FRACTURE MECHANICS

FOURTEENTH SYMPOSIUM

VOLUME I:
Theory and Analysis

Lewis/Sines,
editors

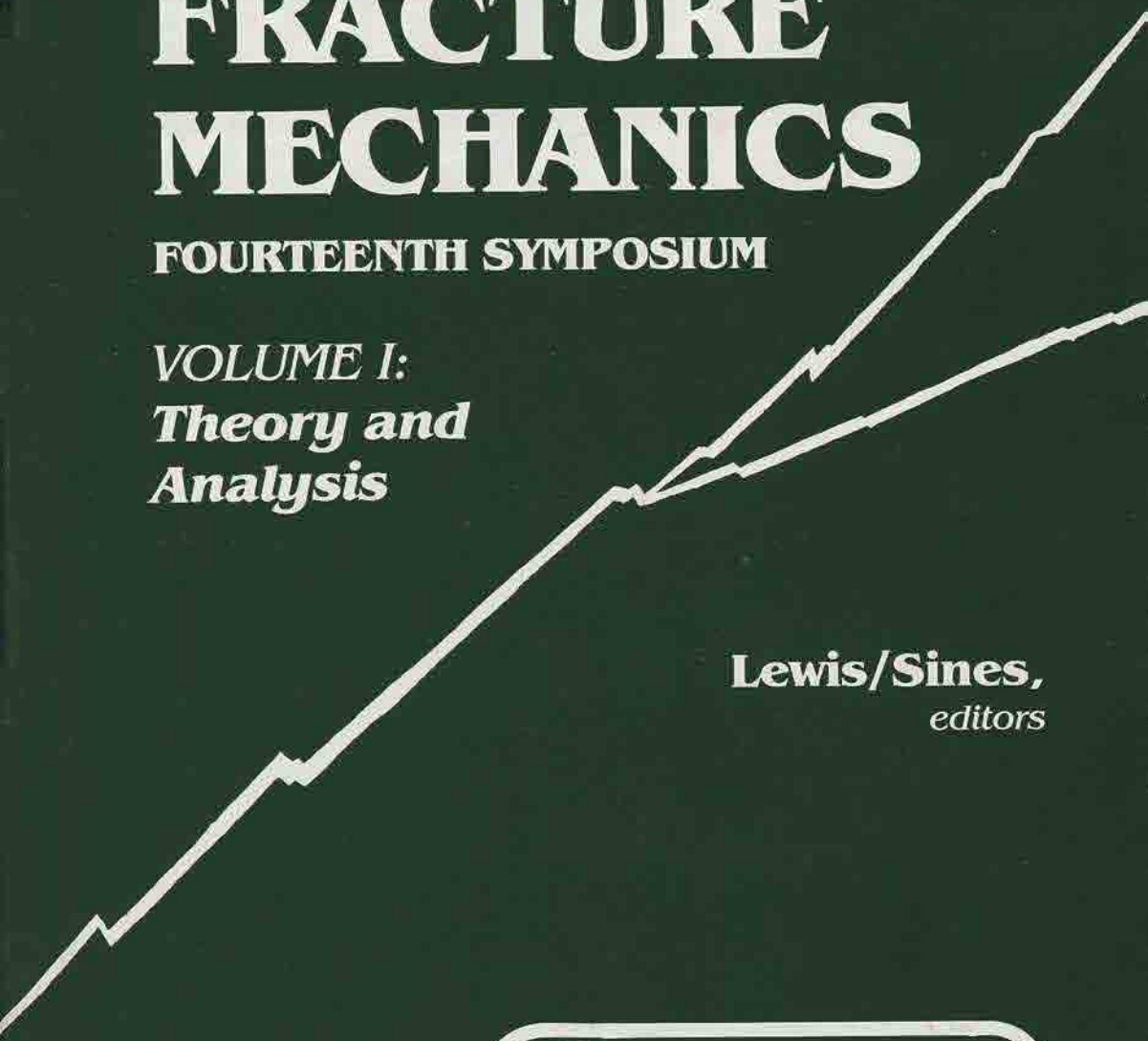

ASTM **STP 791**

FRACTURE MECHANICS: FOURTEENTH SYMPOSIUM—VOLUME I: THEORY AND ANALYSIS

Fourteenth National Symposium on Fracture Mechanics sponsored by ASTM Committee E-24 on Fracture Testing
Los Angeles, Calif., 30 June–2 July 1981

ASTM SPECIAL TECHNICAL PUBLICATION 791
J. C. Lewis, TRW Space and Technology Group, and George Sines, University of California at Los Angeles, editors

ASTM Publication Code Number (PCN)
04-791001-30

1916 Race Street, Philadelphia, Pa. 19103

Library of Congress Catalog Card Number: 82-71747

NOTE

The Society is not responsible, as a body,
for the statements and opinions
advanced in this publication.

Printed in Baltimore, Md. (a)
May 1983

Foreword

The Fourteenth National Symposium on Fracture Mechanics was held in Los Angeles, Calif., 30 June–2 July 1981. ASTM Committee E-24 on Fracture Testing sponsored the symposium. J. C. Lewis, of the TRW Space and Technology Group, and George Sines, of the University of California at Los Angeles, served as symposium chairmen and edited this publication.

Related ASTM Publications

Design of Fatigue and Fracture Resistant Structures, STP 761 (1982), 04-761000-30

Fracture Mechanics for Ceramics, Rocks, and Concrete, STP 745 (1981), 04-745000-30

Fracture Mechanics (Thirteenth Conference), STP 743 (1981), 04-743000-30

Fractography and Materials Science, STP 733 (1981), 04-733000-30

Crack Arrest Methodology and Applications, STP 711 (1980), 04-711000-30

Fracture Mechanics (Twelfth Conference), STP 700 (1980), 04-700000-30

Fracture Mechanics Applied to Brittle Materials (Eleventh Conference), STP 678 (1979), 04-678000-30

Fracture Mechanics (Eleventh Conference), STP 677 (1979), 04-677000-30

A Note of Appreciation to Reviewers

The quality of the papers that appear in this publication reflects not only the obvious efforts of the authors but also the unheralded, though essential, work of the reviewers. On behalf of ASTM we acknowledge with appreciation their dedication to high professional standards and their sacrifice of time and effort.

ASTM Committee on Publications

ASTM Editorial Staff

Janet R. Schroeder
Kathleen A. Greene
Rosemary Horstman
Helen M. Hoersch
Helen P. Mahy
Allan S. Kleinberg
Virginia M. Barishek

Contents

Surface Cracks

Fatigue and Stress Corrosion

SUMMARY

Introduction

In fracture mechanics, as is usually the case in any scientific subject, the increase in literature has been exponential. From the generally accepted beginning in 1913 until the early 1960s, very few papers were written. At about the time of the formation of ASTM Committee E-24 on Fracture Testing of Metals in 1965, publication of information on fracture mechanics began to grow. Committee E-24 and the National Symposia on Fracture Mechanics have played an integral part in this growth.

The decade of the sixties can be characterized as a search for valid test methods and an exploration of fracture theories. The First National Symposium on Fracture Mechanics was held in 1968 at Lehigh University in Bethlehem, Pa.

In the seventies, considerable rethinking and regrouping occurred with the emergence of new concepts such as the R-curve, J-integral, and nonpropagating fatigue crack. During this time, the process was being documented in ASTM Special Technical Publications (STPs) containing the proceedings of the national fracture mechanics symposia for these years.

Currently, we find a more mature fracture mechanics discipline being applied to all aspects of structural integrity. Any failure mechanism in which the final failure occurs by crack growth or in which failure can originate from preexisting cracks is being studied by fracture mechanics disciplinarians. This publication contains papers on such subjects that were presented at the Fourteenth Symposium on Fracture Mechanics, 30 June-2 July 1981, at the University of California at Los Angeles.

Several symposia are held each year on special topics within the fracture mechanics discipline. The organizing committee for this symposium especially wanted it to be open to papers on any fracture subject and, of course, open to papers from other nations. Consequently, this publication represents a broad review of the state of the art of fracture mechanics research worldwide.

Because of the great number of papers received, the proceedings have been divided into two volumes. The papers in the first volume deal primarily with fracture theory and analysis. The second volume contains papers emphasizing testing and applications.

Three special awards were presented at the Fourteenth Symposium. Mr. J. G. Kaufman was awarded Honorary Membership in ASTM; Mr. D. E. McCabe

was presented with the ASTM Award of Merit and honorary title of Fellow; and Dr. J. C. Newman received the George R. Irwin Medal for 1981.

The symposium organizing committee consisted of Mr. W. E. Anderson, Professor B. Gilpin, Professor W. Knauss, Mr. J. C. Lewis, Dr. M. M. Ratwani, Professor G. Sines, Professor R. A. Westmann, and Mr. W. Wilhem. With the exception of Professor Gilpin, each committee member also served as a session chairman. The committee is grateful for the assistance of Professor A. S. Kobayashi, Professor R. P. Wei, and Mr. H. A. Wood who also served as session chairmen. Special thanks are due our banquet speaker, Robert Forgnone, Esq., who spoke on the topic of "Product Liability, or Converting Fracture Mechanics to Dollars."

Finally, the symposium committee wishes to express extra special gratitude to Patricia Schotthoefer of the Special Programs Office of the University Extension for managing all the operational and financial details of the symposium.

J. C. Lewis

Space and Technology Group, TRW, Redondo Beach, Calif. 90278; symposium co-chairman and co-editor.

George Sines

School of Engineering and Applied Science, University of California at Los Angeles, Los Angeles, Calif. 90024; symposium co-chairman and co-editor.

Fracture Theory

R. Chona,[1] *G. R. Irwin,*[1] *and R. J. Sanford*[1]

Influence of Specimen Size and Shape on the Singularity-Dominated Zone

REFERENCE: Chona, R., Irwin, G. R., and Sanford, R. J., **"Influence of Specimen Size and Shape on the Singularity-Dominated Zone,"** *Fracture Mechanics: Fourteenth Symposium—Volume I: Theory and Analysis, ASTM STP 791*, J. C. Lewis and G. Sines, Eds., American Society for Testing and Materials, 1983, pp. I-3-I-23.

ABSTRACT: Improved computational methods have been used to determine, from photoelastic fracture patterns, those stress field parameters (in addition to the stress-intensity factor) that are associated with different fracture test specimen geometries. The variations with crack tip position of these nonsingular terms in modified-compact-tension and rectangular-double-cantilever-beam specimens have been studied. The results have been utilized to formulate criteria that can be used to quantify the concept of the singularity-dominated zone around a crack tip in specimens of finite dimensions.

KEY WORDS: fracture mechanics, photoelastic fracture patterns, stress-intensity factor determination, singularity-dominated zones, generalized Westergaard equations, test specimen geometries, specimen size requirements, nonsingular terms

It is generally recognized that the near-field equations suggested by Irwin [*1*][2] adequately describe the state of stress in the immediate neighborhood of a stationary crack tip, excluding a very small region around the crack tip itself. From a linear elastic viewpoint, all of the stresses in the singularity zone at the crack tip are proportional to the stress-intensity factor, K. Thus, if the crack tip region of interest is small enough, a one-parameter characterization in terms of K is adequate.

Situations arise, however, for which a single-parameter crack tip stress field characterization is not adequate. This can occur due to spreading out of the fracture process zone or a reduction in size of the K-dominated singularity zone at the crack tip. For example, even in a brittle solid, roughening of the fracture due to spreading out of advance cracking and incipient branching can

[1]Instructor, visiting professor, and associate professor, respectively, Department of Mechanical Engineering, University of Maryland, College Park, Md. 20742.

[2]The italic numbers in brackets refer to the list of references appended to this paper.

substantially enlarge the fracture process zone. As a second example, when using isochromatic fringes for the evaluation of K, it is rarely possible to use measurements very close to the crack tip for a number of practical reasons, such as the triaxial nature of the stress field in the immediate neighborhood of the crack tip, light scattering from the dimple (caustic) at the crack tip, crack front curvature, fringe clarity, etc. Thus, the experimental stress analyst frequently is forced to take measurements from regions that border on the validity of the near-field equations. In such cases, it is desirable to define and measure additional stress field parameters.

Considerable work has been done in recent years [*2,3,4*] to investigate the influence of nonsingular terms on the stress field around but not immediately adjacent to the crack tip. The effect of these higher order (that is, nonsingular) terms on the interpretation of fringe patterns obtained from photoelasticity, optical interferometry, and the method of caustics also has been examined [*3,4,5*].

This investigation has been directed towards studying the variations with crack tip position of the nonsingular stress field parameters in commonly used fracture test specimens of two different sizes and geometries. These results then have been utilized to suggest criteria that can be used to quantify the concept of the singularity-dominated zone around a crack tip in specimens of finite dimensions.

Analysis

Stress Field Representation

It has been shown [*4,6*] that the stress state associated with two-dimensional cracks under static opening-mode loading can be described by a generalized form of the Westergaard equations [*7*]. This generalization follows from an Airy stress function of the form

$$F = Re\,\bar{\bar{Z}}(z) + y\,Im\bar{Z}(z) + y\,Im\,\bar{Y}(z) \tag{1}$$

where

$$Z(z) = \frac{d}{dz}\bar{Z}(z) = \frac{d^2}{dz^2}\bar{\bar{Z}}(z) \tag{2}$$

$$Y(z) = \frac{d}{dz}\bar{Y}(z) \tag{3}$$

and

$$z = x + iy \tag{4}$$

It then follows that

$$\sigma_x = Re\,Z - y\,Im\,Z' - y\,Im\,Y' + 2\,Re\,Y \tag{5}$$

$$\sigma_y = Re\,Z + y\,Im\,Z' + y\,Im\,Y' \tag{6}$$

and

$$\tau_{xy} = -y\,Re\,Z' - y\,Re\,Y' - Im\,Y \tag{7}$$

where, for opening mode crack problems, the functions $Z(z)$ and $Y(z)$ are subject to the constraints $Re\ Z(z) = 0$ on the crack faces and $Im\ Y(z) = 0$ along the crack line.

For a single-ended crack, with the origin of coordinates at the crack tip and the negative x-axis coinciding with the crack faces, the functions $Z(z)$ and $Y(z)$ can be represented as

$$Z(z) = \sum_{j=0}^{j=J} A_j z^{j-1/2} \tag{8}$$

and

$$Y(z) = \sum_{m=0}^{m=M} B_m z^m \tag{9}$$

where A_j and B_m are real constants, and the stress-intensity factor, K, is related to A_0, that is, $K = A_0\sqrt{2\pi}$.

Results from specimens which are geometrically similar in their in-plane dimensions can be correlated more easily if Eqs 8 and 9 are rewritten as

$$Z(z) = \frac{K}{\sqrt{2\pi w}}(z/w)^{-1/2} \sum_{j=0}^{j=J} A_j'(z/w)^j \tag{10}$$

and

$$Y(z) = \frac{K}{\sqrt{2\pi w}}(z/w)^{-1/2} \sum_{m=0}^{m=M} B_m'(z/w)^{m+1/2} \tag{11}$$

where A_j' and B_m' are dimensionless real constants ($A_0' \equiv 1$) and w is a characteristic in-plane dimension of the specimen, such as the specimen width.

Determination of the Series Constants from Photoelastic Fracture Patterns

The series representation of the crack tip stress field that is obtained from Eqs 1 to 11 forms the basis for the stress field model used in this study. By combining the governing optical equations for isochromatic fringe patterns with this series representation [*4*], the analysis of isochromatic patterns reduces to the problem of determining the coefficients of the two series $Z(z)$ and $Y(z)$ that produce the best match to the experimental pattern, over the region selected for data acquisition. To determine these coefficients, a procedure based on the least-squares method has been developed [*8,9*].

This procedure can be summarized briefly as follows. A data acquisition

region is selected for a given experimental pattern using the guidelines suggested in Ref *4*. Data points are taken over the entire region in a distributed fashion, and this data set is input to the least-squares algorithm (details of which can be found in Refs *4, 8,* and *9*) to obtain a best-fit set of coefficients. The number of coefficients necessary for an adequate representation of the stress field over the data acquisition region can be estimated by examining, as a function of the number of coefficients, the value of the average fringe order error, $\overline{|\Delta n|}$, which is defined in this study as

$$\overline{|\Delta n|} = \frac{1}{N} \sum_{k=1}^{k=N} |n_i - n_c|_k \tag{12}$$

where n_i is the specified (input) fringe order for a given data point, n_c is the fringe order (at the same point) calculated from the computed set of coefficients, and N is the total number of data points being used. The computed set of best-fit coefficients then can be used to reconstruct an isochromatic fringe pattern which, when compared with the experimental fringe pattern being analyzed, serves as a visual check on the adequacy of the assumed model.

Figure 1 shows an example consisting of the experimental fringe pattern, the data set selected therefrom, and the reconstructed pattern. In this case, the data points have been taken over a region of radius $0.125w$, centered at the crack tip, which is located at $a/w = 0.80$ in a modified-compact-tension specimen. The reconstructed pattern is based upon a six-parameter stress field representation, and can be seen to match the salient features of the experimental pattern over the sampled region around the crack tip.

Previous work by the authors has shown that it is occasionally possible to obtain a best-fit set of coefficients (in a least-squares sense) that is not in fact the correct solution for the fringe pattern being analyzed [*10*]. In those cases, it is advisable to use a sampled least-squares method for analysis of the data,

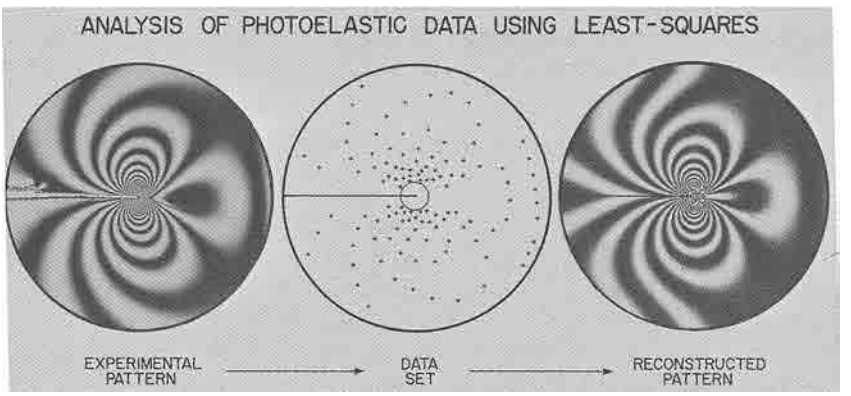

FIG. 1—*An example showing the application of the least-squares method to the analysis of photoelastic fracture patterns.*

and details of this extension of the least-squares method can be found in Refs *10* and *11*. The results reported here were obtained by using the least-squares method to analyze a data set which normally consisted of 120 data points from the selected data acquisition region, with recourse to the sampled least-squares method whenever necessary.

Nonsingular Term Variation in Modified-Compact-Tension and Rectangular-Double-Cantilever-Beam Specimens

Modified-compact-tension (MCT) and rectangular-double-cantilever-beam (RDCB) specimens with the geometry and loading shown in Figs. 2 and 3 were used for this study. The modified-compact-tension specimen is one of the crack-arrest specimens being considered as an ASTM standard [*12*] at the present time, and both MCT and RDCB specimens have been used extensively for fracture testing in previous studies of crack propagation and arrest behaviors [*13-17*].

Saw-cut cracks were extended systematically into the specimen and the photoelastic fringe pattern under static loading recorded at each crack length. The changes in the isochromatic fringe pattern that occur as the crack is ex-

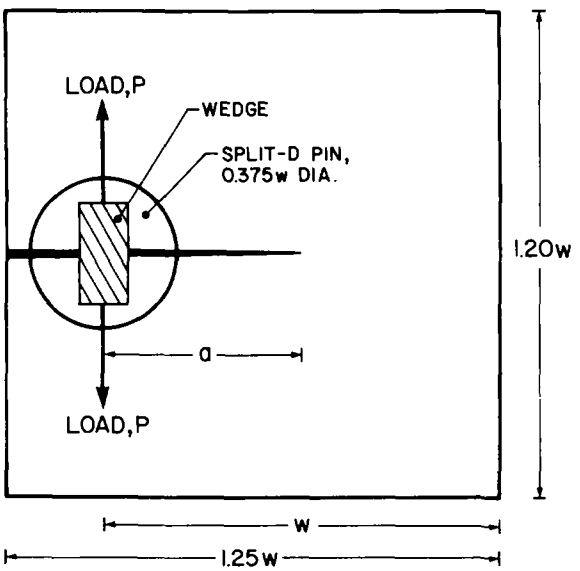

W_s = 4.0 inches = 102 mm

W_L = 8.0 inches = 203 mm

FIG. 2—*The geometry and loading of the MCT specimen used in this study.*

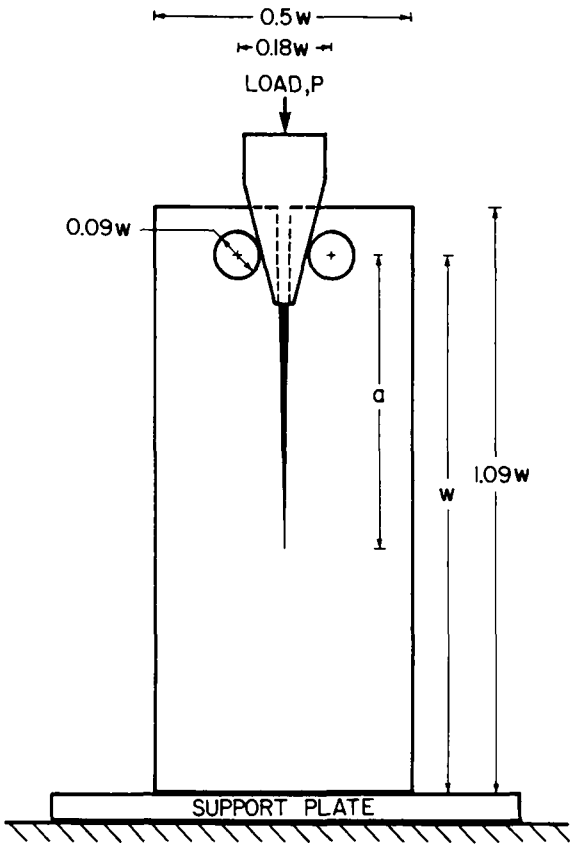

FIG. 3—*The geometry and loading of the RDCB specimen used in this study.*

tended in an MCT specimen are shown in Fig. 4, while Fig. 5 shows the corresponding behavior observed in an RDCB specimen.

These fringe patterns were analyzed, using the least-squares method as previously described, to obtain the first eight coefficients (A_0' to A_3' and B_0' to B_3') of the series stress field representation of Eqs 10 and 11. A total of 120 data points were taken from each fringe pattern recorded, with the data acquisition region having a radius of $0.125w$ in the MCT specimen, and a radius of $0.091w$ in the RDCB specimen. The data acquisition regions used in each case are shown in Figs. 4 and 5 as solid circles.

The changes in the average fringe order error that occur as the number of parameters used is increased from two to eight were examined for each crack length used in the MCT and RDCB specimens. In each case, the error term stabilized by the time the eighth coefficient was introduced, indicating that the stress state had been modelled adequately over the data acquisition region used. Only the first six coefficients from an eight-coefficient, best-fit so-

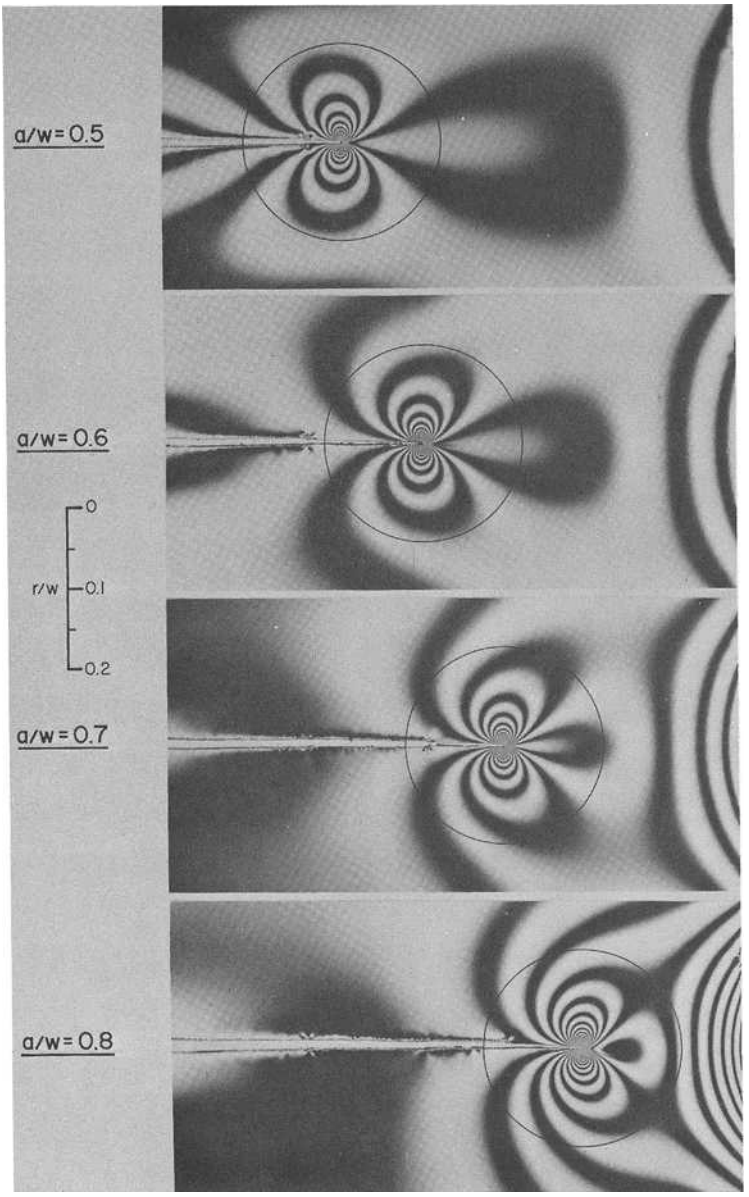

FIG. 4—*Isochromatic fringe pattern variations with crack extension observed in an MCT specimen.*

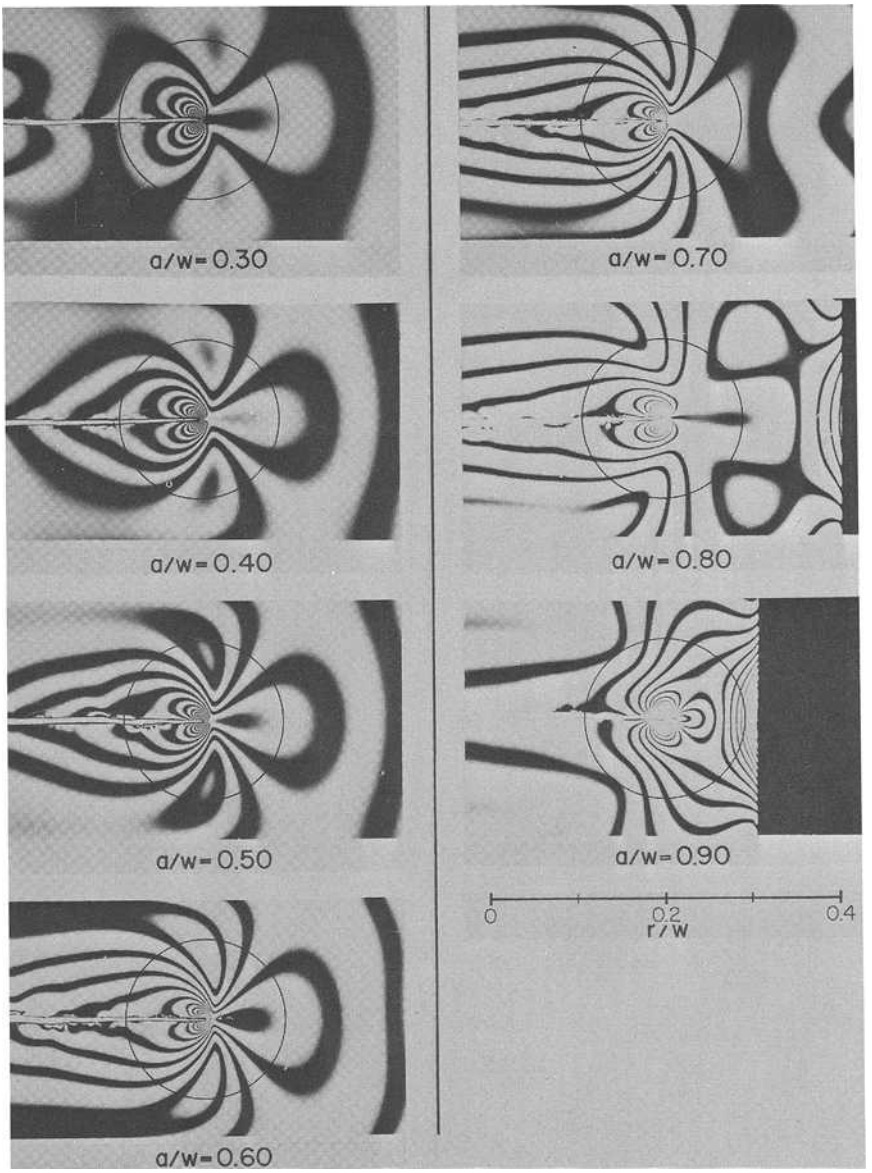

FIG. 5—*Isochromatic fringe pattern variations with crack extension observed in an RDCB specimen.*

lution were used in the subsequent parts of this study, since the last two terms have only a small contribution to the stress field over the data acquisition region used.

The variation with crack tip position, a/w, of the first six normalized coefficients for the MCT and RDCB specimens is shown in Figs. 6 and 7, respectively. The results in both cases show the strong influence of the approaching normal boundary that is manifested in the dramatic increase in the magnitude of the nonsingular terms beyond $a/w = 0.70$. The continuous variation displayed by the nonsingular coefficients in both specimens is consistent with the isochromatic fringe patterns recorded and shown in Figs. 4 and 5. Note that the normalized coefficients for the MCT specimen (Fig. 6) were obtained from specimens of two different sizes [SMCT, $w_S = 102$ mm (4.0 in.); LMCT, $w_L = 203$ mm (8.0 in.)] that were studied to verify experimentally the specimen-size independent form of the stress functions, $Z(z)$ and $Y(z)$, given in Eqs 10 and 11.

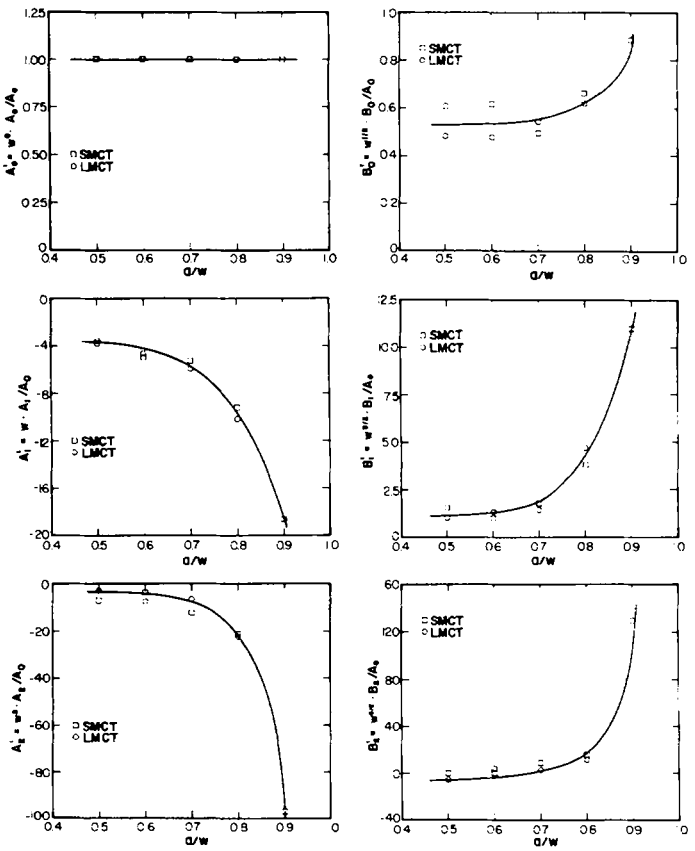

FIG. 6—*The variations with crack tip position of the first six coefficients of the series representation of the stress field as obtained from two different sizes of the MCT specimen.*

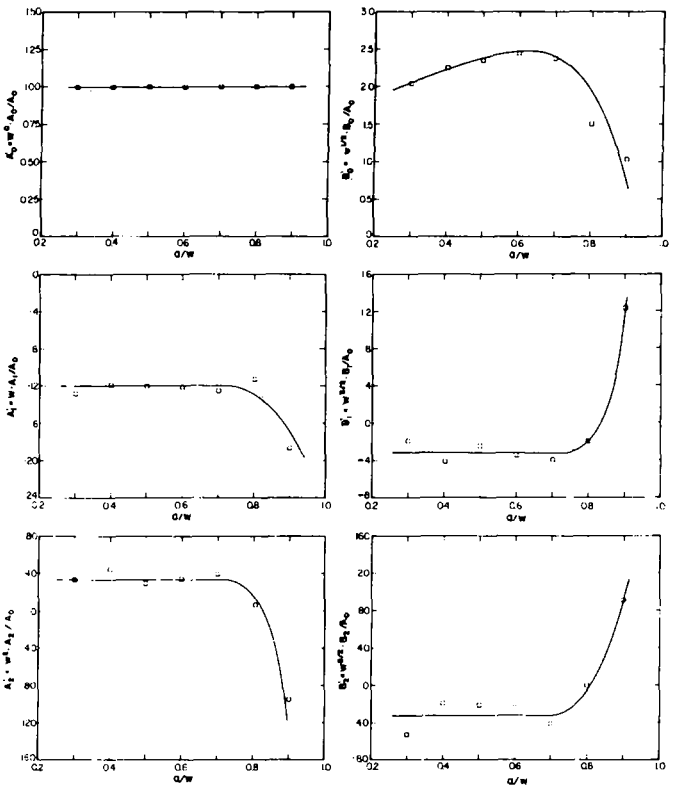

FIG. 7—*The variations with crack tip position of the first six coefficients of the series representation of the stress field as obtained from the RDCB specimen.*

The behavior of the coefficients A_1', B_1', A_2', and B_2' for the RDCB specimen is particularly interesting. The values remain essentially constant from $a/w = 0.30$ to $a/w = 0.70$, after which they begin to change dramatically. Over this span, the boundary of the specimen that is closest to the crack tip is the boundary parallel to the crack line. However, beyond $a/w = 0.75$, the normal boundary becomes the dominant (and the closest) one, and for a very deep crack, $a/w = 0.90$ for example, the nonsingular terms computed for the RDCB specimen approach the values obtained for the MCT specimen in both magnitude and sign. Indications of this also can be obtained from a careful examination of the fringe patterns for deep cracks in the RDCB specimen, which show features similar to those observed for long cracks in the MCT specimen.

Characterization of the Singularity-Dominated Zone in Different Fracture Test Specimens

Within the limits of a singularity-dominated zone, the influence of the singular term should be large relative to the influence of higher-order terms with

regard to both stress magnitude and control of the direction of cracking. The results obtained for the series representation of the stress field in MCT and RDCB specimens were used to develop criteria that are helpful in quantifying the size of the zone within which the $1/\sqrt{r}$-term adequately describes the stress magnitude. In a discussion published in 1967, Wilson [*18*] reported that boundary collocation calculations indicate that the size of this zone is rather small, and the results obtained in this study confirm this observation.

The six-parameter representation of the stress field at different crack lengths in the two specimens was compared to the single-parameter representation ($A_0{}' = 1$, all other coefficients zero) using several different measures such as the Cartesian stress components, the magnitudes and directions of the principal stresses, and the sum and difference of the principal stresses. Regions over which the six-parameter and singular representations differed by less than 2 percent then were constructed and examined to see if they defined a closed region around the crack tip which would serve to define the singularity-dominated zone around the crack tip.

Figure 8 shows, by way of example, the regions around the crack tip at $a/w = 0.60$ in an MCT specimen, for which the six-parameter and singular solutions for σ_x, σ_y, and τ_{xy} differ by less than 2 percent. The use of τ_{xy} as a singularity-dominated zone size criterion has an inherent disadvantage in that, the singular solution always predicts the absence of τ_{xy} along the line $\theta = \pm 60$ deg, thus making the deviation equal to 100 percent along that line, as is apparent from the figure. The difficulties associated with the use of σ_x are not quite so obvious, but become clearer when Fig. 9 is examined.

This figure demonstrates the strong influence of the constant stress term, $B_0{}'$, on the zone size obtained from σ_x, by comparing, at the same crack tip location as in Fig. 8, the zones obtained from (*a*) a 2 percent difference between six-parameter and one-parameter representations, and (*b*) a 2 percent difference between six-parameter and two-parameter representations. Similar behavior also was observed at other crack lengths in the two specimens, and this is illustrated in Fig. 10, in which $B_0{}'$ from MCT and RDCB specimens is plotted as a function of a/w. The same figure also shows the minimum radius, $r_{\min}/w$, of a 2 percent zone based upon σ_x, and the results confirm the unsuitability of σ_x for use as a sole criterion. For example, as the crack approaches the boundary of an RDCB specimen, $B_0{}'$ falls off rapidly due to relaxation, and the zone actually increases substantially in size. This would imply that at $a/w = 0.90$ in an RDCB specimen, the singularity-dominated zone is approximately three times as large as it is at $a/w = 0.50$ in the same specimen.

The strong influence of the $B_0{}'$-term on near-crack-tip behavior is well known [*19,20*] and the results discussed here are another illustration of the importance of this first nonsingular term of the crack-tip stress field. For instance, finite element computations by Larsson and Carlsson [*21*] have shown that, at $a/w = 0.50$ in an MCT specimen of *nearly* similar geometry, the constant-stress term plays a significant role in determining the extent of

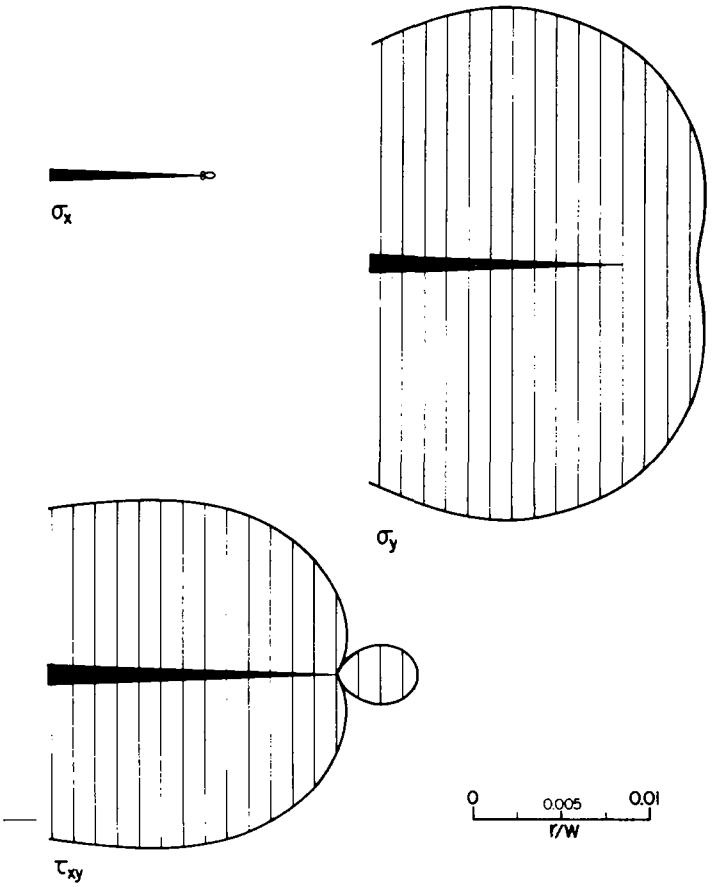

FIG. 8—*Regions surrounding the crack tip at* a/w = *0.60 in an MCT specimen in which the six-parameter and singular representations for the Cartesian stress components differ by less than 2 percent.*

the plastic zone around the crack tip. (Their reported value of $B_0' = 0.52$ agrees well with the results obtained in this study.)

The conclusion drawn from this investigation is that, among the possible criteria for a singularity-dominated zone which are both simple and plausible, the deviation in magnitude of the crack opening stress, σ_y, seems an optimum choice. The zone based upon this criterion is shown in Figs. 11 and 12 for several different crack lengths in the MCT and RDCB specimens, respectively. Note that the two figures are *not* shown to the same scale. Both 2 and 5 percent zones have been shown, and while the former is perhaps better as a mathematical measure, the latter comes closer to engineering standards for acceptable errors. Variations in the shape of the zone behind the crack tip are not important, and this region of the zone has been shown only for completeness.

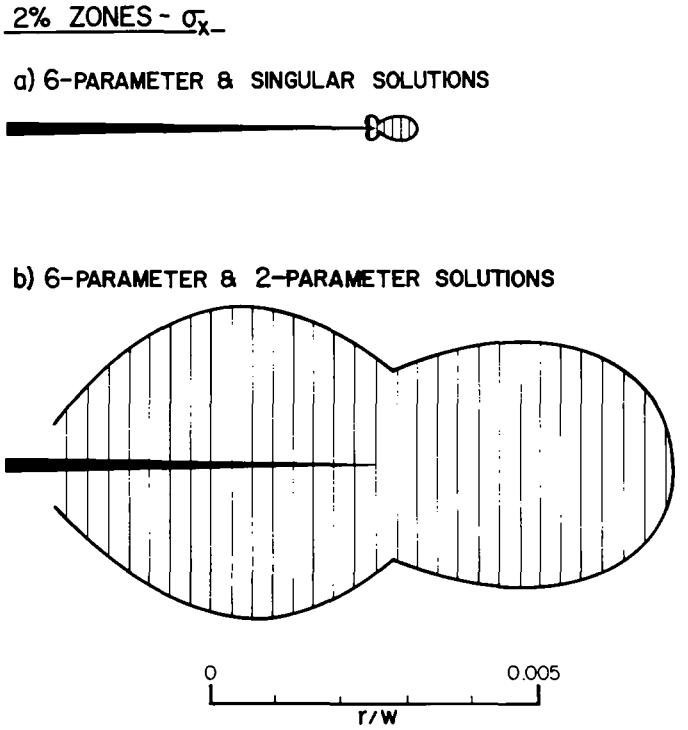

FIG. 9—*Zones of 2 percent difference in* (a) *six-parameter and singular representations, and* (b) *six-parameter and two-parameter representations for* σ_x *for* a/w = *0.60 in an MCT specimen.*

It is observed that the zone is a minimum along $\theta = 0$ deg in both specimens, and it is covenient to define this distance, r_{min}/w, as the singularity-dominated zone size. The behavior of the 2 and 5 percent error zones is approximately linear in their respective values of r_{min}/w, and the subsequent discussion will use only results from the 2 percent zones.

Figure 13 shows the behavior of the quantity r_{min}/w from a 2 percent error zone in σ_y as a function of a/w in the MCT and RDCB specimens. The zone size decreases monotonically with crack length in the MCT specimen, but it remains constant over a large range of crack lengths in the RDCB specimen, before starting to decrease rapidly, and it finally approaches the behavior of the MCT geometry. This behavior is consistent with both the nonsingular term variation and the recorded fringe patterns shown earlier. Over a large part of the useful range of the specimens, the zone size in an MCT specimen is substantially larger than the zone size at the same a/w in an RDCB specimen of the same width, and this may be of importance in making selections of a suitable specimen geometry for testing purposes.

It is even more interesting to examine the behavior of the singularity-

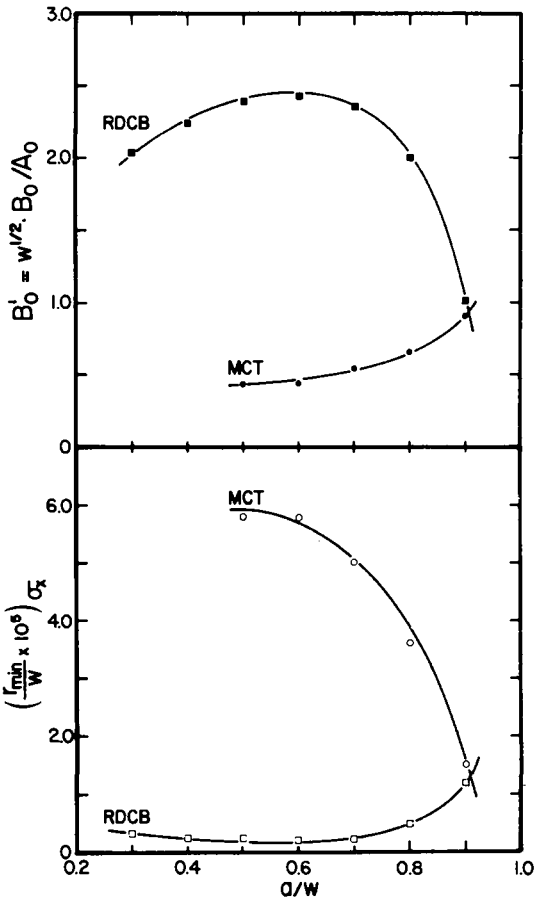

FIG. 10—*The influence of* B_0' *on the singularity-dominated zone size predicted by the use of* σ_x *as a sole criterion.*

dominated zone size as a function of the remaining net ligament, $(w - a)$, and the distance to the nearest boundary, R_{min}. In the MCT specimen

$$R_{min} = \begin{cases} 0.60w, & a/w \leq 0.40 \\ w - a, & a/w \geq 0.40 \end{cases} \tag{13}$$

whereas in the RDCB specimen

$$R_{min} = \begin{cases} 0.25w, & a/w \leq 0.75 \\ w - a, & a/w \geq 0.75 \end{cases} \tag{14}$$

Figure 14 shows, as functions of a/w, r_{min}/R_{min} for the RDCB specimen and $r_{min}/(w - a)$ for the MCT and RDCB specimens. (Note that over the range studied, $r_{min}/(w - a)$ is the same as r_{min}/R_{min} for the MCT specimen.)

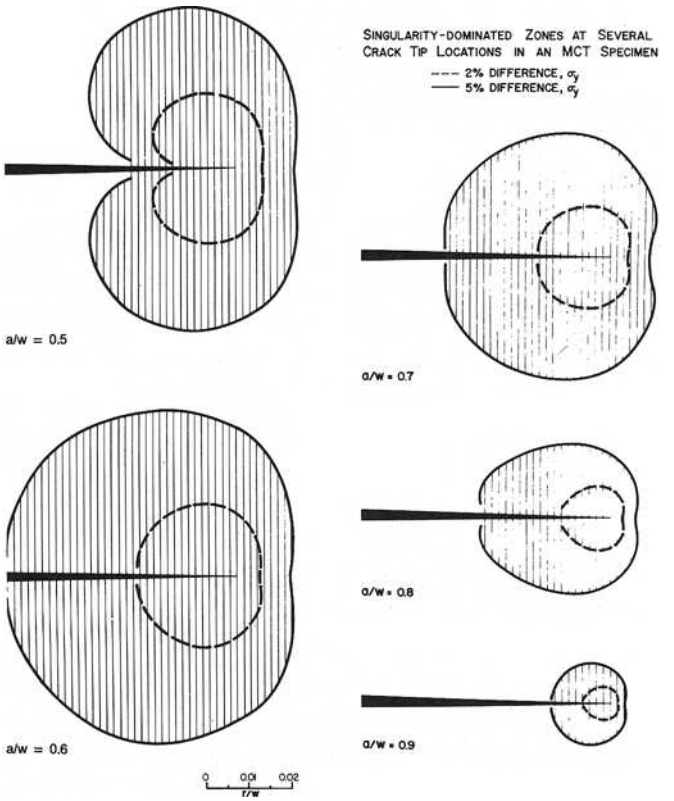

FIG. 11—*The variation with* a/w *in an MCT specimen of the zone surrounding the crack tip in which six-parameter and singular representations for* σ_y *differ by 2 percent (dashed line) and 5 percent (solid line).*

In the case of the MCT specimen, r_{min} is observed to be a constant percentage of the net remaining ligament, with the 2 percent zone having a value of r_{min} equal to 1 percent of $(w - a)$. For the RDCB specimen, the behavior of $r_{min}/(w - a)$ is rather different. The quantity r_{min}/R_{min} is much easier to interpret. Over the range of crack lengths from $a/w = 0.30$ to $a/w = 0.70$, the closest specimen boundary is parallel to the crack line in the RDCB specimen, and hence R_{min} is constant. Consequently, r_{min}/R_{min} remains a constant. At and beyond $a/w = 0.75$, the normal boundary is closest to the crack tip and begins to control the behavior or r_{min}/R_{min}. Beyond $a/w = 0.90$, the approaching normal boundary controls the stress field to such an extent that the behavior of both MCT and RDCB specimens is essentially the same. Indications of this also were obtained from the variation of the nonsingular terms with a/w in the two specimens and from the isochromatic fringe patterns, as noted earlier.

Using a zone size criterion based upon the normal stress, σ_y, the singularity-dominated zone size at the crack tip, for the geometries studied, thus is

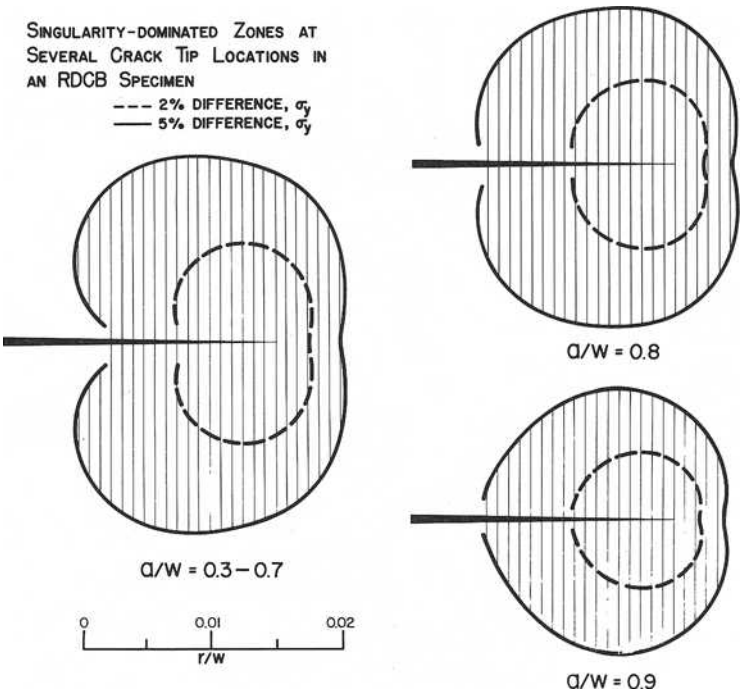

FIG. 12—*The variation with* a/w *in an RDCB specimen of the zone surrounding the crack tip in which six-parameter and singular representations for* σ_y *differ by 2 percent (dashed line) and 5 percent (solid line).*

perceived to be linked closely to the distance from the crack tip to the nearest specimen boundary. It is in fact a constant percentage of this distance, with a transition when the closest boundary shifts from parallel to the crack line to that normal to the direction of crack extension.

Specimen Size Requirements Relative to the Singularity-Dominated Zone Size in Different Fracture Test Specimens

There are certain assumptions inherent in the application of linear-elastic fracture mechanics to engineering materials and practical (finite) specimen types. The usefulness of the results obtained from laboratory testing for initiation and arrest toughnesses, K_c and K_a, depends on the accuracy with which K_c and K_a describe the fracture behavior of real materials, and this, in turn, depends on how well the stress-intensity factor represents the conditions of stress and strain inside the fracture process zone. In this sense, K gives an exact representation only in the limit of zero plastic strain. However, for many practical purposes, a sufficient degree of accuracy may be obtained if the crack front plastic zone is small in comparison with the zone around the crack tip in

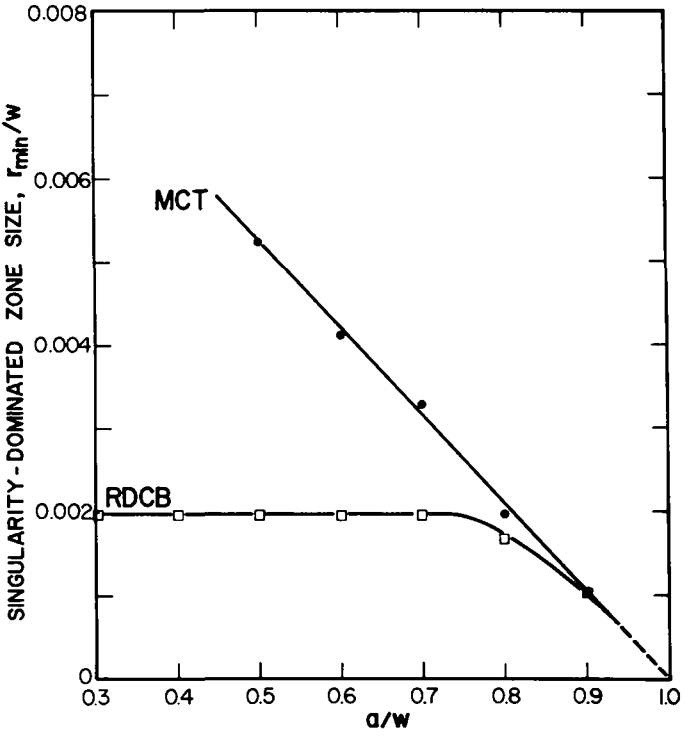

FIG. 13—*The variation with a/w of the singularity-dominated zone size obtained from the use of a 2 percent difference in six-parameter and singular representations for σ_y in MCT and RDCB specimens.*

which the stress-intensity factor yields a satisfactory approximation of the exact elastic stress field in a fracture test specimen [*18,22,23*].

In the past, specimen size requirements relative to enclosure of the fracture process zone by the K-dominated region of the elastic stress field have received only rough estimate treatment. The results presented here represent a preliminary effort towards putting these requirements on a firmer, quantitative footing. For example, ASTM Test for Plane-Strain Fracture Toughness of Metallic Materials (E 399-81) specifies requirements for specimen thickness, B, crack size, a, and net ligament, $(w - a)$, as two and one-half times $(K/\sigma_{YS})^2$, where σ_{YS} is the 0.2 percent offset yield strength obtained by standard testing. These requirements are based upon a plastic zone adjustment factor, r_Y, which is generally accepted in accordance with ASTM Method E 399-81 and ASTM Recommended Practice for R-Curve Determination (E 561-80) [*18,23*] as being characteristic of the plastic strain region around the crack tip. The defining equation for r_Y is

$$r_Y = \frac{1}{2\pi}(K/\sigma_Y)^2 \tag{15}$$

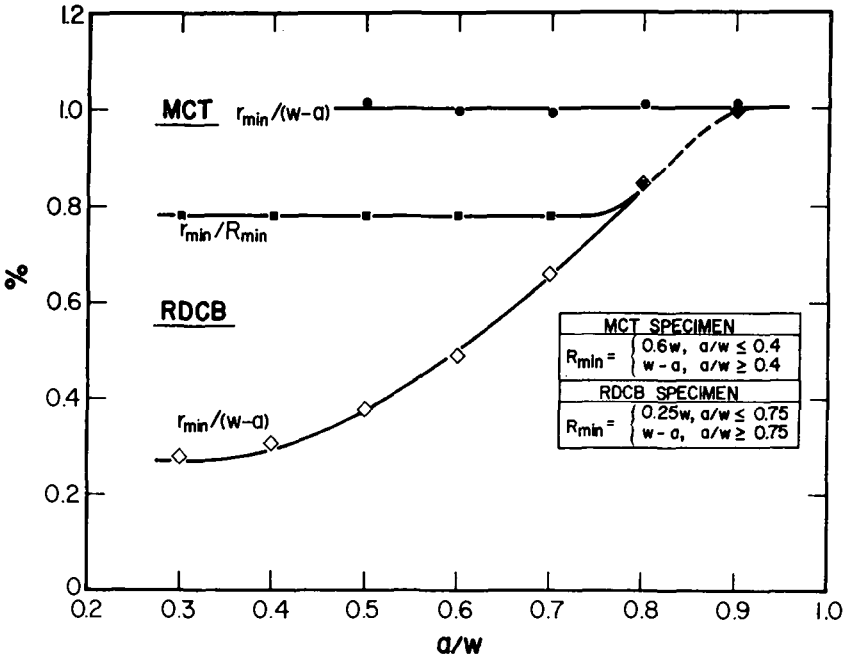

FIG. 14—*The relation between the singularity-dominated zone size in MCT and RDCB specimens and the distance from the crack tip to the boundaries of the specimen.*

where σ_Y is a tensile estimate of the resistance to plastic yielding near the crack tip.

It is useful to compare the plasticity crack size adjustment, r_Y, with the singularity zone size, r_{min}. For conditions of plane strain, $\sigma_Y = 2\sigma_{YS}$ is a reasonable choice, and

$$r_Y = \frac{1}{8\pi}(K/\sigma_{YS})^2 \tag{16}$$

Thus, for an MCT specimen which meets the ASTM Method E 399-81 requirements for in-plane specimen dimensions

$$\frac{r_Y}{w} = \frac{1}{40\pi} = 0.008 \tag{17}$$

The results obtained in this study for r_{min}/w in an MCT specimen, at $a/w = 0.50$, indicate that using a 5 percent deviation in σ_y

$$r_{min}/w = 0.013 \tag{18}$$

Thus, for a given w, the r_Y allowed by ASTM Method E 399-81 size requirements is well within the singularity-dominated region characterized by r_{min}, as illustrated in Fig. 15.

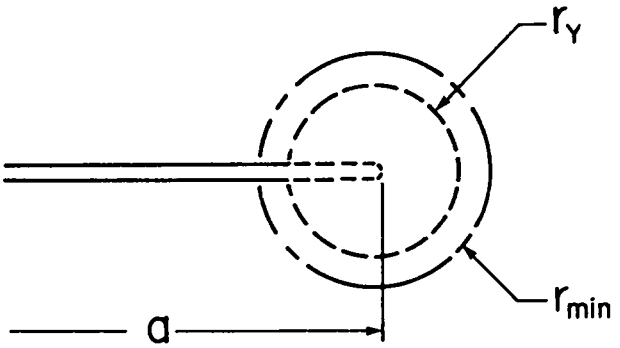

FIG. 15—*The relative sizes of* r_Y *and* r_{min} *for* a/w = 0.50 *in an MCT specimen.*

In the case of an RDCB specimen, r_{min}/w has been shown to be 0.005 over the range $a/w = 0.30$ to $a/w = 0.70$. For r_Y to be just less than r_{min} would require that $w \geq 8\,(K/\sigma_{YS})^2$, where r_Y is defined by Eq 16. The use of an RDCB specimen, therefore, would mean using substantially more material than required for an MCT specimen satisfying the same conditions.

From these comparisons, it is suggested that a relatively simple size requirement for in-plane specimen dimensions can be established, using the singularity zone size, r_{min}. Adequate enclosure of the crack tip plastic zone then can be achieved by adjusting the specimen dimensions such that r_Y is moderately less than r_{min}, the singularity zone size based upon a 5 percent deviation of σ_Y.

Conclusions

The results from this study lead to the following conclusions.

1. The nonsingular terms in the series representation of the stress field can be defined in a specimen-size independent form.
2. For a given specimen geometry, the nonsingular terms display a systematic variation with crack length.

In addition, using the magnitude of σ_y to characterize the singularity-dominated zone size, as suggested here, the following conclusions can be reached.

3. There are significant differences in the size of the singularity-dominated zone between various fracture test specimens.
4. Within any one specimen type, the size of the singularity-dominated zone varies with crack length.
5. The absolute size of the singularity-dominated zone is specimen-size dependent.
6. For the geometries studied, the size of the singularity-dominated zone is a constant percentage of the distance from the crack tip to the nearest specimen boundary, with a transition when the closest boundary shifts from parallel to the crack line to that normal to the direction of crack extension.

7. The singularity-dominated zone size can be used to establish in-plane specimen size requirements for fracture toughness testing consistent with a requirement for the plastic strain region to be within the K-dominated region of the elastic stress field.

Acknowledgments

The authors would like to express their appreciation for the support received from the U.S. Nuclear Regulatory Commission and Oak Ridge National Laboratory through subcontract No. 7778 to the University of Maryland.

The computer time and facilities required were provided by the Computer Science Center at the University of Maryland.

References

[1] Irwin, G. R., *Proceedings of the Society for Experimental Stress Analysis*, Vol. 16, 1958, pp. 93-96.

[2] Etheridge, J. M. and Dally, J. W., *Experimental Mechanics*, Vol. 17, 1977, pp. 248-254.

[3] Rossmanith, H. P. and Irwin, G. R., "Analysis of Dynamic Isochromatic Crack-Tip Stress Patterns," University of Maryland Department of Mechanical Engineering Report, July 1979.

[4] Irwin, G. R. et al, "Photoelastic Studies of Damping, Crack Propagation, and Crack Arrest in Polymers and 4340 Steel," NUREG/CR-1455, University of Maryland, May 1980.

[5] Phillips, J. W. and Sanford, R. J. in *Fracture Mechanics (Thirteenth Conference), ASTM STP 743*, American Society for Testing and Materials, 1981, pp. 387-402.

[6] Sanford, R. J., Mechanics Research Communications, Vol. 6, 1979, pp. 289-294.

[7] Westergaard, H. M., *Transactions*, American Society of Mechanical Engineers, Vol. 61, 1939, pp. A49-A53.

[8] Sanford, R. J. and Dally, J. W., *Engineering Fracture Mechanics*, Vol. 11, 1979, pp. 621-633.

[9] Sanford, R. J., *Experimental Mechanics*, Vol. 20, 1980, pp. 192-197.

[10] Sanford, R. J., Chona, R., Fourney, W. L., and Irwin, G. R., "A Photoelastic Study of the Influence of Non-Singular Stresses in Fracture Test Specimens," NUREG/CR-2179 (ORNL/Sub-7778/2), University of Maryland, Aug. 1981.

[11] Sanford, R. J. and Chona, R. in *Proceedings of the Society of Experimental Stress Analysis Annual Spring Meeting*, Dearborn, Mich., May 1981, pp. 273-276.

[12] ASTM Committee E24.03.04, *Prospectus for a Cooperative Test Program on Crack Arrest Toughness Measurements*, American Society for Testing and Materials, 1977.

[13] Irwin, G. R. et al, "Photoelastic Studies of Crack Propagation and Crack Arrest, NUREG-0342, University of Maryland, Oct. 1977.

[14] Hoagland, R. G. et al in *Fast Fracture and Crack Arrest, ASTM STP 627*, American Society for Testing and Materials, 1977, pp. 177-202.

[15] Hahn, G. T. et al, "Critical Experiments, Measurements, and Analyses to Establish a Crack Arrest Methodology for Nuclear Pressure Vessel Steels," NUREG/CR-0824 BMI-2026, Dec. 1978.

[16] Kalthoff, J. F., Beinert, J., Winkler, S., and Klemm, W. in *Crack Arrest Methodology and Applications, ASTM STP 711*, 1980, pp. 109-127.

[17] Beinert, J. and Kalthoff, J. F., "Experimental Determination of Dynamic Stress Intensity Factors by the Method of Shadow Patterns," *Mechanics of Fracture VII*, Noordhoff International, 1980.

[18] *Plane Strain Crack Toughness Testing of High-Strength Metallic Materials, ASTM STP 410*, W. F. Brown, Jr. and J. E. Srawley, Eds., American Society for Testing and Materials, 1966.

[19] Eftis, J., Subramonian, N., and Liebowitz, H., *Engineering Fracture Mechanics*, Vol. 9, 1977, pp. 189–210.
[20] Liebowitz, H., Lee, J. D., and Eftis, J., *Engineering Fracture Mechanics*, Vol. 10, 1978, pp. 315–335.
[21] Larsson, S. G. and Carlsson, A. J., *Journal of the Mechanics and Physics of Solids*, Vol. 21, 1973, pp. 263–277.
[22] Liu, H. W. in *Fracture Toughness and Its Applications, ASTM STP 381*, American Society for Testing and Materials, 1965, pp. 23–26.
[23] *Review of Developments in Plane Strain Fracture Toughness Testing, ASTM STP 463*, W. F. Brown, Jr., Ed., American Society for Testing and Materials, 1970.

Roland de Wit[1]

A Review of Generalized Failure Criteria Based on the Plastic Yield Strip Model

REFERENCE: de Wit, Roland, **"A Review of Generalized Failure Criteria Based on the Plastic Yield Strip Model,"** *Fracture Mechanics: Fourteenth Symposium—Volume I: Theory and Analysis, ASTM STP 791*, J. C. Lewis and G. Sines, Eds., American Society for Testing and Materials, 1983, pp. I-24–I-50.

ABSTRACT: A review is given of the failure criteria developed by Hahn and Sarrate for through-cracked pressure vessels, whereby they established three failure categories. This work was based on the Dugdale and Bilby-Cottrell-Swinden (D-BCS) model for the crack-tip opening displacement (CTOD) in an infinite plate. The model was extended in an approximate way by Heald-Spink-Worthington (D-BCS-HSW) to finite geometries and structures by combining the effects of plasticity and geometry as multiplicative factors. In this paper the criteria of Hahn and Sarrate are extended to the D-BCS-HSW model. The three failure categories are relabelled: (1) linear-elastic fracture mechanics (LEFM), (2) elastic-plastic fracture mechanics (EPFM), and (3) plastic collapse (PC). The model is plotted in a variety of dimensionless forms and several related developments also are reviewed: (1) the two-criteria approach and universal failure curve, (2) the CTOD design curve, and (3) the Failure Assessment Diagram. Finally, the residual strength diagram for the D-BCS-HSW model is presented. In all these presentations the three failure categories based on Hahn and Sarrate's criteria are included. Thus, it is shown that the D-BCS-HSW model, though approximate, presents a unified picture that embodies many features of fracture mechanics from LEFM through EPFM to PC.

KEY WORDS: collapse, crack opening displacement, cracks, defects, failure, fracture mechanics, plasticity, strength, stress, toughness

Nomenclature

A Area
a Crack size
$\bar{a}$ Equivalent crack size
a_e Effective crack size, $a + r_Y$

[1]National Bureau of Standards, Fracture and Deformation Division, Washington, D.C. 20234.

a_2 Normalized crack size, $(FN\sigma_0/K_R)^2\pi a$
COD Crack opening displacement
CTOD Crack-tip opening displacement
D-BCS Dugdale-Bilby-Cottrell-Swinden
D-BCS-HSW Dugdale-Bilby-Cottrell-Swinden-Heald-Spink-Worthington
E Young's modulus
EPFM Elastic-plastic fracture mechanics
F Geometric factor in stress-intensity factor
FAD Failure assessment diagram
K Stress-intensity factor
K_e Effective stress-intensity factor
K_R Crack-extension resistance or fracture toughness
K_r Risk of failure by linear-elastic fracture mechanics, K/K_R
K_1 Normalized fracture toughness, $(K_R/\sigma_0)/(\pi a)^{1/2}$
K_2 Normalized fracture toughness, $(K_R/FN\sigma_0)/(\pi a)^{1/2}$
L Plastic constraint factor
LEFM Linear-elastic fracture mechanics
L_f Applied failure parameter
L_k Failure parameter by LEFM
L_u Failure parameter by plastic collapse
M Plastic correction factor in K_e
N Geometric factor for nominal stress
PC Plastic collapse
r_Y Plastic-zone adjustment
S_r Risk of failure by plastic collapse, σ/σ_L
W Width
δ CTOD
σ Applied stress or failure stress
σ_L Limit stress at plastic collapse
σ_N Nominal stress
σ_Y Yield stress
σ_0 Flow stress
σ_1 Normalized applied stress, σ/σ_0
σ_2 Normalized nominal stress, σ_N/σ_0

At the Symposium on Fracture Toughness Concepts for Weldable Structural Steel Hahn and Sarrate [*1*][2] established failure criteria for through-cracked vessels. These criteria offered a unified picture of various viewpoints presented at the conference: linear-elastic fracture mechanics (LEFM), plasticity-corrected fracture toughness, and the flow stress criterion. Their work was based on the plastic yield strip model of Dugdale [*2*] as elaborated by Bilby, Cottrell, and Swinden [*3*] for the crack-tip opening displacement

[2]The italic numbers in brackets refer to the list of references appended to this paper.

(CTOD) in an infinite plate (D-BCS model). The viewpoints were fitted into a common framework consisting of three failure categories: (1) linear-elastic behavior, (2) nonlinear elastic behavior, and (3) plastic instability behavior. They established criteria for the dividing line between these failure categories. These criteria were given in terms of the toughness, flow strength, and crack size. The effect of geometry and size of the structure was not taken into account.

Heald, Spink, and Worthington [*4*] extended the D-BCS model to more complicated and finite geometries by introducing a correction factor based on LEFM. They represented the CTOD as the product of two functions, one related to the plasticity of the material and the other to the geometry of the structure, in such a way that for a small crack the correct D-BCS model results, and for a small stress the correct LEFM result is obtained. We have called it the D-BCS-HSW model.

In this paper we have reformulated Hahn and Sarrate's failure criteria in terms of the stress, so that they also can be applied to the case of the finite geometry and size represented by the D-BCS-HSW model. In order to conform better to current usage we have relabelled their three categories: (1) LEFM, (2) elastic-plastic fracture mechanics (EPFM), and (3) plastic collapse (PC). In the Infinite Plate section, we review fracture mechanics for a central crack in an infinite plate and show how Hahn and Sarrate specifically formulated their failure criteria.

In the section on Finite Geometry, we then show how Hahn and Sarrate's criteria can be adapted to the D-BCS-HSW model. It is seen that their ideas can be carried through quite easily by formulating the criteria in terms of the nominal stress.

In the section about Relation to Other Developments, we discuss the relation of the D-BCS-HSW model to several other developments in the literature, and show that they essentially correspond to different forms of plotting the D-BCS-HSW equation. First, we treat Dowling and Townley's [*5*] two-criteria approach and universal failure curve. Next, we show the relation to the CTOD design curve developed by Dawes [*6*] and co-workers at the Welding Institute. Finally, we discuss the failure assessment diagram (FAD) of Harrison et al [*7*], developed at the Central Electricity Generating Board (CEGB).

In the Residual Strength Diagram section, we discuss the residual strength diagram, which is based on examining the failure stress as a function of the crack size. In this paper we examine only the general case, but in a future publication we shall also examine the results obtained for particular geometries.

The D-BCS-HSW model embodies important features of separation mechanics. It reduces to LEFM at one extreme and to PC at the other. In summary, this model presents an even more unified picture than the original one of Hahn and Sarrate.

It has been customary to regard J computations, J_{Ic} and J-R measurements, and the "tearing instability" concept as central components of EPFM. These topics are not discussed in the present paper, but are treated thoroughly in other papers in this publication. Instead, the emphasis in this paper is on the CTOD to provide the transition between linear-elastic and fully plastic behavior. Though it was the interest in the J-integral that led directly to introduction of the term, EPFM, we have extended its meaning to include all fracture behavior that contains elements of both elasticity and plasticity, regardless of the theory used to explain it. In this paper in particular we have used the plastic yield strip model as the central component of EPFM.

Infinite Plate

Linear-Elastic Fracture Mechanics

In LEFM the stress-intensity factor for an infinite plate with a through-crack of length $2a$ is given by (see Tada et al, Ref *8*)

$$K = \sigma(\pi a)^{1/2} \tag{1}$$

where σ is the applied stress. If σ is a tensile stress, then we have an opening mode for the crack, usually denoted as Mode 1. The stress-intensity factor, K, represents the strength of the stress field surrounding the crack tip. Hence, K characterizes the magnitude of the crack-tip stress field. The fracture process of a material may be regarded as "caused" by the surrounding crack-tip stress field environment. Hence, Eq 1 for K also may be interpreted as giving a crack-driving or crack-extension force. Here the term "force" is used in a generalized sense, for K does not have the dimensions of a force. Equation 1 shows that as σ or a is increased, so is the crack-extension force, K. The crack will not actually extend as long as K is less than the crack-extension resistance, K_R. When the crack-extension force begins to exceed the crack-extension resistance, then crack extension occurs. In this paper crack extension will be regarded as failure of the structure. However, these concepts also can be extended to slow stable crack extension (R-curve) before fast fracturing.

The fracture toughness is a generic term for measures of resistance to extension of a crack. Therefore we shall use the terms "fracture toughness" and "crack-extension resistance" interchangeably, and denote it by K_R. In LEFM this material property is denoted by K_{Ic}.

Plastic-Zone Adjustment

The customary formulation of LEFM never can be correct, because it implies an infinite stress at the crack tip. Actually, under the applied stress, σ, a

plastic zone will develop around the crack tip. The effect of this plastic zone is to increase the displacements and lower the stiffness of the plate. In other words, the plate behaves as if it contained a crack of somewhat larger size, which is called the effective crack size, and given by

$$a_e \equiv a + r_Y \tag{2}$$

where r_Y is the plastic-zone adjustment, which is assumed to be small relative to the crack size. Though linear elasticity now has broken down at the crack tip, because of the presence of plasticity, LEFM still gives good elastic results at distances much larger than r_Y from the crack tip. However, the "apparent" stress-intensity factor that best describes the behavior of this far elastic field is given now by an effective stress-intensity factor

$$K_e = \sigma(\pi a_e)^{1/2} \tag{3}$$

which is the LEFM expression for K expressed in terms of the effective crack size, a_e. The plastic-zone adjustment, r_Y, gives a measure of the nominal plastic zone size. Based on a force balance argument, Irwin [*9*] has given the following estimate

$$r_Y \equiv (K_e/\sigma_0)^2/2\pi \tag{4}$$

where σ_0 is the flow stress of the material. Equations 2 to 4 can be combined and solved for K_e to give

$$K_e = \frac{\sigma(\pi a)^{1/2}}{\left[1 - \frac{1}{2}(\sigma/\sigma_0)^2\right]^{1/2}} \tag{5}$$

This relation shows that the effective stress-intensity factor, K_e, is larger than the LEFM stress-intensity factor, K, given by Eq 1. The smaller the flow stress, σ_0, the larger this difference becomes, and the larger the plastic-zone adjustment becomes.

With plasticity present, the magnitude of the surrounding elastic crack-tip stress field is characterized by the effective stress-intensity factor. Hence K_e must now be interpreted as the crack-extension force. Again, the crack will begin to extend when the crack-extension force, K_e, exceeds the crack-extension resistance, K_R. This will occur for smaller values of applied stress, σ, the larger the plasticity, r_Y, or the smaller the flow stress, σ_0.

Plastic Yield Strip Model

In this paper we shall model EPFM by the plastic yield strip model. It was introduced by Dugdale [*2*] and elaborated by Bilby, Cottrell, and Swinden

[3]. This model therefore has become known as the D-BCS model. It assumes that the material yields plastically in a strip ahead of the crack tip. For a central crack in an infinite plate, the model gives an analytic expression for the CTOD, formerly known as crack opening displacement (COD), given by

$$\delta = (8a\sigma_0/\pi E) \ln \sec (\pi\sigma/2\sigma_0) \tag{6}$$

where E is Young's modulus. For small scale yielding it is seen that this CTOD reduces to

$$\delta \to \pi a\sigma^2/E\sigma_0 = K^2/E\sigma_0 \quad \text{for } \sigma/\sigma_0 \to 0 \tag{7}$$

where the equality follows from Eq 1. The relation in Eq 7 now is generalized to define an effective stress-intensity factor by

$$K_e{}^2 = E\sigma_0\delta \tag{8}$$

Thus, from Eqs 1 and 6 the effective stress-intensity factor corresponding to the D-BCS model is taken as follows

$$K_e = \sigma_0 [(8a/\pi) \ln \sec (\pi\sigma/2\sigma_0)]^{1/2} \tag{9}$$

This relation is similar to the Irwin plastic-zone adjusted model in Eq 5 in that

$$\begin{aligned} K_e &> K \quad \text{for } \sigma_0 < \infty \\ K_e &\to K \quad \text{for } \sigma_0 \to \infty \end{aligned} \tag{10}$$

where K is the LEFM stress-intensity factor given by Eq 1.

The relation in Eq 9 and additional expressions for the effective stress-intensity factor, K_e, which we shall derive later, can be visualized directly in terms of the CTOD, δ, by means of Eq 8, that is, in terms of the plastic yield strip model. This shift of nomenclature from δ to K_e and back remains valid in the subsequent sections. Hence Eq 8 can be used to convert K_e-values to δ-values.

Furthermore, the relation in Eq 9 is based on having plastic collapse occurring at $\sigma = \sigma_0$. Plastic collapse or limit load theory assumes elastic-perfectly plastic behavior of the material, that is, there is no work-hardening. Hence the results usually are expressed in terms of the yield stress, σ_Y. Because this provides a pessimistic result for work-hardening materials, it is usual to replace the yield stress by a flow stress, σ_0, which has a value about halfway between the yield stress and the ultimate tensile strength. Furthermore, the effective flow stress may be raised above this particular value due to constraints, such as occur in plane strain. This is frequently expressed in

terms of a constraint factor. In this paper we shall assume that the constraint factor is implied in the flow stress.

To focus on the functional dependence of K_e it is helpful to regard Eq 9 as being made up of two factors as follows

$$K_e(\sigma, \sigma_0, a) = K(\sigma, a)\, M(\sigma/\sigma_0) \tag{11}$$

where $K(\sigma, a)$ is the LEFM value given by Eq 1 and $M(\sigma/\sigma_0)$ is the plastic correction factor given by

$$M(\sigma/\sigma_0) \equiv (2\sigma_0/\pi\sigma)[2 \ln \sec (\pi\sigma/2\sigma_0)]^{1/2} \tag{12}$$

This shows that the D-BCS form for K_e in Eq 9 has the same form as the Irwin K_e in Eq 5, namely, the effective stress-intensity factor, K_e, is the LEFM stress-intensity factor, K, multiplied by a plastic correction factor, M. For $\sigma/\sigma_0 \to 0$, $M \to 1$, so that the D-BCS model approaches the LEFM model at small applied stress.

Failure Criteria

The expression for the effective stress-intensity factor, K_e, represents the crack-extension force. The fracture toughness, K_R, represents the crack-extension resistance and usually is considered to be a material property. In general, it may vary with crack-extension, plate thickness, loading rate, or other parameters. However, we shall assume it constant for the present paper. Hence, when the cracked plate is loaded until

$$K_e = K_R \tag{13}$$

then the crack will begin to extend. This, then, we take as the failure criterion, and the corresponding stress will be the failure stress, sometimes denoted by σ_f. The failure stress for the D-BCS model, therefore, is found from Eq 9 as

$$\sigma = (2/\pi)\, \sigma_0 \cos^{-1} \{ \exp[-(\pi/8a)(K_R/\sigma_0)^2] \} \tag{14}$$

This relation is plotted in dimensionless form as the solid curve labelled D-BCS in Fig. 1. Along the x-axis we have plotted a measure of the fracture toughness, $(K_R/\sigma_0)^2/a$, and along the y-axis the normalized applied stress, σ/σ_0. These are logical choices for dimensionless parameters from Eq 14. Note that σ never exceeds σ_0 for this curve.

The curve represents the expected failure stress for the plate. Hence, for a given crack of size a, in the plate of fracture toughness K_R and flow stress σ_0, if the applied stress, σ, gives a point that falls below the D-BCS curve on this

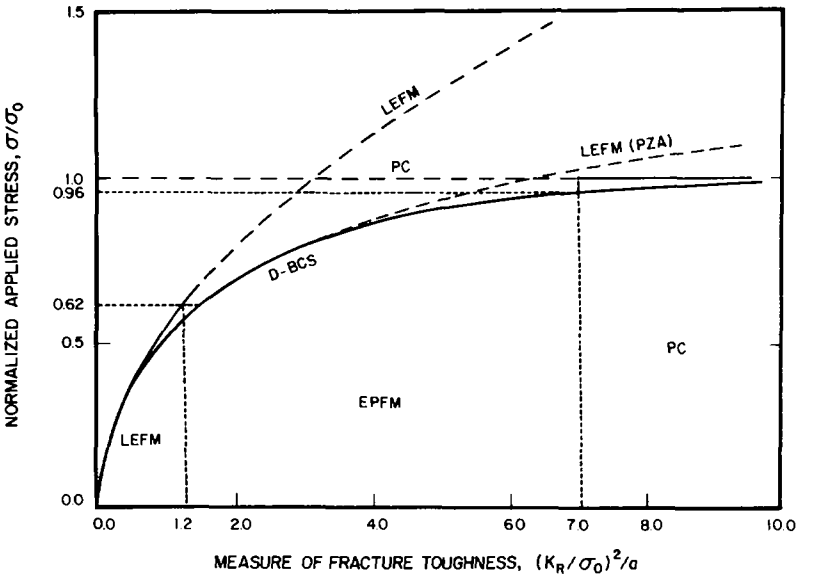

FIG. 1—*Failure categories for the infinite plate. The solid curve is given by the D-BCS-HSW model. The dashed curves represent LEFM and the plastic-zone adjustment [LEFM (PZA)]. The dashed horizontal line represents PC. The dotted lines give the dividing lines between the three failure categories.*

plot, then the structure is considered to be safe, but if the point falls above the curve, then it is assumed that the crack will extend and lead to failure of the plate.

In the same figure, a curve labelled LEFM also is plotted. This curve would be obtained if failure is assumed to occur by brittle fracture, that is, when K in Eq 1 reaches K_R, as described in the section on Linear-Elastic Fracture Mechanics. The failure stress for LEFM, therefore, is given by

$$\sigma = K_R/(\pi a)^{1/2} \tag{15}$$

This relation is plotted in dimensionless form as the dashed curve labelled LEFM in Fig. 1. Note that it approaches the D-BCS curve at small applied stress.

We also have plotted the plastic-zone adjustment for LEFM in Fig. 1. The formula for this model is obtained by substituting Eq 13 in Eq 5 and solving for the failure stress

$$\sigma = K_R/[\pi a + (K_R/\sigma_0)^2/2]^{1/2} \tag{16}$$

This relation is plotted in dimensionless form as the dashed curve labelled LEFM (PZA) in Fig. 1. It gives a much better approximation to the D-BCS

curve then Eq 15, and this shows that the plastic zone adjustment is quite good up to values of $\sigma/\sigma_0 \approx 0.8$.

Finally, PC is considered to occur when the applied stress reaches the flow stress

$$\sigma = \sigma_0 \tag{17}$$

This is the dashed line labelled PC shown in Fig. 1. No knowledge of the fracture toughness is needed for this curve. It simply represents the failure stress when no crack is present. Plastic collapse also is known as plastic instability or ultimate collapse.

Failure Categories

At the Symposium on Fracture Toughness Concepts for Weldable Structural Steel, Hahn and Sarrate [*1*] established failure criteria for through-cracked vessels. Their paper offered a more unified picture of the various viewpoints represented at the conference, such as LEFM, plasticity-corrected fracture toughness, CTOD, the flow strength criterion, etc. These concepts were fitted into a common framework of three failure categories: (1) linear-elastic behavior, (2) nonlinear elastic behavior, and (3) plastic instability behavior. They also established criteria for the dividing lines between these failure categories. These latter criteria were given in terms of the crack size, a, fracture toughness, K_R, and flow stress, σ_0, as follows:

(*a*) Dividing line between categories (1) and (2)

$$(K_R/\sigma_0)^2/a \approx 1.2 \tag{18}$$

(*b*) Dividing line between categories (2) and (3)

$$(K_R/\sigma_0)^2/a \approx 7 \tag{19}$$

In this paper we have relabelled their categories (1) *LEFM*, (2) *EPFM*, and (3) *PC*. These categories and their dividing lines (Eqs 18 and 19) also are shown in Fig. 1. The motivation for these dividing lines was as follows:

(*a*) Hahn and Sarrate established dividing line (Eq 18) between LEFM and EPFM by associating it with the $\sigma/\sigma_0 \approx 0.6$ stress level where the "true" CTOD (Eq 6) departs 20 percent from the "linear-elastic" estimate (Eq 7). This is shown as follows. We substitute Eq 18 into Eq 15, and obtain the stress level criterion

$$\sigma/\sigma_0 \approx 0.62 \tag{20}$$

as illustrated in Fig. 1. From Eqs 1 and 9, we then find

$$(K_0/K)^2 = 8(\sigma_0/\pi\sigma)^2 \ln \sec (\pi\sigma/2\sigma_0) \approx 1.2 \tag{21}$$

This may also be written

$$(K_e^2 - K^2)/K^2 \approx 0.2 \tag{22}$$

which is the 20 percent criterion expressed in terms of the stress-intensity factor rather than CTOD. In Fig. 1, this means that the LEFM and D-BCS curves differ from each other by 20 percent at the dividing line. In support of this dividing line, we note that Heald, Spink, and Worthington [*4*] have stated that the two curves "merge" for $a > (K_R/\sigma_0)^2$. This would correspond to $(K_R/\sigma_0)^2/a < 1$ instead of Eq 18, with a difference of about 15 percent at $\sigma/\sigma_0 \approx 0.56$. We believe that criterion is essentially in agreement with that of Hahn and Sarrate. The conclusion here is that for $\sigma/\sigma_0 < 0.62$ the difference between LEFM and EPFM becomes negligible.

(*b*) For the dividing line (Eq 19) between EPFM and PC, Hahn and Sarrate reported that this was a consensus of various participants at the symposium. If Eq 19 is substituted in Eq 14, we find that at the dividing line

$$\sigma/\sigma_0 \approx 0.96 \quad \text{or} \quad (\sigma_0 - \sigma)/\sigma_0 \approx 0.04 \tag{23}$$

This means that the EPFM curve lies 4 percent below the PC line at the dividing line, as can be seen in Fig. 1. The conclusion here is that for $\sigma/\sigma_0 > 0.96$ the difference between EPFM and PC is negligible.

In establishing these criteria, Hahn and Sarrate did not take into account the effect of the geometry and size of the structure. We shall show how this can be done in the section on Finite Geometry.

Dimensionless Formulation

From Fig. 1, it is apparent that a dimensionless graph displays the essential features of the model quite well. All cases for different values of σ, a, K_R, or σ_0 are reduced to a single plot.

Analytically a dimensionless formulation is also convenient, because it will emphasize the generic form of the equations, and hence highlight the role of the parameters or combination of parameters. We therefore define the normalized applied stress as

$$\sigma_1 \equiv \sigma/\sigma_0 \tag{24}$$

and a normalized fracture toughness by

$$K_1 \equiv (K_R/\sigma_0)/(\pi a)^{1/2} \tag{25}$$

In terms of these dimensionless quantities we can now rewrite the analytic expressions for the three categories as follows:

(*a*) In EPFM Eq 14 then gives the following expression for the normalized applied failure stress of the D-BCS model

$$\sigma_1 = (2/\pi)\cos^{-1}\{\exp[-(\pi K_1)^2/8]\} \tag{26}$$

This would suggest a plot of σ_1 versus K_1. However, we have plotted σ_1 versus πK_1^2 instead in Fig. 1, primarily to illustrate Hahn and Sarrate's criteria for the dividing lines.

(*b*) In terms of the dimensionless quantities, the normalized applied failure stress for LEFM becomes (compare Eq 15)

$$\sigma_1 = K_1 \tag{27}$$

(*c*) Finally, the normalized applied failure stress for PC becomes (compare Eq 17)

$$\sigma_1 = 1 \tag{28}$$

The relations (Eqs 26 to 28) then summarize the three failure categories in the dimensionless formulation.

Finite Geometry

Modified Plastic Yield Strip Model

Heald, Spink, and Worthington [*4*] noted that the D-BCS model (Eq 14) does not account for the effect of the geometry or shape of the structure. They therefore introduced a correction factor into the equation to take this into account. We have called this modification the D-BCS-HSW model.

First recall that in LEFM the effect of geometry or structure can be introduced into the stress-intensity factor by writing it in the generic form

$$K = \sigma(\pi a)^{1/2} F(a/W) \tag{29}$$

where $F(a/W)$ is the geometric factor for the stress-intensity factor and W is the width of the structure. Various handbooks, such as Tada et al [*8*], give analytic expressions for F in many particular geometries. Equation 29 can be

regarded as a generalization of Eq 1 from the infinite plate to arbitrary geometries.

To generalize the D-BCS model (Eq 9) to arbitrary geometries is much more difficult than for the LEFM case. No analytic and only a limited number of numerical solutions have been published. Therefore Heald, Spink, and Worthington proposed an approximate generalization similar to the above one for LEFM. In particular, their procedure is a generalization of the effective stress-intensity factor in Eq 11, as follows

$$\begin{aligned} K_e(\sigma, \sigma_0, a, W) &= K(\sigma, a, W) M(\sigma_N/\sigma_0) \\ &= \sigma(\pi a)^{1/2} F(a/W)\, M(\sigma_N/\sigma_0) \end{aligned} \tag{30}$$

where σ_N is the nominal stress, explained below, $K(\sigma, a, W)$ is the LEFM value given by Eq 29, and $M(\sigma_N/\sigma_0)$ is the plastic correction factor, which has the same form as Eq 12, and is given by

$$M(\sigma_N/\sigma_0) = (2\sigma_0/\pi\sigma_N)\,[2 \ln \sec (\pi\sigma_N/2\sigma_0)]^{1/2} \tag{31}$$

Equation 30 shows that the effective stress-intensity factor, K_e, in the D-BCS-HSW model is the LEFM stress-intensity factor, K, multiplied by a plastic correction factor, M, just as we found for the D-BCS model.

In the previous expressions σ_N is the nominal stress, which is the stress on a net cross-section calculated in a simplified manner without taking into account stress gradients produced by geometric discontinuities, such as cracks. The nominal stress can be related to the applied stress by

$$\sigma = \sigma_N N(a/W) \tag{32}$$

where $N(a/W)$ is the geometric factor for the nominal stress. As with expressions for F, the expressions for N are usually functions of the structural geometry, and most frequently expressed in terms of the parameter a/W. At plastic collapse it is assumed that the nominal stress, σ_N, reaches the flow stress, σ_0, and the applied stress, σ, reaches the limit stress, σ_L, which therefore is given by

$$\sigma_L = \sigma_0 N(a/W) \tag{33}$$

Analytic expressions in this form for various specimen geometries have been given by Chell [*10*] in Table 1 of his paper (where he uses σ_1 for σ_L and $\bar{\sigma}$ for σ_0).

If we substitute Eqs 31 and 32 into Eq 30, we find the following expression for the effective stress-intensity factor of the D-BCS-HSW model

$$K_e = FN\sigma_0\,[(8a/\pi) \ln \sec (\pi\sigma/2N\sigma_0)]^{1/2} \tag{34}$$

This expression has the desirable properties that for LEFM, where $\sigma << \sigma_0$, it reduces to Eq 29, and for the infinite plate, where $F = N = 1$, it reduces to the D-BCS model (Eq 9). Furthermore, Eq 34 is assumed to apply in general to all geometries.

Failure Criteria

The D-BCS-HSW expression for the effective stress-intensity factor, K_e in Eq 34, again can be regarded as the crack-extension force in the finite structure with plasticity. When the applied stress, σ, or the crack size, a, are increased until the crack-extension force, K_e, reaches the value of the crack-extension resistance, K_R, then the crack will start to extend, and by our assumption failure will occur. Hence, if we substitute K_R for K_e in Eq 34 and solve for σ we find the failure stress for the D-BCS-HSW model

$$\sigma = (2/\pi) N\sigma_0 \cos^{-1}\{\exp[-(\pi/8a)(K_R/FN\sigma_0)^2]\} \tag{35}$$

This relation is plotted in dimensionless form as the solid curve labelled D-BCS-HSW in Fig. 2. Along the x-axis we have plotted a measure of the fracture toughness, $(K_R/FN\sigma_0)^2/a$, and along the y-axis the normalized nominal stress, σ_N/σ_0. These are the logical choices for the dimensionless parameters in Eq 35. This curve represents the expected failure stress.

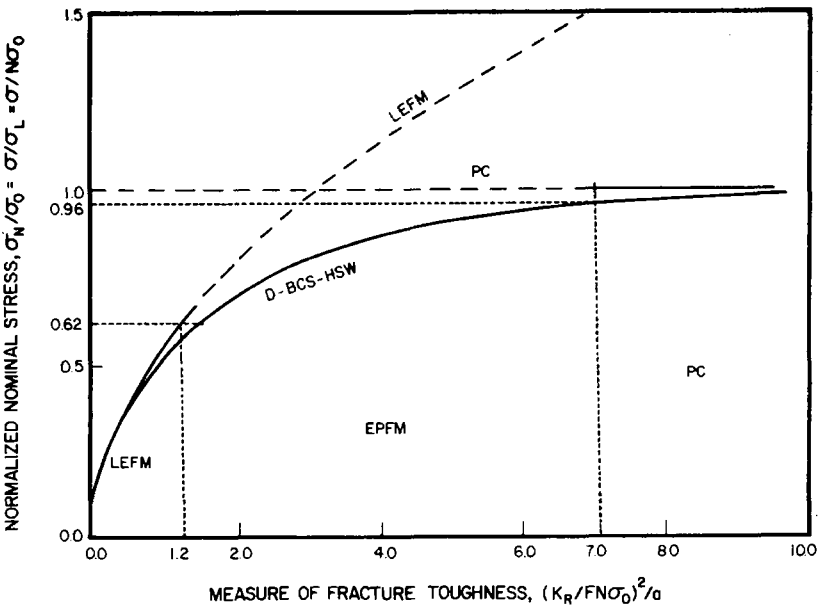

FIG. 2—*Failure categories for finite geometry.*

In the same figure, a curve labelled LEFM also is plotted. This is the curve that would be obtained if one assumes that failure occurs by LEFM, that is, that there is no plasticity at the crack tip. Then the stress-intensity factor, K, given by Eq 29, would represent the crack-extension force, and failure would occur when K reaches K_R. Hence, if we substitute K_R for K in Eq 29, and solve for σ we find the failure stress for LEFM

$$\sigma = (K_R/F)/(\pi a)^{1/2} \tag{36}$$

This relation is plotted as the dashed curve labelled LEFM in Fig. 2. The D-BCS-HSW curve approaches the LEFM curve as the normalized fracture toughness approaches zero.

Finally, PC is considered to occur when the nominal stress reaches the flow stress, or the applied stress reaches the limit stress

$$\sigma_N = \sigma_0 \quad \text{or} \quad \sigma = \sigma_L \tag{37}$$

This is the other dashed line in Fig. 2. Again, no knowledge of fracture toughness is needed for this curve. It simply represents the failure stress when no crack is present. The D-BCS-HSW curve approaches the PC curve as the crack size approaches zero.

It will be noticed that the form of the equations in this section is similar to the form of the equations in the earlier section on Failure Criteria, and that the shape of the curves in Fig. 2 is exactly the same as the shape of the curves in Fig. 1. For this simplified model, the difference between the two figures is only in the labelling of the axes, where in going from Fig. 1 to Fig. 2 the axes have acquired a more general interpretation.

Failure Categories

If the Hahn and Sarrate [*1*] criteria for the dividing lines (Eqs 18 and 19) are applied to the D-BCS-HSW model shown in Fig. 2, then the location of the dividing lines between the categories would depend on the geometry of the structure, through the functions $F(a/W)$ and $N(a/W)$. Hence, it is desirable to generalize these criteria in such a way that they are independent of the geometry. Figure 2 suggests that this can be done as follows:

(*a*) Dividing line between LEFM and EPFM categories

$$(K_R/FN\sigma_0)^2/a \approx 1.2 \quad \text{or} \quad \sigma_N/\sigma_0 \approx 0.62 \tag{38}$$

(*b*) Dividing line between EPFM and PC categories

$$(K_R/FN\sigma_0)^2/a \approx 7 \quad \text{or} \quad \sigma_N/\sigma_0 \approx 0.96 \tag{39}$$

These are now the dividing lines for the three failure categories in the case of finite geometry, as illustrated in Fig. 2. These relations generalize to finite geometries the ideas of Hahn and Sarrate [*1*], discussed in the section on Failure Categories, which were developed for an infinite plate.

We emphasize again that we have ascribed a general meaning to the term EPFM in Eqs 38 and 39, that is, EPFM is used here to describe the elastic-plastic category described by the D-BCS-HSW model. It does not refer to the J-integral approach.

Dimensionless Formulation

Again, it is convenient to have a dimensionless formulation, because it emphasizes the generic form of the equations, and highlights the essential combination of parameters. We define the normalized nominal stress by

$$\sigma_2 \equiv \sigma_N/\sigma_0 = \sigma/\sigma_L = \sigma/N\sigma_0 \tag{40}$$

where the second and third equalities follow from Eqs 32 and 33. Furthermore, we define a second normalized fracture toughness by

$$K_2 \equiv (K_R/FN\sigma_0)/(\pi a)^{1/2} \tag{41}$$

In terms of these dimensionless quantities the analytic expressions for the three categories now can be written as follows:

(*a*) In EPFM, Eq 35 gives the following expression for the normalized nominal failure stress of the D-BCS-HSW model

$$\sigma_2 = (2/\pi)\cos^{-1}\{\exp[-(\pi K_2)^2/8]\} \tag{42}$$

Again, in Fig. 2 we have plotted σ_2 versus πK_2^2 rather than K_2, primarily to show the extension of Hahn Sarrate's criteria for the dividing lines to finite geometries.

(*b*) In terms of the dimensionless quantities, the normalized nominal failure stress for LEFM becomes (compare Eq 36)

$$\sigma_2 = K_2 \tag{43}$$

(*c*) Finally, the normalized nominal failure stress for PC becomes (compare Eq 37)

$$\sigma_2 = 1 \tag{44}$$

Note the striking similarity between Eqs 42 to 44 and Eqs 26 to 28, when the relations are expressed in dimensionless formulation. This is why the curves in Figs. 1 and 2 are identical; only the axes have been relabelled.

Relations to Other Developments

Two-Criteria Approach and Universal Failure Curve

Dowling and Townley [5] attempted to simplify the treatment of structures containing defects by bypassing the post-yield fracture mechanics (EPFM) theories and assuming that the failure stress occurs by one of two mechanisms: this was called the *two-criteria approach*. LEFM can be considered as one extreme form of failure behavior, providing one bound to the problem of fracture analysis. The other bound then is given by the opposite behavior, namely, fully plastic collapse. The two-criteria approach then states that structural failure occurs when the loading system reaches the lower of either the load to cause fracture by LEFM or the load to cause failure by PC. The calculations involved in obtaining these two different loads are independent since in LEFM the material property governing failure is the fracture toughness, K_R, whereas in PC it is the flow stress, σ_0. The former is dependent on crack tip events, whereas the controlling influence in the latter is the net section. In nonwork-hardening materials PC will occur when the average stress across the net section approaches the yield stress (flow stress) and a mechanism exists for PC.

Dowling and Townley further noted that LEFM is a good way of describing the effect of cracks when $\sigma/\sigma_0 < 0.6$. This of course is in agreement with the former assessment of Hahn and Sarrate.

However, Dowling and Townley realized that there is a transition region between their two criteria. They achieved normalization of the data by using the formulation of Heald, Spink, and Worthington [4], that is, the D-BCS-HSW model (Eq 35). This equation was used to describe the behavior of simple specimens in brittle fracture, the transition region, and gross yielding. To describe the behavior of more complex structures, they rewrote this formula to give the *universal failure curve*

$$L_f/L_u = (2/\pi)\cos^{-1}\{\exp[-(\pi^2/8)(L_k/L_u)^2]\} \tag{45}$$

where the symbols L represent failure parameters, such as load, stress, or pressure. For example, the applied failure load could be given by

$$L_f = A\sigma \tag{46}$$

where A is some cross-sectional area. Then the failure load by plastic collapse would be

$$L_u = A\sigma_L \tag{47}$$

and the failure load by brittle fracture

$$L_k = A\sigma K_R/K = AK_R/[(\pi a)^{1/2}F] \tag{48}$$

Hence, Dowling and Townley's universal failure curve (Eq 45) is completely equivalent to the D-BCS-HSW model (Eq 35). This also can be seen as follows. From Eqs 46 and 47 and Eq 40

$$L_f/L_u = \sigma_2 \tag{49}$$

and from Eqs 33, 41, 47, and 48

$$L_k/L_u = K_2 \tag{50}$$

Hence, Eq 45 is identical to Eq 42. This equation is plotted as the solid curve labelled D-BCS-HSW in Fig. 3. This curve again represents the expected failure stress.

Also shown in this figure is the LEFM curve, Eq 38 or 43, which is now a straight line given by

$$L_f/L_u = L_k/L_u \tag{51}$$

and the PC line, Eq 37 or 44, given by

$$L_f/L_u = 1 \tag{52}$$

Furthermore, the three failure categories of Hahn and Sarrate also are shown, separated by the previously discussed dividing lines. These dividing

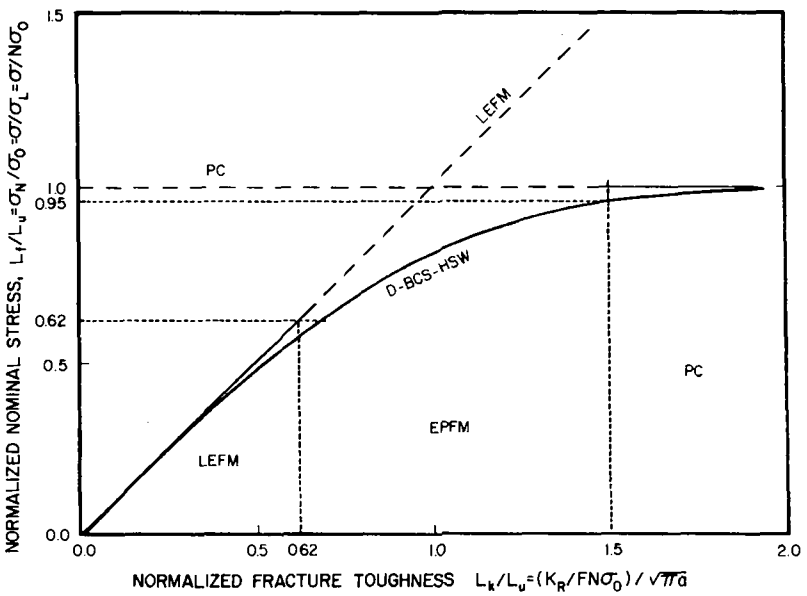

FIG. 3—*The universal failure curve of Dowling and Townley.*

lines now are expressed most conveniently in terms of the dimensionless quantities:

(*a*) Dividing line between LEFM and EPFM categories

$$K_2 \approx (1.2/\pi)^{1/2} \approx 0.62 \quad \text{or} \quad \sigma_2 \approx 0.62 \tag{53}$$

(*b*) Dividing line between EPFM and PC categories

$$K_2 \approx (7/\pi)^{1/2} \approx 1.5 \quad \text{or} \quad \sigma_2 \approx 0.96 \tag{54}$$

Dowling and Townley plotted results of a large number of analyses on the universal failure curve. Extensive evidence was collected confirming that Eq 45 interpolates adequately between the two limiting criteria. There was good agreement between the curve and the experimental points bearing in mind the wide variety of geometries, materials, and toughness levels.

Relation to the Design Curve

As originally propounded, the *CTOD design curve* (formerly known as the COD design curve) aimed to give the practitioner a very simple but assuredly conservative method for defining, for a given material, an acceptable combination of stress level and defect size.

The basis for the CTOD design curve was provided by Burdekin and Stone's [*11*] analysis of the D-BCS model. However, rather than using Eq 9 in terms of the stress, they developed a relationship between a nondimensional value of the CTOD and a normalized strain. The nondimensional CTOD was given by

$$\Phi = \delta E/2\pi\sigma_Y\bar{a} \tag{55}$$

where σ_Y is the yield stress and $\bar{a}$ an equivalent crack size. This analysis applied to an elastic-plastic nonwork-hardening material. However, the experimental values from large-scale tests were generally below the predicted values.

Burdekin and Dawes [*12*] revised the CTOD design curve and used the D-BCS model at small stresses (the toe region) and a linear portion at large strains. Later Dawes [*13*] modified the toe region of the CTOD design curve to a quadratic form that was simple to use. Essentially this corresponded to substituting Eq 7 into Eq 55.

For a more accurate description of the toe region Dawes [*6*] used the equation

$$\Phi/(1 - \bar{a}/W)^2 \approx (4L/\pi^2) \ln \sec (\pi\sigma_N/2L\sigma_Y) \tag{56}$$

where L is a plastic constraint factor. For structural situations with low values of $\bar{a}/W$ this relation was justified by experimental data. We now show

that Eq 56 is equivalent to the developments discussed previously. The plastic constraint factor can simply be taken as the ratio of flow to yield stress

$$L = \sigma_0/\sigma_Y \tag{57}$$

Following Merkle's [*14*] suggestion, that is, comparing Eq 1 with Eq 29, the equivalent crack size, $\bar{a}$, can be related to the actual crack size, a, by the geometric factor for the stress-intensity factor

$$\bar{a} = aF^2 \tag{58}$$

For a crack in tension the geometric factor for the nominal stress can be taken as

$$N = 1 - \bar{a}/W \tag{59}$$

though we would prefer to use the actual crack size, a, in this relation. With the relations in Eqs 57 to 59, it can be seen that Dawes' Eq 56 follows from Eqs 8, 32, 34, and 55. Hence, Dawes' equation is completely equivalent to the D-BCS-HSW model.

In our previous notation the D-BCS-HSW model for the approach in this section is obtained by solving Eq 35 for K_R or, more simply, by substituting Eq 13 in Eq 34

$$K_R = FN\sigma_0\,[(8a/\pi)\ln\sec(\pi\sigma/2N\sigma_0)]^{1/2} \tag{60}$$

The dimensionless form of this relation is found from Eqs 40 and 41 or by solving Eq 42 for K_2

$$K_2 = [(8/\pi^2)\ln\sec(\pi\sigma_2/2)]^{1/2} \tag{61}$$

This relation is plotted as the solid curve labelled D-BCS-HSW in Fig. 4. Again, we also have plotted the dashed LEFM line given by (compare Eqs 36 and 43)

$$K_2 = \sigma_2 \quad \text{or} \quad K_R = \sigma(\pi a)^{1/2}F \tag{62}$$

and the plastic collapse line is given by Eq 37 or 44. The three failure categories of Hahn and Sarrate and their dividing lines are given by the relations in Eqs 53 and 54, as before.

We note that Fig. 4 is a variant of Fig. 3 obtained simply by interchanging the axes. This method of plotting has been used frequently for comparison of experimental data with LEFM or D-BCS-HSW; see, for example, Dawes [*13*], Server and Wullaert [*15*], and deWit and Interrante [*16*].

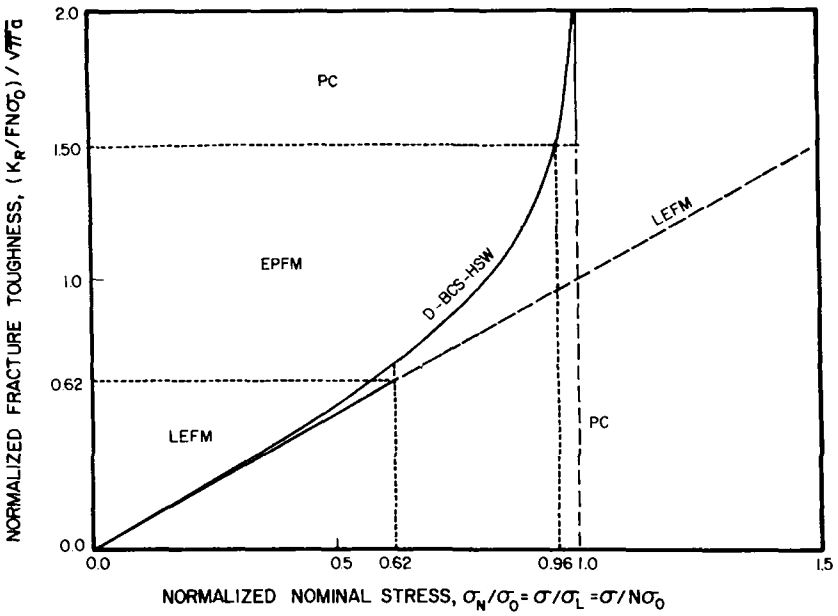

FIG. 4—*General comparison of LEFM, EPFM, and PC.*

Failure Assessment Diagram

Harrison et al [*7*] concluded that the previously mentioned methods were not an ideal presentation. When failure is by LEFM it is abrupt. When failure is the PC it is progressive. Hence, they wanted to clearly separate these two mechanisms in a diagram. The procedures developed within the CEGB were designed to satisfy this function. When the procedures are followed to completion, all necessary plasticity corrections are performed automatically so that the critical conditions are identified properly. Judgment of the degree of safety of the structure is not made by recourse to rigid "safety factors." Instead, the user is encouraged to choose such factors objectively [*17-18*].

The basis of the CEGB procedure, also known as the R6 procedure, is the *FAD*, shown in Fig. 5, on which are plotted two parameters, S_r and K_r, evaluated under the appropriate loading conditions. The parameter S_r is a measure of how close the structure is to failure by PC and is defined by

$$S_r \equiv \sigma/\sigma_L \tag{63}$$

From Eqs 40 and 49 we see that S_r is related to quantities we have defined before by

$$S_r = \sigma_2 = L_f/L_u \tag{64}$$

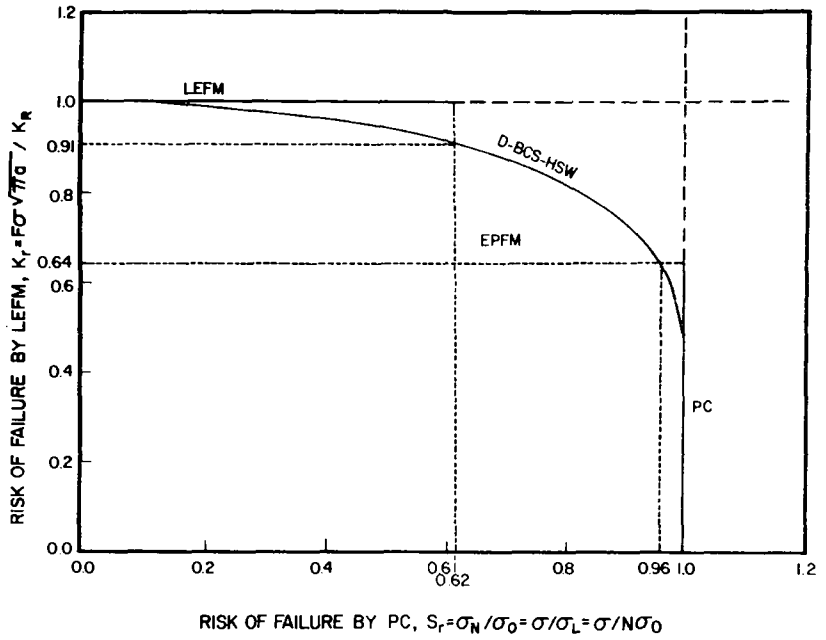

FIG. 5—*The failure assessment diagram of the CEGB.*

The parameter K_r is a measure of how close the structure is to failure by LEFM and is defined by

$$K_r \equiv K/K_R \tag{65}$$

We see that

$$S_r/K_r = K_2 = L_k/L_u \tag{66}$$

from Eqs 29, 33, 41, and 50. If we now substitute σ_2 and K_2 in terms of S_r and K_r as given previously into Eq 61 and solve for K_r we find

$$K_r = S_r[(8/\pi^2) \ln \sec(\pi S_r/2)]^{-1/2} \tag{67}$$

This relation is plotted as the solid curve labelled D-BCS-HSW in Fig. 5. It is called the *failure assessment line*. This line uses the D-BCS-HSW model to interpolate between the two limits of behavior, namely LEFM and PC. In this way, advantage is taken of the observation of Dowling and Townley [5] that structures cannot operate outside the limits imposed by LEFM and PC. The basic assumption of the FAD is that it provides a realistic lower bound failure

locus which is somewhat independent of geometry. If it is regarded as simply an empirical interpolation, this assumption is justified easily by over 150 assessment points [*19*]. In practical applications of this procedure, the two parameters (S_r,K_r) are entered as a coordinate point on the failure assessment diagram in Fig. 5. Failure is conceded if the assessment point falls on or outside the assessment line.

Figure 5 also shows the LEFM line which is given from Eqs 29, 62, and 65 by

$$K_r = 1 \tag{68}$$

and the PC line which is given from Eqs 44 and 64 by

$$S_r = 1 \tag{69}$$

The three failure categories of Hahn and Sarrate also are shown in the figure, separated by the previously discussed dividing lines. These dividing lines now are given in terms of the FAD parameters by using the values of σ_2 for S_r from Eqs 53 and 54 and calculating K_r from Eq 67:

(*a*) Dividing line between LEFM and EPFM categories

$$S_r \approx 0.62 \quad \text{or} \quad K_r \approx 0.91 \tag{70}$$

(*b*) Dividing line between EPFM and PC categories

$$S_r \approx 0.96 \quad \text{or} \quad K_r \approx 0.64 \tag{71}$$

The FAD is another way of expressing the failure line derived from the D-BCS-HSW model. The FAD is the cornerstone of the *failure assessment route* on the format of the American Society of Mechanical Engineers (ASME) Section XI code. This provided a document that was in the format with which engineers are well acquainted and a method based on procedures that also were established and well understood. The assessment route can be applied to ferritic steel structures of any discipline, but its application has been oriented to pressure-bearing components of Nuclear Class 1 status. The route dealt with the treatment of failure in the small-scale and the large-scale yielding regimes. A detailed procedure is set out. The failure assessment route is one approach to assessing the integrity in structures containing defects. Out of the methods available, a route has been selected for establishing the criticality of any flaw and examining the rate of growth of such a flaw. Varying degrees of sophistication can be used, and Harrison et al [*7*] hope that the more simple methods prove to be satisfactory in the majority of cases. They do not claim that the route is fully established. The procedures are continually under review and are updated when knowledge and techniques are improved.

Reviews

The FAD has been well documented. The basic procedures are set out in the basic document by Harrison et al [*7*], which is updated regularly. An early introduction to the method was provided by Harrison and Milne [*17*]. The method and its background has been reviewed extensively more recently by Chell [*10*], Milne [*19*], and Darlaston [*20*]. These reviews also treat various ramifications and extensions of the method. An up-to-date summary was given by Harrison and Milne [*18*].

The design curve also has been documented extensively. Dawes [*6*] has reviewed the CTOD design curve, Burdekin [*21*] has reviewed its application, and Harrison [*22*] has reviewed the state-of-the-art of CTOD testing. Turner [*23*] has reviewed a related *J*-based design curve.

Turner [*24*] also has written an extensive review on all aspects of EPFM.

Residual Strength Diagram

Consider a structure in which a crack develops. Due to the application of repeated loads or due to a combination of loads and environmental attack this crack will grow with time. The longer the crack, the higher the stress concentration induced by it. Due to the presence of the crack the strength of the structure is decreased: it is lower than the original strength it was designed for. The residual strength of the structure decreases progressively with increasing crack size. What is the residual strength as a function of crack size? The answer to this question is already contained in the foregoing sections, but is best clarified by the residual strength diagram shown in Fig. 6.

As a measure of the residual strength we can take the fracture stress. Then Eq 35 represents the residual strength as a function of the crack size. To put this in dimensionless form, we define a normalized crack size by

$$a_2 \equiv (FN\sigma_0/K_R)^2\pi a = K_2^{-2} \tag{72}$$

where the second equality follows from Eq 41. The relation for residual strength then becomes (compare Eq 42)

$$\sigma_2 = (2/\pi)\cos^{-1}\{\exp[-\pi^2/8a_2]\} \tag{73}$$

where we now have taken the normalized stress (Eq 40) as representative of the residual strength. This relation is plotted as the solid curve labelled D-BCS-HSW in Fig. 6. This curve then represents the residual strength of the structure as a function of the normalized crack size. Again, the significance of this curve is that if a point for a given stress and crack size falls below the curve it is safe, but if it falls above this curve failure is predicted.

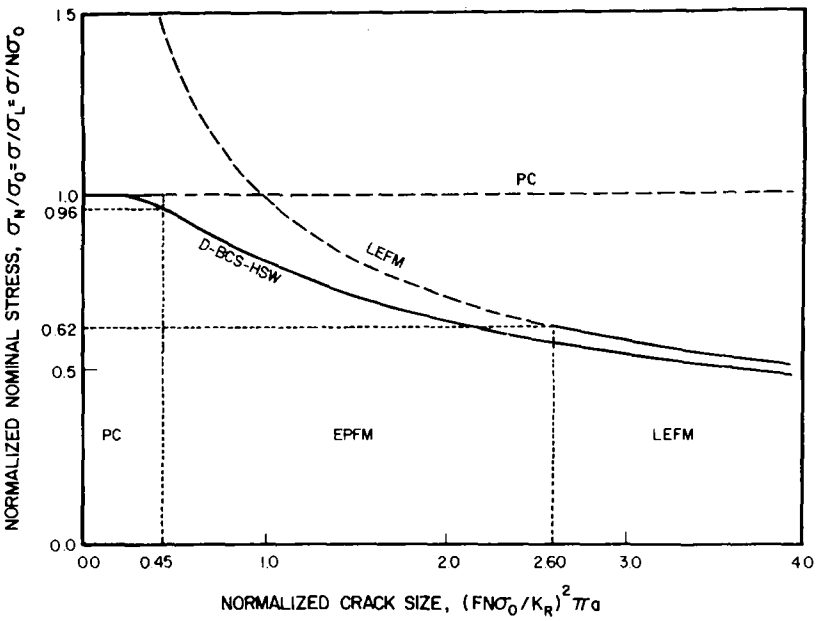

FIG. 6—*The residual strength diagram.*

Also shown in Fig. 6 is the LEFM curve, which is given by

$$\sigma_2 = a_2^{-1/2} \tag{74}$$

from Eqs 36, 40, and 72, and the PC curve, given by

$$\sigma_2 = 1 \tag{75}$$

The three failure categories of Hahn and Sarrate also are shown in the figure, separated by the dividing lines:

(*a*) Dividing line between LEFM and EPFM categories

$$\sigma_2 \approx 0.62 \quad \text{or} \quad a_2 \approx \pi/1.2 \approx 2.6 \tag{76}$$

(*b*) Dividing line between EPFM and PC categories

$$\sigma_2 \approx 0.96 \quad \text{or} \quad a_2 \approx \pi/7 \approx 0.45 \tag{77}$$

The form of the residual strength diagram for comparing data to the D-BCS-HSW model also has been used extensively in the literature, for example, by Heald, Spink, and Worthington [*4*], Dowling and Townley [*5*], and Harrison and Milne [*17*].

The residual strength diagram offers a sensible way to analyze experimental data, for it examines the failure stress as a function of the crack size, that is, the two parameters that would be of most interest to engineers. In this section, this was done in terms of the dimensionless quantities σ_2, Eq 40, and a_2, Eq 72. However, these are rather complicated quantities, involving the functions $F(a/W)$ and $N(a/W)$, which depend on the specific geometry of the structure. In a future publication we shall examine the residual strength diagram for particular geometries in simple terms.

Summary

We have briefly reviewed the fracture mechanics of a central crack in an infinite plate. In that connection we discussed the model developed by Dugdale, Cottrell, Bilby, and Swinden, known as the D-BCS model, which we used in this paper to describe EPFM. The failure criteria of Hahn and Sarrate were related to this model, and it was used to establish three failure categories: (1) LEFM, (2) EPFM, and (3) PC. The criteria for the dividing lines between these categories were given in terms of the fracture toughness, K_R, flow stress, σ_0, and the crack size, a. We reformulated these in terms of the normalized applied stress, σ/σ_0. We also presented a dimensionless formulation of the D-BCS model.

Next, we presented the extension of Heald, Spink, and Worthington of the D-BCS model to finite geometries and structures. This was an approximation patterned after the extension of LEFM for the infinite plate to finite geometry. In this approximation of the effective stress-intensity factor is represented as the product of two terms, one related to the geometry of the structure, and the other to the plasticity of the material. We have called it the D-BCS-HSW model. For a small crack size in a plate it reduces to the D-BCS model and for a small applied stress it reduces to the LEFM result. We generalized the failure criteria of Hahn and Sarrate to the D-BCS-HSW model simply by stating them in terms of the normalized nominal stress. Hence the three failure categories also could be defined quite easily. Two new quantities enter into the formulation of the D-BCS-HSW model, namely, the geometric factor for the stress-intensity factor, F, and the geometric factor for the nominal stress, N, both of which are functions of the geometry of the structure. We also presented a dimensionless formulation of the D-BCS-HSW model, which was formally identical to that for the D-BCS model.

Next, we discussed some related developments in the literature. Dowling and Townley's two-criteria approach and universal failure curve are just another way of presenting the D-BCS-HSW model. Their curve is supported by a large number of data. The relation of the D-BCS-HSW model to Dawes's CTOD design curve was pointed out. Finally, the D-BCS-HSW model is the basis of the FAD developed by Harrison, Loosemore, and Milne at the CEGB. Again, this diagram is justified easily by a large number of

assessment points. For the foregoing related developments, the three failure categories of Hahn and Sarrate and their dividing lines were established.

Finally, the residual strength diagram was presented, where the failure stress is plotted as a function of the crack size. Again, the three failure categories and their dividing lines were established.

Though the term EPFM was introduced into fracture mechanics in connection with developments of the J-integral, we have used it in a more general sense: we have regarded EPFM as any approach to fracture mechanics in the elastic-plastic regime, that is, the regime between LEFM and PC. In this paper the approach we chose was through the plastic yield strip model of Dugdale.

Acknowledgments

This work was sponsored in part by the Federal Railroad Administration Office of Rail Safety Research.

References

[1] Hahn, G. T. and Sarrate, M. in *Practical Fracture Mechanics for Structural Steel, Proceedings of the Symposium on Fracture Toughness Concepts for Weldable Structural Steel*, M. O. Dobson, Ed., United Kingdom Atomic Energy Authority, Risley, 1969, pp. P1-P15.

[2] Dugdale, D. S., *Journal of the Mechanics and Physics of Solids*, Vol. 8, 1960, pp. 100-104.

[3] Bilby, B. A., Cottrell, A. H., and Swinden, K. H., *Proceedings of the Royal Society*, Vol. A272, 1963, pp. 304-314.

[4] Heald, P. T., Spink, G. M., and Worthington, P. J., *Materials Science and Engineering*, Vol. 10, 1972, pp. 129-138.

[5] Dowling, A. R. and Townley, C. H. A., *International Journal of Pressure Vessels and Piping*, Vol. 3, 1975, pp. 77-107.

[6] Dawes, M. G. in *Advances in Elasto-Plastic Fracture Mechanics*, L. H. Larsson, Ed., Applied Science Publishers, London, 1980, pp. 279-317.

[7] Harrison, R. P., Loosemore, K., and Milne, I., "Assessment of the Integrity of Structures Containing Defects," Central Electricity Generating Board Report No. R/H/R6, 1976; Revision 1, 1977; Revision 2, 1980.

[8] Tada, H., Paris, P. C., and Irwin, G. R., *The Stress Analysis of Cracks Handbook*, Del Research Corp., Hellertown, Pa., 1973.

[9] Irwin, G. R. in *Proceedings of the 7th Sagamore Ordnance Materials Research Conference*, Syracuse University Press, Syracuse, N.Y., 1961, pp. IV-63 to IV-78.

[10] Chell, G. G. in *Developments in Fracture Mechanics—I*, G. G. Chell, Ed., Applied Science Publishers, London, 1979, pp. 67-105.

[11] Burdekin, F. M. and Stone, D. E. W., *Journal of Strain Analyis*, Vol. 1, 1966, pp. 145-153.

[12] Burdekin, F. M. and Dawes, M. G. in *Practical Application of Fracture Mechanics to Pressure Vessel Technology*, Proceedings of the Institution of Mechanical Engineers Conference, 1971, pp. 28-37.

[13] Dawes, M. G., *Welding Research Supplement*, Vol. 53, 1974, pp. 369s-379s.

[14] Merkle, J. G., *International Journal of Pressure Vessels and Piping*, Vol. 4, 1976, pp. 197-206.

[15] Server, W. L. and Wullaert, R. A., *Engineering Fracture Mechanics*, Vol. 11, 1979, pp. 477-486.

[16] deWit, R. and Interrante, C. G. in *Proceedings of the CSNI Specialist Meeting on Instrumented Precracked Charpy Testing*, R. A. Wullaert, Ed., Electric Power Research Institute, Palo Alto, Calif., 1981, pp. 5.29-5.42.

[17] Harrison, R. P. and Milne, I. in *Fracture Mechanics in Engineering Practice*, P. Stanley, Ed., Applied Science Publishers, London, 1977, pp. 69-82.
[18] Harrison, R. P. and Milne, I., *Philosophical Transactions of the Royal Society of London*, Vol. A299, 1981, pp. 145-153.
[19] Milne, I. in *Developments in Fracture Mechanics—I*, G. G. Chell, Ed., Applied Science Publishers, London, 1979, pp. 259-301.
[20] Darlaston, B. J. L. in *Advances in Elasto-Plastic Fracture Mechanics*, L. H. Larsson, Ed., Applied Science Publishers, London, 1980, pp. 319-357.
[21] Burdekin, F. M. in *Developments in Pressure Vessel Technology—1: Flaw Analysis*, R. W. Nichols, Ed., Applied Science Publishers, London, 1979, pp. 63-95.
[22] Harrison, J. D., *Metal Construction*, Vol. 12, 1980, Part 1, pp. 415-418; Part 2, pp. 420-422; Part 3, pp. 524-529.
[23] Turner, C. E. in *Advances in Elasto-Plastic Fracture Mechanics*, L. H. Larsson, Ed., Applied Science Publishers, London, 1980, pp. 301-317.
[24] Turner, C. E. in *Post-Yield Fracture Mechanics*, D. G. H. Latzko, Ed., Applied Science Publishers, London, 1979, pp. 23-202.

A. Shukla[1] *and W. L. Fourney*[2]

Influence of Specimen Size and Stress Field on Energy Loss During a Fracture Event

REFERENCE: Shukla, A. and Fourney, W. L., **"Influence of Specimen Size and Stress Field on Energy Loss During a Fracture Event,"** *Fracture Mechanics: Fourteenth Symposium—Volume I: Theory and Analysis, ASTM STP 791*, J. C. Lewis and G. Sines, Eds., American Society for Testing and Materials, 1983, pp. I-51-I-64.

ABSTRACT: The influence of specimen size and stress field on energy loss away from the crack tip was studied using dynamic photoelasticity and fracture mechanics. The method of analysis utilized a balance of energy in the system. Experiments were conducted with three different sizes of modified compact tension (MCT) specimens, and it was found that energy loss increased with specimen size. Energy loss increased from 34 percent of total available energy to 48 percent as the specimen size was doubled.

The influence of stress field on energy loss was modelled by using different starter crack lengths in MCT specimens. It was observed that energy loss as well as crack propagation behavior are dependent on the stress field into which the crack propagates.

KEY WORDS: energy loss, photoelasticity, fracture mechanics, Homalite 100, specimen size, stress field, inefficiency ratio, compliance

The fundamental principles of classical thermodynamics indicate that a loss of energy is inevitable during any irreversible process. Recent work at the University of Maryland [*1,2*][3] has shown that energy loss away from the crack tip is quite significant in a fracture process and accounts for almost 40 percent of the initial strain energy present in a laboratory model. A knowledge of this energy loss is important in numerical studies [*3,4*] that utilize an energy balance approach to predict the stress-intensity factor at arrest and the crack jump distance. The energy loss will, of course, depend on several factors,

[1]Assistant professor, Department of Mechanical Engineering and Applied Mechanics, University of Rhode Island, Kingston, R.I. 02881.

[2]Professor and chairman, Mechanical Engineering Department, University of Maryland, College Park, Md. 20742.

[3]The italic numbers in brackets refer to the list of references appended to this paper.

such as the stress field into which the crack propagates, environmental conditions, specimen material, etc. In this paper we attempt to evaluate experimentally the influence of specimen size and the influence of the stress field on energy loss and crack propagation behavior in Homalite 100 fracture specimens.

It is possible to identify four major sources of energy dissipation away from the crack tip during crack propagation and the initial arrest phase. (1) If the dynamic modulus is different from the static modulus a loss of energy occurs when the system changes either from a static to a dynamic configuration or from a dynamic to a static one. (2) Energy can be lost by high frequency stress waves generated during the sharp drop in K from the high initial value K_Q, to the lower running crack value $K(t)$. (3) Energy is also lost because of the low amplitude stress waves that are released when microcracks form in the fracture process zone. (4) Energy is lost in transformation of energy (for example, from kinetic to potential) and in specimen vibration after crack arrest.

The investigation of energy loss away from the crack tip during rapid fracturing is of special interest with regard to evaluations of crack arrest toughness of structural steel. It is also of interest to predict the size of run-arrest crack extension, which occurs during rapid internal cooling of a cylindrical pressure vessel [5]. To enhance usefulness of this study in these applications, the specimen tested was a wedge loaded modified compact tension (MCT) specimen currently preferred for evaluations of crack arrest toughness. Moreover, this specimen is easy to load and the crack propagates straight without face grooves.

The experimental approach was relatively simple. An MCT specimen was loaded in fixed grip conditions and the initial strain energy U_i was determined. The crack was then initiated and the isochromatic fringe loops associated with the propagating crack were photographed with a high-speed recording system to obtain energy absorbed in forming the fracture surface E_f. After arrest and ring down, the strain energy U_a left in the specimen was determined from the final crack length. Finally, the total energy loss E_d was obtained from the energy balance

$$E_d = U_i - (U_a + E_f) \tag{1}$$

Three different sizes of MCT specimens were used to study the influence of specimen size on energy loss—normal, in accordance with the ASTM Standard Recommended Practice for R-Curve Determination (E 561-81), three-quarters, and 1.5 size. The lateral dimensions of the specimens were scaled so that the compliance characteristics did not change. The initial starter crack length-to-width ratio was kept the same in all experiments so that the cracks propagated into essentially the same state-of-stress field. Within this test series, several experiments were conducted in which the initial stress-in-

tensity factors and the initial strain energy were varied. In that way, the influence of these two parameters on crack jump distance and energy loss were investigated. A separate series of experiments was done in which the position of the starter crack length was varied. The influence of changing the initial crack length and hence the stress state into which the crack propagates was found to be significant with regard to both energy loss and crack jump distance.

Experimental Procedure

Specimen and Loading Fixture

The fracture specimen used throughout this study was an MCT specimen as shown in Fig. 1. The specimen was fabricated from a 12.7-mm-thick sheet of Homalite 100 whose properties have been characterized by Dally and Kobayashi [*6*].

The specimen was loaded with a transverse wedge and a split D, as shown in Fig. 2. The wedge was pulled between the two split D's with a hydraulic cylinder. The split D's were fitted in the circular hole in the MCT specimen. After the specimen was loaded to a specified value of U_i, the wedge was locked into a fixed position. This prevented any interaction between the loading system and the specimen during the fracture event. This condition is important for the validation of Eq 1. Besides locking the wedge, two contacting stops were placed along the load line on the outer edges of the specimen to reduce outward displacement during the propagation and arrest event. Subsequent trials showed there was no significant pressure against these stops prior to crack arrest. The experiment was initiated by drawing a sharp knife edge across the crack tip. Displacements of the split D were monitored with an eddy current transducer during the event to insure that fixed grip conditions were achieved. The fracture event was photographed with a high-speed multiple spark gap camera.

Compliance Calibration

The initial and final strain energy U in the specimen were determined from

$$U = \int_0^{\Delta} P d\Delta \tag{2}$$

which is the area under the load-displacement curves for the MCT specimen with a prescribed crack length a. To determine U, the relation between the load P and the split D displacement Δ was established with a compliance calibration. The load P was measured with a quartz load cell positioned between

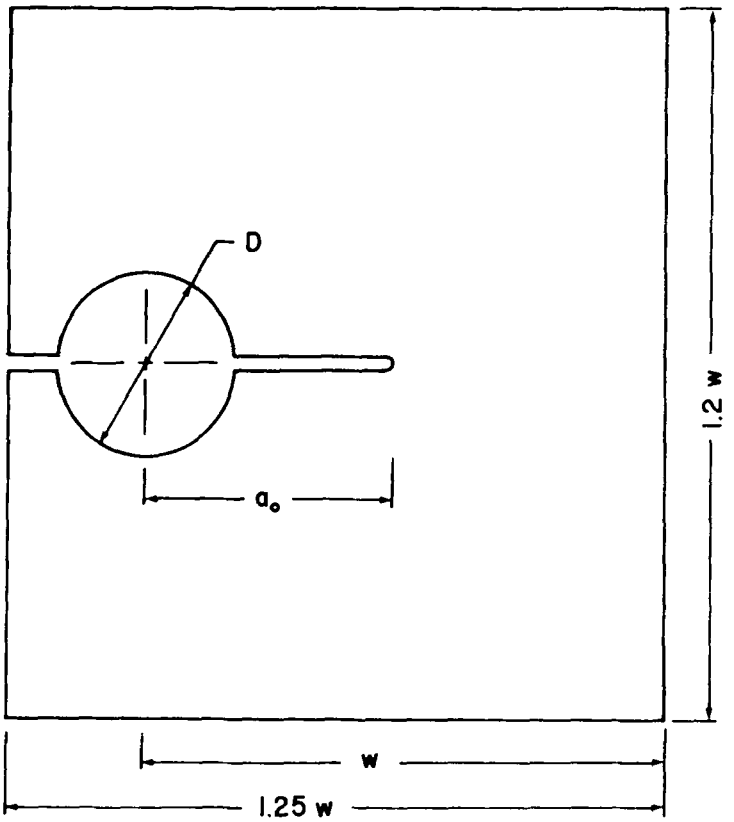

FIG. 1—*Geometry of the fracture specimen used to study the influence of specimen size on energy loss.*

the wedge and the split D fixture. The displacement Δ was measured with an eddy current transducer which bridged the gap on the split D fixture. Accuracies of ± 4 N and ± 0.025 mm were achieved in the determination of P and Δ, respectively. P-Δ curves were obtained for all the specimens, and the results are shown in Fig. 3. The nonlinearity in the curves is mainly due to the hertzian contact indentation between the loading pins and the specimen.

Fracture Energy Determination

The energy absorbed at the crack tip during crack propagation was determined from the photoelastic data obtained during the fracture experiment. Typical isochromatic fringes obtained during the experiment are shown in Fig. 4. These fringes were analyzed to get the value of stress-intensity factor K using a dynamic procedure similar to the one developed by Sanford and Dally [7]. Values of K^2 were plotted as a function of crack tip position for

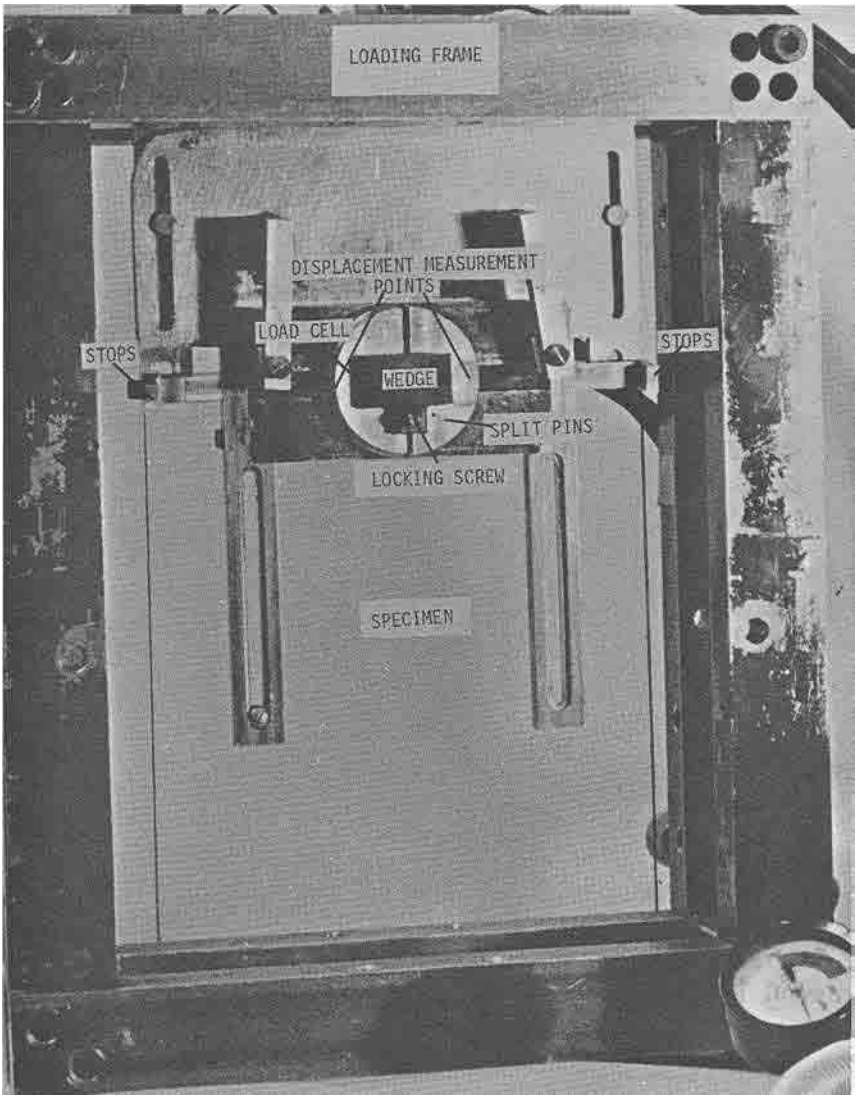

FIG. 2—*Loading fixture with the specimen.*

each experiment. A typical result is shown in Fig. 5. The energy E_f was then determined from

$$E_f = h \int_{a_0}^{a_f} K^2/E \, da \tag{3}$$

where

h = specimen thickness,
E = elastic modulus,

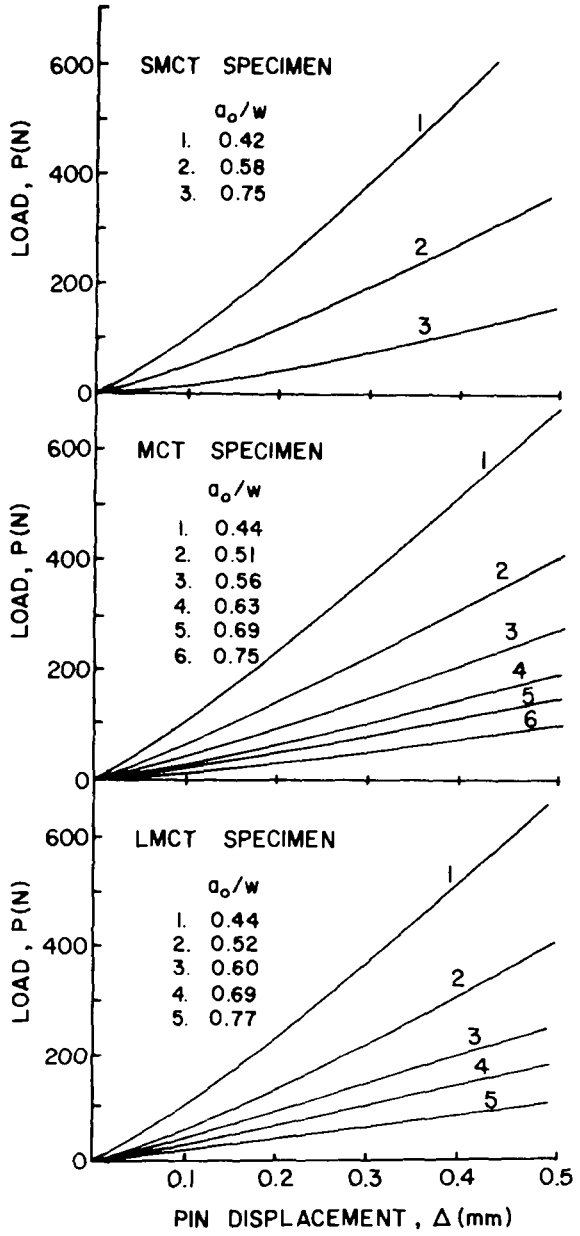

FIG. 3—*Compliance calibration curves for the three MCT specimens.*

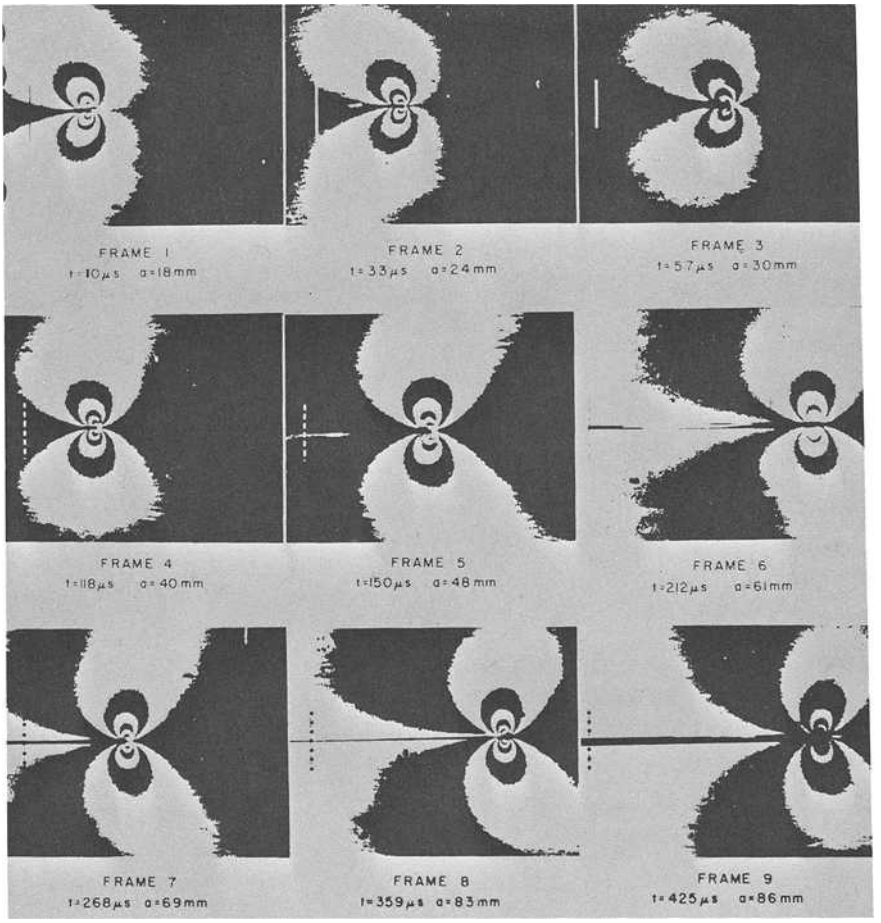

FIG. 4—*Typical isochromatic fringe patterns associated with the running crack.*

a_0 = initial crack length, and
a_f = final crack length.

Results of Dynamic Photoelastic Experiments

Small Modified Compact Specimens (SMCT)

Three experiments were performed to study energy loss and crack propagation in small specimens. The specimens were loaded to an initial strain energy of 0.113, 0.104, and 0.080 J. The photoelastic data obtained during the experiment were analyzed, and the results obtained are shown in Table 1. The results show that about 30 percent of initial strain energy present in the

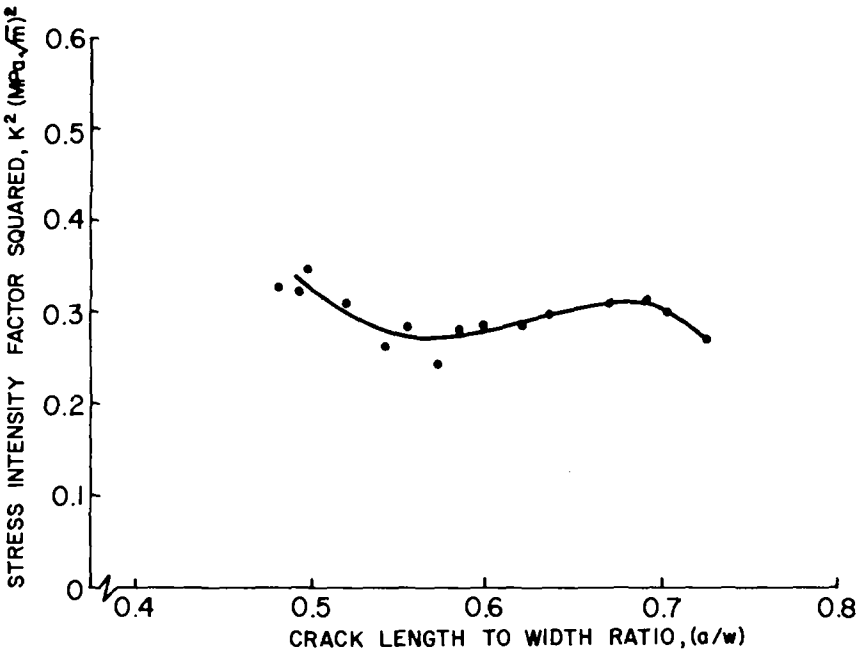

FIG. 5—*Stress intensity factor square,* K^2, *as a function of crack length to width ratio,* a/w.

TABLE 1—*Summary of results for the SMCT specimens.*

Experiment No.	K_Q,[a] MPa√m	A_f,[b] mm²	U_i, J	E_f, J	U_a, J	E_d, J	E_d/U_i, %	E_d/E_f, %	$E_d/(U_i - U_a)$, %
SMCT 1	0.87	934	0.113	0.068	0.014	0.031	28	46	31
SMCT 2	0.82	836	0.104	0.057	0.016	0.031	30	54	35
SMCT 3	0.71	747	0.080	0.043	0.013	0.024	30	56	36

[a] K_Q is the stress-intensity factor associated with the initial starter crack.
[b] A_f is the fracture surface area.

specimen is lost away from the crack tip during propagation and the initial arrest phase. The lost energy increases with the initial energy. Moreover, the ratio of damping energy to fracture energy was about 50 percent for this specimen. If the ratio of the damping loss E_d to the total used energy $(U_i - U_a)$ is defined as the inefficiency of the system, the inefficiency averaged about 34 percent.

Regular Modified Compact Specimens (MCT)

Four experiments were performed to study energy loss in regular sized MCT specimens. The initial strain energy in the specimens was varied from

0.164 to 0.133 J. The results obtained are given in Table 2, and show that about 37 percent of initial strain energy is lost in damping away from the crack tip. The results also verify that damping increases with initial energy. The ratio of damping energy to fracture energy was higher for this specimen as compared to the small specimens, and was about 74 percent. The inefficiency in the specimen was about 42 percent.

Large Modified Compact Specimens (LMCT)

Three experiments were performed with large specimens to complete the study of size effect on damping loss. The initial strain energy in the specimens was varied from 0.208 to 0.129 J. The results obtained are given in Table 3. The results show that about 41 percent of initial strain energy is lost in damping. The results again confirm that damping increased with initial strain energy. The damping energy was comparable to the fracture energy in all three experiments. The inefficiency ratio was higher for the large specimens as compared to the smaller specimens, and averaged about 48 percent.

Discussion of Results

The results obtained from these experiments show that energy loss does increase with specimen size. This would be expected since some energy is lost in internal friction when stress waves travel longer distances in the bigger specimen before they can come back to the crack tip. The inefficiency in the larger specimens was 48 percent, as compared to 42 percent in regular specimens and only 34 percent in smaller specimens. The energy loss was approximately

TABLE 2—*Summary of results for the MCT specimens.*

Experiment No.	K_Q, MPa$\sqrt{m}$	A_f, mm^2	U_i, J	E_f, J	U_a, J	E_d, J	E_d/U_i, %	E_d/E_f, %	$E_d/(U_i - U_a)$, %
MCT 1	0.780	778	0.134	0.059	0.024	0.051	38	86	46
MCT 2	0.813	940	0.140	0.072	0.018	0.050	36	69	39
MCT 3	0.857	1084	0.156	0.084	0.011	0.061	39	73	42
MCT 4	0.890	1157	0.164	0.092	0.012	0.060	37	65	39

TABLE 3—*Summary of results for the LMCT experiments.*

Experiment No.	K_Q, MPa$\sqrt{m}$	A_f, mm^2	U_i, J	E_f, J	U_a, J	E_d, J	E_d/U_i, %	E_d/E_f, %	$E_d/(U_i - U_a)$, %
LMCT 1	0.84	1812	0.208	0.102	0.017	0.089	43	87	47
LMCT 2	0.84	1832	0.197	0.104	0.011	0.082	42	79	44
LMCT 3	0.67	846	0.129	0.042	0.038	0.049	38	116	54

equal to the fracture energy in bigger specimens. In regular MCT specimens the energy loss was 75 percent of E_f, and in smaller specimens energy loss was only 50 percent of E_f. In all the experiments damping increased with increasing initial energy.

The specimen size seems to have a strong influence on the crack propagation behavior. For the same initial stress-intensity factor K_Q the crack jump obtained in bigger specimens was longer than in the small specimens. This is felt to be a result of higher initial strain energy in bigger specimens as compared to the smaller specimens for the same value of K_Q. This can be shown analytically as follows.

For the same initial crack length-to-width ratio [8]

$$\frac{K_{Q_1}}{K_{Q_2}} = \frac{P_1}{P_2}\frac{\sqrt{W_2}}{\sqrt{W_1}}$$

where 1 denotes the small specimen and 2 denotes the large specimen.

Therefore, for $K_{Q_1} = K_{Q_2}$

$$P_1 = P_2\sqrt{\frac{W_1}{W_2}}$$

since $W_1/W_2 < 1$

$$\therefore P_2 > P_1$$

Now, the compliance characteristics do not change if the lateral dimensions are scaled

$$\therefore \Delta_2 > \Delta_1$$

$$\therefore \text{strain energy } U_2 > U_1$$

This result is verified experimentally by the data given in Tables 1, 2, and 3.

Influence of State of Stress on Energy Loss

Six experiments were conducted to study the influence of stress field on energy loss during the fracture event. Previous studies [9] have shown that it becomes increasingly difficult to propagate a crack into a field of increasing compressive stress. This means that a substantial part of an increased initial strain energy is lost in damping as it is not used in forming new fracture surfaces.

The geometry of the specimen used in this study and its compliance characteristics are shown in Fig. 6. In this type of specimen the original compres-

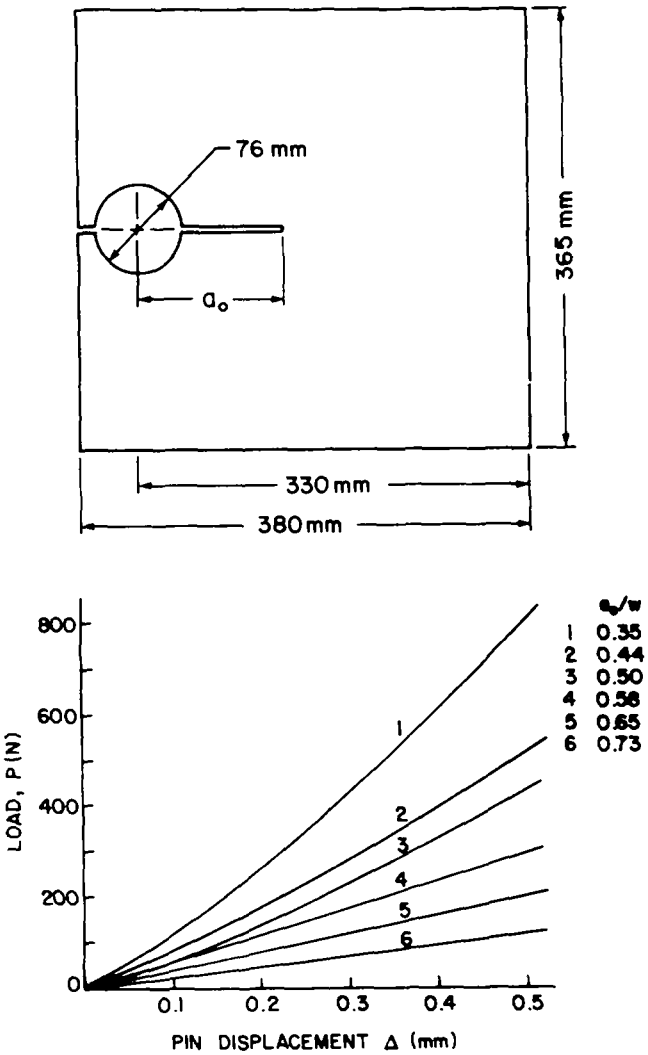

FIG. 6—*Geometry of the specimen used to study the influence of stress field on energy loss and its compliance characteristics.*

sive force at the crack tip position increases as the crack extends deeper into the specimen. Three different initial crack lengths were chosen for the dynamic series of experiments. The ratios of initial crack length to width decided upon were $a_0/W = 0.35$, 0.44, and 0.58. Three experiments were performed for the initial crack length of $a_0/W = 0.35$, two for $a_0/W = 0.44$, and one for $a_0/W = 0.58$. By increasing the initial crack length in the series of experiments, the crack was forced to propagate into an increasingly larger compressive stress field.

Results and Discussion

The data obtained during the dynamic experiments were analyzed to obtain the energy loss during the fracture event. The results shown in Table 4 indicate that energy loss increases with initial crack length. For $a_0/W = 0.35$, the energy loss was 30 percent of initial strain energy. This loss increased to 40 percent for $a_0/W = 0.44$ and to 45 percent for $a_0/W = 0.58$. The results also show that the energy loss becomes more and more comparable to the fracture energy as the initial crack length becomes larger. For the smallest crack length, energy loss was 60 percent of E_f. For intermediate crack length, it was 90 percent of E_f, and for the largest crack length the loss was 127 percent of E_f. The inefficiency increases as the initial crack length is increased. For $a_0/W = 0.35$ the inefficiency is 37 percent, which increased to 46 percent for $a_0/W = 0.44$, and then to 56 percent for $a_0/W = 0.58$.

The experiments also showed that the crack propagation behavior strongly depends on the initial starter crack length. For the same value of K_Q the smaller starter crack length gave a longer crack jump, and consequently a larger fracture surface as shown in Table 4 by the results of experiment B1 and B6 or B2 and B5. This is because the specimen with smaller crack length has more strain energy than the one with larger crack length for the same value of K_Q. Moreover, when the initial crack length is smaller, the crack initially propagates in a more favorable stress field. For longer initial crack length, the compressive gradient in the initial static stress field is steeper and crack propagation through it is more difficult.

Conclusions

Experiments conducted to study the influence of specimen size and stress field on energy loss and crack propagation behavior reached the following conclusions.

TABLE 4—*Summary of results for experiments to study the influence of state of stress on energy loss.*

Experiment No.	a_0/W	K_Q, MPa$\sqrt{m}$	A_f, mm^2	U_i, J	E_f, J	U_a, J	E_d, J	E_d/U_i, %	E_d/E_f, %	$E_d/(U_i - U_a)$, %
B1	0.346	0.844	2065	0.231	0.144	0.017	0.069	30	48	32
B2	0.346	0.789	1645	0.202	0.106	0.031	0.065	32	61	38
B3	0.346	0.710	1168	0.171	0.071	0.051	0.049	29	69	41
B4	0.438	0.677	935	0.159	0.063	0.030	0.065	41	103	50
B5	0.438	0.786	1290	0.201	0.095	0.024	0.081	40	85	46
B6	0.577	0.849	1210[a]	0.210	0.075	0.040	0.095	45	127	56

[a]First arrest.

1. Energy loss away from the crack tip increased with specimen size. The inefficiency increases from 34 to 48 percent with the change from three-quarters sized specimens to 1.5 times normal size.

2. Energy loss is 50 percent of fracture energy in small specimens, and increases to 75 percent in regular sizes, and then to 100 percent in large specimens.

3. All three sizes of specimen show that energy loss increases with initial energy.

4. For the same value of K_Q the crack jump obtained in bigger specimens was longer than in the small specimens.

5. The static compliance characteristics change as expected if the lateral dimensions of the specimen are scaled.

6. Energy loss depends on the initial crack length. The loss increases as the crack length is increased. The inefficiency increased from 37 percent for $a_0/W = 0.35$ to 56 percent for $a_0/W = 0.58$.

7. For the same value of K_Q smaller starter crack lengths gave a longer crack jump distance.

The dynamic fracture data during the experiment were obtained from the time of crack initiation [*10*] to crack arrest. For the range of crack lengths and the size of photoelastic data acquisition region in this specimen geometry, the accuracy in the fracture energy determination was within ± 5 percent.

There are some inherent difficulties in the experiments that introduce error in the results. Some energy might be lost in nonelastic deformation at the loading point. The value of elastic modulus used might not be exactly correct (± 5 percent). It should also be pointed out that a_0/W for SMCT specimens was not exactly the same as for MCT and LMCT specimens, which might change the results for this specimen slightly.

Acknowledgments

The authors wish to thank the Nuclear Regulatory Commission for its support under Subcontract 7778 through Oak Ridge National Laboratory. Partial support was also provided by the Minta Martin Fund at the University of Maryland.

References

[*1*] Dally, J. W. and Shukla, A., *Engineering Fracture Mechanics*, Vol. 13, pp. 807-817.

[*2*] Shukla, A., and Dally, J. W., *Experimental Mechanics*, Vol. 21, No. 4, April 1981, pp. 163-168.

[*3*] Popelar, C. H. and Gehlen, P. C., *International Journal of Fracture*, Vol. 15, No. 2, 1979, pp. 159-178.

[*4*] Kanninen, M. P., Popelar, C., and Gehlen, P. C. in *Fast Fracture and Crack Arrest, ASTM STP 627*, American Society for Testing and Materials, 1977, pp. 19-38.

[5] Cheverton, R. D. and Bolt, S. E., "Pressure Vessel Fracture Studies Pertaining to A PWR LOCA ECC Thermal Shock; Experiments TSE-3 and TSE-4, and Update of TSE-1 and TSE-2 Analysis," Heavy Section Steel Technology Program, Technical Report 46, ORNL/NUREG-22, Oak Ridge National Laboratory/Nuclear Regulatory Commission, Dec. 1977.

[6] Kobayashi, T. and Dally, J. W. in *Fast Fracture and Crack Arrest, ASTM STP 627,* American Society for Testing and Materials, 1977, pp. 257-273.

[7] Sanford, R. J. and Dally, J. W., *Engineering Fracture Mechanics,* Vol. 11, No. 4, 1979, pp. 621-633.

[8] Srawley, J. E., *International Journal of Fracture,* Vol. 12, June 1976, pp. 475-476.

[9] Dally, J. W., Shukla, A., and Kobayashi, T. in *Crack Arrest Methodology and Applications, ASTM STP 711,* American Society for Testing and Materials, 1978, pp. 161-177.

[10] Dally, J. W. and Shukla, A., *Mechanics Research Communications,* Vol. 6, No. 4, 1979, pp. 239-244.

M. G. Vassilaros,[1] *J. A. Joyce,*[2] *and J. P. Gudas*[1]

Experimental Verification of Tearing Instability Phenomena for Structural Materials

REFERENCE: Vassilaros, M. G., Joyce, J. A., and Gudas, J. P., **"Experimental Verification of Tearing Instability Phenomena for Structural Materials,"** *Fracture Mechanics: Fourteenth Symposium—Volume I: Theory and Analysis, ASTM STP 791*, J. C. Lewis and G. Sines, American Society for Testing and Materials, 1983, pp. I-65–I-83.

ABSTRACT: The objective of this investigation was to extend the range of tearing instability validation experiments utilizing the compact specimen to include high-toughness alloys. J-integral (J_I) tests of ASTM A106, ASTM A516 GR70, HY-80, and HY-130 steels were performed in a variably compliant screw-driven test machine. Results were analyzed with respect to the J_I-R curves of the materials, and various models of $T_{applied}$ for the compact specimen. Tearing instability theory was validated for these high-toughness materials. For the cases of highly curved J_I-R curves, it was shown that the actual value of $T_{material}$ at the point of instability should be employed rather than the average $T_{material}$ value. The $T_{applied}$ analysis of Paris and co-workers applied to the compact specimen appears to be nonconservative in predicting the point of instability, whereas the $T_{applied}$ analysis of Ernst and co-workers appears to be accurate, but requires precision beyond that displayed in this program. The generalized Paris analysis applied to the compact specimen and evaluated at maximum load was most consistent in predicting instability.

KEY WORDS: fracture mechanics, ductile fracture, elastic-plastic fracture, tearing instability, HY-80 steel, ASTM A106 steel, ASTM A516 steel, J-integral

Since its introduction by Paris and co-workers in 1979 [*1*],[3] the tearing instability concept has gained increasing analytical and experimental interest [*2,3*]. Tearing instability theory states that a flawed member will tear in a stable manner when loaded beyond J_{Ic} at limit load, where $T_{applied}$ is less than $T_{material}$. Crack instability will occur when $T_{applied}$ equals or exceeds the material tearing modulus. Experimental validation of tearing instability was developed by Paris and co-workers [*2*], and recently by Joyce and Vassilaros for

[1]Metallurgist and branch head, respectively, David Taylor Naval Ship Research and Development Center, Annapolis, Md. 21402.

[2]Associate professor, U.S. Naval Academy, Annapolis, Md. 21402.

[3]The italic numbers in brackets refer to the list of references appended to this paper.

steels, aluminum, and titanium [*3*] where $T_{material}$ was relatively low. The experiments of Joyce and Vassilaros employed the compact specimen in a variably compliant test apparatus where the upper limit of $T_{applied}$ was 30. These results showed that when $T_{applied}$ exceeded $T_{material}$, tearing instability was assured. For the materials included in that experiment, a region of limited instability was observed for a range of $T_{applied}$ below the average $T_{material}$, with a gradual reduction in severity of unstable behavior as $T_{applied}$ was reduced. The existence of limited instability was attributed to the variability of $T_{material}$ about the average value obtained from the J_I-R curve. It was shown that the best correlation of instability with prediction was obtained when $T_{material}$ was defined by the least-squares slope of the whole J_I-R curve which in those experiments extended to 5 mm of crack growth.

The objective of this investigation was to extend the range of tearing instability validation experiments utilizing the compact specimen to include structural alloys with very high fracture toughness and J_I-R curves. Further, the treatment of the experimental results was modified to include analysis of nonlinear J_I-R curves. Emphasis was placed on validating tearing instability with respect to $T_{applied}$ formulations utilizing limit load analysis, and a $T_{applied}$ formulation including specific details of the specimen load-displacement record.

The approach employed in this investigation was to evaluate the instability performance of ASTM A106, ASTM A516 GR70, HY-80, and HY-130 steels using the compact specimen. The experimental approach was similar to that of Joyce and Vassilaros in the use of the variably compliant screw-type test machine in the conduct of conventional unloading-compliance J_I-R curve tests [*3*]. The $T_{applied}$ formulations in this investigation included the generalized expression of Paris and co-workers [*2*], and a modification of this expression where crack-tip opening displacement is limited to crack-tip displacement present when $J = J_{Ic}$. Additionally, the model of Ernst and co-workers [*4*] using the key curve approach assuming separable load-displacement curves was included in this analysis. Analysis of experimental data was performed with both linear and power law function evaluations of $T_{material}$.

Experimental Procedure

Materials

The ASTM A106 steel used in this investigation was supplied in the form of 990-mm pipe product with wall thickness of 95 mm. The ASTM A516 GR70 steel was supplied in the form of 102-mm-thick plate, and the HY steels were supplied in the form of 25-mm plate. The test temperature and mechanical properties of these steels are shown in Table 1.

TABLE 1—*Mechanical properties of steels.*

Material	Modulus, GPa	Flow Stress, MPa	J_{Ic}, kJ/m^2	$T_{material}$, Average over 5 mm of Crack Extension, 20 percent side-grooved Compact Specimens
HY-130	200	1000	150	10
HY-80	200	655	210	70
ASTM A106	200	550	340	170[a]
ASTM A516	200	450	100	50

[a]No side grooves.

Testing Procedure

All the J-integral fracture tests were conducted with 1T compact specimens, shown in Fig. 1, using the single specimen computer interactive unloading compliance method of Joyce and Gudas [5]. The ASTM A106 steel was tested in the L-C orientation, and the remaining steels were tested in the T-L orientation. The results of each unloading compliance test were plots of load versus load line crack-mouth opening displacement, load versus test machine head displacement, and a J_1-R curve that included corrections for specimen rotation [6] and crack growth. J_1 was calculated according to the expression [4]

$$J_{(i+1)} = \left[J_i + \left(\frac{\eta}{b}\right) i \frac{A_{i,i+1}}{B_N}\right]\left[1 - \left(\frac{\gamma}{b}\right) i (a_{i+1} - a_i)\right] \tag{1}$$

where

$\eta = 2 + (0.522)\, b/W$ for compact specimens,
W = specimen width,
$\gamma = 1 + (0.76)\, b/W$,
b_i = instantaneous length of remaining ligament,
B_N = minimum specimen thickness,
a_i = instantaneous crack length, and
$A_{i,i+1}$ = area under the load versus load line displacement record between lines of constant displacement at points i and $i + 1$.

Table 2 presents the test matrix employed in this investigation. Conventional J-integral tests were conducted on at least two and usually three specimens from each of the seven groups shown in Table 2. These tests were conducted in a stiff screw-driven test machine. Each test was concluded after a minimum 5 mm of stable crack extension was measured. The ASTM A106, HY-80, and HY-130 steels were tested at room temperature, and the ASTM A516 steel was tested at 150°C.

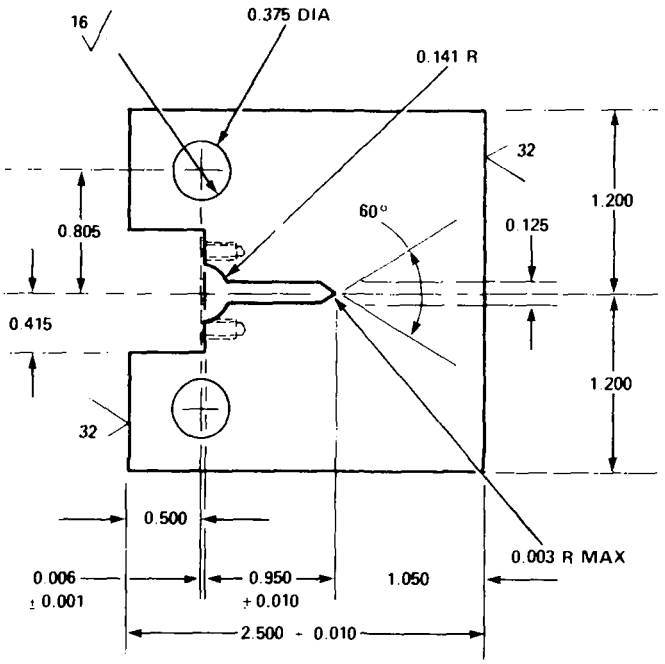

FIG. 1—*Modified compact specimen (ITCT) for J-integral testing.*

TABLE 2—*Test matrix for tearing instability experiments.*

Material	a/W	Side Grooves, %	Test Temperature, °C
HY-130	0.80	0, 20	room temperature
HY-80	0.65	0, 20	room temperature
ASTM A516	0.65	0, 20	150
ASTM A106	0.65	0	room temperature

The tearing instability tests were conducted with a screw-driving test machine which was modified to accept a variable stiffness spring in the load train as shown in Fig. 2, and previously reported by Joyce and Vassilaros [*3*]. The stiffness of the spring was controlled by the span of the two rollers separating the flex plates. Short spans produced high stiffnesses and large spans produced low stiffnesses. This variable stiffness spring controlled the applied tearing force ($T_{applied}$) induced during the fracture tests.

The conventional J-integral test program was modified to calculate the machine compliance and the $T_{applied}$ according to the formulation from Paris and co-workers [*1*]. This $T_{applied}$ expression was a function of the machine stiffness, applied J_I, and crack length from each unloading. The machine compliance was calculated by measuring the total system crosshead deflection versus applied load during the initial loading of a specimen, and sub-

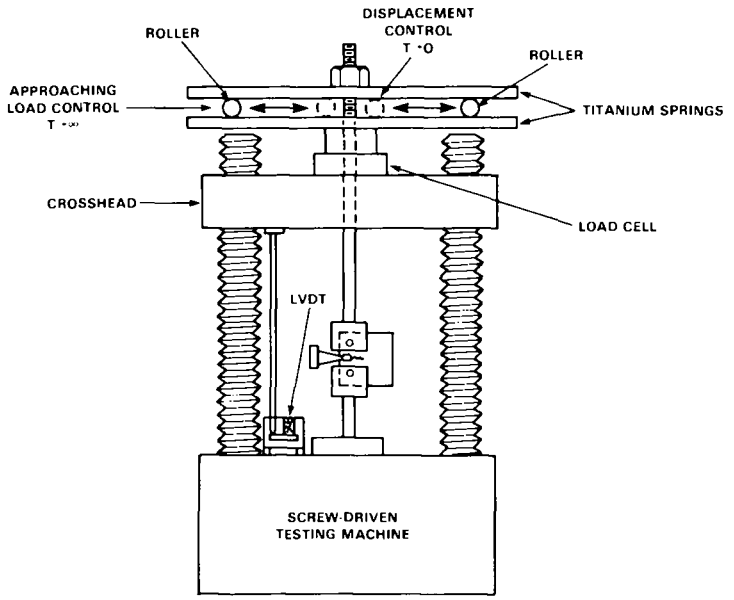

FIG. 2—*Variably compliant test machine arrangement.*

tracting the specimen compliance. In addition to the digitally recorded data, an analog plot of load versus crosshead displacement was recorded during each test. This plot supplemented the load crack-mouth opening displacement curves and was used to identify instability events during each test.

Formulation for $T_{applied}$

Three formulations for $T_{applied}$ were investigated in this study. Two of these were derived from the published work of Paris and co-workers [*1*], which assumed elastic-fully-plastic material behavior to predict $T_{applied}$. These expressions will be referred to as $T_{applied}$ Paris, and $T_{applied}$ Paris (modified), with distinctions to be discussed later. The third formulation was derived from the work of Ernst and co-workers [*4*]. This expression utilizes actual load-displacement data to measure the $T_{applied}$ and is referred to as $T_{applied}$ Ernst. The derivations of the expressions are described later.

The equation for $T_{applied}$ Paris for a compact specimen loaded in a compliant displacement controlled machine was taken from Paris and co-workers [*1*], who gave the general relationship that

$$T_{applied} = \frac{E}{\sigma_0^2}\frac{\partial J}{\partial a} = -\frac{W}{\alpha^* g(a/W)}$$

$$\left[\frac{\partial}{\partial a}[h(a/W) \times f(a/W)] \times \frac{EB}{K_M}\frac{\partial h\,(a/W)}{\partial a} + \frac{\alpha^* JE}{W\sigma_0^2}\frac{\partial g(a/W)}{\partial a}\right] \quad (2)$$

where

E = elastic modulus,

$\sigma_0 = \dfrac{\sigma_{ys} + \sigma_{ut}}{2}$ = flow stress,

B = specimen thickness, and

K_M = test machine stiffness.

The $g(a/W)$ function relates to the plastic component of specimen displacement, Δ_{PL}, such that

$$\Delta_{PL} = \delta_t g(a/W) \tag{3}$$

From the work of Merkle and Corten [7]

$$g(a/W) = \frac{(2W/W - a + \alpha - 1)}{1 + \alpha} \tag{4}$$

where

δ_t = crack opening stretch and

$\alpha = [[4a^2 + 4a(W - a) + 2(W - a)^2]^{1/2} - (a - W)]/(W - a)$.

The $h(a/W)$ function gives the plastic limit load as

$$P_{\text{lim}} = \sigma_0 BW h(a/W) \tag{5}$$

where

$$h(a/W) = (1 - a/W)\alpha \tag{6}$$

Finally, the $f(a/W)$ expression is the elastic compliance expression of the compact specimen taken from Saxena and Hudak [8]

$$f(a/W) = \left(\frac{1 + a/W}{1 - a/W}\right)^2 [2.16299 + 12.219(a/W)^1 - 20.065\,(a/W)^2 - 0.9925\,(a/W)^3 + 20.609\,(a/W)^4 - 9.9314\,(a/W)^5] \tag{7}$$

An expression for δ_t was taken from Paris [1] and Rice [9] as

$$\delta_t = \alpha^* \frac{J}{\sigma_0} \tag{8}$$

where $\alpha^* = 1$ for plane stress, and 0.7 for plane strain. The derivatives required for Eq 2 were obtained from Eqs 3 to 7 in closed form as needed, and

are expressed completely in Ref *1*. This model assumes an elastic-rigid-plastic nonhardening material behavior and accurately defines the T_{applied} only when the specimen is loaded at its limit load. This model is referred to as the Paris model in this work.

A modified Paris model is used to analyze the experimental results reported here in which the previous expression for δ_t is replaced by the following

$$\begin{aligned} \delta_t &= \alpha^* \frac{J}{\sigma_0} \qquad J \le J_{\text{Ic}} \\ \delta_t &= \alpha^* \frac{J_{\text{Ic}}}{\sigma_0} \qquad J > J_{\text{Ic}} \end{aligned} \tag{9}$$

This corresponds to a constant opening angle assumption of crack-tip behavior beyond the point of crack initiation and addresses an apparent limitation of the Paris model which exaggerates the contribution beyond J_{Ic}. Therefore, the only difference between the T_{applied} Paris and Paris (modified) expressions is in the extent of the plastic contribution to T_{applied} beyond J_{Ic}. The Paris (modified) expression exhibits a smaller drop in T_{applied} with crack extension.

The third model used to evaluate T_{applied}, that of Ernst and co-workers [*4*], uses a key curve approach by assuming that the load displacement curve for a compact specimen can be expressed in the form

$$P = \frac{b^2}{W} F(\delta/W, a/W) \tag{10}$$

where δ is the load-line crack-opening displacement (COD) value. This expression assumes that the dependence of the two variables can be separated to give a load-displacement relationship of the form

$$P = \frac{b^2}{W} G(a/W)\, H(\delta/W) \tag{11}$$

Based on experimental results of Landes and co-workers [*10*], $G(a/W)$ is taken by Ernst to have the form

$$G(a/W) = e^{0.522(W-a)/W} = e^{0.522b/W} \tag{12}$$

and

$$P = \frac{b^2}{W} e^{0.522b/W} H(d/W) \tag{13}$$

Substituting this form into the equation for the J-integral and developing an equation for T_{applied} gives [*4*]

$$T_{\text{applied}} = \frac{E}{\sigma_0^2}\frac{dJ}{da} = \frac{E}{\sigma_0^2}\left\{-\gamma\frac{J}{b} + \frac{\eta^2}{b^2} P \frac{1}{H'/WH + K_M/P}\right\} \tag{14}$$

where

$H' = dH/d(\delta/W)$

P is applied load and J is evaluated from Eq 1. The quantity H'/H can be evaluated from the load displacement curve and J-R curve of the specimen as

$$\frac{H'}{H} = \frac{1}{P}\frac{dP}{d\delta} + \frac{\eta^2 P}{b^2}\left(\frac{dJ}{da} + \gamma\frac{J}{b}\right) \tag{15}$$

where

$dP/d\delta$ = the slope of the load displacement curve and
dJ/da = the slope of the material J-R curve.

Calculation of $T_{applied}$ from the Ernst model requires a load-displacement record for each specimen, knowledge of the test machine stiffness, and a J_I-R curve. In this program, the J_I-R curve slope, dJ/da, was evaluated by using the power law fit described by Carlson and Williams [*11*] that

$$J = A_1(\Delta a/B)^A 2 \tag{16}$$

This fit then was applied to the unloading compliance J_I-R curve data as shown in Fig. 3. This equation then is differentiated to give

$$\frac{dJ}{da} = (A_1 \times A_2)\left(\frac{\Delta a}{B}\right)^{(A_2-1)} \tag{17}$$

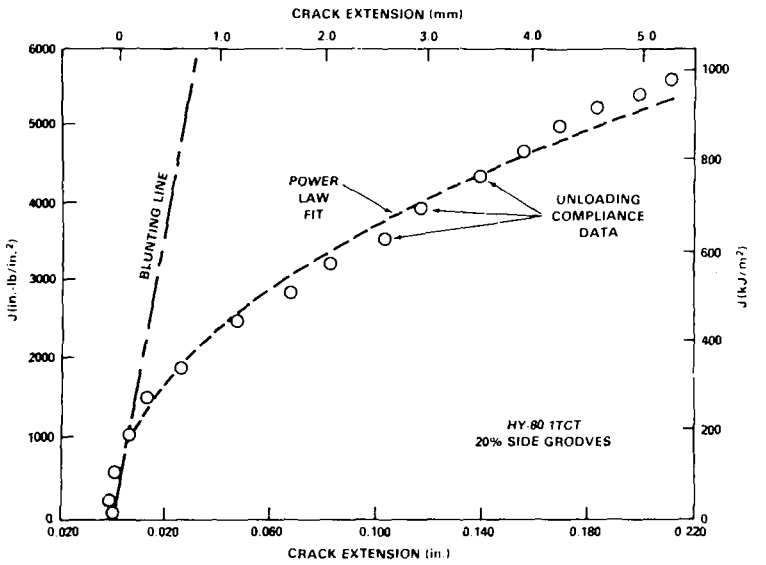

FIG. 3—*Power law fit of J-integral R-curve data for HY-80 steel.*

and

$$T_{\text{mat}} = \frac{E}{\sigma_0^2} \times \frac{dJ}{da} = \frac{EA_1A_2}{\sigma_0^2} \left(\frac{\Delta a}{B} \right)^{(A_2-1)} \tag{18}$$

in terms of the fitting coefficients A_1 and A_2.

Results and Discussion

Description of Specimen Instability Behavior

During the loading of the specimens, three general types of load versus displacement behavior were demonstrated as shown in Fig. 4. The results shown in Fig. 4*a* were from a J_I-R curve test of HY-130 performed in a rigid test machine with the condition that T_{material} was much greater than T_{applied}. The curve was constructed from digital data taken at 0.5-s intervals. These data points were spaced regularly and closely, reflecting stable response of the specimen to the constant crosshead rate used in all these tests.

For the cases where T_{applied} approached T_{material} (but still less than T_{material}) the behavior shown in Fig. 4*b* was observed. This behavior was characterized by repeated rapid steps of crack growth of relatively small magnitude, typically on the order of 0.1 to 0.5 mm, with larger steps being observed as T_{applied} more closely approached T_{material}. The quick jumps of crack growth appeared as gaps in the load versus COD plot shown in Fig. 4*b*. Each jump was accomplished in much less than the 0.5-s data acquisition interval.

The specimens tested with the T_{applied} greater than T_{material} produced the type of load versus displacement shown in Fig. 4*c*. At or near maximum load, instability occurred producing an increment of crack extension large enough either to separate the specimen completely or leave only a small remaining ligament. This sudden unstable crack extension is shown in Fig. 4*c* as the blank region to the right of the load displacement data.

Figs. 4*a* and *b* show that the load displacement records for stable specimens and specimens with limited instability are similar in shape in spite of the presence of the small instabilities, and likewise the J_I-R curves obtained from stable and limited instability specimens are similar in shape, as shown in Fig. 5 for HY-80. This insensitivity of the J_I-R curve to the T_{applied} was seen for all materials tested.

Both macroscopic observation and scanning electron microscopy of all materials studied here showed that the fracture surfaces were fully ductile and very similar whether they resulted from the stable tearing fracture, or the rapid instability. No evidence of cleavage was observed in any of the test specimens either near the beginning of the unstable tearing, or during the growth of the rapidly propagating crack.

The results of the complete series of 32 tests are plotted in Fig. 6, with each

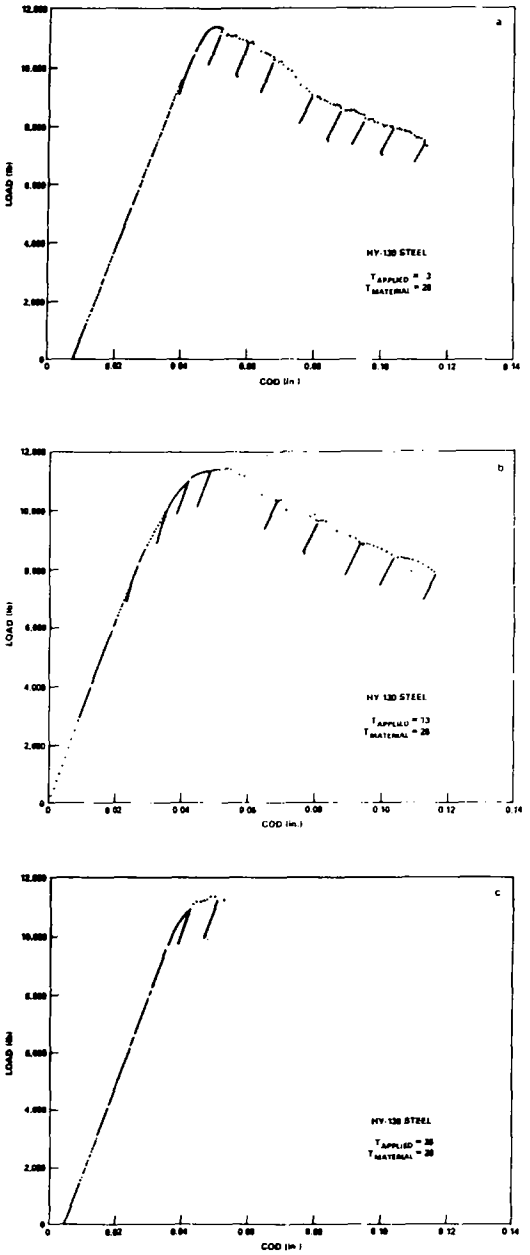

FIG. 4—*Load versus load-line displacement data for HY-130 steel specimens tested under various* $T_{applied}$ *conditions.*

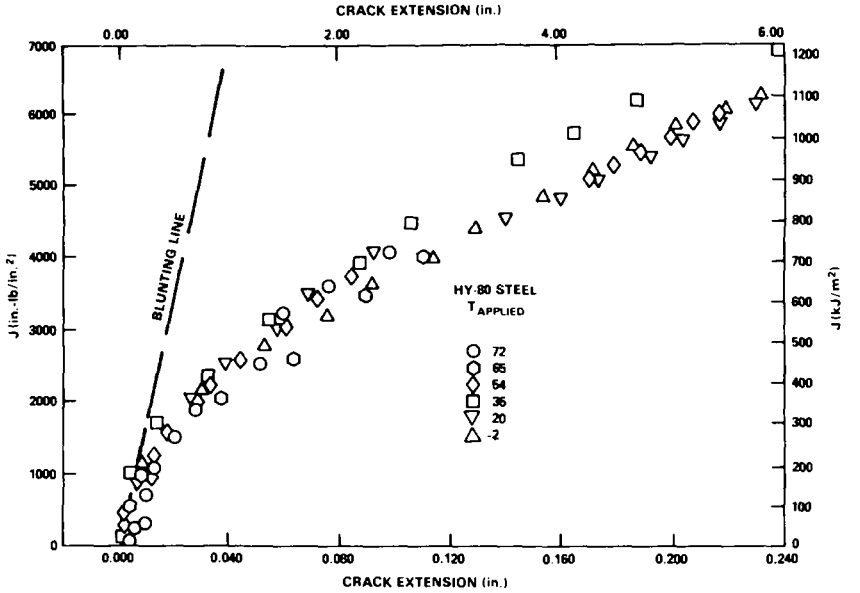

FIG. 5—*J-integral R-curve data for HY-80 steel specimens obtained under various* $T_{applied}$ *conditions.*

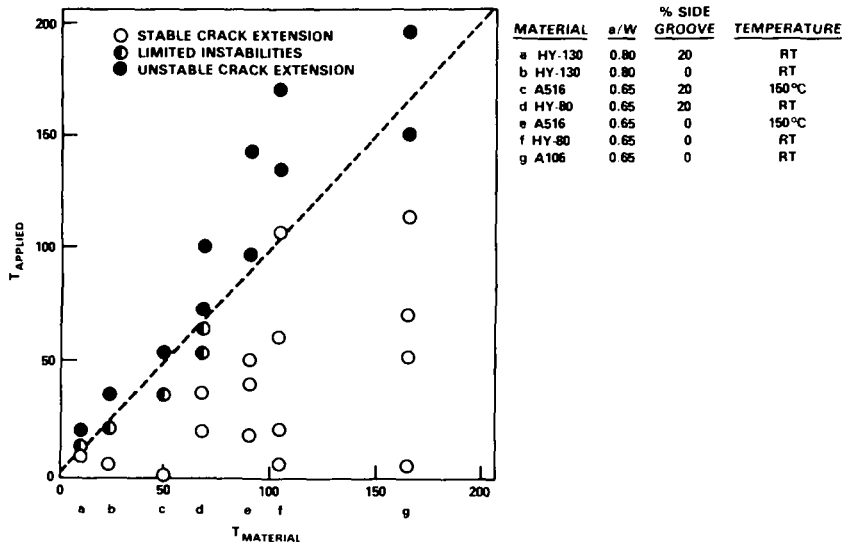

FIG. 6—$T_{applied}$ *versus* $T_{material}$ *calculated from the* J_I*-R curve slope taken to crack extension of 5.0 mm.*

point representing a single specimen. Solid points denote specimens which demonstrated instability to such a degree that the tests were stopped. The half-filled data points represent tests which demonstrated limited instabilities. The open data points represent specimens that behaved in a stable fashion throughout the test, as they would have been expected to behave in a typical stiff test machine. The abscissa of Fig. 6 is the $T_{material}$ obtained from the linear fit of the crack extension portion of a stable J_I-R curve to 5-mm crack extension. The ordinate of Fig. 6 is the $T_{applied}$ calculated at maximum load from the expression of Paris and co-workers [*1*], Eq 2.

There are four points of interest to be drawn from Fig. 6 which reconfirm the conclusion of earlier tearing instability results by Joyce and Vassilaros [*3*]. In the first place, the data demonstrate the effectiveness of the Paris tearing instability criterion in that when $T_{material}$ was less than $T_{applied}$, unstable fracture behavior usually occurred. The second point concerns the effects of side grooves which reduced the $T_{material}$ values when employed. The specimens tested with 20 percent side grooves required a lower $T_{applied}$ to produce unstable behavior when compared to planar specimens of the same material. This is consistent with the results of Gudas and co-workers evaluating the effects of compact specimen geometry on the J_I-R curve of several steels [*12*]. The third key point is the existence of the region of limited instability behavior where $T_{applied}$ approaches $T_{material}$ in value. The relative extent of this region appears to be much smaller than was observed in Ref [*3*] performed on materials with lower $T_{material}$ values ($T_{material}$ less than 30). It appears that the nature of the limited instability regime is a band occupying the region where $T_{applied}$ is slightly less than $T_{material}$, with a width of 10 to 30 "T units." The band appears to disappear when materials with high $T_{material}$ values are tested. This is a result of the relative shrinking of the fixed width of the limited instability region compared to the larger $T_{material}$ values.

The final point in reviewing Fig. 6 is the presence of data denoting crack instability well above the prediction line. These points are not physically realizable, and their existence will be examined with respect to actual J_I-R curves, and the predictions for $T_{applied}$. To carry out this analysis, the first point to be examined will be the method to evaluate $T_{material}$.

The materials tested which had high $T_{material}$ values, such as ASTM A106 and HY-80 steels, are not described accurately by a single $T_{material}$ value resulting from a linear regression analysis due to the significant curvature in their J_I-R curves. This point is illustrated by Fig. 7 which shows $T_{material}$ versus crack extension developed from power-curve fit data from separate tests of HY-130 and ASTM A106 steels. It can be seen that the average $T_{material}$ for ASTM A106 steel is not a reasonable approximation of the $T_{material}$ over the range of crack extension. However, the average $T_{material}$ for HY-130 steel more closely approximates the $T_{material}$ value over the whole range of crack extension. This suggests that the instability analysis of materials with highly

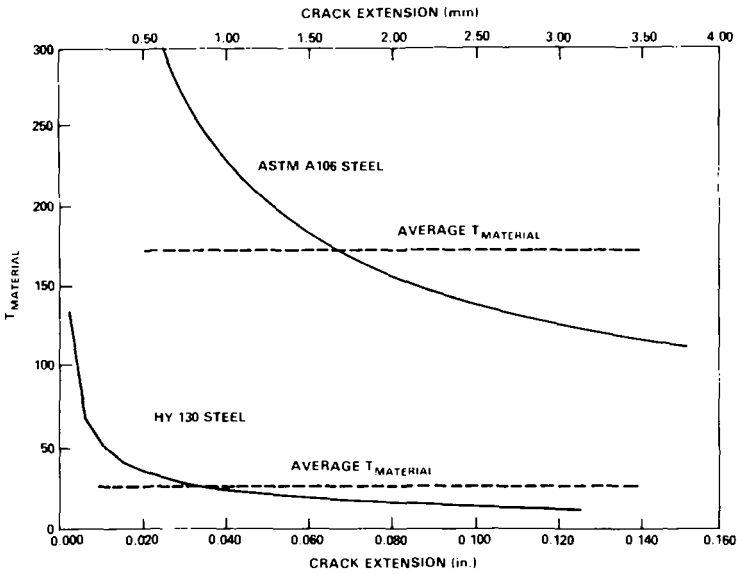

FIG. 7—$T_{material}$ *versus crack extension data for compact specimens of HY-130 and ASTM A106 steels.*

curved J_I-R curves should be performed with the measured $T_{material}$ value at the point of instability.

Reanalysis of the data for the tests resulting in instability for HY-80, ASTM A106, and ASTM A516 steels was carried out by evaluating $T_{material}$ at the point of instability using power curve fits of unloading compliance data from individual specimen tests. Fig. 8 shows an example of such a curve for an HY-80 steel specimen. The first derivative of the power law function, Eq 17, evaluated at the crack extension at instability was used to calculate $T_{material}$. This value then was compared with the $T_{applied}$ value calculated at maximum load from Eq 2. Figure 9 shows the relation between $T_{applied}$ and $T_{material}$ from this reanalysis. This treatment clearly brings the instability points in closer agreement with the prediction. This observation strengthens the validity of the Paris tearing instability theory which predicts immediate instability whenever $T_{applied}$ exceeds $T_{material}$ after maximum load.

The $T_{applied}$ analysis previously reported by Joyce and Vassilaros and utilized in the evaluation of test results in this program was a modification of the generalized formulation of Paris and co-workers [*1*] applied to the compact specimen. One of the objectives of this investigation was to examine more thoroughly the $T_{applied}$ formulations for the compact specimens using the analysis of Paris and co-workers [*1*], and the recent analysis of Ernst and co-workers [*4*]. The $T_{applied}$ formulation from Paris depends on J_I and crack

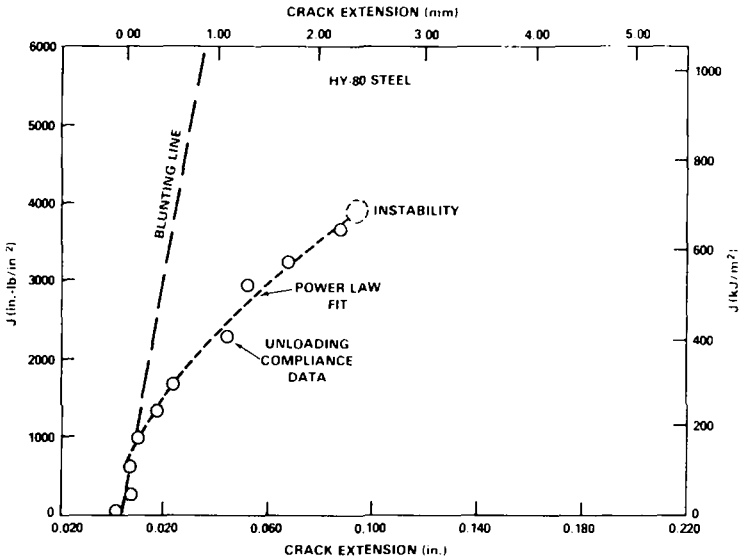

FIG. 8—*Power law fit of J-integral R-curve data for an HY-80 steel specimen which exhibited unstable crack extension.*

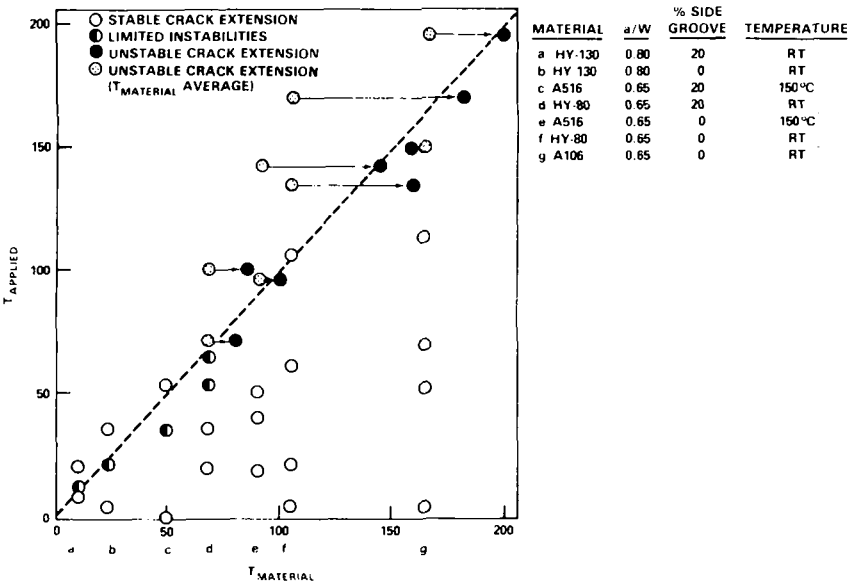

FIG. 9—$T_{applied}$ *versus* $T_{material}$ *calculated at the point of instability.*

length, and varies as these quantities vary throughout the course of a specimen test. The $T_{applied}$ analysis of Ernst depends on these quantities as well as the slope of the load displacement record and the slope of the material J_I-R curve at each instant. Plots of these models of $T_{applied}$, including the third model introduced here for which J_I is limited to be less than or equal to J_{Ic} when evaluating the Paris model, are shown in Figure 10.

Figure 11 shows J_I versus T for two specimen tests of ASTM A106 steel. This J/T analysis is presented in the manner suggested by Paris [*13*], and instability would be expected when the value of $T_{applied}$ exceeds the $T_{material}$ curve. Figure 11*a* shows that in the case where $T_{applied}$ values from all formulations were less than $T_{material}$, stable crack extension was observed during test. In Fig. 11*b*, which shows results of a specimen which exhibited unstable crack extension, the Ernst analysis predicted instability, while the Paris and modified Paris analysis appeared to be unconservative and predicted stable crack extension. The Paris $T_{applied}$ value evaluated at maximum load is noted and seen to be consistent with the Ernst analysis for this case.

Similar data for HY-80 steel specimens exhibiting stable and unstable crack extension are shown in Fig. 12. Again, in this instance, where all three analyses predicted stability, slow stable tearing occurred with the compact specimen. In the case of the instability observed in Fig. 12*b*, the Ernst expression predicted instability at 300 KJ/m^2, whereas the actual instability occurred at a J_I value of 600 KJ/m^2.

To understand this discrepancy, it is illustrative to examine the individual

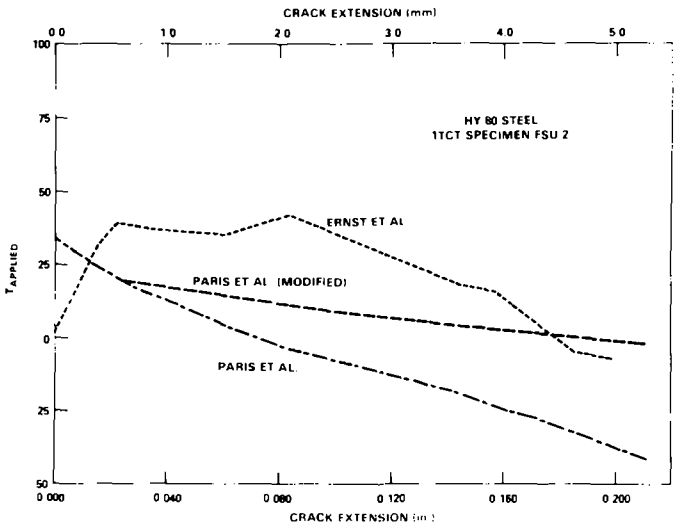

FIG. 10—$T_{applied}$ *versus crack extension according to the models of Paris and co-workers and Ernst and co-workers.*

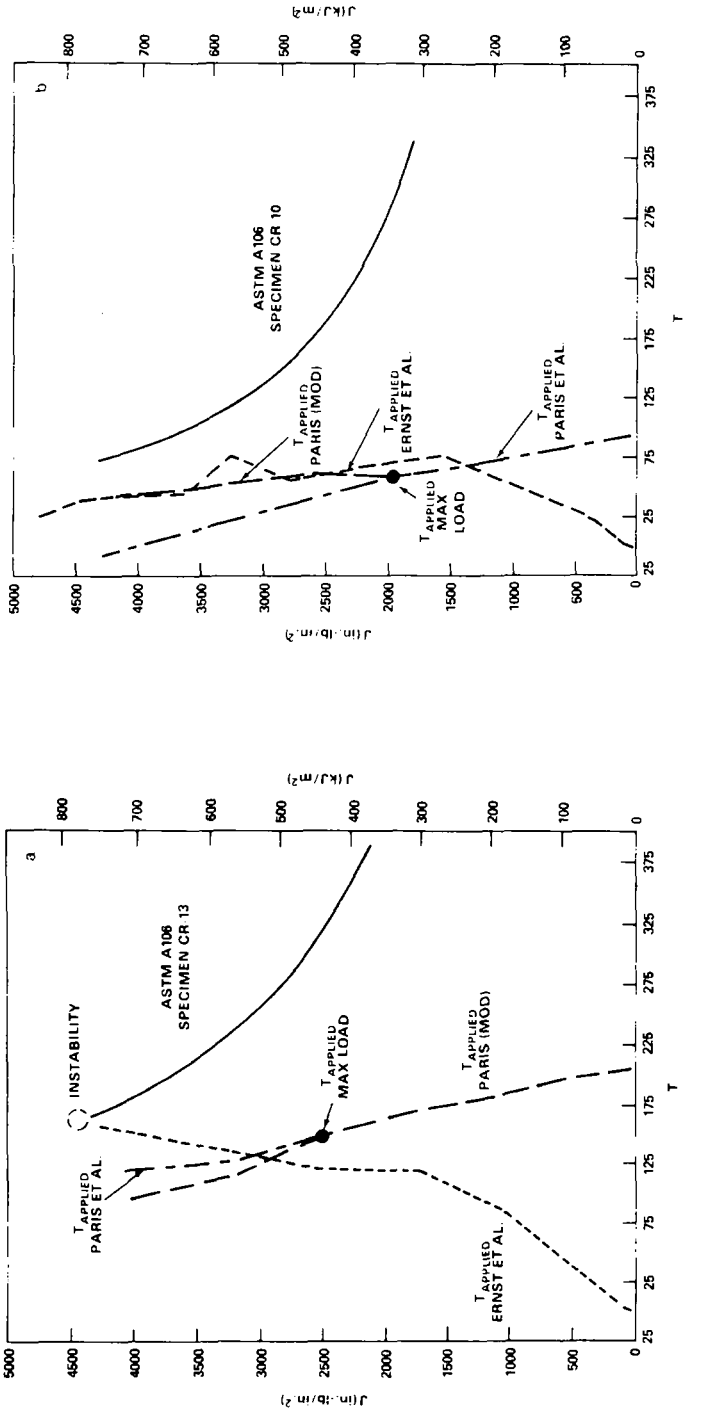

FIG. 11—J_1 *versus* T *for ASTM A106 steel specimens.*

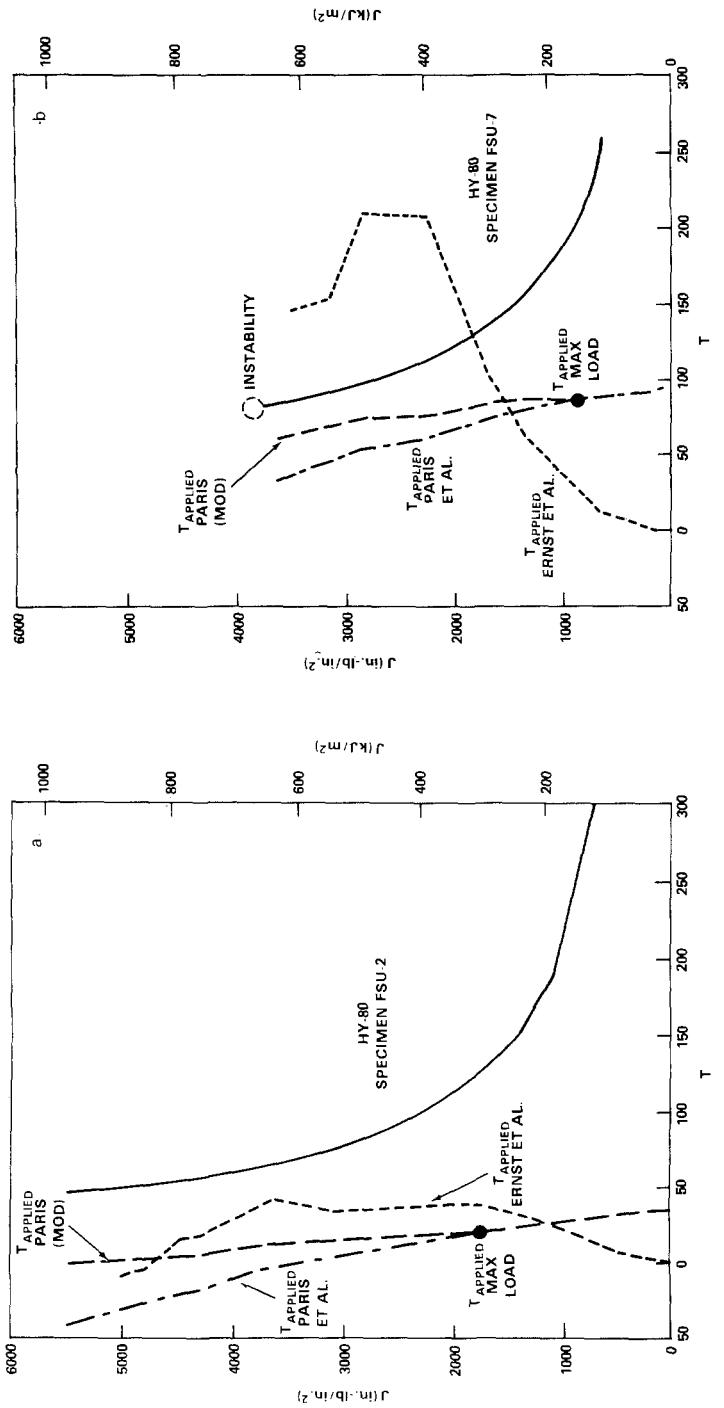

FIG. 12—J_I *versus* T *for HY-80 steel specimens.*

terms of the $T_{applied}$ expressions of Ernst and co-workers. Equations 14 and 15 can be combined and restated as

$$T_{applied} = -\frac{\gamma EJ}{\sigma_0{}^2 b} + \frac{\eta^2 PE}{b^2 \sigma_0 2}\left[\frac{1}{\frac{K_M}{P} + \frac{1}{P}\frac{dP}{d\delta} + \frac{\eta^2 P}{b^2}\left(\frac{dJ}{da} + \gamma\frac{J}{b}\right)^{-1}}\right] \quad (19)$$

For normal tests of tough materials in stiff test machines, the $T_{applied}$ values are small because the K_M/P term is much larger than the other two terms in the bracketed expression. In a reduced stiffness test, all three terms of the bracketed expression can approach the same order of magnitude. At maximum load, the K_M/P term becomes a minimum, and the $1/P\ dP/d\delta$ terms becomes zero, then negative. Cancellation between these terms apparently could produce a singularity in $T_{applied}$ if the denominator of the bracketed term went to zero. For the specimen shown in Fig. 12*b*, the bracketed term approached unity, which is on the order of the error expected in the calculation of 1/P $dP/d\delta$ given the presence of unloadings which perturbed the load-displacement curve as shown in Fig. 4. In certain cases, the algebraic sum of the bracketed terms approaches the order of errors in estimation of the individual terms. In such instances, the $T_{applied}$ values have large uncertainty, which accounts for such discrepencies as noted in Fig. 12*b*.

In reviewing the experimental results and the analysis for $T_{applied}$, the following observations are noted. In the first place, the drop in $T_{applied}$ of the Paris model (and its modification) beyond maximum load was not verified experimentally. It was observed experimentally that instability occurred when $T_{material}$ falls to the value of $T_{applied}$ of the Paris model evaluated at maximum load. All tests in this program were evaluated at this point and this analysis produced the most consistent results.

The Ernst $T_{applied}$ model demonstrated both rising and falling $T_{applied}$ values beyond maximum load. Fluctuations in $T_{applied}$ are relatively large due to the sensitivity to the slope of the specimen load-displacement record, and to errors present in the experimental method employed here to estimate this slope. The Ernst method appears to be accurate, but in this case imprecise due to the experimental method employed in this program. In order to estimate best the point of instability of the compact specimen, the Paris model taken at maximum load appears to provide both conservative and consistent results.

Conclusions

The results of this investigation point to the following conclusions:

1. Tearing instability theory has been validated for materials which have high tearing modulii.

2. The region of limited instability appears to be reduced or eliminated with materials exhibiting high tearing modulii.

3. For the case of highly curved J_I-R curves, the average $T_{material}$ value is not an accurate predictor of instability. Rather, the instantaneous $T_{material}$ value should be employed.

4. The Paris analysis beyond maximum load applied to the compact specimen is nonconservative in predicting the point of instability. The Ernst analysis for $T_{applied}$ appears to be accurate, but requires precision beyond that utilized in this experimental program.

5. The generalized Paris analysis applied to the compact specimen and evaluated at maximum load was most consistent in predicting instability.

Acknowledgments

The authors gratefully acknowledge the support of the Naval Sea Systems Command and H. H. Vanderveldt, and that of the U.S. Nuclear Regulatory Commission and M. Vagins.

References

[1] Paris, P. C., Tada, H., Zahoor, A., and Ernst, H. in *Elastic-Plastic Fracture, ASTM STP 668,* American Society for Testing and Materials, 1979, pp. 5-36.

[2] Paris, P. C., Tada, H., Zahoor, A., and Ernst, H. in *Elastic-Plastic Fracture, ASTM STP 668,* American Society for Testing and Materials, 1979, pp. 251-265.

[3] Joyce, J. A. and Vassilaros, M. G. in *Fracture Mechanics, ASTM STP 743,* American Society for Testing and Materials, 1981, pp. 525-542.

[4] Ernst, H. A., Paris, P. C., and Landes, J. D. in *Fracture Mechanics, ASTM STP 743,* American Society for Testing and Materials, 1981, pp. 476-502.

[5] Joyce, J. A. and Gudas, J. P. in *Elastic-Plastic Fracture, ASTM STP 668,* American Society for Testing and Materials, 1979, pp. 451-468.

[6] "NRL-DPRI Research Program (RP 886-2), Evaluation and Prediction of Neutron Embrittlement in Reactor Pressure Vessel Materials, Annual Progress Report for 1978," J. C. Hawthorne, Ed., National Research Laboratory, Report 327, 30 Aug. 1979, p. 40.

[7] Merkle, J. G. and Corten, H. T., *Journal of Pressure Vessel Technology, Transactions,* American Society of Mechanical Engineers, Vol. 96, Nov. 1974, pp. 286-292.

[8] Saxena, A. and Hudak, S. J., *International Journal of Fracture,* Vol. 14, 1978, pp. 453-468.

[9] Rice, F. R., *The Mechanics of Fracture,* F. Erdogan, Ed., American Society of Mechanical Engineers, 1976.

[10] Landes, J. D., Walker, H., and Clarke, G. A. in *Elastic-Plastic Fracture, ASTM STP 668,* American Society for Testing and Materials, 1979, pp. 266-287.

[11] Carlson, K. W. and Williams, J. A. in *Fracture Mechanics, ASTM STP 743,* American Society for Testing and Materials, 1981, pp. 503-524.

[12] Gudas, J. P., Vassilaros, M. G., Joyce, J. A. Davis, D. A., and Anderson, D. R., "A Summary of Recent Investigations of Compact Specimen Geometry Effects on the J_I-R Curve of High-Strength Steels," NUREG/CR-1813, U.S. Nuclear Regulatory Commission, Nov. 1980.

[13] Paris, P. C., "A Method of Application of Elastic-Plastic Fracture Mechanics to Nuclear Vessel Analysis," NUREG/CR-1947, U.S. Nuclear Regulatory Commission, to be published.

T. H. Gavigan[1] *and R. A. Queeney*[1]

Theoretical Fracture Resistance of Particle-Hardened Brittle Solids

REFERENCE: Gavigan, T. H. and Queeney, R. A., **"Theoretical Fracture Resistance of Particle-Hardened Brittle Solids,"** *Fracture Mechanics: Fourteenth Symposium—Volume I: Theory and Analysis, ASTM STP 791*, J. C. Lewis and G. Sines, Eds., American Society for Testing and Materials, 1983, pp. I-84–I-95.

ABSTRACT: The addition of dispersions of relatively stiff particulates to brittle materials is recognized to increase their fracture resistance as measured with conventional fracture mechanics parameters. Extant analytical models address the problem of particle hardening indirectly. One class of predictions is essentially a rule-of-mixtures approach and is of limited success in predicting particle strengthening. Another predictive model hypothesizes the existence of a line tension associated with the bowing of the crack front line as the crack front encounters particulates on the plane of crack extension; however, this approach fails to predict the measured effects of particle stiffness and particle size. The present analytical model deals directly with the extensibility of a crack on a plane containing particulates of an average size, spacing and stiffness. The elastic strain energy associated with the particulate field is calculated and compared to the energy of the non-particle-containing matrix. The strain energy release rate then is examined for unstable crack extension in the particle-hardened matrix, and the fracture resistance of the composite is compared to that of the plain matrix. The predictions are used to examine experimental data previously generated, and the model is found to be satisfactorily accurate in predicting changes in fracture resistance as particulate character is manipulated.

KEY WORDS: brittle fracture, composite fracture, ceramic inclusions, particulate composites, multiphase material strength, particle hardening, process zones, fracture mechanics

Nomenclature

- ρ Average particulate inclusion radius
- σ Normal stress
- τ Shear stress
- μ Modulus of rigidity

[1]Former graduate student and professor of engineering mechanics, The Pennsylvania State University, University Park, Pa. 16802.

ν Poisson's ratio
u Elastic strain energy density, energy per unit volume
U Total strain energy in relevant material volume
λ Average interparticle spacing
n Number of inclusions lying on given area
a Crack length: Full length for crack emanating on surface, half-length for imbedded cracks
t Structural plate thickness
R Material resistance to crack extension, energy per unit area
T Line tension (force per unit length) associated with crack front lines

The ability of brittle materials to resist catastrophic mechanical failure often can be improved by the addition of a particulate phase, where the elastic stiffness of the particulate phase must exceed that of the brittle matrix. Many metal oxide ceramics and intermetallic ceramic compounds are sufficiently stiff to increase the fracture resistance of the harder and brittle polymers, inorganic glasses, and even selected crystalline ceramics. The mechanical strength parameter being addressed in the design of the composite places restrictions on the choice of particulate material beyond the consideration of particle stiffness. Tensile strength may be dependent not only on the reinforcement character of the particle, but also on the strength of the particle-matrix interface and local residual thermal stresses generated during composite fabrication. By comparison, the resistance of preexisting flaws to unstable extension may be less sensitive to the particles acting as crack initiators. Indeed, raising crack extension resistance may lead to degraded tensile strength in smooth-sided structural members.

Increases in the fracture surface energy when stiff inclusion particulates are added to a brittle material have been demonstrated experimentally by Lange [*1*][2] and Lange and Redford [*2*], among others. Earlier investigators, such as Hasselman and Fulrath [*3*], did not single out the composite's fracture resistance, but rather sought to correlate tensile strength with particulate dispersions by hypothesizing that crack lengths, in the natural flaw population, were altered effectively in length by the presence of nearby particles. The importance of singling out the fracture resistance of the composite was realized first by Lange [*4*], who postulated a line tension associated with a crack front line bowing out between inclusions lying on the crack plane ahead of the crack front line. The line tension concept, analogous to the impedance of a dislocation line pinned by slip plane obstacles, was developed further by Evans [*5*], who developed an analytical model to calculate the line tension.

The present work addresses a different, and more direct, approach to determining the effect that a field of stiff particulate inclusions will have on a material's resistance to the extension of a crack moving through that field.

[2]The italic numbers in brackets refer to the list of references appended to this paper.

Here, the motion of the crack is retarded by the reduced strain energy fields around the stiffer inclusions (stiffer than the matrix material) rather than by the manifestation of the reduced strain energy release rate driving force, a line tension, or crack front curvature potential.

Analytical Model

The particle-strengthened, brittle elastic composite can be visualized as a regular, three-dimensional array of roughly spherical particles of mean radius ρ. The stress distributions around and within a single particle, or inclusion, are well known from an analysis due to Goodier [6]. Figure 1 depicts the isolated spherical inclusion, and appropriate coordinate system, imbedded in a large plate subjected to a tensile boundary traction stress σ. The normal and shear stress components outside of the inclusion are

$$\sigma_{rr} = \sigma\left[-\frac{A\rho^2}{2r^2} + \left(\frac{3B\rho^4}{2r^4} - \frac{2C\rho^2}{r^2}\right)\cos 2\theta\right] + \frac{\sigma}{2}(1+\cos 2\theta)$$

$$\sigma_{o\theta} = \sigma\left[\frac{A\rho^2}{2r^2} - \frac{3B\rho^4}{2r^4}\cos 2\theta\right] + \frac{\sigma}{2}(1-\cos 2\theta) \tag{1}$$

$$\tau_{r\theta} = \sigma\left[\frac{3B\rho^4}{2r^4} - \frac{C\rho^2}{r^2}\right]\sin 2\theta - \frac{\sigma}{2}\sin 2\theta$$

The stresses inside the bonded elastic inclusion are

$$\sigma_{rr} = \frac{\sigma}{2}[(1-A)+(1-B)\cos 2\theta]$$

$$\sigma_{\theta\theta} = \frac{\sigma}{2}[(1-A)-(1-B)\cos 2\theta] \tag{2}$$

$$\tau_{r\theta} = -\frac{\sigma}{2}(1-B)\sin 2\theta$$

The constants A, B, and C are algebraic combinations of the elastic constants of the two phases present, but the constant C does not appear in subsequent analyses, so it will be unspecified here. If the subscripts i and m refer to the inclusion and matrix materials, respectively, the constants A and B are given in terms of the modulus of rigidity μ and Poisson's ratio by

$$A = \frac{(1 - 2\nu_i)\mu_m - (1 - 2\nu_m)\mu_i}{(1 - \nu_i)\mu_m + \mu_i}$$

$$B = \frac{\mu_m - \mu_i}{\mu_m + (3 - 4\nu_m)\mu_i} \tag{3}$$

The strain energy density for plane strain conditions (here, the matrix plate is large in all directions compared to the inclusion size) in Cartesian coordinates is

$$u = \frac{1}{2E}(\sigma_{xx}^2 + \sigma_{yy}^2) - \frac{\nu}{E}(\sigma_{xx}\sigma_{yy}) + \frac{1}{2\mu}\tau_{xy}^2 \tag{4}$$

where E is the Young's modulus of either of the two materials. The strain energy density, integrated over the relevant volume V about the inclusion, will yield the strain energy field in the matrix as well as within the inclusion. The perturbed stresses in Eq 1 are known to die out quickly, certainly by a distance of 4ρ from the inclusion center [6]; thus, strain energy densities be-

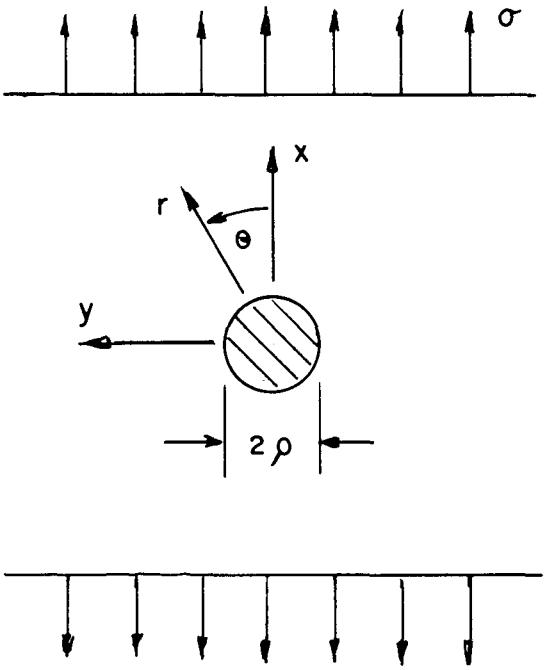

FIG. 1—*Inclusion embedded in a plate subjected to uniform tensile boundary stresses σ.*

yond $r = 4\rho$ are largely those associated with the uniform tensile stress field. Substituting the stresses in Eqs 1 and 2 into the polar coordinate form of Eq 4, and integrating over a volume of radius 4ρ, the total strain energy U_i associated with the inclusion is

$$U_i = \frac{\pi\sigma^2\rho^3}{3E_i}[(1-\nu_i)(1-A)^2 + (1+\nu_i)(1-B)^2] + \ldots + \frac{3\pi\sigma^2\rho^3}{E_m}(1+\nu_m)(A^2+2B^2) \tag{5}$$

The actual composite is to be visualized as in Fig. 2. Each spherical inclusion, of mean radius ρ, is to be centered on the corner of a cube of side λ; thus, λ is the mean interparticle spacing for nearest-neighbor particles. If the locally perturbed stress states associated with each particle rapidly approach the nominal tensile field, as one moves radially outward from the inclusion, the strain energy associated with one particle inclusion (Eq 5) can be safely assumed to be associated with each particle in the composite. In examining a rectangular area segment of length $2a$ by width t, lying on a random plane cutting the composite, it is found that n particles lie in the area segment, where

$$n = \frac{2a}{\lambda} \times \frac{t}{\lambda} = \frac{2at}{\lambda^2} \tag{6}$$

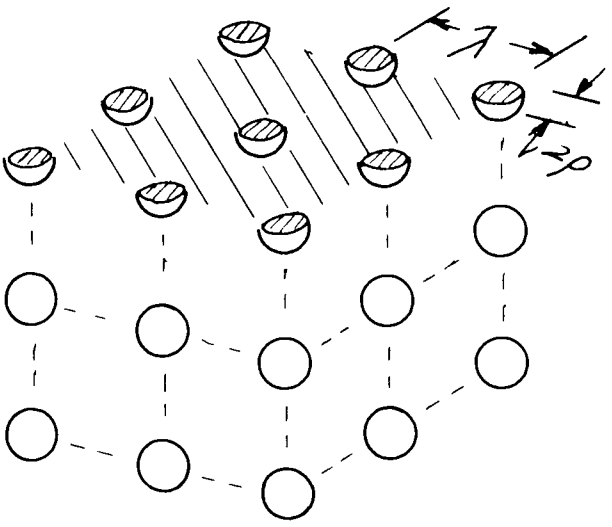

FIG. 2—*Particulate composite with mean particle radius ρ and interparticle spacing λ.*

The total strain energy associated with the n particles on the plane segment, denoted ΣU_i, is

$$\Sigma U_i = nU_i = \frac{2at}{\lambda^2} U_i \tag{7}$$

In his pioneering examination of the driving forces that promote crack extension, Griffith [7] examined crack extension stability by assuming that the strain energy released by the extending crack acted as the driving force for extension. His structural analysis dealt with an infinite plate with biaxial tensile boundary tractions, through-cracked at the center with a flat elliptical flaw as shown in Fig. 3. The decrease in the structural strain energy of the cracked plate, U_c, relative to the unflawed plate, was found to be

$$U_c = \frac{\pi a^2 \sigma^2 \nu t}{2\mu} \tag{8}$$

If the plate of Fig. 3 were to be made of the particulate composite addressed herein, the strain energy is reduced before the introduction of any flaw locally about each of the inclusion particles, the reduction being an amount U_i from

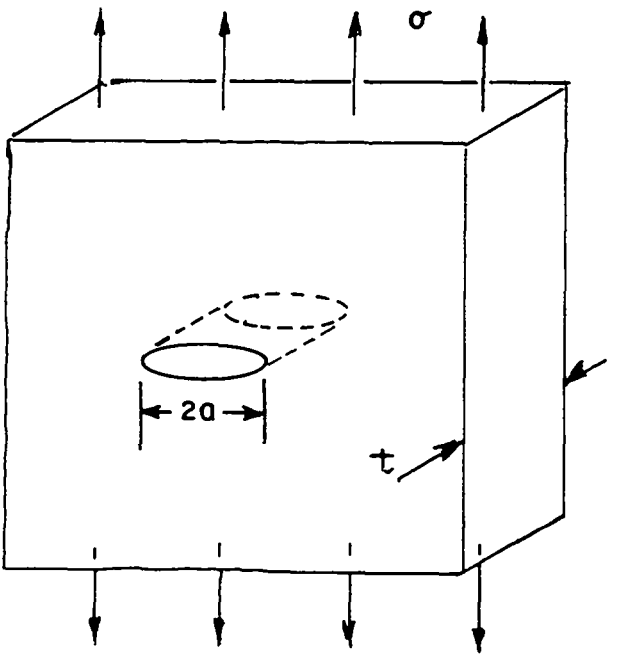

FIG. 3—*Cracked plate examined for crack extension stability.*

Eq 5. With the volume of the introduced flaw, a strain energy reduction equal to ΣU_i (Eq 7) has been realized. Thus, the driving force, or energetic reduction, for flaw extension is

$$U_c - \Sigma U_i = \frac{\pi a^2 \sigma^2 \nu_m t}{2\mu_m} - \frac{2at}{\lambda^2} U_i \tag{9}$$

The stability of the introduced flaw is determined by comparing the change in the structural strain energy (Eq 9) as the flaw extends symmetrically, to the composite's resistance to crack extension, R_c. Instability is expressed as

$$\frac{\partial}{\partial a}(U_c - \Sigma U_i) \geq R_c t$$

or

$$\frac{\partial}{\partial a}\left(\frac{\pi a^2 \sigma^2 \nu_m}{2\mu_m} - \frac{2a}{\lambda^2} U_i\right) \geq R_c \tag{10}$$

For the structural configuration of a flawed plate made of a particulate composite, studied by Griffith [7], Eq 10 predicts a critical fracture stress σ_c equal to

$$\sigma_c = \sigma_o \left[1 - \frac{\rho^3}{a\lambda^2} g(\nu,\mu)\right]^{-1/2} \tag{11}$$

where

σ_o = critical fracture stress for the plate without the strengthening particulate phase and
$g(\nu,\mu)$ = function of elastic response measures of the plate and inclusion materials.

If the brittle plate material without inclusions has a fracture resistance R_o, the fracture resistance of the composite, R_c, is

$$R_c = R_o \left[1 - \frac{\rho^3}{a\lambda^2} g(\nu,\mu)\right]^{-1} \tag{12}$$

Finally, the interplay of the matrix and particulate elastic response, in altering the fracture resistance of the composite, is given by

$$g(\nu,\mu) = \frac{1}{\nu_m}\left[\frac{E_i}{3E_m}(1 - \nu_m)(1 - A)^2 + (1 + \nu_m)(1 - B)^2 + \ldots + 3(1 + \nu_m)(A^2 + 2B^2)\right] \tag{13}$$

Given the physical realities that will be encountered in actual composite fabrication (that is, Poisson's ratio will be very similar for most matrix/particle systems, and the elastic moduli for the same systems will differ by less than an order of magnitude) Eq 13 cannot be reduced to a simpler algebraic form whose strengthening predictions can be made by inspection. Figure 4 is a graphical evaluation of Eq 11, for both matrix and inclusion Poisson ratios of 0.3, various ratios of Young's moduli for the inclusion relative to the matrix, and various volume fractions of inclusions. The mean inclusion particle diameter was set at 1.0 μm for calculating the response curves of Fig. 4.

Discussion

Although the results of more recent investigations of the fracture resistance of particle-reinforced brittle composite abound [*8,9,10*], the earlier work of Lange [*1*] has the most fully tabulated data available for the experimental validation of Eq 12. The composite investigated was a sodium borosilicate glass, reinforced with alumina (Al_2O_3) particles. The present analytical model can be expected to be most accurate for particle volume fractions less than 0.20, to insure noninteractive, particle-to-particle stress fields. The data from Lange [*1*] pertinent to the evaluation of Eq 12, and other useful information, are given in Table 1. The Poisson ratio for the glass is 0.24, and

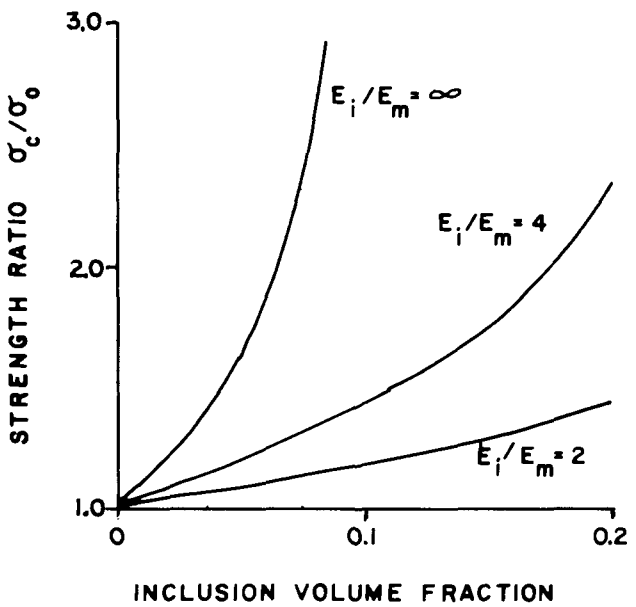

FIG. 4—*Composite critical fracture stress* σ_c *relative to matrix fracture stress* σ_o *for various moduli ratios* E_i/E_m *and volume fractions of inclusions.*

TABLE 1—*Mechanical response data for sodium borosilicate glass with Al_2O_3 reinforcement* [1].

Volume Fraction Al_2O_3	Particle Size ρ, μm	Interparticle Spacing λ, μm	Young's Modulus E, GPa	Fracture Resistance R_c, J/m^2	Fracture Strength, MPa
0.0	...	...	80.6	12.56	93.7
0.10	3.5	12.1	92.5	21.2	109.0
0.10	11.0	38.7	92.5	20.8	107.0
0.10	44.0	153.0	92.5	31.2	71.0

the Al_2O_3 would have a Young's modulus of 145 GPa and a Poisson ratio of 0.16. The factor $g(\nu,\mu)$ (Eq 13) then is calculated to be 22.2 for the glass-Al_2O_3 composite.

The term a, appearing in Eq 12, was introduced as the region in the material wherein the composite loses coherency, or fractures; thus, it corresponds in concept to the "process zone" developed by Pabst [*11*]. The process zone in a brittle material is analogous to the yield zone in a high-strength metallic alloy: it is within this region that the dissipative processes encountered in crack extension occur, providing the expected stress nonlinearity as the tip of a sharp stressed flaw is approached. Pabst [*11*] has estimated the process zone size to be given by

$$a' = \frac{1}{4}\left(\frac{E_c R_c}{TS^2}\right) \tag{14}$$

where TS is the tensile strength of the composite as determined from a four-point bend test of a smooth-sided specimen. Figure 5 compares calculated values of a from Eq 12, using Lange's data in Table 1, to calculated values from Eq 14, also using data from Table 1. The agreement is good, and one can see that the zone size, measured outward from the crack tip, encompasses about one interparticle spacing when determined through the use of Eq 12, as shown in Fig. 6.

In order to describe the same strengthening effect of stiff second phases or inclusions in brittle matrixes, Lange [*4*] proposed a line tension potential associated with the crack front line that is minimized when that line is straight. Lange's prediction for changes in the composite's fracture resistance, for an ideally elastic-brittle material, is

$$R_c = R_o + T/(\lambda - 2\rho) \tag{15}$$

using the terminology defined in this paper, and where T is the line tension tending to straighten out a crack front with inclusion-induced curvature. Evans [*5*] subsequently expanded the same analytical model to predict theo-

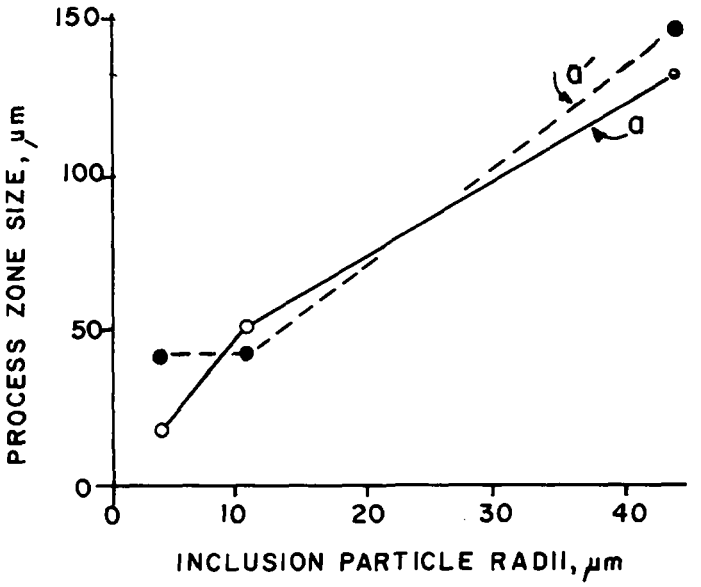

FIG. 5—*Process zone sizes* a *and* a′ *versus particle radii in a sodium borosilicate glass with 10 percent dispersed* Al_2O_3 *by volume.*

retically the value of the line tension T. The physical model upon which these analyses depend demands that a crack front "bow out" between inclusions on the plane of crack extension, in the same manner as a dislocation line behaves as it encounters hard particulates. While the latter phenomenon indeed has been observed widely, the evidence for the existence of the former is very slight. It is both physically and analytically difficult to demand stability of a stressed crack by a virtual extension proceeding as far as a complete semicircular arc swept out as the crack encounters two inclusions.

A physically more realistic approach has been taken recently by Green and Nicholson [*8*], and it is more in the spirit of the present analysis. These writers recognized the importance of the strengthening effect of stiff inclusions in the manner in which they reduce local stress states. Green and Nicholson [*8*] succeed in defining an altered stress-intensity factor for the crack approaching the inclusion, and demonstrate that stiff inclusions reduce the stress-intensity factor, while compliant inclusions (including pores) raise the stress-intensity factor and attract the crack front. Their results are physically and mathematically reasonable, but fall short of actually establishing an instability criterion that is dependent upon the existence of a particle field. It appears to Green and Nicholson [*8*] that a direct force, or stress-intensity factor, approach actually can lead to no more than such an indication of the particle-strengthening phenomenon.

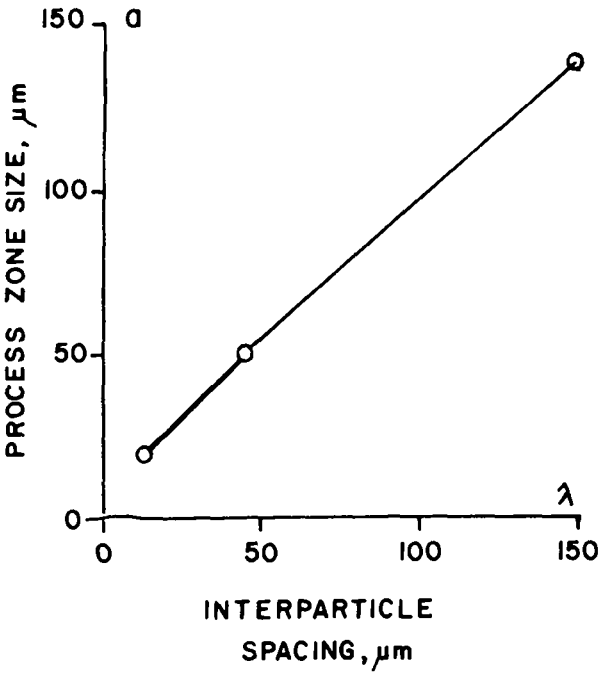

FIG. 6—*Process zone size* a *and interparticle spacing* λ *in a sodium borosilicate glass with 10 percent dispersed* Al_2O_3 *by volume.*

Summary

The present prediction of a particle-bearing composite material's resistance to crack extension is based on the altered strain energy states surrounding the stiff inclusions in the composite particle field. The analytical model restricts the application of the results to composites with less than 0.20 volume fraction of dispersed particulate phase. The composite's fracture resistance R_c is found from

$$R_c = R_o \left[1 - \frac{\rho^3}{a\lambda^2} g(\nu,\mu) \right]^{-1} \tag{12}$$

and the term a has been shown to be the size of the fracture process zone, or region of nonlinear energy dissipation, ahead of the crack tip. Based on the limited examination of experimental data accomplished herein, it appears that the process zone extends a distance of one interparticle spacing plus one particle radius ahead of the crack tip. When the process zone concept has become more thoroughly developed, Eq 12 then can serve as a design equation for optimizing the fracture resistance of these composites. It must be

remembered, however, that other factors may be introduced into a discussion of the fracture resistance of a particulate composite, such as particle-matrix thermal stress generation [*8*].

Finally, various groups currently are seeking to define testing standards for brittle material testing in order to determine fracture resistance parameters with the same confidence that now is identified with the plane strain fracture toughness determination for metallic alloys. These metallic standards clearly recognized the significance of plastic zone size (one type of process zone) relative to specimen dimensions and material response. The same type of testing-material-microstructure relationship will need to be addressed if fracture resistance determinations in brittle composites are to be material response measures only.

References

[*1*] Lange, F. F., *Journal of the American Ceramic Society,* Vol. 54, No. 12, May 1971, pp. 614-620.

[*2*] Lange, F. F. and Redford, K. C., *Journal of Materials Science,* Vol. 6, No. 9, Sept. 1971, pp. 1197-1203.

[*3*] Hasselman, D. P. H., and Fulrath, R. M., *Journal of the American Ceramic Society,* Vol. 49, No. 2, Feb. 1966, pp. 68-72.

[*4*] Lange, F. F., *Philosophical Magazine,* Vol. 22, No. 179, Nov. 1970, pp. 983-992.

[*5*] Evans, A. G., *Philosophical Magazine,* Vol. 26, No. 6, Dec. 1972, pp. 1327-1344.

[*6*] Goodier, J. N., *Journal of Applied Mechanics,* Vol. 1, No. 1, 1933, pp. 39-44.

[*7*] Griffith, A. A., *Philosophical Transactions of the Royal Society of London,* Vol. 221A, No. 4, 1920, pp. 163-198.

[*8*] Green, D. J. and Nicholson, P. S. in *Fracture Mechanics of Ceramics,* R. C. Bradt, D. P. H. Hasselman, and F. F. Lange, Eds., Plenum, New York, 1978, pp. 945-960.

[*9*] Nadeaa, J. S. and Bennett, R. C. in *Fracture Mechanics of Ceramics,* R. C. Bradt, D. P. H. Hasselman, and F. F. Lange, Eds., Plenum, New York, 1978, pp. 961-972.

[*10*] Swearengen, J. C., Beauchamp, E. K., and Eagan, R. J. in *Fracture Mechanics of Ceramics,* R. C. Bradt, D. P. H. Hasselman, and F. F. Lange, Eds., Plenum, New York, 1978, pp. 973-987.

[*11*] Pabst, R. F., Steep, J., and Claussen, N. in *Fracture Mechanics of Ceramics,* R. C. Bradt, D. P. H. Hasselman, and F. F. Lange, Eds., Plenum, New York, 1978, pp. 821-830.

M. P. Wnuk[1] *and T. Mura*[1]

Extension of a Stable Crack at a Variable Growth Step

REFERENCE: Wnuk, M. P. and Mura, T., **"Extension of a Stable Crack at a Variable Growth Step,"** *Fracture Mechanics: Fourteenth Symposium—Volume I: Theory and Analysis, ASTM STP 791*, J. C. Lewis and G. Sines, Eds., American Society for Testing and Materials, 1983, pp. I-96-I-127.

ABSTRACT: This study has been inspired by two proposed models for stable crack growth described by Sih and Kiefer (1979) and Wnuk and Sedmak (1980). Basic assumptions of the second model are reexamined and refined. Although the mathematical analyses involved in both approaches are widely different, it is shown that the physical assumptions underlying these two models are analogous. Both treatments assume a "quantum" nature of crack growth by representing extension of a stable crack as a sequence of steps each of which is executed as a finite jump in the current crack length. While Sih and Kiefer employed the numerical approach to treat the three-dimensional (3D) elastic-plastic fracture problem, here a highly idealized line-plasticity model, modified by an addition of the final stretch growth law, is used.

In earlier final stretch model the quantities essential in the formulation of the growth law, such as the growth step Δ and the opening constants δ or $\tilde{J}$, were assumed to be material constants. Now it is demonstrated that the first of these assumptions may be relaxed and replaced by a more general requirement of the constancy of the ratios COD/Δ or J/Δ. Indeed, a self-consistent theory may be constructed if only the ratio of a certain measure of the apparent material fracture toughness to the size of the growth step is maintained constant throughout the slow growth phase.

It is shown that variations in the growth step result in *reduction* of the true and apparent fracture toughnesses associated with the quasi-static crack, which are represented respectively by the tearing modulus $\alpha\ \tilde{\delta}/\Delta$ and any suitable resistance parameter such as J-integral, COD, or extent of the plastic zone generated at the crack front. It is concluded that the models that are based on ideal plasticity and that ignore variations in the growth step tend to overestimate material ability to sustain a stable crack, and thus lead to non-conservative predictions regarding occurrence of terminal instability.

KEY WORDS: ductile fracture, stability, analysis, stable crack growth, damage, non-elastic material behavior, resistance curve, fracture mechanics

[1]Visiting professor and professor, respectively, Civil Engineering Department, Technological Institute of Northwestern University, Evanston, Ill. 60201.

Rice [*1*][2] has pointed out that in order to account for the nonlinear effects exhibited by the material located immediately ahead of the fracture front it is necessary to modify the continuum view applied to the entire solid containing a crack by focusing attention on the small domain that is about to be penetrated by the crack front. This domain is expected to behave differently from the remaining part of the bulk solid, or "matrix," and further studies of such nonlinear regions indicate a certain "inner structure" within the end zone. As it turns out, the deterioration of strength from its maximum level to zero occurs over a material element of *finite* dimension, say the growth step Δ, which shall be referred to as "disintegration" or "process" zone, or a "unit cell." The size of such a disintegration zone may widely vary from one material to another, as it is determined by the microstructural parameters such as the average spacing between the inclusions in metallic alloys (roughly equal to several grain diameters), the characteristic width of the bundle of molecular chains in polymers, the average spacing between the microcracks in rocks and ceramics, and finally, the aggregate dimension in mortars and concretes. Since this infinitesimal disintegration element is usually embedded within a larger nonlinear zone that precedes the moving crack tip, it is appropriate to speak about "structured end zone" as suggested by Rice [*1*].

This concept is illustrated in Fig. 1, in which four possible representations of the structured end zone are shown schematically. The essential features of all these schemes are as follows: (1) the restraining stress $S(x_1)$ prevailing within the end zone is either uniform and equal to an effective stress σ_0, or it falls off linearly to zero over the length β, which will be identified later with the growth step Δ; (2) the relative magnitudes of the process zone (β) and the end zone (R) vary from one scheme to another. The first two cases shown, Fig. 1*a* and *b*, for which $\Delta \ll R$, pertain to the ductile limit of material behavior in quasi-brittle fracture, which the other two, Fig. 1*c* and *d*, for which the growth step is on the same order of magnitude as the size of the end zone, $\Delta \simeq R$, correspond to a brittle limit of material behavior. Of course, all four representations shown in Fig. 1 are only certain idealizations of the actual stress distribution pictured in Fig. 2.

Neither the exact nature of the stress distribution within the outer part of the nonlinear zone ($\beta \leq x_1 \leq R$), nor its deterioration within the process zone ($0 \leq x_1 \leq \beta$) is known. This insufficient knowledge, however, does not prevent us from postulating certain plausible models, such as those shown in Fig. 1. A detailed analysis of these models will enable us to draw meaningful conclusions regarding an apparent fracture toughness (R-curve) associated with a quasi-static crack extending at the subcritical K-factor levels, that is, below the K-factor required for a spontaneous (unstable) fracture. Our objective in this study is to provide relationships between various fracture

[2]The italic numbers in brackets refer to the list of references appended to this paper.

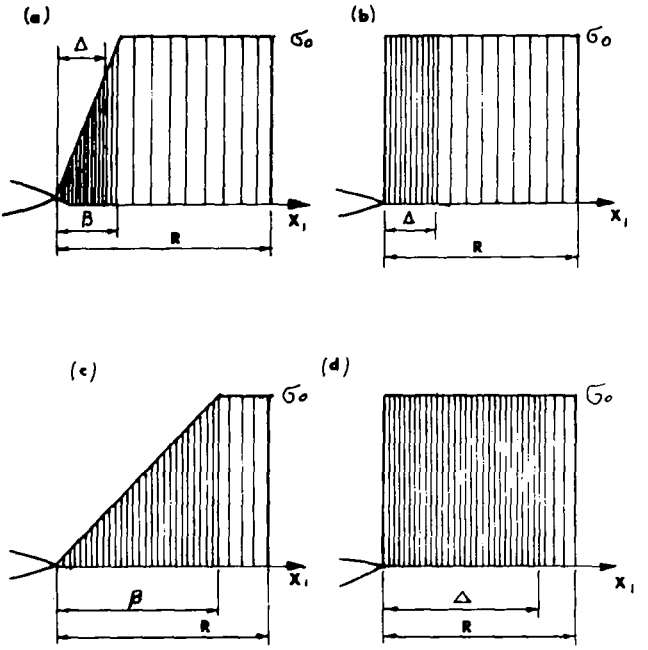

FIG. 1—*Schematic representation of idealized stress distributions simulating the stress transmitted across the nonlinear zone.*

parameters, and in particular to predict their variations during the stable crack growth phase and at the point of terminal instability for any given loading condition and geometrical configuration.

Fracture Criterion

According to Wnuk [2], failure of a volume element located on the prospective path of the crack front is linked to the incremental work dissipated within the process zone just prior to the collapse of this zone. If t_f denotes the instant at which the control volume element breaks down, then the incremental accumulation of damage occurs within the time interval $t_f - \delta t \leq t \leq t_f$, in which the increment δt ($= \Delta/\dot{a}$) corresponds to the time used by the crack front to traverse its own process zone. Size of such hypothetical zone, over which an intensive straining occurs before the crack may advance, is characterized by the length Δ, which is assumed to be microstructural constant. An alternative way of stating the basic physical assumption underlying the final stretch criterion of fracture may be expressed as follows: amount of irreversible deformation $\hat{\delta}$ generated per increment of crack extension Δ does not depend on the preceding deformation states, and therefore it is invariant to the amount of crack growth.

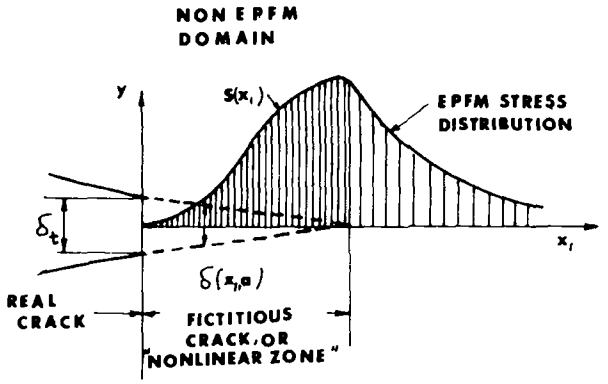

FIG. 2—*Qualitative representation of the actual stress distribution occurring within the near crack tip region. "EPFM" stands for "elastic-plastic fracture mechanics."*

It is readily demonstrated that both statements given previously, the first one involving the energy absorbed within the process zone during an incremental crack extension, and the second one employing an increment of irreversible deformation generated during a single growth step, are in fact equivalent. They are also equivalent to the requirement of elevating the strain at a certain distance ahead of the crack front to the critical level, as suggested by McClintock [*3*] for a quasi-static Mode III crack.

A more recent interpretation of this criterion of fracture within the subcritical range was given by Kfouri and Miller [*4*], and then by Kfouri and Rice [*5*], who reduced the energy balance equation, set up for a quasi-static crack extending in an elastic-plastic solid, to an equality between the rate of energy supplied by the external field, $\mathcal{G}^{\Delta}$, which is only a small fraction of the total work dissipated within the nonlinear zone, namely

$$\mathcal{G}^{\Delta} = \lim_{\delta a \to \Delta} \frac{2}{\delta a} \int_{a}^{a+\delta a} S(x)\, \delta u_y [x, a]\, dx \tag{1}$$

and the energy absorbed within the disintegration zone, $\hat{\mathcal{G}}$, called also the "essential work of fracture," compare Broberg [*6*] and Cotterell [*7*]. The quantity $\hat{\mathcal{G}}$ is regarded to be a material property that represents the true material resistance to crack progagation, in contrast to the apparent fracture toughness parameter $\mathcal{G}_R$, used by other investigators. Note that the integration in Eq 1 is performed with respect to the coordinate x related to the distance measured from the crack tip (x_1) as follows: $a + x_1 = x$, while the symbol $\delta u_y(x, a)$ denotes variation of the displacement normal to the crack plane due to an incremental crack growth δa. It is worthy to note that despite the continuum mechanics framework employed in the derivation of the energy separation rate, the quantity $\mathcal{G}^{\Delta}$ turns out to be distinctly dependent on

the assumed growth step, Δ, and in particular it vanishes for $\Delta \to 0$. Therefore, a notion of continuous crack extension must be replaced by a discrete process that is visualized as a sequence of "jumps," each of which equals a finite quantum of crack extension, Δ. This view is in complete agreement with the final stretch concept of Wnuk [2], since the energy balance criterion

$$2\int_{a}^{a+\delta a} S(x)\,\delta u_y[x, a]\,dx = \hat{\mathcal{G}}\delta a \tag{2}$$

may indeed be reduced for quasi-brittle solids, that is, when $R \ll a$, to the final stretch condition for a propagating subcritical crack, namely

$$u_y[a + \Delta, a + \Delta] - u_y[a + \Delta, a] = \hat{\delta}/2 \tag{3}$$

in which the quantity $\hat{\delta}$, final stretch, is assumed to be a material constant and is used as a measure of the local (true) fracture toughness. The quantity δa in the upper limit of the integral in Eq 2 has been identified with the finite growth step Δ.

To prove the equivalence of Eqs 2 and 3, we note that within the so called "small-scale yielding range" (when $R \ll a$) one may calculate the energy separation rate $\mathcal{G}^{\Delta}$ either by integration of the product $S(x) \times [\delta\, u_y(x, a)/\delta a]$ with respect to the spatial coordinate x, or by an integration of the product $S(x, t)\dot{u}_y(x, t)$, evaluated at a fixed x, with respect to time. This latter integral is evaluated over an interval corresponding to the lapse of time between the two successive states (compare Fig. 3):

State 1—crack length $= a$,
distance of the control point from the crack front $= \Delta$, and
time, $t_1 = t_f - \delta t$, in which $\delta t = \Delta/\dot{a}$.

State 2—crack length $= a + \Delta$,
distance of the control point from the crack front $= 0$, and
time, $t_2 = t_f$

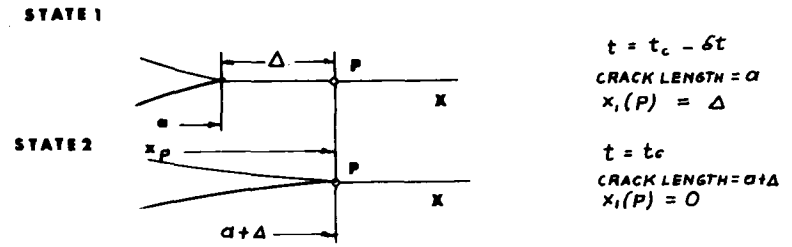

FIG. 3—*Two successive states considered in the derivation of the energy separation rate,* $\mathcal{G}^{\Delta}$. P *is the control point at which the energy dissipation rate is being evaluated.*

Therefore, the energy balance Eq 2 may be rewritten in this way

$$\mathcal{G}^{\Delta} = 2\left\{\int_{t_1}^{t_2} S(x, t)\,\dot{u}_y(x, t)\,dt\right\}_{x=x_p} \tag{4}$$

For a constant restraining force $S = \sigma_Y$ this expression assumes the form

$$\mathcal{G}^{\Delta} = 2\sigma_Y [u_y(x, t_f) - u_y(x, t_f - \delta t)]_{x=x_p} \tag{5}$$

Let us now replace the coordinate x by the coordinate x_1, which is anchored at the tip of a moving crack, and employ a new notation for the function u_y, namely

$$u_y \rightarrow u(x_1, a) \tag{6}$$

Then State 1 is designated by $x_1 = \Delta$ and the current crack length a, while State 2 is defined by $x_1 = 0$ and the crack length $a + \Delta$. With this notation the displacements $u_y(t_1)$ and $u_y(t_2)$, which correspond to the two successive states considered, are

$$\begin{aligned} u_y(t_1) &= u_y[x_p, a] &&= u(\Delta, a) \\ u_y(t_2) &= u_y[x_p, a + \Delta] &&= u(0, a + \Delta) \end{aligned} \tag{7}$$

Inserting these expressions into Eq 5 and recalling that the constant $\hat{\mathcal{G}}$ was given by the product of the effective yield stress σ_Y and the final stretch $\hat{\delta}$, we obtain the equation $u(0, a + \Delta) - u(\Delta, a) = \hat{\delta}/2$, which indeed is the final stretch criterion postulated by Wnuk [*2*].

Distribution of Displacements Corresponding to Structured Crack-Tip Zone

Constant Growth Step Considerations

In this section we shall discuss the consequences of the assumption of existence of a structured crack-tip zone, weakened by the microcracks and other microdefects that lead to a breakdown of the stress and strain fields predicted by the continuum elastic-plastic fracture mechanics. For this reason we shall at times refer to this region as "nonlinear zone." According to the schematic representations shown in Fig. 1 the nonlinear zone may be visualized as a composite domain consisting of two subregions. The smaller of the two (in Fig. 1*a* and *b*) is the disintegration zone, which is well embedded within the nonlinear region, $\Delta \ll R$. Situations depicted in Fig. 1*c* and *d* refer to the case when the sizes of both subregions almost coincide, $\Delta \simeq R$.

It should be emphasized that in a quasi-static problem considered here, extension of fracture is accompanied by a continuous redistribution of the strains prevailing within the nonlinear zone. The global effect of such redistribution is the change in length of the nonlinear region associated with a growing crack. Therefore, we anticipate that to each increment of crack length δa, one may ascribe an increment in the extent of the nonliner zone, δR. Determining the rate of such redistribution, $\delta R/\delta a$, is one of the primary objectives of this section. The quantity $\delta R/\delta a$ is in fact a measure of the resistance to cracking. Since the function $R = R(a)$ describes an apparent material toughness associated with a stable crack, we shall now proceed to determine both the unknown quantities: the rate dR/da and the function $R(a)$.

If the stable phase of crack growth is to exist at all, the rate dR/da has to be a positive quantity. However, as we will show in the next section, a transition into unstable fracture usually occurs at a certain value of dR/da greater than zero, but low enough to be matched by the energy supply rate, determined from the intensity of the external field.

Let us now derive the equations governing motion of a quasi-static crack. For a Mode I crack the basic required input is the distribution of the displacements normal to the crack plane generated within the nonlinear zone and associated with one of the distributions of the restraining forces shown in Fig. 1. Let us first consider the case of a uniform distribution of the stress over the entire end zone, $S(x_1) = \sigma_Y$ (see Fig. 1*c* and *d*). The profile of the nonlinear zone subjected to such uniform restraining stress was given (for example) by Rice [*8, 9*], and it is a known function of the coordinate x_1 and the extent of the nonlinear zone R, namely

$$u_y(x_1, R) = \frac{4\sigma_Y}{\pi E_1}\left\{\sqrt{R(R - x_1)} - \frac{x_1}{2}\log\frac{\sqrt{R} + \sqrt{R - x_1}}{\sqrt{R} - \sqrt{R - x_1}}\right\} \tag{8}$$

Here the coordinate x_1 varies within the interval $(0, R)$, while the symbol E_1 denotes Young's modulus for plane stress, and it equals $E(1 - \nu^2)^{-1}$ for the plane-strain situation. The extent of the nonlinear zone, R, may be considered here as an external field parameter related to the intensity K of the near-tip stress field as follows

$$R = \pi K^2/8\sigma_Y{}^2 \tag{9}$$

At this point we should add that since during the stable phase of crack growth the intensity of the stress field K equals at all times the material resistance to cracking K_R, we may also interpret Eq 9 as a relation between the toughness K_R and the resistance parameter R, that is

$$R(a) = \pi K_R{}^2(a)/8\sigma_Y{}^2 \tag{10}$$

Note that the displacement $u_y(x_1, R)$ attains the maximum value at the crack tip, that is, at $x_1 = 0$

$$u_{\text{tip}} = u_y(0, R) = \frac{4\sigma_Y}{\pi E_1} R \tag{11}$$

while it vanishes at $x_1 = R$. It should be emphasized that while for a stationary crack the length R has a certain fixed value, in the case of a quasi-static crack the toughness parameter R is a time-dependent quantity. It is convenient to employ the current crack length a as a time-like variable, and therefore we shall consider R to be a function of a, that is, $R = R(a)$. This is an a priori unknown function and it will be subject to determination.

It may be demonstrated that Eq 8 results as a limiting case, when $\beta \to 0$, from a more general expression considered by Knauss [*10*] in his study of time-dependent fracture, and valid for a bilinear distribution of the restraining stress

$$\begin{aligned} S(x_1) &= (\sigma_Y/\beta)x_1 \qquad 0 \le x_1 \le \beta \\ &= \sigma_Y \qquad\qquad\quad \beta \le x_1 \le R \end{aligned} \tag{12}$$

Knauss' expression reduced to an inviscid case reads

$$u_y(x_1, R) = \frac{8\sigma_Y}{\pi E_1} R g(\hat{r}) F(r, \hat{r}), \qquad 0 \le r \le 1 \tag{13}$$

in which $r = x_1/R$, $\hat{r} = \beta/R$, while the functions g and F are defined as follows

$$\begin{aligned} g(\hat{r}) &= \frac{2}{3}\left[1 + \frac{1-\hat{r}}{1+\sqrt{1-\hat{r}}}\right] \\ F(r, \hat{r}) &= C_r + \frac{1}{2}A_r\left[\frac{\hat{r}-r}{2}\log\left|\frac{C_r + C_0}{C_r - C_0}\right| - C_0 C_r\right] \\ &\quad + \frac{A_r}{4\hat{r}}\left[\frac{\hat{r}^2 - r^2}{2}\log\left|\frac{C_r - C_0}{C_r + C_0}\right| - \frac{r^2}{2}\log\left|\frac{C_r + 1}{C_r - 1}\right|\right. \\ &\quad \left. - (1 - C_0)(1 + r)C_r + \frac{1}{3}(1 - C_0^3)C_r\right] \end{aligned} \tag{14}$$

The auxiliary quantities A_r, C_r, and C_0 are defined

$$A_r = \frac{\left(\frac{3}{2}\right)\hat{r}}{1 - (1 - \hat{r})^{3/2}}$$

$$C_r = (1 - r)^{1/2} \tag{15}$$

$$C_0 = (1 - \hat{r})^{1/2}$$

The relation analogous to Eq 9, which connects the extent of the nonlinear zone R and the K-factor (or, the material toughness K_R), now takes on the form

$$R = \frac{\pi}{8}\left(\frac{K}{\sigma_Y}\right)^2 \frac{\frac{9}{4}\hat{r}^2}{[1 - (1 - \hat{r})^{3/2}]^2}, \qquad \hat{r} = \beta/R \tag{16}$$

At $\beta = 0$, that is, at $\hat{r} = 0$, this form reduces to Eq 9, while for the other extreme case, at $\beta \to R$, or $\hat{r} \to 1$, we obtain

$$R = \left(\frac{9}{4}\right)\frac{\pi}{8}\left(\frac{K}{\sigma_Y}\right)^2 \tag{17}$$

Before we proceed with the derivation of the equation defining the resistance curve, let us note that Eq 13 describing the distribution of the opening displacement within the nonlinear zone associated with a quasi-static crack may be written in the following general way

$$u(x_1, a) = \frac{4\sigma_Y}{\pi E_1} R(a) f(r, \hat{r}), \qquad 0 \le r \le 1 \tag{18}$$

in which

$$\begin{aligned} f(r, \hat{r}) &= 2g(\hat{r})\, F(r, \hat{r}) \\ r &= \frac{x_1}{R} \\ \hat{r} &= \frac{\beta}{R} \\ R &= R(a) \end{aligned} \tag{19}$$

Let us now evaluate the displacements $u_y(t_1)$ and $u_y(t_2)$ that enter into the fracture criterion of Eq 3. It is readily seen that the displacement $u_y(t_2)$ can be identified with the opening displacement at the crack tip at the instant when the current crack length equals $a + \Delta$, say $u_y(t_2) = [u_{tip}]\, a + \Delta$. Combining this with Eq 18 yields

$$u_y(t_2) = u(0, a + \Delta) = R(a + \Delta) f_2[R(a + \Delta)] \tag{20}$$

Here, both the parameter R and the function f_2 are to be evaluated at the current crack length $a + \Delta$, thus

$$\begin{aligned} R &= R(a + \Delta) \\ f_2 &= \{2g(\hat{r})\, F(0, \hat{r})\}_{\hat{r}=\beta/R(a+\Delta)} \end{aligned} \tag{21}$$

On the other hand, the displacement $u_y(t_1)$ should be evaluated at a certain distance from the crack front, $x_1 = \Delta$, and at the instant when the current crack length equals a. If the distance β is identified with the growth step Δ, then $x_1 = \Delta$ corresponds to $r = \hat{r}$, and we obtain

$$u_y(t_1) = u(\Delta, a) = \frac{4\sigma_Y}{\pi E_1} R(a) f_1[R(a)] \tag{22}$$

in which

$$\begin{aligned} f_1[R(a)] &= \{f(\hat{r}, \hat{r})\}_{R=R(a)} \\ &= \{2g(\hat{r})\, F(\hat{r}, \hat{r})\}_{R=R(a)} \end{aligned} \tag{23}$$

To apply the fracture criterion of Eq 3, we need to evaluate the difference

$$u_y(t_2) - u_y(t_1) = \frac{4\sigma_Y}{\pi E_1} \{R(a + \Delta) f_2[R(a + \Delta)] - R(a) f_1[R(a)]\} \tag{24}$$

In order to relate the functions appearing in braces in Eq 24 and containing the arguments a and $a + \Delta$, we use the Taylor expansion and arrive at the form

$$u_y(t_2) - u_y(t_1) = \frac{4\sigma_Y}{\pi E_1} \left\{ R f_2 + \left[f_2 + R \frac{df_2}{dR} \right] \frac{dR}{da} \Delta - R f_1 \right\}_{R=R(a)} \tag{25}$$

in which both quantities f_1 and f_2 are known functions of the resistance parameter R evaluated at the current crack length a. The form of Eq 25 is quite general and it enables us to set up the equations that describe motion of a quasi-static crack, and predict the variations of the material resistance to

cracking developed during the early stages of stable fracture. The range of validity of these expressions will be limited to the "quasi-brittle" case, since we are discussing here only the so-called "small-scale yielding" case, as it is appropriate for the class of materials under consideration.

Applying Eqs 5 and 25, we evaluate the energy separation rate associated with a discontinuously growing crack

$$\mathcal{G}^{\Delta} = \frac{8\sigma_Y^2}{\pi E_1}\left\{Rf_2 + \left[f_2 + R\frac{df_2}{dR}\right]\frac{dR}{da}\Delta - Rf_1\right\} \tag{26}$$

Alternately, we may evaluate the final stretch $\hat{\delta}$ generated during an incremental (but finite) crack extension $\delta a = \Delta$, that is

$$\hat{\delta} = \frac{8\sigma_Y}{\pi E_1}\left\{Rf_2 + \left[f_2 + R\frac{df_2}{dR}\right]\frac{dR}{da}\Delta - Rf_1\right\} \tag{27}$$

It is noteworthy that the quantity $\mathcal{G}^{\Delta}$ rather strongly depends on the choice of the growth step Δ, and in particular it vanishes when Δ is allowed to approach zero. We are, therefore, led to a conclusion that existence of a certain finite growth step is a necessary condition for propagation of a quasi-static crack occurring in a solid that possesses a certain granular structure. Once again, we emphasize that in this case the limits of applicability of the continuum mechanics are surpassed and a small volume of the material immediately adjacent to the fracture front obeys a new, yet not well understood, constitutive law.

Generalization of the classical energy balance equation, as proposed by other investigators [2,4-7], suggests an equality between the energy separation rate $\mathcal{G}^{\Delta}$ associated with a discontinuously growing crack, and the essential work of fracture, $\hat{\mathcal{G}}$, given as a product of the effective stress σ_Y and the final stretch. Therefore, if we set $\mathcal{G}^{\Delta} = \hat{\mathcal{G}}$ or, equivalently $u_y(t_2) - u_y(t_1) = \hat{\delta}/2$, and use Eqs 26 and 27, we may cast the equation governing motion of a stable crack in this general form

$$\frac{R}{\Delta}(f_2 - f_1) + \left[f_2 + R\frac{df_2}{dR}\right]\frac{dR}{da} = M \tag{28}$$

Here, the functions $f_1(\Delta, R)$ and $f_2(\Delta, R)$ do not depend on a particular loading condition or crack configuration, and they are known once the distribution of the restraining stress transmitted across the nonlinear zone (see Figs. 1 and 2) is chosen. The constant M appearing on the right side of Eq 28 will be named "tearing modulus" and it will be used as a measure of the *true* material resistance to cracking. The greater is the constant M, the more pronounced will be the phase of stable crack extension preceding onset of the

catastrophic fracture. It is so because both the resistance to slow crack growth and the span between the lower and the upper toughness levels are directly proportional to the nondimensional modulus M. The experimental data collected by numerous investigators show that modification of microstructure, which enhances material toughness, strongly affects the tearing modulus. This phenomenon may be better understood if we relate the tearing modulus appearing in Eq 28 to other material properties, namely

$$M = \frac{\pi}{8}\frac{E_1}{\sigma_Y}(\hat{\delta}/\Delta) \quad \text{or}$$
$$= \frac{\pi}{8}\frac{E_1}{\sigma_Y{}^2}(\hat{\mathcal{G}}/\Delta) \tag{29}$$

We see that the ratio of a true toughness (measured either by $\hat{\delta}$ or by $\hat{\mathcal{G}}$) to the crack growth step becomes a decisive factor that discriminates between a brittle and a tough material. Still another interpretation of the quantity M has been suggested by Wnuk [*11,12*]

$$M = \left(\frac{\pi}{8}\right)\left(\frac{\epsilon^f}{\epsilon_Y}\right) \tag{30}$$

in which ϵ^f denotes the ultimate strain attained in a uniaxial tension test, while the strain ϵ_Y is the strain at yield. With certain additional assumptions, we will soon show that stable cracking is possible only if the nondimensional modulus M exceeds the minimum value $M_{\min}$. For brittle solids this minimum value of M turns out to be about unity, and thus the initially stable cracking is possible for those materials in which $M > 1$, while for $M \leq 1$ the point of fracture initiation coincides with the spontaneous crack propagation.

Case A: Constant Restraining Stress

To illustrate the usefulness of the equations derived previously, and in particular to show how the differential equation, Eq 28, may be put to work, let us derive a governing equation for an R-curve under an assumption of the simplest form of distribution of the stress within the nonlinear zone, namely $S(x_1) = \sigma_Y$ over the entire length of the end zone, $0 \leq x_1 \leq R$. It is readily seen that in this case according to Eq 28 we have

$$u_y(t_2) = \frac{4\sigma_Y}{\pi E_1} R(a + \Delta) \tag{31}$$

and

$$u_y(t_1) = \frac{4\sigma_Y}{\pi E_1}\left\{\sqrt{R(R-\Delta)} - \frac{\Delta}{2}\log\frac{\sqrt{R}+\sqrt{R-\Delta}}{\sqrt{R}-\sqrt{R-\Delta}}\right\}_{R=R(a)} \tag{32}$$

Hence it follows $f_2 = 1$ and $df_2/dR = 0$, while

$$Rf_1(\Delta, R) = \sqrt{R(R-\Delta}} - \frac{\Delta}{2}\log\frac{\sqrt{R}+\sqrt{R-\Delta}}{\sqrt{R}-\sqrt{R-\Delta}} \tag{33}$$

Therefore, the governing equation of the problem under consideration, that is, Eq 28, reduces as follows

$$\begin{aligned}\frac{dR}{da} &= M - \frac{R}{\Delta} + \sqrt{\frac{R}{\Delta}\left(\frac{R}{\Delta}-1\right)} \\ &\quad + \frac{1}{2}\log\frac{\sqrt{R/\Delta}-\sqrt{R/\Delta-1}}{\sqrt{R/\Delta}+\sqrt{R/\Delta-1}}\end{aligned} \tag{34}$$

This nonlinear first-order differential equation defines an R-curve for an arbitrary loading condition and crack configuration. It may be integrated numerically for a prescribed initial condition at

$$a = a_0, \qquad R = R_{\text{ini}} \tag{35}$$

It is important to note that there are no restrictions imposed on the ratio Δ/R, and due to this fact we may now consider two limiting cases, each of which corresponds to a different class of materials. These extreme cases are as follows: (*a*) ductile behavior occurring when the process zone is entirely embedded in the nonlinear end zone, that is, when $\Delta \ll R$; and (*b*) brittle behavior occurring when the process zone is on the same order of magnitude as the entire end zone, that is, when $\Delta \simeq R$.

For the first case Eq 34 reduces to the form given by Wnuk [*2*] for metals of limited ductility, and then in an almost identical form by Rice and Sorensen [*13*] and Rice et al [*14*], namely

$$\frac{dR}{da} = M - \frac{1}{2} - \frac{1}{2}\log(4R/\Delta) \tag{36}$$

This equation appears to provide a successful description of stable phase of ductile fracture in metals, and its extensive discussion was provided by Rice and Sorensen [*13*].

In case of the other extreme material behavior, pertaining to inelastic brit-

tle fracture, the size of the process zone almost coincides with the extent of the entire nonlinear end zone. For such a limiting case, when $\Delta \to R$, Eq 34 degenerates to a simple form

$$\frac{dR}{da} = M - \frac{R}{\Delta} + \frac{2}{3}\left(\frac{R}{\Delta} - 1\right)^{3/2} \tag{37}$$

or

$$\frac{dR}{da} \simeq M - \frac{R}{\Delta}, \qquad \Delta \to R \tag{38}$$

We note that the minimum value of the tearing modulus at which stable fracture phase is still possible is determined from the requirement

$$\left(\frac{dR}{da}\right)_{\text{ini}} \geq 0 \tag{39}$$

which leads to

$$\begin{aligned} M_{\min} &= R_{\text{ini}}/\Delta - \frac{2}{3}\left(\frac{R_{\text{ini}}}{\Delta} - 1\right)^{3/2} \quad \text{from Eq 37} \\ &= R_{\text{ini}}/\Delta \quad \text{from Eq 38} \end{aligned} \tag{40}$$

In the case of very brittle solids the most reasonable assumption that one can make regarding toughness parameter at the onset of crack extension, R_{ini}, is to let the growth step Δ be equal to the extent of the nonlinear zone at the threshold of fracture growth. When it is assumed that $R_{\text{ini}} \simeq \Delta$, we have $M_{\min} = 1$. Figure 4 shows three possible developments of events immediately following the onset of fracture extension. Only one of them is stable when $M > M_{\min}$ and $dR/da > 0$, while the other two imply unstable fracture, which begins right at the initiation point and is not preceded by any slow crack growth. These are the cases obtained for $M = M_{\min}$, marked by a horizontal line, and for $M < M_{\min}$ shown by a descending resistance curve. For both the latter cases the slope dR/da is either zero or negative.

Examples of integration of Eq 34, which defines an R-curve for an arbitrary Δ/R ratio, performed at various sizes of the growth step relative to the extent of the nonlinear zone at the onset of crack extension R_{ini}, are shown in Fig. 5. It is seen that the assumed ratio Δ/R_{ini} rather strongly affects the shape of the resistance curves obtained from Eq 34, and it also has a pronounced effect on the shape of the Q-curves shown in Fig. 6. The curves illustrate variations of the external load during stable crack extension in a

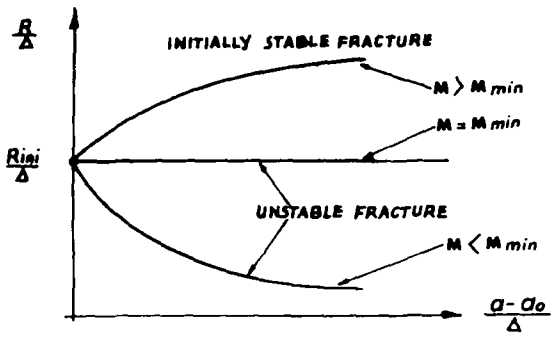

FIG. 4—*Effect of the tearing modulus* M *and its limiting value* M_{min} *on stability of crack extension in a quasi-brittle solid.*

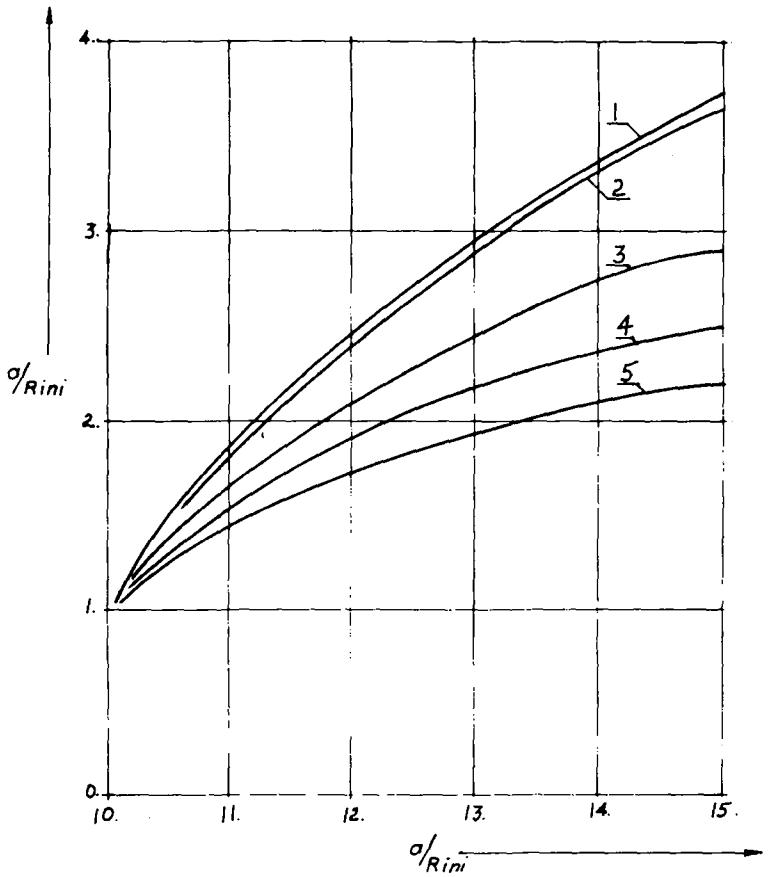

FIG. 5—*Resistance curves obtained by numerical integration of Eq 34 at* $a_0 = 10\Delta$ *and* Δ/R_{ini} *ratios 0.2 (Curves 1 and 2), 0.4 (Curve 3), 0.6 (Curve 4), and 0.8 (Curve 5). The tearing modulus for all five curves was assumed to equal the minimum modulus multiplied by a constant,* $L = 1.5$. *Curve 1 was obtained by integration of a asymptotic Eq 36 valid for* $R/\Delta \gg 1$.

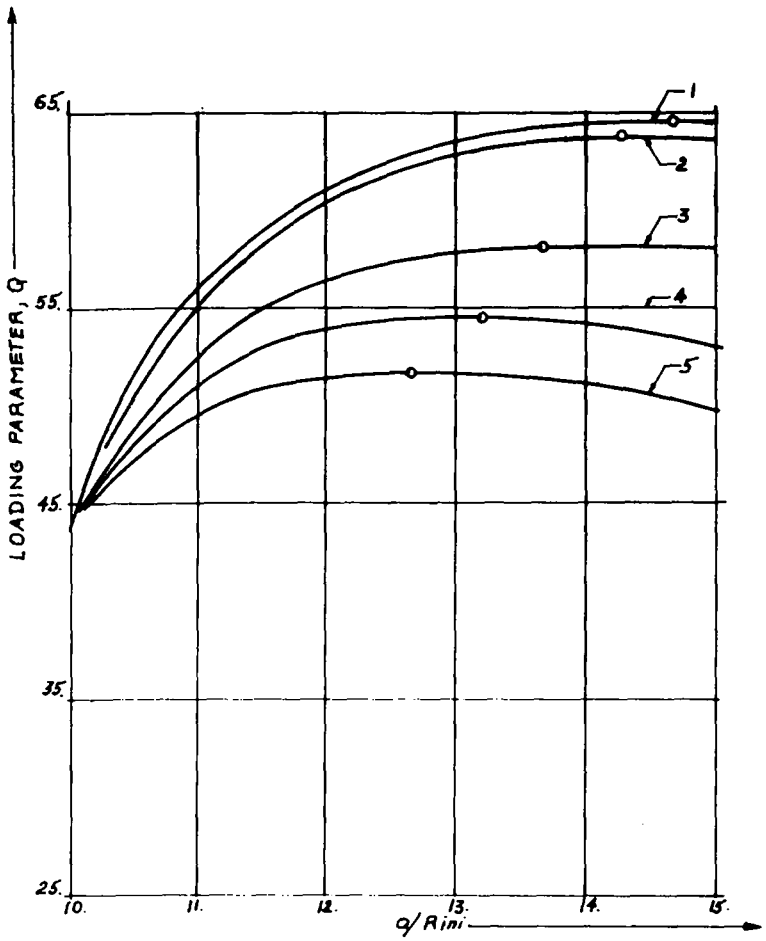

FIG. 6a—*Load versus current crack length curves; terminal instability points attained under load controlled condition are marked by circles. Note that the range shown is insufficient to reach the instability in a displacement-controlled test.*

four-point bend specimen. (Data used for plotting were derived from the R-curves shown in Fig. 5.) The curves in Fig. 6 represent the nondimensional loading parameter $Q(= \pi\sigma/2\sigma_Y)$ as a function of the increment of crack length, $\Delta a = a - a_0$. If the shape factor ϕ, which relates specimen geometry to the K-factor, $K = \sigma\sqrt{a}\phi(a)$, is known, then Q-curve may be obtained from an R-curve in the following way

$$Q(a) = \phi^{-1}\left\{\frac{2\pi R(a)}{a}\right\}^{1/2} \tag{41}$$

The maxima of the Q-curves (marked in Fig. 6*a* circles) correspond to the points of terminal instability attained in a load controlled test, while the stars

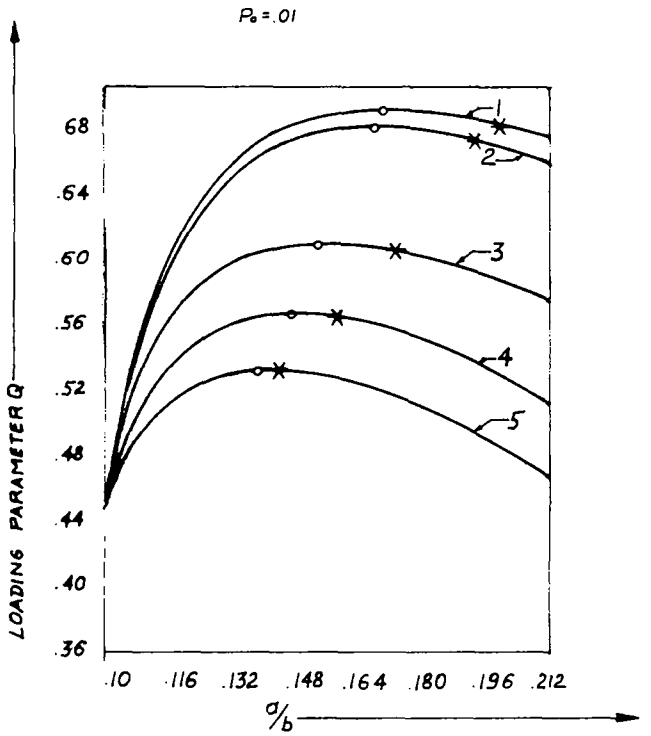

FIG. 6b—*Same curves as Fig. 6a, but the range of stable crack growth has been extended to show the terminal instability points attained in a displacement controlled test (marked by stars).*

are used to designate the points of terminal instability reached in a displacement controlled test.

Case B: Bilinear Restraining Stress

The intricate form of Eqs 13 and 15 prohibits a direct calculation of a resistance curve when the ratio of the size of the inner section of the nonlinear zone ($0 \leq x_1 \leq \beta$) to the extent of the entire end zone ($x_1 = R$) is an arbitrary fraction. However, it is possible to provide certain limiting expressions for an R-curve, analogous to those given by Eqs 36 and 37, which were obtained from considerations based on an assumption of a uniform stress distribution prevailing over the entire end zone.[3] If we consider first the limit

[3]If β is allowed to shrink to zero, that is, when the bilinear distribution of S-stresses is replaced by a linear reduction of the effective stress σ_0 to zero over the length of the end zone, the governing equation for an R-curve reads

$$\frac{dR}{da} = M - \rho + \frac{2\rho - 1}{2\rho^2}\sqrt{\rho(\rho - 1)} + \frac{1}{4\rho^2}\log\frac{\sqrt{\rho} - \sqrt{\rho - 1}}{\sqrt{\rho} + \sqrt{\rho - 1}}$$

of ductile material behavior ($\Delta \ll R$), then the equation defining an R-curve for a bilinear restraining stress assumes the form

$$\frac{dR}{da} = M + 1 - \frac{1}{4\rho^2}\log(4\rho), \qquad \rho = R/\Delta \tag{42}$$

This form is similar to Eq 36 for quasi-static stable fracture in metals.

We shall now focus on the other limiting case corresponding to the brittle behavior, obtained when $\Delta \simeq R$. The equation describing a quasi-static crack (Eq 9) reduces to a simple form

$$\frac{dR}{da} = M - \rho + \frac{4}{3}\left(\frac{\rho - 1}{\rho}\right)^{3/2}, \qquad \rho = R/\Delta \tag{43}$$

which, without a significant loss of accuracy, may be further simplified

$$\frac{dR}{da} \simeq M - \frac{R}{\Delta} \tag{44}$$

This form is identical with the expression obtained for the limiting case of Δ approaching R (Eq 38). Again, the minimum tearing modulus is predicted as

$$M_{\min} = R_{\text{ini}}/\Delta \tag{45}$$

while the upper bound for fracture toughness R_{ss} is related to the growth step Δ and the modulus M as follows

$$R_{ss} = M \times \Delta \tag{46}$$

Figure 7*a* shows an example of the R-curves obtained from the equations discussed here in the limit of Δ approaching R, and Fig. 7*b* illustrates the variations of the loading parameter Q, as predicted by the equations derived from both the models considered previously (Cases A and B). The configuration chosen for plotting Fig. 7*b* is that of four point bend specimen. It is seen that the differences between the two curves are not significant.

Effect of Variable Growth Step on the Resistance Curve

In the preceding section we have shown that the effect of any particular assumption regarding the distribution of the restraining force that prevails over the process zone has negligible effect on the resistance curve resulting from integration of the governing equation (Eq 28). Such is not the case, however, when one chooses to alter the size of the (constant) growth step. By examination of Figs. 5 and 6 it is visible that an increase in the growth step relative to

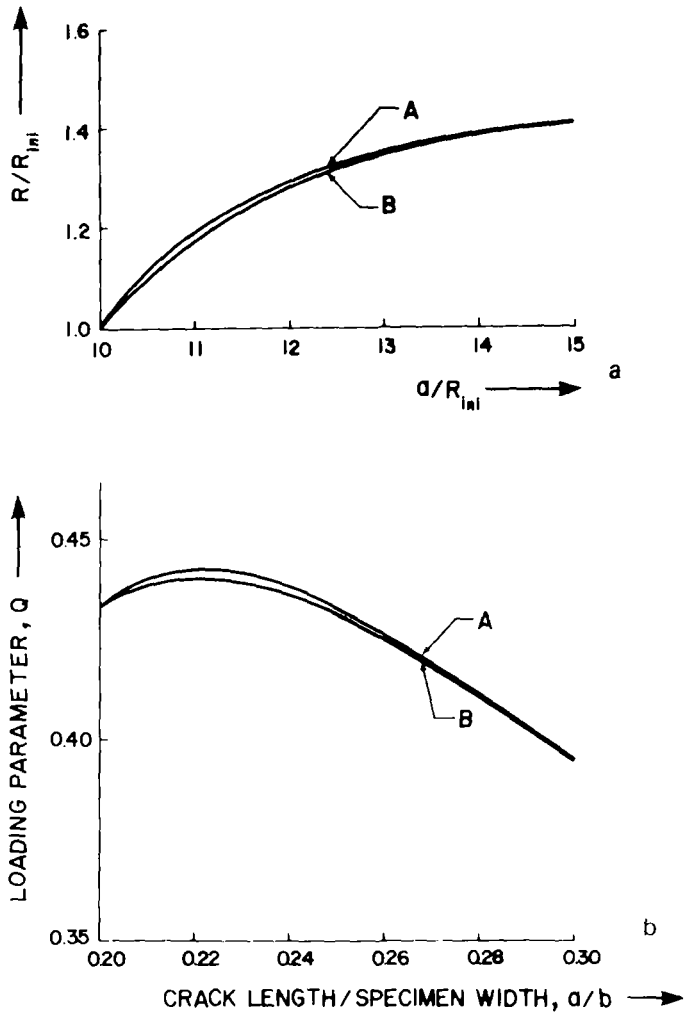

FIG. 7—(a) *Resistance curves and* (b) Q-*curves shown for the two cases of restraining force distribution;* $S(x_1) = \sigma_Y$, *Case A, and Case B, the bilinear stress* S. *Only the limit of brittle material behavior is shown,* $\Delta \rightarrow$ R. *Configuration used to graph the Q-curves is that of a four-point bend specimen.*

the size of the end zone R leads to a considerable change in material response during a stable fracture phase: for Δ much less than R a ductile behavior occurs, while for Δ approaching R one arrives at the limit of the very brittle fracture. It is not the absolute value of the growth step that matters, but its relation to the size of the plastic zone is a decisive parameter.

In earlier treatments of the subject of ductile fracture [*2,11,12,15,16*] the growth step was assumed to be a material property, usually identified with the size of the process zone, and thus related to the microstructure and in-

variant to the amount of stable cracking. Recently, however, it has been suggested by Sih[4] and Curran [*17*] that during a single ductile tear test, in which a crack grows at first in a stable manner due to enlargement and coalescence of voids generated on the prospective fracture path, the size of the growth step may vary from a certain initial value Δ_i up to a much higher level corresponding to brittle fracture, say Δ_f. It is a fact that at the point of terminal instability the physical nature of fracture undergoes a transition, as its mode changes from tearing (ductile mode) to cleavage (brittle mode). Between these two limits of the growth step, Δ_i and Δ_f, one would expect a gradual variation of the quantity Δ, just as one expects the gradual change in the apparent toughness parameters such as R, J-integral, or crack-opening displacement (COD).

Curran [*17*] has pointed out that as a result of continuous strain redistribution ahead of the crack front which progresses discontinuously due to subsequent acts of void coalescence, the increment of crack extension becomes larger as the crack approaches the terminal instability point. The suggested relation between the growth step and an apparent toughness parameter [*17*] was of the kind

$$\Delta = C_1 J_R(a) \quad \text{or} \quad CR(a) \tag{47}$$

in which the constants C_1 and C involve microstructural variables. Such an assumption, although it may appear simplistic, agrees with the outcome of the studies done by Sih and Kiefer [*18*], who suggested that each increment of crack extension is accompanied by an increment in the energy density factor S (chosen as an apparent toughness parameter), so that the ratio of the two, $S/\delta a$ remains constant during the entire phase of stable crack growth. Such a requirement results from Sih's criterion of crack growth, in which the constancy of the strain-energy density along the crack border is postulated. Since the strain-energy density, chosen as a measure of true toughness, is expressed as a ratio of factor S and a small distance $\hat{x}_1$ from the crack tip (identifiable with the process zone size), the constancy of the ratio $S/\delta a$ during the stable crack extension follows naturally.

Following these suggestions we shall now relax the requirement of a constant growth step and repeat briefly the considerations presented in the preceding section leading to derivation of an R-curve. Only one type of distribution of the restraining force will be considered, namely $S(x_1) = \sigma_Y$. For this case the displacements $u_y(t_2)$ and $u_y(t_1)$, which enter into the final stretch crack growth law, may be expressed in terms of R and the R/Δ ratio for any given crack length as follows

[4]Sih, G. C., private communication, 1980.

$$u_y(t_1) = \frac{4\delta_Y}{\pi E_1}\{Rf_1[R/\Delta]\}_{R=R(a)}$$
$$u_y(t_2) = \frac{4\sigma_Y}{\pi E_1} R(a + \Delta) \tag{48}$$

If we now replace the R/Δ ratio by the microstructural constant C^{-1} and apply the final stretch criterion of fracture, as given by Eq 3 or 28, we arrive at

$$\frac{R}{\Delta}\left[1 - f_1\left(\frac{R}{\Delta}\right)\right] + \frac{dR}{da} = \left(\frac{\pi E_1}{8\sigma_Y}\right)\left(\frac{\hat{\delta}}{\Delta}\right) \tag{49}$$

or simply

$$\frac{dR}{da} = M_{\text{ini}}/(R/R_{\text{ini}}) - F_1(C^{-1}) \tag{50}$$

Here, the function F_1 denotes C^{-1} $[1 - f_1(C^{-1})]$, and for the considered near-tip deformation field it reads

$$F_1(C^{-1}) = C^{-1} + \sqrt{C^{-1}(C^{-1} - 1)} + \frac{1}{2}\log\frac{\sqrt{C^{-1}} - \sqrt{C^{-1} - 1}}{\sqrt{C^{-1}} + \sqrt{C^{-1} - 1}} \tag{51}$$

Note that the effective tearing modulus $M_{\text{ini}}/(R/R_{\text{ini}})$ becomes now a function of the amount of crack growth just as R is a function of a. Therefore, an index "ini" has been added to emphasize the variation in modulus M. Its value at the onset of crack propagation is defined as follows

$$M_{\text{ini}} = \left(\frac{\pi E_1}{8\sigma_Y}\right)\left(\frac{\hat{\delta}}{\Delta_i}\right) \tag{52}$$

Since the quantity $F_1(C^{-1})$ is now a constant, Eq 50 may be easily integrated in a closed form. The result is

$$\frac{a - a_0}{R_{\text{ini}}} = F_1^{-2}(C^{-1})\left\{\left(1 - \frac{R}{R_{\text{ini}}}\right)F_1(C^{-1}) + M_{\text{ini}}\log\left|\frac{M_{\text{ini}} - F_1(C^{-1})}{M_{\text{ini}} - (R/R_{\text{ini}})F_1(C^{-1})}\right|\right\} \tag{53}$$

This expression is valid for any value of the constant C taken from the interval (0,1). When $R \gg \Delta$, that is, when C^{-1} is much larger than one, Eq 51 simplifies

$$F^* = [F_1(C^{-1})]_{R \gg \Delta} = \frac{1}{2} + \frac{1}{2}\log(4C^{-1}) \tag{54}$$

while for $R \simeq \Delta$ we obtain another asymptotic form

$$F_* = [F_1(C^{-1})]_{R \simeq \Delta} = C^{-1} - \frac{2}{3}(C^{-1} - 1)^{3/2} \tag{55}$$

Since the form of Eq 53 remains unchanged for these two limiting cases, all one needs to do in order to discuss the two limits of material behavior is to substitute the Eq 54 or Eq 55 for $F_1(C^{-1})$ into Eq 53.

To facilitate such a discussion Figs. 8*a* and *b* show some computer-generated results of simultaneous integration of Eqs 34 and 50, which define an R-curve obtained at a constant and at a variable growth step, respectively, during stable crack extension. It is seen that the assumption of a variable Δ has a pronounced effect on the final outcome of the analysis, that is, the shape of an R-curve. As might be anticipated, the change in material response indicated by assumption of a variable growth step is toward a more brittle behavior. A reduced slope of an R-curve signifies a lesser material resistance to cracking and a diminished amount of stable crack extension. This point is borne out in a yet more obvious way by inspection of Figs. 9*a* and *b*, which show a number of load versus Δa curves, or so-called Q-curves, corresponding to the two cases considered, that is, a constant and a variable growth step. The critical loads attained at the point of transition to fast brittle-like fracture are far *below* those predicted by the equations obtained in the preceding section concerned with the constant Δ case. A similar conclusion pertaining to modification of an R-curve was reached by Ernst [*19*].

A sharp contrast between the results of both approaches discussed here is revealed when the upper bound for the apparent fracture toughness (R_{ss} or K_{ss}) is calculated. Setting dR/da equal zero in Eq 34 or in Eq 50 implies attainment of steady-state situation at which toughness no longer depends on the amount of crack growth. This condition determines the upper toughness limit, which according to Eq 34 valid for a constant Δ, assumes the form

$$F_1\left(\frac{R_{ss}}{\Delta_{ss}}\right) - M_{\text{ini}} = 0 \tag{56}$$

while for a variable Δ it follows from Eq 50

$$R_{ss} = R_{\text{ini}} \frac{M_{\text{ini}}}{F_1(C^{-1})} \tag{57}$$

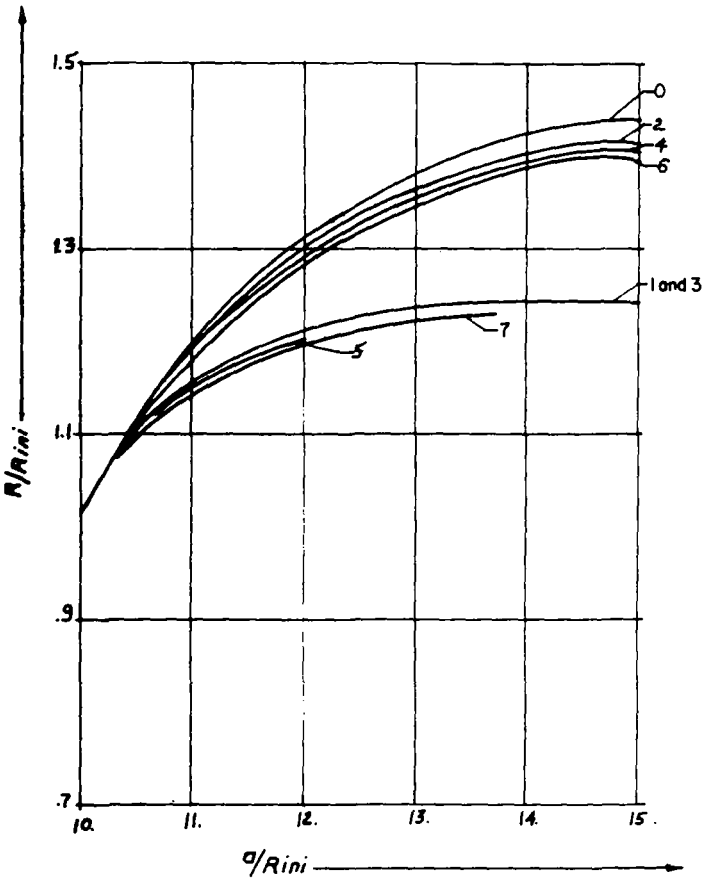

FIG. 8a—*Curves grouped in the upper "band" represent the* R-*curves (designated by even numbers) obtained under an assumption of a constant* Δ *and at these initial conditions:* $C^{-1} = R_{ini}/\Delta_i = R/\Delta = 1.1$ *(Curves 0 and 1), 1.08 (Curves 2 and 3), 1.06 (Curves 4 and 5), and 1.04 (Curves 6 and 7). The lower band of (overlapping) curves corresponds to the assumption of a variable* Δ, *and it has been obtained at the same initial conditions as the curves derived for a constant growth step.*

Solutions to Eq 56 have to be sought numerically, at least for the range of R_{ss} on the same order of magnitude as Δ_{ss}. Within the range of $R_{ss} \gg \Delta_{ss}$, however, one may obtain an explicit relationship

$$R_{ss} = \frac{\Delta_{ss}}{4} \exp\{2M_{\text{ini}} - 1\} \tag{58}$$

This expression leads to unreasonably high values of R_{ss}/Δ_{ss} for a class of ductile solids in which the tearing moduli are much greater than one (note a

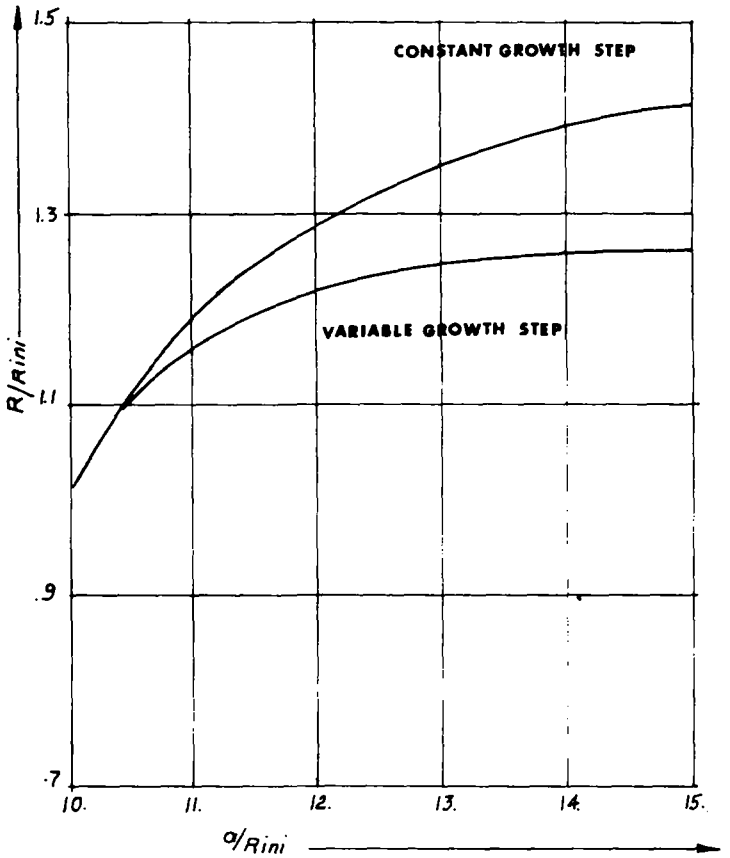

FIG. 8*b*—*Example of two R-curves obtained under assumption of a constant* Δ *and a variable* Δ. *The initial parameter* R_{ini}/Δ_i *was assumed 1.04 for both curves.*

rapid exponential increase of the curve labeled "a" shown in Fig. 10). This deficiency is corrected when Eq 57 is used to evaluate the upper toughness bound. Figures 10*a* and *b* show the distinct difference between the upper toughness levels (R_{ss}/Δ_{ss}) obtained from the solutions corresponding to a constant and a variable growth step.

It is noteworthy that Eq 50, which governs an R-curve and was derived from an assumption of a variable growth step, may be cast into a simple form

$$\frac{dR}{da} = \frac{A_1}{R} - B_1 \tag{59}$$

in which the constants A_1 and B_1 are related to the microstructural properties as follows

$$A_1 = M_{\text{ini}} R_{\text{ini}}$$

$$B_1 = F_1(C^{-1}) \tag{60}$$

$$C^{-1} = R_{\text{ini}}/\Delta_i$$

Multiplying Eq 59 by a constant factor

$$\lambda = 8n\sigma_Y^2/\pi E_1 \tag{61}$$

where n is a numerical factor varying within the range 1 to 2.6 depending on the near-tip state of stress and the degree of material strain hardening, gives

$$\frac{dJ_R}{da} = \frac{A}{J_R} - B \tag{62}$$

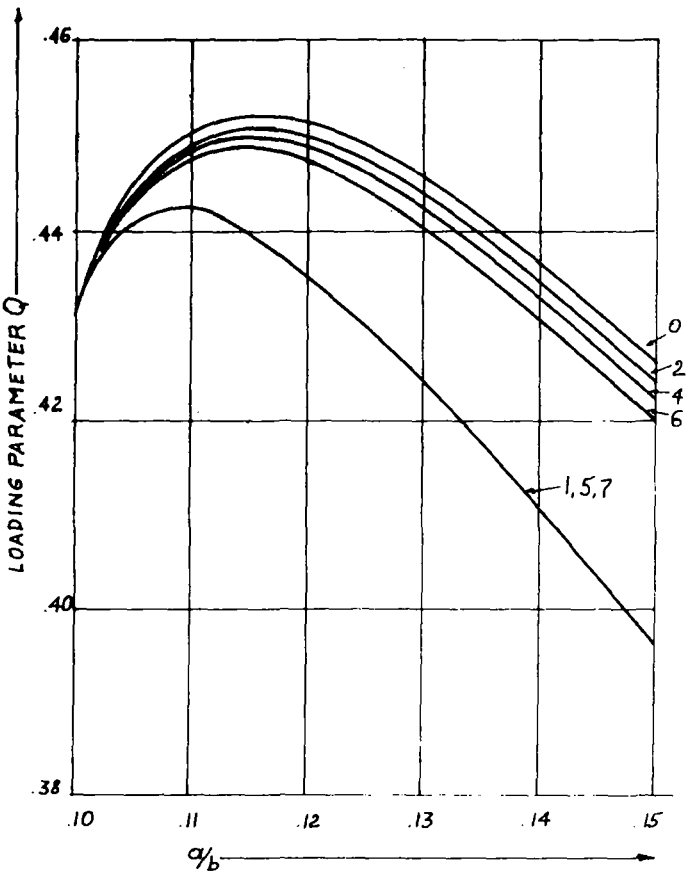

FIG. 9a—Q-curves resulting from the resistance curves shown in Fig. 8a.

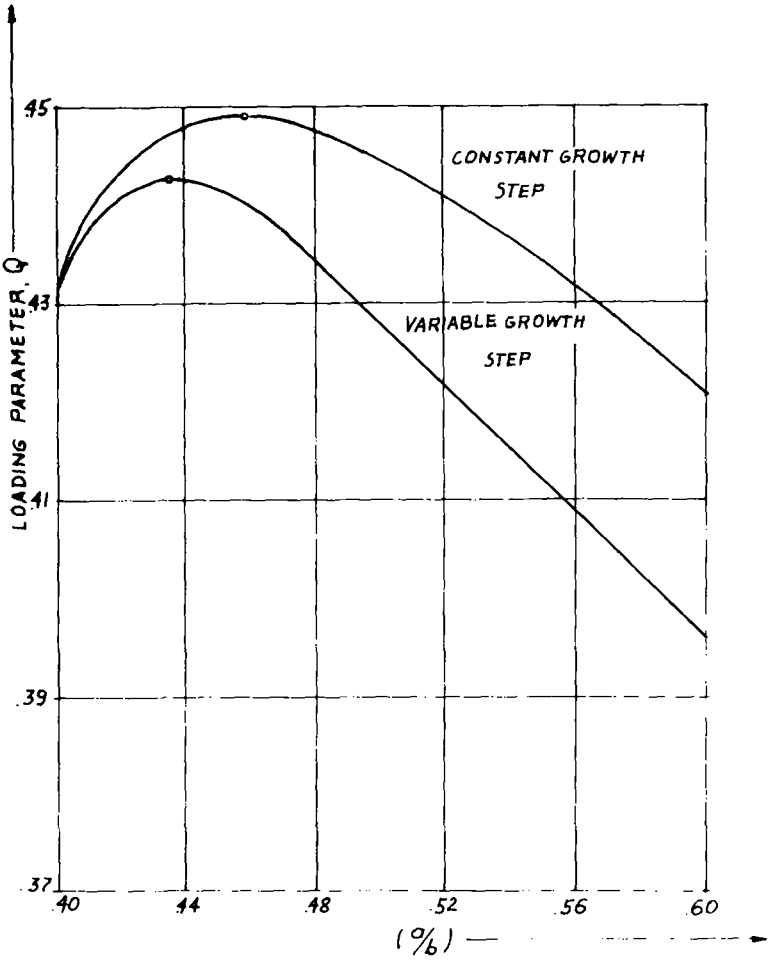

FIG. 9*b*—Q-*curves resulting from the resistance curves shown in Fig. 8*b. *Both sets of curves correspond to a four-point bend specimen configuration, and* Q *denotes a nondimensional loading parameter,* $Q = \pi\sigma/2\sigma_Y$.

Here the constants A and B relate to other material properties as implied by Eqs 60 and 61. These constants may also be readily determined experimentally by matching an empirical J_R versus Δa curve with that predicted by Eq 62. Three examples of this (almost perfect) fit are provided by Figs. 11 to 13. Since the A533B steel (see Fig. 11) and the weld deposit (see Fig. 12) represent two opposite extremes in material behavior, a ductile one and a brittle one, we may conclude that both these limits of material response under fracture are contained in the present mathematical model and they are correctly represented by Eq 62. This observation provides an additional argument in favor of admitting a variable growth step during early stage of crack extension, as suggested by Eq 47.

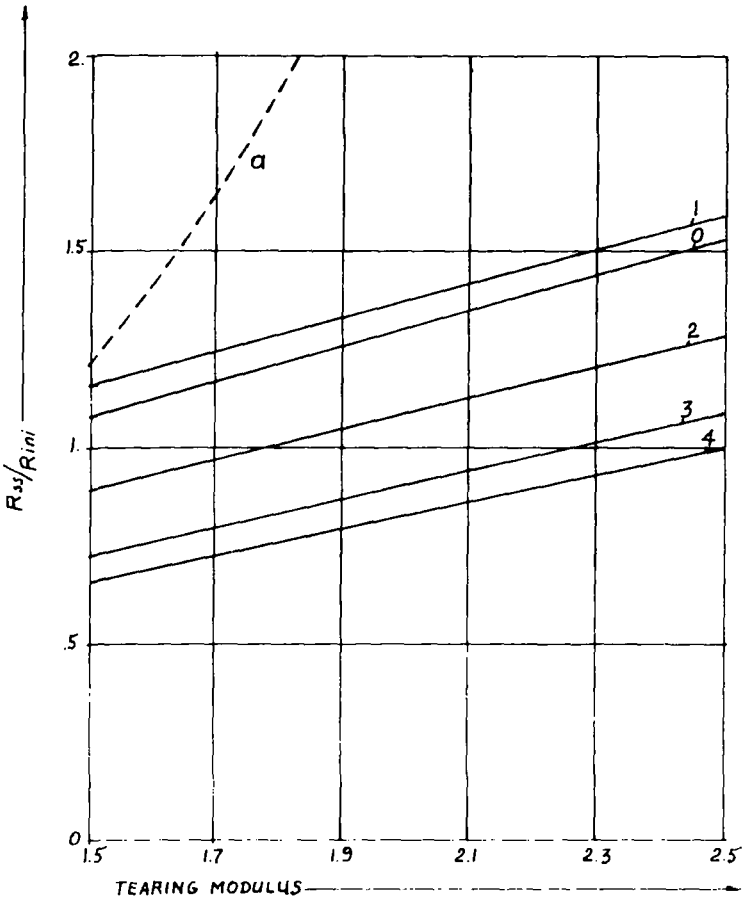

FIG. 10*a*—*Strong and weak dependence of the upper toughness limit* (R_{ss}/R_{ini}) *on the tearing modulus* M, *as predicted according to constant* Δ *approach, Curve "a," and variable* Δ *approach, Curves 0 and 1 to 4. Curve 0 corresponds to a limiting case of an* R-*curve derived from the asymptotic form of the differential equation defining apparent material resistance, valid for* $R/\Delta \gg 1$ *(note that Curves 0 and 1 converge for larger values of the tearing modulus* M*). The parameter* A *has been assumed as follows:* $A = \delta_{ini}/\hat{\delta} = 1$ *(Curves 0 and 1), 2 (Curve 2), 3 (Curve 3), and 4 (Curve 4). Note that the line* $R_{ss} = R_{ini}$ *separates stable from unstable fracture processes, the latter occurring below* $R_{ss}/R_{ini} = 1$.

Conclusions

The model developed here is based on an assumption that the fracture zone formed during the early stages of fracture in inelastic solids is represented by a "fictitious" crack, or a "damage band" of finite width, preceding the dominant crack and able to transfer stress. Such extension of a natural crack is referred to as a "nonlinear zone" in which the laws of elastic plastic fracture mechanics break down.

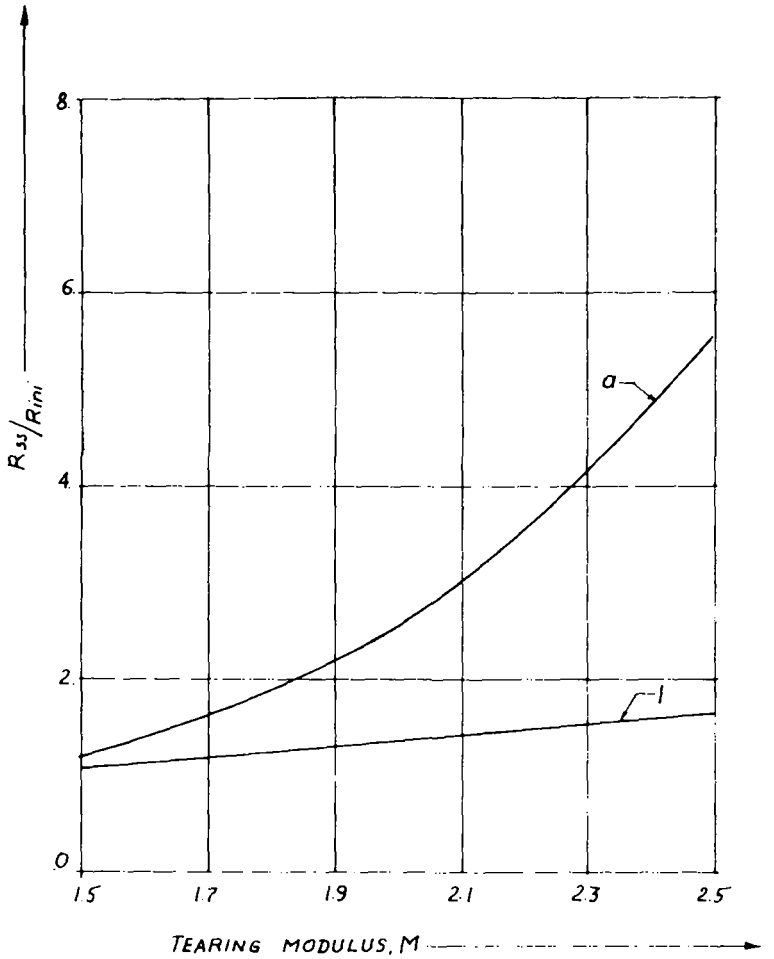

FIG. 10*b*—*Enlargement of Curves "a" and 1 taken from Fig. 10a shows an exponential and a linear relationship between the upper toughness limit* R_{ss} *and the tearing modulus* M.

The stress transferring ability of the damage zone depends on the separation distance created between the two opposite boundaries of a newly formed fracture zone. Although detailed information regarding the distribution of stress prevailing within the nonlinear zone is lacking, it is shown that certain plausible models may be constructed and employed to derive the differential equations that define a resistance curve.

It is suggested that the "essential work of fracture" or so-called "final stretch," which serves as a measure of irreversible deformation, be calculated at each step of an advancing crack. Hence the variations of the toughness parameter with the extent of stable crack growth (an *R*-curve) may be predicted.

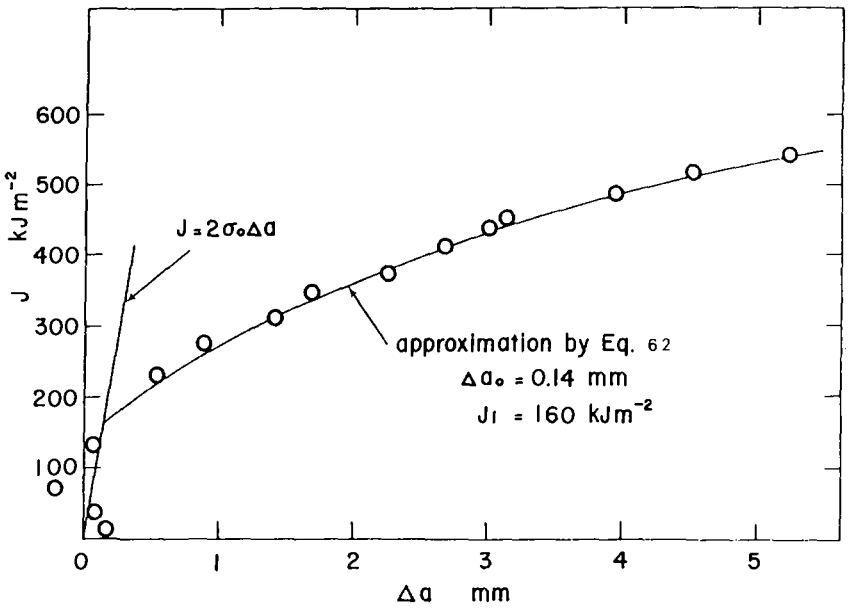

FIG. 11—*Example of a resistance curve for a ductile metal (A533B steel) tested at room temperature). Constants entering Eq 62 are* A = *173 kJ/m² mm,* B = *3 kJ/m² mm. Data points marked by the circles are according to Vassilaros et al [20].*

Such an approach requires that crack growth occur by a series of rapid but intermittent steps. Equations governing the discontinuous motion of a crack are provided, and the stability conditions for fracture developing either under a load-controlled or a displacement-controlled test are discussed briefly. If the domain of intensive straining in which the final act of fracture takes place (the so-called "process zone") is identified with a finite increment of crack length, Δ, then it appears necessary to regard the growth step to depend not only on the microstructure (in which case Δ would be a material constant), but also to reflect the variations of the state of stress prevailing at the tip of a propagating crack. An assumption of a variable Δ seems to gain support from an independent study of microvoid kinetics [*17*].

Variations in the growth step of a quasi-static crack are shown to have a rather pronounced influence on the shape of a resistance curve within the small-scale yielding range. When a modification of the resistance curve is taken into account and examined in view of the stability conditions, the previous models of ductile tear process turn out to be nonconservative. The existing solutions, which assume perfect plasticity to describe a near-tip deformation field such as those resulting from the final stretch model or from the Prandtl slip line field around a propagating crack, as suggested by Rice and Sorensen [*13*], appear to overestimate material ability to sustain stable tearing process prior to occurrence of brittle-like cleavage fracture.

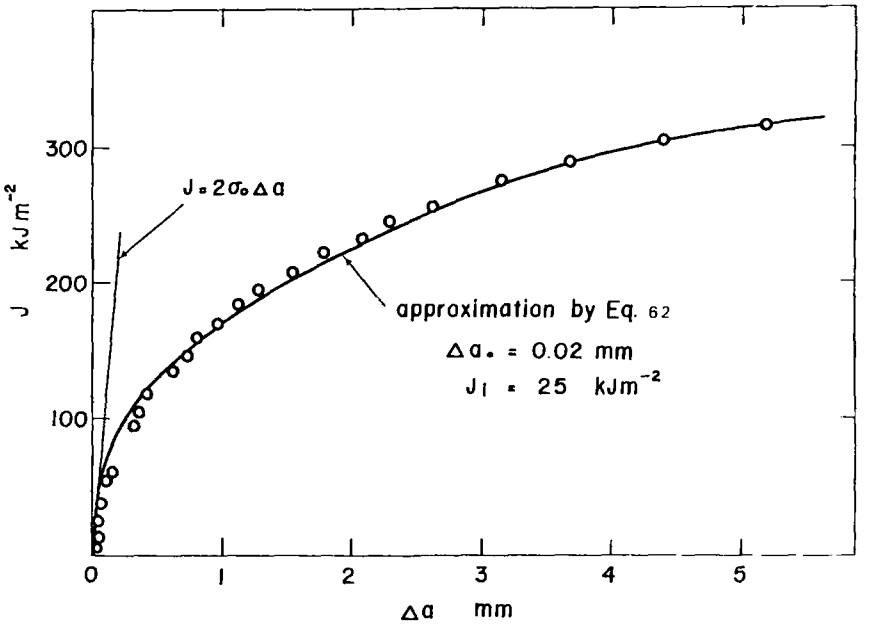

FIG. 12—*Example of a resistance curve for a relatively brittle metal (weld deposit used for A533B steel). Constants entering Eq 62 are* A = 550 kJ/m^2 *mm,* B = 20 kJ/m^2 *mm. Data points are taken from Loss et al [21].*

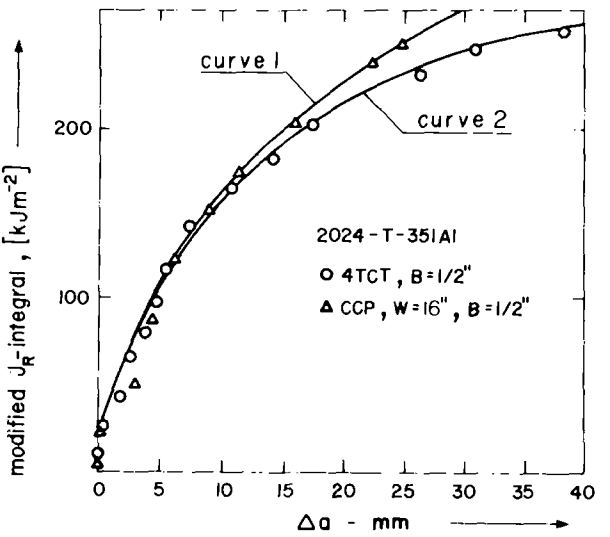

FIG. 13—*Curves 1 and 2 correspond to a center cracked panel (Curve 1) and to a compact tension specimen (Curve 2) made of an aluminum alloy 2024-T-351Al. The data points are taken from Ref* 19, *while the continuous curves are drawn according to Eq 62.*

An unreasonably high steady-state level of fracture toughness K_{ss} predicted by the two approaches discussed is considerably reduced when the restriction concerning a constant growth step is relaxed and a variable Δ is considered instead.

Acknowledgments

One of the authors (MPW) would like to thank the Office of Naval Research (ONR) for supporting this study under ONR Grant No. N00014-81-K-0215.

References

[1] Rice, J. R., "The Mechanics of Quasi-Static Crack Growth," Technical Report No. 63, prepared for U.S. Department of Energy, Brown University, Providence, R.I., Oct. 1978.

[2] Wnuk, M. P. in *Proceedings of International Conference on Dynamic Crack Propagation*, G. C. Sih, Ed., Lehigh University, 1972, pp. 273-280.

[3] McClintock, F. A., *Journal of Applied Mechanics*, Vol. 25, 1958, pp. 582-588.

[4] Kfouri, A. P. and Miller, K. J., *Proceedings of the Institution of Mechanical Engineers*, Vol. 190, 1976, p. 571.

[5] Kfouri, A. P. and Rice, J. R. in *Proceedings of 4th International Conference on Fracture*, D. M. R. Taplin, Ed., Pergamon Press, New York, 1978, Vol. 1, p. 41.

[6] Broberg, K. R. in *Proceedings of International Conference on Fracture Mechanics and Technology*, G. C. Sih and C. L. Chow, Eds., Sijthoff and Noordhoff, The Netherlands, 1977, pp. 837-858.

[7] Cotterell, B. in *Proceedings of International Conference on Fracture Mechanics and Technology*, G. C. Sih and C. L. Chow, Eds., Sijthoff and Noordhoff, The Netherlands, 1977, Vol. 2, pp. 785-795.

[8] Rice, J. R. in *Proceedings of the First International Conference on Fracture Mechanics*, T. Yokobori, T. Kawasaki, and J. L. Swedlow, Eds., Japanese Society for Strength and Fracture of Materials, Toyko, 1966, Vol. 1, p. 309.

[9] Rice, J. R. in *Fracture: An Advanced Treatise*, H. Liebowitz, Ed., Vol. 2, *Mathematical Fundamentals*, Chapter 3, Academic Press, New York, 1968, pp. 191-311.

[10] Knauss, W. G. in *Proceedings of Symposium on Fracture at Battelle Memorial Institute*, M. F. Kanninen, Ed., 1974, pp. 501-541.

[11] Wnuk, M. P., *Journal of Applied Mechanics*, Vol. 48, 1981, pp. 500-508.

[12] Wnuk, M. P., "Extension of a Stable Crack in Inelastic Solids," Annual Progress Report, Technological Institute, Northwestern University, Evanston, Ill., sponsored by Office of Naval Research Grant N00014-81-K-0215, Aug. 1981.

[13] Rice, J. R. and Sorensen, E. P., *Journal of the Mechanics and Physics of Solids*, Vol. 26, 1978, pp. 163-186.

[14] Rice, J. R., Drugan, W. J., and Sham, T. C., "Elastic Plastic Analysis of Growing Cracks," Technical Report No. 65, Brown University, Providence, R.I., 1979.

[15] Wnuk, M. P., *Transactions of American Society of Mechanical Engineers, Journal of Applied Mechanics*, Vol. 41, 1974, pp. 234-242.

[16] Wnuk, M. P., *International Journal of Fracture Mechanics*, Vol. 15, No. 6, 1979, pp. 553-581.

[17] Curran, D., "Dependence of the J-R Curve on Microstructure," Poulter Lab, Technical Report 003-81, SRI International, Menlo Park, Calif., 1981.

[18] Sih, G. C. and Kiefer, B. V., "Nonlinear Response of Solids Due to Crack Growth and Plastic Deformation" in *Proceedings of Symposium on Nonlinear and Dynamic Fracture, II*, G. C. Sih, Ed., American Society of Mechanical Engineers, 1979.

[19] Ernst, H. A. in this publication, pp. I-499-I-519.

[20] Vassilaros, M. G., Joyce, J. A., and Gudas, J. P. in *Fracture Mechanics (12th Conference), ASTM STP 700*, American Society for Testing and Materials, 1980, pp. 251-270.

[21] Loss, F. J., "Structural Integrity of Water Reactor Pressure Vessel Boundary Components," Quarterly Progress Report, Naval Research Laboratory Washington, D.C., 1979.

Bibliography

Kfouri, A. P., *Journal of the Mechanics and Physics of Solids*, Vol. 27, 1979, pp. 135-150.

Kfouri, A. P., *International Journal of Fracture Mechanics*, Vol. 15, No. 1, 1979, pp. 23-29.

Miller, K. J. and Kfouri, A. P. in *Elastic-Plastic Fracture, ASTM STP 668*, American Society for Testing and Materials, 1979, pp. 214-228.

Wnuk, M. P. and Sedmak, S., in *Fracture Mechanics (13th Conference), ASTM STP 743*, American Society for Testing and Materials, 1981, pp. 236-249.

Stress-Intensity Factors

H. P. Rossmanith[1] *and A. Shukla*[2]

Transient Mode I and Mixed-Mode Stress-Intensity Factors During Elastic Crack-Wave Interaction

REFERENCE: Rossmanith, H. P. and Shukla, A., **"Transient Mode I and Mixed-Mode Stress-Intensity Factors During Elastic Crack-Wave Interaction,"** *Fracture Mechanics: Fourteenth Symposium—Volume I: Theory and Analysis, ASTM STP 791*, J. C. Lewis and G. Sines, Eds., American Society for Testing and Materials, 1983, pp. I-131-I-156.

ABSTRACT: A detailed experimental photoelastic investigation of the history of dynamic Mode I and apparent mixed-mode stress-intensity factor during the passage of elastic stress waves over the crack tip is presented. Experimental recordings of isochromatic fringe pattern about static and moving crack tips permit the determination of the history of the complex stress-intensity factor $K = K_1 - iK_2$ which is associated with a mixed-mode crack stress loading.

A first cracking time and a first branching time problem is formulated for stationary and moving cracks. The dependence of the local state of stress at the crack tip on the rate of change of the overall stress field is discussed.

KEY WORDS: dynamic photoelasticity, stress waves, wave diffraction, crack propagation, fracture mechanics, stress-intensity factor, mixed-mode crack loading

Nomenclature

The following nomenclature for the various types of elastic waves generated will be adopted throughout this investigation.

P	Primary/longitudinal/dilatational/irrotational wave
S	Secondary/transversal/shear/rotational wave
R	Rayleigh wave
V	von Schmidt wave or head wave
+(−)	Upper (lower) crack face
$X_d^Z Y$, $X_r^Z Y$	Diffracted (d) and reflected (r) wave of type X at crack tip Z due to an incident wave of type Y (X, Y = P, S)
$R_{\pm} X$	Rayleigh wave traveling along upper (+) or lower (−) crack wall and generated by an incident wave of type X

[1]Associate professor, Institute of Mechanics, Technical University of Vienna, Vienna, Austria.
[2]Assistant professor, Department of Mechanical Engineering and Applied Mechanics, University of Rhode Island, Kingston, R.I. 02881.

For reasons of clarity the formal formation of a secondary lower Rayleigh wave is illustrated:

$P \rightarrow S_d{}^A P \rightarrow R\_{}^B S^A P$ characterizes the generation of a Rayleigh wave propagating along the lower crack face and generated by diffraction about crack tip B of the shear wave $S^A P$ which was generated by diffraction about crack tip A of the incident P-pulse.

r, θ	Polar coordinate system attached to the crack tip
x_0, y_0	Coordinates of wave source in the reference coordinate system
c	Crack speed
c_1, c_2	Wave propagation speeds (P, SV)
c_t	Terminal crack speed
a, l	Crack length
t	Time
w	Net ligament
t_e, x_e	Time and location of crack wave encounter
t_b, a_b	Time and location of crack branching
Δt	Duration of crack wave encounter
t^*	Time-like variable
f_σ	Material fringe value
h	Plate thickness
$N^{(i)}, N$	Photoelastic fringe order for isochromatics associated with incident and total wave fields, respectively
σ_1, σ_2	Principal normal stresses
τ_m	Maximum in-plane shear stress
SIF	Stress-intensity factor
K_{dc}	SIF for running crack subjected to static prestress and stress wave loading
K_{do}	SIF for stationary crack of equivalent length subjected to static prestress and stress wave loading
K_{sc}	SIF for running crack subjected to static prestress (no wave)
K_{so}	SIF for stationary crack subjected to static prestress
K_{br}	SIF just prior to crack branching
K_1	Mode I SIF
K_2	Mode II SIF
K	$K_1 - iK_2$ Mixed-mode stress-intensity factor
P, S	Refer to corresponding wave type

Relations among SIF's

$$K_{sc}(l, c) = k(c)\, K_{so}(l, o)$$
$$K_{dc}(t, c) = k(c)\, K_{do}(t, o)$$

$k(c)$ = universal function of the crack tip velocity

K_d	Dynamic fracture toughness
$\mathcal{G}$	Strain energy release rate

$\mathcal{G}_c$ Critical value of $\mathcal{G}$
$g(c)$ Auxiliary function
$\mathcal{G}_D$ Dynamic material resistance
K_D $(\mathcal{G}_D E)^{1/2}$

Crack-wave interaction processes are important in many fields of research. At times of increasing demand for energy, fracture mechanics and wave propagation play an active role in the exploitation of new and profitable energy resources. Of particular significance are geothermal heat exploitation, oil shale research, and surface and underground mining operations. Knowledge of crack-wave interaction enables one to optimize fragmentation and consequently reduce the cost of mining operations.

Rock formations found at quarry sites and oil shale sites from stacks of layered rock with bedding planes and joint sets present. Upon detonation of an explosive, the wave pattern generated in layered media is extremely complicated and static and running cracks interact with incident and reflected elastic wave systems. Depending on the nature of the wave the cracks may initiate, accelerate, or decelerate during the interaction phase. In particular situations crack path instability may induce crack branching.

During the past decade considerable work has been devoted to the problem of a crack subjected to stress wave loading. Most of the analytical results of crack-wave interaction compiled and critically reviewed in Ref *1*[3] are related to the transient response of cracks to impact loads and scattering of waves about stationary and moving cracks. Very recent analytical work on wave diffraction at stationary crack tip is due to Brock [*2-4*] and Harris [*5,6*]. The results of the latter author's investigations of the transient response of cracks to impinging cylindrical wave fronts emitted from a source at finite distance from the crack tip and the associated diffraction problem are of particular interest in the photoelastic crack wave interaction problem.

Experimental investigations of crack wave interaction date back to the work by Schardin [*7*], Kerkhof and co-workers [*8*], and others. Photoelastic studies and research in dynamic crack-wave interaction are rather limited. An experimental photoelastic investigation concerning the interaction between a stationary crack and an impinging dilatational wave is due to Smith [*9*]. The stress intensification at the tips of the crack was evaluated and found to be significantly higher than in the corresponding static case. The dynamic stress-intensity factor reduces to the static value for the case of a very high wave length to crack length ratio. Photoelastic studies by Rossmanith and Shukla [*10,11*] focus attention on the dynamic interaction between static and running cracks and stress waves impinging in a direction normal, tangential, and oblique to the prospective crack propagation plane.

This paper deals with the determination of the history of the apparent

[3]The italic numbers in brackets refer to the list of references appended to this paper.

mixed-mode stress-intensity factor $K = K_1 - iK_2$ at stationary or moving crack tips during wave diffraction. A first-cracking-time and first-branching-time problem is formulated in the stress-intensity factor $K_1 - K_2$-plane for stationary and moving crack tips. In addition, the influence of the rate of change of the stress field applied onto mixed-mode cracking is discussed. Dynamic photoelasticity has been used as a means for recording the sequences of isochromatic fringe patterns and thus visualizing the highly complex interaction process between stress waves and cracks.

Theoretical Considerations

During blasting or an earthquake phenomenon several types of elastic waves are generated. The longitudinal and shear waves spread out in hemispherical wave fronts with the spacing of their wave fronts in accord with their differing velocities. Miller and Pursey [*12*] have computed the partition of energy among the dilatational, shear, and surface waves due to an oscillating normal point force. Woods's [*13*] representation in Fig. 1*a* shows the geometric attenuation of the displacement amplitudes with radial distance. The "shear window" indicates the portion of the shear wave arc along which the amplitude is greatest. In addition, a circular Rayleigh surface wave front carrying the major part of the input energy in a thin layer just underneath the

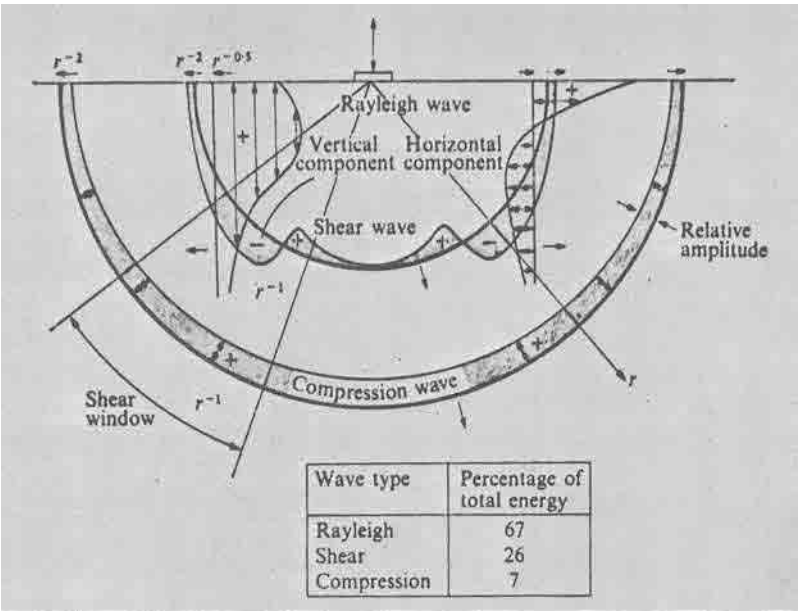

FIG. 1*a*—*Distribution of displacement and energy in dilatational, shear, and surface waves from a harmonic normal load on a half-space for* $\nu = 1/4$ *(after Ref* 13*).*

free surface propagates in a radial direction from the locus of excitation. Although the results shown in Fig. 1*a* pertain to spherical wave emission (with geometric attenuation of the stress of the order r^{-1} and $r^{-0.5}$ for body waves and surface waves, respectively) similar results will hold for the two-dimensional analogue (with cylindrical stress field attenuation of the orders $r^{-1/2}$ and r^{0} for body and surface waves, respectively). Thus Fig. 1*b* shows a dynamic photoelastic recording of the wave system generated during explosive excitation at the free surface of a half-plane model of Homalite 100 where the P, S, V, and R-waves can be identified clearly. Their associated wave propagation velocities are $c_P = 2150$ m/s, $c_S = c_V = 1230$ m/s, and $c_R = 1110$ m/s, respectively.

The stress field associated with the incident P-wave is compressive in the leading part and tensile in the trailing part of the wave with a ratio of stress biaxiality $\sigma_r/\sigma_\theta = \sigma_1/\sigma_2 = 2.5$. The stress field associated with SV-wave is pure shear and its intensity distribution is extremely nonuniform, showing two distinctive symmetrical maxima.

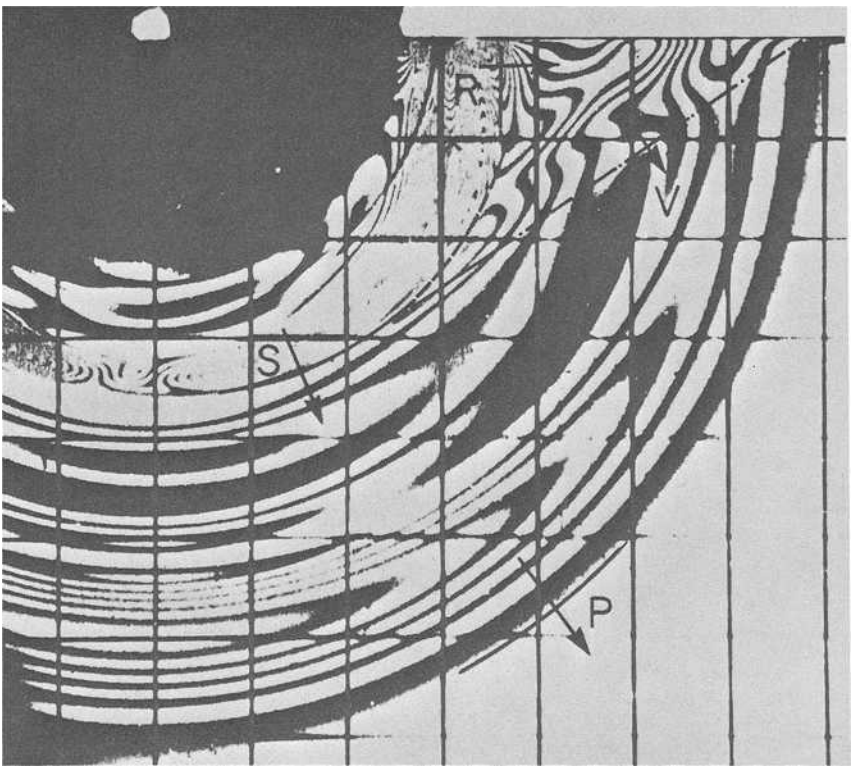

FIG. 1*b*—*Dynamic photoelastic recording of wave emission during explosive point force excitation at the free surface of a half-plane.*

The Diffraction Problem

When elastic waves are generated and propagated in a heterogeneous solid they are diffracted at the geometric discontinuities which most often are cracks or inclusions or both. The diffraction process may give rise to high elevation of local stresses. This stress amplification becomes extremely severe when the discontinuity is a crack and might lead to unstable crack propagation. The incident wave can be either a P-wave (polarized in the direction of the incoming wave), or an S-wave which may be decomposed into an SH-wave (polarized parallel to the horizontal x-z crack plane) and an SV-wave (polarized parallel to the vertical xy-plane). Plane dynamic photoelasticity deals with P- and SV-wave propagation. Figure 2 shows the standard diffraction problem of cylindrical wave pulse impinging on a static or moving semi-infinite crack.

In fracture mechanics the deformation of the crack surfaces induced by the wave interaction process are classified into three modes: Mode I (normal opening mode deformation), Mode II (in-plane shearing mode deformation), and Mode III (antiplane shearing mode deformation). In connection with (obliquely) impinging P- and SV-waves the first two fracture modes occur in various combinations in isotropic materials. General wave diffraction at crack tips gives rise to a mixed-mode transient fracture problem which for

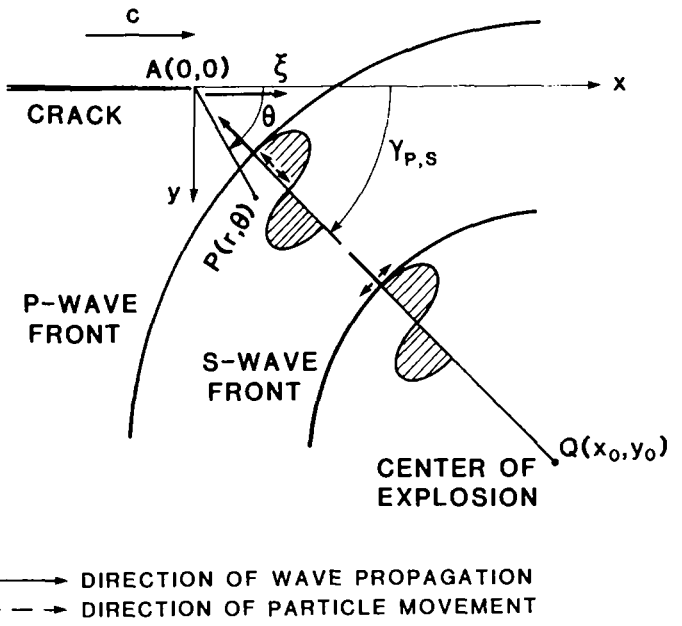

FIG. 2—*Classical diffraction problem of cylindrical wave pulse impinging on a static or moving semi-infinite crack.*

analysis purposes is divided conveniently into a symmetric part (Mode I) and an antisymmetric part (Mode II) [5,6].

Consider the propagation of elastic waves and their interaction with a static or running crack as shown in Fig. 2. The input waves are diffracted and scattered about the crack tip A. Regardless of the type of incident waves, whether P- or SV-waves, diffraction gives rise to the generation of both P- and SV-waves. The total stress field $\sigma_{ij}(x,y,t)$ is composed of the stress fields of the incident wave $\sigma_{ij}^{(i)}(x,y,t)$ and the scattered field associated with the diffracted P- and SV-waves $\sigma_{ij}^{(s)}(x,y,t)$

$$\sigma_{ij}(x,y,t) = \sigma_{ij}^{(i)}(x,y,t) + \sigma_{ij}^{(s)}(x,y,t) \tag{1}$$

with an appropriate radiation condition for the scattered field and the associated wave function satisfies the Helmholtz equation [14]. In addition, boundary conditions appropriate for stress-free crack surfaces are to be described. In the immediate vicinity (singularity region) of the crack tip the plane stresses due to a scattered P- or SV pulse are assumed to be of the form

$$\sigma_{ij}^{(s)}(t,c) = \sum_{n=1}^{n=2} \frac{K_n(t,c)}{\sqrt{2\pi r}} f_{ij}^{n}(\Theta,c) + 0(1) \tag{2}$$

where t and c denote time and crack speed, $K_n(t,c)$ is the dynamic time-dependent stress-intensity factor, and n denotes the mode of fracture.

The total local crack-tip stress field in the region $\{|\Theta| < \pi/2; r < c_p t\}$ is obtained by substituting Eq 2 into Eq 1. Restriction to the close crack tip vicinity $r/a < 0.1$, that is, neglecting higher order terms except for the one associated with r^0 in the stress σ_{xx}, α_0, and using the relation for the maximum in-plane shear stress, $\tau_m = (\sigma_1 - \sigma_2)/2$, the expected shape of the isochromatics near the crack tip is found to be [15,16]

$$\tau_m^2 = \left(\frac{Nf_\sigma}{2h}\right)^2 = F\{K_1, K_2, \sigma_1^{(i)} - \sigma_2^{(i)}, \Theta, \alpha_0\} \tag{3}$$

with

$$\sigma_1^{(i)} - \sigma_2^{(i)} = \frac{N^{(i)} f_\sigma}{h} \tag{4}$$

The function F is quadratic in K_1 and K_2 and is given in Refs 15 and 16. The quantity N is the order of the isochromatic fringe at the crack tip. When the incident wave (P) shows rotational symmetry as for a subsurface wave source employed in Ref 9, $N^{(i)}$ may be obtained at a point on the incident wave front corresponding to the location of the crack tip but remote from the actual crack tip. If the wave source is located on a free surface, the resulting P- *and*

SV-waves show nonuniform angular distributions for the wave amplitudes. Then, a convenient engineering approach to the measurement of $N^{(i)}$ is to measure the fringe order along the prospective angular coordinate of wave-crack interaction at an earlier phase of wave propagation, that is, in an earlier frame of the sequence of photoelastic fringe patterns as shown in Fig. 3. Amplitude and wave shape then have to be corrected for the geometric dispersion and changed crack tip location for the running crack between the measurement phase and the interaction phase.

Moving cracks interacting with P- and SV-waves have been investigated by

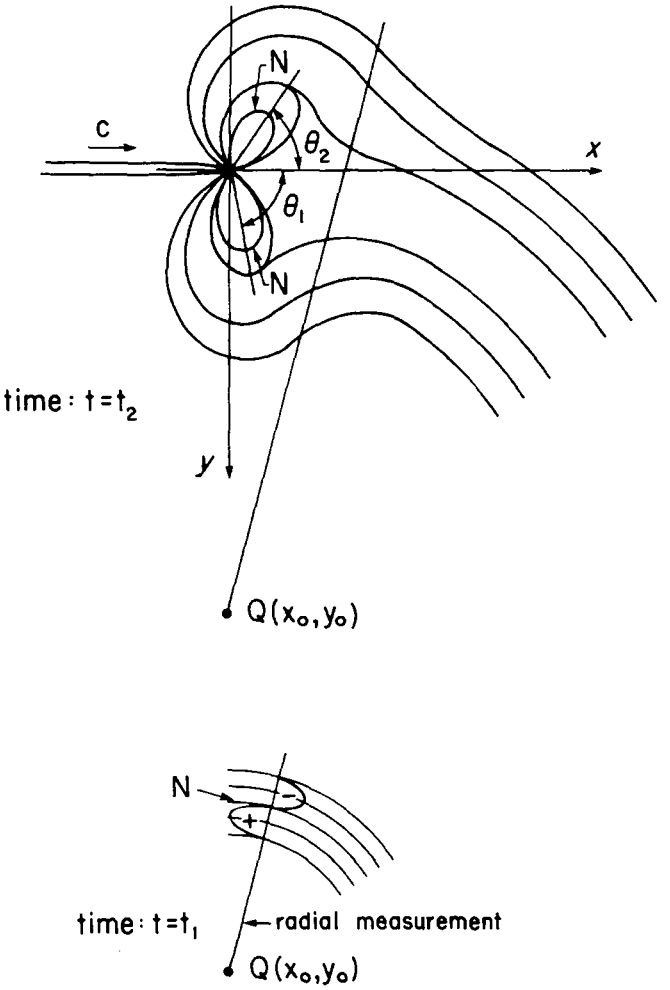

FIG. 3—*Measurement of fringe orders* $N^{(i)}$ *and* N *associated with wave diffraction about a static or running crack tip.*

Chen and Sih [*1*] and Freund [*17*]. For plane harmonic waves the treatment for running cracks is similar to the method for stationary cracks except that the problem is formulated with respect to a set of moving coordinates. At least for the singular solution the $r^{-1/2}$ stress singularity is the same as that of a stationary crack while the angular variation of the stress field around the crack tip is increasingly distorted with increasing crack velocity.

The dynamic stress-intensity factors K_1 and K_2 for the moving crack-wave interaction process are complicated functions of the circular frequency ω, input wave amplitudes σ and τ, angles of incidence γ_p and γ_s, and crack speed c. If the influence of input P- and SV-wave in K_1 and K_2 is separated, the dynamic stress-intensity factors for incidence of P- or SV-wave can be represented in the form [*1*]

P-wave incidence

$$K_p = \bar{K}_{1p} - i\bar{K}_{2p} = \sigma\sqrt{\lambda_p}\,(K_{1p} - iK_{2p})\,G_p\,(\omega, \alpha_p, \gamma_p, a/L) \quad (5a)$$

SV-wave incidence

$$K_s = \bar{K}_{1p} - i\bar{K}_{2s} = \tau\sqrt{\lambda_s}\,(K_{1s} - iK_{2s})\,G_s\,(\omega, \alpha_s, \gamma_s, a/L) \quad (5b)$$

where λ_p and λ_s are the wave length of the P- and S-wave, respectively, and the functions G_p and G_s are given in Ref *1*. It can be noted that the peaks of the individual contributions K_{jp} and K_{js} do not coincide but occur at different angles. This phase difference in $\bar{K}_1$ and $\bar{K}_2$ which depends on the crack speed, angle of incidence, etc., has a significant influence on the crack path stability under dynamic mixed-mode conditions. For cracks of finite length and wave pulses the functions depend also on the crack length-to-pulse length ratio a/L, where L is a characteristic length of the pulse. Typical values of L from explosive model studies are $L = 25$ to 26 mm and a crack length of $a = 50$ to 100 mm.

Photoelastic Study of Running Crack-Wave Interaction

Experimental Procedure

Dynamic photoelasticity was utilized to study running crack-wave interaction in a single-edge-notched specimen. Photoelasticity provides whole field data during the propagation period which contains the instantaneous stress-intensity factor, the crack tip position, and the change in the state of stress across the section due to crack movement and crack-wave interaction.

The geometry of the single-edge-notched (SEN) specimens used in the running crack wave interaction study is shown in Fig. 4.

The specimens were fabricated from a 9.5-mm-thick sheet of a brittle polyester, Homalite 100. This polyester becomes temporarily birefringent when subjected to a state of stress and gives rise to optical interference fringes when

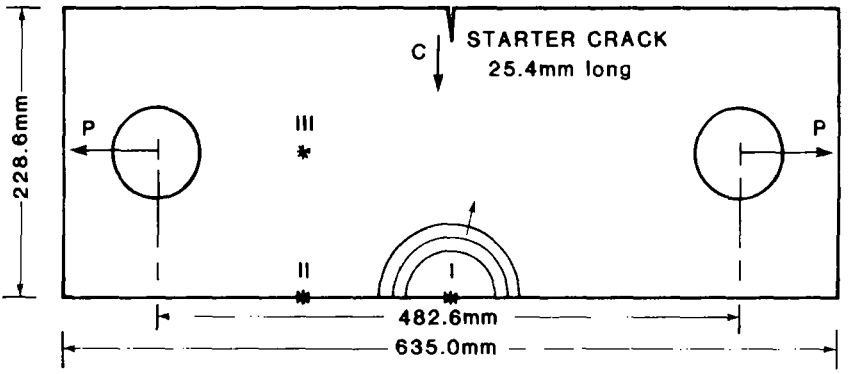

FIG. 4—*Geometry of SEN specimen and loci of explosive wave source.*

viewed in a circular polariscope. These fringes are known as isochromatics and represent the line along which the maximum shear stress is a constant.

A blunt starter crack was saw-cut into the specimen, as shown in Fig. 4, and the crack tip was rounded to inhibit premature initiation at high values of K_Q. The crack then was initiated by drawing a sharp blade across the tip. As the crack propagated, it interrupted a silver conductive paint line on the model and triggered the multiple-spark Cranz-Schardin camera and the explosive after prescribed delay times [*18*]. The Cranz-Schardin camera used provides 16 frames at discrete times during the dynamic event. The sparks provide light pulses about 500 ns in duration and thus effectively stop the motion of the fringes during the exposure time. A framing rate of about 200 000 frames per second was used in the experiments. This provided an observation period of 90 μs which was well matched with the interaction process being studied.

The dynamic mechanical and optical properties of Homalite 100 were determined by Metcalf and Kobayashi [*19*] and are given in Table 1.

Elastic Wave Diffraction About a Running Crack: Nonoblique Incidence

Consider the specimen geometry of Fig. 5 with the wave source located at Point 1. At some prescribed delay time after crack initiation elastic waves radiate from the center of explosion as shown in Figs. 1 and 2. During the interaction phase the normal to the wave front and the crack path are colinear but oppositely oriented. The dynamic stress-intensity factor, K_{dc}, for Mode I extension of a half-plane crack is given by a universal function of crack tip velocity $k(c)$ times the stress-intensity factor, K_{do}, appropriate for a crack of fixed length, equal to the instantaneous length, subjected to the given applied loading, whether this loading is time-dependent or time-independent

TABLE 1—*Dynamic mechanical and optical properties of Homalite 100* [19].

Plate wave velocity	$c_1 \equiv c_p$, m/s	2150
Shear wave velocity	$c_2 \equiv c_s$, m/s	1230
Rayleigh wave velocity	c_R, m/s	1110
Static Young's modulus	E_s, GPa	3.86
Dynamic Young's modulus	E_d, GPa	4.83
Dynamic shear modulus	μ, GPa	1.84
Dynamic Poisson's ratio	ν	0.31
Mass density	ρ, kgs^2m^{-4}	122
Minimum stress-intensity factor	K_{Im}, $MNm^{-3/4}$	0.42
Static material fringe value	$f_{\sigma s}$, MPa-m/fringe	19.3
Dynamic material fringe value (λ = 492 nm)	$f_{\sigma d}$, MPa-m/fringe	21.9

[*17*]. Assuming that a similar relation could be applied approximately to a crack of finite length in a finite specimen, one obtains

$$K_{dc}(t, l) = k(c) K_{do}(t, l) \tag{6}$$

where $K_{dc}(t, l)$ is a dynamic stress-intensity factor for the running crack which was subjected to a stress wave with pulse shape given in Fig. 5 at time zero, becoming l in length and reaching speed c at time t, and $K_{do}(t, l)$ is a dynamic stress-intensity factor at time t for a stationary crack of length equal to the instantaneous length of the running crack and has been subjected to the identical stress wave at time zero. In a first engineering approximation the function $k(c)$ [*17*] may be represented by $k(c) = 1 - c/c_R$ for $0 < c/c_R < 1$ where c_R is the speed of the Rayleigh wave.

Postulating that crack propagation occurs and continues when the value of the dynamic stress-intensity factor exceeds a critical value—the dynamic fracture toughness, K_d—one obtains as a fracture criterion

$$K_{do}(t, l) \times (1 - c/c_R) = K_d \tag{7}$$

Since experimental measurements have shown that the crack speed in the SEN-crack-wave interaction problem was constant, the spatially fixed x-coordinate attached to the tip of the starter crack is eliminated in favor of the coordinate $\xi = x - ct$ where the (ξ, y) coordinate system moves along with the crack tip. Suppose now that the crack begins to move at time $t = 0$ with constant speed c, whereas the P-wave is emitted at $t = t_0$ $(t_0 > 0)$ at a distance w from the tip of the starter crack and spreads with speed c_1. The time t_e and the place x_e of the first encounter are then $t_e = w/c - t_0(1 - c/c_1)^{-1}$ and $x_e = ct_e$. The duration of crack-wave interaction is given by $\Delta t = \lambda(c_1 + c)^{-1}$ with λ the wave pulse length as shown in Fig. 5.

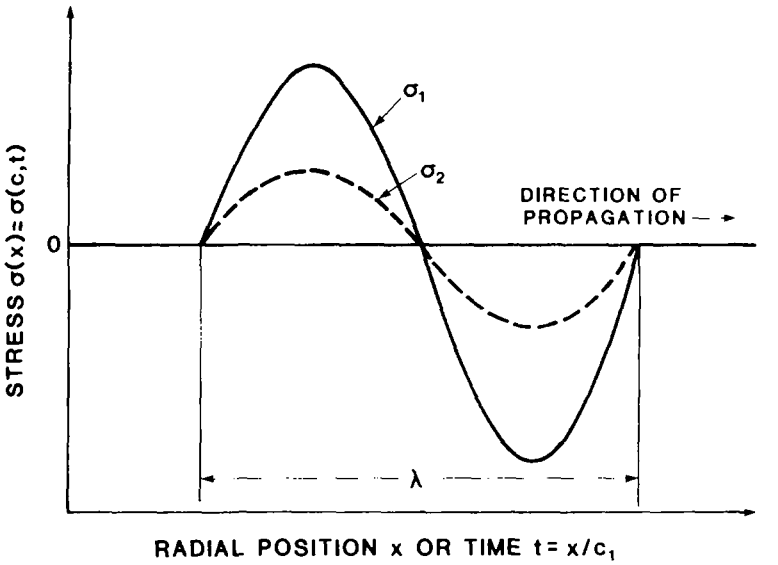

FIG. 5—*Approximate stress distribution along the line of symmetry for a P-wave.*

The dynamic stress-intensity factor associated with a constant-speed running crack subjected to stress loading with a real time pulse profile

$$\sigma(q) = \nu N(q) + N_0 = \sum_{n=0}^{N} \alpha_n q^n \tag{8}$$

where ν, α_n are real constants and $N(q)$ is obtained from isochromatic fringe pattern evaluation, as given by Ref *17*

$$K_{dc}(t^*, c) = Ak(c) \int_{0-}^{t^*} (t^* - q)^{1/2} \sigma'(q) dq \tag{9}$$

and A is a constant. The time-like quantity $t^* \equiv t + c(t - \tau)/c_1$ is a measure of the time that would have elapsed since the incident wave hit the crack tip if the crack tip had always been at its instantaneous position. The quantity τ is considered the time delay between wave incidence and crack initiation; for the running crack wave interaction problem it holds $\tau = 0$, hence, $t^* \equiv t(1 + c/c_1)$. $\sigma'(q)$ is a description of the actual wave profile in Eq 8 and the variable q measures distance behind the wavefront on a real time basis.

Combination of Eqs 8 and 9 renders

$$K_{dc}(t^*, c) = A\nu k(c) \int_{0-}^{t^*} (t^* - q)^{1/2} N'(q) dq \tag{10}$$

$$= A\,k(c) \sum_{n=0}^{N} \alpha_n' t^{n+3/2} \tag{11}$$

where the α_n' form a set of real coefficients.

The result for a simple step pulse $\sigma'(q) = H(q)\sigma_0$

$$K_{dc}(t^*, c) = A\,k(c)\sigma_0 t^{*1/2} \qquad t^* > 0 \tag{12}$$

serves as a basis for the evaluation of the stress-intensity factor $K_{dc}^{\sqcap\!\sqcup}(t^*, c)$ induced by the square pulse

$$\sigma_y(x) = \sigma_0\,[H(x) - (1 + \delta)H(x - \lambda_1) + \delta H(x - \lambda_1 - \lambda_2)] \tag{13}$$

as shown in Fig. 6.

The distribution of $K_{dc}^{\sqcap\!\sqcup}(t^*, c) = \beta\sigma_0 k(c)\,K_{do}^{\sqcap\!\sqcup}(t^*, 0)$ is given by

$$K_{do}^{\sqcap\!\sqcup}(t^*, 0) = \begin{cases} t^{*1/2} & \text{for} \quad T_0 \le t^* \le T_1 \\ t^{*1/2} - (1+\delta)(t^* - T_1)^{1/2} & \text{for} \quad T_1 \le t^* \le T_2 \\ t^{*1/2} - (1+\delta)(t^* - T_1)^{1/2} + \delta\,(t^* - T_2)^{1/2} & \text{for} \quad T_2 \le t \end{cases} \tag{14}$$

where T_0, T_1, and T_2 denote the arrival times of the stress pulse jumps.

The total dynamic stress-intensity factor for the Mode I crack wave interaction problem is composed of the sum of the stress-intensity factor for the crack running in an SEN specimen subjected to time-independent loading in the form of body forces or remotely applied tractions and the stress-intensity factor variation due to stress wave loading

$$K_{dc}^{(tot)}(t^*, c) = K_{sc}(t^*, c)/\text{no wave} + K_{dc}(t^*, c)/\text{wave} \tag{15}$$

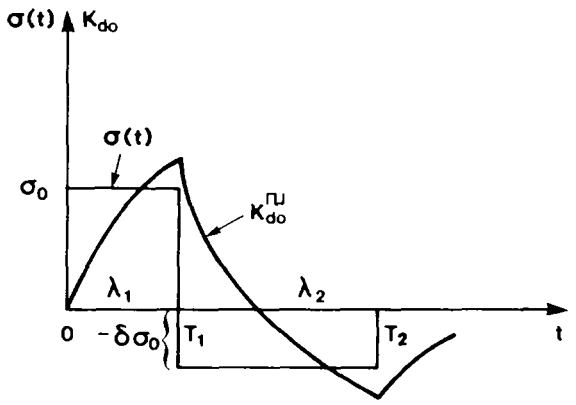

FIG. 6—*Square shaped stress pulse and associated static stress-intensity factor* $K_{do}^{\sqcap\!\sqcup}$.

The strain energy release rate for the present case [*17*]

$$\mathcal{G}(t^*, c) = \frac{1 - \nu^2}{E} A_1(c) [K_{dc}^{(tot)}(t^*, c)]^2 = g(c)\, \mathcal{G}(t^*, 0) \tag{16}$$

and the fracture criterion

$$\mathcal{G}(t^*, c) = \mathcal{G}_D \tag{17}$$

allow a derivation for the equation of motion for the crack tip. The function $g(c)$ is given in Ref *17*. The dynamic material resistance or critical strain energy release rate $\mathcal{G}_D$ may be considered independent of the crack speed c for $c/c_R < 1/4$ of the $\mathcal{G}_D - c$ relationship shown in Fig. 7 for Homalite 100 [*18,20,21*].

The crack tip equation of motion follows from Eqs 15 to 17 and is given by

$$\mathcal{G}_D E/[(1 - \nu^2)(K_{so}(t^*, 0) + K_{do}(t^*, 0))^2] = g(c) \tag{18}$$

which must be augmented by appropriate initial conditions.

A low-velocity propagating crack ($c/c_R < 1/4$) with $\mathcal{G}_D = \mathcal{G}_c$ fixed would experience an oscillating variation in crack speed with no crack arrest provided in Eqs 13 and 14 δ is small enough to assume that $(K_{dc}^{(tot)})\min > K_D$. In the plateau region of the $c - \mathcal{G}_D$ relationship of Fig. 7 large increases in $\mathcal{G}_D$ causes only very small changes in crack speed c, hence $g(c) =$ constant in Eq 18. If the moving crack is subjected only to time-dependent external trac-

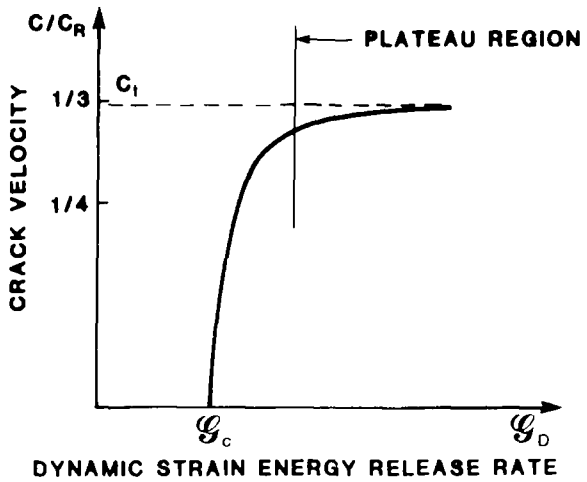

FIG. 7—*Crack speed* c *versus dynamic strain energy release rate* $\mathcal{G}$ *as obtained for Homalite 100 from an SEN-type fracture test specimen* [18].

tions, the resulting variation in K_{so} would require corresponding variations in $\mathcal{G}_D$. This type of behavior has in fact been observed in fracture experiments with Homalite 100. In the no-wave running crack problem the transition region $1/4 < c/c_R < 1/3$ is associated with the beginning of fracture surface roughening. Fracture surface roughening and the development of unsuccessful part-through crack branches becomes more severe for increasing K_{so}-values in the plateau region. When K_{so} exceeds a critical value, the branching stress-intensity factor K_{br}, successful crack branching occurs and two or more cracks propagate individually with the motion of each one governed by an equation of motion similar to Eq 18.

Assume that the crack propagates with terminal (plateau) velocity c_t, hence $g(c) = g(c_t) =$ constant. The SEN specimen geometry is characterized by monotonically increasing K-values and induces crack branching at a distance from the top of the starter crack at time t_{bo}. An incident stress wave scattered about the crack tip moving with speed c_t generates variations of K_{dc} that cause, in general, oscillating fracture surface roughening patterns. If, however, K_{sc} is large enough, the impinging tensile (compressive) stress wave will enhance (delay) crack branching by reducing (increasing) the time t_b and the distance a_b for branching. Stress wave effects onto branching may be characterized by branching delay and shift parameters, $\beta_t = (t_b)\text{wave}/(t_b)\text{no wave}$, and $\beta_a = (a_b)\text{wave}/(a_b)\text{no wave}$, respectively.

The K versus a/w relationship for stress wave-crack interaction is shown in Fig. 8 for nonobliquely incident stress waves. The impact of three types of incident stress waves onto the total dynamic stress-intensity factor is illustrated. A tensile step pulse $\sigma_y(t, x) = \sigma_0 H(x + ct - w)$ encountering the crack tip at position $x = a_b/w$ increases the stress-intensity factor above its critical value K_{br} to yield branching at position a_b/w. Assuming that $K_{so}(a/w, 0)$ may be approximated by

$$K_{so}(a/w, 0) = \kappa_0 + \kappa_1(a/w) + \kappa_2(a/w)^2 + \ldots \tag{19}$$

crack branching will occur when $K_{so}(a_b/w, 0) = K_{br}\, k^{-1}(c)$. Setting $\kappa_i \equiv 0 (i \geq 2)$, the crack bifurcates at position $(a_b/w)\text{no wave} = \kappa/\kappa_1$ with $\kappa = K_{br}k^{-1}(c) - \kappa_0$. For step stress wave interaction at time $t = t_i$ (Case A in Fig. 8) with $K_{dc}(t^*, c)$ given by Eq 12, the locus of crack branching is determined from the condition

$$K_{br} = K_{sc}(a_b/w, c) + K_{dc}(t^*, c)$$

$$= k(c)\{K_{so}(a_b/w, 0) + A\sigma_0[w/c(a_b/w - a_i/w)(1 + c/c_1)]^{1/2}\} \tag{20}$$

with a_1/w the position of crack wave encounter.

The linear approximation for (a_b/w) wave is given by

$$(a_b/w)\text{wave} = (a_b/w)\text{no wave} + \gamma + \{2\gamma(a_b/w)\text{no wave} + \gamma^2 - \beta\}^{1/2} \tag{21}$$

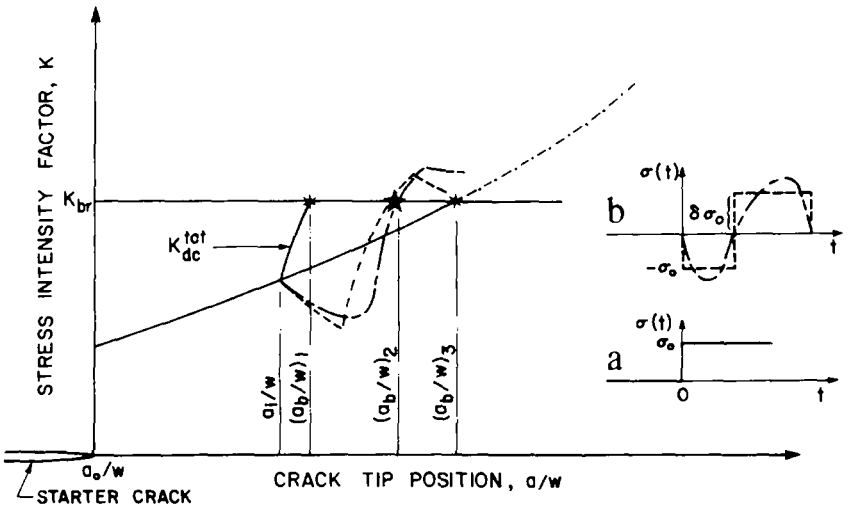

a_1 Tensile step stress wave $\sigma_y(t, x) = \sigma_0 H(x + ct - w)$
b_1 Experimentally recorded stress wave profile and associated squared pulse (Eq *13*).
FIG. 8—*Dynamic stress-intensity factor* $K_{dc}^{(tot)}$ *versus crack tip position* a/w *for running crack-stress wave interaction showing enhance of branching.*

with

$$\gamma = A^2\sigma_0^2 \frac{w}{c} (1 + c/c_1)/(2\kappa_1^2)$$

$$\beta = A^2 \sigma_0^2 \frac{w}{c} (1 + c/c_1) \frac{a_i}{w} \kappa_1^{-2} \tag{22}$$

and

$$t_b = a_b/c \tag{23}$$

Expressions similar to Eqs 20 and 21 may be obtained for more general wave forms. Crack-wave interaction with real waves obtained from explosive wave sources (Fig. 8*b*) showing a leading biaxial compressive pulse followed by a biaxial tensile pulse may lead to branching enhancement ($\beta_a < 1$) or delay ($\beta_a > 1$) depending on the time of encounter of crack tip and wave front.

This is demonstrated clearly in Fig. 8. The sequence of isochromatic fringe patterns shown in Fig. 9 are associated with a very early time of encounter with σ_0 too small to enforce stress wave branching. Running crack-explosive wave interaction experiments yielded (a_b/w)no wave $= 0.68$ and (a_b/w)wave $= 0.45$ for $a_i/w = 0.15$, where $c = 380$ m/s and $c_1 = 2150$ m/s for Homalite 100; hence, $\beta_a \simeq 2/3$.

Nonoblique incident P-wave diffraction at a high speed running crack tip is depicted in the fringe patterns shown in Fig. 9. The fringe pattern presented in Fig. 9*a* shows the mutual far field interaction as the crack tip normally approaches the P-wave front at time $t = 65$ μs after initiation of the crack. The crack tip is surrounded by a butterfly isochromatic fringe pattern which is typical for Mode I cracks propagating at nearly terminal velocity ($c = 380$ m/s) in an SEN specimen characterized by increasing K-values as the crack proceeds. When the P-wave front is scattered at the moving crack tip both a PP-wave and an SP-wave are generated by diffraction. The second photograph (Fig. 9*b*) shows the phase when the crack tip traverses the peak of the leading compressive pulse of the P-wave (Frame 6, $t = 85$ μs). Notice that the classical butterfly isochromatics have been distorted completely by the transient stress field component which acts parallel to the crack line. An unstable quadruple fringe pattern is generated during the passage of the compressive half of the P-pulse.

The final photograph of this sequence (Fig. 9*c*) depicts the situation where the crack tip traverses the trailing tensile pulse of the P-wave. The strong increase of crack tip fringe order from $N = 5$ in Fig. 9*a* to the visible order $N = 8$ in Fig. 9*c* indicates an essential increase of the stress-intensity factor.

Oblique Incidence

Scattering of obliquely incident stress waves about a stationary or moving crack tip gives rise to apparent mixed-mode stress conditions at the crack tip. The explosively generated stress waves, P- and S- waves, radiate from the source at Point II as shown in Fig. 4. During the crack-wave interaction phase the angle between the crack line and the normal to the wave front is constant for plane wave fronts but changes for cylindrical wave fronts and for a moving crack. Assuming the crack to propagate in its plane even when subjected to mixed-mode stress conditions, an assumption which is clearly contradictory to experimental results, the mathematical treatment becomes very involved [17], incorporating two universal functions $k_1(c)$ and $k_2(c)$ for Mode I and Mode II, respectively. Relations for dynamic stress-intensity factors K_{1dc} and K_{2dc} may be derived which are similar to Eq 6 for the symmetric mode

$$K_{idc}(t, c) = k_i(c)\, K_{ido}(t, 0) \qquad (i = 1, 2) \tag{24}$$

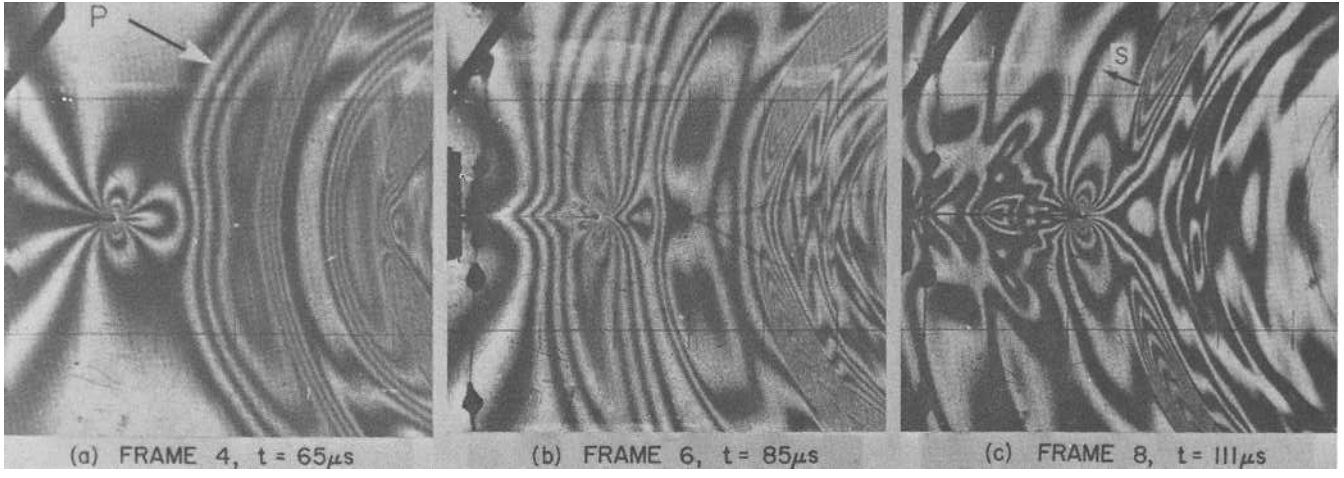

(*a*) Mutual far-field interaction as the crack tip approaches the wave front
(*b*) Crack tip traversing the leading compressive pulse of the P-wave
(*c*) Crack tip traversing the trailing tensile pulse of the P-wave

FIG. 9—*Diffraction of a nonobliquely incident P-wave about a high velocity running crack-tip (crack speed* $c = 380$ *m/s; P-wave velocity* $c_l = 2150$ *m/s) in Homalite 100.*

and the expression for the mixed-mode strain energy release rate G reads (compare Eq 16)

$$\mathcal{G}(t^*, c) = \frac{1 - \nu^2}{E} [A_1(c) (K_{1dc}{}^{tot}(t^*, c))^2 + A_2(c) (K_{2dc}(t^*, c))^2] \quad (25)$$

Experiments with DCB-type specimens with unstable crack propagation occurring in the sense of crack path instability suggest Mode I stress conditions at the very crack tip provided the crack moves in a time-independent load-induced stress field. Dynamic photoelastic fringe recordings showing transient stress fields such as generated by stress waves as well as the shapes of the associated shadow spots seem to induce an apparent dynamic Mode II contribution as expressed by Eq 25. Dynamic recordings of the shadow-spot surrounding a crack tip moving at high speed along a curved path in a static stress field reveal perfectly symmetrical shapes of the caustic.[4] The presence of a considerable transient Mode II contribution to the stress-intensity factor is evidenced by the asymmetrical shape of the pseudo-shadow spot shown in Fig. 10*a* and by the dominant mixed-mode isochromatic fringe pattern enlargement of Fig. 11*c* shown in Fig. 10*b*; Fig. 10*c* is the associated analytically generated fringe pattern [*16*].

The sequence of photographs in Fig. 11 shows the diffraction of an obliquely incident longitudinal (P) wave about the tip of a high-velocity running crack. Frame 1 (Fig. 11*a*) shows the crack tip moving in the static SEN-stress field surrounded by the classical butterfly-shaped isochromatic fringe system. The wave system approaches from the right lower corner. The P-wave impinges the crack tip at an angle of about 30 deg with respect to the crack line. The wave-induced stress field is superimposed onto the stress field caused by the loading of the specimen. The stress components of the P-wave can be split into three components which act normal, parallel, and tangential to the crack. The normal compressive stress component gives rise to an opening mode crack deformation. The stress field acting parallel to the crack line plays an important role in the crack path stability, whereas the tangential stress component causes in-plane shearing deformation of the crack walls (Mode II).

Analysis of the isochromatic near crack tip fringe patterns (Figs. 11*a* and *b*) on the basis of a (static) mixed-mode analysis reveals a dominant Mode I-mixed mode crack problem with the sign of the transient stress field parallel to the crack line changing from negative (compression in Fig. 11*b*) to positive (tension in Fig. 11*c*). The crack path exhibits waviness with the curvature apparently changing sign between Frame 3 (Fig. 11*b*) and Frame 4 (Fig. 11*c*). The geometric features of the resulting wavy crack path may be utilized to determine an apparent mixed-mode ratio function $m(t) = K_{II}/K_I$ of the interaction process.

[4]Kalthoff, J. F., private communication, IWM Freiburg, 1980.

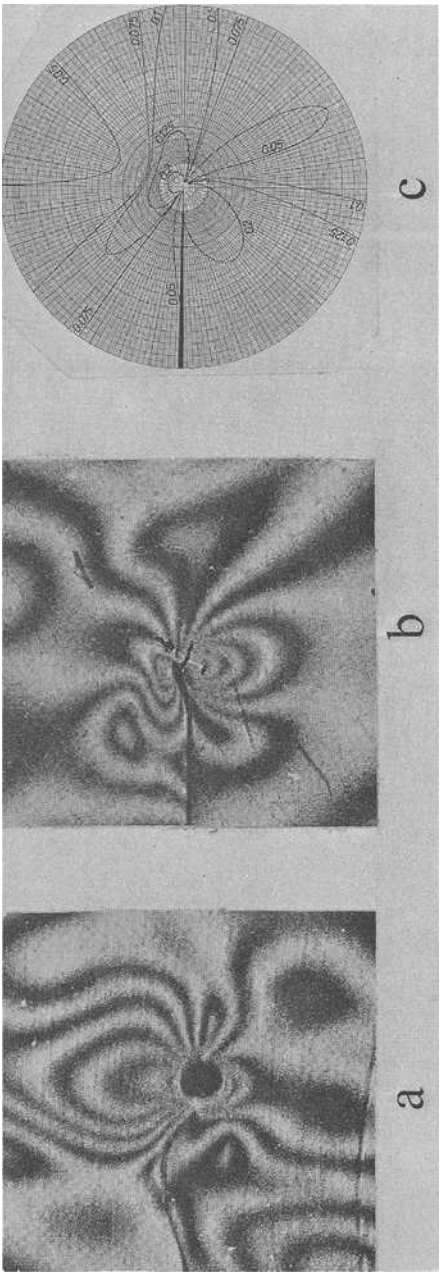

FIG. 10—*Asymmetrical pseudo shadow spot* (a) *and experimentally recorded* (b) *and analytically generated* (c) *isochromatic fringe pattern associated with a moving crack tip subjected to transient mixed-mode stress conditions.*

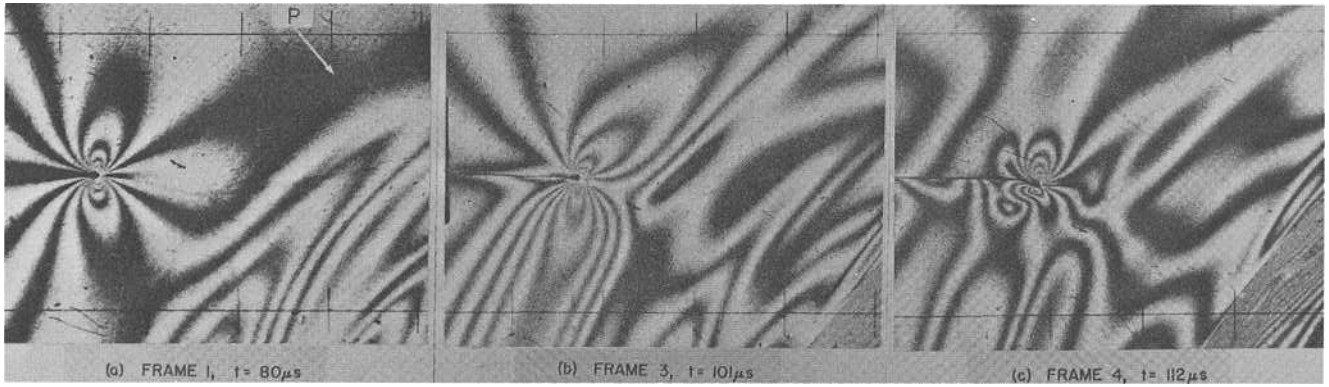

(*a*) Far-field interaction of moving crack tip stress field and incident leading compressive P-wave pulse
(*b*) Compressive P-pulse generates a dynamic mixed-mode stress pattern around the crack-tip
(*c*) Dynamic mixed-mode stress field showing crack path waviness due to P-wave interaction

FIG. 11—*Diffraction of an obliquely incident P-wave about a high-velocity running crack tip (crack speed* $c = 380$ *m/s; P-wave velocity* $c_1 = 2150$ *m/s) in Homalite 100.*

Oblique SV-wave scattering about a moving crack is depicted in the sequence of photographs shown in Fig. 12. In Fig. 12*a* (Frame 7, $t = 141$ μs), the crack tip is surrounded by nearly pure Mode I isochromatic fringes as the crack approaches the oblique incident SV-wave. The angle of incidence is greater than the critical angle, and the wave is diffracted at the crack tip in Fig. 12*b* (Frame 8, $t = 153$ μs), giving rise to a diffracted and reflected wave system. Oblique SV-wave scattering gives rise to apparent mixed-mode stress concentrations at the moving crack tip. The SV-wave induced Mode I stress intensity becomes very large, and momentarily the value of the strain energy release rate approaches a critical limit. The crack finally divides into two or eventually several individual branches when the requirements for a branching criterion

$$\mathcal{G}_{\text{br}} = \mathcal{G}(t^*, c) \tag{26}$$

are met. Branching of running cracks subjected to mixed-mode loading conditions is shown in Fig. 12*c* (Frame 11, $t = 182$ μs), and also has been investigated in Ref 22. An alternate branching criterion would postulate crack division to occur when the strain energy disappearance rate G_{D} associated with the system of branches would become larger than the value of G_{D} for the single running crack [*23*].

Obliquely incident stress wave scattering about stationary and running crack tips suggests formulation of a first-cracking-time problem or first-branching-time problem similar to a first-passage-time problem in other fields of mechanics. An appropriately selected fracture criterion as well as branching criterion constitutes two limiting curves F and B, respectively, in the (complex) $K_1 - K_2$ plane as shown in Fig. 13. Any wave-crack interaction process is associated with a path in this plane crossing the fracture (F)-limit at fracture initiation, and passing the branching (B)-limit when branching occurs. All Mode I processes are restricted to the axis $K_2 \equiv 0$. The K-paths for the special case of nonoblique step tensile pulse interaction with a moving crack (Fig. 9) is indicated by interrupted lines. The associated first-branching-time is given by Eq 23. Solid and dash-dot curves are associated with oblique incident P and SV wave interaction corresponding to Figs. 11 and Fig. 12, respectively.

It should be pointed out that Mode II contributions to form an apparent mixed-mode stress-intensity factor as obtained from theoretical and experimental investigations may rest upon entirely different phenomenon. All dynamic mathematical analyses of crack advancement to date assume uniform or nonuniform crack extension along the crack plane and do not account for crack path curvature, thus introducing a crack path deviation-induced apparent Mode II contribution. Finite-element analyses of dynamic crack propagation along curved crack paths are not available in the literature to date. Photoelastic or other optical fringe recordings of moving crack tips along

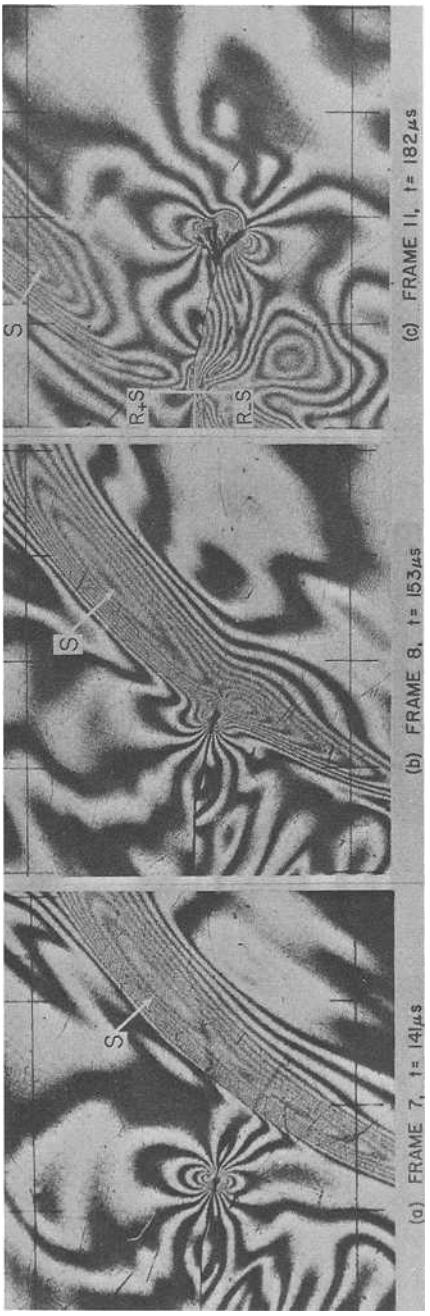

(*a*) Oblique SV-wave approaching the crack tip
(*b*) SV-wave scattering about moving crack tip
(*c*) Multiple crack branching due to the joint action of SV-wave and reflected tensile P-waves from the specimen boundary.

FIG. 12—*Diffraction of an obliquely incident SV-wave about a high-velocity crack.*

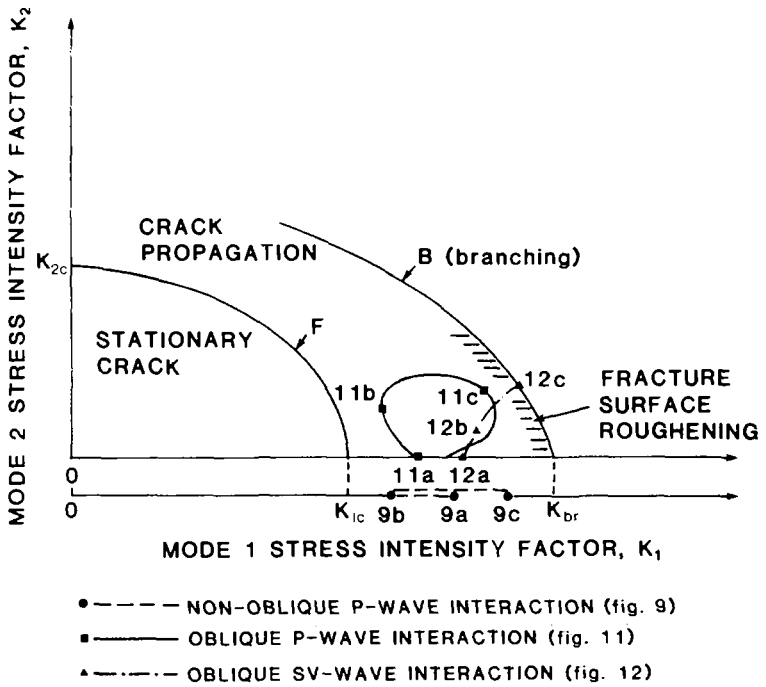

FIG. 13—*Mixed-mode* $K_1 - K_2$*-plane showing fracture and branching boundaries and K-paths for crack-wave interaction problems.*

curved paths including the method of caustics show asymmetrical fringes in the far field or even in the close field, and the shapes of the shadow spots are asymmetrically distorted. This, however, does not imply that the very close vicinity around the crack tip is in mixed-mode, nor does it prevent the crack tip from propagating under pure Mode I conditions even in a highly transient stress field. Ratios $m(t)$ evaluated from larger isochromatic fringe loops of a globally mixed-mode isochromatic crack-tip fringe pattern show a tendency towards increasing influence of K_2. Hence, Fig. 14 has to be reinterpreted in the sense that the paths K connecting Figs. 11*a, b,* and *c* and 12*a, b,* and *c* pertain to a particular fringe order (that is, to a very specific region of validity of the analysis employed). The use of a completed dynamic stress field solution including the essential nonsingular terms would remove this complexity. This, however, is at the present time beyond the limit of running-crack interaction analysis and will be the subject of future research.

Conclusions

Dynamic photoelasticity was employed to provide whole field data for stress wave scattering about moving crack tips in prestressed SEN fracture

test specimens. The isochromatic data were analyzed to obtain qualitative estimates of the stress intensity at the crack tip. P-waves impinging non-obliquely on the moving crack give rise to Mode I type crack deformation. The associated stress-intensity factor K_1 caused by static preload of the specimen is lowered during the passage of the leading compressive pulse of the explosively generated P-wave, but K_1 increases when the trailing tensile P-pulse passes over the crack tip. The energy content of the trailing tensile plus and the dynamic stress-intensity factor at the position of crack-wave encounter if there was no wave present determine the dynamic propagation behavior of the crack and control delayed or enhanced occurrence of crack branching.

Oblique incident SV-wave scattering causes a transient apparent mixed-mode stress field, which in turn causes the crack to deviate from its originally stable straight crack path [*12*]. Finally, crack branching is possible for oblique SV-wave-crack interaction. A suitable representation of crack wave interaction is provided by a stress-intensity factor path $K(K_1, K_2)$ in a $K_1 - K_2$-plane. Engineering approximations for first-cracking and first-branching-time problems have been formulated for general plane-stress wave loading employing Freund's fundamental solutions. Although in these experiments the crack is of finite length and the specimen is finite, the results are surprisingly favorable even though certain restrictive assumptions have been made.

Acknowledgments

The authors were supported in this research program by the Department of Energy under Contract No. DE AP21-79MC-12577. Part of the support for H. P. Rossmanith was provided from the Fonds zur Förderung der Wissenschaftlichen Forschung in Austria under Contract No. 3864. The research work was conducted by the authors at the Photomechanics Laboratory, University of Maryland.

References

[*1*] Chen, P. E. and Sih, G. C., "Elastodynamic Crack Problems," *Mechanics of Fracture*, Vol. 4, G. C. Sih, Ed., Noordhof.

[*2*] Brock, L. M., *International Journal of Engineering Science*, Vol. 13, 1975, pp. 851-859.

[*3*] Brock, L. M., "Intensity of the Strain Energy Density about a Crack Edge Due to P-Wave and SV-Wave Diffraction," *Journal of Applied Mechanics*, to be published.

[*4*] Brock, L. M., *International Journal of Engineering Science*, Vol. 13, 1975, pp. 951-958.

[*5*] Harris, J. G., *Zeitschrift für Angewandte Mathematik and Physik*, Vol. 31, 1980, pp. 367-383.

[*6*] Harris, J. G., "Elastodynamic Diffraction and Radiation Problems," Ph.D. dissertation, Northwestern University, Evanston, Ill., 1979.

[*7*] Schardin, H., *Ergebnisse der kinematographischen Unlersuchung des Glasbruchvorganges*, Glastechn, Berichte 23, 1950, pp. 1-10, 67-79, 325-336.

[*8*] Kerkhof, F. in *Linear Fracture Mechanics*, G. C. Sih et al., Eds., Envo Publishing, 1976, pp. 303-321.

[*9*] Smith, D. G., "A Photoclastic Investigation of Stress Wave Loading of a Crack," Society for Experimental Stress Analysis, Spring Meeting 1971, Salt Lake City, Utah.

[10] Rossmanith, H. P. and Shukla, A., "Dynamic Photoelastic Investigation of Interaction of Stress Waves with Running Cracks," *Experimental Mechanics*, to be published.
[11] Rossmanith, H. P. and Shukla, A., "Photoelastic Investigation of Stress Wave Diffraction about Stationary Crack Tips," *Journal of the Mechanics and Physics of Solids*, to be published.
[12] Miller, G. F. and Pursey, H., *Proceedings of the Royal Society*, Series A, Vol. 233, 1955, pp. 55-69.
[13] Woods, R. D., *Journal of the Soil Mechanics and Foundations Division*, Proceedings of the American Society of Civil Engineers, Vol. 94, 1968, pp. 951-979.
[14] Graff, K. F., *Wave Motion in Elastic Solids*, Ohio State University Press, 1975.
[15] Sanford, R. J. and Dally, J. W., *Engineering Fracture Mechanics*, Vol. 11, No. 4, 1979, pp. 621-633.
[16] Rossmanith, H. P., *Acta Mechanica*, Vol. 34, 1979, pp. 1-38.
[17] Freund, L. B., *Journal of the Mechanics and Physics of Solids*, Vol. 21, 1973, pp. 47-61; Vol. 22, 1974, pp. 137-146.
[18] Irwin, G. R., Dally, J. W., Kobayashi, T., Fourney, W. L., Etheridge, M. J., and Rossmanith, H. P., *Experimental Mechanics*, Vol. 19, 1979, pp. 121-128.
[19] Metcalf, J. and Kobayashi, T. in *Crack Arrest Methodology and Applications, ASTM STP 711*, American Society for Testing and Materials, 1978, pp. 128-145.
[20] Rossmanith, H. P., *Journal of Applied Mechanics*, Vol. 47, 1980, pp. 795-800.
[21] Rossmanith, H. P. and Irwin, G. R., "Analysis of Dynamic Isochromatic Crack-Tip Stress Patterns," University of Maryland, Department of Mechanical Engineering Report, July 1979.
[22] Rossmanith, H. P., "Crack Propagation and Branching," *Proceedings*, International Symposium on the Strain Energy Density Criterion in Memory of the Late Professor Laszlo Gillemot, Budapest, Hungary, 17-19 Sept. 1980.
[23] Irwin, G. R. and Rossmanith, H. P., "Application of the Maximum Energy Disappearance Rate Principle to Crack Extension," *Mechanical Research Committee*, to be published.

R. C. Shah[1] *and F. T. Lin*[1]

Stress-Intensity Factors of Stiffened Panels with Partially Cracked Stiffeners

REFERENCE: Shah, R. C. and Lin, F. T., **"Stress-Intensity Factors of Stiffened Panels with Partially Cracked Stiffeners,"** *Fracture Mechanics: Fourteenth Symposium—Volume I: Theory and Analysis, ASTM STP 791*, J. C. Lewis and G. Sines, Eds., American Society for Testing and Materials, 1983, pp. I-157–I-171.

ABSTRACT: Theory and numerical procedure are presented to determine the stress-intensity factors for a partially cracked typical stiffener and a partially cracked splice stiffener in a stiffened panel subjected to a uniaxial uniform remote stress normal to the crack. The translational spring element and the beam element with special boundary conditions are investigated for the simulation of flexible fasteners. The finite-element procedure was applied to the problem. From the finite-element solution, the stress-intensity factors were determined by using the displacement method and the strain energy release rate method. Results are presented as stress-intensity configuration factors, Y, for various values of crack lengths, stiffening ratios, stiffener spacings, and fastener flexibilities. The crack growth lives computed from finite-element solutions are compared with test data of panels containing a partially cracked typical stiffener subjected to constant amplitude cyclic loading and spectrum loading. The correlation between the test data and the analyses is very good.

KEY WORDS: stiffened panel, finite-element method, partially cracked stiffener, flexible fastener, stress-intensity factors, configuration factor, fracture mechanics

The assessment of structural reliability in the design of modern aircraft requires the considerations of structural response to loading when cracking is present. The existence of alternate load paths in a built-up structure has resulted in what is termed as a fail-safe design. In most instances, this has produced a fairly high level of load-carrying capability in the presence of extensive damage. Any quantitative analysis of behavior of the cracked structure (that is, crack growth and residual strength) requires that one have

[1]Principal engineer and senior specialist engineer, respectively, The Boeing Company, Mail Stop 21-43, Seattle, Wash. 98124.

available the stress-intensity factor (SIF) solution for the geometry, boundary conditions, and loading in question. The determination of this SIF is the primary task in any fracture analysis. Most of the work done on stiffened panels with cracks involves cracks in skin with intact or broken stiffeners [*1-6*].[2] Very little analytical or experimental work has been done on a partially cracked stiffener [*7*]. Here, stiffened panels containing a partially cracked typical (Z) stiffener and a partially cracked splice (I) stiffener are analyzed with the finite-element analysis for various crack lengths, stiffening ratios, bay widths, and fastener system flexibility parameters. SIF's are presented in graphical forms for partially cracked stiffeners for previously mentioned parameters.

Problems of small cracks originating from the edge of the skin flange, or from either or both sides of the fastener hole are not adressed here. SIF solutions for these cases are discussed and available elsewhere [*8, 9*].

Formulation of Modeling Procedure

The purpose of the work described here is to analyze a stiffened panel containing a partially cracked stiffener as shown in Figs. 1 and 2. Equally spaced stiffeners are attached to the skin with equally spaced fasteners. The skin and stiffeners are subjected to a remote uniform uniaxial stress, normal to the crack. Fasteners are flexible and their deformations must be accounted for accurately to reflect the load transferred from the cracked stiffener to the skin. Two different kinds of elements are used to simulate the flexible fasteners in the analysis of stiffened panels. They are the translational spring element, and the beam element with special boundary conditions. The translational spring element is shown in Fig. 3*a*. The element has two structural nodes. Each structural node has three translational stiffnesses. The stiffness matrix for this element expressed in rectangular Cartesian coordinates is

$$k = \begin{bmatrix} k_{ax} & 0 & 0 & -k_{ax} & 0 & 0 \\ 0 & k_{vy} & 0 & 0 & -k_{vy} & 0 \\ 0 & 0 & k_{vz} & 0 & 0 & -k_{vz} \\ -k_{ax} & 0 & 0 & k_{ax} & 0 & 0 \\ 0 & -k_{vy} & 0 & 0 & k_{vy} & 0 \\ 0 & 0 & -k_{vz} & 0 & 0 & k_{vz} \end{bmatrix}$$

[2]The italic numbers in brackets refer to the list of references appended to this paper.

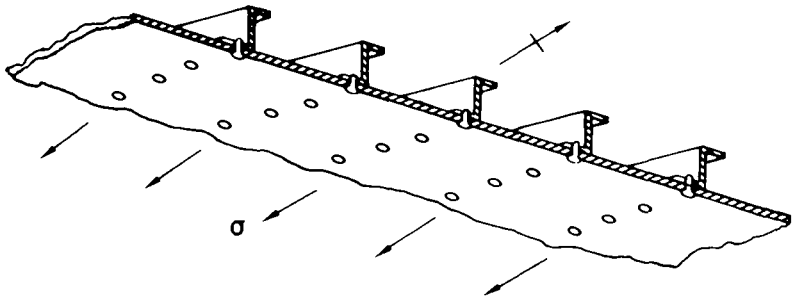

(a) Half of Stiffened Panel

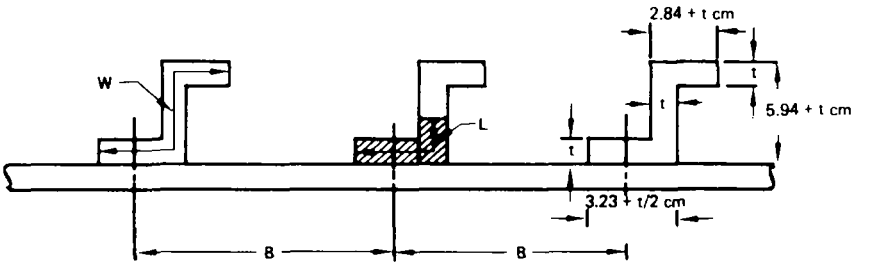

(b) Section at Centerline of Panel

FIG. 1—*Stiffened panel with a partially cracked typical stiffener.*

where

k_{ax} = translational stiffness in the axial direction,
k_{vy} = translational stiffness in y direction, and
k_{vz} = translational stiffness in z direction.

The beam element as shown in Fig. 3*b* is assumed to be a straight bar capable of resisting axial force, bending moments about the two principal axes in the plane of its cross section, and a twisting moment about its centroidal axis. The element has three translational freedoms and three rotational freedoms at each node. The fastener was idealized with this beam element with the end conditions fixed such that it behaved as a cantilever beam, that is, three rotational displacements equal to zero at the fixed end and three bending moments equal to zero at the free end. The flexibility coefficient, f, for a cantilever beam under an end load is given by

$$f = \frac{l^3}{3EI}$$

where

E = Young's modulus for the fastener material,
l = the fastener length, and
I = the moment of inertia.

Both of these elements were used to simulate flexible fasteners in a stiffened panel with a bay-centered crack. Results for both finite-element analyses with fasteners simulated as spring elements or beam elements were identical. The beam element was used to simulate fasteners thereon.

Application of Procedure

The purpose of this work was to determine SIF's for a partially cracked typical (Z) or splice (I) stiffener and to determine stress concentration factors

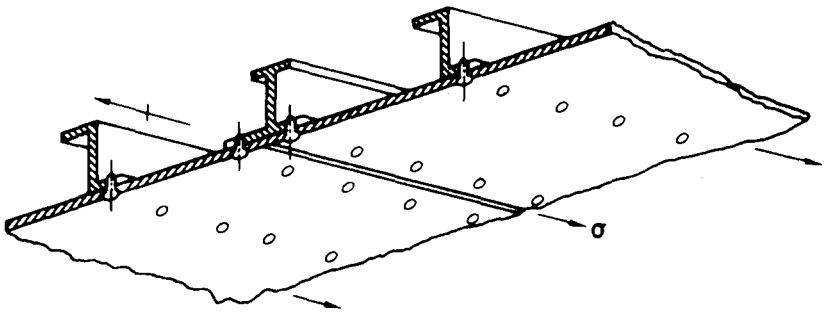

(a) Half of Stiffened Panel

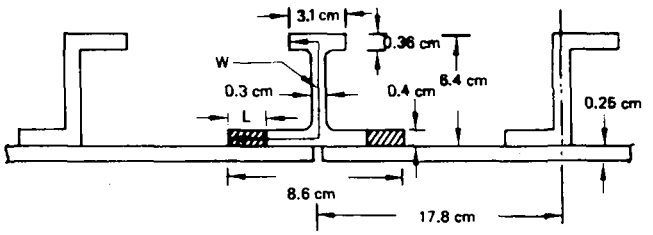

(b) Section at Centerline of Panel

FIG. 2—*Stiffened panel with a partially cracked splice stiffener.*

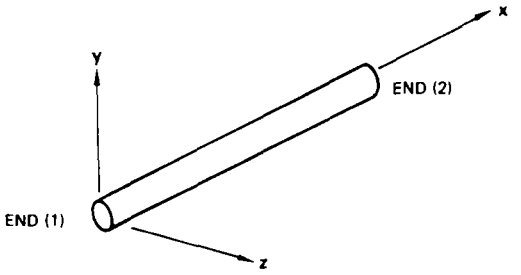

(a) Translational Spring Element

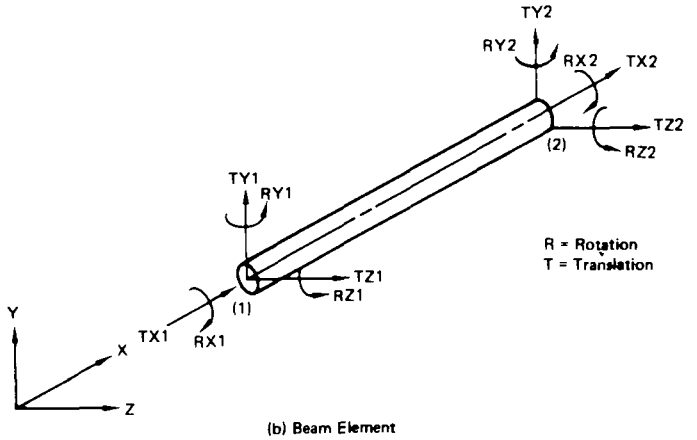

(b) Beam Element

FIG. 3—*Fastener idealization.*

(SCF's) in the skin and adjacent stiffeners as the crack extends in the stiffener (see Figs. 1 and 2). Finite-element analyses were conducted for a stiffened panel containing a partially cracked stiffener, as shown in Figs. 1 and 2. The bay width, skin thickness, and stiffener dimensions used are dimensions very typically found on the lower wing surface of military transport, cargo, and commercial aircrafts and are shown in Figs. 1 and 2. The crack length, L, is measured from the edge of the skin-flange of the stiffener along the centerline of the cross section. Width W is the developed width of the stiffener, as shown in Figs. 1 and 2.

A typical finite-element idealization is shown in Fig. 4. This is a three-dimensional geometric idealization. However, analysis itself is two-dimensional in nature. General bending plate elements were used to idealize the skin and stiffener for the case of a partially cracked Z stiffener. The element with uncoupled membrane and bending stiffness has five degrees of freedom per node (the element has no in-plane bending stiffness). It assumes constant

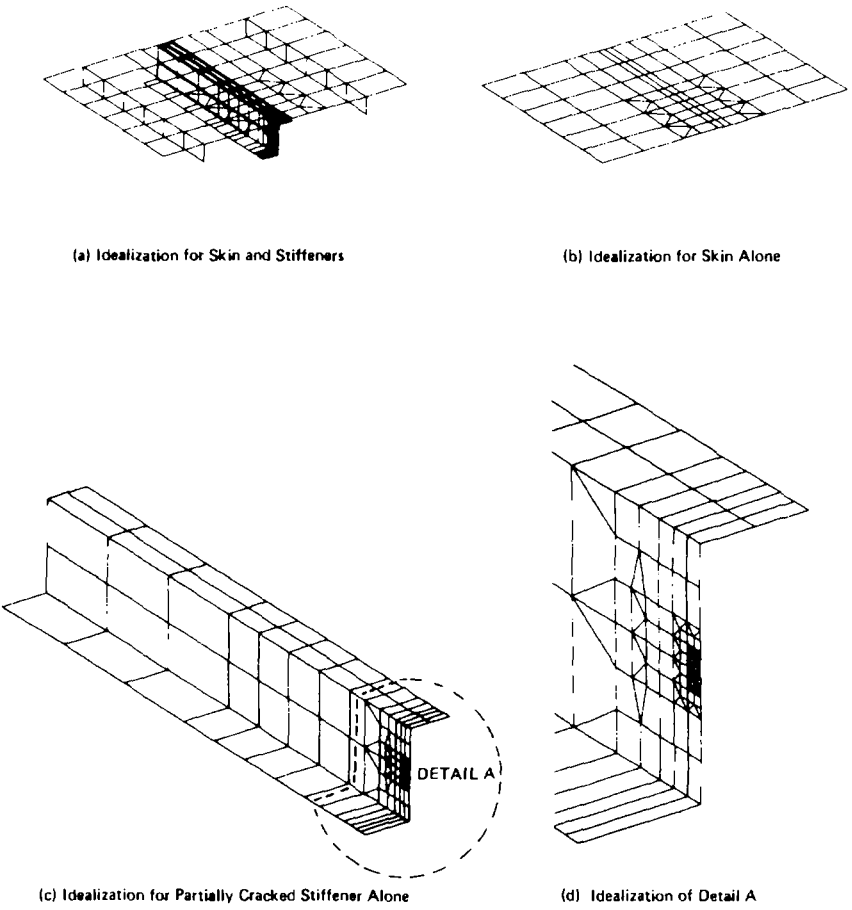

FIG. 4—*Finite-element idealization for a partially cracked stiffener.*

membrane strain and linear curvature. For partially cracked I stiffener, membrane plate elements were used to idealize the skin and stiffener and cracks are assumed to grow symmetrically. Beam elements with special boundary conditions are used to simulate the flexible fasteners. For each case, seven completely different finite-element idealizations were constructed for seven crack lengths ranging from 1.9 cm (0.75 in.) to 9.4 cm (3.7 in.). In order to have the accurate stress-strain distribution in the crack-tip region, the mesh patterns were rearranged for each value of crack length. Since steep stress gradients exist in the vicinity of a crack tip, the clement sizes in the crack-tip region were reduced and the smallest elements, which were squares with each side about 0.13 cm (0.05 in.) long, were used at the crack tip. The typical finite-element idealization shown in Fig. 4 consisted of 265 nodes, 285

elements, and 1231 degrees of freedom. The skin and stiffeners were subjected to a remote uniform tension of 6.89 MPa (1 ksi).

Special crack-tip elements, such as eight-node quadratic isoparametric quadrilateral element with quarter point singularity, were used for cracked panels subjected to membrane or in-plane stress only [*10*]. The analysis in hand considers bending stiffness also. No special two-dimensional crack-tip elements were available with this capability. Hence, regular elements were used, as described previously, to model the crack-tip region. For the sake of uniformity, regular elements also were used for the partially cracked splice stiffener.

Stress intensity factors, K, were determined by the displacement method and the strain energy release rate method. The K-values calculated by the strain energy release rate method are approximately 7.5 percent higher than K calculated by the displacement method. The results shown in the illustrations are based on the displacement method.

Results and Discussion

The parameters that were found to have a significant effect on the SIF's are crack length, L, stiffening ratio, R_s, stiffener spacing, B, fastener flexibility, f, fastener pitch, p, and stiffener cross-section dimensions. Stiffening ratio R_s is defined as the ratio of cross-sectional area of a Z stiffener to one bay area of skin. R_{sp} is defined as the ratio of cross-sectional area of the I stiffener to the cross-sectional area of a Z stiffener. Results in Fig. 5 for a partially cracked Z stiffener show that SIF remains nearly constant while the crack is in the skin flange. As the crack grows in the web or the top flange, SIF increases with the increasing crack length. Results in Fig. 5 also show that varying R_s from 0.4 to 1.0, SIF increases by less than 14 percent for a given crack length with respect to that for $R_s = 0.4$. Finite-element analyses also were conducted for $B = 25.4$ cm (10.0 in.). Comparison of results showed that SIF increased approximately 2 percent for small cracks [$L = 2.54$ cm (1.0 in.)] and 4 percent for larger cracks [$L = 8.2$ cm (3.25 in.)] as B increased from 17.8 cm (7.0 in.) to 25.4 cm (10.0 in.).

Effect of fastener flexibility also was investigated. Standard fastener flexibility encountered in practice is 2 to 10. Using $ftE = 6$ as a baseline, it was found that effect of fastener flexibility on SIF was less than -9 to $+8$ percent for $ftE = 2$ to $ftE = 10$, respectively. As expected, it was found that SIF of a partially cracked stiffener increased as the flexibility of the fastener increased. With the increased flexibility of the fastener system, less load was transferred from the cracked stiffener to the intact skin.

The SIF's obtained for R_s values of 0.4, 0.7, and 1.0 are given in Fig. 6 for a partially cracked splice stiffener. Results in Fig. 6 show that SIF increases rapidly as the two crack tips in the skin flanges move closer to each other and join together. Once the crack extends in the vertical web and free flange, SIF remains nearly unchanged.

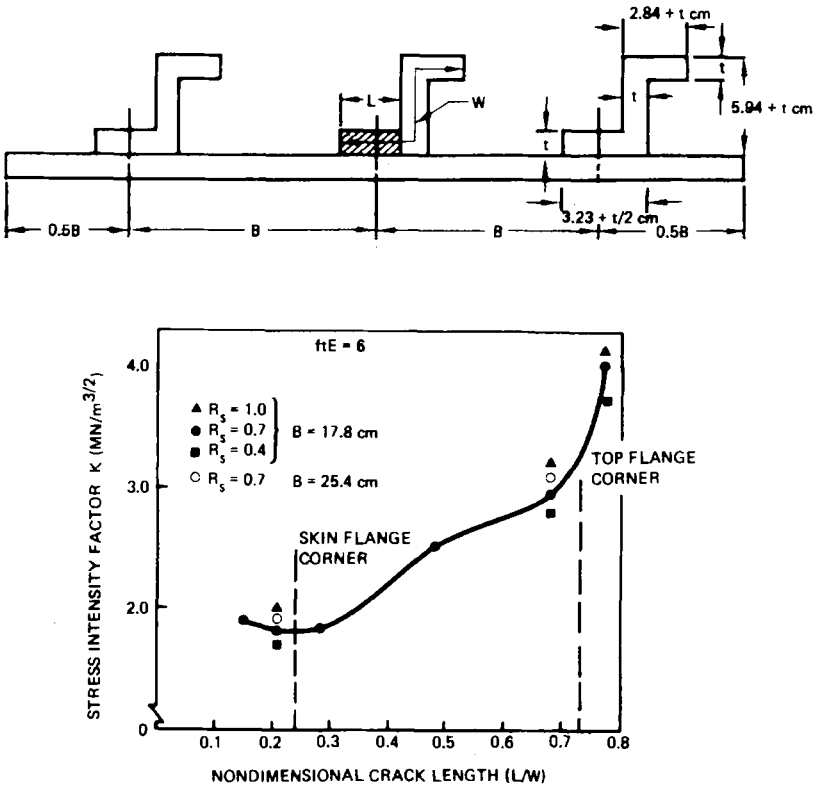

FIG. 5—*SIF's for a partially cracked typical stiffener.*

The nondimensional stress-intensity configuration factor, Y, is defined as follows

$$Y = \frac{K}{\sigma\sqrt{\pi L}}$$

where σ is the applied uniaxial uniform stress and L is the crack length. Plots of Y versus L/W, R_s, B, and ftE are given in Figs. 7 and 8 for a partially cracked Z stiffener and a partially cracked I stiffener, respectively. Y is expressed as follows

$$Y = y_0 y_1 y_2$$

As seen from Fig. 7 for a partially cracked Z stiffener, y_0 accounts for the effect of stiffening ratio R_s for various L/W, y_1 accounts for variations in stiffener spacing B, and y_2 accounts for the change in fastener flexibility

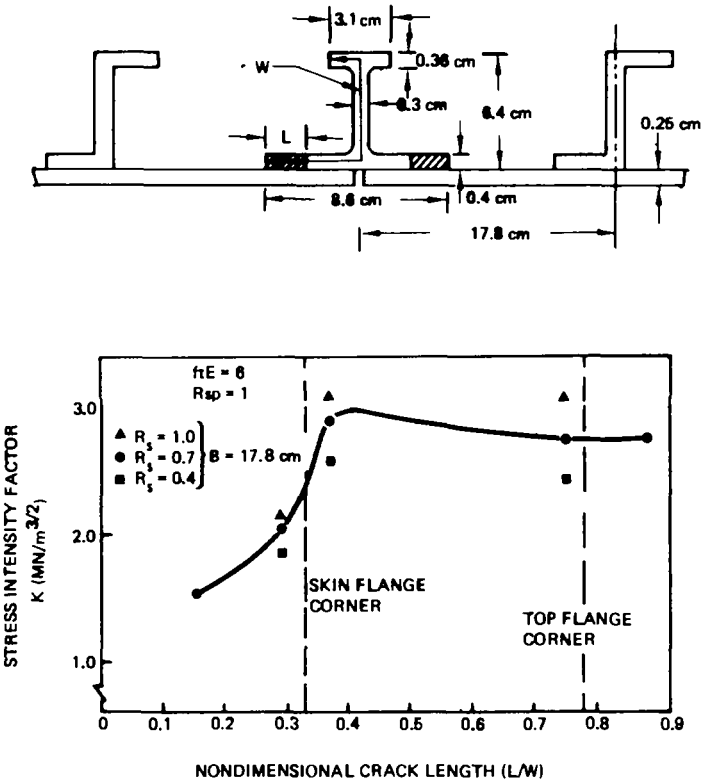

FIG. 6—*SIF's for a partially cracked splice stiffener.*

parameter, ftE. Fastener flexibility is represented in the nondimensional form as ftE.

Stress-concentration factors, C, for the skin near the cracked stiffener were obtained and are shown in Figs. 9 and 10. As expected, results show that as L/W increases, skin stress-concentration factor C increases for a given R_s. Also for a given L/W, C increases with increasing R_s. This is expected as more load is transferred from stiffener to skin. Effect of the fastener flexibilities of practical interest on C was small. For $ftE = 4$, C was about 3 percent higher than C shown in Fig. 9 for $ftE = 6$. For $ftE = 10$, C was about 3 percent lower than C for $ftE = 6$. The stress-concentration factor C increases about 11 percent as bay width B increases from 17.8 cm (7.0 in.) to 25.4 cm (10.0 in.). Factors C are useful in computing SIF for secondary cracks in the skin near the cracked stiffener. SIF for a small crack in the skin near a partially cracked stiffener is computed as follows

$$K = K \text{ (for crack in the skin with uncracked stringer)} \times C$$

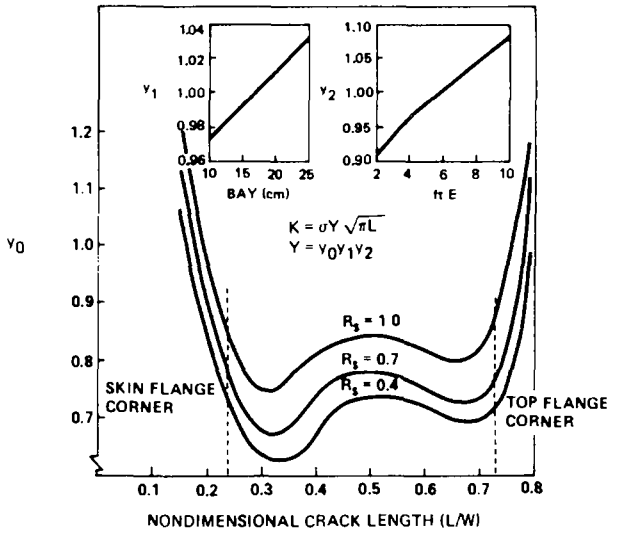

FIG. 7—*Stress-intensity configuration factors for a partially cracked typical stiffener.*

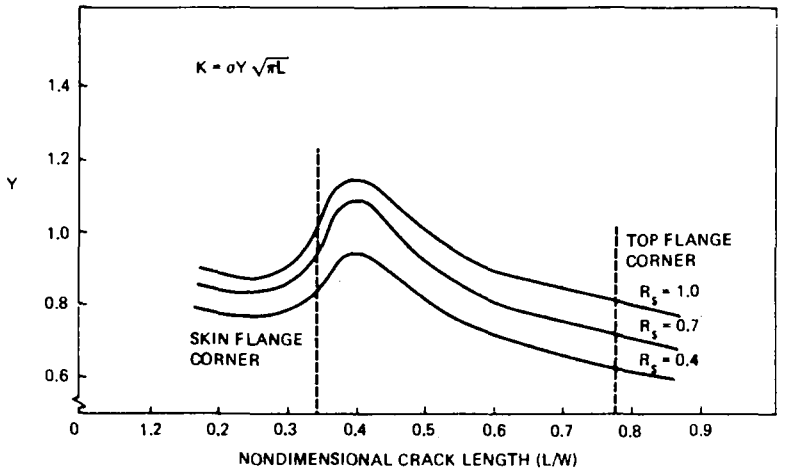

FIG. 8—*Stress-intensity configuration factors for a partially cracked splice stiffener.*

Industry practice in computing K for the partially cracked stiffener is to use the SIF solution for a single edge cracked panel with or without the free edge of the panel near the crack restrained. Results of the present anlayses show that the previously used methods (based on compounding solutions from known solutions) overestimate K by as much as 60 to 200 percent depending on whether edge restraint is used or not. Effect on the crack prop-

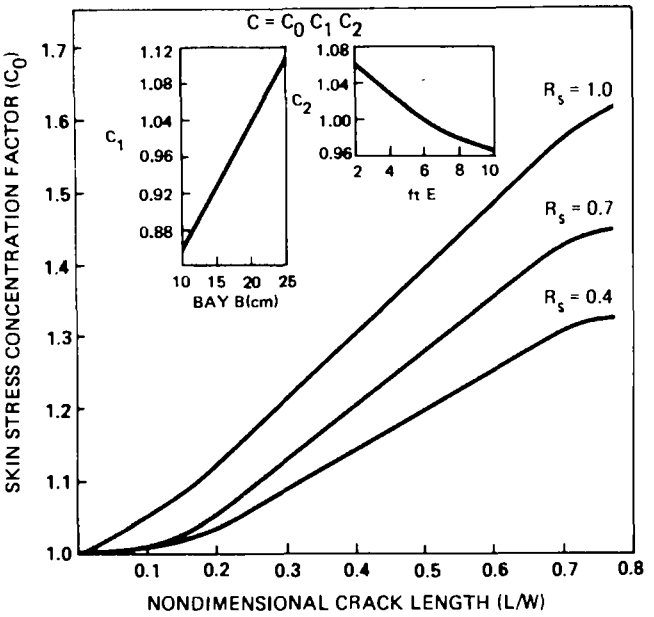

FIG. 9—*Skin stress-concentration factors for a partially cracked typical stiffener.*

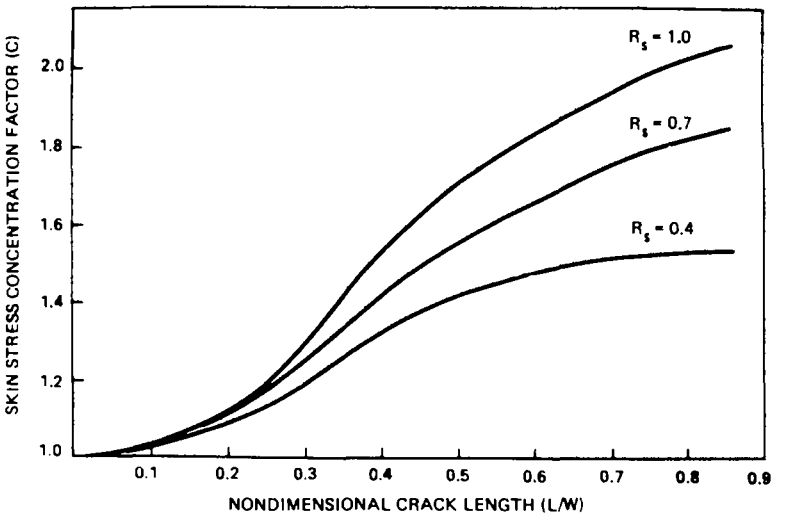

FIG. 10—*Skin stress-concentration factors for a partially cracked splice stiffener.*

agation life is much more severe as it is proportional to K^n where n is always greater than 2.

Application

SIF's obtained in Fig. 7 are used to compute crack growth for two stiffened panels with partially cracked typical stiffeners tested previously at Boeing. Panel 1, consisting of 2024-T3 aluminum skin and 7075-T6 aluminum Z stiffeners, was tested under constant amplitude cyclic loading. Typical bay width B was 17.8 cm (7.02 in.) and stiffening ratio R_s was 0.57. Major pertinent dimensions and cyclic loads are shown in Fig. 11. Initial length of the crack in the stiffener was 3.1 cm (1.20 in.). The crack growth rate relationship for the test panel material was not determined. The average crack growth rate

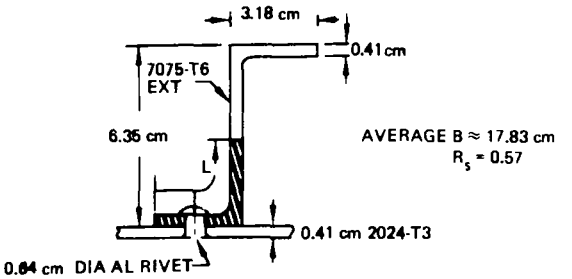

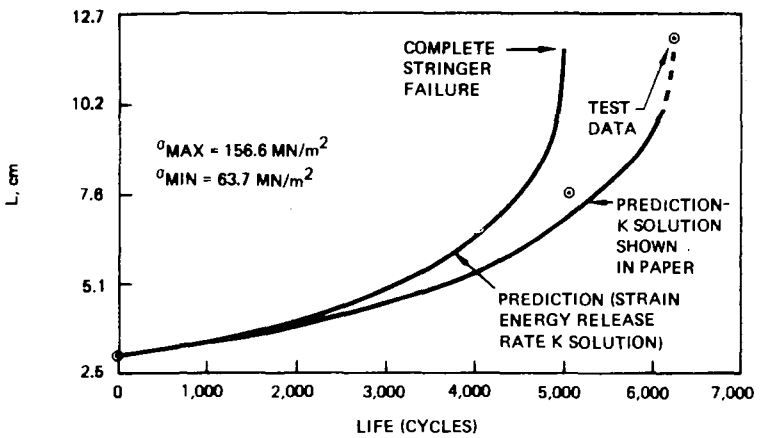

FIG. 11—*Comparison of crack growth computed from finite-element solution and test data.*

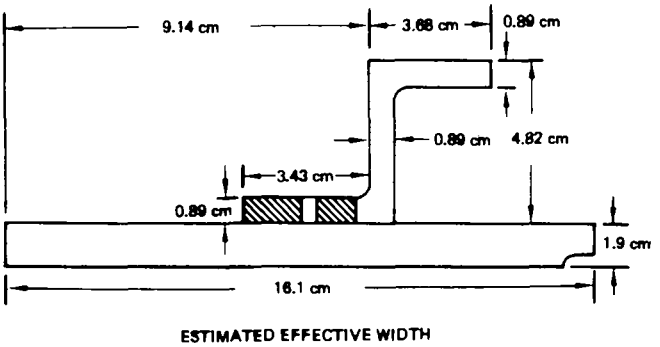

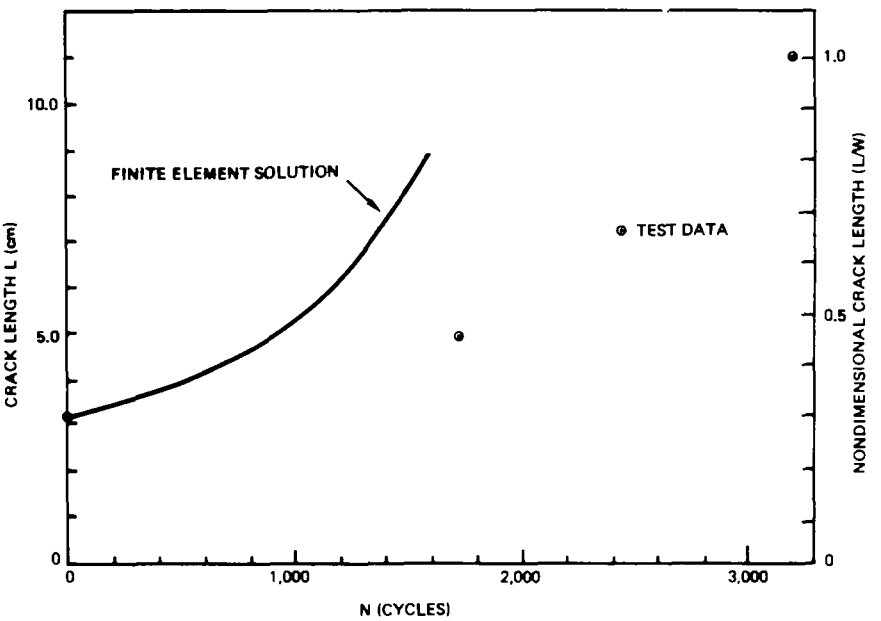

FIG. 12—*Comparison of crack growth computed from finite-element solution and test data.*

relationship for 7075-T6 aluminum alloy used at Boeing for ambient laboratory environment is utilized here and is given by the following equation

$$\frac{dL}{dN} = 9.77 \times 10^{-10}(1 - R)^{2.22} K_{\max}{}^{3.7}$$

Crack growth life computed from SIF values in Fig. 7 are shown in Fig. 11 along with measured crack lengths from the test. Figure 11 also shows crack

growth life computed from SIF solutions based on strain energy release rates. As mentioned before, SIF's based on strain energy release rates were approximately 7.5 percent higher than the SIF's computed from the crack opening displacements shown in Fig 7. Computed crack growth lives correlate very well with the test crack growth life.

Figure 12 contains a comparison of computed crack growth life to the test life of Test Panel 2. Panel 2 was tested under a complex spectrum loading representing cyclic loads at the lower wing skin of a military cargo aircraft. Pertinent details are given in Fig. 12. Predicted crack growth life correlates quite well with test life, considering a scatter of 50 percent is common in cyclic tests and prediction capability of crack growth life for spectrum loadings.

It should be emphasized that average crack growth rates for the stiffener material were used and no actual test data for crack growth rates for test panel materials were available.

Conclusions

SIF's are obtained for partially cracked Z and I stiffeners for a stiffened panel subjected to uniform uniaxial tension. SIF's are presented in design charts as a function of crack length, stiffening ratio, stiffener spacing, and fastener flexibility.

Results of this work show that using SIF solutions based on the traditionally used single-edge-notch solution significantly overestimate SIF.

Crack growth lives predicted for partially cracked stiffeners in stiffened panels subjected to constant amplitude cyclic loading and spectrum loading correlate very well with the test results.

Acknowledgments

This work is part of a Boeing Independent Research and Development program. The authors wish to thank W. L. Engstrom, R. V. Sanga, and D. E. Strand for their interest and helpful discussions.

References

[1] Bhatt, S. J., "Analysis of Load Transfer in Skin Stiffener Panels," Boeing Document D6-17821, The Boeing Company, Seattle, Wash., 1966.

[2] Poe, C. C., "Stress Intensity Factor for a Cracked Sheet with Riveted and Uniformly Spaced Stringers," NASA TR R-358, National Aeronautics and Space Administration, Washington, D.C., 1971.

[3] Swift, T. in *Damage Tolerance in Aircraft Structures, ASTM STP 486*, American Society for Testing and Materials, 1971, pp. 164-214.

[4] Sanga, R. V., "The 747 Fail-Safe Structural Verification Program," presented at 7th International Committee on Acronautical Fatigue Symposium, London, England, 1973.

[5] Ratwani, M. M. and Wilhem, D. P., "Development and Evaluation of Methods of Plane Stress Fracture Analysis," AFFDL-TR-73-42, Air Force Flight Dynamics Laboratory, Wright-Patterson AFB, Ohio, 1977.

[6] Swift, T., "Damage Tolerance Analysis of Redundant Structures," Douglas Paper 6673, McDonnell Douglas Co., 1978.

[7] Brussat, T. R., Chiu, S. T., and Creager, M., "Flaw Growth in Complex Structure, Vol. 1, Technical Discussion," AFFDL-TR-77-49, Air Force Flight Dynamics Laboratory, Wright-Patterson AFB, Ohio, 1977.

[8] Shah, R. C. in *Mechanics of Crack Growth, ASTM STP 590*, American Society for Testing and Materials, 1976, pp. 429-459.

[9] Rooke, D. P. and Cartwright, D. J., *Compendium of Stress Intensity Factors*, Her Majesty's Stationery Office, London, England, 1976.

[10] Schwab, P. M. and Shah, R. C. "Stress Intensity Factors for a Skin Crack Centered on a Broken Stiffener or Near a Spar Cap," Boeing Document D180-25063-1, The Boeing Company, Seattle, Wash., 1979.

T. M. Hsu[1] *and K. Kathiresan*[1]

Analysis of Cracks at an Attachment Lug Having an Interference-Fit Bushing

REFERENCE: Hsu, T. M. and Kathiresan, K., **"Analysis of Cracks at an Attachment Lug Having an Interference-Fit Bushing,"** *Fracture Mechanics: Fourteenth Symposium—Volume I: Theory and Analysis, ASTM STP 791*, J. C. Lewis and G. Sines, Eds., American Society for Testing and Materials, 1983, pp. I-172-I-193.

ABSTRACT: An analytical procedure was presented for computing the stress-intensity factors for a crack emanating from an attachment lug having an interference-fit bushing. The procedure consists of two major steps. First, the effective unflawed stress distribution on the prospective crack surface was obtained by superimposing the residual hoop stresses due to the installation of an interference-fit bushing on the tangential stresses obtained due to the application of pin loading. Next, a crack was introduced in this stress field by removing the tractions on the crack faces and computing the corresponding effective stress-intensity factor using the developed Green's function. It was found that the installation of an interference-fit bushing caused an increase in the effective stress-intensity factor ratio ($R_{eff} = K_{min}/K_{max}$), and a significant decrease in the effective stress intensity factor range ($\Delta K_{eff} = K_{max} - K_{min}$). This would result in reduction of the fatigue crack growth rate. The effects of the rigidity and the thickness of the bushing on the stresses and the effective stress-intensity factors also were presented.

KEY WORDS: stress-intensity factor, stress analysis, attachment lug, residual stress, crack propagation, fracture mechanics

In aircraft structures, lug-type joints are used frequently to connect major structural components or in linkage structure. The lug joint normally is connected by a single pin, creating a simple joint that is easy to assemble and disassemble. However, the elastic gross section stress concentration for a normal lug can be very high, which results in a relatively short crack initiation period and crack growth life. To improve such life, the concept of installing an interference-fit bushing to introduce fatigue-reducing residual

[1]Staff engineer and senior engineer, respectively, Advanced Structures Department, Lockheed-Georgia Co., Marietta, Ga. 30063.

stresses around the hole of the lug prior to pin fitting has been used in aircraft attachment lug design practices. For a given fatigue load cycle, the installation of an interference bushing can reduce the effective tangential stress range at the likely location of crack initiation, resulting in improvement in fatigue and crack growth life. It also can reduce fretting damage on the hole wall of the lug.

Despite improved damage-tolerance design capabilities and practices and despite much improved nondestructive inspection techniques, some cracks still occur and cannot be detected during routine maintenance inspection. Under service loading, such cracks will grow, and fracture can occur if the crack length reaches a critical size before it can be detected and the part repaired or replaced. Since attachment lugs are some of the most fracture-critical components in aircraft structure, the consequences of a structural lug failure can be very severe. Therefore, it is important to develop an analytical procedure for assessing or designing durable attachment lugs to help ensure aircraft operational safety.

Recently, several papers have been published on the analyses of cracks at attachment lugs that do not have interference-fit bushings. Schijve and Hoeymaker [*1*][2] and Wanhill [*2*] derived empirical K-solutions from the growth rate data for through-cracks under constant-amplitude loading using a backtracking method. Liu and Kan [*3*] and Kirkby and Rooke [*4*] used the simple compounded solution method that involves superimposing known solutions to estimate the stress-intensity factors. Aberson and Anderson [*5*] used special crack-tip singularity elements to compute the stress-intensity factors for a crack in a nonsymmetrical aft lug of an engine pylon. Pian et al [*6*] used the hybrid finite-element method to compute the K-values for cracks oriented in various angles from the axial direction of straight lugs. Impellizzeri and Rich [*7*] modified the exact weight function derived by Buecker [*8*], for an edge crack in a semi-infinite plate, to include a series of geometry correction factors. Then they [*7*] computed the K-values using the weight function method. Hsu [*9*] used the finite-element method with the inclusion of a high-order crack-tip singularity element to determine the pin-bearing pressure distributions and the stress-intensity factors for cracks in straight and tapered attachment lugs, having a neat fit between the pin and the lug. This analysis can account accurately for the change of pin-bearing pressure distribution with the change in crack length, and provides K-values that are in good agreement with the available data.

Very few solutions are available for estimating the stress-intensity factors for cracks at attachment lugs having an interference-fit bushing. The purpose of this study is to develop a procedure for estimating the stress-intensity factors for a crack emanating from such a lug.

[2]The italic numbers in brackets refer to the list of references appended to this paper.

Analytical Procedures

Generation of the Green's Function

It is well known that the linear superposition method can be used to obtain the stress-intensity factors for a crack structure. The principle of superposition of linear elasticity implies that, for calculating stress-intensity factors, loading the crack faces with $\sigma(x)$ is equivalent to loading the cracked body with loads which produce $\sigma(x)$ on the prospective crack faces in the absence of a crack.

Figure 1 shows the scheme of the linear superposition method. The stress-intensity factor of the problem in Fig. 1*a* is equivalent to the sum of that of the problems in Figs. 1*b* and 1*c*. Since Fig. 1*b* is crack free, the stress-intensity factor in Fig. 1*a* is equivalent to that of Fig. 1*c*. By idealizing the stress in Fig. 1*c* as N discrete loads, $P_1, \ldots, P_N$, then the stress-intensity factor, for a given crack length, a, can be computed from the following equation

$$K(a) = \sum_{i=1}^{N} K_i = \sum_{i=1}^{N} k_i(x_i, a)\, P_i(x_i) \tag{1}$$

where $k_i(x_i, a)$ is the normalized stress-intensity factor due to the i^{th} load, P_i, applied at location x_i. For an arbitrarily distributed stress, $\sigma(x)$, instead of discrete forces, P_i, Eq 1 becomes

$$K(a) = \int_0^a k(x,a) \times \sigma(x)\, dx \tag{2}$$

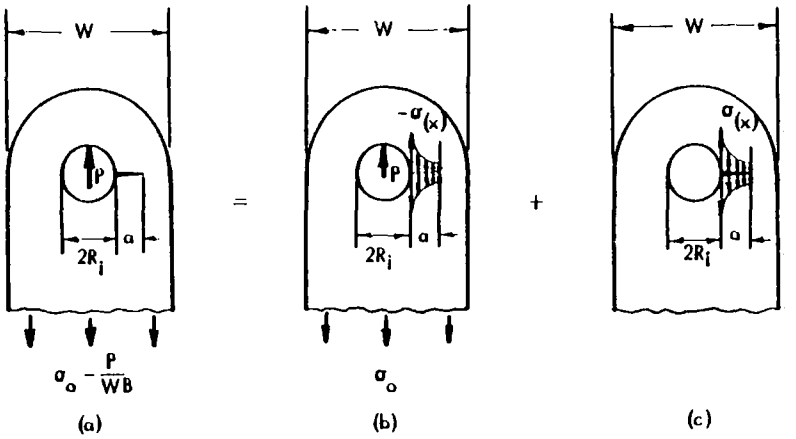

FIG. 1—*Schematic of linear superposition method.*

In Eq 2, $k(x,a)$ is the weight function (or Green function). Bueckner [*10*] and Rice [*11*] defined the weight function as

$$k(x,a) = \frac{H}{2\bar{K}(a)} \times \frac{\partial u(x,a)}{\partial a} \tag{3}$$

for a symmetrical load system on a linearly elastic body containing a crack of length a. In Eq 3, H is an appropriate elastic modulus; it is $E/(1 - \nu^2)$ for plane strain and E for generalized plane stress. $\bar{K}(a)$ is the known stress-intensity factor, and $u(x,a)$ is the y-component of the crack surface displacement at x. The weight function was shown [*10,11*] to be unique for a given structural geometry and crack size, regardless of the loading condition. Therefore, it can be developed for one load condition and then used to determine the stress-intensity factor for any other load condition. As discussed by Hsu and Rudd [*12*], the closed-form weight function for cracks emanating from a hole is not available. They developed the Green's function from the stress-intensity factors computed using the high-order singularity element for a double-radial crack emanating from an open hole and subjected to concentrated loads on and perpendicular to the crack surface. This approach also accounts for the effect of hole curvature, the finite width, and the shape of the lug head. Therefore, it can be used to develop the weight function for through-the-thickness cracks emanating from the hole of attachment lugs.

By defining $G = k\sqrt{a/\pi}$ and $\zeta = x/a$ and substituting them into Eq 2, one obtains

$$K(a) = \sigma_0\sqrt{\pi a} \int_0^1 \bar{\sigma}(\zeta)\, G(a,\zeta) \times d\zeta \tag{4}$$

where σ_0 is the uniform far-field stress and $\bar{\sigma} = \sigma/\sigma_0$ is the normalized, unflawed stress distribution on the prospective crack surface.

The Green's function, G, for a single radial crack emanating from a circular hole of the lug and subjected to a pair of concentrated forces on the crack surfaces, as shown in Fig. 2, can be obtained from the computed stress-intensity factor using two-dimensional, cracked finite-element analysis for various width-to-hole diameter ratios, W/D, and crack length a/R_i and x/a ratios as follows

$$G\left(\frac{a}{R_i}, \frac{x}{a}, \frac{W}{D}\right) = k(x,a)\sqrt{a/\pi} \tag{5}$$

Due to the limitation of finite-element methodology, when the concentrated forces are applied close to the crack tip, say $x/a > 0.9$, the corresponding weight functions were obtained using the edge crack model as shown in Fig.

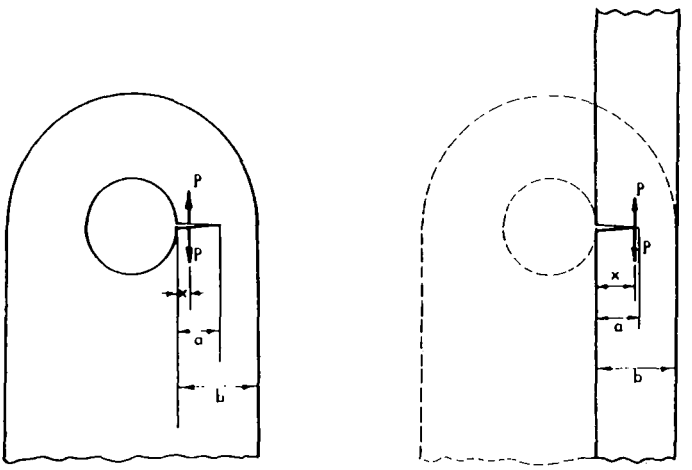

(a) FOR P APPLIED AWAY FROM CRACK TIP (b) FOR P APPLIED CLOSE TO CRACK TIP

FIG. 2—*Models for generating the Green's function.*

$2b$. The weight function, G_1, for such edge cracks is available in Ref. *13*, and can be written as

$$G_1 = \frac{2}{\pi}\left\{\frac{3.52(1-x/a)}{(1-a/b)^{3/2}} - \frac{4.35-5.28x/a}{\left(1-\frac{a}{b}\right)^{1/2}} + \left[\frac{1.30-0.30(x/a)^{3/2}}{\sqrt{1-(x/a)^2}} + 0.83 - 1.76x/a\right]\left[1-(1-x/a)\frac{a}{b}\right]\right\} \quad (6)$$

In the conventional finite-element method, the external force can be applied only at nodal points. When the crack length is small, it becomes cumbersome to refine the model such that there will be enough nodes along the crack faces for the purpose of computing the K and G values. Therefore, an alternate approach is used. For each crack length a, the K and G values were calculated at each available nodal point on the crack face, say x_j/a, using the model shown in Fig. 2*a* and Eq 5. The weight function for an edge crack in a finite-width strip as shown in Fig. 2*b* was calculated at the same locations x_j/a using Eq 6. From this, the ratio of the weight function for a curved attachment lug and the weight function for a straight strip was obtained for each x_j/a value, that is

$$r(x_j/a) = G(x_j/a)/G_1(x_j/a) \tag{7}$$

When x_j/a approaches 1, say $x_j/a = 0.9999$, one would anticipate that $r(0.9999) = 1.0$. The high order polynominal then was used to represent the computed ratio r using the least-square curve fitting procedure, that is

$$r\left(\frac{x}{a}\right) = \sum_{i=1}^{M} C_i\left(\frac{x}{a}\right)^{i-1} \tag{8}$$

The weight function at any location on the entire crack surface then can be computed using Eq 6 and 8 as

$$G\left(\frac{x}{a}\right) = r\left(\frac{x}{a}\right) \times G_1\left(\frac{x}{a}\right) \tag{9}$$

The results obtained using the aforementioned procedure are shown in Figs. 3 to 5 for single through-the-thickness cracks in straight attachment lugs having width-to-hole diameter ratios, W/D, of 1.5, 2.25, and 3.0, respectively. The symbols shown in these three figures are the discrete values obtained using the finite-element method and the curves are obtained using Eq 9. As seen from these figures, this alternate approach gives an excellent estimation of G values at any desired location. A similar approach can be used to generate the Green's function for different W/D ratios. For any a/R_i ratio different from those computed values, an interpolation or extrapolation technique can be used to obtain the corresponding Green's function.

With a knowledge of the Green's function, G, Eq 2 can be used to compute the stress-intensity factors for a crack emanating from the attachment lug having an interference-fit bushing, provided the effective unflawed stress (residual stress plus applied stress) on the prospective crack surface can be determined with the crack absent.

Unflawed Stress Analysis

The installation of an interference-fit bushing creates a compressive radial stress and a tensile hoop stress in the lug in a manner similar to a thick cylinder under internal pressure. On this basis, an approach similar to that of Seely and Smith [*14*] for a thick-wall cylinder under internal pressure is used to compute the residual stresses in the lug due to the installation of an interference-fit bushing. Before the residual stresses in the lug can be computed, the pressure, P_s, on the surface of contact between the bushing and the lug must be determined.

Let R_o and R_i denote outer and inner radii of the lug, and r_o and r_i denote outer and inner radii of the bushing before the interference-fit installation, respectively. Let R_1 be the inner radius of the lug and also the outer radius of

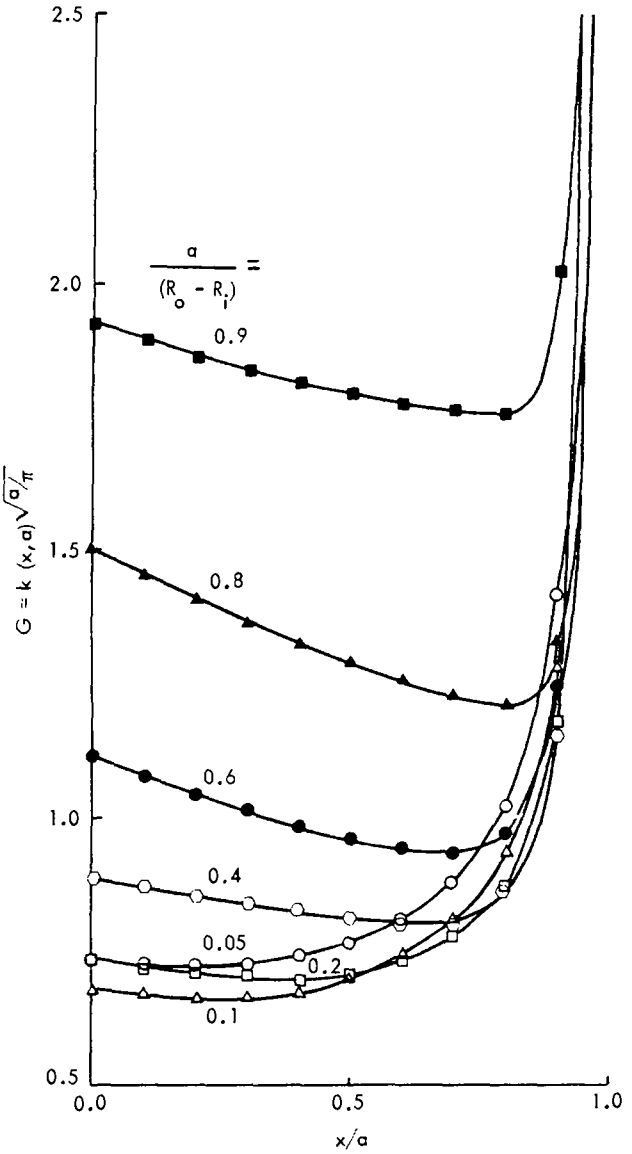

FIG. 3—*Green's functions for a single through-crack at a straight attachment lug having* W/D *ratio of 1.50.*

the bushing after the installation, and let δ be the difference in the original two values of inner radius of the lug, R_i, and the outer radius of the bushing, r_o, that is

$$\delta = r_o - R_i \tag{10}$$

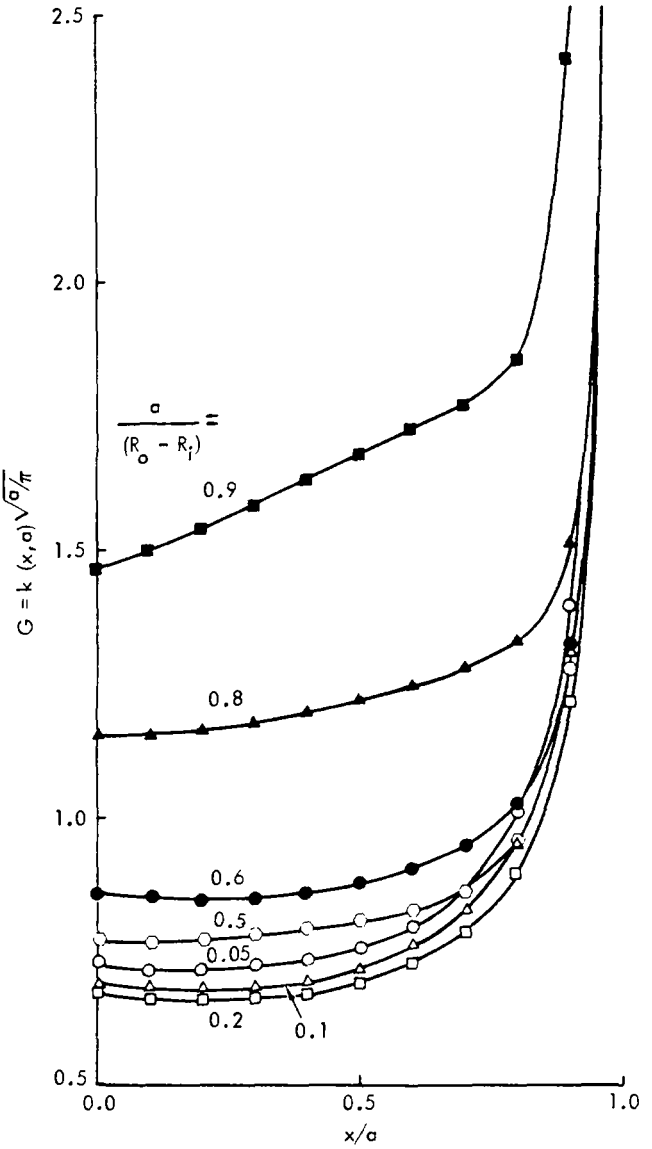

FIG. 4—*Green's functions for a single through-crack at a straight attachment lug having* W/D *ratio of 2.25.*

After fitting the bushing, the inner radius of the lug will be larger than its initial value by an amount, δ_1, which is related to the unknown contact pressure as

$$\delta_1 = \frac{P_s R_1}{E_L}\left(\frac{R_o^2 + R_1^2}{R_o^2 - R_1^2} + \mu_L\right) \tag{11}$$

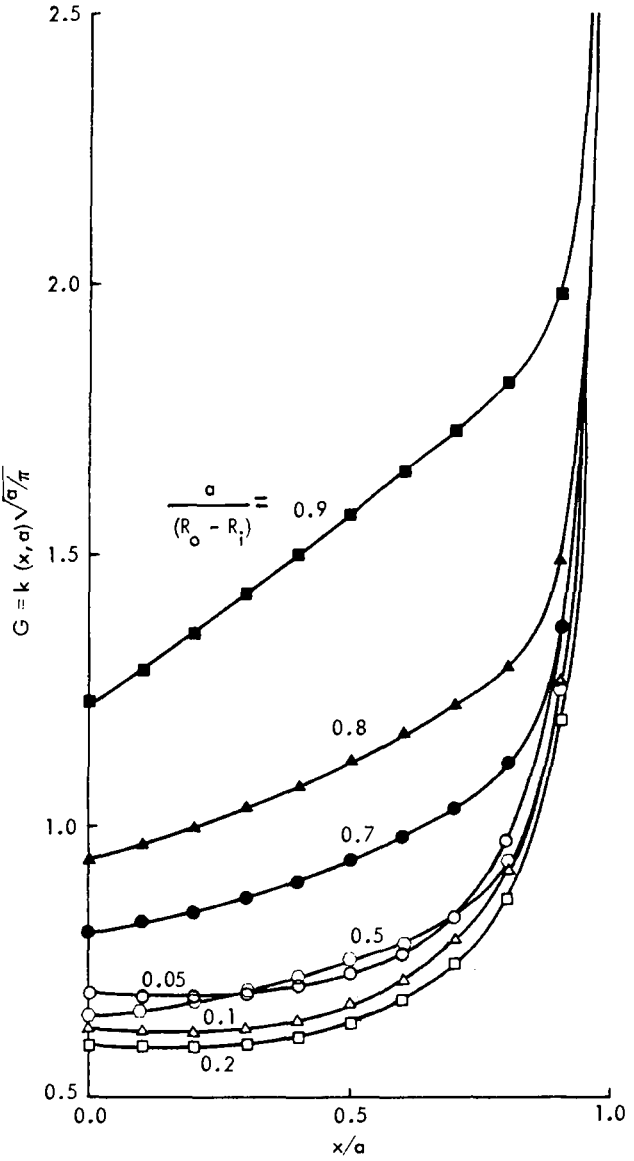

FIG. 5—*Green's functions for a single through-crack at a straight attachment lug having* W/D *ratio of 3.00.*

where E_L and μ_L are the Young's modulus and the Poisson ratio of the lug. At the same time, the outer radius of the bushing will be changed (decreased) by an amount, δ_2, which is given by the following equation

$$\delta_2 = \frac{P_s R_1}{E_B}\left(\frac{R_1^2 + r_i^2}{R_1^2 - r_i^2} - \mu_B\right) \tag{12}$$

where E_B and μ_B are the Young's modulus and the Poisson's ratio of the bushing.

At the completion of the fitting process, the difference in these original radii, δ, disappears as a result of the changes in the lengths δ_1 and δ_2. Therefore, the sum of the magnitudes of δ_1 and δ_2 is equal to δ, that is

$$\delta = \frac{P_s R_1}{E_L}\left[\left(\frac{R_o^2 + R_1^2}{R_o^2 - R_1^2} + \mu_L\right) + \frac{E_L}{E_B}\left(\frac{R_1^2 + r_i^2}{R_1^2 - r_i^2} - \mu_B\right)\right] \tag{13}$$

The contact pressure is obtained from Eq 13 as

$$P_s = \delta E_L / R_1\left[\left(\frac{R_o^2 + R_1^2}{R_o^2 - R_1^2} + \mu_L\right) + \frac{E_L}{E_B}\left(\frac{R_1^2 + r_i^2}{R_1^2 - r_i^2} - \mu_B\right)\right] \tag{14}$$

With contact pressure determined, the residual stresses in the lug due to the installation of an interference-fit bushing can be calculated using the following equations

$$\sigma_\theta = \frac{P_s R_1^2}{R_o^2 - R_1^2}\left[\frac{R_o^2}{(R_1 + x)^2} + 1\right] \tag{15}$$

and

$$\sigma_r = \frac{P_s R_1^2}{R_o^2 - R_1^2}\left[\frac{R_o^2}{(R_1 + x)^2} - 1\right] \tag{16}$$

where x is the radial distance measured from the hole wall surface.

Equations 14, 15, and 16 are used to compute the residual tangential stresses along the x-axis in the attachment lugs due to the installation of interference-fit bushings having various dimensions and rigidities. Results are presented in Figs. 6, 7, and 8. Figure 6 shows the effect of the amount of radial interference on the residual stress along the x-axis in the aluminum lug having a constant bushing thickness of 0.09 in.[3] and constant ratio of bushing rigidity to lug rigidity (E_B/E_L) of 3.0. As shown by Fig. 6, the increase in the amount of radial interference increases the magnitude of the residual tangential stress. Figure 7 presents the residual tangential stress as a function of the normalized distance along the x-axis in an attachment lug for an E_B/E_L ratio ranging from 1.0 to 3.0. The result indicates that, for a constant bushing thickness and a constant level of radial interference, the increase in the bushing-to-lug rigidity ratio increases the magnitude of residual stress. The effect of bushing thickness on the residual stress in the attachment lug having a constant E_B/E_L ratio and the same amount of radial interference is

[3]SI unit conversion table is furnished at the end of the text.

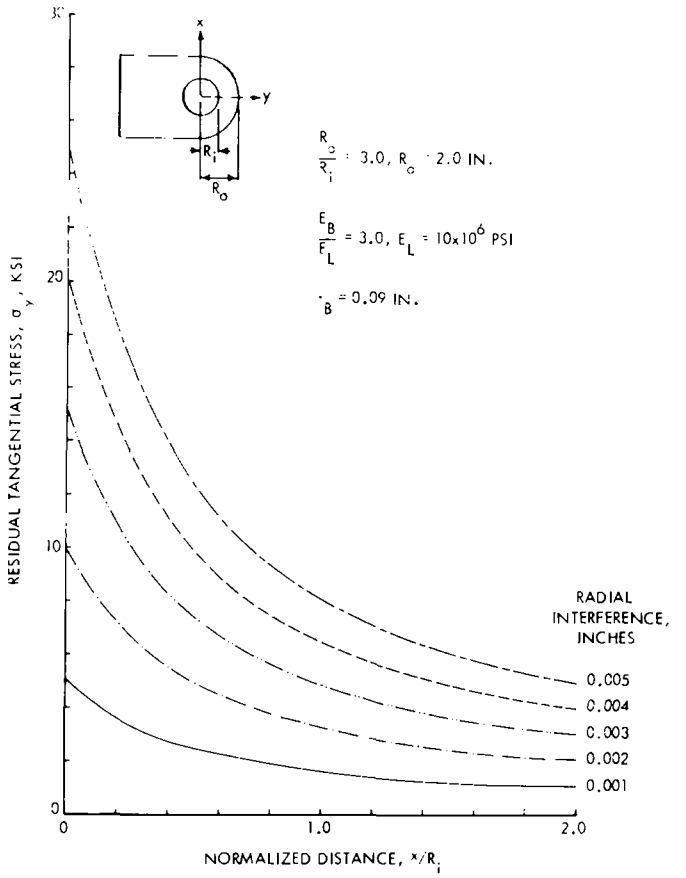

FIG. 6—*Stress distribution along the x-axis in attachment lugs due to installation of variable levels of interference-fit bushings.*

shown in Fig. 8; the increase in the bushing thickness increases the residual stress in the lug.

The tangential stresses due to the application of the pin loading were computed using the finite-element method. In the calculation, it is assumed that the bushing and the lug remain contact, and that no slippage occurs along the hole wall surface during the application of the load. The computed applied stresses are shown in Figs. 9 and 10. Figure 9 show the tangential stress normalized by the far-field applied stress as a function of normalized distance along the x-axis in the attachment lug having a constant bushing thickness and various bushing rigidity ratios. As shown in this figure, the increase in the rigidity of the bushing decreases the applied tangential stress. Figure

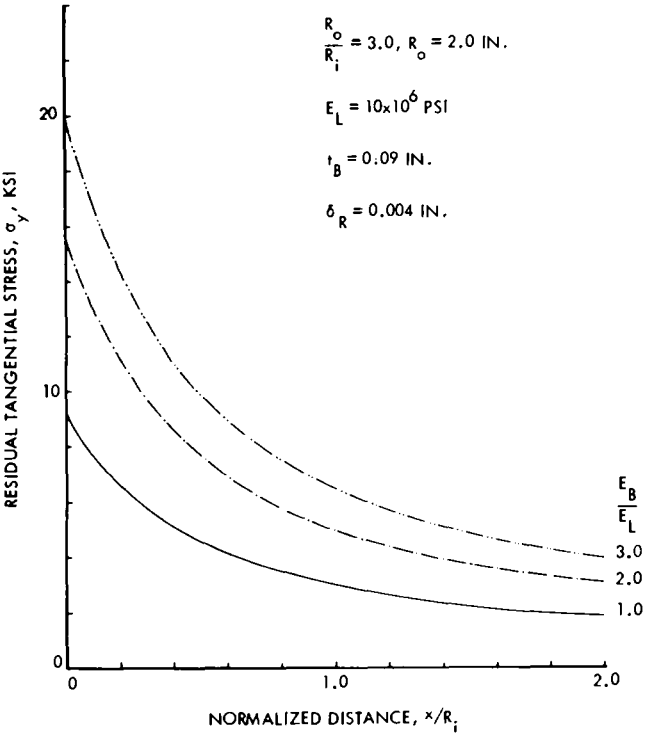

FIG. 7—*Stress distribution along the* x-*axis in attachment lugs due to installation of interference-fit bushings with various rigidities.*

10 presents similar results for an attachment lug having a constant E_B/E_L ratio and various bushing thicknesses. The results indicated that the increase in the bushing thickness reduces the applied tangential stress.

Within the levels of radial interference used in this study, it is found that the tangential stresses due to the application of the far-field loading are independent of the level of interference. This is true as long as there is no separation between the interference-fit bushing and the lug, and the total effective stress (residual stress plus applied stress) does not exceed the material yield strength. If the total effective stress exceeds the material yield strength, a nonlinear, elastic-plastic, finite-element analysis such as Ref. *15* should be conducted to obtain the total effective stress. Within the range of practical interest, only the linear analysis is performed in the current study. The total effective tangential stresses then were used to compute the effective stress-intensity factors for a crack emanating from an attachment lug having an interference-fit bushing by using Eq 4.

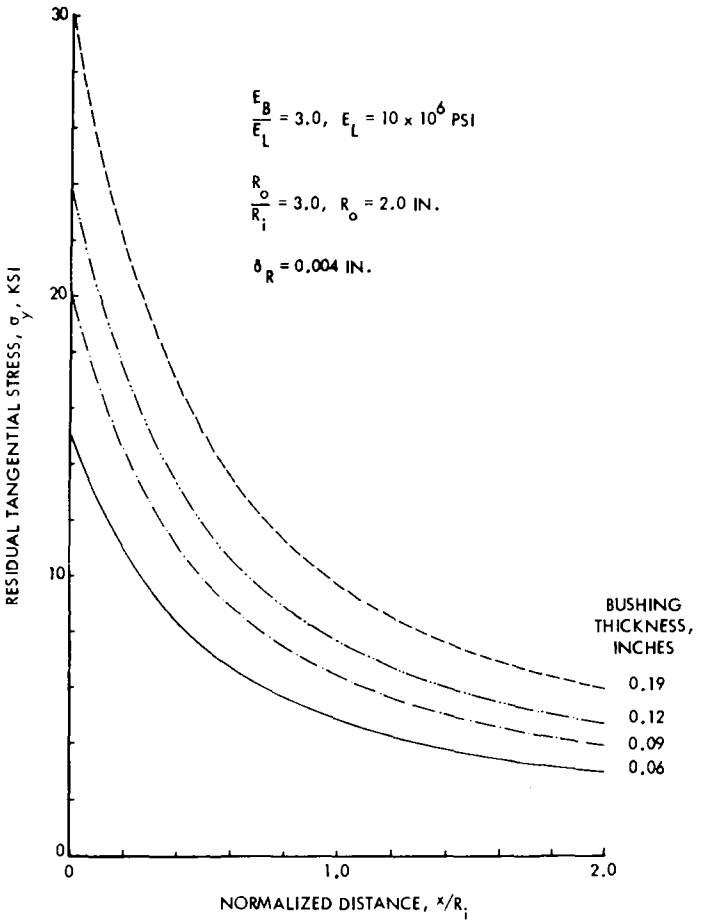

FIG. 8—*Stress distribution along the x-axis in attachment lugs due to installation of interference-fit bushings with various thicknesses.*

Analysis of Stress-Intensity Factors

The effective stress-intensity factors were computed using Eq 4, and the typical results are presented in Figs. 11, 12, and 13 for the lugs subjected to far-field loading of 8 ksi[3] and a minimum-to-maximum load ratio of zero (R = 0). Figure 11 compares the effective stress-intensity factor ranges for a lug having an interference-fit bushing with a similar lug without a bushing. It is clear from Fig. 11 that the installation of the interference-fit bushing causes an increase in the effective stress-intensity factor ratio, $R_{eff} = K_{min}/K_{max}$, and a significant decrease in the stress-intensity factor range, ΔK. This combination will result in the reduction of fatigue crack growth rate.

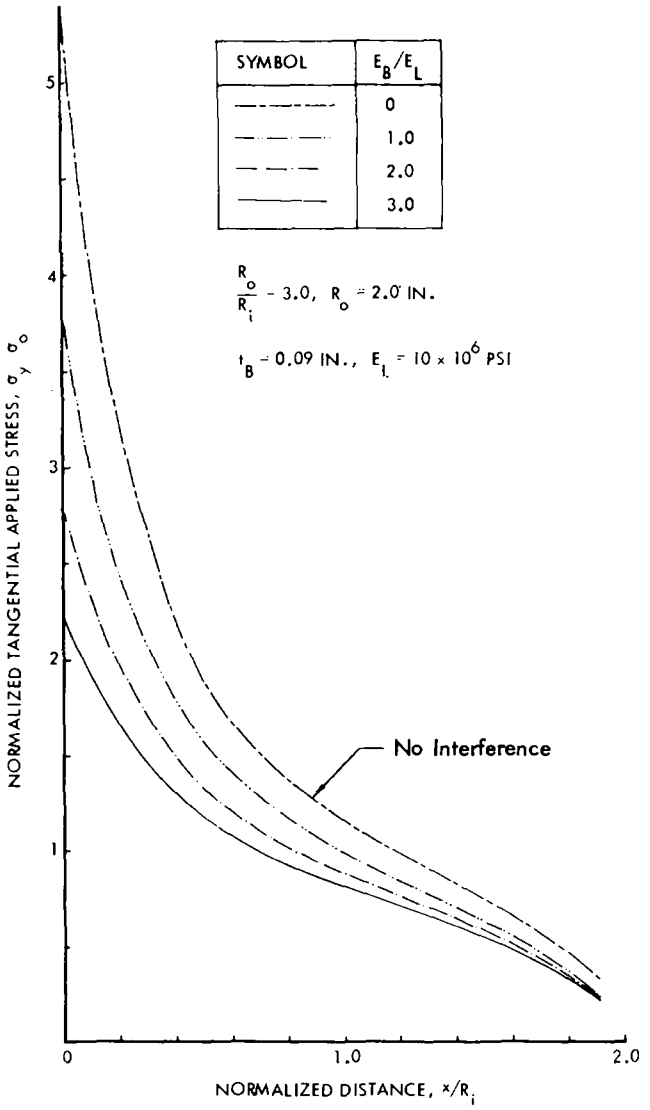

FIG. 9—*Normalized stress distribution along the x-axis in attachment lug having various bushing rigidities caused by far-field applied loading.*

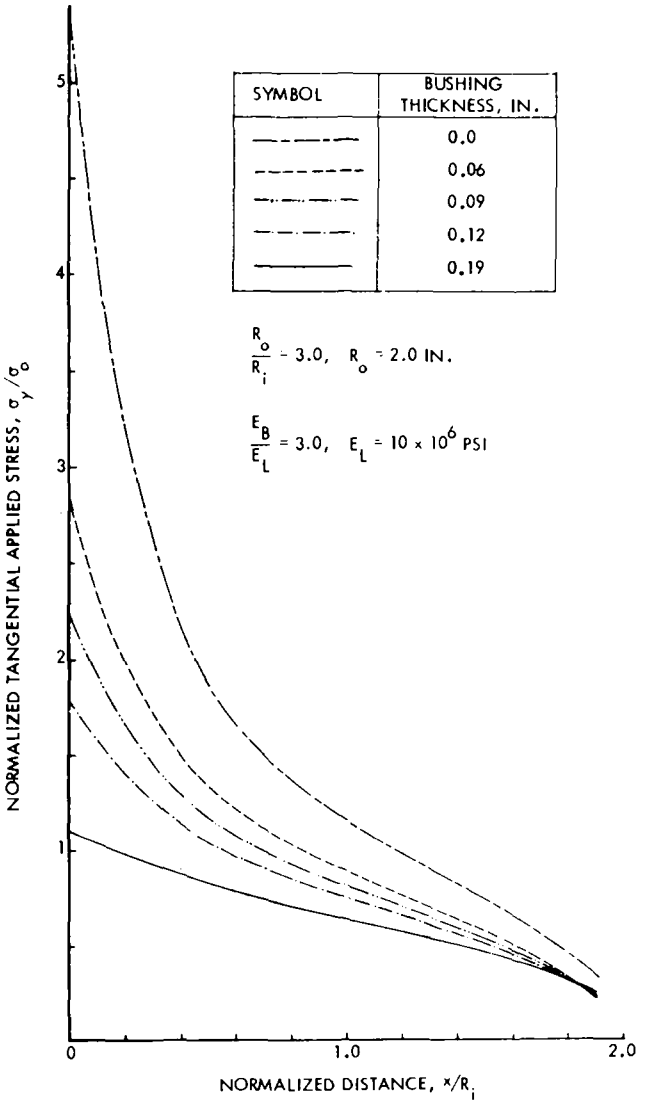

FIG. 10—*Normalized stress distribution along the x-axis in attachment lug having various bushing thicknesses caused by far-field applied loading.*

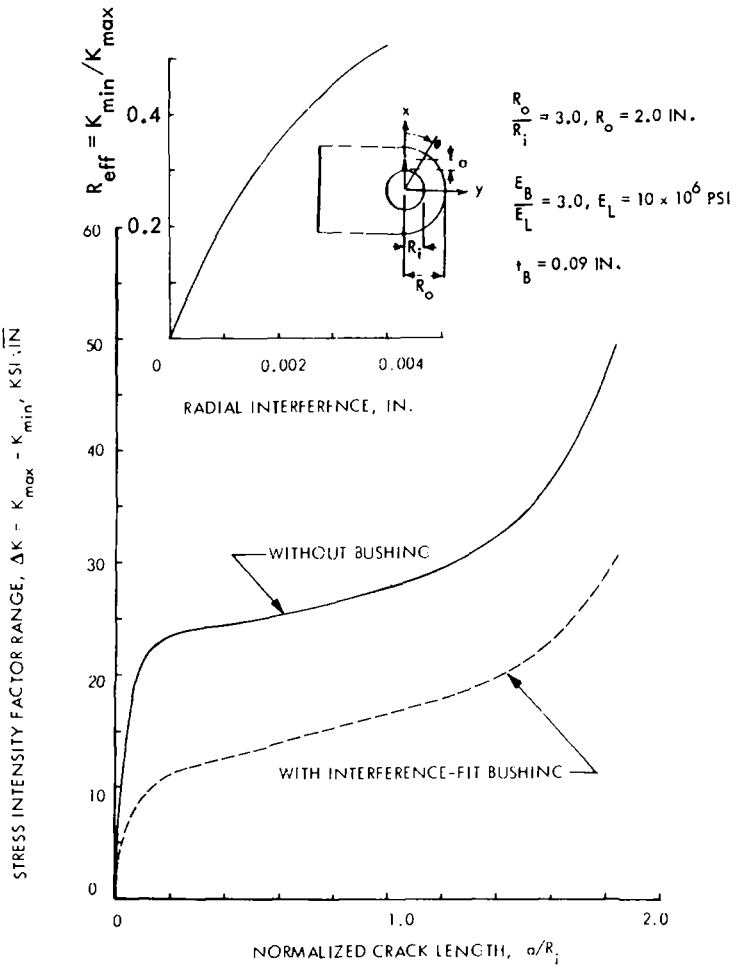

FIG. 11—*Effective stress-intensity factor range and ratio of a single through-crack at attachment lug with and without interference-fit bushing (σ_0 = 8 ksi and R = 0).*

The effect of a/R_i on R_{eff} also was investigated, and was found to change the value of R_{eff} by less than 4 percent for interference levels considered in this paper. The effects of the bushing-to-lug rigidity ratio on the effective stress-intensity factor range are shown in Fig. 12. Similar results on the effect of bushing thickness on the effective ΔK are presented in Fig. 13. Based on the results shown in Figs. 12 and 13, it may be concluded that: (1) for the same amount of radial interference and a constant thickness of the bushing, when the rigidity of the bushing increases, the effective stress-intensity factor range decreases; (2) for the same amount of radial interference and a specific

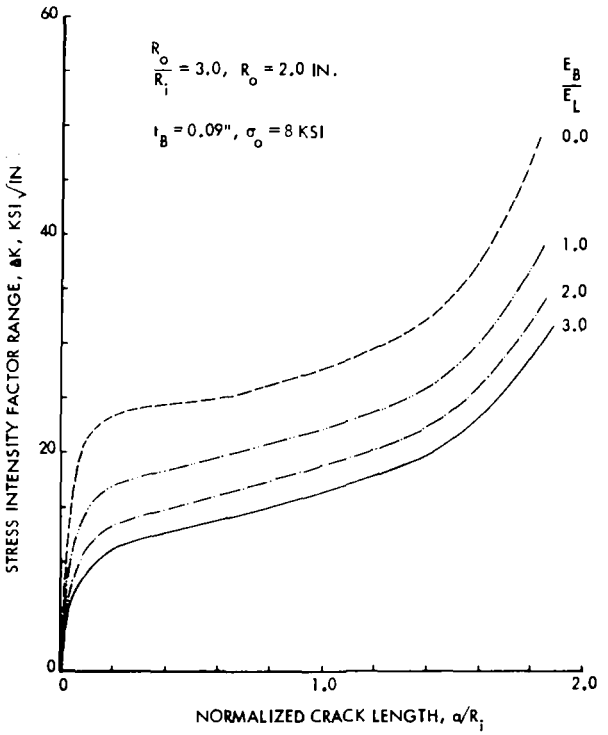

FIG. 12—*Stress-intensity factor ranges of cracks at attachment lug having 0.004-in. interferences bushing and various* E_B/E_L *ratios.*

rigidity of the bushing, the increase in the bushing thickness decreases the effective stress-intensity factor range.

An experimental program has been defined to provide data to evaluate and verify the analysis. A straight 7075-T6 aluminum lug will be used in the text, and the experimental stress-intensity factors will be reduced from the crack growth rate data to be generated using a backtracking method [*16*] of calibrating the crack growth rate, da/dN, and the stress-intensity factor range, ΔK. When the reduced K-values become available, they will be used to correlate with the analysis, and the results will be reported in the near future.

Conclusions

An analytical procedure using the Green's function approach has been presented for computing the stress-intensity factors for a crack emanating from an attachment lug having an interference-fit bushing. Based on the analysis conducted, the following conclusions have been reached:

1. The installation of an interference-fit bushing caused an increase in the effective stress-intensity factor ratio ($R_{\text{eff}} = K_{\min}/K_{\max}$), and a significant

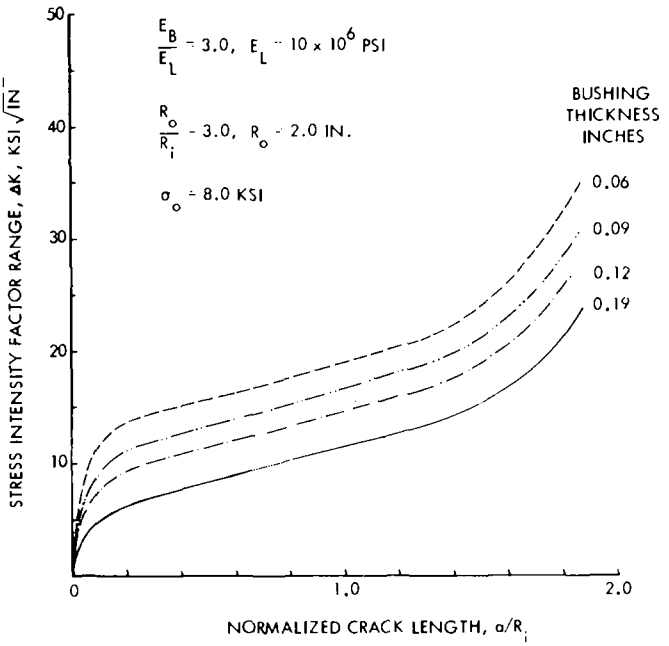

FIG. 13—*Stress-intensity factor ranges of cracks at attachment lug having 0.004-in. radial interference bushing subjected to far-field loading of 8 ksi and* R = *0.1.*

decrease in the effective stress-intensity range ($\Delta K_{eff} = K_{max} - K_{min}$). This would result in the reduction of fatigue crack growth rate, and hence improve the fatigue crack growth life.

2. For the same amount of radial interference between the bushing and the lug, the effective stress-intensity factor range can be further decreased by the proper choice of a bushing either (*a*) having a specific thickness but a higher rigidity, or (*b*) having a specific rigidity but a greater thickness.

SI Unit Conversion Table	
1 in.	= 0.0254 m
1 ksi	= 6.895 MPa
1 psi	= 0.006895 MPa
1 ksi $\sqrt{\text{in.}}$	= 1.0989 MPa $\sqrt{\text{m}}$

References

[*1*] Schijve, J. and Hoeymakers, A. H. W., "Fatigue Crack Growth in Lugs and the Stress Intensity Factor," Report LR-273, Delft University of Technology, Delft, The Netherlands, July 1978.

[*2*] Wanhill, R. J. H. and Lof, C. F., "Calculation of Stress Intensity Factors for Corner

Cracking in a Lug," *Fracture Mechanics Design Methodology*, Advisory Group for Aerospace Research and Development (ARGARD), CP221, Paper No. 8, Feb. 1977.
[3] Liu, A. F. and Kan, H. P. in *Proceedings of the Fourth International Conference on Fracture*, Waterloo, Ont., Canada, June 19-24, Vol. 3, 1977, pp. 657-664.
[4] Kirkby, W. T. and Rooke, D. P., *Fracture Mechanics in Engineering Practice*, Applied Scientific Publishers, London, 1977, p. 339.
[5] Aberson, J. A. and Anderson, J. M. in *Third NASTRAN User's Colloquium*, NASA TMX-2893, National Aeronautics and Space Administration, 1973, pp. 531-550.
[6] Pian, T. H. H., Mar, J. W., Orringer, O., and Stalk, G., "Numerical Computation of Stress Intensity Factors for Aircraft Structural Details by the Finite Element Method," AFFDL-TR-76-12, Air Force Flight Dynamics Laboratory, May 1976.
[7] Impellizzeri, L. F. and Rich, D. L. in *Fatigue Crack Growth Under Spectrum Loads, ASTM STP 595*, American Society for Testing and Materials, 1976, pp. 320-336.
[8] Bueckner, H. F., *Zeitschrift für Angewandte Mathematik und Mechanik*, Vol. 51, 1971, pp. 97-109.
[9] Hsu, T. M., "Analysis of Cracks at Attachment Lugs," presented at the American Institute of Aeronautics and Astronautics/American Society of Mechanical Engineers, 21st Structures, Structural Dynamics, and Materials Conference, Seattle, Wash., 12-14 May 1980.
[10] Bueckner, H. F., *Zeitschrift für Angewandte Mathematik und Mechanik*, Vol. 50, 1970, pp. 529-545.
[11] Rice, J. R., *International Journal of Solids and Structures*, Vol. 8, 1972, pp. 751-758.
[12] Hsu, T. M. and Rudd, J. L. in *Proceedings of the Fourth International Conference on Fracture*, Waterloo, Ont., Canada, Vol. 3, 1977, pp. 139-148.
[13] Tada, H., Paris, P. C., and Irwin, G. R., *The Stress Analysis of Cracks Handbook*, Del Research Corp., 1973.
[14] Seely, F. B. and Smith, J. O., *Advanced Mechanics of Materials*, 2nd Ed., Wiley, New York, 1960.
[15] Rudd, J. L., Hsu, T. M., and Aberson, J. A., "Analysis and Correlation of Crack Growth from Interference-Fit Fastener Holes," *Numerical Methods in Fracture Mechanics, Proceedings of the First International Conference*, University College of Swansea, West Glamorgan, U.K., Jan. 9-13, 1980.
[16] James, L. A. and Anderson, W. E., *Engineering Fracture Mechanics*, Vol. 1, 1969, pp. 565-568.

DISCUSSION

A. P. Parker[1] *(written discussion)*—The authors have addressed a complex problem. This problem encompasses Weight (or Green's) functions, pin-fit, and bushing effects. Taking these various aspects in turn, I believe that it is important to emphasize the following points.

1. The authors have derived a Green's function for a cracked lug by applying discrete pairs of point forces, symmetrically located on the crack surfaces, at a total of eight stations along the crack line. The Green's functions for each crack length then were obtained by "fitting" the numerical data

[1]Materials Branch, Royal Military College of Science, Shrivenham, Swindon, Wiltshire, England.

points. By employing a Weight function approach it is possible to obtain *all* of the Green's function data for each crack length from only two computer runs.[2,3]

2. The modelling of a multiply connected geometry by using the Green's function for a singly connected geometry of the equivalent width is likely to give inaccurate answers at longer crack lengths, unless the additional restraint of the multiply connected region is incorporated.[4] The authors employ this model for near-tip loading, and should indicate the amount of error which this may involve.

3. In the case of contact problems in which the required unflawed crack line distribution is a function of crack length, it is incorrect to employ crack line loading arising from boundary conditions applicable to the unflawed state. Quoting from Parker[5]:

> The derivation of further stress-intensity factor solutions from the weight function depends on a knowledge of stresses along the crack line in an unflawed configuration which has other boundary conditions identical to those in the cracked structure. If incorrect crack-line stresses are used, any solution so obtained is, in general, invalidated. K_I solutions to statically indeterminate configurations cannot be obtained unless the redistribution of boundary stresses caused by the presence of the crack is known.

The authors should indicate the likely error arising from this incorrect modelling.

4. In circumstances in which displacement boundary conditions are to be applied, it may be advantageous to employ the alternative weight function formulation applicable to such boundary conditions.[6]

5. The increased R ratio with interference fit bushing is anticipated on the grounds that the loading tends to increase K_{min}/K_{max}. However, the significant reduction in stress-intensity range is not fully explained. I assume that it is because the pin-load distribution in the nonbushed lug is mitigated by the bushing, producing a more constant variation of direct stress around the hole boundary. Such a dramatic influence of arc of contact is noted elsewhere.[5] Would the authors comment on the hole boundary stress distribution in lugs with, and without, interference fit bushing?

[2]Andrasic, C. P. and Parker, A. P. in "Weight Functions for Cracked, Curved Beams", *Proceedings, Conference on Numerical Methods in Fracture Mechanics*, Swansea, U. K., 1980, pp. 67-82.

[3]Parks, D. M. and Kamenetzky, E. M., *International Journal for Numerical Methods in Engineering*, Vol. 14, 1979, pp. 1693-1706.

[4]Parker, A. P., Underwood, J. H., Throop, J., and Andrasic, C. P., in this publication, pp. 1-216-I-237.

[5]Parker, A. P., "The Mechanics of Fracture and Fatigue in Some Common Structural Configurations," Technical Note MAT/18, Royal Military College of Science, Shrivenham, England, 1979.

[6]Parker, A. P. "The Mechanics of Fracture and Fatigue—An Introduction," E and FN Spon, London, 1981.

T. M. Hsu and K. Kathiresan (authors' closure)—In response to the discussion of Dr. Parker, we would like to thank him for stressing the complexity of the problem addressed in the paper and bringing some of his recent works related to the present topic to our notice. We offer the following comments for the rest of his discussion.

It was recognized in the very early stage of the work that the change in arc of contact of the pin and use of singly connected geometry for near-tip loading will play important roles in the analysis as the crack length increases (Ref *9* of the paper). It also was conjectured that the effect of such incorrect boundary condition or modeling on the estimation of stress-intensity factors will be minimal for higher W/D ratios. In other words, the redistribution of stresses along the prospective crack surface due to the extension of the crack will be very small, at least for higher W/D ratios. As anticipated, the stress-intensity factors estimated by the Green's function method and the direct evaluation of stress-intensity factors through the finite-element method by modeling both the lug and the pin, accounting proper arc of contact, agreed well for W/D ratios of 3.0 and 2.25, the differences between them being less than 1 and 2 percent, respectively. However, for a lower W/D ratio of 1.5, the difference was of 10 to 15 percent, values estimated by the Green's function being higher. Consequently, the Green's function was scaled down in a consistent form to reflect the effect of incorrect boundary conditions and errors arising from other means due to the extension of crack length. Thus, while the statements are true, they could be taken into account in a rational form in order to obtain reasonably accurate solutions.

The significant reduction in the stress-intensity factor range due to the installation of interference-fit bushing can be explained as follows. In the present analysis, the effective stresses are obtained as the sum of the residual stresses due to the interference-fit bushing and the stresses due to the application of the load by the pin. While the stresses due to the interference fit remain constant, the magnitude of the variable stresses due to the loading and unloading of the pin may seem not to have a significant reduction. The magnitude of the variable stresses in the lug is reduced by the following factors. The installation of the bushing reduces the hole radius, thereby reducing the stress concentration factor. The boundary of the lug hole is at a distance t_B from the bushing boundary, in the radial direction. This also contributes to lower stresses at the lug hole boundary, as the tangential stresses decrease rapidly in the radial direction. Other important factors in reducing the stresses at the lug hole boundary are the properties of the bushing, such as its rigidity and thickness. As the thickness or the rigidity of the bushing is increased, the stresses at the lug hole boundary will be reduced. In effect, the bushing bears the beatings of the pin, thereby reducing the stress or stress-intensity factor range significantly in the lug. As far as the lug hole boundary stress distribution is concerned, in the present analysis, it again will be the superposition of the residual stresses due to the installation of interference-fit

bushing and the stresses due to the pin load, the latter being reduced significantly due to the previously mentioned reasons.

Finally, we would like to comment that several assumptions were made in the present analysis, such as no separation between the interference-fit bushing and the lug, and the effective stresses do not exceed the yield strength of the lug material, etc. It is very hard to pin down and make error estimates due to each contributing factor. The analysis procedure was developed such that the errors due to several contributing factors are minimal and could be used effectively for designing fracture resistant lugs for aerospace and other mechanical applications. An experimental program using 7075-T6 aluminum lug is underway, and the results presented in the present paper will be correlated with that of the experiments, and will be reported in the near future. Also, effort is underway to make a nonlinear, elastic-plastic analysis such as in Ref *15* of the paper when the total effective stresses exceed the material yield strength.

S. L. Pu[1] *and M. A. Hussain*[2]

Stress-Intensity Factors for Radial Cracks in a Partially Autofrettaged Thick-Wall Cylinder

REFERENCE: Pu, S. L. and Hussain, M. A., **"Stress-Intensity Factors for Radial Cracks in a Partially Autofrettaged Thick-Wall Cylinder,"** *Fracture Mechanics: Fourteenth Symposium—Volume I: Theory and Analysis, ASTM STP 791*, J. C. Lewis and G. Sines, Eds., American Society for Testing and Materials, 1983, pp. I-194–I-215.

ABSTRACT: Using a finite-element method and thermal simulation, stress-intensity factors are determined for a uniform array of equal depth radial cracks emanating from the internal boundary of a pressurized, autofrettaged thick-wall cylinder. The computation of the same by methods of load relief and weight function also are examined. The combination of finite elements and weight functions is found very effective and is used in this paper for multiple-radial cracks in a partially autofrettaged tube. Extensive numerical results are presented for a cylinder having an external diameter twice that of the internal diameter. It shows that the autofrettaged tube with two diametrically opposed cracks remains, in general, the weakest configuration. For more than two cracks, the higher the number of cracks is, the smaller the stress-intensity factor will be.

KEY WORDS: stress-intensity factors, multiple cracks, thick-wall cylinder, quadrilateral isoparametric element, weight function, load relief factor, fracture mechanics

Nomenclature

a	Inner radius, used as length unit in this analysis
b	Diameter ratio or normalized outer radius
c	Normalized depth of cracks
E	Young's modulus of the tube material
K	Opening mode stress-intensity factors (SIF)
$K(p_o)$, $K(p_i)$	SIF due to uniform tension p_o and internal pressure p_i
K_c	SIF due to crack face loading p_c

[1]Mathematician, U.S. Army Armament Research and Development Command, Large Caliber Weapon Systems Laboratory, Benet Weapons Laboratory, Watervliet, N.Y. 12189.
[2]Applied mathematician, Corporate Research and Development Center, General Electric Co., Schenectady, N.Y. 12345.

$K_c(p)$, $K_c(pr^{-2})$ SIF due to $p_c = p$, $p_c = pr^{-2}$, respectively

$K_c(\epsilon = 0.9)$ SIF due to p_c corresponding to a 90 percent overstrain residual stress

K_m SIF for m equally spaced radial cracks emanating from a hole in an infinite plate

$K_{m.f}$ K_m when the infinite plate is replaced by a cylinder of finite thickness

N Number of radial cracks

r, θ Polar coordinates centered at the center of the tube

r_c Radius to the tip of a crack, $r_c = 1 + c$

t Wall thickness of the cylinder, $t = b - 1$

T, T_o, T_ρ Temperature at r, $r = a$ and $r = \rho$, respectively

α Linear thermal expansion coefficient

ϵ Percentage of overstrain, $\epsilon = (\rho - 1)/t$, $0 \leq \epsilon \leq 1$

ν Poisson's ratio

ρ Radius of elastic-plastic interface during pressurization

σ_o Uniaxial yield stress of the tube material

σ_r, σ_θ Normal stress in the radial and tangential direction, respectively

In a previous paper [*1*],[3] stress-intensity factors have been obtained, using 12-node quadrilateral, isoparametric elements, for a uniform array of equal depth radial cracks originating at the internal boundary of a pressurized thick-wall cylinder. To increase the maximum pressure a cylinder can contain, it is a common practice to produce a favorable residual stress in the cylinder by an autofrettage process. It is important to find the effect of residual stresses on the stress-intensity factor for a cylinder with multiple cracks.

Using the concept of thermal simulation [*2*], the autofrettage residual stresses are simulated by active thermal loads. It is shown that the stress-intensity factor for multiple radial cracks in a tube with residual stresses can be computed by the same finite-element method.

Slight changes in geometrical configurations or loading conditions require new computations. To obviate this problem, which is a shortcoming of the finite-element method, load relief [*3*] and weight function methods [*4,5*] are examined. For a small number of radial cracks, the method of load relief enables us to estimate the stress intensity for N other than two fairly accurately by making use of the finite-element result for $N = 2$. When N or crack depth is large it is shown in this paper that the load relief factor is not reliable because it varies with the nature of the load.

For a given geometrical configuration it is useful to use the weight function method. In the present approach the restrictive assumption that the crack opening displacement is a conic section [*6,7*] is circumvented. There are only

[3]The italic numbers in brackets refer to the list of references appended to this paper.

three types of hoop stress, namely: constant, $1/r^2$, and $\log(r)$, in an uncracked cylinder subjected to internal pressure, uniform tension on the outer boundary, and the autofrettage residual stress. This eliminates the need to assume the crack face pressure as a simple polynomial [*8*]. It enables us to obtain stress-intensity factors for each type of crack face pressure from three linear algebraic equations using three finite-element results for the given geometry. The stress-intensity factor can be calculated readily for any combination of internal pressure and any degree of autofrettage.

When the radial cracks progress beyond the elastic-plastic interface produced during the autofrettage overstrain, the algebraic equation for stress-intensity factor breaks down because the crack face pressure cannot be represented by a simple expression. Modifications are derived for such cases based on the crack-opening displacement near a crack tip being parabolic [*9*].

Extensive numerical results are presented for multiply cracked cylinders having an external diameter twice that of the internal diameter. Results agree with those obtained by other methods for the nonautofrettaged [*10*] and fully autofrettaged [*11*] cases. In addition, results are given for the partially autofrettaged cases.

Residual Stress and Thermal Simulation

For the case of plane strain, the stress distribution of a partially autofrettaged tube, using the von Mises yield criterion for the incompressible material, is given by [*12*]

$$\sigma_r(r) = \begin{cases} \dfrac{\sigma_o}{\sqrt{3}} \left\{ \left(2\log \dfrac{r}{\rho} - 1 + \dfrac{\rho^2}{b^2} \right) - P_1 \left(\dfrac{1}{b^2} - \dfrac{1}{r^2} \right) \right\} & 1 \le r \le \rho \quad (1) \\ \dfrac{\sigma_o}{\sqrt{3}} (\rho^2 - P_1) \left(\dfrac{1}{b^2} - \dfrac{1}{r^2} \right) & \rho \le r \le b \quad (2) \end{cases}$$

$$\sigma_\theta(r) = \begin{cases} \dfrac{\sigma_o}{\sqrt{3}} \left\{ 2\log \dfrac{r}{\rho} + 1 + \dfrac{\rho^2}{b^2} - P_1 \left(\dfrac{1}{b^2} + \dfrac{1}{r^2} \right) \right\} & 1 \le r \le \rho \quad (3) \\ \dfrac{\sigma_o}{\sqrt{3}} (\rho^2 - P_1) \left(\dfrac{1}{b^2} + \dfrac{1}{r^2} \right) & \rho \le r \le b \quad (4) \end{cases}$$

where

$$P_1 = P_1(\rho) = \frac{b^2}{b^2 - 1} \left(1 - \frac{\rho^2}{b^2} + 2\log \rho \right) \quad (5)$$

If the same hollow cylinder is subjected to a thermal load

$$T(r) = \begin{cases} T_o - \dfrac{(T_o - T_\rho)}{\log \rho} \log r & 1 \le r \le \rho \\ T_\rho & \rho \le r \le b \end{cases} \tag{6}$$

the thermal stresses are given by [2]

$$\sigma_r(r) = \begin{cases} \dfrac{E\alpha(T_o - T_\rho)}{2(1-\nu)\log \rho} \left\{ \left(2\log \dfrac{r}{\rho} - 1 + \dfrac{\rho^2}{b^2} \right) - P_1 \left(\dfrac{1}{b^2} - \dfrac{1}{r^2} \right) \right\} & 1 \le r \le \rho \quad (7) \\ \dfrac{E\alpha(T_o - T_\rho)}{2(1-\nu)\log \rho} (\rho^2 - P_1) \left(\dfrac{1}{b^2} - \dfrac{1}{r^2} \right) & \rho \le r \le b \quad (8) \end{cases}$$

$$\sigma_\theta(r) = \begin{cases} \dfrac{E\alpha(T_o - T_\rho)}{2(1-\nu)\log \rho} \left\{ 2\log \dfrac{r}{\rho} + 1 + \dfrac{\rho^2}{b^2} - P_1 \left(\dfrac{1}{b^2} + \dfrac{1}{r^2} \right) \right\} & 1 \le r \le \rho \quad (9) \\ \dfrac{E\alpha(T_o - T_\rho)}{2(1-\nu)\log \rho} (\rho^2 - P_1) \left(\dfrac{1}{b^2} + \dfrac{1}{r^2} \right) & \rho \le r \le b \quad (10) \end{cases}$$

The thermal stresses and the autofrettage residual stresses become equivalent if the temperature gradient of the thermal load and the uniaxial yield stress of the cylinder material has the following relation

$$\frac{E\alpha(T_o - T_\rho)}{2(1-\nu)\log \rho} = \frac{2\sigma_o}{\sqrt{3}} \tag{11}$$

where T_o or T_ρ may be assigned arbitrarily.

In many instances there is a redistribution of residual stresses due to changes of geometrical configurations such as the presence of keyways, holes, riflings, and cracks. The stress redistribution may be difficult to find. In case of cracks, it may be difficult to obtain stress-intensity factors. For simple problems, the method of superposition may be used to compute the stress redistribution as well as the stress-intensity factors involving cracks. Several examples are given in Ref *13*. An alternative, thermal simulation method is proposed in Ref *2* replacing the residual stress by an active thermal load. The method of thermal simulation shows in Ref *13* that the thermal stress redistribution is equivalent to the residual stress redistribution. For more complicated problems, the thermal simulation method has the advantage over the method of superposition by eliminating the computation of residual stresses acting on the surface of the crack which would be present in

the uncracked body under external loads. In this paper the thermal simulation is used to compute stress-intensity factors for multiple, radial cracks in a fully autofrettaged tube.

Finite Element Method

The finite-element technique has become an important numerical method for practical problems in structural mechanics because of its ability to treat very general geometrical configurations and loading conditions. The trend is to use high order elements requiring a small number of elements for high degree of accuracy. The plane problem of a uniform array of equal depth radial cracks emanating from the bore of a pressurized, nonautofrettaged tube has been solved using 12-node quadrilateral, isoparametric elements [*1*]. The collapsed singular elements developed by the authors [*14*] are used around the crack tip. The finite element results of stress-intensity factors agree well with results in Refs *15* and *10* using the modified mapping collocation method. Tracy, in a private communication, pointed out a discrepancy of five percent for the case of four cracks with crack depth $c/t = 0.5$ in a tube having outer diameter twice that of inner diameter.

In the previous work [*1*], the finite element meshes are generated automatically by a computer program for various values of N and c/t. There is a possibility of excessive distortion of elements for some values of N and c/t. According to Sickles and Gifford [*16*], isoparametric elements suffer a loss of accuracy when distorted from a rectangular shape. They recommended a "45-degree rule" as a guide to construct the element mesh. Because of these reasons and our interest in very shallow radial cracks, we have used the enriched quadrilateral elements [*17*] as crack tip elements in this study. A typical finite element idealization is shown in Fig. 1*a*. For shallow cracks, the section containing the crack tip changes slightly as shown in Fig. 1*b*. When thermal simulation is used with the finite-element method, the circle $r = \rho$ must be a side of quadrilateral elements in the finite element idealization since thermal loads are different in the two regions of $r < \rho$ and $r > \rho$. The actual finite element idealization for a particular geometry and thermal loads may be modified slightly from those shown in Fig. 1.

The finite element computer program APES, an acronym for Axisymmetric/Planar Elastic Structures, is used for all finite element computations in this paper. This powerful computer program has been improved continuously with new features including the addition of thermal loading for fracture analysis [*18*]. The APES results for stress-intensity factors for inside diameter radial cracks for a cylinder of $b = 2$ are given in Table 1 for three types of loading, namely (1) uniform tension p_o on outside diameter, (2) uniform pressure p_i on inside diameter (no crack face pressure), and (3) thermal loading equivalent to a 100 percent overstrain residual stress [*2*]. The new results for uniform tension on outside diameter serve as a check to the previously re-

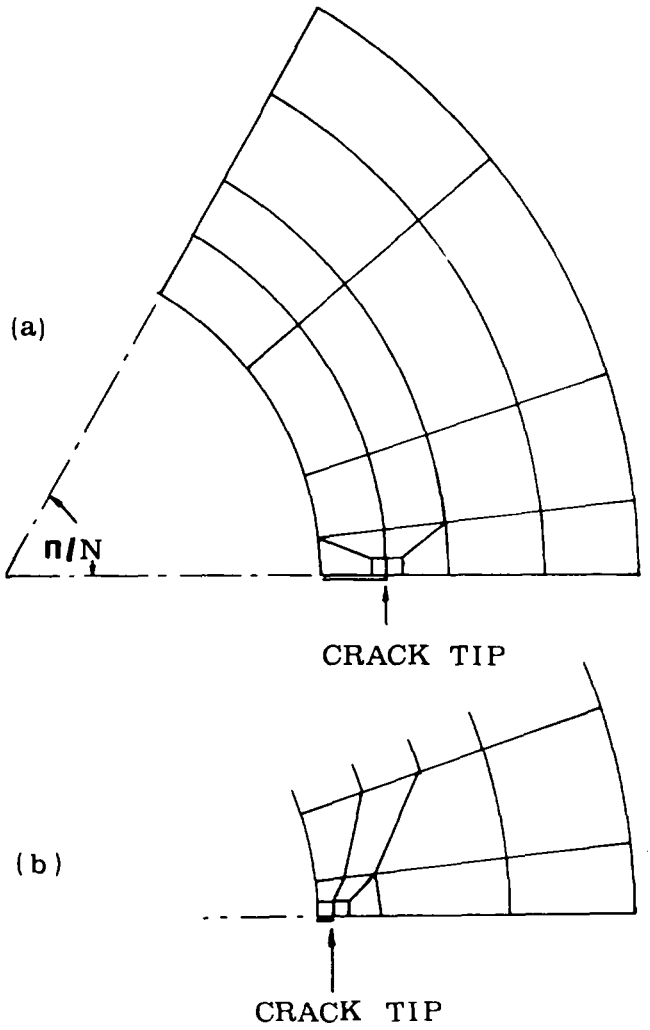

FIG. 1—(a) *A typical finite element idealization.* (b) *Idealization for very shallow cracks.*

ported results using collapsed singular crack tip elements [*1*]. The new results agree within three percent of those reported in Refs *15* and *10*. For instance, the result for $b = 2$, $N = 4$, $c/t = 0.5$, which was $K(p_o)/p_o\sqrt{\pi c} = 2.990$ in Ref *1*, is now $K(p_o)/p_o\sqrt{\pi c} = 3.149$ which agrees with Tracy's $H_1 = 1.18$ [*10*] within 0.1 percent.

An explanation is in order regarding negative stress-intensity factors shown in Table 1. A crack remains closed in a compressive residual stress region. The stress-intensity factor (SIF) is zero. The crack will open when a sufficiently large internal pressure is applied. The negative value of SIF is con-

TABLE 1—*Dimensionless SIF,* $K(p_o)/p_o\sqrt{\pi c}$, $K(p_i)/p_i\sqrt{\pi c}$, *and* $K_c(\epsilon = 1)/\sigma_o\sqrt{\pi c}$ *obtained from APES for a cylinder* b = 2 *for various* N *and* c/t.

Loading	$c/t = 0.05$	$c/t = 0.1$	$c/t = 0.2$	$c/t = 0.3$
		$N = 1$		
p_o	2.874	2.825	2.828	2.890
p_i	1.703	1.711	1.667	1.646
100% overstrain	−0.967	−0.896	−0.758	−0.650
		$N = 2$		
p_o	2.891	2.874	3.014	3.279
p_i	1.762	1.745	1.766	1.872
100% overstrain	−0.980	−0.919	−0.813	−0.745
		$N = 3$		
p_o	2.878	2.860	2.882	3.034
p_i	1.762	1.731	1.689	1.728
100% overstrain	−0.980	−0.907	−0.776	−0.683
		$N = 4$		
p_o	2.866	2.826	2.782	2.833
p_i	1.764	1.710	1.629	1.611
100% overstrain	−0.981	−0.895	−0.745	−0.628
		$N = 6$		
p_o	2.843	2.753	2.578	2.504
p_i	1.753	1.665	1.507	1.418
100% overstrain	−0.975	−0.871	−0.684	−0.539
		$N = 10$		
p_o	2.792	2.590	2.217	2.056
p_i	1.721	1.566	1.291	1.155
100% overstrain	−0.957	−0.817	−0.575	−0.417
		$N = 20$		
p_o	2.548	2.062	1.635	1.538
p_i	1.570	1.243	0.944	0.854
100% overstrain	−0.871	−0.641	−0.401	−0.284
		$N = 30$		
p_o	2.224	1.687	1.363	1.282
p_i	1.367	1.014	0.782	0.709
100% overstrain	−0.756	−0.515	−0.322	−0.228
		$N = 40$		
p_o	1.959	1.465	1.169	1.124
p_i	1.195	0.879	0.670	0.621
100% overstrain	−0.659	−0.442	−0.277	−0.197

venient in measuring the crack resistance against the opening by internal pressure, and it should be understood as such.

The combination of the finite-element method and thermal simulation can be used to compute SIF for any degree of partial autofrettage. However, it is expensive and time consuming to use finite element for parametric studies. Therefore, we seek alternative methods for the computation of SIF for radial cracks in a partially autofrettaged tube in the following two sections.

Method of Load Relief Factor

Baratta [*3*] extended the coefficient of load relief of Neuber [*19*] to estimate SIF arising from multiple cracking in a thick-wall cylinder. He defined the ratio

$$R = \frac{K_m}{K_n} \tag{12}$$

as the load relief factors, with K_m and K_n based on a solution due to Tweed and Rooke [*20*]. Assuming that this R value remains nearly constant from an infinitely thick cylinder to a cylinder with finite thickness, he can estimate $K_{m,f}$ since $K_{n,f}$ is known for $n = 1$ and $n = 2$ from Bowie and Freese [*15*]. His estimates, based on the crude assumption, have a discrepancy as high as 20 percent with our finite element results for the same geometry and loading. Parker and Farrow [*21*] obtained R values for various numbers of cracks using our results in Ref *1*. They assume that R values vary with geometrical configurations, but they are independent of loading. Therefore, they can obtain SIF for N inside diameter radial cracks for a 100 percent overstrained tube by applying the load relief factors to the solution of SIF for a 100 percent autofrettaged tube with two inside diameter radial cracks due to Grandt [*22*].

If the load relief factor works for a fully autofrettaged tube, then it should work for a partially overstrained tube also. Our study reveals that R values do vary with the nature of load. Strictly speaking, the concept of load relief factor does not work. However, R values vary within ± 5 percent, except for large values of N and c/t, for a thick-wall cylinder subjected to the following three types of loading: (1) uniform tension p_o on outside diameter, (2) uniform pressure p_i on inside diameter, and (3) residual stress due to 100 percent overstrain. Table 2 gives R values for various values of N and c/t under these three types of loading. From Table 2 it can be seen that R values remain nearly constant for any given N and c/t no matter if the loading is p_o on outside diameter or p_i on inside diameter. This property enables us to estimate fairly accurately the SIF for p_i from values for p_o and vice versa. The R values corresponding to the 100 percent overstrain residual stress agree within two percent with R values for p_o if $N \leq 4$ and $c/t \leq 0.3$. Therefore,

TABLE 2—*Load relief factor* $R = K_N/K_{N=2}$ *for a cylinder of* $b = 2$ *subjected to three types of loading.*

Loading	$c/t = 0.05$	$c/t = 0.1$	$c/t = 0.2$	$c/t = 0.3$
		$N = 1$		
p_o	0.994	0.983	0.938	0.881
p_i	0.967	0.980	0.943	0.897
100% overstrain	0.987	0.976	0.932	0.873
		$N = 3$		
p_o	0.996	0.995	0.956	0.925
p_i	1.000	0.992	0.956	0.923
100% overstrain	1.000	0.987	0.954	0.918
		$N = 4$		
p_o	0.992	0.983	0.923	0.864
p_i	1.002	0.980	0.922	0.860
100% overstrain	1.002	0.974	0.917	0.844
		$N = 6$		
p_o	0.984	0.958	0.855	0.764
p_i	0.995	0.954	0.853	0.757
100% overstrain	0.995	0.948	0.841	0.723
		$N = 10$		
p_o	0.966	0.901	0.735	0.627
p_i	0.977	0.897	0.731	0.617
100% overstrain	0.977	0.889	0.707	0.560
		$N = 20$		
p_o	0.882	0.718	0.543	0.469
p_i	0.891	0.713	0.534	0.456
100% overstrain	0.889	0.697	0.493	0.381
		$N = 30$		
p_o	0.769	0.587	0.452	0.391
p_i	0.776	0.581	0.443	0.379
100% overstrain	0.772	0.561	0.396	0.307
		$N = 40$		
p_o	0.678	0.510	0.388	0.343
p_i	0.678	0.504	0.379	0.331
100% overstrain	0.672	0.481	0.340	0.264

SIF may be estimated for $N \leq 4$, $c/t \leq 0.3$ for partially autofrettaged cases from R values for p_o and from known results of SIF for $N = 2$ for the same crack depth c/t and loading. The error may exceed ten percent if the load relief factor method is used to estimate SIF for cracked tubes with autofret-

tage residual stress from R values obtained for p_o on outside diameter for $N \geq 10$ and $c/t \geq 0.2$. For loading conditions other than the three types mentioned, the method of load relief factor should be applied with care.

Weight Function Method

Bueckner [*4*] and Rice [*5*] have shown that knowledge of the SIF and displacement field for a flaw geometry enable construction of a weight function which depends only on geometry. With the weight function one may obtain SIF for any other symmetric loading applied to the same geometry. Grandt has applied this technique to obtain SIF for a large plate containing radial hole cracks [*7*] and for radially cracked rings [*22*] loaded with arbitrary symmetric crack pressure. The SIF K for a specified crack face loading $p_c(x)$, based on the weight function approach, is given by

$$K = \frac{H}{K^*} \int_0^c p_c(x) \frac{\partial v}{\partial c}\, dx \tag{13}$$

where H is a constant, $H = E$ for plane stress and $H = E/(1 - \nu^2)$ for plane strain, K^* is the known SIF for a given loading applied to the flaw geometry of interest, x is the distance from the edge of the hole, and v is the crack opening profile corresponding to the known SIF K^*. In Eq 13 the only undefined term is the partial derivative $\partial v/\partial c$. The finite-element results of the y-component of displacement at nodal points along the crack face are not enough for the determination of the crack profile. Grandt used the assumption of conic sections due to Orange [*6*]. Andrasic and Parker [*23*] used the method of virtual crack extension [*24*] and B-spline curve fitting. In this paper the loading of the cracked tube is limited to a combination of internal pressure and autofrettage residual stresses; a set of algebraic equations is used in lieu of the determination of $\partial v/\partial c$.

The crack face loading $p_c(x)$ in Eq 13 for a cracked tube subjected to the autofrettage residual stress is given by the hoop stress, Eqs 3 and 4, for an uncracked, overstrained tube

$$\frac{p_c(x)}{\sigma_o} = \frac{\sigma_\theta(x)}{\sigma_o}$$

$$= \begin{cases} \dfrac{1}{\sqrt{3}}[(2 - P_1) - P_1(1 + x)^{-2} + 2\log(1 + x)] & 0 \leq x \leq \epsilon t \quad (14) \\ \dfrac{1}{\sqrt{3}}[(\rho^2 - P_1)b^{-2} + (\rho^2 - P_1)(1 + x)^{-2}] & \epsilon t \leq x \leq t \quad (15) \end{cases}$$

For $\epsilon = 1$, substituting from Eq 14 into Eq 13, the following is obtained

$$\frac{K_c(\epsilon = 1)}{\sigma_o\sqrt{\pi c}} = \frac{1}{\sqrt{3\pi c}}[\{2 - P_1(b)\}K_c(1) - P_1(b)K_c(r^{-2}) + 2K_c(\log r)] \quad (16)$$

where

$$K_c(1) = \frac{H}{K^*}\int_0^c \frac{\partial v}{\partial c}dx \quad (17)$$

$$K_c(r^{-2}) = \frac{H}{K^*}\int_0^c (1+x)^{-2}\frac{\partial v}{\partial c}dx \quad (18)$$

$$K_c(\log r) = \frac{H}{K^*}\int_0^c [\log(1+x)]\frac{\partial v}{\partial c}dx \quad (19)$$

These may be termed as functional intensity factors. From Lamé solution, the hoop stress in an uncracked cylinder subjected to uniform tension p_o on outside diameter is

$$\frac{\sigma_\theta}{p_o} = \frac{b^2}{b^2 - 1}\left(1 + \frac{1}{r^2}\right) \quad (20)$$

The same stress under internal pressure p_i is

$$\frac{\sigma_\theta}{p_i} = \frac{1}{b^2 - 1}\left(1 + \frac{b^2}{r^2}\right) \quad (21)$$

Substituting σ_θ for p_c in Eq 13, the SIF for a radially cracked cylinder subjected to p_o or p_i is given by one of the following

$$\frac{K(p_o)}{p_o\sqrt{\pi c}} = \frac{b^2}{b^2 - 1}\frac{K_c(1)}{\sqrt{\pi c}} + \frac{b^2}{b^2 - 1}\frac{K_c(r^{-2})}{\sqrt{\pi c}} \quad (22)$$

$$\frac{K(p_i)}{p_i\sqrt{\pi c}} = \frac{1}{b^2 - 1}\frac{K_c(1)}{\sqrt{\pi c}} + \frac{b^2}{b^2 - 1}\frac{K_c(r^{-2})}{\sqrt{\pi c}} \quad (23)$$

If the left-hand sides of Eqs 22 and 23 are determined numerically from the finite-element method, then $K_c(1)$ and $K_c(r^{-2})$ can be solved. Inserting these values into Eq 16, $K_c(\log r)$ can be solved if $K_c(\epsilon = 1)$ is known from the finite-element computation.

Once $K_c(1)$, $K_c(r^{-2})$, and $K_c(\log r)$ are known for a given geometry (b, N,

and c/t are fixed), the SIF for the flawed cylinder subjected to a residual stress corresponding to a given ϵ ($\neq 1$) can be computed from

$$\frac{K_c(\epsilon)}{\sigma_o\sqrt{\pi c}} = \frac{1}{\sqrt{3\pi c}}[\{2 - P_1(\rho)\}K_c(1) - P_1(\rho)K_c(r^{-2}) + 2K_c(\log r)] \quad (24)$$

provided $c \leq \epsilon t$.

In case $c > \epsilon t$, the crack face pressure is a combination of Eqs 14 and 15; therefore, Eq 24 is not valid. If $c/t = \epsilon + \delta$ and $0 < \delta \ll 1$, we may use Eq 24 to compute an approximate SIF and then use the following equation to compute a corrective SIF, K_δ

$$\frac{K_\delta}{\sigma_o\sqrt{\pi c}} = \frac{1}{\sqrt{3\pi c}} \frac{H}{K^*} \int_{\epsilon t}^{(\epsilon+\delta)t} p_c(x) \frac{\partial v}{\partial c} dx \quad (25)$$

where

$$p_c(x) = (-1 + 2\log\rho) + \rho^2(1 + x)^{-2} - 2\log(1 + x) \quad (26)$$

The final result of SIF for a small $\delta > 0$ is the sum of $K_c(\epsilon)$, Eq 24, and K_δ, Eq 25.

An approximate method for K_δ is based on the Westergaard near field solution [*25*]. The crack opening displacement $v(\xi)$ near a crack tip due to an arbitrary load is given in terms of SIF K^* at the crack tip by

$$v(\xi) = \frac{2K^*}{H}\left(\frac{2\xi}{\pi}\right)^{1/2} \quad (27)$$

The derivative with respect to the crack length is

$$\frac{\partial v}{\partial c} = \frac{K^*}{H}\left(\frac{2}{\pi}\right)^{1/2}(\xi^{-1/2} + \xi^{1/2}/c) \quad (28)$$

The length variable ξ is defined by

$$\xi = -(x - c) \quad (29)$$

Substituting from Eqs 26 and 28 into 25 and using Eq 29, we have

$$\frac{K_\delta}{\sigma_o\sqrt{\pi c}} = \frac{1}{\sqrt{3\pi c}}\sqrt{2/\pi}\{(-1 + 2\log\rho)(I_1 + I_1') + \rho^2(I_2 + I_2') - 2(I_3 + I_3')\} \quad (30)$$

where

$$I_1 = 2\sqrt{\delta t}, \qquad I_1' = \frac{2}{3c}(\delta t)^{3/2} \tag{31}$$

$$\left.\begin{aligned} I_2 &= \frac{1}{1+c}\left[\frac{\sqrt{\delta t}}{\rho} - \frac{(1+c)^{-1/2}}{2}\log D(\rho)\right] \\ I_2' &= \frac{1}{c}\left[\frac{\sqrt{\delta t}}{\rho} + \frac{(1+c)^{-1/2}}{2}\log D(\rho)\right] \end{aligned}\right\} \tag{32}$$

$$\left.\begin{aligned} I_3 &= -2\left[(2-\log\rho)\sqrt{\delta t} + (1+c)^{1/2}\log\frac{\sqrt{1+c}-\sqrt{\delta t}}{\sqrt{1+c}+\sqrt{\delta c}}\right] \\ I_3' &= \frac{2}{3c}\left[\sqrt{\delta t}(\delta t\{\log\rho - 2(1+c) - 2\delta t/3\}) - (1+c)^{3/2}\log D(\rho)\right] \end{aligned}\right\} \tag{33}$$

with

$$D(\rho) = [2(1+c) - \rho - 2\sqrt{\delta t(1+c)}]/\rho \tag{34}$$

It should be noted that Eq 30 is independent of N. It works for small N and δ. If N is small, it may work for a relatively larger δ. But when N is large, the crack interaction is strong, and δ must be small.

Numerical Results

Using Eqs 16, 22, and 23 and finite element results in Table 1, we obtain values of $K_c(p)/p\sqrt{\pi c}$, $K_c(pr^{-2})/p\sqrt{\pi c}$, and $K_c(p \log r)/p\sqrt{\pi c}$. Figures 2 through 4 are plots of these values as a function of c/t for various values of N. The use of these graphs and Eq 24 gives $K_c(\epsilon)/\sigma_o\sqrt{\pi c}$ for any value of ϵ, $\epsilon t \geq c$, for a given geometry. A graph of $K_c(\epsilon)/\sigma_o\sqrt{\pi c}$ versus ϵ is shown in Fig. 5 for various c/t and for $N = 2$ and $N = 40$. Figure 6 is another way of presenting $K_c(\epsilon)/\sigma_o\sqrt{\pi c}$ in which ϵ is fixed but N varies.

The numerical results given previously are enough for an estimate of SIF for any assigned values of N, c/t, and ϵ. For example, if the SIF is desired for $N = 8$, $c/t = 0.15$, and $\epsilon = 0.75$, readings are taken from Figs. 2 through 4 as follows: $K_c(p)/p\sqrt{\pi c} = 1.03$, $K_c(pr^{-2})/p\sqrt{\pi c} = 0.86$, and $K_c(p \log r)/p\sqrt{\pi c} = 0.091$. For $\epsilon = 0.75$ we have from Eqs 5 and 24 $K_c(\epsilon = 0.75)/\sigma_o\sqrt{\pi c} = -0.67$. In another example, if the SIF for $N = 2$, $c/t = 0.30$, and $\epsilon = 0.25$ is desired, we first compute $K_c(\epsilon = 0.25)/\sigma_o\sqrt{\pi c}$ from Eq 24 with $K_c(1)/\sqrt{\pi c} = 1.41$ from Fig. 2, $K_c(r^{-2})/\sqrt{\pi c} = 1.05$ from Fig. 3, and $K_c(\log$

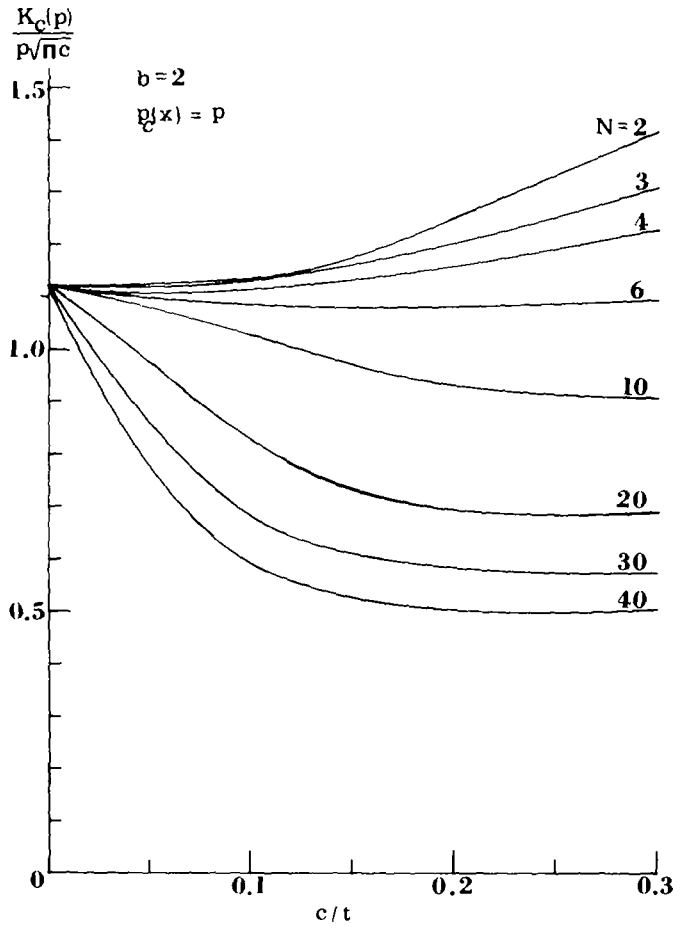

FIG. 2—*Stress-intensity factors as a function of* c/t *for* N *radial cracks subjected to the crack face pressure* $p_c(x) = p$.

$r)/\sqrt{\pi c} = 0.22$ from Fig. 4. The result from Eq 24 is $K_c(\epsilon = 0.25)/\sigma_o\sqrt{\pi c} = -0.12$. In this case since $c/t > \epsilon$, we have to compute $K_\delta/\sigma_o\sqrt{\pi c}$ from Eqs 30 through 34 with $\delta t = 0.05$. The corrective SIF is $K_\delta/\sigma_o\sqrt{\pi c} = -0.023$ and the desired SIF is $K_c(\epsilon = 0.25)/\sigma_o\sqrt{\pi c} = -0.143$. A finite element computation is performed for the case; the result is also -0.143. If in the previous example $\epsilon = 0.20$ is desired, that is, $\delta t = 0.1$, Eq 24 gives $K_c/\sigma_o\sqrt{\pi c} = -0.0209$ and Eq 30 gives $K_\delta/\sigma_o\sqrt{\pi c} = -0.0668$. The final result is $K_c(\epsilon = 0.2)/\sigma_o\sqrt{\pi c} = -0.088$ which is 5.6 percent less than the finite element result $K_c(\epsilon = 0.2)/\sigma_o\sqrt{\pi c} = -0.093$. This indicates that δ must be fairly small for Eq 30 to be valid. For the geometry $N = 10$, $c/t = 0.3$, the finite element computation gives $K_c(\epsilon = 0.3)/\sigma_o\sqrt{\pi c} = -0.079$ and $K_c(\epsilon = 0.25)/\sigma_o\sqrt{\pi c} =$

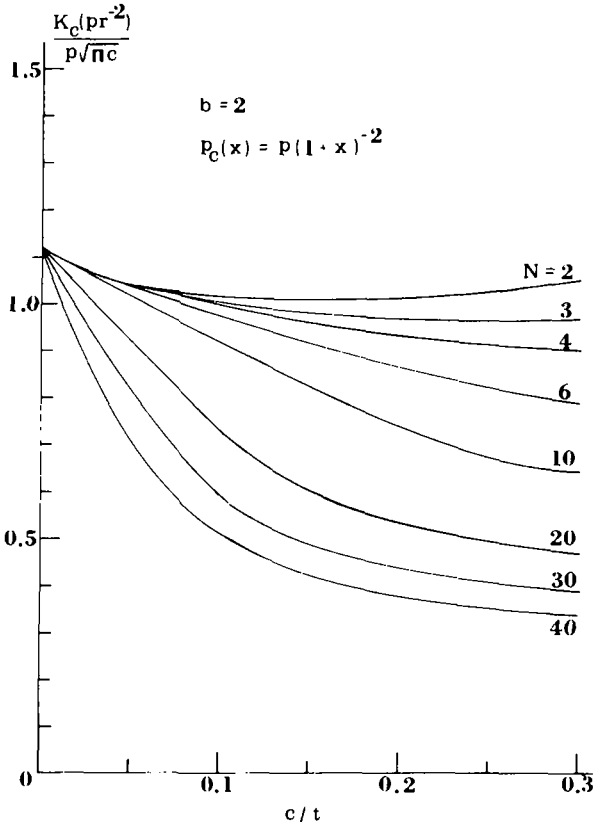

FIG. 3—*Stress-intensity factors as a function of* c/t *for* N *radial cracks subjected to the crack face pressure* $p_c(x) = p(1 + x)^{-2}$.

−0.044. The corresponding values computed from Eq 24 and from Eqs 24 and 30 are −0.080 and −0.0477.

The SIF's due to a combination of residual stress and internal pressure on inside diameter and on crack faces can be computed readily by linear superposition. If the applied pressure is $p_i = \sigma_o/f$, where f is a constant, the resultant SIF's for $f = 1.5$ and 3, for $N = 1$ and 40, and for $\epsilon = 1.0$ are shown in Fig. 7. We purposely keep the negative SIF for shallow cracks in the case of $f = 3$ and $\epsilon = 1.0$. The correct SIF should be zero, which means that a single crack or a set of multiple cracks remains closed due to the high compressive residual stress near the bore. The negative SIF gives a little more information than SIF = 0. The graph also shows a high SIF for $N = 1$ than that for $N = 40$ for a given ϵ and f. One may conclude that it is worse to have a single radial crack than to have a large number of radial cracks for an autofrettaged tube. This conclusion is similar to that found in the study of nonautofrettaged

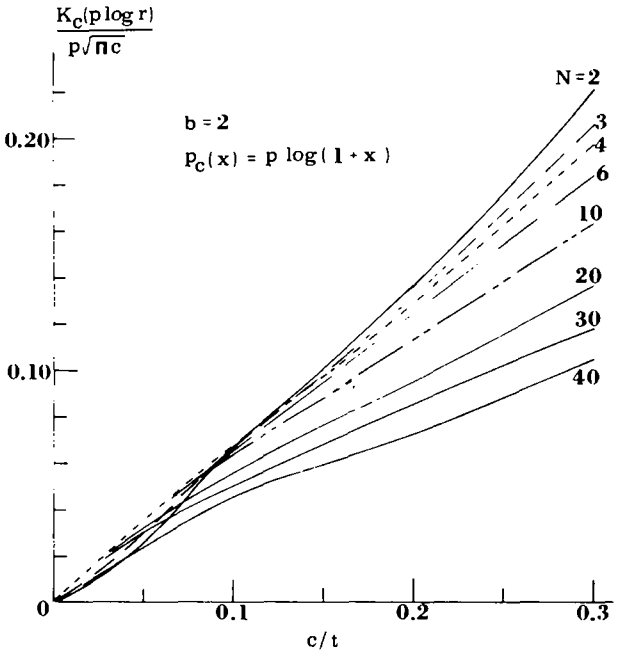

FIG. 4—*Stress-intensity factors as a function of* c/t *for* N *radial cracks subjected to the crack face pressure* $p_c(x) = p \log (1 + x)$.

tubes. With some slight modification, the method used here can be applied to multiple outside diameter cracks. The modifications and numerical results for outside diameter cracks are to be reported elsewhere.

Conclusions

The finite-element method together with the thermal simulation can be used to compute the SIF for multiple radial cracks emanating from the bore of a partially autofrettaged tube. The finite element results of $K(p_o)$, $K(p_i)$, and $K_c(\epsilon = 1.0)$ can lead to a system of algebraic equations for solving $K_c(1)$, $K_c(r^{-2})$, and $K_c(\log r)$. Using these results, the weight function concept gives an alternative method for the determination of SIF for any degree of partial autofrettage provided that the crack depth c/t is not greater than the percentage of autofrettage ϵ. A correction formula is supplied for the SIF when c/t is slightly greater than ϵ when N is small. These expressions yield quite accurate results and can save a great deal of computing time.

The SIF results of this study show that a cylinder with dual cracks is, in general, the weakest configuration against fracture. For more than two cracks, the SIF decreases as the number of cracks increases. This conclusion

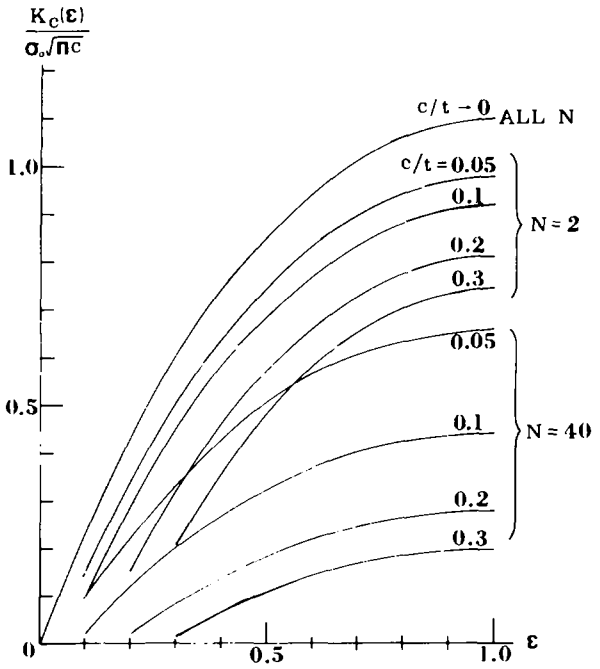

FIG. 5—*Stress-intensity factors as a function of* ϵ *in an autofrettaged cylinder of* b = 2.

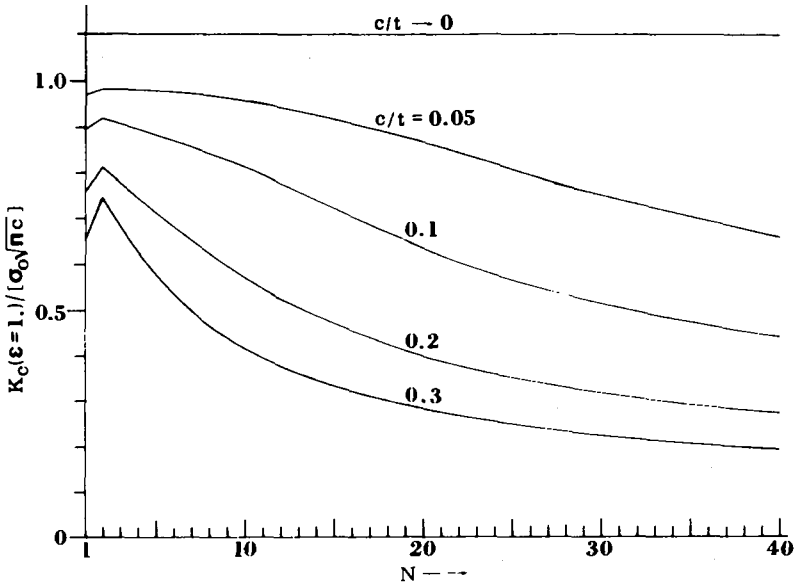

FIG. 6—*Stress-intensity factors as a function of* N *in a fully autofrettaged cylinder of* b = 2.

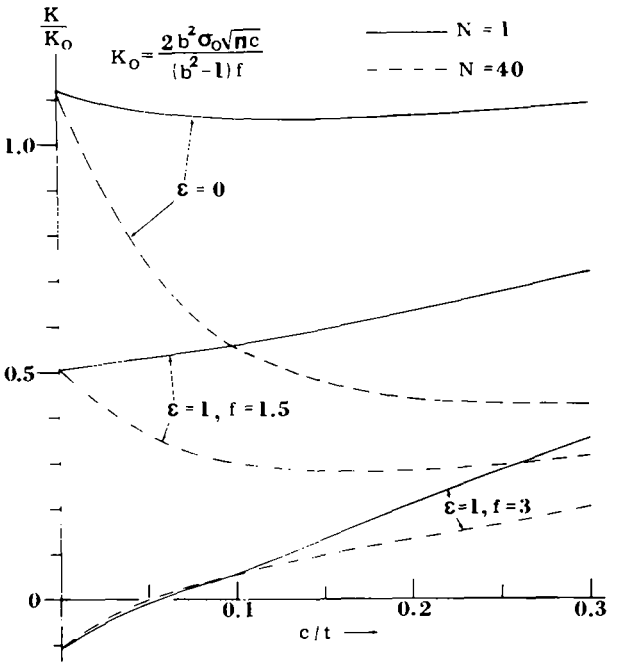

FIG. 7—*Stress-intensity factors in an autofrettaged cylinder of* b = 2 *subjected to internal pressure* σ_0/f *on inside diameter and on crack faces.*

for an autofrettage cylinder of an elastic-ideally plastic material remains the same as that concluded for a nonautofrettaged cylinder [*1*].

Experimental studies of SIF for multiply cracked cylinders reported in Refs *26* and *27* confirmed the previously mentioned conclusion. A compliance K calibration for a pressurized cylinder with a radial crack suggested by Underwood et al [*28*] may be extended to multiply cracked cylinders with or without autofrettage to provide further experimental verification.

An important use of the SIF study of a cracked cylinder is to estimate the remaining useful life of the cylinder. Based on the well-known crack propagation laws of Paris-Erdogen [*29*], it is obvious that the fatigue life of an autofrettaged cylinder is prolonged because of the reduction in both the maximum SIF and the range of stress intensity due to the compressive residual stress introduced by the autofrettage process. An experimental study of pressure cycling 0 to 331 MPa (0 to 48 ksi) a cylinder (b/a = 2, a = 8.75 cm) with multiple notches [0.008 cm (0.003 in.) cut, 0.64 cm (0.25 in.) deep, and 50.8 cm (20 in.) long], was conducted by Joseph Throop of our laboratory to measure the remaining fatigue lives. For the case of a single notch, cycles to failure were 1550, 3834, and 8490 for cylinders with 0, 30, and 60 percent overstrain, respectively. This confirms our prediction that the fatigue life is

prolonged considerably by the process of autofrettage. In multiple cracking experiments, it was virtually impossible to achieve uniform crack propagation. The final failure inevitably was dominated by one crack no matter if it was started from two or four notches. Therefore, no meaningful conclusion could be drawn from measured cycles to failure except a set of data for non-autofrettaged cylinders. The measured cycles to failure for initially one-, two-, and four-notch cases were 1550, 1143, and 1463, respectively. It agrees with the SIF prediction of Ref *1* that dual crack case is the weakest configuration and the SIF for a single crack case is close to that of three-crack, or four-crack case.

References

[*1*] Pu, S. L. and Hussain, M. A. in *Fracture Mechanics (11th Conference), ASTM STP 677*, American Society for Testing and Materials, 1979, pp. 685-699.

[*2*] Hussain, M. A., Pu, S. L., Vasilakis, J. D., and O'Hara, P., *Journal of Pressure Vessel Technology*, Vol. 102, No. 3, 1980, pp. 314-318.

[*3*] Baratta, F. I., *Engineering Fracture Mechanics*, Vol. 10, 1978, pp. 691-697.

[*4*] Bueckner, H. F., *Zeitschrift Angewandte für Mathematik und Mechanik*, Vol. 50, 1970, pp. 529-546.

[*5*] Rice, J. R., *International Journal of Solids and Structures*, Vol. 8, 1972, pp. 751-758.

[*6*] Orange, T. W. in *Stress Analysis and Growth of Cracks, ASTM STP 513*, American Society for Testing and Materials, 1972, pp. 71-78.

[*7*] Grandt, A. F., *International Journal of Fracture*, Vol. 11, 1975, pp. 283-294.

[*8*] Grandt, A. F., *International Journal of Fracture*, Vol. 14, 1978, pp. R221-R229.

[*9*] Paris, P. C. and Sih, G. C. in *Fracture Toughness Testing and Its Applications, ASTM STP 381*, American Society for Testing and Materials, 1965, pp. 39-81.

[*10*] Tracy, P. G., *Engineering Fracture Mechanics*, Vol. 11, 1979, pp. 291-300.

[*11*] Parker, A. P. and Andrasic, C. P., "Stress Intensity Prediction For a Multiply-Cracked, Pressurized Gun Tube With Residual and Thermal Stresses," presented at Solid Mechanics Symposium, Cape Cod, Mass., 1980.

[*12*] Hill, R., *The Mathematical Theory of Plasticity*, Oxford at the Clarendon Press, 1950.

[*13*] Pu, S. L. and Hussain, M. A., "Residual Stress Redistribution Caused by Notches and Cracks in a Partially Autofrettaged Tube," submitted to *Journal of Pressure Vessel Technology.*

[*14*] Pu, S. L. and Hussain, M. A., *International Journal of Numerical Methods in Engineering*, Vol. 12, 1978, pp. 1727-1742.

[*15*] Bowie, O. L. and Freese, C. E., *Journal of Engineering Mechanics*, Vol. 4, 1972, pp. 315-321.

[*16*] Sickles, J. B. and Gifford, L. N., "A Further Study of Accuracy Loss in Distorted Isoparametric Finite Elements," DTNSRDC Report M-50, 1979.

[*17*] Gifford, L. N., Jr., "APES—Second Generation Two-Dimensional Fracture Mechanics and Stress Analysis by Finite Elements," DTNSRDC Report 4799, 1975.

[*18*] Gifford, L. N., Jr., "APES—Finite Element Fracture Mechanics Analysis: Revised Documentation," DTNSRDC Report 79/023, 1979.

[*19*] Neuber, H., "Theory of Notch Stresses," AEC TR 4547, 1958.

[*20*] Tweed, J. and Rooke, D. P., *Journal of Engineering Science*, Vol. 13, 1975, pp. 653-662.

[*21*] Parker, A. P. and Farrow, J. R., "Stress Intensity Factors For Multiple Radial Cracks Emanating From the Bore of an Autofrettaged or Thermally Stressed Thick Cylinder," Materials Branch Technical Note MAT/20, Royal Military College of Science, Swindon, Wiltshire, England, 1979.

[*22*] Grandt, A. F. "Two Dimensional Stress Intensity Factor Solutions For Radially Cracked Rings," Technical Report AFML-TR-75-121, Air Force Materials Laboratory, Wright-Patterson Air Force Base, Ohio, 1975.

[*23*] Andrasic, C. P. and Parker, A. P., "Weight Functions for Cracked Curved Beams," Sec-

ond International Conference on Numerical Methods in Fracture Mechanics, Swansea, U.K., 1980.
[24] Parks, D. M. and Kamenetzky, E. M. *International Journal for Numerical Methods in Engineering*, Vol. 14, 1979, pp. 1693-1706.
[25] Westergaard, H. M., *Journal of Applied Mechanics*, Transactions of the American Society of Mechanical Engineers, 1939.
[26] Goldthorpe, B. D., "The Application of Fatigue Mechanics to Gun Barrel Fatigue Life Prediction," Symposium on the Relevance of Fracture Toughness to the Design and Reliability of Military Equipment, The Welding Institute, Cambridge, England, June 1973.
[27] Crymble, T. G., Goldthorpe, B. D., and Austin, B. A. in *High Pressure Engineering*, H. LI. D. Pugh, Ed., Institution of Mechanical Engineers, London, 1975, pp. 341-348.
[28] Underwood, J. H., Lasselle, R. H., Scanlon, R. D., and Hussain, M. A., "A Compliance K Calibration for a Pressurized Thick-Wall Cylinder With a Radial Crack," Watervliet Arsenal Report WVT-7026, 1970.
[29] Paris, P. C. and Erdogan, F., *Journal of Basic Engineering*, Transactions of the American Society of Mechanical Engineers, Vol. 85, 1963, pp. 528-534.

DISCUSSION

A. P. Parker[1] *(written discussion)*—The authors have addressed a geometry and loading which also has been a concern of ours for some time. The numerical technique we have adopted to solve the multiply cracked, partially autofrettaged thick cylinder is modified mapping-collocation (MMC),[2] combined with a simple procedure involving superposition of the stress intensity due to pressure acting alone, and the stress intensity due to full autofrettage acting alone (that is, the 100 percent overstrain case).

Results for internal pressure and for full autofrettage were presented graphically by Parker and Andrasic.[2] Numerical values for these cases have been supplied to the authors. Results for partial autofrettage with internal pressure and both internal and external cracks were presented by Parker et al,[3]

[1]Materials Branch, Royal Military College of Science, Shrivenham, Swindon, Wiltshire, England.

[2]Parker, A. P. and Andrasic, C. P., "Stress Intensity Prediction for a Multiply Cracked, Pressurized Gun Tube with Residual and Thermal Stresses," Army Symposium on Solid Mechanics, AMMRC MS 80-5, Army Materials and Mechanics Research Center, Sept. 1980.

[3]Parker, A. P., Sleeper, K. A., and Andrasic, C. P., "Safe Life Design of Gun Tubes: Some Numerical Methods and Results," U.S. Army Numerical Methods Conference, Huntsville, Ala., Feb. 1981.

the necessary superposition being given by Eq 4 in Neal et al[4] (internal cracks) and Eq 12 in Parker[5] (external cracks).

Would the authors indicate the extent of agreement between their finite element calculations and our MMC predictions?

S. L. Pu and M. A. Hussain (authors' closure)—We appreciate the opportunity of discussion from the question raised by Professor Parker regarding the agreement between their SIF predictions based on MMC technique and our finite element calculations. It originally was planned to include in the paper a comparison of results by these two methods. Since the numerical results supplied by Professor Parker were not received on time, we had to change the plan to include the comparison in a follow-up paper.[6] Tables 3 and 4, shown here, are taken from Footnote 6. The agreement is quite well with a maximum relative error less than four percent. The finite element values are consistently higher than MMC values.

TABLE 3—*Comparison of* $K_1/p_i\sqrt{\pi c}$ *for inside diameter cracks in a cylinder of* b/a = 2, *subject to bore pressure* p_i. *Finite element (FE) (this study) versus modified mapping collocation (Tracy[7]).*

	1 Crack		2 Cracks		4 Cracks	
c	FE	MMC	FE	MMC	FE	MMC
0.1	2.83	2.80	2.87	2.83	2.83	2.75
0.2	2.83	2.77	3.01	2.96	2.78	2.75
0.3	2.89	2.88	3.28	3.23	2.83	2.77
0.4	3.02	2.99	3.56	3.55	2.95	2.99
0.5	3.19	3.15	4.00	4.00	3.15	3.15[a]

[a]This value is based on $H_1 = 1.18$ in a private communication prior to the publication of Footnote 7. The value $H_1 = 1.31$ in Footnote 7 is probably a typographic error.

[4]Neal, D. M., Parker, A. P., and Lenoe, E. M., "Gun Tube Fatigue Life Estimates: Influence of Residual Stress, Crack Growth Law, and Load Spectra," U.S. Army Numerical Methods Conference, Huntsville, Ala., Feb. 1981.

[5]Parker, A. P., "Stress Intensity and Fatigue Crack Growth in Multiply Cracked, Pressurized, Partially Autofrettaged Thick Cylinders," to be published in *Fatigue of Engineering Materials and Structures.*

[6]Pu, S. L., "Stress Intensity Factors for Radial Cracks at Outer Surface of a Partially Autofrettaged Cylinder Subjected to Internal Pressure," U.S. Army Armament Research and Development Command, Technical Report ARLCB-TR-82003, Benet Weapons Laboratory, Watervliet, N.Y., 1982.

[7]Tracy, P. G., *Engineering Fracture Mechanics*, Vol. 11, 1979, pp. 291-300.

TABLE 4—*Comparison of* $K_I/(-\sigma_o\sqrt{\pi c})$ *for inside diameter cracks in a fully autofrettaged cylinder of* b/a = 2. *Finite element (FE) (this study) versus modified mapping collocation*[a] *(Parker and Andrasic*[8]*).*

	4 Cracks		6 Cracks		10 Cracks		40 Cracks	
c	FE	MMC	FE	MMC	FE	MMC	FE	MMC
0.05	0.981	0.967	0.975	0.959	0.957	0.941	0.659	0.670
0.1	0.895	0.871	0.871	0.847	0.817	0.794	0.442	0.432
0.2	0.745	0.722	0.684	0.662	0.575	0.557	0.277	0.271
0.3	0.628	0.609	0.539	0.521	0.417	0.403	0.197	0.191

[a]MMC results were supplied by Parker in a private communication, then multiplied by $2/\sqrt{3}$ to convert from Tresca yield criterion to von Mises criterion.

[8]Parker, A. P. and Andrasic, C. P., "Stress Intensity Prediction For a Multiply Cracked, Pressurized Gun Tube With Residual and Thermal Stresses," Army Symposium on Solid Mechanics, AMMRC MS 80-5, Army Materials and Mechanics Research Center, 1980, and supplemental data supplied in private communications, 1981.

A. P. Parker,[1] *J. H. Underwood,*[2] *J. F. Throop,*[2] *and C. P. Andrasic*[3]

Stress Intensity and Fatigue Crack Growth in a Pressurized, Autofrettaged Thick Cylinder

REFERENCE: Parker, A. P., Underwood, J. H., Throop, J. F., and Andrasic, C. P., **"Stress Intensity and Fatigue Crack Growth in a Pressurized, Autofrettaged Thick Cylinder,"** *Fracture Mechanics: Fourteenth Symposium—Volume I: Theory and Analysis, ASTM STP 791*, J. C. Lewis and G. Sines, Eds., American Society for Testing and Materials, 1983, pp. I-216–I-237.

ABSTRACT: Stress-intensity factors are determined using the modified mapping collocation (MMC) method for a single, radial, straight-fronted crack in a thick cylindrical tube that has been subjected to full autofrettage treatment (100 percent overstrain). By superposition of these results and existing solutions, stress-intensity factors are determined for the same geometry with internal pressure and any amount of overstrain from 0 to 100 percent.

Correction factors for crack shape and nonideal material yielding are determined from various sources for the pressurized, autofrettaged tubes containing semielliptical cracks. These results are employed in the life prediction of pressurized thick tubes with straight-fronted and semicircular cracks, for various amounts of autofrettage. Experimentally determined lifetimes for tubes having 0 and 30 percent nominal overstrain are significantly greater than the predictions for both straight-fronted and semicircular cracks. This is related to multiple initiation and early growth of cracks from the notch.

Experimentally determined lifetimes for a tube with 60 percent nominal overstrain are somewhat less than predicted. This effect is partially explained by additional experimental work, which shows that the angle of opening of rings cut from autofrettaged tubes is somewhat less than the ideal predictions. The latter effect is attributed to the Bauschinger effect and the associated reduced yield strength in compression during the unloading of tubes during the autofrettage process.

KEY WORDS: crack growth, fatigue cracks, cylinders, fracture (materials), fracture mechanics, residual stress, stress-intensity factor

[1] Guest scientist, U.S. Army Materials and Mechanics Research Center, Watertown, Mass.; from The Royal Military College of Science, Shrivenham, SN6 8LA, England.

[2] Research engineer, U.S. Army Research and Development Command, Watervliet, N.Y. 12189.

[3] Research scientist, The Royal Military College of Science, Shrivenham, SN6 8LA, England.

Nomenclature

a	Crack depth
A	Autofrettage
c	Surface crack length
C	Coefficient in Paris' crack growth law
E	Modulus of elasticity
G	$E/2(1 + \nu)$
H_C	Correction factor defined in Eq 11
K	Stress-intensity factor
K_{I}	Opening mode stress-intensity factor
K_{II}	Sliding mode stress-intensity factor
$\bar{K}$	Nondimensionalizing stress-intensity factor
K_0	Nondimensionalizing stress-intensity factor
ΔK	Stress-intensity factor range
ℓn	Natural logarithm
m	Exponent in Paris' crack growth law
max	Maximum
min	Minimum
N	Number of loading cycles
P	Pressure
PB	Pure bending
PT	Pure tension
r	Radius
R_1	Tube inner radius
R_2	Tube outer radius
R_A	Tube autofrettage radius
R_D	Tube reversed yielding radius
t	Theoretical
Y	Yield stress
z	Complex variable, $x + iy$
α	Proportion of tension
β	Proportion of bending
γ	Tube opening angle (radians)
ζ	Parameter plane
θ	Angular coordinate
κ	$3 - 4\nu$ (plane strain), $(3 - \nu)/(1 + \nu)$ (plane stress)
λ	Yield stress in tension/yield stress in compression
ν	Poisson's ratio
ξ	Parameter plane
σ	Direct stress
τ	Shear stress
ϕ	Complex stress function
ψ	Complex stress function

Fatigue crack growth arising from the cyclic pressurization of thick-wall cylinders tends to produce radial fatigue cracks emanating from the bore. A knowledge of the crack tip stress-intensity factor, K, is necessary in order to predict the fatigue crack growth rate, critical length, and lifetime of such cracks. It is common practice to produce an advantageous stress distribution by autofrettage (overstrain) of the cylinder in order to slow or prevent crack growth. This autofrettage process may involve plastic strain throughout the wall thickness, or any lesser proportion of the wall thickness, depending upon the degree of overstrain applied to the cylinder by overpressure or by an oversized mandrel-swage process.

An accurate stress-intensity solution for pressurized, autofrettaged thick cylinders is a fundamental requirement for crack growth rate and life prediction. Some of the work relating to two- and three-dimensional K solutions is reviewed by Tan and Fenner [*1*].[4] Of the various types of solutions, the errors associated with collocation and integral equation solutions are of order 1 percent while 4 percent would be more typical of finite-element and boundary-element methods. However, there may be more significant uncertainties in crack growth and life prediction. Some key factors, and the factors considered here, are the shape of the crack during the fatigue lifetime of the component, uncertainty over the exact proportion of overstrain in the tube, and a residual stress distribution that generally does not conform with the predictions of an idealized elastic-plastic analysis, particularly the assumption of the same magnitude of yield strength in tension and compression.

In this paper it is proposed that accurate two-dimensional K solutions may be modified in order to predict stress-intensity factors, and hence crack growth rates, for semielliptical cracks in pressurized thick-wall cylinders with residual stress distributions. Such predictions may be compared with experimental crack growth data, and some measure of the extent of overstrain may be obtained by cutting autofrettaged tubes radially and measuring the angle of opening.

Calculation of Stress-Intensity Factors

Stress-intensity factors for the plane (two-dimensional) geometry illustrated in Fig. 1*a* were obtained by the modified mapping collocation (MMC) method. This method is described in detail in Ref *2*. Briefly, complex variable methods due to Muskhelishvili [*3*] are utilized. Stresses and displacements within a body are given in terms of the complex stress functions $\phi(z)$ and $\psi(z)$ by

$$\sigma_x + \sigma_y = 4 \text{ Re } \{\phi'(z)\} \tag{1}$$

$$\sigma_y - \sigma_x + 2i\,\tau_{xy} = 2[\overline{z}\phi''(z) + \psi'(z)] \tag{2}$$

[4] The italic numbers in brackets refer to the list of references appended to this paper.

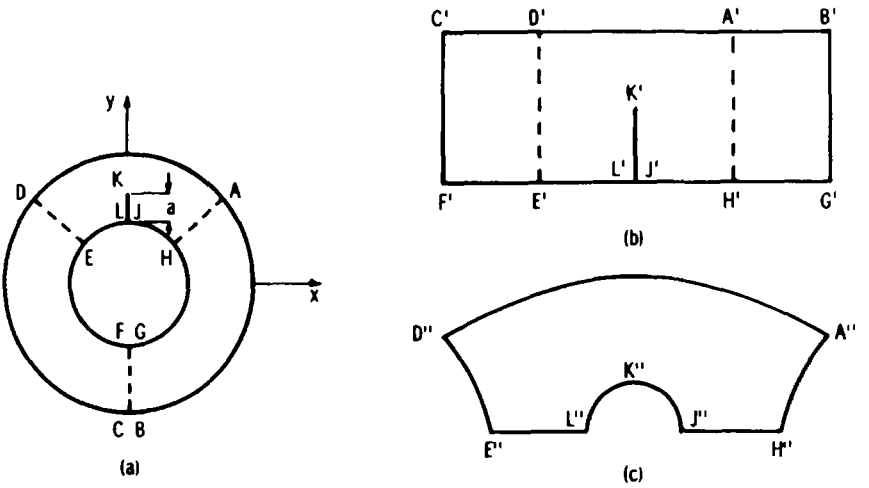

FIG. 1—*Cracked thick cylinder geometry showing partitioning and mapping schemes:* (a) *z (physical)-plane,* (b) ξ*-plane, and* (c) ζ*-plane.*

$$2G(u + iv) = \kappa\phi(z) - \overline{z\phi'(z)} - \overline{\psi(z)} \tag{3}$$

where the complex variable $z = x + iy$, x and y are the physical coordinates, primes denote differentiation, and bars represent the complex conjugate. Also

$$G = \frac{E}{2(1 + \nu)}$$

$$\kappa = 3 - 4\nu \text{ (plane strain)}, \qquad \kappa = \frac{3 - \nu}{1 + \nu} \text{ (plane stress)}$$

where G is the shear modulus, E the elastic modulus, and ν is Poisson's ratio, while the resultant force over an arc s is

$$f_1 + if_2 = i\int_s (X_n + iY_n)ds = \phi(z) + \overline{z\,\phi'(z)} + \overline{\psi(z)} \tag{4}$$

where $X_n\,ds$ and $Y_n\,ds$ are the horizontal and vertical components of force acting on ds.

The solution of the cracked, autofrettaged cylinder was carried out similarly to Tracy [4]. A complex mapping transforms straight lines parallel to the real axis in the ξ-plane to curved lines in the physical (z)-plane; in particular, the real axis in the ξ-plane is mapped to an arc of radius R_1, centered at the origin in the z-plane (Fig. 1). A further mapping is introduced, which maps the unit

semicircle plus its exterior in the ζ-plane to the crack plus its exterior in the ξ-plane, as in Fig. 1*b,c*. The analytic continuation arguments of Muskhelishvili are used to ensure traction-free conditions along $F'L'$ and $J'G'$ and hence FL and JG in the physical plane (Fig. 1).

For certain geometries it is necessary to use partitioning [*2*] to obtain the desired accuracy. The partitioning of the cylinder is shown in Fig. 1. In general, each region has its own complex stress and mapping function. Since there is symmetry about the imaginary axis, only Region I and that part of Region II to the right of the imaginary axis need be considered. When partitioning is used, it is necessary to "stitch" along common boundaries, by imposing equilibrium and compatibility of displacements.

In the MMC method the infinite series representations of the stress functions are truncated to a finite number of terms. Force conditions are imposed at selected boundary points, which give conditions on the unknown coefficients in the stress functions. Thus, each boundary point produces two rows in the main matrix A, and two corresponding elements in the boundary conditions vector $\mathbf{b}$, where

$$A\mathbf{x} = \mathbf{b}$$

and $\mathbf{x}$ is the vector of unknown coefficients. The common ("stitched") boundary points are used to obtain conditions relating the unknown coefficients. Each common boundary point gives four rows in A and four corresponding zeros in $\mathbf{b}$. In general, A is a matrix of ℓ rows and m columns, where ℓ and m depend upon the number of boundary points and unknown coefficients, respectively. It was found that convergence is generally better when $2m < \ell < 2.5$ m, and this conforms with other work [*5*]. A least-square error minimization procedure was used to solve the overdetermined set of linear equations. When the coefficients for the stress function in the cracked region are known, the crack-tip stress-intensity factor, K, may be determined from [*6*]

$$K = K_{\mathrm{I}} - iK_{\mathrm{II}} = 2(2\pi)^{1/2} \operatorname*{Limit}_{z \to z_c} (z - z_c)^{1/2} \times \phi'(z) \tag{5}$$

where K_{I} and K_{II} are opening and sliding mode stress-intensity factors, respectively, and z_c is the location of the crack tip.

We now consider the various loadings and combinations of loadings that will be necessary for the solution of the pressurized, autofrettaged tube.

Loading A: Internal Pressure Acting in Bore and Cracks

An accurate MMC opening mode stress-intensity solution, K_{I}, is available for this configuration [*7*] and is shown as the upper curve in Fig. 2. This MMC solution was obtained by superposition of an all-round tension field on the outer boundary. The results are presented in dimensionless form as $K_{\mathrm{I}}/\bar{K}_p$, where

$$\tilde{K}_p = \frac{2R_2^2}{(R_2^2 - R_1^2)} p(\pi a)^{1/2} \tag{6}$$

and where R_2 is the outer radius, R_1 is the inner radius, a is the crack depth, and p is the internal pressure acting in both bore and crack. Also shown, for the purposes of comparison, are points from a solution due to Grandt [8] based on an approximate weight function method that was also employed in the derivation of additional solutions referred to in the next section.

Loading B: Ideal Autofrettage Residual Stresses in Uncracked Tube

An MMC program, based on the formulation outlined in this section, was used to calculate the stress-intensity results for full autofrettage (100 percent overstrain), shown as the lower curve in Fig. 2. This was based on the ideal,

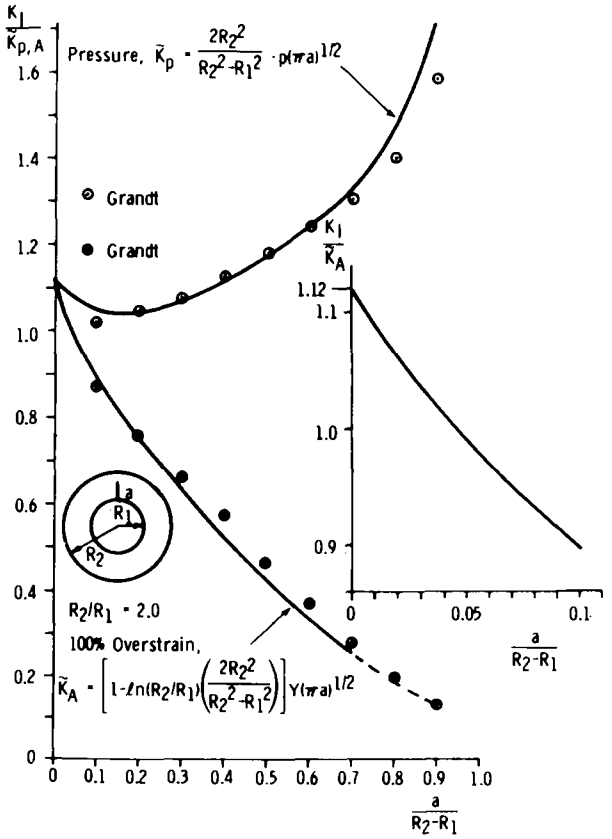

FIG. 2—*Stress-intensity factors for a single, straight-fronted, radial crack in a thick cylinder.* (Inset) *Short crack length convergence for 100 percent overstrain.*

elastic-plastic solution [*9*], where the distribution of hoop stress (σ_θ) in the uncracked tube is given by

$$\sigma_\theta = -Y \ln (R_2/R_1)\left[1+\frac{R_1^2}{R_2^2-R_1^2}\left(1+\frac{R_2^2}{r^2}\right)\right]+Y[1+\ln (r/R_1)] \qquad (7)$$

and Y is the uniaxial yield strength of the material (Tresca's criterion) or 1.15 $\times$ yield strength (von Mises' criterion). Points obtained from a solution by Grandt are shown for comparison purposes. The approximate results of Grandt [*10*] for a cracked tube of the same dimensions subjected to steady-state thermal loading were modified in accordance with Ref *11* to make possible a comparison with the calculated autofrettage results. The modification is based on the fact that the residual stress distribution for 100 percent overstrain is identical to that for steady state thermal loading, apart from a simple multiplying constant. Agreement is generally within 5 percent.

A particularly important feature of the MMC formulation outlined at the beginning of this section is the accuracy of the results at shallow crack depths. Many available results are not quoted for $a/(R_2 - R_1) < 0.1$, or even 0.2, and are therefore of limited use for life prediction purposes. The inset in Fig. 2 shows the calculated results for 100 percent overstrain in the range $0 < a/(R_2 - R_1) \leq 0.1$, and indicates good convergence to the limiting value of 1.12. Since as much as 80 percent of gun tube lifetime may be expended in this range, it is clearly very important to seek accurate results at shallow crack depths. It is apparent that this solution provides the required accuracy. The results for full autofrettage are presented in dimensionless form as $K_1/\tilde{K}_A$ where

$$\tilde{K}_A = \left[1 - \ln (R_2/R_1)\left(\frac{2R_2^2}{R_2^2-R_1^2}\right)\right] Y (\pi a)^{1/2} \qquad (8)$$

Loading C: Internal Pressure and Ideal Autofrettage

The total stress intensity in a pressurized, fully autofrettaged (100 percent overstrain) tube is given by the superposition of the results in Fig. 2, thus

$$K_{\text{full autofrettage + pressure}} = K_p + K_A \qquad (9)$$

where K_p is the stress intensity with pressure in bore and crack, and K_A is the stress-intensity contribution due to the 100 percent overstrain residual stress field acting alone.

In the event that the tube has been subjected to less than 100 percent overstrain, the plastic flow during the autofrettage process will extend to a radius R_A, and the stress-intensity factor in this case is given by [*12*]

$$K_{\text{partial autofrettage + pressure}} = \left[1 + \frac{Y}{p}\,\ell n(R_2/R_A) - \frac{Y}{p}\,(R_2^2 - R_A^2/2R_2^2\right] \cdot K_p + K_A, \qquad a \leq R_A - R_1 \tag{10}$$

where R_A can be obtained from the expression [*12*]

$$p = Y\ell n(R_A/R_1) + \frac{Y}{2R_2^2}\,(R_2^2 - R_A^2)$$

Results for 0, 30, 60, and 100 percent overstrain, with $Y/p = 3.55$, $R_2/R_1 = 2.0$, based on the superposition of results given in Fig. 2, are shown in Fig. 3. These curves indicate the very significant reduction in stress intensity as a result of the ideal autofrettage process. Indeed, for the particular value $Y/p = 3.55$, 100 percent overstrain causes a negative total stress intensity (that is, crack closure) for crack depths up to $a/(R_2 - R_1) = 0.08$.

Correction for the Crack Shape Effects

Thus far we have ignored the effect of crack shape on stress intensity, assuming a through crack. We now consider the crack to be semielliptical, semimajor axis c, depth a, as shown in Fig. 4. In order to modify the two-

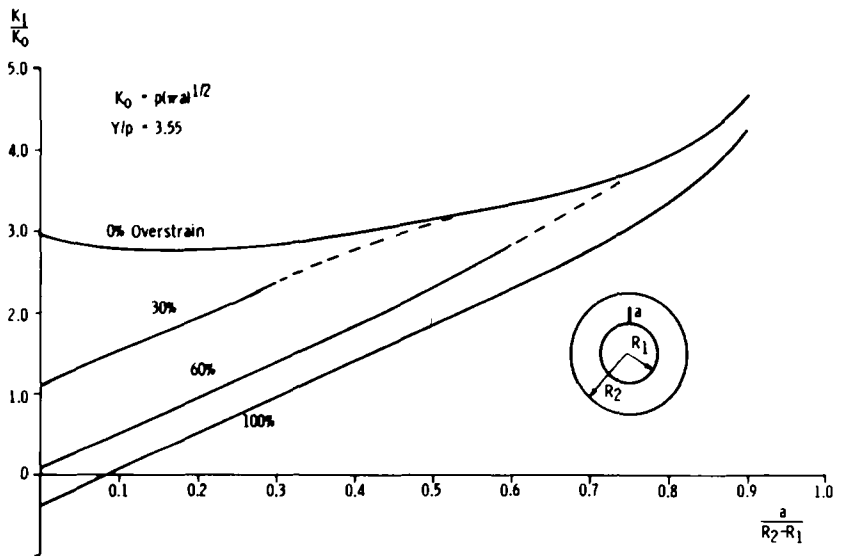

FIG. 3—*Stress-intensity factors for a single, straight-fronted crack in a pressurized thick cylinder with 0, 30, 60, and 100 percent overstrain.*

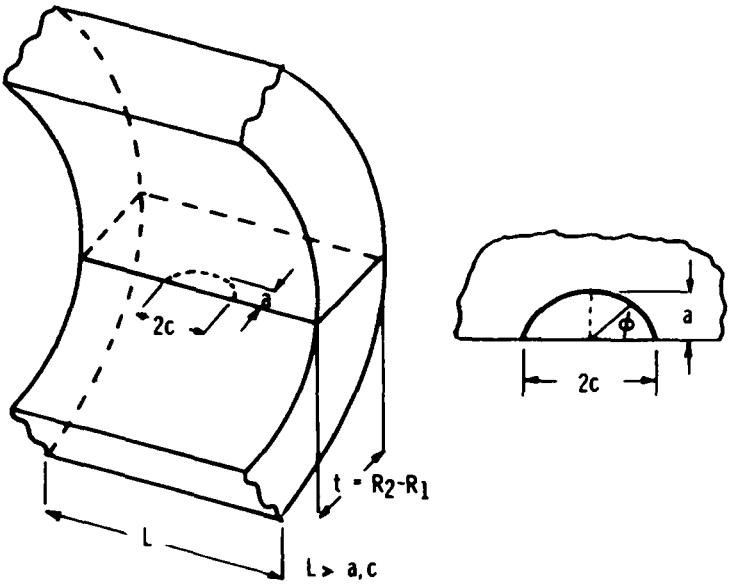

FIG. 4—*Semielliptical crack in a thick cylinder.*

dimensional results to account for crack shape we employ two sets of work, namely the extensive results for semielliptical cracks in a flat plate under tension or bending, due to Newman and Raju [*13*], and the limited results for a semielliptical crack in a pressurized thick cylinder, due to Tan and Fenner [*1*] and Atluri and Kathiresan [*14*].

First, consider the flat plate containing a semielliptical crack. From the results given in Ref *13*, we may define a correction factor for the plate in pure tension H_{PT} given by

$$H_{PT} = \frac{K_{PT}}{\tilde{K}_{PT}}$$

where K_{PT} is the stress-intensity factor for semielliptical crack in a plate in tension and $\tilde{K}_{PT}$ is the stress-intensity factor solution for a straight-fronted through crack given in Ref *15*. Curves of the correction factor H_{PT} are shown in Fig. 5*a*.

Similar correction factors for the flat plate under pure bending H_{PB} are defined by

$$H_{PB} = \frac{K_{PB}}{\tilde{K}_{PB}}$$

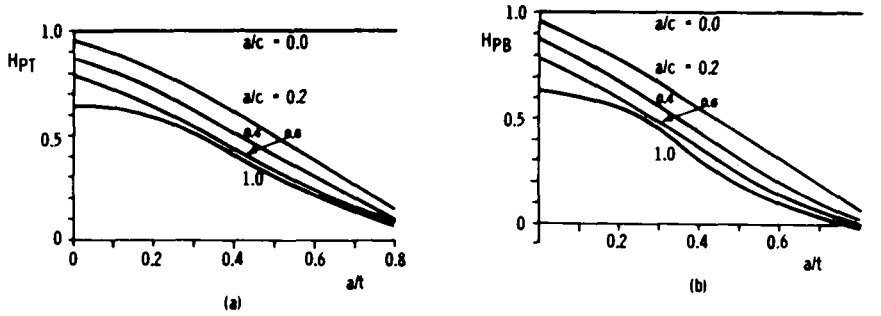

FIG. 5—(a) *Crack shape factors for a plate in tension ($\phi = \pi/2$), after Ref* 13. (b) *Crack shape factors for a plate in pure bending ($\phi = \pi/2$), after Ref* 13.

where K_{PB} is the stress-intensity factor for a semielliptical crack in a plate in pure bending and $\tilde{K}_{PB}$ is the solution for a straight-fronted through crack [*15*]. Curves of the correction factor H_{PB} are shown in Fig. 5*b*.

It is proposed that, at shallow crack depths, the correction factors applicable to the thick cylinder may be obtained by appropriate superpositions of H_{PT} and H_{PB}, given by

$$H_C = \alpha H_{PT} + \beta H_{PB} \tag{11}$$

where the multiplying factors α and β are obtained by calculating the proportions of tension and bending in the uncracked tube that act over the prospective crack line. In order to test this hypothesis, consider the case of a tube subjected to internal pressure. In this case the crack-line loading comprises hoop stresses due to the internal pressure [*12*] plus a contribution from the pressure, p, which infiltrates the crack, thus the total crack line loading is

$$\sigma_\theta = p\left[1 + \frac{R_1^2}{R_2^2 - R_1^2}\left(1 + \frac{R_2^2}{r^2}\right)\right]$$

as shown in Fig. 6*a*. Using a straight line approximation, for the range $0 < a/(R_2 - R_1) \leq 0.2$, the proportion of tension loading is given by $\alpha = 1.72/2.66$ while the proportion of pure bending, $\beta = 0.94/2.66$, hence the correction factor H_c is determined as

$$H_C = 0.645\, H_{PT} + 0.355\, H_{PB}$$

Correction factors determined on this basis are plotted in Fig. 6*b* for the case $a/c = 0.8$. Also shown are the equivalent correction factors obtained for the same configuration by Tan and Fenner [*1*], using boundary-element methods.

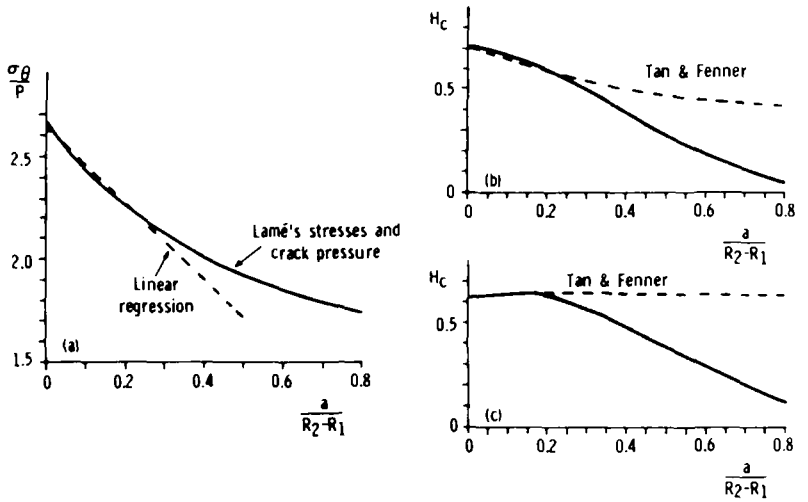

FIG. 6—(a) *Method of calculating proportion of tension and bending, pressure in bore and cracks.* (b) *Crack shape factors for pressure in bore and cracks,* a/c = *0.8,* $\phi = \pi/2$. (c) *Crack shape factors for pressure in bore and cracks,* a/c = *0.8,* $\phi = 0$.

Agreement is within 2 percent at $a/(R_2 - R_1) = 0.2$. For deeper cracks the difference between plate and cylinder results becomes appreciable because of the differences in constraint, discussed in the next paragraph. It is important to emphasize that the proportion of the tube in which the majority of component lifetime is expended is well represented by the model, that is, for $a/(R_2 - R_1) \leq 0.3$. The equivalent correction factors for K at the point $\phi = 0$ (the free surface of the plate) are shown in Fig. 6*c* and exhibit similar characteristics to those of Fig. 6*b*.

The significant difference between the cylinder and plate shape factors in Fig. 6*b* is attributed to the significantly greater constraint of a cylinder compared with a plate, particularly for straight-fronted, deep cracks. This difference can be demonstrated by comparing K for a straight-fronted, $a/(R_2 - R_1) = 0.8$ crack in a pressurized cylinder with $R_2/R_1 = 2.0$ with the K for a straight-fronted, $a/(R_2 - R_1) = 0.8$ crack in a plate with approximately the same combination of tension and bending loading as that of the pressurized cylinder. The K for the cylinder can be obtained from Ref *7* or from Fig. 2, and is shown in Table 1. The K for the plate with cylinder loading is obtained using the expressions for pure tension and pure bending [*15*] as follows

$$K_{\text{plate}} = K_{PT} + K_{PB}$$

The tension and bending stresses in K_{PT} and K_{PB} are determined as $\sigma_{PT} = 2.0\ p$ and $\sigma_{PB} = 0.5\ p$, by using a linear approximation of the entire cylinder loading plot shown in Fig. 6*a*. The K for the plate with a straight crack is

TABLE 1—*Comparison of* K *values for deeply cracked cylinder and plate.*

	K for $a/(R_2 - R_1) = 0.8$, Straight Crack	H_c from Fig. 6*b* for $a/(R_2 - R_1) = 0.8$, $a/c = 0.8$	K for $a/(R_2 - R_1) = 0.8$, $a/c = 0.8$, Semielliptical Crack
Pressurized cylinder	$6.99\,p(a)^{1/2}$	0.42	$2.9\,p(a)^{1/2}$
Plate with approximate cylinder loading	$46.7\,p(a)^{1/2}$	0.07	$3.3\,p(a)^{1/2}$

several times that of the cylinder, which indicates that the plate is much less constrained. Therefore, the increase in constraint corresponding to a semielliptical rather than a straight crack will be much larger for a plate than for a cylinder. This results in the much smaller H_c for a plate than for a cylinder, as observed in Fig. 6*b*. When the final comparison is made in Table 1, K for deep semielliptical cracks in a cylinder and a similarly loaded plate are about the same, as might be expected.

In order to obtain a range of correction factors applicable to thick cylinders, the procedure outlined by Eq 11, Fig. 6, and related discussion was used to obtain correction factors from Newman's work for the case of internal pressure and full autofrettage (100 percent overstrain). These results for relatively short cracks were combined, using engineering judgment, with those of Tan and Fenner for longer cracks to obtain correction factors for use over a wide range of crack length. The results for pressure, L_P, are shown in Fig. 7*a* and *b*, for $\phi = \pi/2$ and 0.0, respectively, and the results for autofrettage, L_A, are shown in Fig. 7*c* and *d* for $\phi = \pi/2$ and 0.0, respectively. In the case of pressure (Fig. 7*a* and *b*), we may compare in each figure with the solutions due to Atluri and Kathiresan [*14*] at two points, namely $a/c = 1.0$ and $a/t = 0.5$ and 0.8. For $\phi = \pi/2$ agreement is within 8 percent; however, for $\phi = 0$ the correction factors differ by 25 percent, reflecting wide disagreement between investigators on K solutions at the free surface [*13,14*].

It is thus possible to calculate the stress-intensity factor for any combination of pressure, ideal partial autofrettage, and crack shape by correcting the stress-intensity factors presented in Fig. 2 in accordance with Eq 10 and correction factors L_p and L_A to obtain

$$K_{\text{partial autofrettage + pressure (3D)}} = L_p \left[1 + \frac{Y}{p} \ell n(R_2/R_A) - \frac{Y}{p} (R_2^2 - R_A^2/2R_2^2 \right] \cdot K_p + L_A K_A \tag{12}$$

Effects of Nonideal Residual Stress Distribution

The residual stress distribution predicted by Eq 7 may not occur in practice [*16,17*]. Nonideal Bauschinger effects and uncertainty over the exact amount

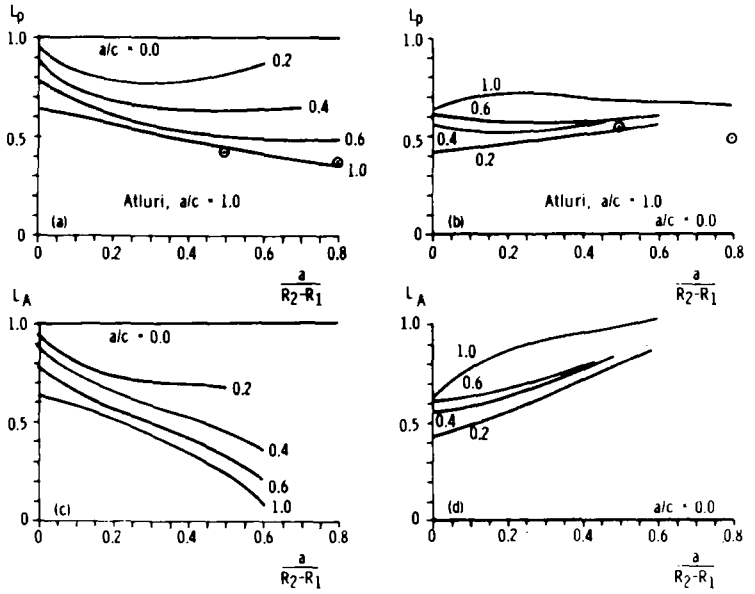

FIG. 7—(a) *Crack shape factors,* L_p, *for pressure in bore and cracks,* $\phi = \pi/2$; *two data points from Ref* 14, a/c = *1.0.* (b) *Crack shape factors,* L_p, *for pressure in bore and cracks,* $\phi = 0$; *two data points from Ref* 14, a/c = *1.0.* (c) *Crack shape factors,* L_a, *for 100 percent overstrain,* $\phi = \pi/2$. (d) *Crack shape factors,* L_a, *for 100 percent overstrain,* $\phi = 0$.

of autofrettage on unloading may produce a different stress distribution. In earlier work [*16*] a constant reduction factor of 0.7 was applied to the autofrettage contribution to stress-intensity factor to account for primarily the Bauschinger effect.

In the present work it is proposed that these effects may be considered in a different manner. If an unflawed autofrettaged tube is cut along a radius, it will spring apart, the theoretical angle of opening γ_t being given for 100 percent overstrain and using the von Mises' yield criterion as [*18*]

$$\gamma_t^{100 \text{ percent}} = \frac{8\pi Y}{\sqrt{3E}} \tag{13}$$

In the case of partial overstrain, the total moment acting over the cut ends is reduced by a factor F. Details of the calculation of F are contained in the Appendix. The theoretical angle of opening for partial overstrain $\gamma_t^{\text{percent}}$ is given by

$$\gamma_t^{\text{percent}} = F\gamma_t^{100 \text{ percent}} \tag{14}$$

A graphical representation of F for a tube having $R_2/R_1 = 2.0$ is shown in Fig. 8. The angle (and moment) ratio F between partial and 100 percent overstrain does not vary much with R_2/R_1. In fact, for tubes in the range $1.8 \leq R_2/R_1 \leq 2.2$ the deviation from the curve in Fig. 8 is only 1 percent, and of course it still goes asymptotically to the limit of 1.0 at 100 percent overstrain, and to zero at 0 percent overstrain.

We propose that a comparison of the ratio of measured opening angle to $\gamma_t^{100 \text{ percent}}$ with the ratio F provides an indication of the nonideality of the residual stress distribution in actual autofrettage cylinders. The data points shown in Fig. 8 make this comparison. Each point represents an autofrettaged steel cylinder of the type described in Ref *16*. A section was removed from each cylinder, and the opening angle was measured using an optical comparator. The ratio of measured angle to 100 percent overstrain theoretical angle was calculated using the measured value of yield strength, Y, for each tube.

The important features of the comparison between experiment and theory in Fig. 8 are the following:

1. The experimental results are generally near or above the theoretical curve for relatively low overstrain and generally below the curve for high overstrain. This can be explained by the Bauschinger effect, since for high overstrain and the associated large amount of tensile yielding, the Bauschinger effect would result in significant reverse yielding and less than expected residual stress and opening angle.

2. The two sets of experimental results designated by dashed lines indicate less than expected opening angle and residual stress with increasing R_2/R_1.

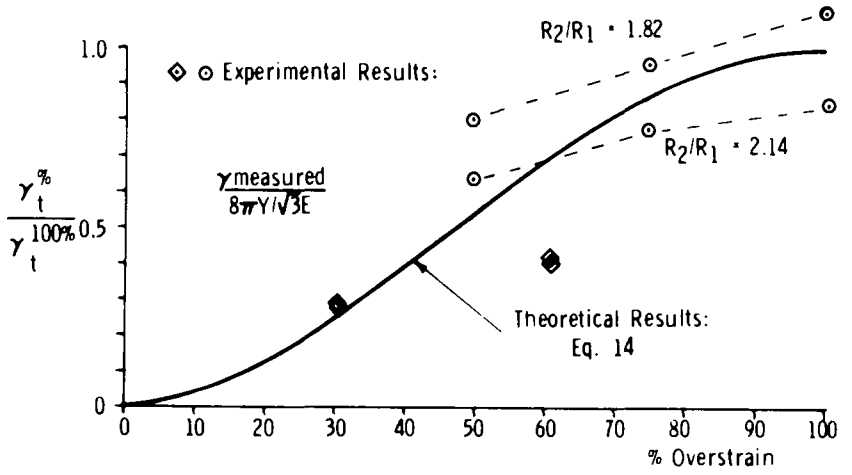

FIG. 8—*Ratio of opening angle for partial overstrain to the theoretical value for 100 percent overstrain.*

This also is consistent with the Bauschinger effect, using a similar rationale as with the first feature, that is, larger R_2/R_1 result in more tensile yielding, more reverse yielding, and less than expected residual stress.

Also shown in Fig. 8 are the measured-to-theoretical angle ratios from the 30 and 60 percent overstrained tubes of the experimental work described here. Note that the average of the two angle measurements for 60 percent overstrain is about 0.6 of the theoretical value. This would suggest that, at least as a first approximation, the contribution of overstrain to the total K could be reduced by this 0.6 factor, and a shorter than expected fatigue life would result. This is discussed further in the comparison of experimental and theoretical results.

Life Calculations

The fatigue growth rate of cracks subjected to cyclic loading may be expressed in terms of Paris' law [*19*]

$$\frac{da}{dN} = C(\Delta K)^m \tag{15}$$

where da/dN is the fatigue crack growth per loading cycle, C and m are empirical constants, and ΔK is the range of stress intensity defined by

$$\Delta K = K_{max} - K_{min}, \qquad (K_{min} \geq 0)$$

$$\Delta K = K_{max}, \qquad (K_{min} < 0)$$

where K_{max} and K_{min} are the maximum and minimum values of stress intensity during the loading cycle. Note that the possibility of "overlapping" or touching of the crack surfaces at some point on the crack line remote from the crack tip [*20*] is not considered in this paper. During the lifetime of a particular cracked cylinder, the crack will propagate from some initial depth a_i to some final depth a_f, where a_f is generally the total wall thickness of the cylinder, $R_2 - R_1$. In order to predict the fatigue life, Eq 15 is rearranged to give

$$\int_{a_i}^{a_f} \frac{da}{C(\Delta K)^m} = N_f - N_i \tag{16}$$

Crack growth (a versus N) predictions are made for two examples that are near the extremes of crack geometry encountered in thick cylinders: a single nearly straight-fronted crack and a single semicircular crack. The predictions are compared with ultrasonic crack growth measurements from cylinders in which internal radius R_1 is 90 mm, R_2/R_1 is 2.0, and the cyclic pressurization is 0 to 331 MPa. The cylinder material is ASTM A723 forged steel, with yield strength of 1175 MPA, −40°C Charpy impact energy of 34 J, reduction in area

of 50 percent [*21*]. These properties can be slightly different after overstrain, due to the plastic strain, which can be up to 1 percent at the inner radius of a 100 percent overstrained cylinder. Considering this small amount of plastic strain relative to reduction in area, no significant effect on fatigue life is expected as the result of the material property changes due to the overstrain process.

In general, the integral of Eq 16 was evaluated numerically using Simpson's rule. For the particular steel employed in the experimental crack growth rate work, the measured constants are $C = 6.52 \times 10^{-12}$ and $m = 3.0$ for crack growth in metres per cycle and ΔK in MPa $m^{1/2}$.

Single, Nearly Straight-Fronted Crack

Figure 9 shows a versus N predictions based on the K results presented in Fig. 3 for a single, straight-fronted radial crack, initial depth 6.4 mm. The solid lines in Fig. 9 are predictions for 0 and 30 percent overstrain. The dashed line shows experimental results, originally reported in Ref *21*, for a tube with zero nominal overstrain in which a single notch was cut using electro-discharge machining to a depth of 6.4 mm and a half surface length, c, of 254 mm.

For this example it is possible [*22*] to integrate Eq 16 directly if a simple, shallow crack K-expression is used, that is, one with $K_p/\tilde{K}_p$ at a constant value. From Fig. 2, $K_p/\tilde{K}_p = 1.05$ at $a/R_2 - R_1 = 0.2$ is a reasonable choice, considering that most of the cylinder life is expended at relatively low values of a. Doing so and combining with Eqs 6 and 12 gives the following expression for fatigue life of a tube with no overstrain

$$N_f - N_i = \frac{2\left[\frac{1}{\sqrt{a_i}} - \frac{1}{\sqrt{a_f}}\right]}{C\left[\frac{K_p}{\tilde{K}_p}(\pi)^{1/2}\left(\frac{2R_2^2}{R_2^2 - R_1^2}\right)L_p\, p\right]^3} \tag{17}$$

For values of a_i, C, R_2, R_1, and p in this example and setting $L_p = 1.0$, the result is the dotted line in Fig. 9, very close to the more general analysis. For the conditions of this comparison, the simpler analysis of Eq 17, although less rigorous and general, is adequate and easier to use.

The lack of agreement between the two analytical predictions and the experiment would be improved if the shape factor, L_p, was significantly less than unity. The initial shape is described by $(a/c)_i = 0.025$ and the final shape is $(a/c)_f = 0.18$. Referring to Fig. 7*a* and considering that most of the cylinder life is expended with low values of both a/c and $a/R_2 - R_1$, L_p is estimated to be between 0.95 and 1.0. So even with this factor to the third power in Eq 17, it cannot account for the differences in Fig. 9.

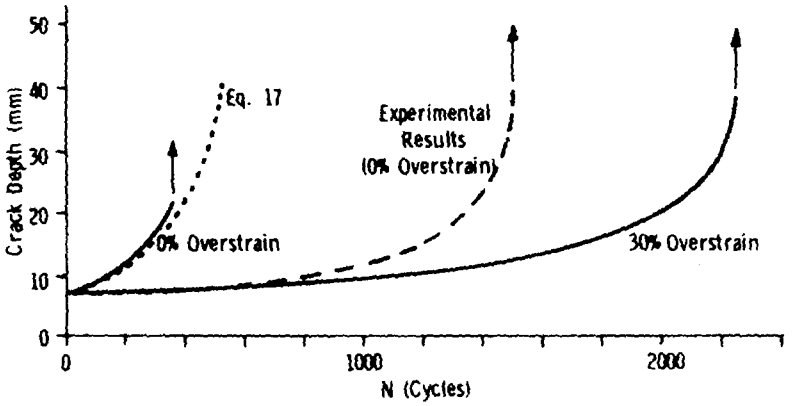

FIG. 9—*Fatigue crack growth* (a *versus* N) *in thick cylinder with single, straight-fronted crack: experimental results and predictions.*

Single, Semicircular Crack

Figure 10 shows a versus N predictions, based on the K-values presented in Fig. 2, as modified in accordance with Eq 12, utilizing correction factors L_p and L_a from Fig. 7*a* and *c* respectively, for $a/c = 1.0$. The K-values are representative of the stress intensity at the deepest point of a semicircular crack of initial depth 6.4 mm in a thick cylinder, and therefore implicitly assume that the crack retains its semicircular shape during the life of the tube. This as-

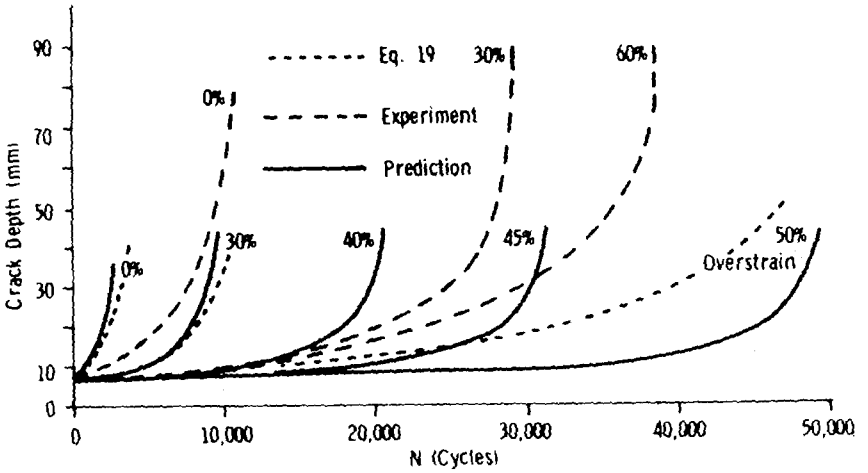

FIG. 10—*Fatigue crack growth* (a *versus* N) *in thick cylinder with single, semicircular crack; experimental results and predictions.*

sumption appears to be justified on the basis of experimental observations [*16*]. The predictions are made for zero, 30, 40, 45, and 50 percent overstrain, while the dashed lines indicate experimental results [*16*] for the same initial crack depth for actual tubes with zero, 30, and 60 percent nominal overstrain.

For this example it is also possible to obtain a closed form expression for fatigue life, analogous to Eq 17. By combining Eqs 6, 8, and 10 it can be shown that the ratio of the K expression for an autofrettaged and pressurized cylinder to that of a pressurized cylinder with no autofrettage is the following

$$\frac{K_{p+A}}{K_p} = 1 + \frac{Y}{p}\left[\ell n\left(\frac{R_2}{R_A}\right) + \delta \ell n \frac{R_1}{R_2} + \frac{R_A^2 - \delta R_1^2 - (1-\delta)R_2^2}{2R_2^2}\right] \quad (18)$$

where δ is defined as $(K_A/\tilde{K}_A)/(K_p/\tilde{K}_p)$, the ratio of the K solutions in Fig. 2.

Using Eq 18 in a life expression in the form of Eq 17 gives

$$N_f - N_i = \frac{2\left[\frac{1}{\sqrt{a_i}} - \frac{1}{\sqrt{a_f}}\right]}{C\left[\frac{K_p}{\tilde{K}_p}(\pi)^{1/2}\left(\frac{2R_2^2}{R_2^2 - R_1^2}\right)\left(1 + \frac{Y}{P}\cdot\left[\ell n\left(\frac{R_2}{R_A}\right) + \delta \ell n \frac{R_1}{R_2} + \frac{R_A^2 - \delta R_1^2 - (1-\delta)R_2^2}{2R_2^2}\right]\right)\bar{L}_p\right]^3} \quad (19)$$

which should give a good estimate of fatigue life for an autofrettaged, pressurized cylinder in which a shallow semielliptical crack dominates the life. Results from this shallow crack expression are shown in Fig. 10 for 0, 30, and 50 percent overstrain. A mean $\bar{L} = 0.53$ was used, since L_p and L_A are close to this value for $a/R_2 - R_1$ 0.2 (see Fig. 7*a* and *c*). The predictions of the shallow crack analysis, Eq 19, are close to those of the more general analysis. The lack of agreement between the two analytical predictions and the experiments is discussed in the next section.

Discussion and Conclusions

Life prediction for cracked tubes requires an accurate knowledge of stress-intensity factor at short crack depths. In this paper, two-dimensional solutions for cracked tubes with various amounts of residual stress (overstrain) were obtained by use of the MMC technique, which gives good convergence to the known analytic solution at very small crack depths.

The solutions were extended to include three-dimensional semielliptical

cracks in thick cylinders by calculating the proportion of tension and bending in the cylinder and applying appropriate correction factors determined for cracked plates in tension and bending. Comparison with limited available three-dimensional solutions for thick cylinders indicates good agreement at short to medium crack lengths, $a/R_2 - R_1 \leq 0.3$, where most of the fatigue lifetime is expended. The approach adopted is, however, not restricted to thick cylinders, and may have general application in fracture mechanics design. Indeed, the thick cylinder may be a sort of limiting configuration in which maximum errors would be anticipated because of the large degree of restraint offered by the doubly connected body.

The calculations of lifetime for nonautofrettaged, pressurized tubes with nearly straight-fronted and semicircular cracks predict lives of about one quarter of those determined experimentally. Possible explanations for this effect are the following:

1. The possibility that full pressure does not infiltrate the crack. This is not considered likely, because the experimental work was deliberately designed to avoid this effect. Also it would be far more noticeable in the autofrettage case if it were occurring because of the compressive stress closing the crack.

2. Residual stresses in the nonautofrettage tube. Again, this is not considered likely. When cut radially, nonautofrettaged tubes do not exhibit any tendency to spring open, indicating negligible gross residual stresses.

3. Multiple, small, semielliptical cracks along the notch boundary. This is considered a probable explanation. Such a form of multiple crack growth would result in slower overall crack growth than that of a single crack, until the individual semielliptical cracks linked to form a single continuous crack front.

Lifetimes calculated on the basis of the ideal residual stress field indicate extreme sensitivity to the amount of overstrain. Note in Fig. 10 that an increase from 30 to 50 percent overstrain increases the predicted life by a factor of five, while an increase from 30 to 60 percent overstrain increases measured life by a factor of 1.4. So there is clearly much less increase in life due to increased overstrain than would be expected from the calculations. We believe this effect is directly related to the less than expected opening angle measured from cylinders with 60 percent overstrain, discussed in relation to Fig. 8. The preferred explanation for the deviations of opening angle and lifetime from calculated values is the reduction in the residual stress field due to reversed yielding near the inner radius caused by the Bauschinger effect. This would manifest itself as a reduction in opening angle, particularly at large overstrains, and a relatively larger reduction in lifetime, since most of the lifetime is expended at shallow depths at which the hoop stresses are reduced most significantly.

Acknowledgments

The first author performed work on this paper during an attachment to the Engineering Mechanics Laboratory, U.S. Army Materials and Mechanics Re-

search Center. The fourth author acknowledges support from a U.K. Ministry of Defense research contract as a Research Scientist at the Royal Military College of Science.

APPENDIX

Opening of Cut Tubes with Partial Autofrettage, No Reversed Yielding

The residual stresses in an autofrettaged tube, internal radius R_1, external radius R_2, and autofrettage radius R_A are [9]

$$\sigma_{\theta 1} = -p + Y(1 + \ell n(r/R_1) - p\left(\frac{R^2}{R_2^2 - R_1^2}\left[1 + \frac{R_2^2}{r^2}\right]\right), \qquad R_1 \le r \le R_A \tag{20}$$

$$\sigma_{\theta 2} = \left[\frac{YR_A^2}{2R_2^2} - \frac{pR_1^2}{R_2^2 - R_1^2}\right]\left[1 + \frac{R_2^2}{r^2}\right], \qquad R_A \le r \le R_2 \tag{21}$$

where p, the autofrettage pressure, is given by

$$p = Y\ell n(R_A/R_1) + \frac{Y}{2R_2^2}(R_2^2 - R_A^2) \tag{22}$$

The total moment acting over any radial cut is given by

$$M = \int_{R_1}^{R_2} \sigma_\theta \times r \times dr$$

or

$$M = \int_{R_1}^{R_A} \sigma_{\theta 1}\, r \times dr + \int_{R_A}^{R_2} \sigma_{\theta 2}\, r \times dr \tag{23}$$

Since the opening angle of fully autofrettaged tubes of any radius ratio, R_2/R_1, provided reversed yielding does not occur, is given by $8\pi Y/\sqrt{3E}$ [18], and the amount of opening is proportional to the applied bending moment, it is possible to produce a nondimensional plot of theoretical angle of opening for a cut tube with partial autofrettage, for any radius ratio. The curve for $R_2/R_1 = 2.0$ is shown in Fig. 8. Deviations from this curve for $1.8 \le R_2/R_1 \le 2.2$ are less than 1 percent of the maximum opening.

Opening of Cut Tubes with Partial, Autofrettage, with Reversed Yielding

If the material of the tube has a reduced yield strength in compression of $-\lambda Y$, it may undergo reversed yielding out to a radius R_D after removal of the autofrettage pressure, p. In this case the residual stresses are [23]

$$\sigma_{\theta 3} = -\lambda Y\,(1 + \ell n(r/R_1)), \qquad R_1 \le r \le R_D \tag{24}$$

$$\sigma_{\theta 4} = -\left\{p - (1+\lambda)Y\ell n\left(\frac{R_D}{R_1}\right)\right\}\frac{R_D^2}{R_2^2 - R_D^2}\left[1 + \frac{R_2^2}{r^2}\right]$$

$$-p + Y(1 + \ell n(r/R_1)), \qquad R_D \le r \le R_A \tag{25}$$

$$\sigma_{\theta 5} = \left[\frac{YR_A^2}{2R_2^2} - \left\{p - (1+\lambda)Y\ell n\left(\frac{R_D}{R_1}\right)\right\}\frac{R_D^2}{R_2^2 - R_D^2}\right]$$

$$\cdot\left[1 + \frac{R_2^2}{r^2}\right], \qquad R_A \le r \le R_2 \tag{26}$$

where R_D is calculated in an iterative fashion from

$$\frac{p}{Y} = (1+\lambda)\left[\frac{R_2^2 - R_D^2}{2R_2^2} + \ell n(R_D/R_1)\right] \tag{27}$$

Once again, the total moment acting over any radial cut is given by Eq 23, thus when reversed yielding occurs

$$M = \int_{R_1}^{R_D} \sigma_{\theta 3}\, r \times dr + \int_{R_D}^{R_A} \sigma_{\theta 4}\, r \times dr + \int_{R_A}^{R_2} \sigma_{\theta 5}\, r \times dr \tag{28}$$

The reduction in opening arising from a Bauschinger effect equivalent to $\lambda = 0.5$ can be calculated, leading to a plot similar to Fig. 8. The maximum reduction in opening is approximately 8 percent as a result of this magnitude of Bauschinger effect. Deviations from this figure do not exceed 1 percent for $1.8 \le R_2/R_1 \le 2.2$.

References

[1] Tan, C. L. and Fenner, R. T., *International Journal of Fracture*, Vol. 16, No. 3, 1980, pp. 233-245.

[2] Andrasic, C. P. and Parker, A. P. in *Numerical Methods in Fracture Mechanics, Proceedings of the Second International Conference*, D. R. J. Owen and A. R. Luxmoore, Eds., Swansea, England, 1980, pp. 67-82.

[3] Muskhelishvili, N. I., *Some Basic Problems of the Mathematical Theory of Elasticity*, Noordhoff, New York, 1973.

[4] Tracy, P. G., *Engineering Fracture Mechanics*, Vol. 11, 1979, pp. 291-300.

[5] Eason, E. D., *International Journal for Numerical Methods in Engineering*, Vol. 10, 1976, pp. 1021-1046.

[6] Sih, G. C., Paris, P. C., and Erdogan, F., *Journal of Applied Mechanics*, Vol. 29, 1962, pp. 306-312.

[7] Bowie, O. L. and Freese, C. E., *Engineering Fracture Mechanics*, Vol. 4, No. 2, 1972, pp. 315-321.

[8] Grandt, A. F., *International Journal of Fracture*, Vol. 14, 1978, pp. R221-R229.

[9] Hill, R., *The Mathematical Theory of Plasticity*, Clarendon Press, Oxford, 1950.

[10] Grandt, A. F., "Two Dimensional Stress Intensity Factor Solutions for Radially Cracked Rings," AFML-TR-75-121, Air Force Materials Laboratory, Wright-Patterson Air Force Base, Ohio, 1975.

[11] Parker, A. P. and Farrow, J. R., *Engineering Fracture Mechanics*, Vol. 14, 1981, pp. 237-241.

[12] Parker, A. P., "Stress Intensity and Fatigue Crack Growth in Multiply Cracked, Pressur-

ized, Partially Autofrettaged Thick Cylinders," *Fatigue of Engineering Materials and Structures*, Vol. 4, No. 2, 1982.

[13] Newman, J. C. and Raju, I. S., "Analyses of Surface Cracks in Finite Plates Under Tension or Bending Loads," NASA TP 1578, National Aeronautics and Space Administration, Washington, D.C., 1979.

[14] Atulri, N. and Kathiresan, K., *Nuclear Engineering and Design*, Vol. 51, 1979, pp. 163-176.

[15] Rooke, D. P. and Cartwright, D. J., *Compendium of Stress Intensity Factors*, Her Majesty's Stationery Office, London, 1976.

[16] Underwood, J. H. and Throop, J. F., "Residual Stress Effects on Fatigue Cracking of Pressurized Cylinders and Notched Bending Specimens," Fourth International Congress of the Society of Experimental Stress Analysis, Boston, Mass., May 1980.

[17] Milligan, R. V., Koo, W. H., and Davidson, T. E., *Journal of Basic Engineering, Transactions of the American Society of Mechanical Engineers*, Vol. 88, 1966, pp. 480-488.

[18] Parker, A. P. and Farrow, J. R., *Journal of Strain Analysis*, Vol. 15, No. 1, 1980, pp. 51-52.

[19] Paris, P. C. and Erdogan, F., *Journal of Basic Engineering, Transactions of the American Society of Mechanical Engineers*, Vol. 85, 1963, pp. 528-534.

[20] Parker, A. P. in *Residual Stress Effects in Fatigue, ASTM STP 776*, American Society for Testing and Materials, 1982, pp. 13-31.

[21] Throop, J. F., *Proceedings of the National Conference on Fluid Power*, Fluid Power Society, Chicago, 1972, pp. 115-131.

[22] Underwood, J. H. and Throop, J. F. in *Part-Through Crack Fatigue Life Prediction, ASTM STP 687*, American Society for Testing and Materials, 1979, pp. 195-210.

[23] Parker, A. P., Sleeper, K. A., and Andrasic, C. P., "Safe Life Design of Gun Tubes: Some Numerical Methods and Results," U.S. Army Numerical Analysis and Computers Conference, Huntsville, Ala., ARO Report 81-3, 1981, pp. 311-333.

J. C. Newman, Jr.,[1] *and I. S. Raju*[2]

Stress-Intensity Factor Equations for Cracks in Three-Dimensional Finite Bodies

REFERENCE: Newman, J. C., Jr., and Raju, I. S., **"Stress-Intensity Factor Equations for Cracks in Three-Dimensional Finite Bodies,"** *Fracture Mechanics: Fourteenth Symposium—Volume I: Theory and Analysis, ASTM STP 791*, J. C. Lewis and G. Sines, Eds., American Society for Testing and Materials, 1983, pp. I-238-I-265.

ABSTRACT: This paper presents empirical stress-intensity factor equations for embedded elliptical cracks, semielliptical surface cracks, quarterelliptical corner cracks, semielliptical surface cracks at a hole, and quarterelliptical corner cracks at a hole in finite plates subjected to remote tensile loading. These equations give stress-intensity factors as a function of parametric angle, crack depth, crack length, plate thickness, and, where applicable, hole radius. The stress-intensity factors used to develop the equations were obtained from current and previous three-dimensional finite-element analyses of these crack configurations. A wide range of configuration parameters was included in the equations. The ratio of crack depth to plate thickness ranged from 0 to 1, the ratio of crack depth to crack length ranged from 0.2 to 2, and the ratio of hole radius to plate thickness ranged from 0.5 to 2. The effects of plate width on stress-intensity variations along the crack front also were included, but generally were based on engineering estimates. For all combinations of parameters investigated, the empirical equations were generally within 5 percent of the finite-element results, except within a thin "boundary layer" where the crack front intersects a free surface. However, the proposed equations are expected to give a good estimate in this region because of a study made on the boundary-layer effect. These equations should be useful for correlating and predicting fatigue crack growth rates as well as in computing fracture toughness and fracture loads for these types of crack configurations.

KEY WORDS: cracks, surface cracks, corner cracks, crack propagation, fracture, stress analysis, fatigue (materials), stress-intensity factors, finite elements

Nomenclature

- a Depth of crack
- b Width or half-width of cracked plate (see Fig. 2)

[1]Senior scientist, National Aeronautics and Space Administration, Langley Research Center, Hampton, Va. 23665.

[2]Associate research professor, The George Washington University, Joint Institute for Advancement of Flight Sciences, National Aeronautics and Space Administration, Langley Research Center, Hampton, Va. 23665.

c Length or half-length of crack (see Fig. 2)
F Boundary-correction factor on stress intensity
F_c Boundary-correction factor for corner crack in a plate
F_e Boundary-correction factor for embedded crack in a plate
F_s Boundary-correction factor for surface crack in a plate
F_{sh} Boundary-correction factor for surface crack at a hole in a plate
F_{ch} Boundary-correction factor for corner crack at a hole in a plate
f_w Finite-width correction factor
f_ϕ Angular function derived from embedded elliptical crack solution
g_i Curve fitting functions defined in text
h Half-length of cracked plate
K_I Stress-intensity factor (Mode I)
M_i Curve fitting functions defined in text
Q Shape factor for an elliptical crack
R Radius of hole
S Remote uniform tensile stress
t Thickness or half-thickness of plate (see Fig. 2)
ν Poisson's ratio
ϕ Parametric angle of the ellipse

In aircraft structures, fatigue failures usually occur from the initiation and propagation of cracks from notches or defects in the material that are either embedded, on the surface, or at a corner. These cracks propagate with elliptic or near-elliptic crack fronts. To predict crack-propagation life and fracture strength, accurate stress-intensity factor solutions are needed for these crack configurations. But, because of the complexities of such problems, exact solutions are not available. Instead, investigators have used approximate analytical methods, experimental methods, or engineering estimates to obtain the stress-intensity factors.

Very few exact solutions for three-dimensional cracked bodies are available in the literature. One of these, an elliptical crack in an infinite solid subjected to uniform tension, was derived by Irwin [*1*][3] using an exact stress analysis by Green and Sneddon [*2*]. For finite bodies, all solutions have required approximate analytical methods. For a semicircular surface crack in a semi-infinite solid and a semielliptical surface crack in a plate of finite thickness, Smith, Emery, and Kobayashi [*3*] and Kobayashi [*4*], respectively, used the alternating method to obtain stress-intensity factors along the crack front. Raju and Newman [*5,6*] used the finite-element method, and Heliot, Labbens, and Pellissier-Tanon [*7*] used the boundary-integral equation method to obtain the same information. For a quarterelliptic corner crack in a plate, Tracey [*8*] and Pickard [*9*] used the finite-element method; Kobayashi and Enetanya [*10*] used the alternating method. Shah [*11*] estimated the stress-intensity factors

[3]The italic numbers in brackets refer to the list of references appended to this paper.

for a surface crack emanating from a circular hole. For a single corner crack emanating from a circular hole in a plate, Smith and Kullgren [*12*] used a finite-element-alternating method to obtain the stress-intensity factors. Hechmer and Bloom [*13*] and Raju and Newman [*14*] used the finite-element method for two-symmetric corner cracks emanating from a hole in a plate. All of these approximate results, except that for the surface crack [*6,9*] and the corner crack [*9*], were presented in the form of curves or tables. However, for ease of computation, results expressed in the form of equations are preferable.

This paper presents empirical equations for the stress-intensity factors for a wide variety of three-dimensional crack configurations subjected to uniform tension as a function of parametric angle, crack depth, crack length, plate thickness, and hole radius (where applicable). An example is shown in Fig. 1. These crack configurations, shown in Fig. 2, include the following: an embedded elliptical crack, a semielliptical surface crack, a quarterelliptical corner crack, a semielliptical surface crack at a hole, and a quarterelliptical corner crack at a hole in finitie plates subjected to remote tensile loading. The equations were based on the stress-intensity factors obtained from three-dimensional finite-element analyses conducted herein and from the literature [*5,14*], and cover a wide range of configuration parameters. The ratio of crack

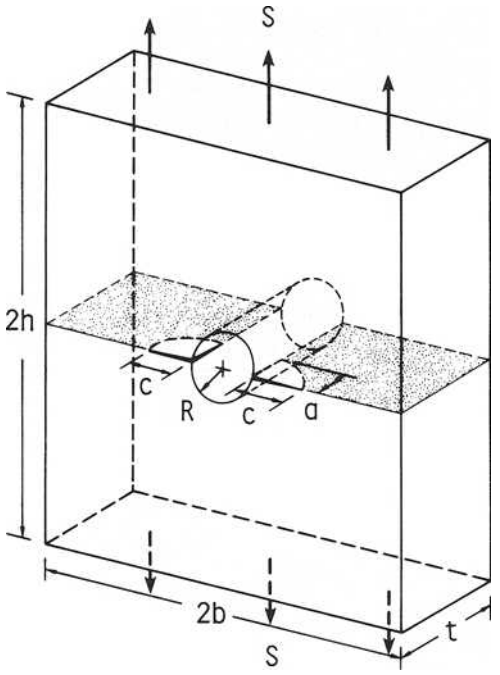

FIG. 1—*Corner cracks at the edge of a hole in a finite plate subjected to remote tension.*

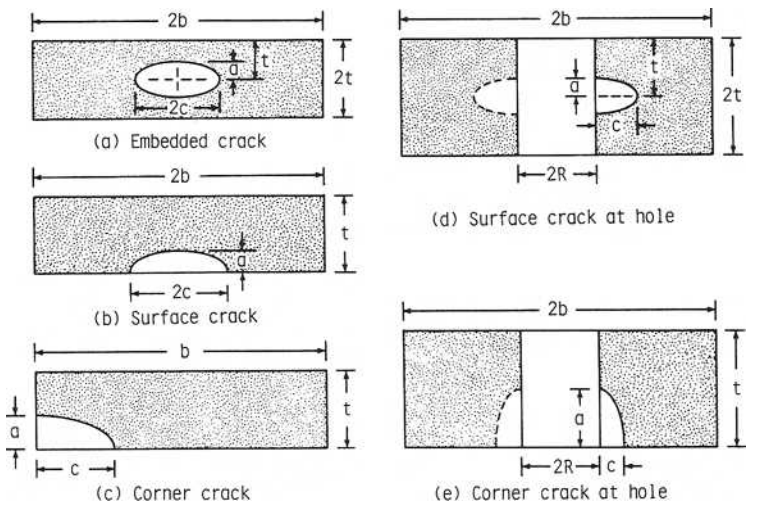

FIG. 2—*Embedded-, surface-, and corner-crack configurations (all cracks have elliptical fronts).*

depth to plate thickness (a/t) ranged from 0 to 1, the ratio of crack depth to crack length (a/c) ranged from 0.2 to 2, and the ratio of hole radius to plate thickness (R/t) ranged from 0.5 to 2. The effects of plate width (b) on stress-intensity variations along the crack front also were included, but generally were based on engineering estimates.

Three-Dimensional Finite-Element Analyses

Three-dimensional finite-element analyses [*5,14*] using linear-strain and singularity elements were used to calculate the Mode I stress-intensity factor variation along the crack front for an embedded elliptical crack, a quarterelliptical corner crack, and a semielliptical surface crack at a hole in a finite plate subjected to remote tensile loading (see Fig. 2). The finite-element models used for these configurations were the same as those used in Refs *5* and *14* for surface cracks and corner cracks at holes. The only differences were the boundary conditions that were imposed on certain faces of the models. For embedded cracks and surface cracks at holes, the normal displacements on three planes of symmetry were fixed (set equal to zero), except for the crack surface. For a corner crack in a plate, the normal displacements on the two faces that intersect the crack were free.

The stress-intensity factors were obtained from the finite-element analyses by using a nodal-force method, the details of which are given in Refs *5* and *15*. In this method, the nodal forces normal to the crack plane and ahead of the crack front were used to evaluate the stress-intensity factors.

The stress-intensity factor, K_I, at any point along the crack front in a finite-thickness plate was taken to be

$$K_I = S\sqrt{\pi \frac{a}{Q}}\, F\left(\frac{a}{t}, \frac{a}{c}, \frac{R}{t}, \phi\right) \tag{1}$$

where Q is the shape factor for an ellipse and is given by the square of the complete elliptic integral of the second kind [2]. In the finite-element models, the width (b) and length (h) of the plate were taken to be large enough so that they would have a negligible effect on stress intensity. The boundary correction, F, accounts for the influence of various boundaries and is a function of crack depth, crack length, hole radius (where applicable), plate thickness, and the parametric angle of the ellipse. Figure 3 shows the coordinate system used to define the parametric angle.

Very useful empirical expressions for Q have been developed by Rawe (see Ref 6). The expressions are

$$Q = 1 + 1.464\left(\frac{a}{c}\right)^{1.65} \quad \text{for } \frac{a}{c} \leq 1 \tag{2a}$$

$$Q = 1 + 1.464\left(\frac{c}{a}\right)^{1.65} \quad \text{for } \frac{a}{c} > 1 \tag{2b}$$

The maximum error in the stress-intensity factor by using these equations for Q was about 0.13 percent for all values of a/c. (Rawe's original equation was written in terms of $a/2c$).

The boundary-correction factors, F, obtained from the present finite-ele-

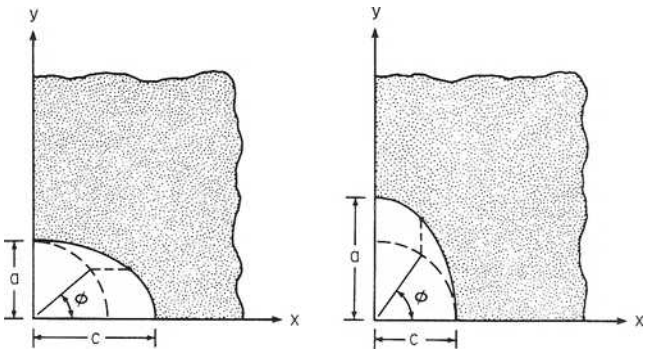

FIG. 3—*Coordinate system used to define parametric angle.*

ment results for the embedded elliptical crack and the quarterelliptic corner crack in a finite plate subjected to uniform tension are given in Tables 1 and 2, respectively, for various parametric angles and several a/c and a/t ratios. Tables 3 and 4 give the boundary-correction factors for two-symmetric semielliptical surface cracks emanating from a circular hole in a finite plate subjected to uniform tension for R/t equals 1 and 2, respectively.

TABLE 1—*Boundary correction factors, F, for embedded elliptical crack in a plate subjected to tension (c/b ≤ 0.2; h/b = 1; ν = 0.3).*

		a/t		
a/c	$2\phi/\pi$	0.2	0.5	0.8
0.2	0	0.450	0.473	0.514
	0.125	0.531	0.556	0.605
	0.25	0.643	0.678	0.745
	0.375	0.750	0.794	0.884
	0.5	0.838	0.893	1.015
	0.625	0.905	0.978	1.176
	0.75	0.951	1.042	1.329
	0.875	0.978	1.083	1.438
	1.0	0.987	1.097	1.480
0.4	0	0.632	0.660	0.721
	0.125	0.656	0.685	0.749
	0.25	0.715	0.748	0.821
	0.375	0.789	0.826	0.905
	0.5	0.857	0.900	0.995
	0.625	0.914	0.964	1.105
	0.75	0.954	1.014	1.211
	0.875	0.978	1.046	1.285
	1.0	0.987	1.056	1.312
1.0	0	0.986	1.009	1.060
	0.125	0.986	1.009	1.058
	0.25	0.986	1.008	1.050
	0.375	0.986	1.006	1.035
	0.5	0.986	1.006	1.036
	0.625	0.986	1.008	1.059
	0.75	0.986	1.010	1.093
	0.875	0.986	1.012	1.114
	1.0	0.986	1.013	1.121
2.0	0	0.709	0.713	0.720
	0.125	0.703	0.707	0.714
	0.25	0.686	0.690	0.697
	0.375	0.658	0.662	0.669
	0.5	0.622	0.625	0.633
	0.625	0.579	0.582	0.592
	0.75	0.536	0.539	0.552
	0.875	0.503	0.506	0.522
	1.0	0.490	0.494	0.511

TABLE 2—*Boundary correction factors, F, for corner crack in a plate subjected to tension (c/b ≤ 0.2; h/b = 1; ν= 0.3).*

		a/t		
a/c	2φ/π	0.2	0.5	0.8
0.2	0	0.555	0.761	1.288
	0.125	0.633	0.840	1.340
	0.25	0.753	0.988	1.522
	0.375	0.871	1.141	1.705
	0.5	0.973	1.277	1.850
	0.625	1.055	1.397	2.008
	0.75	1.115	1.495	2.118
	0.875	1.159	1.580	2.263
	1.0	1.156	1.610	2.450
0.4	0	0.791	0.990	1.397
	0.125	0.774	0.952	1.297
	0.25	0.824	0.997	1.310
	0.375	0.893	1.067	1.346
	0.5	0.964	1.140	1.384
	0.625	1.026	1.210	1.458
	0.75	1.075	1.273	1.528
	0.875	1.117	1.334	1.627
	1.0	1.132	1.365	1.788
1.0	0	1.162	1.275	1.487
	0.125	1.111	1.207	1.378
	0.25	1.079	1.160	1.290
	0.375	1.064	1.134	1.219
	0.5	1.059	1.121	1.180
	0.625	1.063	1.123	1.191
	0.75	1.078	1.140	1.231
	0.875	1.109	1.176	1.301
	1.0	1.159	1.233	1.416
2.0	0	0.800	0.826	0.862
	0.125	0.787	0.811	0.837
	0.25	0.756	0.776	0.793
	0.375	0.722	0.738	0.750
	0.5	0.683	0.697	0.704
	0.625	0.640	0.653	0.660
	0.75	0.600	0.612	0.624
	0.875	0.579	0.590	0.611
	1.0	0.586	0.597	0.625

Stress-Intensity Factor Equations

In the following sections, the empirical stress-intensity factor equations for embedded elliptical cracks, semielliptical surface cracks, quarterelliptical corner cracks, semielliptical surface cracks at a hole, and quarterelliptical corner cracks at a hole in finite plates (see Fig. 2) subjected to remote tension are presented. The particular functions chosen were obtained from systematic

TABLE 3—*Boundary correction factors, F, for surface crack at center of hole in a plate subjected to tension [(R + c)/b ≤ 0.2; h/b > 1.6; ν = 0.3; R/t = 1].*

		a/t		
a/c	2φ/π	0.2	0.5	0.8
0.2	0	0.641	0.607	0.593
	0.125	0.692	0.662	0.643
	0.25	0.836	0.775	0.771
	0.375	1.011	0.905	0.919
	0.5	1.196	1.032	1.094
	0.625	1.405	1.178	1.293
	0.75	1.651	1.362	1.528
	0.833	1.905	1.583	1.765
	0.917	2.179	1.885	2.050
	0.958	2.288	2.121	2.336
	1.0	1.834	1.958	2.329
0.4	0	1.030	0.872	0.840
	0.125	1.076	0.912	0.872
	0.25	1.202	1.007	0.959
	0.375	1.376	1.131	1.074
	0.5	1.578	1.275	1.234
	0.625	1.804	1.452	1.426
	0.75	2.040	1.667	1.668
	0.833	2.238	1.891	1.914
	0.917	2.396	2.141	2.201
	0.958	2.376	2.255	2.411
	1.0	1.844	1.923	2.224
1.0	0	2.267	1.806	1.615
	0.125	2.276	1.818	1.619
	0.25	2.301	1.851	1.630
	0.375	2.343	1.905	1.646
	0.5	2.404	1.980	1.730
	0.625	2.481	2.079	1.852
	0.75	2.566	2.206	2.049
	0.833	2.620	2.321	2.250
	0.917	2.622	2.415	2.452
	0.958	2.468	2.370	2.512
	1.0	1.950	1.957	2.203
2.0	0	1.944	1.606	1.394
	0.125	1.931	1.600	1.389
	0.25	1.897	1.582	1.377
	0.375	1.840	1.553	1.357
	0.5	1.763	1.514	1.333
	0.625	1.669	1.468	1.313
	0.75	1.580	1.434	1.310
	0.833	1.498	1.404	1.313
	0.917	1.426	1.387	1.332
	0.958	1.313	1.321	1.294
	1.0	1.042	1.082	1.077

TABLE 4—*Boundary correction factors, F, for surface crack at center of hole in a plate subjected to tension [(R + c)/b ≤ 0.2; h/b > 1.6; ν = 0.3; R/t = 2].*

		a/t		
a/c	$2\phi/\pi$	0.2	0.5	0.8
0.2	0	0.800	0.680	0.634
	0.125	0.864	0.743	0.690
	0.25	1.046	0.877	0.832
	0.375	1.272	1.037	1.002
	0.5	1.508	1.206	1.213
	0.625	1.766	1.410	1.469
	0.75	2.041	1.662	1.787
	0.833	2.279	1.932	2.109
	0.917	2.474	2.238	2.463
	0.958	2.439	2.375	2.699
	1.0	1.791	1.947	2.380
0.4	0	1.290	1.058	0.972
	0.125	1.346	1.107	1.010
	0.25	1.498	1.227	1.118
	0.375	1.704	1.384	1.263
	0.5	1.932	1.568	1.470
	0.625	2.165	1.785	1.722
	0.75	2.378	2.026	2.031
	0.833	2.516	2.237	2.319
	0.917	2.564	2.418	2.595
	0.958	2.417	2.416	2.705
	1.0	1.776	1.894	2.258
1.0	0	2.620	2.188	1.990
	0.125	2.626	2.199	1.996
	0.25	2.642	2.232	2.009
	0.375	2.667	2.280	2.026
	0.5	2.700	2.341	2.121
	0.625	2.732	2.410	2.246
	0.75	2.753	2.483	2.437
	0.833	2.733	2.527	2.599
	0.917	2.643	2.521	2.716
	0.958	2.409	2.381	2.662
	1.0	1.862	1.888	2.192
2.0	0	2.136	1.922	1.712
	0.125	2.121	1.911	1.704
	0.25	2.075	1.879	1.681
	0.375	2.000	1.826	1.643
	0.5	1.899	1.756	1.594
	0.625	1.777	1.671	1.541
	0.75	1.659	1.593	1.499
	0.833	1.552	1.522	1.461
	0.917	1.456	1.463	1.434
	0.958	1.325	1.360	1.351
	1.0	1.041	1.088	1.089

curve-fitting procedure by using double-series polynomials in terms of a/c, a/t, and angular functions of ϕ. For cracks emanating from holes, polynomial equations in terms of c/R and ϕ also were used. The limits on a/c, a/t, R/t, R/b, c/b, and ϕ in the equations were determined from either the analysis or engineering estimates.

Embedded Elliptical Crack

The empirical stress-intensity factor equation for an embedded elliptical crack in a finite plate (shown in Fig. 2*a*) subjected to tension was obtained by fitting to the finite-element results presented in Table 1. To account for limiting behavior as a/c approaches zero or infinity, the results of Irwin [*1*] also were used. The equation is

$$K_I = S\sqrt{\pi \frac{a}{Q}}\, F_e\left(\frac{a}{c}, \frac{a}{t}, \frac{c}{b}, \phi\right) \tag{3}$$

for $0 \le a/c \le \infty$, $c/b < 0.5$, and $-\pi \le \phi \le \pi$ provided that a/t satisfies

$$\begin{aligned} &\frac{a}{t} < 1.25\left(\frac{a}{c} + 0.6\right) \quad \text{for } 0 \le \frac{a}{c} \le 0.2 \\ &\frac{a}{t} \le 1 \quad \text{for } 0.2 \le \frac{a}{c} \le \infty \end{aligned} \tag{4}$$

The function F_e accounts for the influence of crack shape (a/c), crack size (a/t), finite width (c/b), and angular location (ϕ), and was chosen as

$$F_e = \left[M_1 + M_2\left(\frac{a}{t}\right)^2 + M_3\left(\frac{a}{t}\right)^4\right] g f_\phi f_w \tag{5}$$

The term in brackets gives the boundary-correction factors at $\phi = \pi/2$ (where $g = f_\phi = 1$). The function f_ϕ was taken from the exact solution for an embedded elliptical crack in an infinite solid [*1*] and f_w is a finite-width correction factor. The function g is a fine-tuning curve-fitting function. For $a/c \le 1$

$$M_1 = 1 \tag{6}$$

$$M_2 = \frac{0.05}{0.11 + \left(\frac{a}{c}\right)^{3/2}} \tag{7}$$

$$M_3 = \frac{0.29}{0.23 + \left(\frac{a}{c}\right)^{3/2}} \tag{8}$$

$$g = 1 - \frac{\left(\frac{a}{t}\right)^4}{1 + 4\left(\frac{a}{c}\right)} |\cos \phi| \tag{9}$$

and

$$f_\phi = \left[\left(\frac{a}{c}\right)^2 \cos^2 \phi + \sin^2 \phi\right]^{1/4} \tag{10}$$

The finite-width correction, f_w, from Ref *6* was

$$f_w = \left[\sec\left(\frac{\pi c}{2b}\sqrt{\frac{a}{t}}\right)\right]^{1/2} \tag{11}$$

for $c/b < 0.5$. (Note that for the embedded crack, t is defined as one half of the full plate thickness.) For $a/c > 1$

$$M_1 = \sqrt{\frac{c}{a}} \tag{12}$$

and

$$f_\phi = \left[\left(\frac{c}{a}\right)^2 \sin^2 \phi + \cos^2 \phi\right]^{1/4} \tag{13}$$

The functions M_2, M_3, g, and f_w are given by Eq 7, 8, 9, and 11, respectively.

As a/c approaches zero and ϕ equals $\pi/2$, the stress-intensity factor equation reduces to

$$K_I = S\sqrt{\pi a}\left[1 + 0.455\left(\frac{a}{t}\right)^2 + 1.261\left(\frac{a}{t}\right)^4\right] \tag{14}$$

for $c/b = 0$. Equation 14 is within 1 percent of the accepted solution [*16*] for $a/t < 0.55$ and within 3 percent for $a/t < 0.8$.

As a/c approaches infinity and ϕ equals zero, the equation reduces to

$$K_I = S\sqrt{\pi c}\left[\sec\left(\frac{\pi c}{2b}\sqrt{\frac{a}{t}}\right)\right]^{1/2} \tag{15}$$

Equation 15 is the accepted solution [*16*] for this configuration as a/t approaches unity.

A typical comparison between the proposed equation and the finite-element results for an embedded elliptical crack is shown in Fig. 4 for $a/c = 0.4$ and various a/t ratios. The boundary-correction factor, F_e, is plotted against the parametric angle. At $\phi = 0$ and $\pi/2$, the equation (solid curves) is within 2 percent of the finite-element results (symbols). (Herein "percent error" is defined as the difference between the equation and the finite-element results normalized by the maximum value for that particular case. This definition is necessary because the stress-intensity factors in some cases vary from small to large values along the crack front.) The dashed curve shows the exact solution for an elliptic crack in an infinite solid [*1*]. These results indicate that the finite-element solution for $a/t = 0.2$ is probably about 1.5 percent below the exact solution. Because the proposed equation is slightly higher than the finite-element results, the equation should be very accurate.

Semielliptical Surface Crack

An empirical equation for the stress-intensity factors for a semielliptical surface crack in a finite plate (shown in Fig. 2*b*) subjected to tension was obtained from Ref *6*. This equation was fitted previously to the finite-element results

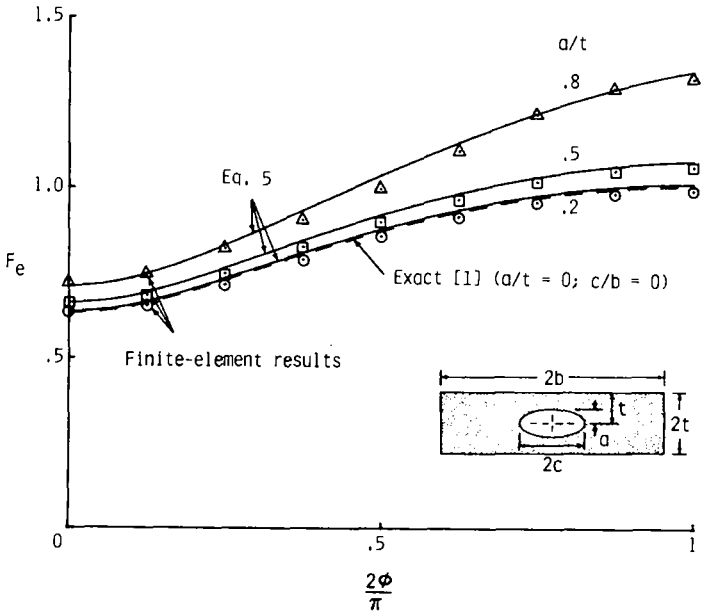

FIG. 4—*Distribution of boundary-correction factors along crack front for an embedded elliptical crack (a/c = 0.4; c/b = 0.1).*

from Raju and Newman [5] for a/c values from 0.2 to 1. An equation for a/c greater than unity was developed herein. To account for the limiting behavior as a/c approaches zero, the results of Gross and Srawley [17] for a single-edge crack also were used. The equation is

$$K_I = S\sqrt{\pi\frac{a}{Q}}F_s\left(\frac{a}{c}, \frac{a}{t}, \frac{c}{b}, \phi\right) \tag{16}$$

for $0 \le a/c \le 2$, $c/b < 0.5$, and $0 \le \phi \le \pi$, again, provided that a/t satisfies Eq 4. The function F_s was chosen to be

$$F_s = \left[M_1 + M_2\left(\frac{a}{t}\right)^2 + M_3\left(\frac{a}{t}\right)^4\right] g f_\phi f_w \tag{17}$$

For $a/c \le 1$

$$M_1 = 1.13 - 0.09\left(\frac{a}{c}\right) \tag{18}$$

$$M_2 = -0.54 + \frac{0.89}{0.2 + \left(\frac{a}{c}\right)} \tag{19}$$

$$M_3 = 0.5 - \frac{1}{0.65 + \frac{a}{c}} + 14\left(1 - \frac{a}{c}\right)^{24} \tag{20}$$

$$g = 1 + \left[0.1 + 0.35\left(\frac{a}{t}\right)^2\right](1 - \sin\phi)^2 \tag{21}$$

and f_ϕ is given by Eq 10. The finite-width correction, f_w, is again given by Eq 11. (The 24th power in Eq 20 was needed to fit the behavior as a/c approaches zero.) Equations 17 through 21 were taken from Ref 6.

For $a/c > 1$

$$M_1 = \sqrt{\frac{c}{a}}\left(1 + 0.04\frac{c}{a}\right) \tag{22}$$

$$M_2 = 0.2\left(\frac{c}{a}\right)^4 \tag{23}$$

$$M_3 = -0.11\left(\frac{c}{a}\right)^4 \tag{24}$$

$$g = 1 + \left[0.1 + 0.35\left(\frac{c}{a}\right)\left(\frac{a}{t}\right)^2\right](1 - \sin\phi)^2 \tag{25}$$

and f_ϕ and f_w are given by Eqs 13 and 11, respectively.

Figure 5 shows the distribution of boundary-correction factors, F_s, along the crack front for a semielliptical surface crack with $a/c = 2$ for two a/c ratios. The proposed equation (solid curves) is within 3 percent of the finite-element results (symbols).

For $a/c \leq 1$, Ref *6* gives a more complete comparison between the proposed equation and the finite-element results. In Ref *6*, the equation also was used to predict surface crack-growth patterns under tension fatigue loads. These predicted crack-growth patterns were in good agreement with measurements made on steel, titanium alloy, and aluminum alloy materials. In Ref *18*, the equation also was used to correlate surface-crack fracture data for a brittle epoxy material within ±10 percent over a wide range of crack shapes (a/c) and crack sizes (a/t).

Quarterelliptical Corner Crack

The empirical stress-intensity factor equation for a quarterelliptical corner crack in a finite plate (shown in Fig. 2*c*) subjected to tension was obtained by

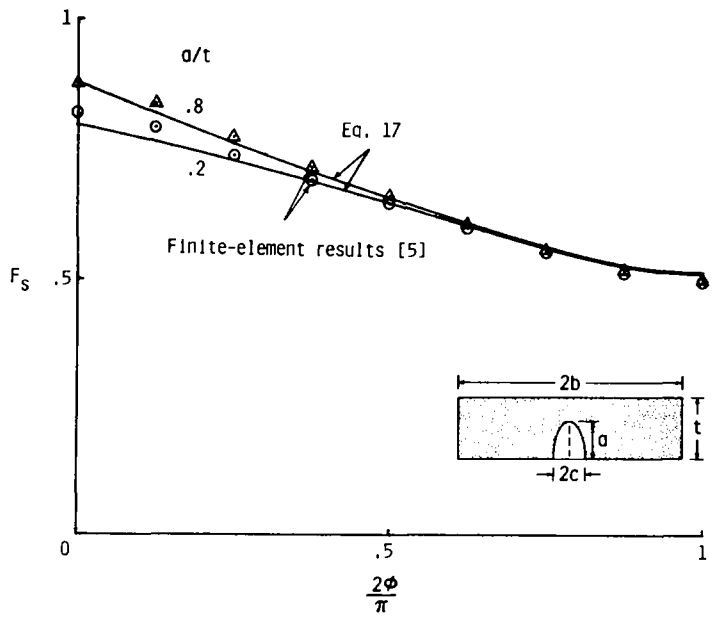

FIG. 5—*Distribution of boundary-correction factors along crack front for a semielliptical surface crack (a/c = 2; c/b = 0.04).*

fitting to the finite-element results presented in Table 2. The equation is

$$K_I = S\sqrt{\pi \frac{a}{Q}} F_c\left(\frac{a}{c}, \frac{a}{t}, \phi\right) \tag{26}$$

for $0.2 \leq a/c \leq 2$, $a/t < 1$, and $0 \leq \phi \leq \pi/2$ for $c/b < 0.2$. The function F_c was chosen as

$$F_c = \left[M_1 + M_2\left(\frac{a}{t}\right)^2 + M_3\left(\frac{a}{t}\right)^4\right] g_1 g_2 f_\phi \tag{27}$$

(Although the effects of width are significant, f_w is not included in Eq 27 because results on finite-width plates were not available for comparison.) For $a/c \leq 1$

$$M_1 = 1.08 - 0.03\left(\frac{a}{c}\right) \tag{28}$$

$$M_2 = -0.44 + \frac{1.06}{0.3 + \left(\frac{a}{c}\right)} \tag{29}$$

$$M_3 = -0.5 + 0.25\left(\frac{a}{c}\right) + 14.8\left(1 - \frac{a}{c}\right)^{15} \tag{30}$$

$$g_1 = 1 + \left[0.08 + 0.4\left(\frac{a}{t}\right)^2\right](1 - \sin\phi)^3 \tag{31}$$

$$g_2 = 1 + \left[0.08 + 0.15\left(\frac{a}{t}\right)^2\right](1 - \cos\phi)^3 \tag{32}$$

and f_ϕ is given by Eq 10.

For $a/c > 1$

$$M_1 = \sqrt{\frac{c}{a}}\left(1.08 - 0.03\frac{c}{a}\right) \tag{33}$$

$$M_2 = 0.375\left(\frac{c}{a}\right)^2 \tag{34}$$

$$M_3 = -0.25\left(\frac{c}{a}\right)^2 \tag{35}$$

$$g_1 = 1 + \left[0.08 + 0.4\left(\frac{c}{t}\right)^2\right](1 - \sin\phi)^3 \tag{36}$$

$$g_2 = 1 + \left[0.08 + 0.15\left(\frac{c}{t}\right)^2\right](1 - \cos\phi)^3 \tag{37}$$

and f_ϕ is given by Eq 13.

Figure 6 shows boundary-correction factors obtained by several investigators for a quartercircular corner crack in a finite-thickness plate ($a/t = 0.2$) under tension loading. The present finite-element results are shown as solid circular symbols and the proposed equation is shown as the solid curve. Tracey [*8*] and Pickard [*9*] also used the finite-element method, but the width (b) and half-length (h) of their models were equal to the plate thickness (see dashed and dash-dot lines in the insert in Fig. 6). Kobayashi [*10*] used the alternating method, but the a/c ratio was 0.98. Pickard's results were 1 to 3 percent higher than the present finite-element results. Part of the difference is due to a width- and length-effect in Pickard's model. The present results are expected to be about 1.5 percent below the exact solution. Near $\phi = 0$ and $\pi/2$, Tracey's and Kobayashi's results are 5 to 13 percent higher than present results. All results are in good agreement (within 3 percent) at the midpoint ($\phi = \pi/4$).

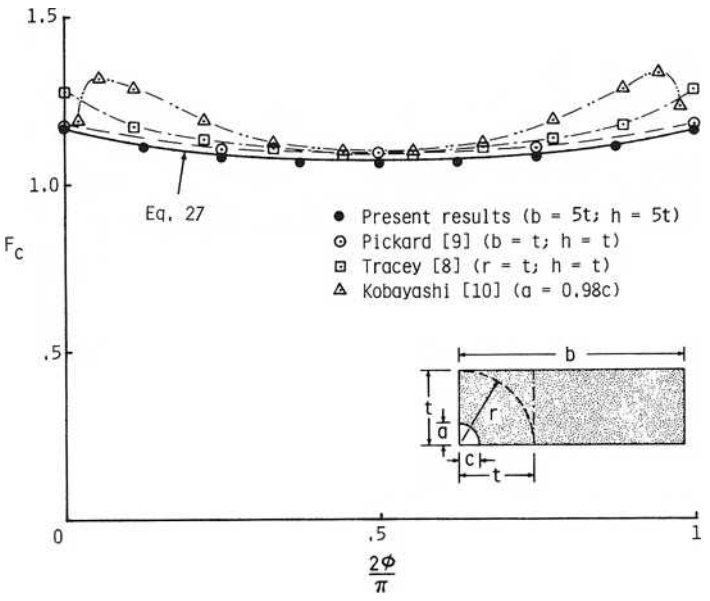

FIG. 6—*Comparison of boundary-correction factors for quartercircular corner crack in a plate subjected to tension (*a/c = *1;* a/t = *0.2).*

Figures 7 and 8 show the distribution of boundary-correction factors, F_c, along the crack front for a quartercircular ($a/c = 1$) and semielliptical ($a/c = 0.2$) corner crack, respectively, in a finite plate subjected to tension. The figures show the results for several a/t ratios. The proposed equation (solid curves) is generally within about 2 percent of the finite-element results (symbols), except near the intersection of the crack front with the free surfaces ($\phi = 0$ and $\pi/2$). Near these points, the equations is generally higher than the finite-element results, the maximum difference being about 5 percent. These low values at the free surfaces are probably due to a boundary-layer effect [*19*] and this behavior is discussed in the appendix.

Semielliptical Surface Crack at Hole

Two-Symmetric Surface Cracks—The empirical stress-intensity factor equation for two-symmetric semielliptical surface cracks at the center of a hole in a finite plate (shown in Fig. 2*d*) subjected to tension was obtained by fitting to the finite-element results presented here (Tables 3 and 4). The equation is

$$K_I = S\sqrt{\pi \frac{a}{Q}} F_{sh}\left(\frac{a}{c}, \frac{a}{t}, \frac{R}{t}, \frac{R}{b}, \frac{c}{b}, \phi\right) \tag{38}$$

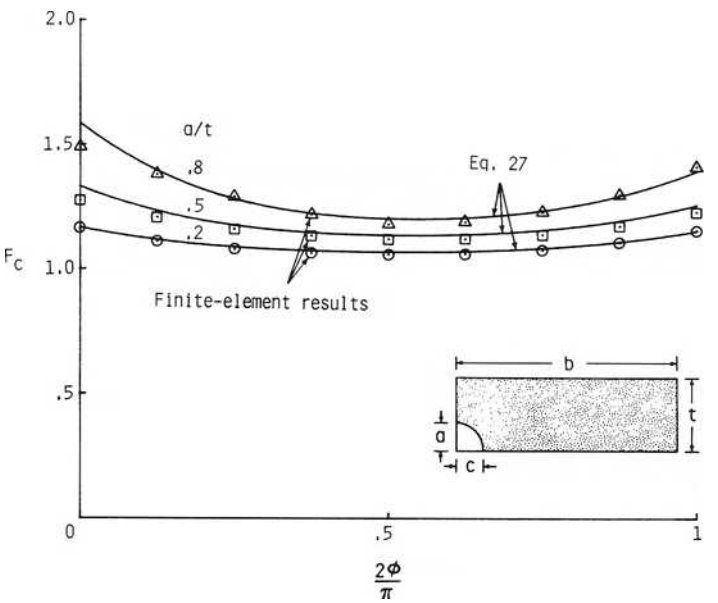

FIG. 7—*Distribution of boundary-correction factors along crack front for quartercircular corner crack (*a/c = *1;* c/b = *0.04).*

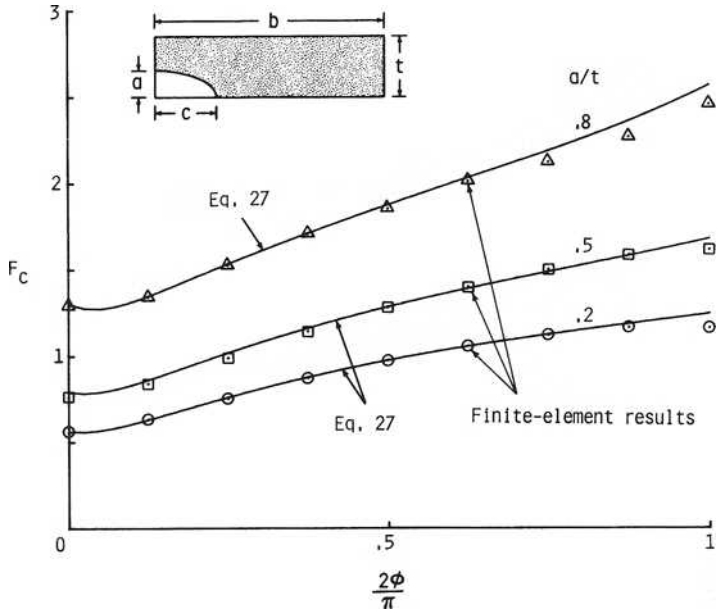

FIG. 8—*Distribution of boundary-correction factors along crack front for quarterelliptic corner crack* (a/c = 0.2; c/b = 0.2).

for $0.2 \leq a/c \leq 2$, $a/t < 1$, $0.5 \leq R/t \leq 2$, $(R + c)/b < 0.5$, and $-\pi/2 \leq \phi \leq \pi/2$. (Note that here t is defined as one half of the full plate thickness.) The function F_{sh} was chosen as

$$F_{sh} = \left[M_1 + M_2\left(\frac{a}{t}\right)^2 + M_3\left(\frac{a}{t}\right)^4\right] g_1 g_2 g_3 f_\phi f_w \tag{39}$$

For $a/c \leq 1$

$$M_1 = 1 \tag{40}$$

$$M_2 = \frac{0.05}{0.11 + \left(\frac{a}{c}\right)^{3/2}} \tag{41}$$

$$M_3 = \frac{0.29}{0.23 + \left(\frac{a}{c}\right)^{3/2}} \tag{42}$$

$$g_1 = 1 - \frac{\left(\frac{a}{t}\right)^4}{1 + 4\left(\frac{a}{c}\right)} \cos\phi \tag{43}$$

$$g_2 = \frac{1 + 0.358\lambda + 1.425\lambda^2 - 1.578\lambda^3 + 2.156\lambda^4}{1 + 0.08\lambda^2} \tag{44}$$

where

$$\lambda = \frac{1}{1 + \frac{c}{R}\cos(0.9\phi)} \tag{45}$$

$$g_3 = 1 + 0.1(1 - \cos\phi)^2\left(1 - \frac{a}{t}\right)^{10} \tag{46}$$

The function f_ϕ is given by Eq 10. (The 10th power in Eq 46 was needed to fit the behavior as a/t approaches zero.) The finite-width correction, f_w, was taken as

$$f_w = \left[\sec\left(\frac{\pi R}{2b}\right)\sec\left(\frac{\pi(2R + nc)}{4(b - c) + 2nc}\sqrt{\frac{a}{t}}\right)\right]^{1/2} \tag{47}$$

where $n = 1$ is for a single crack, $n = 2$ is for two-symmetric cracks, and the hole is located in the center of the plate. This equation was chosen to account for the effects of width on stress concentration at the hole [*20*] and for crack eccentricity [*16*]. For $a/c > 1$

$$M_1 = \sqrt{\frac{c}{a}} \tag{48}$$

The functions M_2, M_3, g_1, g_2, g_3, and λ are given by Eqs 41 through 46, and the functions f_ϕ and f_w are given by Eqs 13 and 47, respectively.

Estimates for a Single-Surface Crack—The stress-intensity factors for a single-surface crack located at the center of a hole can be estimated from the present results for two-symmetric surface cracks by using a conversion factor developed by Shah [*11*]. The relationship between one- and two-surface cracks was given by

$$(K_I)_{\substack{\text{one}\\\text{crack}}} = \sqrt{\frac{\frac{4}{\pi} + \frac{ac}{2tR}}{\frac{4}{\pi} + \frac{ac}{tR}}}\,(K_I)_{\substack{\text{two}\\\text{cracks}}} \tag{49}$$

where K_I for two cracks must be evaluated for an infinite plate ($f_w = 1$) and then the finite-width correction for one crack must be applied. Shah had assumed that the conversion factor was constant for all locations along the crack front, that is, independent of the parametric angle.

Comparison with Another Stress-Intensity Solution—Figure 9 shows a comparison between the present results and those estimated by Shah [*11*] for two-symmetric semicircular ($a/c = 1$) and semielliptical ($a/c = 0.2$) surface cracks emanating from a hole in a plate subjected to tension. The present results (solid symbols) show the distribution of boundary-correction factors, F_{sh}, as a function of the parametric angle. The open symbols show the results estimated by Shah. The proposed equation (solid curves) is in good agreement with the results estimated by Shah, but the equation is about 5 percent higher (based on peak value) than the present results in the midregion for the semielliptic crack. Near the intersection of the crack front with the free surface ($\phi = \pi/2$), the present results show a sharp reduction. As previously mentioned, this reduction is probably due to a boundary-layer effect (see Appendix). However, as mentioned in the Appendix, further mesh refinement in this region caused the stress-intensity factors to be higher very near the intersection point, but lower at the surface. Also, the stress-intensity factors in the interior region $0 \leq 2\phi/\pi < 0.8$ were unaffected by mesh refinement. Therefore, the equation was fitted in the interior region ($2\phi/\pi < 0.8$) only. However, the pro-

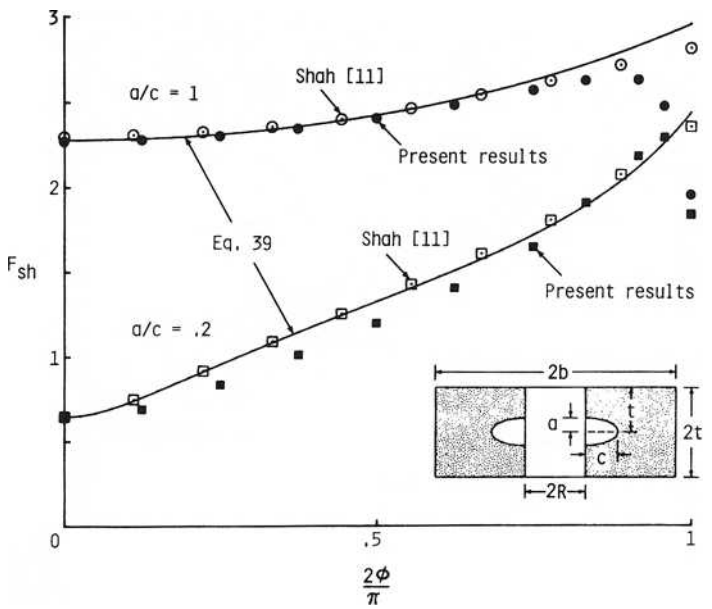

FIG. 9—*Comparison of boundary-correction factors for semielliptical surface cracks at a hole subjected to tension* (R/t = *1;* a/t = *0.2;* R/b < *0.05).*

posed equation, extrapolated to the surface, is probably a good estimate for the limiting behavior due to mesh refinement.

The influence of crack shape (a/c) on the distribution of boundary-correction factors is shown in Fig. 10. The open symbols show the estimated results from Shah [*11*]. The solid symbols show the present finite-element results for $a/c = 2$. The solid curves show the results from the proposed equation for a semielliptical surface crack at a hole with $R/t = 0.5$. The agreements are very good.

Effects of Crack Depth-to-Plate Thickness—Figure 11 shows the distribution of boundary-correction factors, F_{sh}, along the crack front for two-symmetric semicircular surface cracks at a hole ($R/t = 1$) with various a/t ratios. The proposed equation (solid curves) is generally within a few percent of the finite-element results (symbols), except near the intersection of the crack front with the hole surface ($\phi = \pi/2$). Here, again, the proposed equation is expected to give a good estimate for the limiting behavior due to mesh refinement in this region.

Quarterelliptical Corner Crack at a Hole

Two-Symmetric Corner Cracks—The empirical stress-intensity factor equation for two-symmetric quarterelliptical corner cracks at a hole in a finite plate

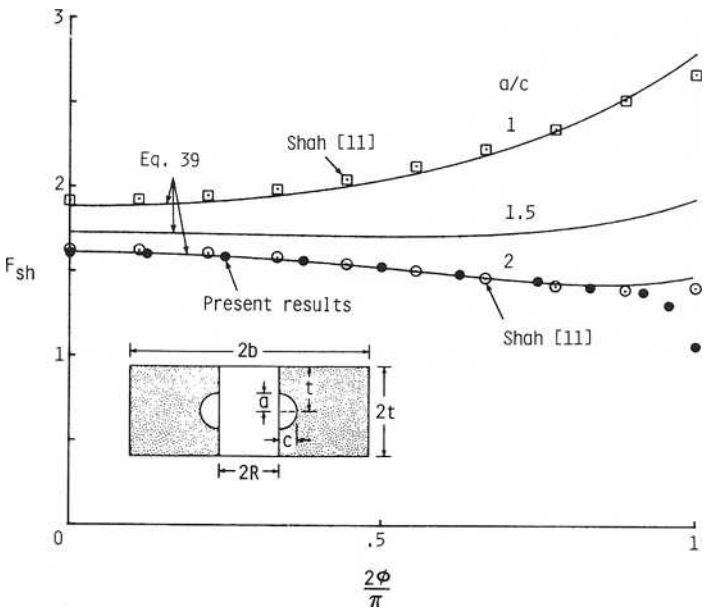

FIG. 10—*Comparison of boundary-correction factors for semielliptical surface cracks at a hole subjected to tension as a function of* a/c *(*R/t = *0.5;* a/t = *0.2;* R/b < *0.1).*

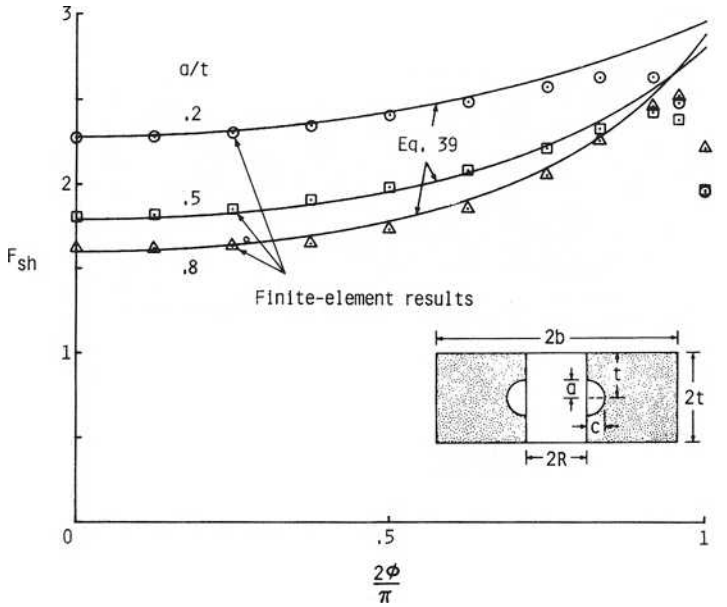

FIG. 11—*Distribution of boundary-correction factors along crack front for semicircular surface cracks at a hole (*R/t = *1;* a/c = *1;* R/b < *0.1).*

(shown in Fig. 2*e*) subjected to tension was obtained by fitting to the finite-element results in Ref *14*. The equation is

$$K_I = S\sqrt{\pi\frac{a}{Q}}\,F_{ch}\left(\frac{a}{c}, \frac{a}{t}, \frac{R}{t}, \frac{R}{b}, \frac{c}{b}, \phi\right) \tag{50}$$

for $0.2 \le a/c \le 2$, $a/t < 1$, $0.5 \le R/t \le 1$, $(R + c)/b < 0.5$, and $0 \le \phi \le \pi/2$. The function F_{ch} was chosen as

$$F_{ch} = \left[M_1 + M_2\left(\frac{a}{t}\right)^2 + M_3\left(\frac{a}{t}\right)^4\right] g_1 g_2 g_3 f_\phi f_w \tag{51}$$

For $a/c \le 1$

$$M_1 = 1.13 - 0.09\left(\frac{a}{c}\right) \tag{52}$$

$$M_2 = -0.54 + \frac{0.89}{0.2 + \frac{a}{c}} \tag{53}$$

$$M_3 = 0.5 - \frac{1}{0.65 + \frac{a}{c}} + 14\left(1 - \frac{a}{c}\right)^{24} \tag{54}$$

$$g_1 = 1 + \left[0.1 + 0.35\left(\frac{a}{t}\right)^2\right](1 - \sin\phi)^2 \tag{55}$$

$$g_2 = \frac{1 + 0.358\lambda + 1.425\lambda^2 - 1.578\lambda^3 + 2.156\lambda^4}{1 + 0.13\lambda^2} \tag{56}$$

where

$$\lambda = \frac{1}{1 + \frac{c}{R}\cos(0.85\phi)} \tag{57}$$

The function g_3 is given by

$$g_3 = \left(1 + 0.04\frac{a}{c}\right)[1 + 0.1(1 - \cos\phi)^2]\left[0.85 + 0.15\left(\frac{a}{t}\right)^{1/4}\right] \tag{58}$$

Functions f_ϕ and f_w are given by Eqs 10 and 47, respectively. For $a/c > 1$

$$M_1 = \sqrt{\frac{c}{a}}\left(1 + 0.04\frac{c}{a}\right) \tag{59}$$

$$M_2 = 0.2\left(\frac{c}{a}\right)^4 \tag{60}$$

$$M_3 = -0.11\left(\frac{c}{a}\right)^4 \tag{61}$$

$$g_1 = 1 + \left[0.1 + 0.35\left(\frac{c}{a}\right)\left(\frac{a}{t}\right)^2\right](1 - \sin\phi)^2 \tag{62}$$

Functions g_2 and λ are given by Eqs 56 and 57. The function g_3 is given by

$$g_3 = \left(1.13 - 0.09\frac{c}{a}\right)[1 + 0.1(1 - \cos\phi)^2]\left[0.85 + 0.15\left(\frac{a}{t}\right)^{1/4}\right] \tag{63}$$

The functions f_ϕ and f_w are given by Eqs 13 and 47, respectively.

Estimates for a Single-Corner Crack—The stress-intensity factors for a single-corner crack at a hole can be estimated from the present results for two-symmetric corner cracks by using the Shah conversion factor (Eq 49). Raju and Newman [*14*] have evaluated the use of the conversion factor for some corner crack-at-a-hole configurations. The stress-intensity factor obtained using the conversion factor were in good agreement with the results from Smith and Kullgren [*12*] for a single-corner crack at a hole.

Effects of Plate Thickness and Crack Shape—Figures 12 and 13 show the distribution of boundary-correction factors, F_{ch}, along the crack front for two-symmetric quarterelliptical corner cracks at a hole. The effects of crack size (a/t) on the distribution are shown in Fig. 12. The finite-element results are shown as symbols and the proposed equation is shown as the solid curves. Again, the equation is in good agreement with the finite-element results, except near $\phi = 0$ and $\pi/2$. Here again the boundary-layer effect [*19*], as mentioned previously, is causing low values of boundary-correction factors. Further mesh refinement in this region is shown in the Appendix to give higher boundary-correction factors near the free surface, but lower values at the surface. Thus, the equation is expected to give a good estimate in these regions.

The effects of crack shape (a/c) on the distribution of boundary-correction factors are shown in Fig. 13. Again, the proposed equation (solid curves) is in

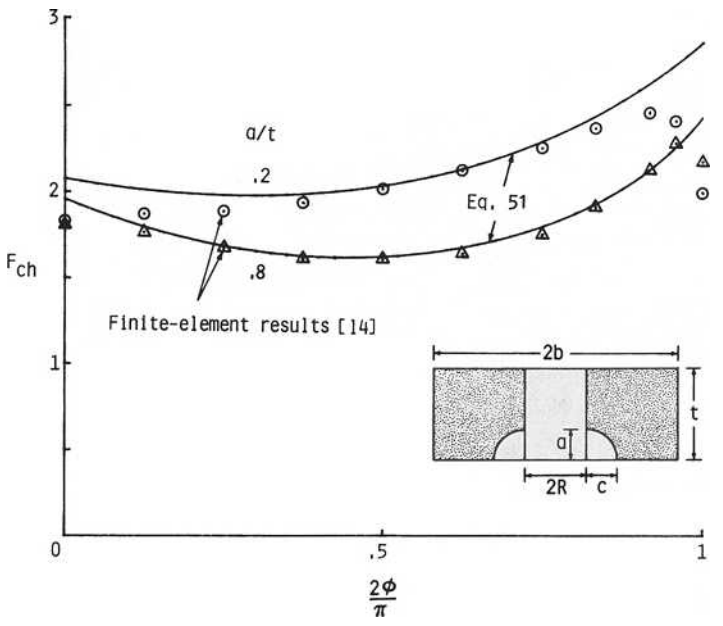

FIG. 12—*Distribution of boundary-correction factors along crack front for quartercircular corner cracks at a hole (*R/t = *0.5;* a/c = *1;* R/b < *0.1).*

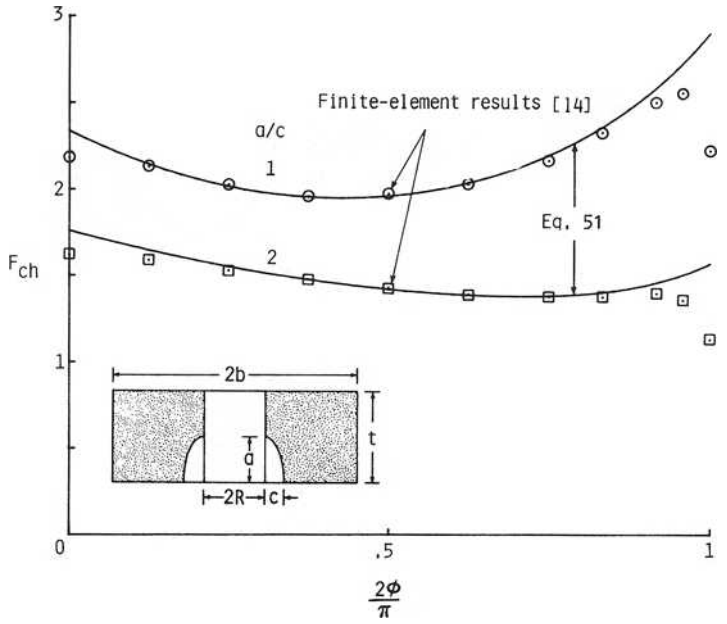

FIG. 13—*Distribution of boundary-correction factors along crack front for quarterelliptical corner cracks at a hole (*R/t = *1;* a/t = *0.8;* R/b < *0.1).*

good agreement with the finite-element results (symbols), except near the intersection points ($\phi = 0$ and $\pi/2$).

In summary, for all combinations of parameters investigated and $a/t \leq 0.8$, the equations were within a few percent of the finite-element results. The maximum error was about 5 percent, except where the crack front intersects a free surface. For $a/t > 0.8$, the accuracy of the equations has not been established because there are no solutions available for comparison. However, their use in that range appears to be supported by estimates based on a part-through crack approaching a through crack. The effects of plate width on stress-intensity variations along the crack front also were included, but generally were based on engineering estimates. Table 5 gives the range of applicability of ϕ, a/t, a/c, R/t, and $(R + c)/b$ for the proposed equations.

Concluding Remarks

Stress-intensity factors from three-dimensional finite-element analyses were used to develop empirical stress-intensity factor equations for a wide variety of crack configurations subjected to remote uniform tension. The following configurations were included: an embedded elliptical crack, a semielliptical surface crack, a quarterelliptical corner crack, a semielliptical surface crack at

TABLE 5—*Range of applicability for stress-intensity factor equations.*

Configuration	Equation	ϕ	a/t	a/c	R/t	$(R + c)/b$
Embedded crack in plate	3	$-\pi$ to π	...[a]	0 to ∞	...	<0.5[b]
Surface crack in plate	16	0 to π	...[a]	0 to 2	...	<0.5[b]
Corner crack in plate	26	0 to $\pi/2$	<1	0.2 to 2	...	<0.2[b]
Surface crack at hole[c]	38	$-\pi/2$ to $\pi/2$	<1	0.2 to 2	0.5 to 2	<0.5
Corner crack at hole[c]	50	0 to $\pi/2$	<1	0.2 to 2	0.5 to 1	<0.5

[a] $a/t < 1.25\,(a/c + 0.6)$.
[b] $R = 0$.
[c] One or two-symmetric cracks.

the center of a hole, and a quarterelliptical corner crack at the edge of a hole in finite plates. The empirical equations cover a wide range of configuration parameters. The ratio of crack depth to plate thickness (a/t) ranged from 0 to 1, the ratio of crack depth to crack length (a/c) ranged from 0.2 to 2, and the ratio of hole radius to plate thickness (R/t) ranged from 0.5 to 2. The effects of plate width (b) on stress-intensity variations along the crack front also were included, but were based on engineering estimates.

For all configurations for which ratios of crack depth to plate thickness do not exceed 0.8, the equations are generally within 5 percent of the finite-element results, except where the crack front intersects a free surface. Here the proposed equations give higher stress-intensity factors than the finite-element results, but these higher values probably represent the limiting behavior as the mesh is refined near the free surface. For ratios greater than 0.8, no solutions are available for direct comparison; however, the equations appear reasonable on the basis of engineering estimates.

The stress-intensity factor equations also were compared with other solutions reported in the literature for some of the configurations investigated. The proposed equations were in good agreement with some of the reported results. For limiting cases, as crack depth-to-plate thickness (a/t) or crack depth-to-crack length (a/c) approach limits, the proposed equations reduce to exact or accepted solutions.

The stress-intensity factor equations presented herein should be useful for correlating and predicting fatigue crack growth rates as well as in computing fracture toughness and fracture loads for these types of crack configurations.

Acknowledgments

The authors thank T. E. Edmunds and A. C. Pickard of Rolls-Royce Limited, Bristol, England for their in-depth review of the equations in this report and for their comments on limiting solutions for small cracks. Their comments led to certain improvements in some of the equations.

APPENDIX

Boundary-Layer Effect on Stress-Intensity Factors

Hartranft and Sih [*19*] proposed that the stress-intensity factors in a very thin "boundary layer" near the intersection of the crack with a free surface drop off rapidly and equal zero at the free surface. To investigate the boundary-layer effect, a semicircular surface crack emanating from a hole was considered. Three different finite-element models were analyzed with 8, 10, and 14 wedges. A wedge is a slice of the finite-element model used to define a layer of elements [*5*]. The width of a wedge is measured by a parametric angle. Larger numbers of wedges result in smaller wedge angles and more degrees of freedom. The 8-wedge model had eight equal wedges ($\Delta\phi = \pi/16$). The other models had nonuniform wedges and were obtained by refining the 8-wedge model near the free surface ($\phi = \pi/2$). The smallest wedge angle for the 10 and 14-wedge models was $\pi/48$ and $\pi/180$, respectively. The stress-intensity factors obtained from the three models are shown in Fig. 14. These results show that the stress intensities near the free surface were affected by mesh refinement. They were higher near the free surface but lower at the surface with smaller wedge angles. However, the stress-intensity distributions in the interior ($2\phi/\pi < 0.8$) were unaffected by mesh refinements.

Further mesh refinements near the free surface should give higher stress intensities near the free surface but lower values at the surface. Thus, the proposed equation (solid curve) is expected to give a good estimate for the limiting behavior due to mesh refinement.

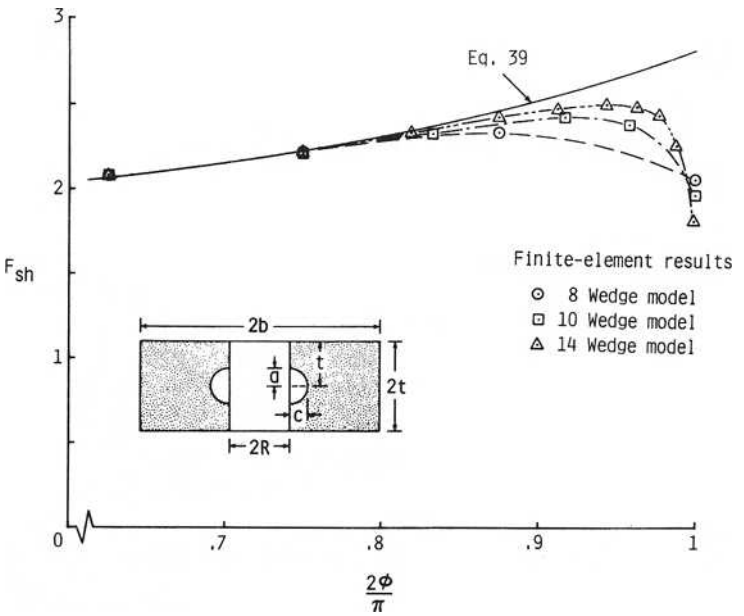

FIG. 14—*Effects of mesh refinement near the free surface on the distribution of boundary-correction factors for surface cracks at a hole* (R/t = *1*; a/c = *1*; a/t = *0.5*; R/b < *0.05*).

References

[1] Irwin, G. R., *Journal of Applied Mechanics, Transactions of the American Society of Mechanical Engineers,* Vol. 29, No. 4, 1962, pp. 651-654.

[2] Green, A. E. and Sneddon, I. N., *Proceedings of the Carbridge Philosophical Society*, Vol. 47, 1950, pp. 159-164.

[3] Smith, F. W., Emery, A. F., and Kobayashi, A. S., *Journal of Applied Mechanics*, Vol. 34, No. 4, *Transactions of the American Society of Mechanical Engineers,* Vol. 89, Series E, Dec. 1967, pp. 953-959.

[4] Kobayashi, A. S., *Proceedings of the Second International Conference on Mechanical Behavior of Materials*, American Society for Metals, 1976, pp. 1073-1077.

[5] Raju, I. S. and Newman, J. C., Jr., *Engineering Fracture Mechanics Journal,* Vol. 11, No. 4, 1979, pp. 817-829; see also NASA TM X-72825, National Aeronautics and Space Administration, Washington, D.C., Aug. 1977.

[6] Newman, J. C., Jr. and Raju, I. S., "Analyses of Surface Cracks in Finite Plates Under Tension or Bending Loads," NASA TP-1578, National Aeronautics and Space Administration, Washington, D.C., Dec. 1979.

[7] Heliot, J., Labbens, R., and Pellissier-Tanon, A., *International Journal of Fracture*, Vol. 15, No.6, Dec. 1979, pp. R197-R202.

[8] Tracey, D. M., *International Journal of Fracture*, Vol. 9, 1973, pp. 340-343.

[9] Pickard, A. C., "Stress Intensity Factors for Cracks with Circular and Elliptic Crack Fronts Determined by 3D Finite Element Methods," PNR-90035, Rolls-Royce Limited, May 1980.

[10] Kobayashi, A. S. and Enetanya, A. N. in *Mechanics of Crack Growth, ASTM STP 590*, American Society for Testing and Materials, 1976, pp. 477-495.

[11] Shah, R. C. in *Mechanics of Crack Growth, ASTM STP 590*, American Society for Testing and Materials, 1976, pp. 429-459.

[12] Smith, F. W. and Kullgren, T. E., "Theoretical and Experimental Analysis of Surface Cracks Emanating from Fastener Holes," AFFDL-TR-76-104, Air Force Flight Dynamics Laboratory, Feb. 1977.

[13] Heckmer, J. L. and Bloom, J. M., "Determination of Stress Intensity Factors for the Corner-Cracked Hole Using the Isoparametric Singularity Element," *International Journal of Fracture*, Oct. 1977.

[14] Raju, I. S. and Newman, J. C., Jr., *Fracture Mechanics (11th Conference), ASTM STP 677*, American Society for Testing and Materials, 1979, pp. 411-430.

[15] Raju, I. S. and Newman, J. C., Jr., Three-Dimensional Finite-Element Analysis of Finite-Thickness Fracture Specimens, NASA TN D-8414, National Aeronautics and Space Administration, Washington, D.C., May 1977.

[16] Tada, H., Paris, P. C., and Irwin, G. R., *The Stress Analysis of Cracks Handbook*, Del Research Corp., 1973.

[17] Gross, B. and Srawley, J. E., "Stress-Intensity Factors for Single-Edge-Notch Specimens in Bending or Combined Bending and Tension by Boundary Collocation of a Stress Function," NASA TN D-2603, National Aeronautics and Space Administration, Washington, D.C., 1965.

[18] Newman, J. C., Jr. and Raju, I. S., *Engineering Fracture Mechanics Journal,* Vol. 15, No. 1, 1981, pp. 185-192.

[19] Hartranft, R. J. and Sih, G. C., *International Journal of Engineering Science*, Vol. 8, No. 8, 1970, pp. 711-729.

[20] Howland, R. C. J., *Philosophical Transactions of the Royal Society of London,* Series A, Vol. 229, Jan. 1930, pp. 49-86.

Surface Cracks

C. W. Smith[1] *and G. C. Kirby*[1]

Stress-Intensity Distributions for Natural Cracks Approaching Benchmark Crack Depths in Remote Uniform Tension

REFERENCE: Smith, C. W. and Kirby, G. C., **"Stress-Intensity Distributions for Natural Cracks Approaching Benchmark Crack Depths in Remote Uniform Tension,"** *Fracture Mechanics: Fourteenth Symposium—Volume I: Theory and Analysis, ASTM STP 791*, J. C. Lewis and G. Sines, Eds., American Society for Testing and Materials, 1983, pp. I-269–I-280.

ABSTRACT: A series of frozen stress photoelastic experiments on large flat plates containing surface cracks was conducted during which cracks were grown to depths approximating those prescribed as benchmark depths in uniform remote tension. Crack shapes and stress-intensity distributions were obtained and compared with analytical results. It was found that (1) cracks grown in uniform remote tension retain their semielliptic shape but exhibit nonself-similar flaw growth, (2) stress-intensity factor (SIF) distributions compare favorably with results from finite element models, and (3) benchmark geometries cannot be obtained from cracks grown under uniaxial loading.

KEY WORDS: stress-intensity factors, surface cracks, photoelastic analysis, three-dimensional crack problems, surface flaws, benchmark geometries, fracture mechanics

It is generally acknowledged that the majority of service failures found in load-carrying components are preceded by a period of subcritical crack growth under cyclic or repeated loading, during which period a subcritical crack is enlarged into one of critical size. Moreover, a substantial percentage of starter cracks occurs at component surfaces because of exposure to a variety of extraneous environmental and mechanical effects. G. R. Irwin, in a classic paper in 1962 [*1*],[2] characterized such a crack in a large body as semielliptic in shape and provided a stress-intensity factor (SIF) distribution for such a shape in a half-space. While such a characterization has been generally accepted by the fracture mechanics community for small cracks in large bodies, this approach

[1] Professor and graduate research assistant, respectively, Department of Engineering Science and Mechanics, Virginia Polytechnic Institute and State University, Blacksburg, Va. 24061.

[2] The italic numbers in brackets refer to the list of references appended to this paper.

has been questioned when cracks grow to dimensions of the order of the body dimensions. In such a case, the problem falls into the three-dimensional (3D) finite, cracked body problem class which has remained intractable to efforts of analysts to provide closed form solutions.

The importance of surface flaws in fracture control rationale has led to a great deal of study such as found in Refs *2, 3,* and *4,* but most of the work has focused upon the semielliptic flaw shape and has implied self-similar crack growth.[3] However, a recent compilation of current data, shown in Fig. 1 [*5–9*], on subcritical surface crack growth in finite thickness plates reveals that, in general, the crack growth is nonself-similar and depends upon the aspect ratio of the starter crack.

Because of the practical importance of the surface crack problem and its resistance to tractability in an analytical sense, the first author of this paper and his colleagues some years ago began to study ways of adapting experimental techniques towards a goal of modelling subcritical crack growth to predict both crack shape and SIF distribution where neither are known *a priori*. The method has evolved from over a decade of laboratory experience and involves a marriage between a modified form of Irwin's near field equations of linear elastic fracture mechanics (LEFM) with the techniques of frozen stress photoelasticity. In modelling 3D crack shapes, however, real cracks are used, and a small, irreversible nonlinear zone always surrounds the crack tip. Conversely (as is well known to photoelasticians), when cracks are simulated with sharp machined notches in which material is removed from the body, the frozen stress process is completely reversible. When real cracks are used, the first author and his colleagues have found that, under certain conditions, the crack shapes produced under monotonic load in the photoelastic models exactly overlay those produced by fatigue loading in geometrically similar metal models [*10–11*].

In a previous publication [*12*], the authors and their colleagues reported on the influence of the deviations of crack shapes from semielliptic shapes upon SIF distributions. However, they were attempting to produce benchmark aspect ratios prescribed by the Battelle Three-Dimensional Fracture Workshop [*13*] and they found it necessary to apply flexural loads to achieve the proper aspect ratios. This led to the conclusion that the aspect ratios recommended by the Battelle Workshop could not be obtained from uniform remote extensional loading. It also left unanswered the question of the degree of deviation from the semielliptic crack shape and self-similar flaw growth that one can expect from purely uniform extensional loading.

The present study utilizes the frozen stress method to assess the extent to which the classic semielliptic flaw shape and SIF distribution is retained as the flaw depths in wide plates are increased from approximately one third to three

[3] That is, crack shape remains semielliptic with same aspect ratio during growth.

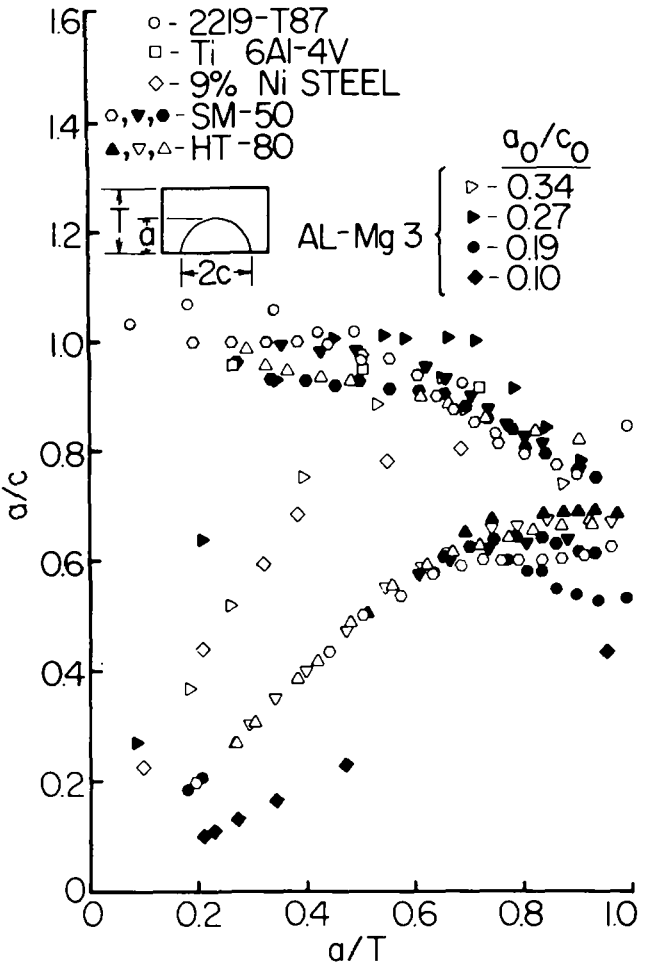

FIG. 1—*Test data on fatigue surface crack growth under uniaxial tension: 2219-T87 [5]; Ni steel [6]; Ti-6Al-4V [7]; SM-50, HT-80 [8]; Al-Mg 3 [9].*

quarters of the plate depth under remote uniform extension. No attempt is made to control the aspect ratio during this flaw growth. Results are compared with the finite element results of Raju and Newman [5] for semielliptic flaws.

Analytical Foundation and Test Procedures

The details of the frozen stress method have been described elsewhere [*14,15*]. Its application to the Mode I problem is briefly restated here for the convenience of the reader.

For the case of Mode I loading, one begins with equations of the form

$$\sigma_{ij} = \frac{K_I}{r^{1/2}} f_{ij}(\theta) + \sigma_{ij}^{o}(r, \theta) \qquad (i, j = n, z) \tag{1}$$

for the stresses in a plane mutually orthogonal to the crack surface and the crack border referred to a set of local rectangular Cartesian coordinates as pictured in Fig. 2, where the terms containing K_I, the SIF, are identical to Irwin's equations for the plane case, and σ_{ij}^{o} represent the contribution of the regular stresses to the stress field in the measurement zone. The σ_{ij}^{o} are normally taken to be constant for a given point along the crack border, but may vary from point to point. Observing that stress fringes tend to spread approximately normal to the crack surface, as shown in Fig. 3, Eq 1 is evaluated along $\theta = \pi/2$ (Fig. 2) and

$$\tau_{max} = 1/2\,[(\sigma_{nn} - \sigma_{zz})^2 + 4\sigma_{nz}^2]^{1/2} \tag{2}$$

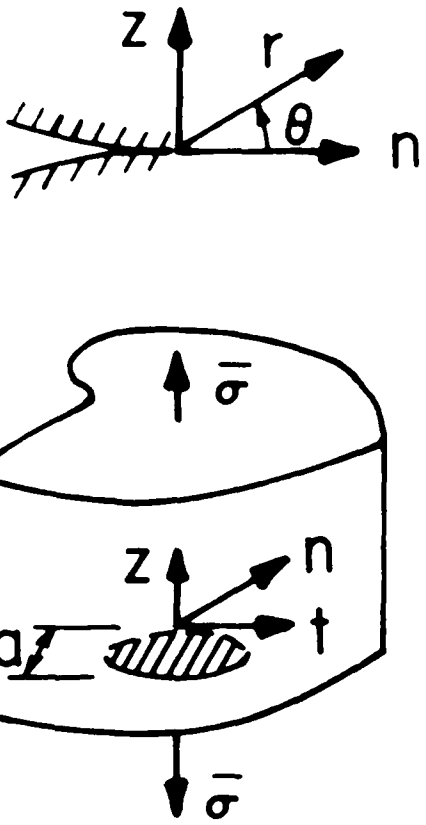

FIG. 2—*General problem notation.*

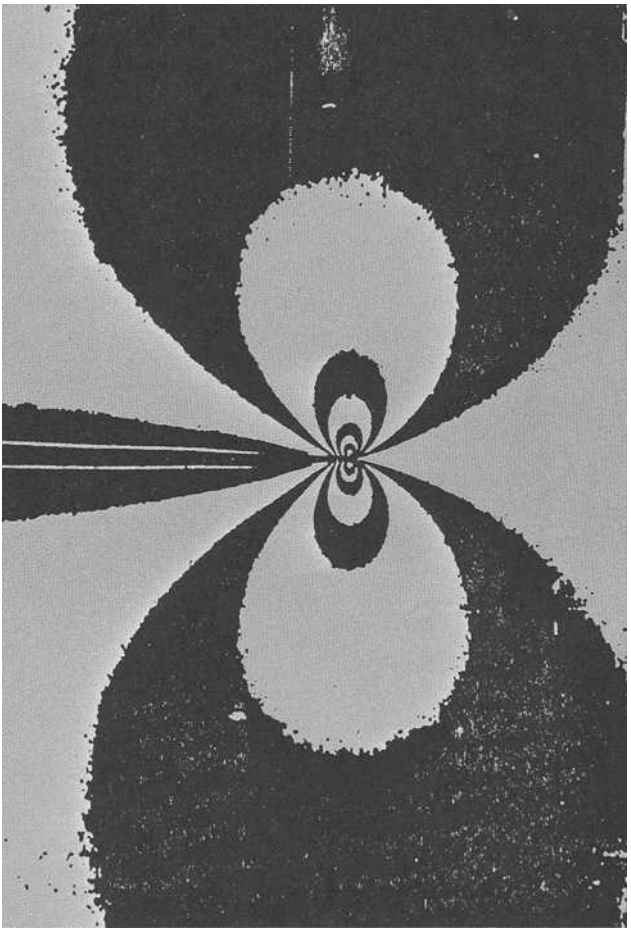

FIG. 3—*Spreading of Mode I isochromatics.*

which, when truncated to the same order as Eq 1, leads to the two-parameter equation

$$\tau_{\max} = \frac{A}{r^{1/2}} + B \quad \text{where } A = K_I/\sqrt{8\pi} \quad \text{and} \quad B = f(\sigma_{ij}^o) \tag{3}$$

which can be rearranged into the normalized form

$$\frac{K_{AP}}{q(\pi a)^{1/2}} = \frac{K_I}{q(\pi a)^{1/2}} + \frac{f(\sigma_{ij}^o)(8)^{1/2}}{q}\left(\frac{r}{a}\right)^{1/2} \tag{4}$$

where $K_{AP} = \tau_{max} (8\pi)^{1/2}$ and, from the Stress-Optic Law, $\tau_{max} = Nf/2t'$ where N is the stress fringe order, f is the material fringe value, t' is the slice thickness in the t direction, q is the remote loading parameter (such as uniform stress, pressure, etc.), and a is the characteristic crack depth. Equation 4 prescribes that, within the zone dominated by Eq 1 with σ_{ij}^{o} as described previously, a linear relation exists between the normalized apparent SIF and the square root of the normalized distance from the crack tip. Thus, one need only locate the linear zone in a set of photoelastic data and extrapolate across a very near field nonlinear zone to the crack tip in order to obtain the SIF. An example of this approach using data from one of the tests described later in this paper is given in Fig. 4.

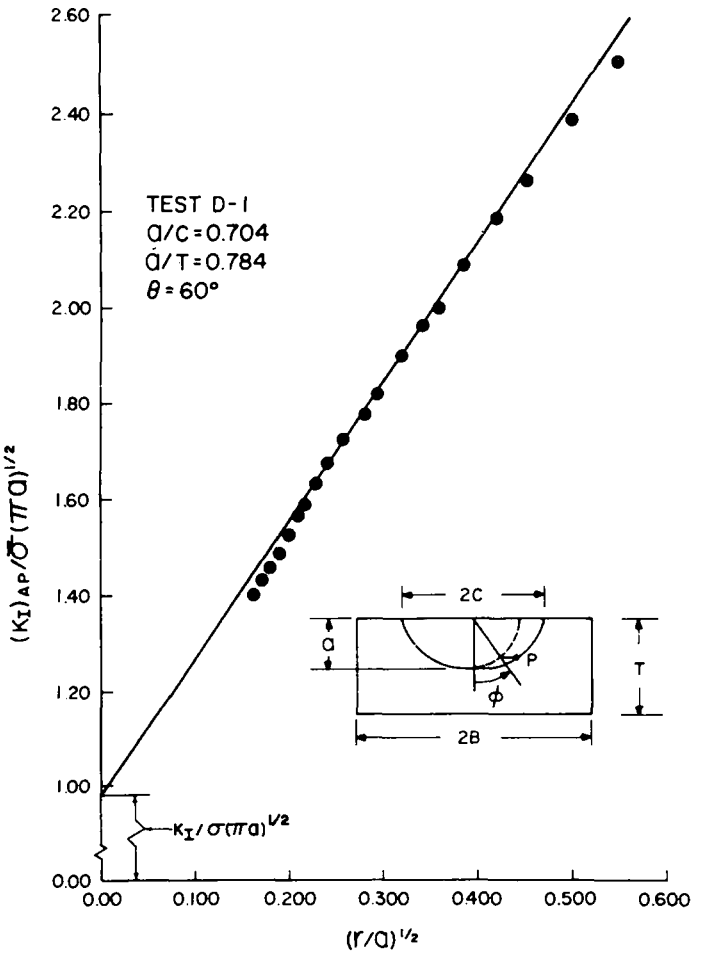

FIG. 4—*Estimation of normalized SIF from optical data.*

In applying the method, starter cracks are inserted at desired locations by striking a sharp blade held normal to the specimen surface, causing a crack to propagate dynamically into the specimen normal to the specimen surface, after which the crack arrests. The cracked model is then placed in an oven in a loading device, heated to critical temperature, and then loaded monotonically until the crack begins to grow. The crack will take the shape dictated by the loads and geometry, and when it reaches the desired size (several times larger than the initial crack), loads are reduced, terminating crack growth. Upon cooling under load, the frozen cracked model containing crack-tip stress fringe and deformation fields is obtained. All slices for analysis are taken parallel to the *nz* plane (Fig. 2), coated with matching index fluid, and analyzed in a crossed circular polariscope with white light, using the Tardy method and reading tint of passage at $\times 10$ magnification.

Experimental Results

Small starter cracks were placed in the center of five wide plates with lengths several times plate width. Crack geometries studied are given in Table 1. Each plate was loaded above critical temperature in remote uniform tension normal to the crack plane through a dead weight system consisting of a row of pins connected to nylon lines through fishing swivels. The moderately shallow and intermediate cracks maintained perfect elliptical shapes throughout their growth. In fact, even the deep crack in Fig. 5 showed only a slight deviation from the semielliptic shape. However, as suggested by Fig. 1, the crack growth was not self-similar (that is, aspect ratios changed during growth).

Using the procedures described in the previous section, SIF values were estimated at intervals along the crack borders for each test. Results are shown in Figs. 6, 7, and 8. Also shown are the results from a 3D finite-element model of the semielliptic crack developed by Newman and Raju [5]. The experimental results reveal a maximum experimental scatter of approximately ± 6 per-

TABLE 1—*Crack geometries.*

Test	$\bar{\sigma}$, MPa	a, mm	c, mm	a/c	a/T	c/B
			Moderately Shallow Flaws			
S-1	0.19	5.33	5.54	0.96	0.39	0.10
S-2	0.24	5.26	5.33	0.99	0.39	0.14
			Intermediate Flaws			
I-1	0.19	8.36	11.46	0.73	0.61	0.32
I-2	0.16	7.67	9.78	0.78	0.62	0.51
			Deep Flaws			
D-1	0.076	11.51	15.62	0.74	0.78	0.21

Note—Conversion factors: 1 psi = 0.006895 MPa; 1 in. = 25.400 mm.

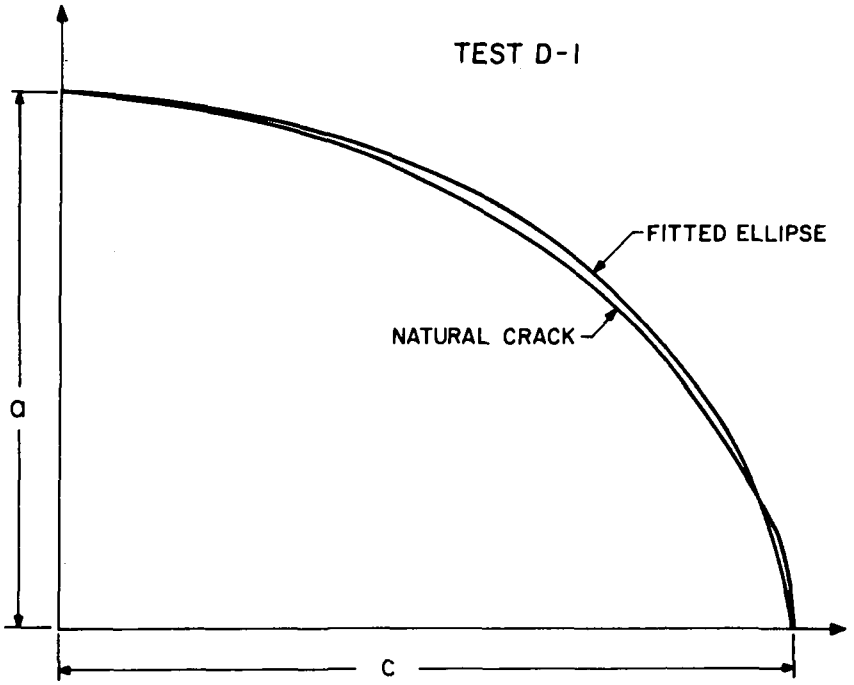

FIG. 5—*Deviation of flaw shape from semiellipse (a/T ≃ 0.80).*

cent. The center of this scatter band appears to lie 5 to 10 percent above the Newman-Raju theory. In this connection, it should be noted that the value of Poisson's ratio (ν) for the photoelastic material above critical temperature is nearly 0.5. By using $\nu = 0.3$ and 0.45 in several surface crack numerical analyses, Newman and Raju have found that the higher value of Poisson's ratio causes an elevation of the SIF by an average of about 6 percent, ranging from 6.7 percent at midcrack to 5.7 percent at the surface, for $a/T = 0.8$ and $a/c = 0.7$. Based upon these estimates, the authors conjecture that most of the elevation of the experimental results above the analytical model results is likely due to the Poisson's ratio effect since Newman and Raju used $\nu = 0.3$. Since virtually no deviation from the semielliptic crack shape was observed in these experiments, we surmise that deviations produced in Ref *12* (and the corresponding changes in SIF distribution) resulted from the flexing operation used to produce the crack shapes prior to tensile loading.

Summary and Conclusions

A series of five photoelastic stress freezing experiments was conducted on wide, long plates containing centrally located natural surface cracks that entered from one side of each plate. Loads were applied through a dead weight

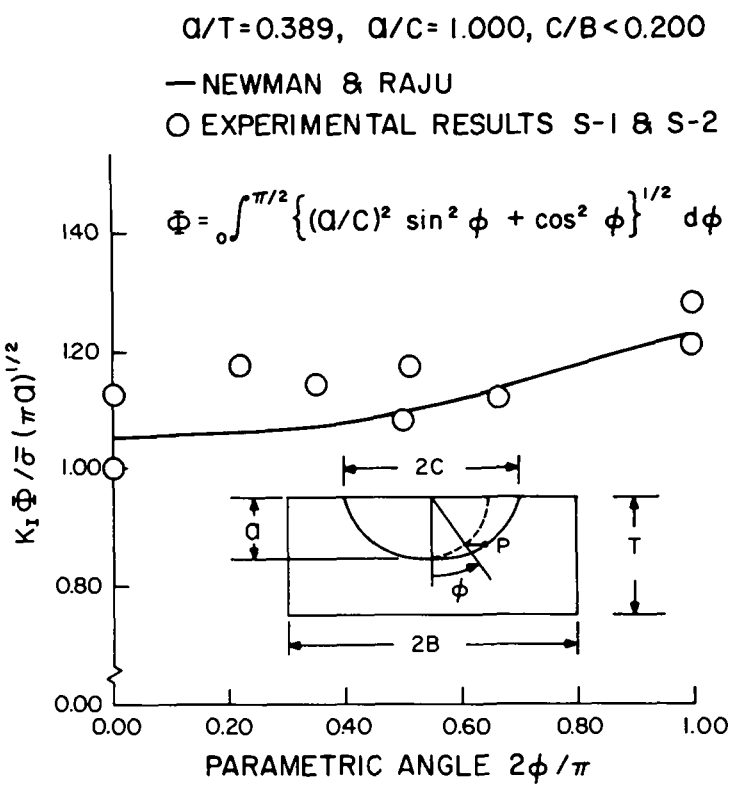

FIG. 6—*Variation of SIF around moderately shallow flaw.*

system to produce a uniform remote uniaxial tension normal to the crack plane. By removing slices mutually orthogonal to the crack plane and the crack border, SIF values were estimated at points along the crack borders after the border shapes were obtained. Results suggest the following conclusions.

1. For uniform remote simple tension on large plates, surface cracks maintain nearly perfect semielliptic shapes up through 75 percent of the plate depth. However, aspect ratios prescribed by the Battelle Benchmark Committee will not be realized by crack growth under uniform tension.

2. Corresponding SIF distributions averaged some 5 to 10 percent higher than those from finite-element elastic models where $\nu = 0.3$ was used. This elevation is probably due to the fact that $\nu \simeq 0.5$ for the photoelastic material above critical temperature.

The experimental method has its own limitations when used to predict subcritical fatigue cracking in metals, as follows:

1. The photoelastic material is elastic (except very near the crack tip) and is incompressible.

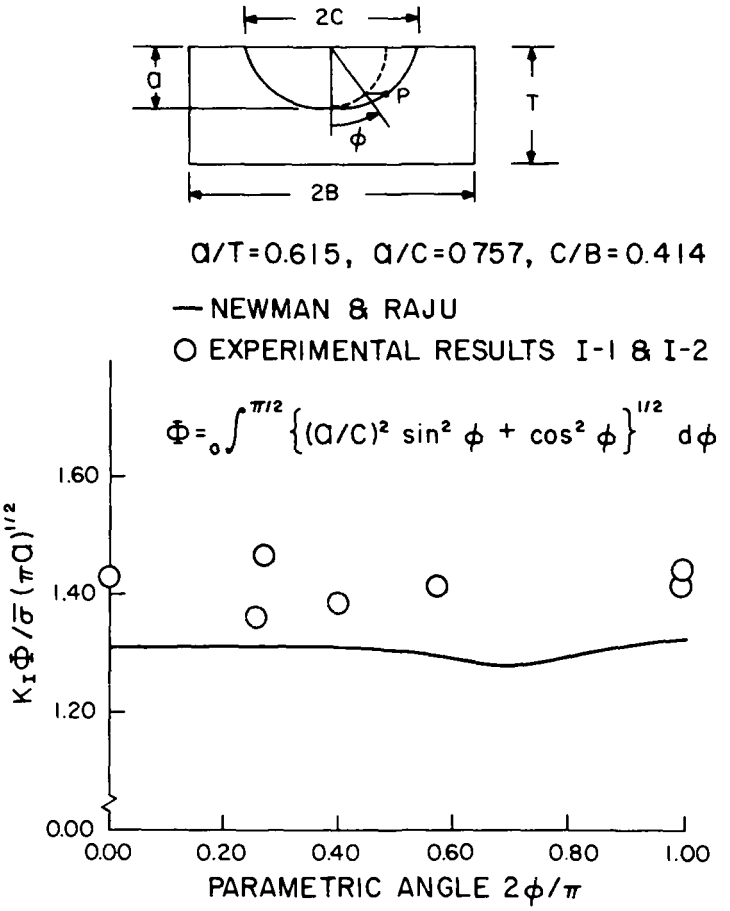

FIG. 7—*Variation of SIF around moderately deep flaw.*

2. Starter crack aspect ratios and model geometry must be the same for photoelastic and metal models.
3. Fatigue loading must be tension-tension.
4. Closure effects must be small.

Despite these limitations, the use of real cracks in frozen stress models offers a window on the geometrical and loading effects upon subcritical crack growth in complex 3D problems and a means of obtaining estimates of both crack shapes and SIF distributions where neither are known *a priori*.

Acknowledgments

The authors wish to acknowledge the significant work of J. C. Newman, Jr. and I. S. Raju, and the joint support of the Virginia Polytechnic Institute and

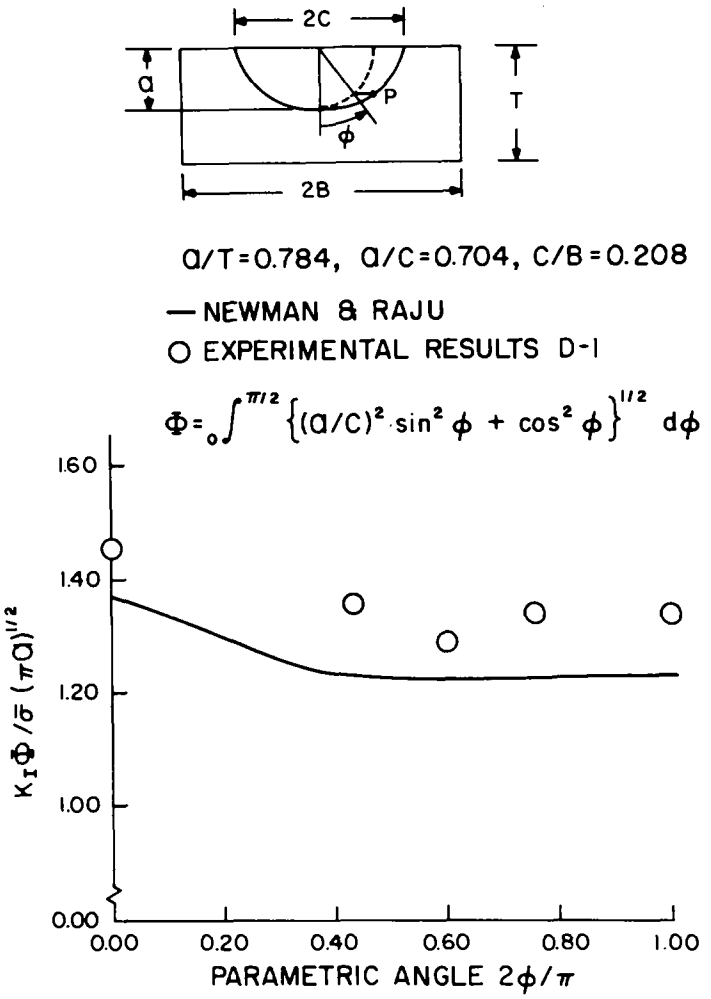

FIG. 8—*Variation of SIF around deep flaw.*

State University Research Division and the National Science Foundation, the latter under Eng. 76-20824-01.

References

[1] Irwin, G. R., *Journal of Applied Mechanics, Transactions of the American Society of Mechanical Engineers*, Series E, Vol. 29, Dec. 1962, pp. 651-654.

[2] Swedlow, J. L., Eds., "The Surface Crack: Physical Problems and Computational Solutions," *Symposium Proceedings*, American Society of Mechanical Engineers Committee for Computing in Applied Mechanics of the Applied Mechanics Division, Nov. 1972.

[3] Chang, J. B., Ed., *Part-Through Crack Fatigue Life Prediction, ASTM STP 687*, American Society for Testing and Materials, 1979.

[4] McGowan, J. J., Ed., *Journal of Experimental Mechanics*, Aug. 1980, pp. 253-264.

[5] Newman, J. C. and Raju, I. S., "Analysis of Surface Cracks in Finite Plates Under Tension or Bending Loads," NASA TP/1578, National Aeronautics and Space Administration, Washington, D.C., Dec. 1979.

[6] Nishioka, K., Hirakawa, K., and Kitaura, I., "Fatigue Crack Propagation of Various Steels," The Sumitomo Search No. 17, pp. 39-55, 1977 (available as ICAF-993).

[7] Hoeppner, D. W., Pettit, D. E., Fedderson, C. E., and Hyler, W. S., "Determination of Flaw Growth Characteristics of Ti-6Al-4V Sheet in the Solution Treated and Aged Condition," NASA CR-65811, National Aeronautics and Space Administration, Washington, D.C., 1965.

[8] Kobayashi, K., Narumoto, A., Tanoka, M., and Funakoshi, T. in *Proceedings of the Third International Conference on Pressure Vessel Technology*, Part II, 1977, pp. 807-814.

[9] Sommer, E., Hodulak, L., and Kordisch, H., *Journal of Pressure Vessel Technology*, Vol. 99, No. 1, 1977, pp. 106-111.

[10] Smith, C. W. and Peters, W. H., *Developments in Theoretical and Applied Mechanics*, Vol. 9, May 1978, pp. 225-234.

[11] Smith, C. W. and Peters, W. H. in *Preprints of the 6th International Conference on Experimental Stress Analysis*, Sept. 1978, pp. 861-864.

[12] Smith, C. W., Peters, W. H., Kirby, G. C., and Andonian, A. in *Fracture Mechanics, ASTM STP 743*, American Society for Testing and Materials, 1981, pp. 422-437.

[13] Hulbert, L. E., Eds., *Proceedings of a Workshop on Three-Dimensional Fracture Analysis*, Battelle-Columbus Laboratories, Ohio, Sept. 1976.

[14] Smith, C. W., *Fracture Mechanics and Technology*, G. C. Sih and C. L. Chow, Eds., Sijthoff and Noordhoff, Alphen aan den Rijn, The Netherlands, Vol. 1, 1979, pp. 591-605.

[15] Smith, C. W. in *Mechanics of Fracture*, Vol. 7, Martinus Nijhoff Publishers, 1981, pp. 163- 188.

E. Y. Lim,[1] *D. D. Dedhia,*[2] *and D. O. Harris*[1]

Approximate Influence Functions for Part-Circumferential Interior Surface Cracks in Pipes

REFERENCE: Lim, E. Y., Dedhia, D. D., and Harris, D. O., **"Approximate Influence Functions for Part-Circumferential Interior Surface Cracks in Pipes,"** *Fracture Mechanics: Fourteenth Symposium—Volume I: Theory and Analysis, ASTM STP 791*, J. C. Lewis and G. Sines, Eds., American Society for Testing and Materials, 1983, pp. I-281-I-296.

ABSTRACT: Approximate influence functions are presented for a part-circumferential semielliptical interior surface crack in a circular pipe. The influence functions are derived from the crack surface opening displacements obtained by the use of boundary integral equation techniques. Such functions are useful in evaluating stress-intensity factors for cracks in bodies subjected to complex stress conditions, and convenient curve fits suitable for numerical calculations are provided. The stress intensities are obtainable for arbitrary stresses by numerical integration techniques. Comparisons with existing solutions indicate that the influence functions provide results of suitable accuracy for engineering purposes. The results indicate that the stress-intensity factor is not strongly dependent on the parameter R_i/h or on whether the crack is longitudinal or circumferential. Details of the variation of K along the crack front are not obtainable from the influence functions, only "root-mean-square (RMS)-averaged" values are generated. However, such values are useful in the analysis of the growth of semielliptical cracks, and the results presented should be of wide use in the analysis of such cracks under complex stress conditions.

KEY WORDS: cracks, stress-intensity factors, influence functions, pipes, fracture mechanics

Nomenclature

- a Maximum crack depth
- a_j Length of crack in j direction
- A Crack area
- b Half surface length of crack
- F A parameter in curve fit of g_2

[1]Division managers, Science Applications, Inc., Palo Alto, Calif. 94304.
[2]Materials scientist, Science Applications, Inc., Sunnyvale, Calif., 94086.

g_1 A function in influence function formulation
g_2 A function in influence function formulation
h Pipe wall thickness
h_a Influence function associated with depth direction ($\bar{K}_a$)
h_b Influence function associated with length direction ($\bar{K}_b$)
H Equals $E/(1 - \nu^2)$; E = Young's modulus, ν = Poisson's ratio
$\bar{K}_a$ RMS-averaged stress-intensity factor associated with depth direction
$\bar{K}_b$ RMS-averaged stress-intensity factor associated with length direction
R_i Inside radius of pipe
S Equals $[(x/a)^2 + (y/b)^2]^{1/2}$
U Strain energy in cracked stressed body
w Crack surface opening displacement
x Spatial coordinate into pipe wall
y Spatial coordinate in crack plane and normal to x
α Equals a/h
β Equals b/a
γ Equals R_i/h
ΔA_a Incremental change in crack area for a crack growing only in a direction
ΔA_b Incremental change in crack area for a crack growing only in b direction
ζ Equals $1/\beta$
ξ Equals $[1 - (x/a)^2 - (y/b)^2]$
σ Normal stress on crack plane
ϕ Elliptical angle along crack front (equals 0 at point of maximum crack depth)
Φ Complete elliptic integral of the second kind
ψ Equals $1 - (2/\pi) \tan^{-1} (y/b)/(x/a)$

Stress-intensity factor solutions for semielliptical surface cracks in cylindrical bodies are useful in the analysis of crack growth. Considerable information on stress intensities (K) for such surface cracks is available, with selected examples supplied in Refs *1* to *5*.[3] However, if information on part-circumferential cracks is desired, current K solutions suffer from one or more of the following deficiencies: applicable only to flat plates or longitudinal cracks; applicable only for selected crack depths and lengths; applicable only for uniform stress; or applicable only at point of maximum crack penetration.

In order to overcome these deficiencies, and to provide a general K solution for part-circumferential cracks, approximate influence (or weight) functions [*6*] were determined for this crack geometry. The purpose of this paper is to present the results obtained, along with some closely related results that were generated in the process. Part-circumferential cracks are of interest, be-

[3]The italic numbers in brackets refer to the list of references appended to this paper.

cause most piping welds are circumferential, and cracks tend to be concentrated in and grow in welds.

The developed influence functions are not capable of providing complete information on the variation of the stress-intensity factor along the crack front in the case of three-dimensional problems. Only "root-mean-square (RMS)-averaged" values of K are provided. However, such averaged values are suitable for analysis of subcritical crack growth [*7–9*] and therefore provide sufficient information for many purposes. The influence functions are determined from the crack surface opening displacement for an arbitrary stress. In the case of part-circumferential surface cracks, numerical techniques must be utilized. Hence, detailed information on crack surface opening displacements for a given stress is generated as part of the calculations.

The numerical results for the crack surface opening displacement were generated by boundary integral equation (BIE) techniques [*10–13*] for uniform normal stress on the crack plane. This also provides the variation of K along the crack front for this stress system. K was evaluated for both circumferential and longitudinal cracks in order to allow comparisons with previous solutions. The crack surface opening displacements for part-circumferential cracks then were used to determine approximate influence functions for this geometry, and a convenient curve fit is provided. Additional comparisons with selected earlier results are presented which indicate that the influence functions provide suitably accurate results that are applicable to a wide variety of crack sizes subjected to arbitrary stresses.

Review of Influence Functions

The theory of influence functions for cracks in three-dimensional bodies has been covered elsewhere [*6, 14–16*] and will be reviewed only briefly here. The part-circumferential crack geometry shown in Fig. 1 will be analyzed, with attention on the case of symmetry with respect to the line AB. Such a crack is said to possess "two-degrees-of-freedom" associated with growth in the depth (a) and length (b) directions. In this case, the following equations apply

$$\bar{K}_a = \int_A h_a(x, y, a, b)\sigma(x, y)dA \tag{1}$$

$$\bar{K}_b = \int_A h_b(x, y, a, b)\sigma(x, y)dA \tag{2}$$

h_a and h_b are the influence functions associated with growth in the depth and length directions, respectively. The RMS-averaged stress intensities are related to the local value of K through the relationships

$$\bar{K}_a^2 = \frac{1}{\Delta A_a} \int_0^{\pi/2} K^2(\phi) d[\Delta A_a(\phi)] \tag{3}$$

$$\bar{K}_b^2 = \frac{1}{\Delta A_b} \int_0^{\pi/2} K^2(\phi) d[\Delta A_b(\phi)] \tag{4}$$

The parameters $\Delta A_a(\phi)$ and $\Delta A_b(\phi)$ are associated with incremental area changes for cracks growing only in the depth and length directions, respectively [*6, 7, 14-17*]. Equations 1 to 4 can be summarized conveniently as follows

$$\bar{K}_j = \int_A h_j(x, y, a, b)\sigma(x, y)dA$$

$$= \left[\frac{1}{\Delta A_j} \int_0^{\pi/2} K^2(\phi) d[\Delta A_j(\phi)] \right]^{1/2} \tag{5}$$

Following the development of Cruse and Besuner [*7, 14, 16*], the influence function h_j is given by

$$h_j = \frac{\partial w}{\partial a_j} \Big/ \left[\frac{1}{H} \frac{\partial A}{\partial a_j} \frac{\partial U}{\partial a_j} \right]^{1/2} \tag{6}$$

where $a_1 = a$ and $a_2 = b$. h_j can be evaluated from numerical solutions for crack surface displacements for a reference stress system. In order to mini-

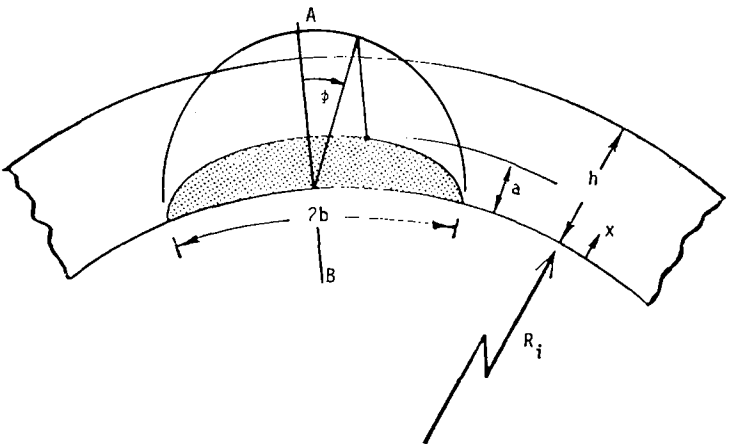

FIG. 1—*Geometry of part-circumferential internal surface crack considered in this investigation.*

mize errors in development of the desired influence functions, the known influence function for an embedded elliptical crack in an infinite body will be utilized, with "corrections" made to account for the free surfaces of the pipe.

Consider the following four solutions to the elliptical crack.

	Crack Surface Displacement	Strain Energy	Influence Function
Exact solution for embedded crack	w^*	U^*	h_j^*
Numerical solution for embedded crack	$\hat{w}$	$\hat{U}$	...
Numerical solution for surface crack	$\tilde{w}$	$\tilde{U}$	...
Exact solution for surface crack	w	U	h_j

In these solutions, w^* and U^* are known, and w and U are the desired end result. The following are assumed to hold

$$\frac{U}{U^*} = \frac{\tilde{U}}{\hat{U}} \equiv g_1(a, b) \tag{7}$$

$$\frac{w}{w^*} = \frac{\tilde{w}}{\hat{w}} \equiv g_2(a, b, x, y) \tag{8}$$

The functions g_1 and g_2 are obtained from numerical results for the part-circumferential surface crack and embedded crack with same a and b (but in an infinite body). Once g_1 and g_2 are known, Eq 7 and 8 can be substituted into Eq 6 to provide the following end result

$$h_j = h_j^* \left[g_2 + w^* \frac{\partial g_2}{\partial a_j} \Big/ \frac{\partial w^*}{\partial a_j} \right] \Big/ \left[g_1 + U^* \frac{\partial g_1}{\partial a_j} \Big/ \frac{\partial U^*}{\partial a_j} \right]^{1/2} \tag{9}$$

Hence, the desired approximate influence function is known once the functions g_1 and g_2 are evaluated. For the sake of completeness, the following closed-form results for the embedded crack are included [*14,16,17*]

$$w^* = \frac{2\sigma a}{H\Phi} \xi^{1/2} \tag{10}$$

$$U^* = \frac{4\pi\sigma^2 a^2 b}{3H\Phi} \tag{11}$$

uniform stress

$$h_a^* = \frac{\left[\frac{1}{a} - \frac{1}{\Phi} \frac{\partial \Phi}{\partial a} + \frac{x^2}{a^3 \xi} \right] \xi^{1/2}}{\pi b \left[\frac{1}{3} \Phi \left(\frac{2}{a} - \frac{1}{\Phi} \frac{\partial \Phi}{\partial a} \right) \right]^{1/2}} \tag{12}$$

$$h_b^* = \frac{\left[-\frac{1}{\Phi}\frac{\partial \Phi}{\partial b} + \frac{y^2}{b^3 \xi}\right]\xi^{1/2}}{\pi\left[\frac{ab}{3}\Phi\left(\frac{1}{b} - \frac{1}{\Phi}\frac{\partial \Phi}{\partial b}\right)\right]^{1/2}} \tag{13}$$

Φ is the complete elliptic integral of the second kind, which is defined as follows

$$\Phi(a/b) \equiv \int_0^{\pi/2}\left[1 - \left(1 - \frac{a^2}{b^2}\right)\sin^2\theta\right]^{1/2} d\theta \tag{14}$$

A convenient approximation of Φ is

$$\Phi(a/b) \sim \left[1 + 1.464\left(\frac{a}{b}\right)^{1.65}\right]^{1/2} \tag{15}$$

This approximation is good for $a < b$, and is accurate to within 0.13 percent for a/b between 0 and 1.

Approximate Influence Functions and Related Results

Crack surface opening displacements for the geometry of interest are required to obtain the desired influence functions. The necessary numerical results were generated by use of the BIE technique [*10-13*]. Cracks with $\alpha = a/h = 0.25$, 0.4, 0.5, 0.6, 0.8, and $\beta = b/a = 1$ to 6 were analyzed. A uniform stress on the crack plane was considered, and the variations of K along the crack front were determined from the opening displacements along the row of nodes in the BIE mesh closest to the crack front [*17*]. The distance between this row and the crack front was $a/10$. Typically, about 120 nodes and 360 degrees-of-freedom were employed. Reference *17* provides additional details, including information on the BIE mesh employed.

In order for the generated results to be comparable to previous solutions, longitudinal cracks were analyzed first. Figure 2 shows typical results for the variation of K along the crack front, and provides comparisons with previous work [*2,3*]. Good agreement is observed in this figure. Calculations were then performed for part-circumferential cracks, with Fig. 3 presenting typical results. This figure shows that the variation of K along the crack front does not depend strongly on the crack orientation or value of R_i/h. These points are discussed in detail in Ref *17*. Additionally, the magnitudes of K for longitudinal and part-circumferential cracks were observed to be nearly the same [*17*], thereby indicating that crack orientation does not have a strong influence for the range of semielliptical crack sizes considered.

The values of $\bar{K}_a$ and $\bar{K}_b$ for uniform stress on a part-circumferential crack were evaluated from the known $K(\phi)$ by use of Eqs 3 and 4. The results are

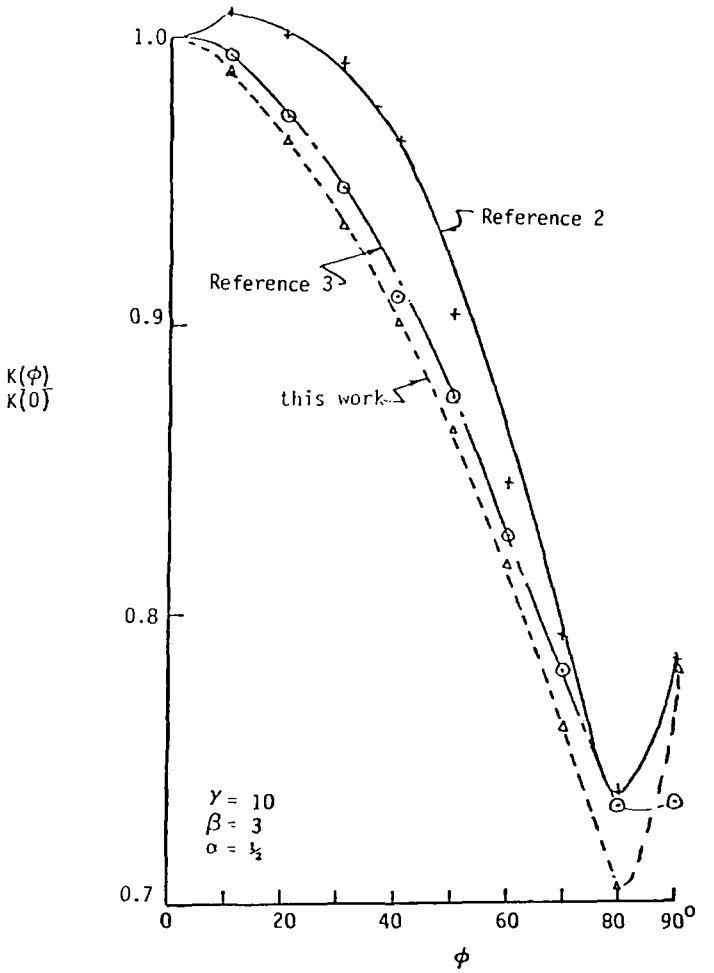

FIG. 2—*Comparison of normalized variation of* K *along crack front of semielliptical interior surface longitudinal crack in a pipe.*

presented as data points in Figs. 4 and 5. Also shown in Figs. 4 and 5 are the results of a polynomial curve fit. In addition to the indicated data points, values of $\bar{K}_a$ and $\bar{K}_b$ for an embedded crack in an infinite body were used as additional data points for $\alpha = 0.01$ in the curve fit. This improves the fit by providing additional data for small α. The use of embedded crack results should produce errors no larger than 12 percent, which is an accuracy consistent with other sources of error in this work. The curve fit for uniform stress is included in the Appendix, and is felt to be of suitable accuracy for $\alpha = 0$ to 0.8 and $\beta = 1$ to 6. The curve fit should be fairly accurate as α exceeds 0.8, because the $(1 - \alpha)^{-1/2}$ singularity for a centrally located circular crack ap-

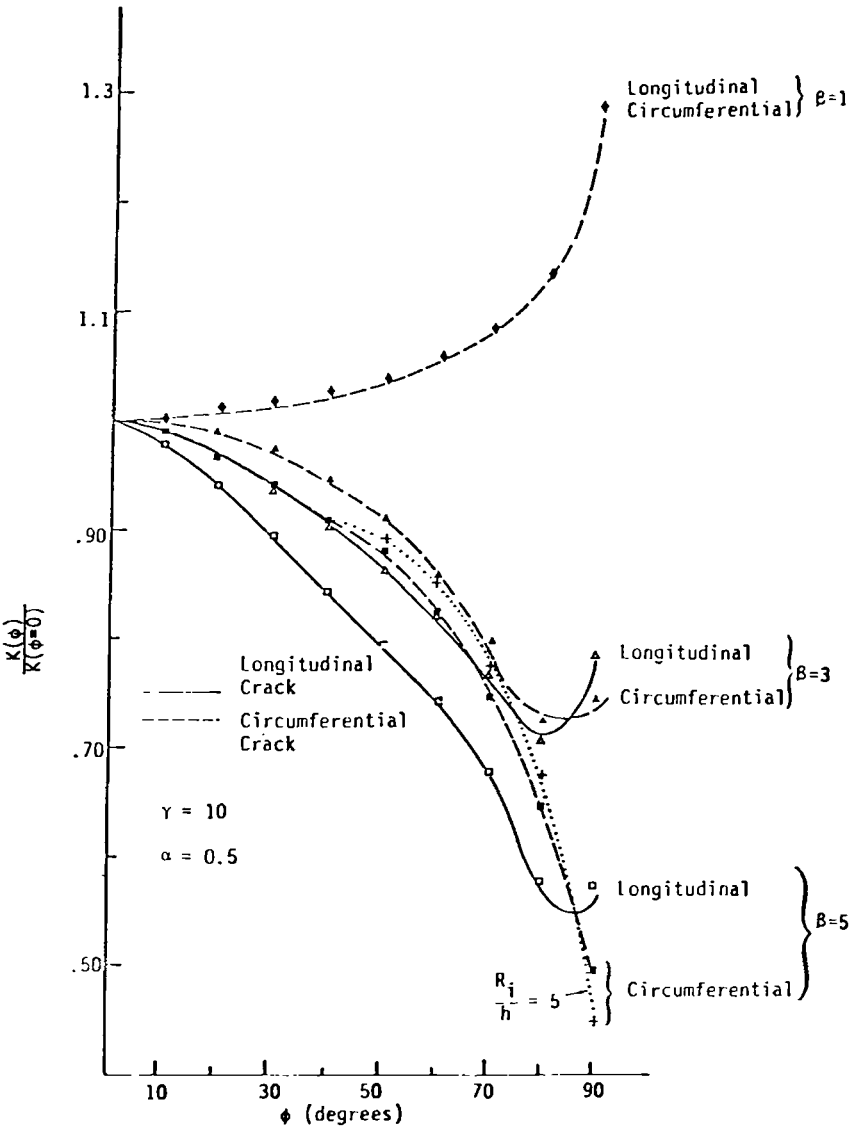

FIG. 3—*Normalized variation of* K *along the crack front for various longitudinal and circumferential semielliptical cracks in pipes as obtained by BIE calculations.*

proaching the outside surface of a circular cylindrical bar [*18*] has been incorporated into the curve fit. K for a complete circumferential crack [*19,20*] also is included in Fig. 4, which shows that K for the part-circumferential crack is always considerably below the corresponding complete circumferential crack.

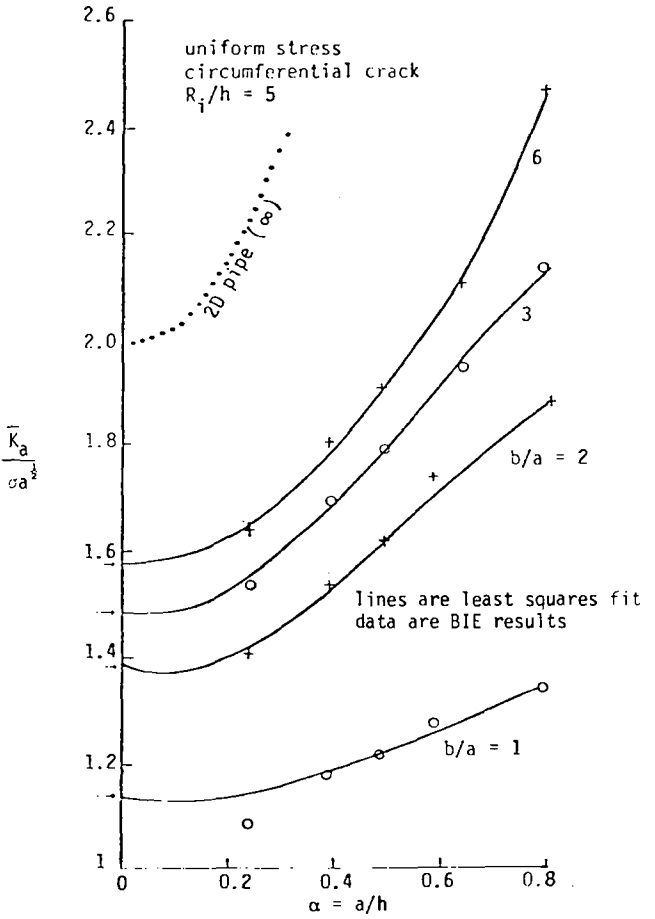

FIG. 4—$\bar{K}_a/\sigma a^{1/2}$ *for a part-circumferential crack in a pipe with uniform stress in the pipe wall.*

The functions g_1 and g_2 in Eqs 7 and 8 then were evaluated from numerical results for the crack surface opening displacements at nodal points of the BIE mesh. The strain energy, $\tilde{U}$, was evaluated from the relation

$$\tilde{U}(a, b) = \tfrac{1}{2}\sigma \int_A \tilde{w}(x, y, a, b)\, dxdy \tag{16}$$

A linear least squares regression analysis was performed for g_1, and the resulting curve fit, which is most accurate for $\alpha < 0.8$ and $\beta = 1$ to 6, is included in the Appendix.

The function g_2 depends on four independent variables. Besuner's [*16*]

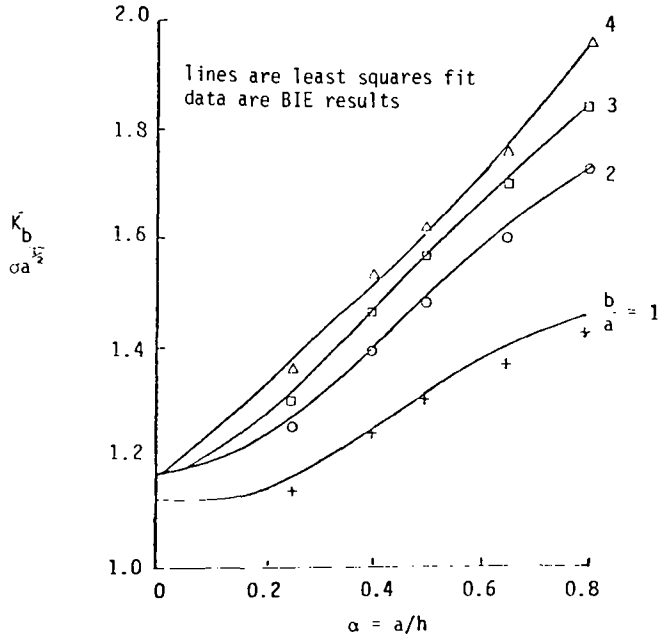

FIG. 5—$\bar{K}_b/\sigma a^{1/2}$ *for a part-circumferential crack in a pipe with uniform stress in the pipe wall.*

formulation for a semielliptical surface crack in a half-space was modified to account for the finite thickness, and the resulting curve fit is included in the Appendix.

The functions g_1 and g_2 now are defined. This, in turn, defines the desired approximate influence functions by use of Eq 9 in conjunction with Eqs 10 to 13. Figure 2 indicates that the BIE calculations of $K(\phi)$ were of suitable accuracy. However, this comparison does not check the accuracy of g_1 and g_2. Such checks will be provided in the following section.

Additional Comparisons

Results presented earlier and additional discussions in Refs *17* and *20* suggest that the values of K determined from the BIE calculations are of reasonable accuracy. However, they do not provide a check on the suitability of the curve fits for g_1 and g_2. Such checks can be made in two ways: (1) using Eqs 1 and 2 to generate $\bar{K}_a$ and $\bar{K}_b$ for uniform stress and comparing the results with Figs. 4 and 5; and (2) using previous results for power law stresses from Refs *2* and *3* in conjunction with Eqs 3 and 4 and comparing the results with those generated for corresponding stress systems by use of the approximate influence functions in Eqs 1 and 2.

Numerical integration over semielliptical crack areas is required, and the functions h_i and h_i^* are singular at the crack front. Reference *17* presents an efficient scheme for integrating over semielliptical areas functions with the known type of singularity. Checks of the integration scheme demonstrate it to be highly accurate [*17*].

Comparisons of results for uniform stress obtained by different means are presented in Figs. 6 and 7. The agreement between the two sets of results is seen to be best for deeper cracks of small aspect ratio.

Figures 8 and 9 present comparisons with Heliot's results [*2*] for power law stresses on longitudinal cracks in pipes with R_i/h of 10. Good agreement is observed, which indicates the suitable accuracy of the approximate influence functions. Figures 8 and 9 compare longitudinal cracks with $R_i/h = 10$ to circumferential cracks with $R_i/h = 5$. However, as discussed previously and in Ref *17*, these variables do not have a strong influence on K. Hence, the comparisons of Figs. 8 and 9 are felt to provide strong evidence of the accuracy of the influence functions.

The major usefulness of the approximate influence functions is in the analysis of crack growth under complex stress conditions, such as thermal or

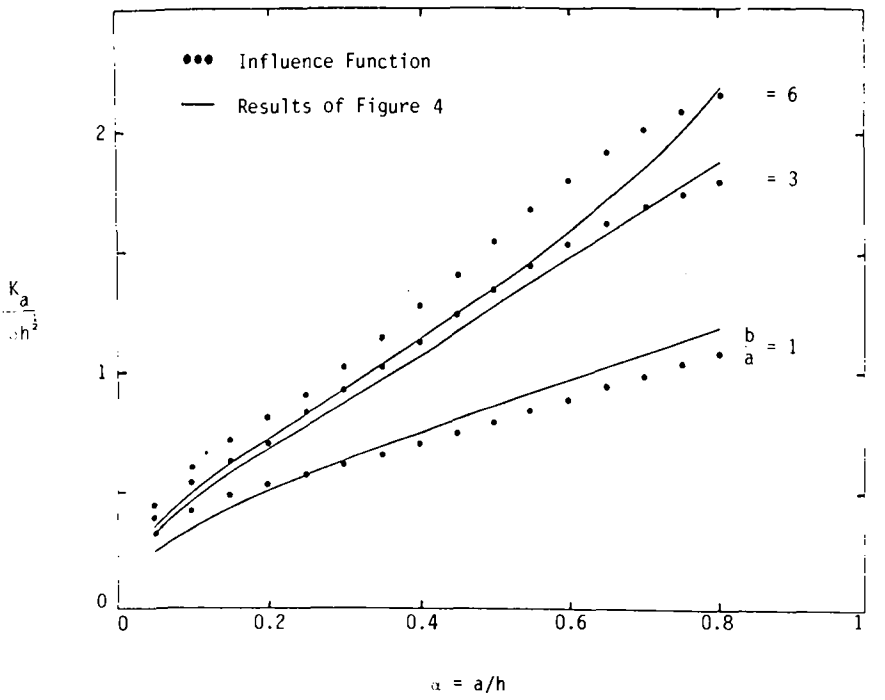

FIG. 6—*Comparison of* $\bar{K}_a$ *for part-circumferential crack in a pipe with uniform stress in the pipe wall as determined by two means. The lines are for results directly from BIE calculations (Fig. 4). Data points are obtained by use of* h_a *and Eq 1.*

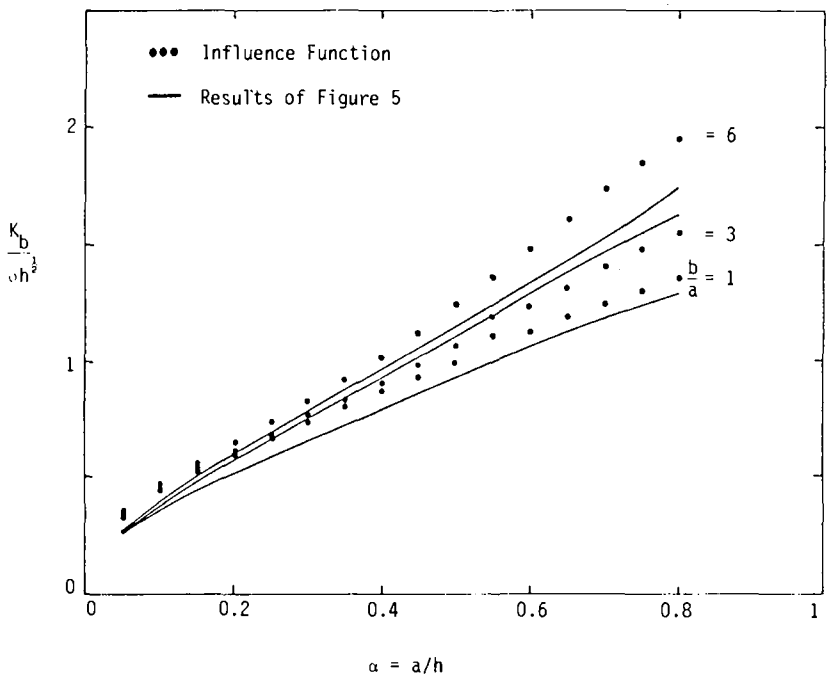

FIG. 7—*Comparison of* $\bar{K}_b$ *for part-circumferential crack in a pipe with uniform stress in the pipe wall as determined by two means. The lines are for results directly from BIE calculations (Fig. 5). Data points are obtained by use of* h_b *in Eq 2.*

residual stresses. In such cases of strong thickness gradients of the stresses, the influence functions can easily and economically provide stress-intensity factors that are of sufficient accuracy for engineering purposes. This circumvents the need to perform numerical calculations for each of the complex stress systems of interest. Applications of the influence functions to analysis of fatigue crack growth in the presence of thermal stresses are presented in Refs *17* and *21*. Reference *22* discusses their application to the analysis of the influence of welding residual stresses on the growth of stress-corrosion cracks.

Summary and Conclusions

Approximate influence functions are presented for part-circumferential semielliptical cracks located at the inside surface of a pipe. These influence functions were derived from numerical calculations based on boundary integral equations. Convenient curve fits of the results are presented. Comparisons with previous solutions indicate the results are of suitable accuracy for engineering purposes. The following additional conclusions can be drawn:

1. The variation of the stress-intensity factor with position on the crack front is not strongly dependent on the crack orientation (that is, longitudinal versus circumferential).
2. The magnitude of K is not strongly dependent on the crack orientation.
3. The value of K is only weakly dependent on R_i/h, for the range considered in this work ($R_i/h = 5$ to 10). (Additional results in Ref *17* indicate that this conclusion can be extended to the range $R_i/h > 5$).

The approximate influence functions should be useful in a wide variety of analyses of the behavior of semielliptical cracks growing under complex stress conditions.

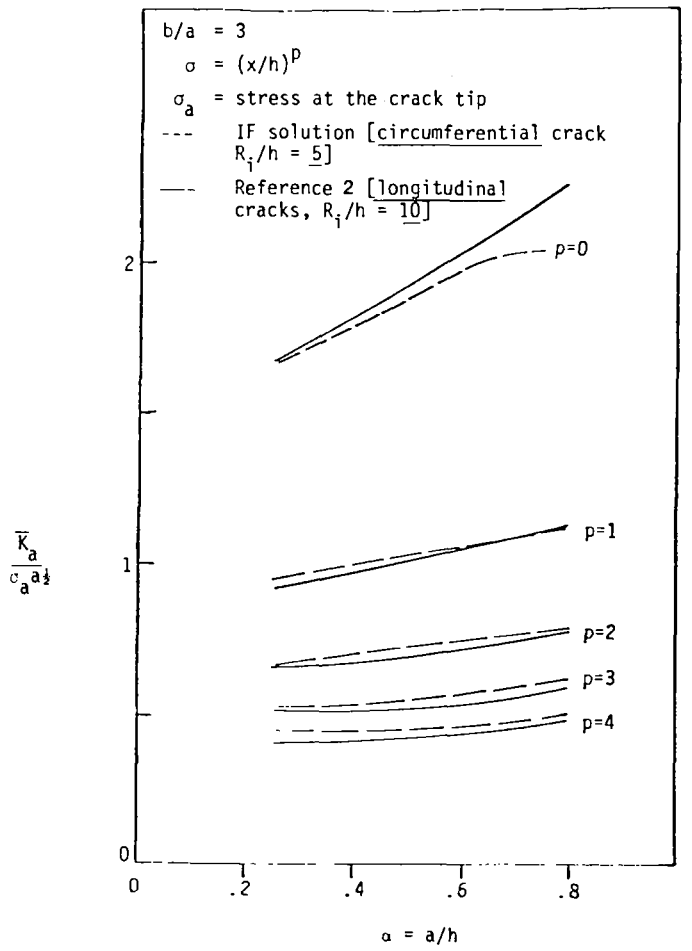

FIG. 8—*Comparison of influence function solutions for uniform (p = 0) and nonuniform stresses with existing solutions. Note somewhat different geometries involved.*

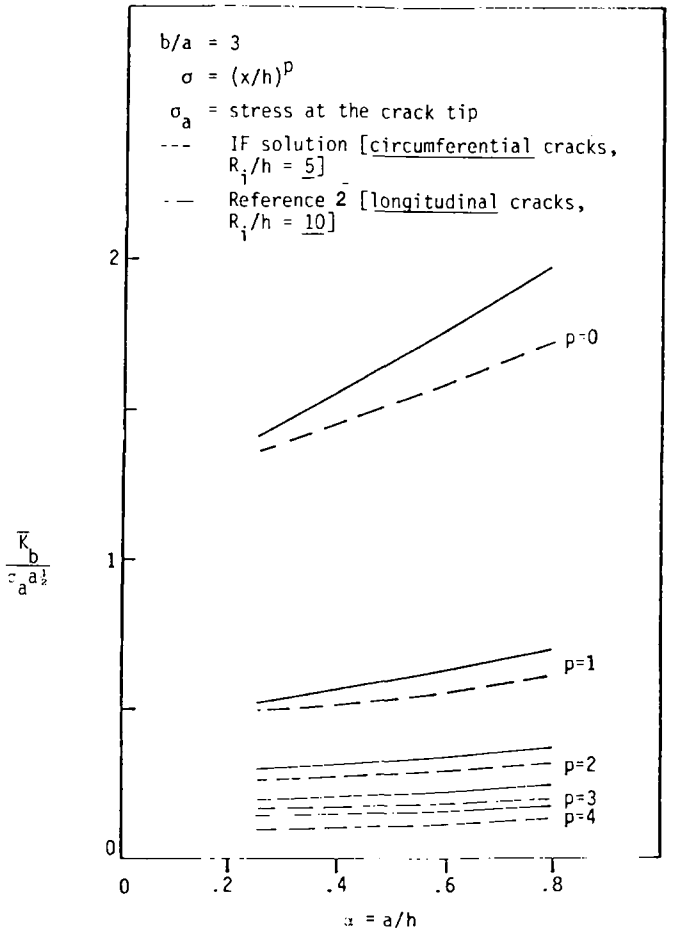

FIG. 9—*Comparison of influence function solutions for uniform (p = 0) and nonuniform stresses with existing solutions. Note somewhat different geometries involved.*

Acknowledgments

The support provided by Lawrence Livermore National Laboratory, as part of their Load Combinations Program, is gratefully acknowledged. The assistance provided by T. A. Cruse of Pratt and Whitney Aircraft, East Hartford, Conn., and P. M. Besuner of Failure Analysis Associates, Palo Alto, Calif. in supplying the boundary integral equation code was indispensable to this work. Additionally, the discussions with P. M. Besuner regarding approximations for influence functions were invaluable. Finally, considerable assistance in this work was provided by R. Northrup of Science Applications, Inc. (SAI) and the University of Cincinnati.

APPENDIX

Curve Fits

Stress Intensities Due to Uniform Stress

The values of $\bar{K}_a$ and $\bar{K}_b$ for part-circumferential interior surface cracks in pipes with uniform axial stress can be approximately evaluated from the following expression

$$\frac{\bar{K}_i}{\sigma a^{1/2}} = [d_0 + d_1\zeta + d_2\zeta^2 + d_3\zeta^3 + \alpha(e_0 + e_1\zeta + e_2\zeta^2 + e_3\zeta^3) + \alpha^2(f_0 + f_1\zeta + f_2\zeta^2 + f_3\zeta^3) + \alpha^3(g_0 + g_1\zeta + g_2\zeta^2 + g_3\zeta^3)] /(1 - \alpha)^{1/2} \quad (17)$$

The values of the coefficients are different for $\bar{K}_a$ and $\bar{K}_b$, and are as follows.

	$\bar{K}_a$	$\bar{K}_b$		$\bar{K}_a$	$\bar{K}_b$
d_0	1.6561	1.1260	f_0	0.042060	−3.1601
d_1	−0.39440	0.23200	f_1	13.568	25.091
d_2	−0.46115	−0.28484	f_2	−23.844	−41.651
d_3	0.33664	0.063055	f_3	11.147	21.397
e_0	−0.78383	1.2214	g_0	0.48946	1.6496
e_1	−0.48680	−7.6912	g_1	−18.201	−20.361
e_2	−0.57149	10.601	g_2	33.969	35.868
e_3	1.1149	−4.9324	g_3	−17.301	−18.949

Function g_1

The values of g_1 can be approximated from the following curve fit

$$g_1 = (0.9701 + 0.3414\beta) + \alpha(-0.00176 + 0.39924\beta - 0.05512\beta^2) + \alpha^2(-0.16095 + 0.4112\beta - 0.15460\beta^2 + 0.01936\beta^3) \quad (18)$$

Function g_2

The value of g_2 can be approximated from the following curve fit

$$g_2 = [A_0(\alpha) + A_1(\alpha)S^{1.5}\psi^{0.15} + A_2(\alpha)S^{1.5}\psi^{0.3} + A_3(\alpha)S^{2.5}\psi^{0.15} + A_4(\alpha)S^{2.5}\psi^{0.3} + A_5(\alpha)(\zeta - 1) + A_6(\alpha)(\zeta - 1)^2]F \quad (19)$$

where

$A_0 = 0.99568 + 0.71745\alpha,$
$A_1 = 3.99268 - 22.1411\alpha + 44.2643\alpha^2 - 32.8078\alpha^3,$
$A_2 = -3.5431 + 17.3427\alpha - 40.5886\alpha^2 + 31.5185\alpha^3,$
$A_3 = -2.5527 + 2.3462\alpha + 0.27447\alpha^2,$

$$A_4 = 2.5948 - 0.6154\alpha,$$
$$A_5 = -0.17706 - 0.5857\alpha,$$
$$A_6 = -0.1378 + 0.09001\alpha,$$
$$S = [(x/a)^2 + (y/b)^2]^{1/2},$$
$$\psi = 1 - 2/\pi \left[\tan^{-1} \left(\frac{y/b}{x/a} \right) \right], \text{ and}$$
$$F = 1 + 0.15 \left(\frac{a-x}{h} \right) (y/b)^2 (1 + 0.2\alpha)(2\beta - 1.99).$$

References

[1] Newman, J. C., Jr. in *Part-Through Crack Fatigue Life Prediction, ASTM STP 687,* American Society for Testing and Materials, 1979, pp. 16–42.

[2] Heliot, J., Labbens, R. C., and Pellisier-Tanon, A. in *Fracture Mechanics (11th) Conference), ASTM STP 677,* American Society for Testing and Materials, 1979, pp. 341–364.

[3] McGowan, J. J. and Raymund, M. in *Fracture Mechanics (11th Conference), ASTM STP 677,* American Society for Testing and Materials, 1979, pp. 365–380.

[4] Atluri, S. N., Kathiresan, K., Kobayashi, A. S., and Nakagaki, M., "Inner Surface Cracks in an Internally Pressurized Cylinder Analyzed by a Three Dimensional Displacement-Hybrid Finite Element Method," *Third International Conference on Pressure Vessel Technology, Part II, Materials and Fabrication,* American Society of Mechanical Engineers, New York, 1977.

[5] Kobayashi, A. S., Polvnicha, N., Emery, A. F., and Love, W. J., *Journal of Pressure Vessel Technology,* 1977, pp. 83–89.

[6] Rice, J. R., *International Journal of Solids and Structures,* Vol. 8, 1972, pp. 751–758.

[7] Cruse, T. A. and Besuner, P. M., *Journal of Aircraft,* Vol. 12, No. 4, 1975, pp. 369–375.

[8] Cruse, T. A., Meyers, G. J., and Wilson, P. B. in *Flaw Growth and Fracture, ASTM STP 631,* American Society for Testing and Materials, 1977, pp. 174–189.

[9] Cruse, T. A. et al in *Part-Through Crack Fatigue Life Prediction, ASTM STP 687,* American Society for Testing and Materials, 1979, pp. 3–15.

[10] Rizzo, F. J., *Quarterly of Applied Mathematics,* Vol. 25, 1967, pp. 83–95.

[11] Cruse, T. A., *International Journal of Solids and Structures,* Vol. 5, 1969, pp. 1259–1274.

[12] Cruse, T. A., "An Improved Boundary-Integral Equation Method for Three Dimensional Elastic Stress Analysis," Report SM-73-19, Department of Mechanical Engineering, Carnegie-Mellon University, Pittsburgh, Pa., 1973.

[13] *Boundary Integral Equation Method: Computational Applications in Applied Mechanics,* T. A. Cruse and F. J. Rizzo, Eds., American Society of Mechanical Engineers, New York, 1975.

[14] Besuner, P. M., *Nuclear Engineering and Design,* Vol. 43, No. 1, 1977, pp. 115–154.

[15] Besuner, P. M. in *Mechanics of Crack Growth, ASTM STP 590,* American Society for Testing and Materials, 1976, pp. 403–419.

[16] Besuner, P. M. et al, "BIGIF: Fracture Mechanics Code for Structures," Report EPRI NP-838, Electric Power Research Institute, Palo Alto, Calif., 1978.

[17] Harris, D. O., Lim, E. Y., and Dedhia, D. D., "Probability of Pipe Fracture in the Primary Coolant Loop of a PWR, Vol. 5: Probabilistic Fracture Mechanics Analysis," Report NUREG/CR 2189, Vol. 5, U.S. Nuclear Regulatory Commission, Washington, D.C., 1981.

[18] Tada, H., Paris, P. C., and Irwin, G. R., *The Stress Analysis of Cracks Handbook,* Del Research Corp., Hellertown, Pa., 1973.

[19] Labbens, R., Pellisier-Tanon, A., and Heliot, J. in *Mechanics of Crack Growth, ASTM STP 590,* American Society for Testing and Materials, 1976, pp. 368–384.

[20] Harris, D. O. and Lim, E. Y. in *Fracture Mechanics (13th Conference), ASTM STP 743,* 1981, pp. 375–386.

[21] Dedhia, D. D., Harris, D. O., and Lim, E. Y., in this publication, pp. I-308–I-326.

[22] Harris, D. O., "Stress-Corrosion Crack Growth in the Presence of Residual Stresses," presented at 28th Sagamore Army Materials Research Conference on Residual Stress and Stress Relaxation, Lake Placid, N.Y., 1981, to be published in conference proceedings.

M. Jolles[1] *and V. Tortoriello*[2]

Geometry Variations During Fatigue Growth of Surface Flaws

REFERENCE: Jolles, M. and Tortoriello, V., **"Geometry Variations During Fatigue Growth of Surface Flaws,"** *Fracture Mechanics: Fourteenth Symposium—Volume I: Theory and Analysis, ASTM STP 791*, J. C. Lewis and G. Sines, Eds., American Society for Testing and Materials, 1983, pp. I-297-I-307.

ABSTRACT: Recent investigations have indicated that fatigue growth of surface flaws cannot be adequately predicted solely by stress-intensity factor (SIF) analysis. This is due to variations in the stress field triaxiality along the flaw border. A fatigue growth analysis of surface cracks is performed accounting for the variation in stress field triaxiality using the concepts of crack closure. Changes in the geometric parameters describing the flaw size and shape are studied for remote tensile load. For an isotropic material where the Paris equation adequately describes the fatigue crack growth rates, it is found that all subcritical flaws, regardless of initial geometry, extend such that they eventually will have identical size and shape, and that the process is independent of stress range and material properties. Experiments were performed to assess the accuracy of the analysis. Accounting for the constraint variation through the use of the concepts of crack closure yields excellent results.

KEY WORDS: fracture mechanics, fatigue (materials), surface flaw, fatigue crack growth

One of the most common flaw types found in structural components is the surface flaw, which is often observed to have a shape close to that of a semiellipse. Although much attention has been focused on the surface flaw problem [*1,2*],[3] accurate analysis of the fatigue growth of such surface flaws under constant amplitude loading has been slow to develop. This has been due to complicating factors such as the lack of a closed form solution for the stress-intensity factor, multidirectional and nonself-similar crack growth, and variations in the stress-intensity factor and stress field triaxiality along the flaw border.

Recent studies [*3*] have shown that fatigue growth of semielliptical surface

[1]Head, Fracture Mechanics Section, Naval Research Laboratory, Washington, D.C. 20375. Formerly associate professor, University of Missouri.

[2]Captain, Escuela Superior de la Fuerza Aerea Venzzolana, Caracas 1010, Venezuela. Formerly graduate student, University of Missouri.

[3]The italic numbers in brackets refer to the list of references appended to this paper.

flaws is not adequately predicted solely by stress-intensity factor analysis. Although a variation in the fatigue resistance of the material along the flaw border would account for the observed differences, many metals are isotropic. Thus, the variation in constraint along the flaw border, from plane stress at the plate surface to that of plane strain at the point of maximum flaw penetration, must be an important factor affecting observed fatigue crack growth behavior.

An analysis of the fatigue growth of semielliptical surface flaws is performed, accounting for the variation in constraint along the flaw border. Changes in the geometric parameters describing the flaw size and shape are investigated, and the analysis is compared with results of experiments.

Analytical Considerations

A semielliptical surface flaw in a finite plate is shown in Fig. 1, where a is the crack depth, c the crack half-length at the free surface, w the width, and t the plate thickness. The parametric angle ϕ is used to locate a point on the flaw border.

The point of intersection of the flaw and the free surface, point c, and the point of maximum flaw penetration, point a, occur at $\phi = 0$ and $\pi/2$, respectively. Note that flaw extension at point c will be in the $\phi = 0$ direction while the crack extension at point a will be in the $\phi = \pi/2$ direction. Thus, it is convenient to study the fatigue growth of the surface flaw by analyzing crack extension at points a and c.

The crack growth rate at these points can be related to the stress-intensity factor range (ΔK) through the Paris [4] relation

$$\frac{da}{dN} = C(\Delta K_a)^n \tag{1}$$

$$\frac{dc}{dN} = C(\Delta K_c)^n \tag{2}$$

where C and n are material properties which depend on the stress ratio.

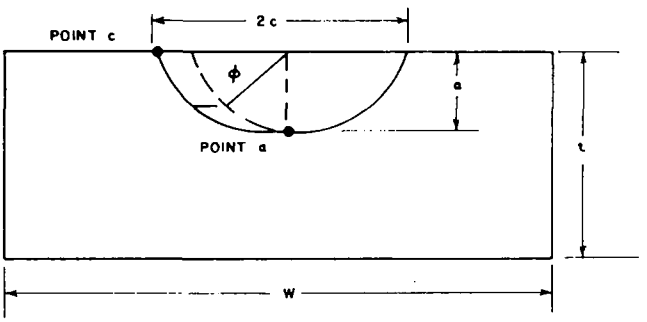

FIG. 1—*Surface flaw geometry.*

The stress-intensity factor under remote tensile loading (σ) is given by Newman and Raju [5] as

$$K = \sigma\left(\frac{\pi a}{Q}\right)^{1/2} F\left(\frac{a}{t}, \frac{a}{c}, \frac{c}{w}, \phi\right) \tag{3}$$

Since the plate width is often large as compared with crack length ($w \gg c$), the primary parameters describing the crack geometry are the aspect ratio (a/c) and the relative depth (a/t).

Equation 1, 2, and 3 can be combined and written in incremental form as

$$\Delta a = \left(\frac{F_a}{F_c}\right)^n \Delta c \tag{4}$$

Thus, geometry variations during fatigue growth of surface flows can be studied by assuming a small amount of crack length extension (Δc), determining the corresponding amount of crack depth increase (Δa), and repeating the process incrementing the values of a and c until a final desired flaw size is attained. An example of this procedure is in the Appendix.

The results of an analysis of an initially shallow, semicircular surface flaw ($a/t = 0.01$, $a/c = 1$) are presented in Fig. 2. A value of $n = 3$, typical for a crack growth rate exponent in metals, was assumed. Although observations of surface cracks are that shallow semicircular flaws will remain semicircular [6, 7], the analysis predicts a decreasing aspect ratio. Thus, the observed crack growth at point c is slower than predicted by the analysis.

In the absence of anisotropic crack growth rate properties (C and n are equal in Eqs 1 and 2), the variation in constraint along the flaw border can account for the observed differences in flaw growth. The plane stress condition occurring at point c results in more extensive yielding [8] than that occurring at point a, which generally will be in a region of plane strain. Fatigue crack closure, as first noted by Elber [9], is caused by plastic deformation left in the wake of the advancing crack tip. Thus, the relative increase in yielding causes greater crack closure to occur at point c than at point a. Then, the effective stress range at point c is smaller than at point a and results in slower crack growth at the point of flaw intersection with the plate surface, which is consistent with the observed behavior.

In order to account for the constraint variation along the flaw border, the fatigue crack growth rates are related to the range of the stress-intensity factor when the flaw is fully open, ΔK_{eff} by

$$\frac{da}{dN} = C(\Delta K_{\text{eff}_a})^n \tag{5}$$

$$\frac{dc}{dN} = C(\Delta K_{\text{eff}_c})^n \tag{6}$$

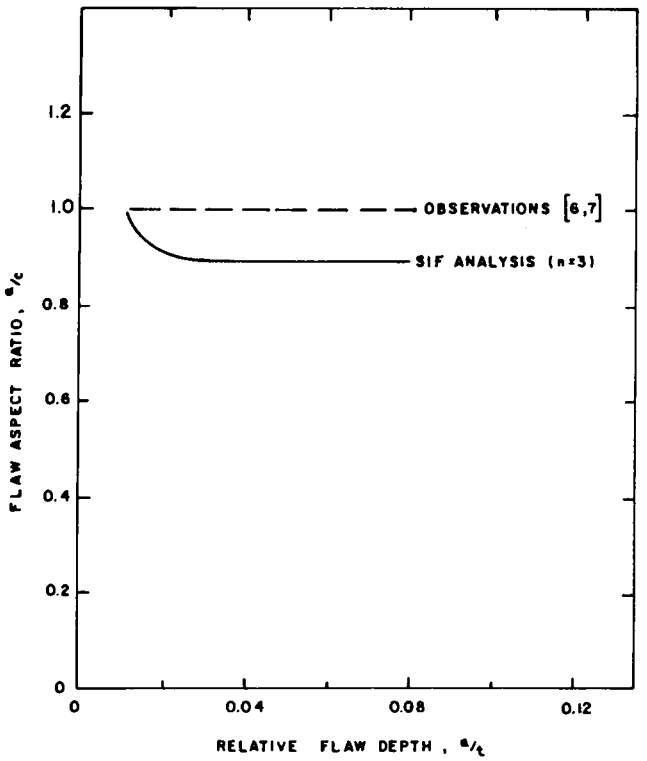

FIG. 2—*Crack geometry changes neglecting effects of constraint variation.*

where C and n can be shown now to be material constants independent of the stress ratio. Elber [*10*] demonstrated that the extent of crack closure during constant amplitude tensile loading can be quantified by a crack closure parameter

$$U = \frac{\Delta K_{\text{eff}}}{\Delta K} \tag{7}$$

Equations 3, 5, 6, and 7 can be combined and written in incremental form as

$$\Delta a = \left(\frac{U_a F_a}{U_c F_c}\right)^n \Delta c \tag{8}$$

This is similar to Eq 4, yet accounts for the effects of constraint variation by allowing the crack closure parameter at the point of flaw intersection with the plate surface, U_c, to be a different value than the crack closure parameter at the point of maximum flaw penetration, U_a.

Using Eq 8 and the procedure described previously to analyze surface crack fatigue growth, a shallow semicircular surface flaw will remain semicircular if $U_c/U_a = 0.91$ as shown in Fig. 3. This analysis then can be performed to determine changes in geometry during fatigue growth of surface flaws over a wide range of initial geometries using the ratio $U_c/U_a = 0.91$.

Surface Flaw Growth Behavior

Analyses were performed to study changes in geometry during fatigue growth of shallow surface flaws of initial relative flaw depth $a/t = 0.01$ and various initial aspect ratios. The results, shown in Fig. 3, indicate that all flaws tend to grow as to attain a semicircular shape.

The influence of the back surface of the plate on flaw growth behavior can be seen in Fig. 4. Here, fatigue crack growth analyses were performed on cracks of initial relative flaw depth $a/t = 0.2$ and a range of initial aspect ratios. An initially semicircular flaw no longer will remain semicircular, but will extend with a decreasing aspect ratio. However, it is interesting to note

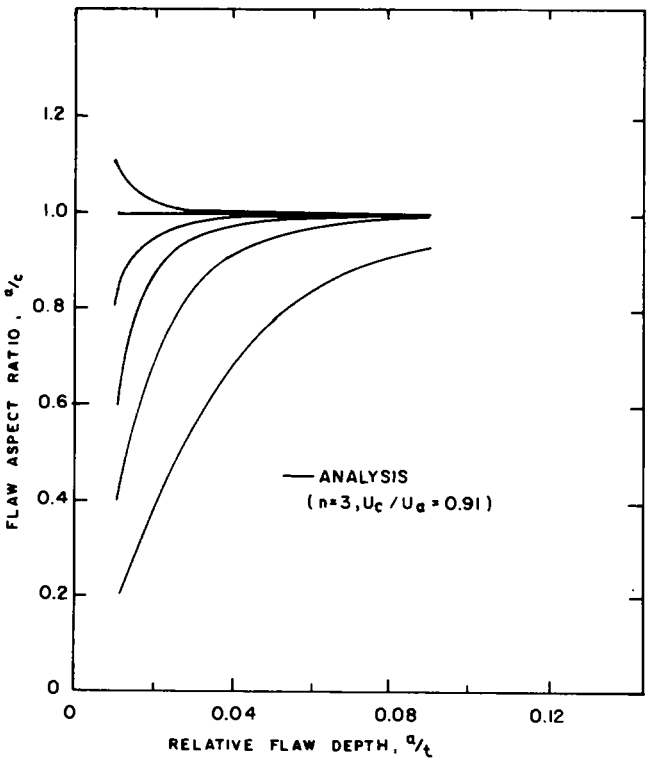

FIG. 3—*Geometry histories of shallow flaws.*

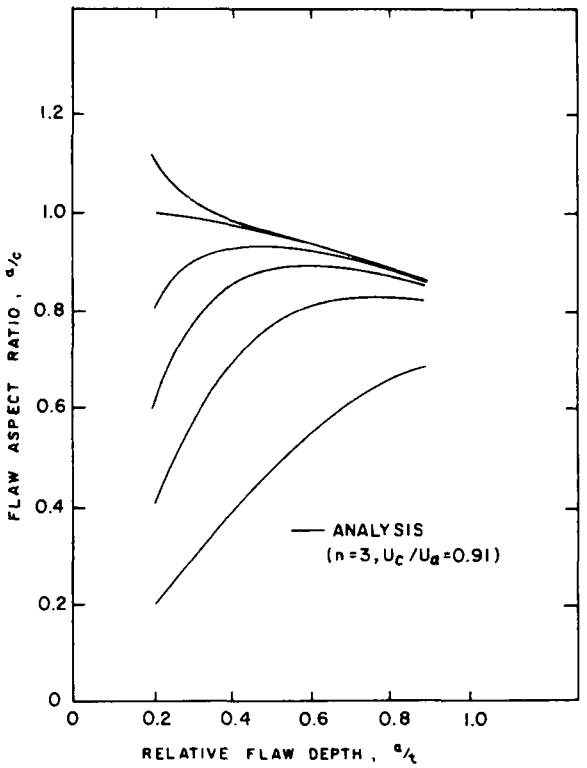

FIG. 4—*Geometry histories of surface flaws.*

that the growth pattern of the initially shallow semicircular flaw remains an asymptote for the growth patterns of all other initial geometries.

A closer examination of the parameters affecting the crack geometry history would be appropriate. As can be seen from Eq 8, flaw shape extension is independent of the stress range and the crack growth rate constant, C, and depends only on the current flaw geometry and the crack growth rate exponent, n. The influence of the exponent is assessed by performing analyses on an initial flaw geometry ($a/t = 0.2$ and $a/c = 1$) assuming a range of values of the exponent typical of metals. The results of such analyses indicate that the geometric history of the flaw is affected only slightly by a large change in the exponent. Thus, the future geometric parameters of an existing flaw depend almost entirely on the current flaw geometry and not on the material properties or stress range.

Although the analysis presented is for materials with isotropic fatigue crack growth properties and a simple power law relationship between the fatigue crack growth rate and effective stress-intensity factor range, the analy-

sis can be generalized by selecting another functional relation for Eqs 5 and 6 and varying the material constants from Eq 5 to 6.

Experiments

Experiments were conducted to assess the accuracy of the analysis. Eight fatigue crack growth rate tests were conducted on 2024-T351 aluminum to determine the range of ΔK_{eff} for which Eqs 5 and 6 are applicable as well as the crack growth rate exponent, n. The results are presented in Fig. 5. It is apparent that, for this material, if $3 \leq \Delta K_{eff} \leq 18$ MPam$^{1/2}$ the analytic procedure will be valid. A least squares analysis results in $n = 3.76$. Note that when an effective stress-intensity factor range is used, the measured fatigue crack growth rates are independent of the stress ratio.

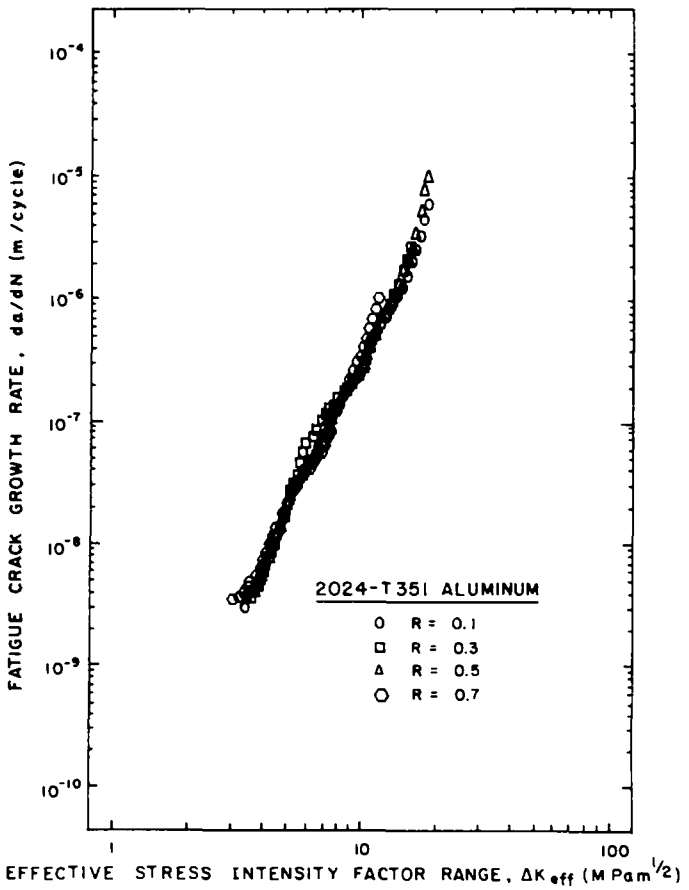

FIG. 5—*Fatigue crack growth rate results for 2024-T351 aluminum.*

Ten surface flaw specimens were fabricated of 2024-T351 aluminum. The specimens had a width $w = 2.54$ cm and a thickness $t = 1.27$ cm or 2.54 cm. A notch of the desired initial flaw geometry was electro-discharge machined (EDM) in each specimen.

Each specimen then was fatigued in a servohydraulic test system at a stress ratio $R = 0.1$ and a frequency of 10 Hz. Crack extension was monitored along the plate surface. Periodically, the minimum load was increased for 300 cycles to a level which would result in a fatigue crack growth rate of approximately 25 nm/cycle. This results in the creation of a contrasting marker band on the fracture surface which can be used to examine flaw growth after completion of the fatigue loading.

The fracture surfaces were observed and the dimensions a and c measured for each marker band using a travelling microscope. The first marker band served as the initial crack geometry for purposes of the analyses.

The initial and final flaw geometry and loading parameters for each experiment are summarized in Table 1. The range of ΔK_{eff} achieved during all experiments is within the limits qualified previously.

The results of the experiments and corresponding analyses are shown in Fig. 6, presented in two graphs for clarity. As can be noted in Fig. 6, excellent agreement is obtained between the experimentally observed flaw geometry histories and those predicted by the analyses. The asymptotic trend of the crack geometry histories is also apparent.

Summary and Conclusions

Geometry variations during fatigue growth of surface flaws have been investigated. It is apparent that fatigue growth of surface flaws cannot be predicted solely by a stress-intensity factor analysis due to the variation in stress field triaxiality along the flaw border. Accounting for the constraint variation through the use of the concepts of crack closure yields excellent results.

Surface flaws tend to grow as to attain a geometry identical with that observed of a crack which is initially shallow and semicircular. Although fatigue life depends on the magnitude of loading, material properties, and flaw size and shape, the geometry history will depend primarily on the initial flaw geometry for the conditions studied.

Including the effects of constraint variation in surface flaw analyses also should improve fatigue life predictions.

Acknowledgments

The authors wish to thank J. C. Newman, Jr. for many helpful discussions and providing the cited stress-intensity factor solutions.

TABLE 1—*Flaw geometry and loading parameters.*

Experiment Number	Initial Geometry		Maximum Stress, MPa	Final Geometry				Range of ΔK_{eff}, $MPam^{1/2}$
				Experiment		Analysis		
	a/t	*a/c*		*a/t*	*a/c*	*a/t*	*a/c*	
1	0.12	1.02	124	0.22	0.99	0.22	0.99	6.07 to 8.45
2	0.13	0.90	124	0.40	0.95	0.40	0.95	6.66 to 14.91
3	0.12	0.68	124	0.45	0.94	0.45	0.94	6.21 to 17.98
4	0.16	0.58	124	0.41	0.88	0.41	0.89	7.11 to 15.49
5	0.22	0.64	124	0.55	0.88	0.55	0.88	6.04 to 12.51
6	0.24	1.14	117	0.70	0.90	0.70	0.89	5.35 to 14.87
7	0.28	1.01	110	0.64	0.92	0.64	0.91	5.29 to 12.08
8	0.24	1.02	117	0.80	0.85	0.80	0.86	4.75 to 14.37
9	0.30	0.57	90	0.71	0.81	0.71	0.83	4.94 to 14.77
10	0.11	0.82	124	0.43	0.94	0.43	0.94	5.67 to 15.82

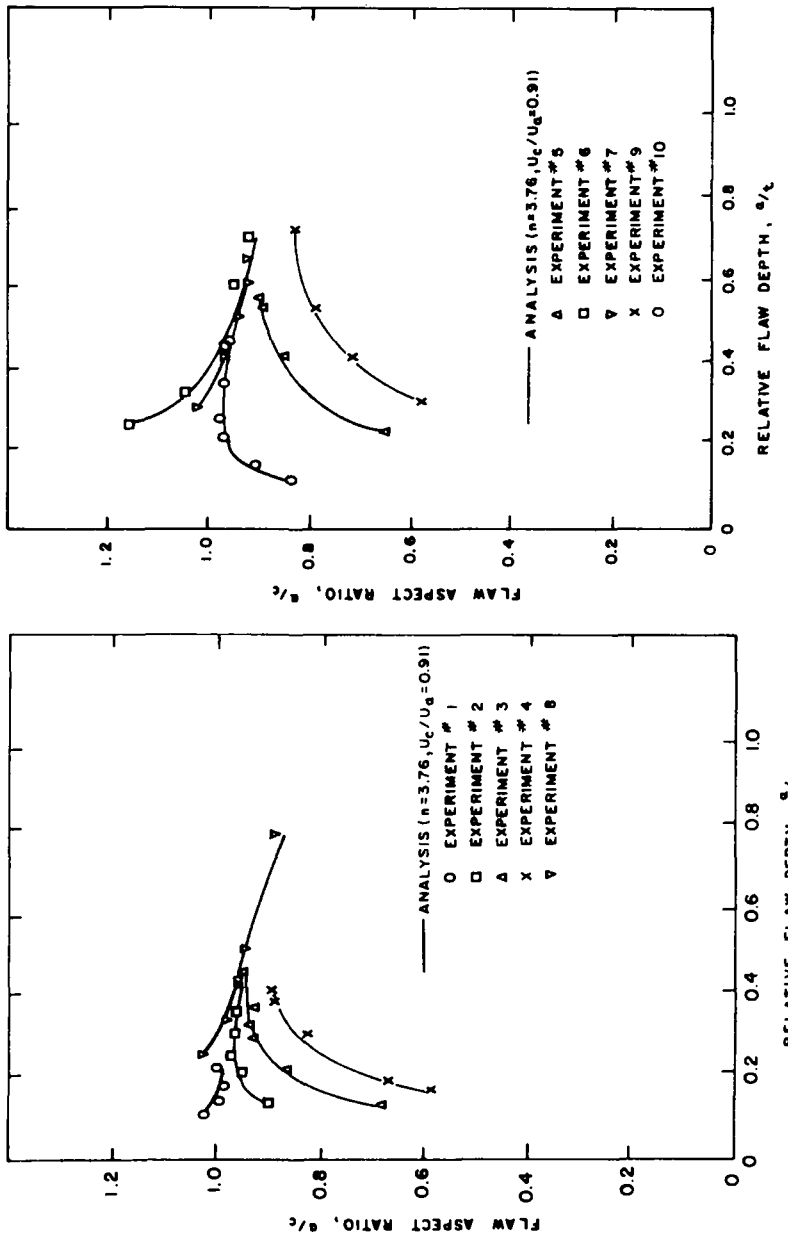

FIG. 6—*Comparison of geometry histories of experiments with analyses.*

APPENDIX

An example of the application of Eq 8 for the analysis of surface flaw fatigue growth is appropriate. The initial geometry of Experiment 1 is $a = 3.10$ mm, $c = 3.05$ mm, and $t = 25.4$ mm. Then, the relative flaw depth $a/t = 0.12$ and the flaw aspect ratio $a/c = 1.02$ as shown in Table 1. For this geometry, Ref 5 is used to find $F_a = 1.124$ and $F_c = 1.242$. Using $U_c/U_a = 0.91$ and the crack growth rate exponent $n = 3.76$ for the material of interest, the crack depth increase (Δa) can be determined for a small, arbitrary crack length extension, $\Delta c = 0.25$ mm.

Rewriting Eq 8

$$\Delta a = \left(\frac{U_a F_a}{U_c F_c}\right)^n \Delta c = \left(\frac{1}{0.91}\,\frac{1.124}{1.242}\right)^{3.76} (0.25) = 0.243 \text{ m} \tag{9}$$

Then, the new crack depth $a = 3.10 + 0.243 = 3.343$ mm and crack length $c = 3.05 + 0.25 = 3.30$ mm. The new relative flaw depth, $a/t = 0.13$ and aspect ratio, $a/c = 1.01$. The procedure is repeated, using the new crack geometry, to yield the analytical results shown in Fig. 6.

References

[1] Swedlow, J. L., Ed., *The Surface Crack: Physical Problems and Computational Solutions*, American Society of Mechanical Engineers Special Publication, 1972.

[2] Chang, J. B., Ed., *Part-Through Crack Fatigue Life Prediction, ASTM STP 687*, American Society for Testing and Materials, 1979.

[3] Hodulak, L., Kordisch, H., Kunzelmann, S., and Sommer, E. in *Fracture Mechanics, ASTM STP 677*, 1979, pp. 399-410.

[4] Paris, P. C. in *Fatigue—An Interdisciplinary Approach*, Syracuse University Press, 1964, pp. 107-132.

[5] Newman, J. C., Jr. and Raju, I. S., "Analyses of Surface Cracks in Plates Under Tension or Bending Loads," NASA TP 1578, National Aeronautics and Space Administration, 1979.

[6] Corn, D. L., *Engineering Fracture Mechanics*, Vol. 3, No. 1, 1971, pp. 45-52.

[7] Yen, C. S. and Pendleberry, S. L., *Materials Research Standards*, Vol. 2, No. 11, 1962, pp. 913-916.

[8] Aurich, D., *Engineering Fracture Mechanics*, Vol. 7, No. 4, 1975, pp. 761-765.

[9] Elber, W., *Engineering Fracture Mechanics*, Vol. 2, No. 1, 1970, pp. 37-46.

[10] Elber, W. in *Damage Tolerance in Aircraft Structures, ASTM STP 486*, American Society for Testing and Materials, 1971, pp. 230-242.

D. D. Dedhia,[1] *D. O. Harris,*[2] *and E. Y. Lim*[2]

Influence of Nonuniform Thermal Stresses on Fatigue Crack Growth of Part-Through Cracks in Reactor Piping

REFERENCE: Dedhia, D. D., Harris, D. O., and Lim, E. Y., **"Influence of Nonuniform Thermal Stresses on Fatigue Crack Growth of Part-Through Cracks in Reactor Piping,"** *Fracture Mechanics: Fourteenth Symposium—Volume I: Theory and Analysis, ASTM STP 791*, J. C. Lewis and G. Sines, Eds., American Society for Testing and Materials, 1983, pp. I-308–I-326.

ABSTRACT: The growth of part-through part-circumferential semielliptical surface cracks in nuclear primary piping of finite wall thickness is computed. Crack extension is considered to be controlled by root mean square (RMS)-averaged stress-intensity factors associated with each axis of the semielliptical crack, which allows the consideration of varying aspect ratio with crack depth. Crack extension due to nonuniform through-wall stresses is computed by the use of a recently developed influence function for circumferential cracks in pipes. The crack growth due to uniform and nonuniform stresses is presented by the use of crack trajectories, which pictorially display the change in crack geometry with stress history. These trajectories are presented for crack growth due to heat-up and cool-down and reactor trip transients of a nuclear plant. These crack growth trajectories for uniform stress are presented in a manner that makes it possible to compute crack growth for any stress history.

KEY WORDS: aspect ratio, cracks in pipes, circumferential cracks, crack growth trajectories, influence functions, nonuniform stresses, RMS stress-intensity factors, semielliptical cracks, uniform stresses, fatigue crack growth, fracture mechanics

Nomenclature

ΔA_i	Increment of crack area for crack extending in i-direction
a	Maximum depth of a semielliptical crack
da/dn	Fatigue crack growth rate
b	Half surface length of a semielliptical crack

[1]Science Applications, Inc., Sunnyvale, Calif. 94086.
[2]Science Applications, Inc., Palo Alto, Calif. 94304.

C Parameter in fatigue crack growth relation
h Pipe wall thickness
K Stress intensity factor
K' Equals $(K_{max} - K_{min})/(1 - R)^{1/2}$
$\bar{K}_i$ RMS-averaged stress-intensity factor associated with crack extension in the i degree-of-freedom direction
$\delta\bar{K}_i$ Stress-intensity factor ($\bar{K}_i$) due only to radial gradient thermal stresses
LOCA Loss-of-coolant accident
m Exponent in fatigue crack growth relation
n Number of stress cycles
R Load ratio $= K_{min}/K_{max}$
x Distance into pipe wall
α Equals $\Delta n\, C\, \sigma_e^m\, h^{m/2}$
σ_{max} Maximum stress during a fatigue cycle
σ_{min} Minimum stress during a fatigue cycle
σ_e Effective cyclic stress $= [\sigma_{max}(\sigma_{max} - \sigma_{min})]^{1/2}$
ϕ Elliptic angle of position along crack front

The growth of part-through surface cracks in reactor piping and pressure vessels is a problem of considerable interest in analysis of the reliability of such components. This is especially true of nuclear reactors, where failure of the pressure boundary can have particularly undesirable consequences. A means of accounting for the complex stresses that occur during the operation of a nuclear plant is of interest, as well as a means of accounting for possible changes of the crack aspect ratio (length-to-depth ratio) that can occur as the crack extends. Previous work [*1,2,3*][3] in related areas generally suffers from one or more of the following drawbacks:

1. It was restricted to uniform stress through the wall, or at most a linear variation of stress.
2. It considered aspect ratio to remain constant during crack growth.
3. It based the growth rate on local values of stress-intensity factor at the plate surface and the point of deepest crack penetration.
4. It considered only cracks in a half-space.

These restrictions are all dropped in the current paper. Crack extension is considered to be controlled by a root mean square (RMS)-averaged stress intensity factor associated with each axis of semielliptical surface crack (two-degrees-of-freedom model) rather than the local value. This allows the aspect ratio to change as the crack grows. Additionally, the use of the recent influence function developed for circumferential cracks in pipes [*4*] allows arbitrary stresses through the pipe wall of finite thickness to be treated.

[3]The italic numbers in brackets refer to the list of references appended to this paper.

The relative influence of uniform and radial gradient thermal stresses (nonuniform) on fatigue crack growth is ascertained and displayed by the use of "crack growth trajectories" that pictorially display how the shapes of semielliptical cracks change with cyclic loading of various types. Uniform stresses tend to grow cracks deeper, whereas nonuniform radial gradient thermal stresses (which tend to be largest at the inside surface) grow cracks longer. This effect is shown schematically in Figure 1, and is quantified in this paper. Such results are of interest in discussions of the types of cracks expected to be found in reactor piping, and are of relevance in estimation of the relative probability of "leak-before-break" in pressurized components subjected to complex stresses.

Stress-Intensity Factors and Crack Growth Rate

The rate at which a and b (length and depth of a crack) will grow depends on the cyclic values of K along the crack front, as well as the fatigue crack growth characteristics of the material. The growth characteristic for cases where K is uniform along the crack front for austenitic stainless steel primary piping material (A304 and A316) were reviewed [5] and the results could be summarized by

$$\frac{da}{dn} = C\left[\frac{\Delta K}{(1-R)^{1/2}}\right]^m = CK'^m \tag{1}$$

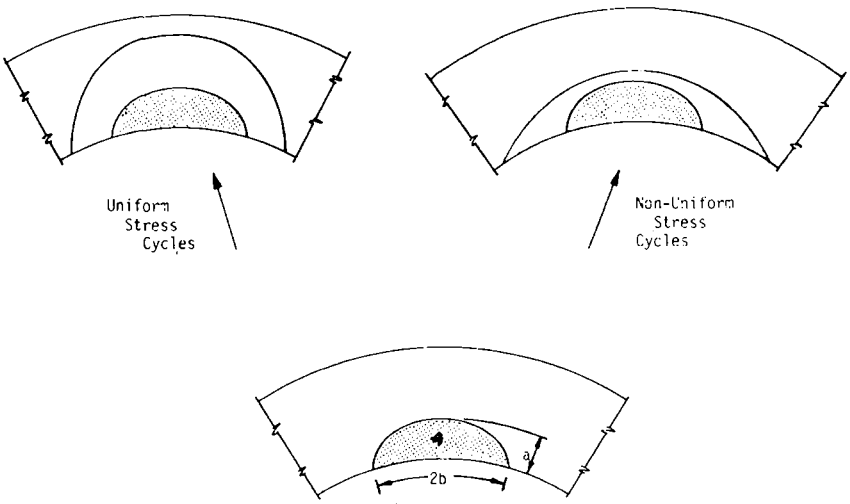

FIG. 1—*A schematic diagram showing fatigue crack growth of a semielliptical crack in pipe, due to uniform through-wall and nonuniform radial gradient thermal stresses.*

where

da/dn = fatigue crack growth rate, m/cycle,
ΔK = cyclic stress-intensity factor = $K_{max} - K_{min}$, MPa $\sqrt{m}$,
R = load ratio = K_{min}/K_{max}, and
C, m = empirical constants.

K' is the effective cyclic stress-intensity factor that accounts for the effect of cyclic stress intensity as well as the load ratio on fatigue crack growth rate. The values of C and m were obtained by statistical analysis [5] of the relevant experimental data to be 1.59×10^{-13} and 4, respectively (for da/dn in m/cycle, and K in MPa-$m^{1/2}$). This growth law will be assumed to be applicable to part-through cracks as well, but the stress-intensity factors to be employed must be defined carefully, because K varies along the crack front. Consideration of a local growth rate controlled by the local values of K would be analytically prohibitive, and probably unrealistic. Semielliptical cracks would not necessarily remain semielliptic for complex stresses, and stress-intensity factor solutions for nonelliptical cracks would be required. Therefore, it will be assumed that the growth of a and b need only be considered, with appropriate selection of the controlling stress-intensity factors. The following are two possibilities. (1) The growth of a is controlled by the cyclic value of K at the point of maximum crack penetration, and the growth of b is controlled by the cyclic K at the surface, or, in other words, by the local values of K. (This approach was adopted by Nair [6] in a closely related investigation that was limited to simpler stress distributions than considered here); (2) The growth of a and b are controlled separately by some average stress intensity along the crack front that is associated with growth in each of these directions.

Suggested averaged values are the RMS-averaged values [7-10] associated with each degree-of-freedom. This seems to be a more realistic assumption than the use of simply the local values. Therefore, these RMS-averaged values of stress-intensity factors associated with each degree of freedom will be assumed to govern the rate of growth of a and b. Basically, the RMS-averaged values, which are denoted as $\bar{K}$, are defined as follows

$$\bar{K}_a^2 = \frac{1}{\Delta A_a} \int_0^{\pi/2} K^2(\phi)\, d\,[\Delta A_a(\phi)] \tag{2}$$

$$\bar{K}_b^2 = \frac{1}{\Delta A_b} \int_0^{\pi/2} K^2(\phi)\, d\,[\Delta A_b(\phi)] \tag{3}$$

An added advantage of this approach is that $\bar{K}_a$ and $\bar{K}_b$ can be evaluated for arbitrary stresses on the crack plane by the use of influence function [4, 7-11]. An influence function is defined as the stress-intensity factor arising from a unit point load on the crack surface. This function can be evaluated from

information on the opening displacements on the crack surface for an arbitrary state of stress. This is fully explained in Ref *4*.

In accordance with the preceding consideration, the fatigue crack growth rates will be assumed to be governed by the following equations

$$\frac{da}{dn} = C\,[\bar{K}'_a]^m \tag{4}$$

and

$$\frac{db}{dn} = C\,[\bar{K}'_b]^m \tag{5}$$

Results and Discussion

Uniform Stress

The applicability of the fracture mechanics solutions obtained is demonstrated by evaluating the crack growth rates in nuclear primary piping. First, the crack growth calculations are performed for uniform through-the-wall stresses. The cyclic crack growth results are plotted on a graph with a/b as one coordinate and normalized crack depth, (a/h) as another coordinate. The normalized crack depth would lie between zero and one. The limits on a/b are also zero and one; the upper limit on $a/b = 1$ means that the cracks that are shorter than twice the depth are omitted from consideration. This coordinate system is displayed in Fig. 2. Any crack with an a/h coordinate equal to one would be a through-wall defect and cause a leak. The loci of all cracks that would cause a double-ended guillotine break, or loss-of-coolant accident (LOCA), are shown as a dotted region. The position of the dashed line (one of the boundaries of the dotted region) depends on the stresses on the pipe and the failure criteria employed.

Typical crack growth trajectories also are displayed in Fig. 2. The trajectories are the loci of points showing the variation of crack dimensions with time as the crack grows under the cyclic loads. The crack depth variable is monotonically increasing, while the value of a/b either increases or decreases during the crack propagation, depending on the current crack geometry and the nature of the applied stress.

As shown in Fig. 2, any of the cracks in the sample space when subjected to cyclic loads of sufficient magnitude for enough number of cycles, would eventually cause a failure, either as a through-wall leak or a catastrophic complete pipe severance. Figure 2 shows that many of the failures would occur as part-through defects that would develop into a leak (trajectories intersecting the $a/h = 1$ line). If these leaks are not detected, the length of the crack would continue to increase (a/b decreasing) and ultimately reach the large LOCA re-

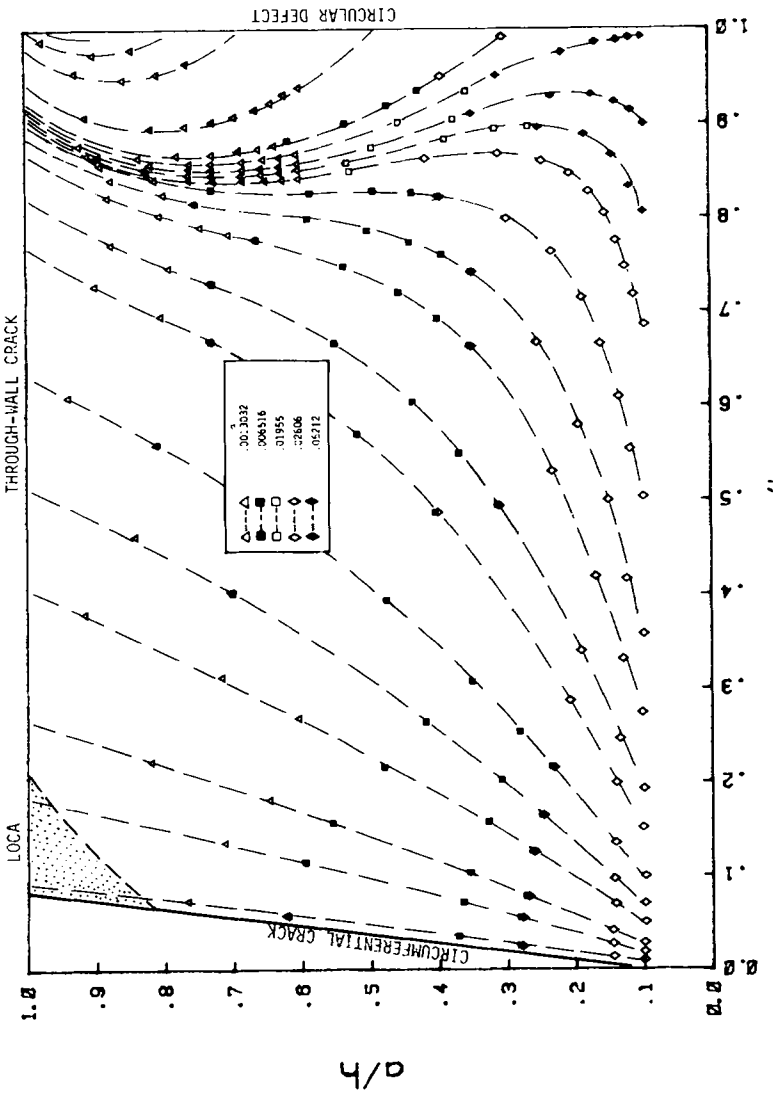

FIG. 2—*Fatigue crack growth trajectories for uniform through-wall stresses* (m = 4).

gion. Cracks which exhibit this sequence of leak and LOCA are said to have experienced "leak before break." It is apparent from Fig. 2 that for uniform through-the-wall stress loading, most of the failures that could occur would experience a "leak before break." On the other hand, it is possible to have a combination of initial crack size and stress histories that lead to large LOCA without first undergoing a leak. The cracks leading to a direct LOCA necessarily would have to be initially very long, that is, almost completely circumferential.

As shown in Fig. 2, for the cracks with a/b less than about 0.85, the crack depth increases faster than the half-crack-length b and the a/b (inverse of aspect ratio) approaches a constant value of about 0.85. For cracks with a/b larger than 0.85, a/b actually decreases, again approaching the value of about 0.85. This is true for $m = 4$. The crack growth trajectories for $m = 6$ and $m = 2$ are displayed in Figs. 3 and 4. The only noticeable difference in the trajectories is that for $m = 6$, the cracks approach a/b of 0.8, and for $m = 2$, this value of a/b is about 0.9.

For uniform through-the-wall stresses, the crack growth data are plotted for predetermined values of C, m, fatigue cycles, and effective stress (σ_e). This procedure makes it possible to use the crack growth rate calculations for any other values of C and effective stress, as explained in the following equations.

The crack growth rate (da/dn) is given as

$$\frac{da_i}{dn} = C\left[\frac{\bar{K}_{\max} - \bar{K}_{\min}}{\left(1 - \frac{\bar{K}_{\min}}{\bar{K}_{\max}}\right)^{1/2}}\right]^m = C\,[\bar{K}_{\max}{}^2\,(\bar{K}_{\max} - \bar{K}_{\min})^2]^{m/4} \tag{6}$$

Since $\bar{K}_i$ solutions, for uniform stress are given as [4,5] $\bar{K}_i = \sigma a^{1/2} \times f_i\,(a/h, a/b)$

$$\frac{da_i}{dn} = C\,[f_i^4(a/h, a/b) \times a^2]^{m/4}\,[\sigma_{\max}{}^2\,(\sigma_{\max} - \sigma_{\min})^2]^{m/4}$$

$$= C\,[f_i^4(a/h, a/b) \times a^2]^{m/4}\,(\sigma_e{}^4)^{m/4} \tag{7}$$

where $\sigma_e = [\sigma_{\max}\,(\sigma_{\max} - \sigma_{\min})]^{1/2}$.

For Δn cycles

$$\Delta a_i = \Delta n \times C\,[f_i^4\,(a/h, a/b)\,a^2]^{m/4}\,(\sigma_e{}^4)^{m/4}$$

$$= \alpha[f_i^4\,(a/h, a/b)(a/h)^2]^{m/4} \tag{8}$$

where $\alpha = \Delta n \times C \times \sigma_e{}^m \times h^{m/2}$.

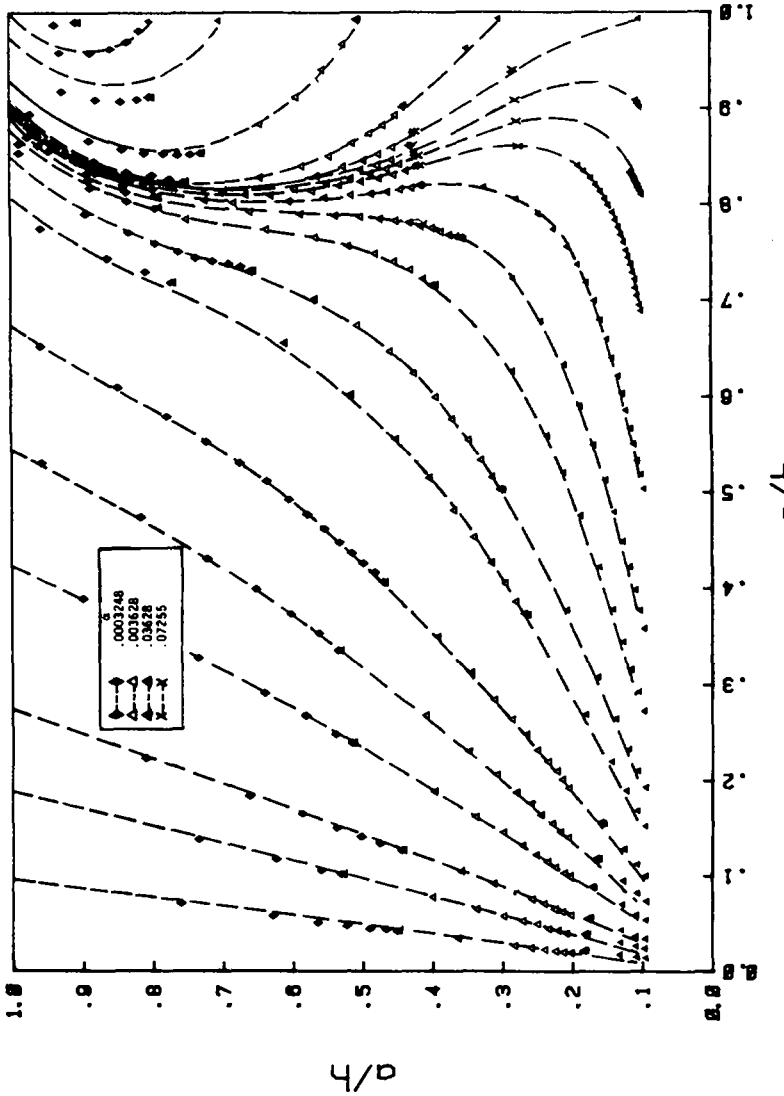

FIG. 3—*Fatigue crack growth trajectories for uniform through-wall stresses* (m = 6).

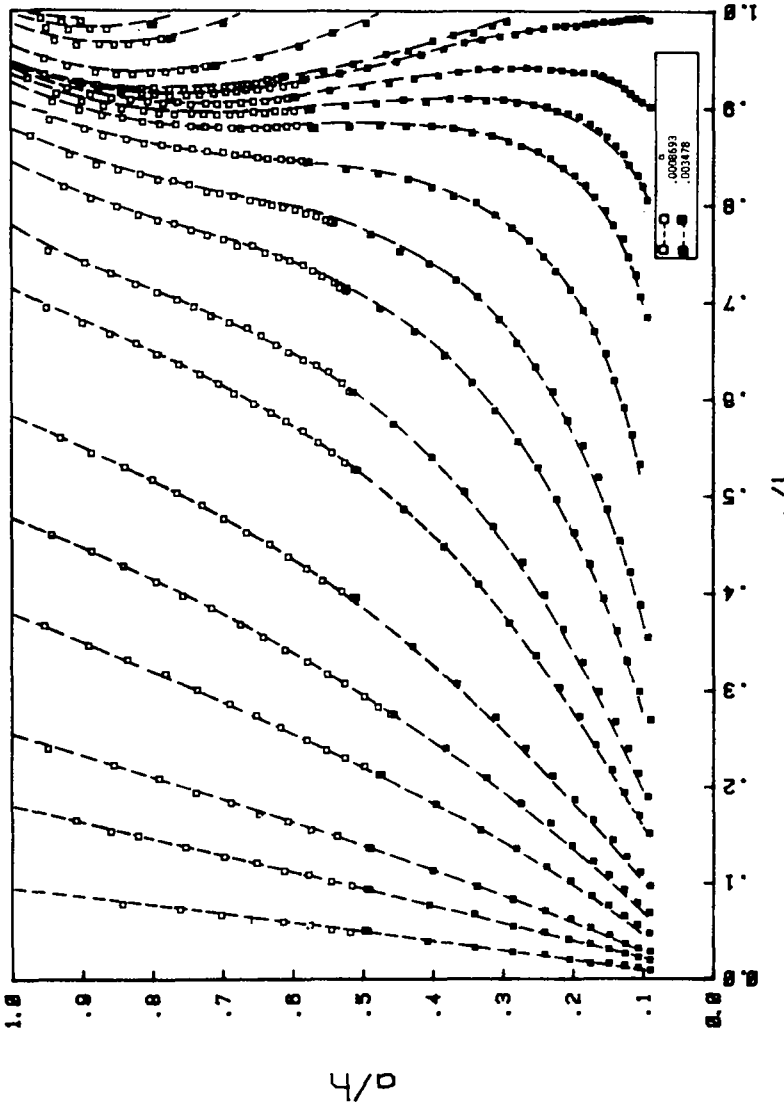

FIG. 4—*Fatigue crack growth trajectories for uniform through-wall stresses* (m = 2).

Δa and Δb are computed for a given α and plotted $a/h - a/b$ space. Any two adjoining symbols on a trajectory define the Δa and Δb for a given α. This kind of plot makes it possible to compute the effect of another C and σ_e on crack growth rate, using the crack growth trajectories. A specific example of this computation is given in the Appendix.

Nonuniform Stresses

Sudden changes in the coolant temperature in the primary nuclear piping following a reactor transient produce axisymmetrical radial gradient thermal stresses. Figure 5 shows such stresses for various times from the start of a reactor trip from full power (a reactor transient). These stresses were obtained [*12*] by a numerical procedure that employed the time-temperature variation.

The method of influence function [*4,11*] then was used to calculate the RMS stress-intensity factors ($\bar{K}_a$ and $\bar{K}_b$) for each time interval. These calculations of $\bar{K}_a$ and $\bar{K}_b$ were performed for a range of crack geometries. For each crack geometry, the RMS stress-intensity factors change with time and go through a maximum. This is very much like a fatigue cycle, and hence, maximum excursions of $\bar{K}_a$ and $\bar{K}_b$ are of interest. The maximum excursion due solely to the temperature fluctuations are denoted as $\delta\bar{K}_a$ and $\delta\bar{K}_b$, and are shown for a range of crack geometries in Figs. 6 and 7. For numerical computations, the maximum $\delta\bar{K}_a$ and $\delta\bar{K}_b$ are curve fitted as functions a/h and a/b. These maximum values of $\delta\bar{K}_a$ and $\delta\bar{K}_b$ are plotted (Figs. 6 and 7) as a function of a/h for a selected value of b/a.

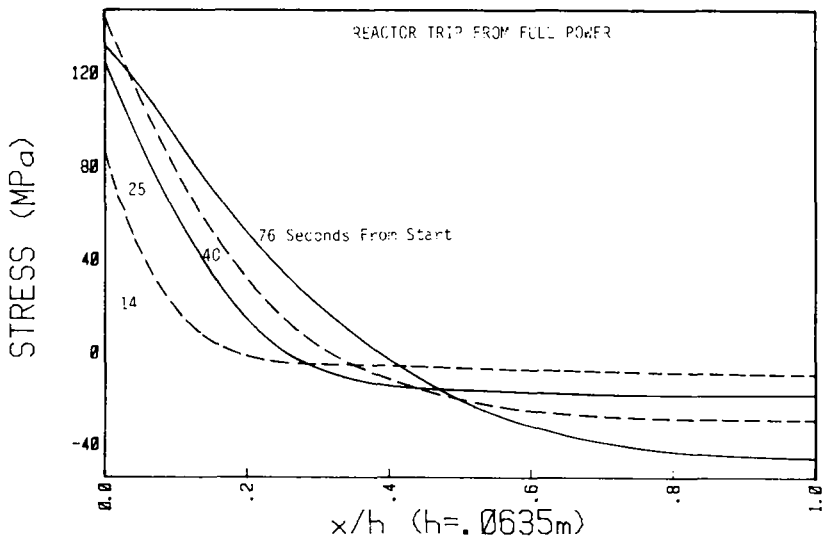

FIG. 5—*Radial gradient thermal stresses at various times from the start of the transient for 0.0635-m-thick pipe.*

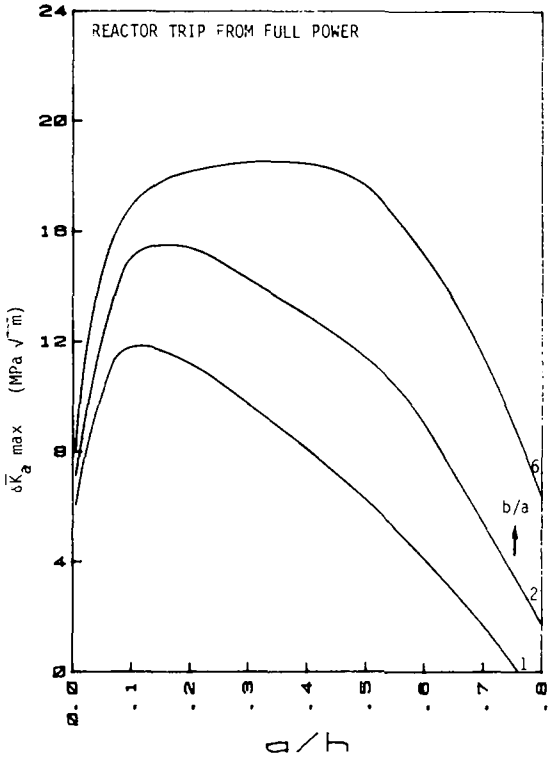

FIG. 6—*Maximum* $\delta\bar{K}_a$ *during reactor trip as a function of crack geometry for a pipe wall thickness of 0.0635 m.*

Some interesting observations can be drawn from Figs. 6 and 7. One is that $\delta\bar{K}_b$ is generally larger than $\delta\bar{K}_a$ for the same crack, except for very shallow and very long cracks. This means that only very shallow and very long cracks will grow in the same manner as due to uniform stress. That is, for the cracks in this category, crack depth will increase faster than b (half-crack-length). For all the other cracks, b will increase faster than a. That is, they will grow more in the circumferential direction than in the depth direction. This is displayed vividly in Fig. 8, which presents the fatigue crack growth due to a given number of transients (all of them reactor trips, in this case). A very striking feature of the fatigue crack growth due to radial gradient thermal stresses is that these would produce the long cracks that would result in a sudden and complete pipe severance, rather than a leak-before-break. This is because the largest stresses occur at inner pipe walls with a steep gradient into the wall (see Fig. 5).

Another interesting feature of the $\bar{K}_a$ for a reactor trip is that the stress-intensity factors for shallow cracks can be larger than for the deep cracks. This is demonstrated (Fig. 8) by the fact that as the crack becomes deeper, it takes

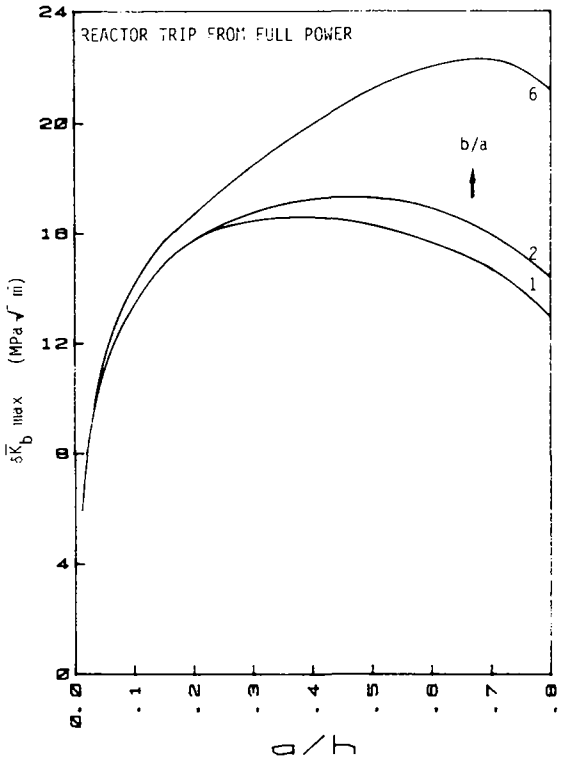

FIG. 7—*Maximum* $\delta\bar{K}_b$ *during reactor trip as a function of crack geometry for a pipe wall thickness of 0.0635 m.*

more and more cycles to grow it by the same amount. This apparent anomaly is due to the steep stress gradients through the pipe wall. The stresses decrease with increasing thickness, and the tip of very deep cracks might even see some compressive stresses. This produces lower $\bar{K}_a$ for deeper cracks; on the other hand, $\bar{K}_b$ remains high for deeper cracks, meaning that the deeper cracks would continue to grow in the circumferential direction, which again points to such transients tending to lead to direct pipe breaks more than uniform stress cycles.

The foregoing analysis to produce the crack growth trajectories was based on uniform and nonuniform stress cycles separately. The cracks in the primary coolant piping in actuality would be subjected to both uniform and nonuniform stress cycles. The crack growth trajectories for stress histories involving both uniform and nonuniform stress cycles is shown in Fig. 9. The nonuniform stress cycle was the one discussed earlier (reactor trip), whereas the uniform stress cycle corresponds to the actual calculated stresses produced during the heat-up and cool-down transient of a nuclear power plant, the ef-

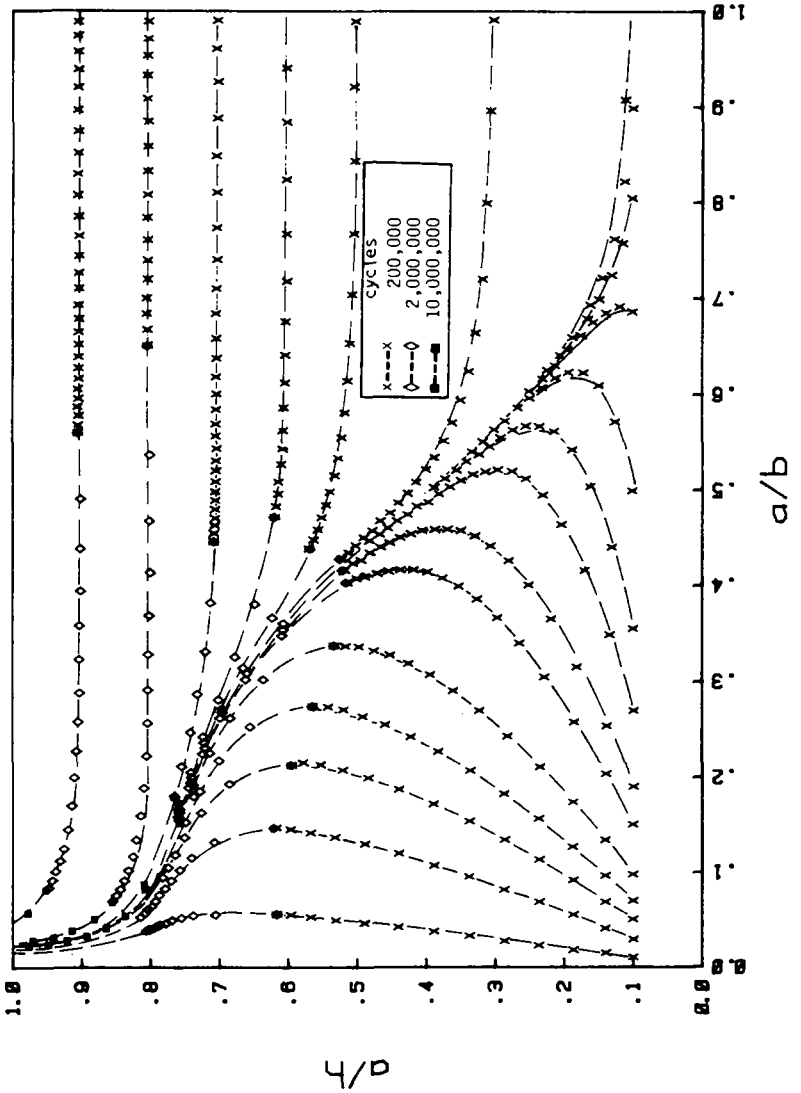

FIG. 8—*Fatigue crack growth trajectories for radial gradient thermal stresses due to reactor trip* ($C = 1.59 \times 10^{-13}$, $m = 4$).

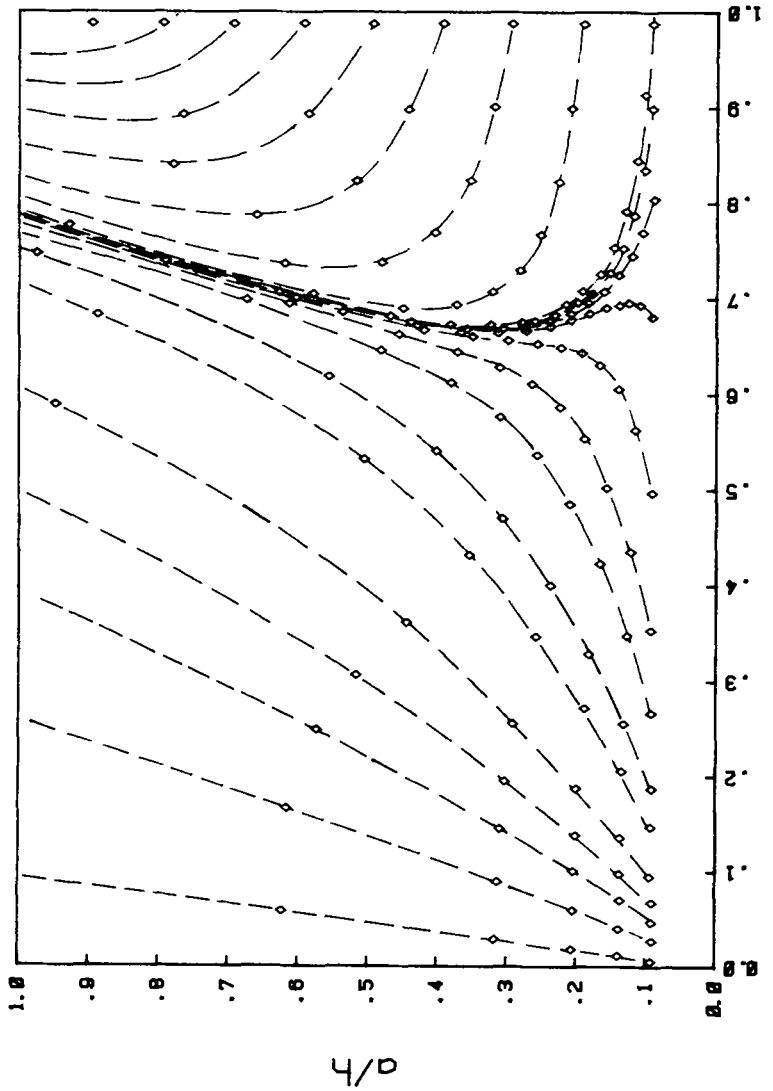

FIG. 9—*Fatigue crack growth trajectories for a combination of uniform and nonuniform stress cycles produced by heat-up and cool-down and reactor trip, respectively.* σ_e *for uniform stress cycles is 96.747 MPa.* $C = 1.59 \times 10^{-13}$. *Change in crack geometry between two points is due to 150 000 uniform stress cycles with a nonuniform stress cycle for every uniform stress cycle* (m = 4).

fective cyclic stress (σ_e) for which is 96.747 MPa. The trajectories are plotted (in Fig. 9) assuming one reactor trip occurring after every heat-up and cool-down transient, that is, one nonuniform stress cycle for every uniform stress cycle. It is seen that the crack growth behavior is dominated by uniform stress cycles. With this combination of uniform and nonuniform stress cycles, most of the cracks would grow to leak and very few of initial crack geometries could lead to direct pipe severance, as was the case with uniform stress cycles (see Figs. 2, 3, or 4). Even when two to five cycles of nonuniform stress are considered for every uniform stress cycle, as shown in Figs. 10 and 11, there is only a small change in the trajectories. Most of the cracks would still leak first. The cracks approach a/b ratio of about 0.6 instead of 0.7 in the previous case (see Fig. 8).

With sufficient number of heat-up and cool-down and reactor trip transients (two of the most severe [5] as far as the fatigue crack growth is concerned), all the cracks would grow to failure. However, the computed crack growth in primary nuclear piping due to these transients is very small. For example, it would take about 20 000 years for an initial crack of $a/h = 0.37$ to grow to $a/h = 0.48$, with only a small change in this aspect ratio. This is based on five heat-up and cool-down and ten reactor trips occurring every year, the rate typical [5] of a pressurized water reactor.

Summary and Conclusions

The growth of part-through part-circumferential semielliptical surface cracks in nuclear primary piping of finite wall thickness was ascertained. Crack extension was considered to be controlled by RMS-averaged stress-intensity factors associated with each axis of the semielliptical crack rather than the local value. This allowed the aspect ratio to change with crack extension. Additionally, the use of a recent influence function developed for circumferential cracks in pipes allowed the arbitrary stresses through the pipe wall of finite thickness to be treated.

The influence of uniform and radial gradient thermal stresses on crack growth was computed and displayed through crack growth trajectories that display the changes in semielliptical crack growth geometry with stress history. These trajectories showed that the uniform stress cycles tend to grow cracks through the thickness for all cracks with length-to-depth ratio of greater than 2.5, thus resulting in most of the cracks leading to leaks in pipes rather than direct pipe severence. Nonuniform thermal stresses, on the other hand, tend to grow cracks more in length direction leading to direct pipe severance. These trajectories were obtained for an actual calculated primary piping stress history, and the results were dominated by uniform stress cycles, with the actual crack growth during the lifetime of a reactor being predicted to be negligibly small.

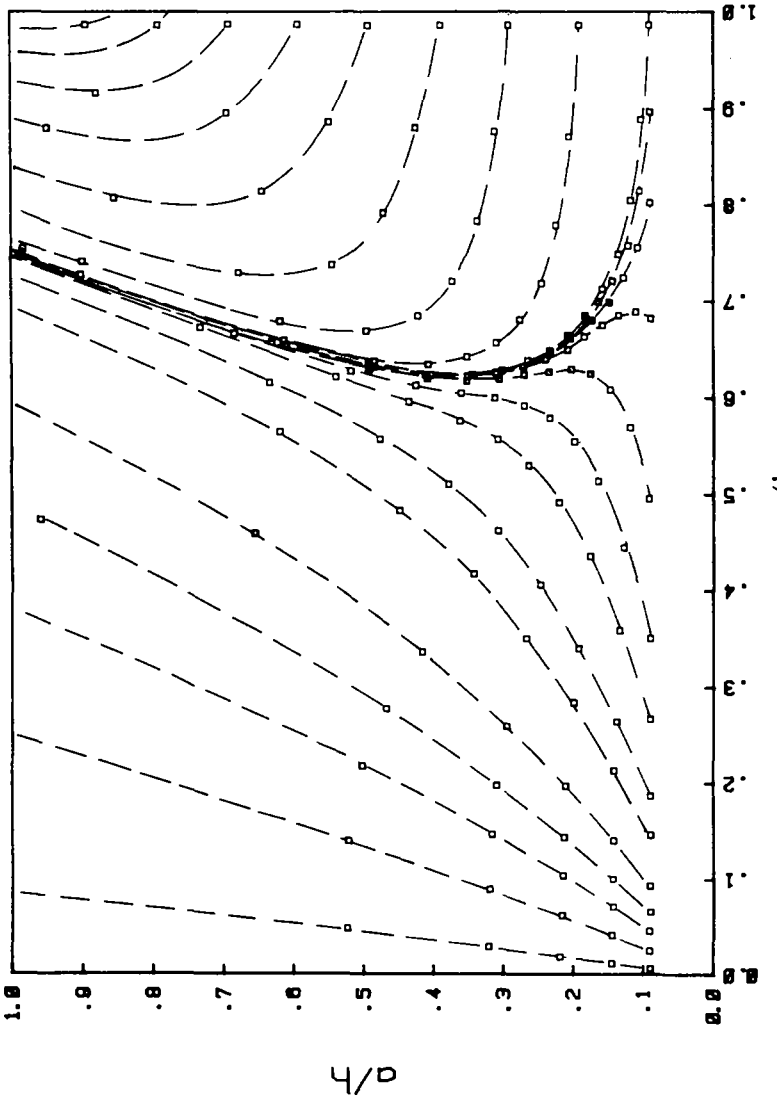

FIG. 10—*Fatigue crack growth trajectories for a combination of uniform and nonuniform stress cycles produced by heat-up and cool-down and reactor trip, respectively.* σ_e *for uniform stress cycles is 96.747 MPa.* $C = 1.59 \times 10^{-13}$. *Change in crack geometry between two points is due to 100 000 uniform stress cycles with two nonuniform stress cycles for every uniform stress cycle* (m = 4).

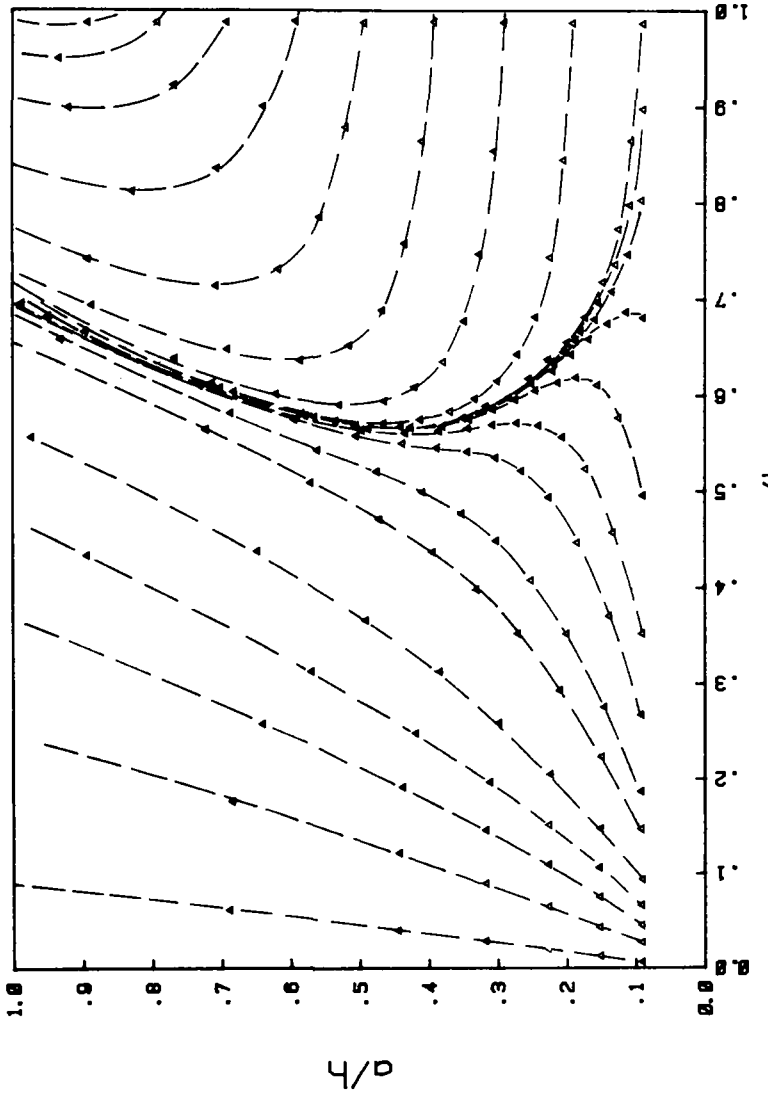

FIG. 11—*Fatigue crack growth trajectories for a combination of uniform and nonuniform stress cycles produced by heat-up and cool-down and reactor trip, respectively.* σ_e *for uniform stress cycles is 96.747 MPa.* $C = 1.59 \times 10^{-13}$. *Change in crack geometry between two points is due to 50 000 uniform stress cycles with five nonuniform stress cycles for every uniform stress cycle* ($m = 4$).

Acknowledgment

This work was supported in part by the Lawrence Livermore National Laboratory under the Load Combinations Program.

APPENDIX

This appendix illustrates the use of crack growth trajectories to compute the number of cycles required to grow a crack from a defined point on a given crack growth trajectory. For example, for $m = 4$, let us compute the number of heat-up to cool-down cycles required to grow a crack from the point indicated by an arrow in Fig. 2 to the next point on the trajectory. This corresponds to initial conditions of $a/h = 0.315$, $a/b = 0.495$, and final conditions of $a/h = 0.369$, $a/b = 0.545$. From Fig. 2, the value of α for these two points is 0.006516. Consider the heat-up and cool-down cycle to have $\sigma_{max} = 104.2$ MPa and $\sigma_{min} = 14.34$ MPa. Then

$$\sigma_e = [\sigma_{max}(\sigma_{max} - \sigma_{min})]^{1/2} = 96.7 \text{ MPa} \tag{9}$$

Let $C = 1.59 \times 10^{-13}$ and pipe wall thickness $h = 0.0635$ m. The following number of cycles then are required to produce the amount of crack growth considered

$$\Delta n = \alpha/(C\sigma_e^m h^{m/2}) = 0.006516/(1.59 \times 10^{-13} \times 96.7^4 \times 0.0635^2)$$

$$= 1.16 \times 10^5 \text{ cycles} \tag{10}$$

Thus, 116 000 cycles of heat-up to cool-down will grow an initial crack of $a = 0.315h = 20$ mm, $b = 40$ mm to a size of $a = 0.369h = 23.4$ mm, $b = 43.0$ mm. The manner in which a crack changes shape as it grows is given by the crack trajectory. The number of cycles required to grow a crack between two points on a given trajectory for any combination of C, σ_e and h can be computed from information on the corresponding value of α.

References

[1] Swedlow, J. L., Ed., *The Surface Crack: Physical Problems and Computational Solutions*, American Society of Mechanical Engineers, New York, 1972.

[2] *Part-Through Crack Fatigue Life Prediction, ASTM STP 687*, American Society for Testing and Materials, 1979.

[3] "Study on the Safety Assessment of Fatigue Strength of Pressure Vessels and Piping Systems in Nuclear Plants," Report No. JWES-AE-7707 (NCR Translation No. 351), Japan Welding Engineering Society, 1977.

[4] Lim, E. Y., Dedhia, D. D., and Harris, D. O., this publication, pp. I-281–I-297.

[5] Harris, D. D., Lim, E. Y., and Dedhia, D. O., "Probability of Pipe Fracture in the Primary Coolant Loop of a Pressurized Water Reactor Plant, Vol. 5; Probabilistic Fracture Mechanics Analysis," Report NUREG/CR 2189, U.S. Nuclear Regulatory Commission, Washington, D.C., 1981.

[6] Nair, P. I., *Transactions of the American Society of Mechanical Engineers, Journal of Engineering Materials and Technology*, Vol. 101, April 1979, pp. 53–58.

[7] Besuner, P. M. in *Mechanics of Crack Growth, ASTM STP 590*, American Society for Testing and Materials, 1976, pp. 403–419.

[8] Besuner, P. M., *Nuclear Engineering and Design*, Vol. 43, No. 1, Aug. 1977, pp. 115–154.

[9] Cruse, T. A., and Besuner, P. M., *Journal of Aircraft*, Vol. 12, No. 4, April 1975, pp. 369–375.

[*10*] Cruse, T. A., Meyers, G. J., and Wilson, R. B. in *Flaw Growth and Fracture, ASTM STP 631*, American Society for Testing and Materials, 1977, pp. 174-189.
[*11*] Rice, J. R., *International Journal of Solids and Structures*, Vol. 8, 1972, pp. 751-758.
[*12*] Chan, A. L., Rybicki, E. F., and Curtis, D. J., "Investigation of Non-Seismic Stresses in a Pressurized Water Reactor Primary Piping System," Report No. SAI-005-81-SJ, Science Applications, Inc., San Jose, Calif., submitted to Lawrence Livermore National Laboratory, Load Combination Program: Project I, Event Decoupling, Jan. 1981.

Fatigue and Stress Corrosion

S. Suresh,[1] *J. Toplosky,*[2] *and R. O. Ritchie*[3]

Environmentally Affected Near-Threshold Fatigue Crack Growth in Steels

REFERENCE: Suresh, S., Toplosky, J., and Ritchie, R. O., **"Environmentally Affected Near-Threshold Fatigue Crack Growth in Steels,"** *Fracture Mechanics: Fourteenth Symposium—Volume I: Theory and Analysis, ASTM STP 791*, J. C. Lewis and G. Sines, Eds., American Society for Testing and Materials, 1983, pp. I-329-I-347.

ABSTRACT: Environmentally affected fatigue crack propagation in steels is described for *ultralow growth rates* (below 10^{-6} mm/cycle) in terms of the role of crack surface corrosion debris in promoting crack closure. It is shown that the reported effects of gaseous and aqueous environments (air, water, hydrogen, helium, etc.) on near-threshold crack growth in lower strength steels are consistent primarily with an oxide-induced crack closure mechanism. Moist atmospheres, such as humid air and water, are shown to promote the formation of oxide deposits within the crack, which at low load ratios are thickened by fretting-assisted oxidation to maximum thicknesses comparable with crack-tip opening displacements. Using ultrasonic techniques, this is shown to increase closure loads and to lower effective alternating stress intensities at the crack tip. Observations that near-threshold growth in dry helium is similar to that in dry hydrogen gas and faster than in air, are shown to be consistent with such concepts since both environments provide a dry atmosphere limiting oxide formation. Extensive data on near-threshold corrosion-fatigue crack growth in ultrahigh-strength (300-M) and lower-strength (2¼Cr-1Mo and SA516) steels are examined in the context of this mechanism, and it is found that the threshold for no crack growth (ΔK_o) is consistent with a maximum excess oxide thickness approximately equal to the pulsating crack-tip displacement (ΔCTOD). The implications of this and other microscopic mechanisms of closure are discussed in the light of microstructural and environmental influences on near-threshold fatigue.

KEY WORDS: fatigue (materials), cracking, fracturing, crack propagation, load ratio, environment, crack closure, alloy steels, pressure vessel steels, thresholds, fracture mechanics

[1]Metallurgist/research engineer, Materials and Molecular Research Division, Lawrence Berkeley Laboratory, University of California, Berkeley, Calif. 94720. Formerly research assistant, Massachusetts Institute of Technology, Cambridge, Mass. 02139.

[2]Research assistant, Department of Mechanical Engineering, Massachusetts Institute of Technology, Cambridge, Mass. 02139.

[3]Professor, Department of Materials Science and Mineral Engineering and Lawrence Berkeley Laboratory, University of California, Berkeley, Calif. 94720. Formerly associate professor, Massachusetts Institute of Technology, Cambridge, Mass. 02139.

Nomenclature

a	Crack length
d	Crack surface oxide thickness
da/dN	Fatigue crack growth rate
ΔCTOD	Pulsating (cyclic) crack-tip opening displacement
E	Elastic modulus
ΔK	Alternating stress-intensity factor ($K_{max} - K_{min}$)
ΔK_{eff}	Effective alternating stress-intensity factor ($K_{max} - K_{cl}$)
ΔK_o	Threshold stress intensity for no detectable cyclic crack growth
K_{cl}	Stress intensity to cause closure of fatigue crack
K_{1c}	Plane strain fracture toughness
K_{Iscc}	Threshold stress intensity for environmentally assisted cracking
K_{max}^T	transition maximum stress intensity for hydrogen-assisted growth
K_{max}	Maximum stress-intensity factor
K_{min}	Minimum stress-intensity factor
N	Number of cycles
R	Load ratio (K_{min}/K_{max})
UTS	Tensile strength
Y_c	Cyclic yield strength

Recently a new approach to modelling corrosion-fatigue crack growth has been proposed based on the concept that if corrosion deposits form within growing cracks to a size comparable with crack-tip opening displacements, significant crack closure can result which reduces effective alternating stress intensities at the crack tip [*1–3*].[4] This concept, termed *oxide-induced crack closure,* has been found to be pertinent in explaining somewhat surprising observations reported recently on environmentally affected fatigue crack growth at near-threshold levels (that is, below 10^{-6} mm/cycle), where, for instance, seemingly aggressive environments are found in certain materials to retard crack growth [*1–4*]. For example, near-threshold fatigue crack propagation has been found (*a*) to be *slower* in water [*3,5,6*] and *faster* in helium gas compared to air in lower-strength steels [*1–3,7*], (*b*) to be marginally *slower* in dry hydrogen gas compared to air in ultrahigh-strength steels [*4,8*], and (*c*) in general to be susceptible only to an environmental contribution to cracking at low load ratios [*1,3*]. Such observations are at first sight inconsistent with classical mechanisms of corrosion fatigue, involving such processes as hydrogen embrittlement or active path corrosion (that is, metal dissolution) [*9*]. It appears that with the ultralow growth rates, small crack-tip displacements, and high frequencies generally associated with crack propagation at alternating stress intensities (ΔK) approaching the threshold for no detectable crack growth (ΔK_o), conventional wisdom on environmentally-

[4]The italic numbers in brackets refer to the list of references appended to this paper.

assisted cracking becomes questionable and alternative competing mechanisms, such as oxide-induced crack closure, become more predominant.

According to the oxide-induced crack closure model [*1–3*], near-threshold growth rates are faster in dry hydrogen gas because of an absence of water vapor compared to moist air. Moist environments result in the formation of readily observable oxide films within the crack, which are thickened at low load ratios by "fretting oxidation [*10*]." The latter process is essentially a continual breaking and reforming of the oxide scale on the crack surfaces due to abrasion and "smashing" together of these surfaces, and is a result of plasticity-induced crack closure [*11*] and the Mode II crack-tip displacements characteristic of near-threshold crack growth [*12*]. Consistent with this mechanism, oxide films have been measured to be between 3 to 20 times thicker than oxide formed naturally on freshly bared specimens held in the same environment for similar periods of time [*3,10*]. Such corrosion deposits, which are much less predominant in dry atmospheres or at high load ratios (where plasticity-induced closure is insignificant), provide a mechanism for increased crack closure. By allowing earlier contact between mating fracture surfaces during unloading, closure loads are raised such that the effective stress intensity range at the crack tip is reduced, that is, the presence of the foreign debris effectively raises K_{min}. This mechanism, however, is specific only to stress intensity ranges where oxide thicknesses are of the order of cyclic crack-tip opening displacements (ΔCTOD), for example, at near-threshold levels.

The objective of the present paper is to review some new observations on environmentally influenced near-threshold fatigue crack growth in both ultrahigh-strength and lower-strength steels in the context of such alternative corrosion fatigue mechanisms. In particular, direct experimental measurements of oxide-induced crack closure are described, and the significance of this microscopic closure is discussed in terms of effects of microstructure and environment on near-threshold fatigue crack growth behavior.

Experimental Procedures

In this investigation, alloy steels covering a wide range of yield strengths from 327 to 1740 MPa were examined. These were an ultrahigh-strength silicon-modified AISI 4340 steel (300-M), two lower-strength 2¼Cr-1Mo pressure vessel steels, namely quenched and tempered ASTM A542 Classes 2 and 3, and a normalized ASTM A516 Grade 70 pipeline steel.[5] The 300-M alloy was oil quenched from 870°C, and tempered at 300°C and at 650°C (hereafter referred to as T300 and T650, respectively) to give tempered

[5]For brevity, the lower strength steels are referred to in the text by their American Society of Mechanical Engineers (ASME) designations, namely SA542-2, SA542-3, and SA516-70, respectively.

martensitic structures. The lower strength steels, which were heat-treated according to appropriate ASTM standards, displayed duplex ferritic/pearlitic (SA516), bainitic (SA542-3), and martensitic (SA542-2) microstructures. Room temperature mechanical properties are shown in Table 1; full details of microstructures and heat-treatment procedures are described elsewhere [*13-15*].

Near-threshold fatigue testing was performed with 12.7-mm-thick compact specimens[6] (T-L orientation), cycled under load control at frequencies between 0.5 and 50 Hz (sine wave). Tests were conduced at load ratios ($R = K_{min}/K_{max}$) between 0.05 and 0.75 in carefully controlled room temperature environments of moist air (30 percent relative humidity), distilled water, and purified and dehumidified hydrogen and helium gases. Gaseous atmopheres were held at 138 kPa pressure in a small O-ring sealed chamber, locally mounted on the specimen, with gas purity maintained using an extensive purification system including molecular sieves, cold traps, and heat-bakeable lines [*15*]. Near-threshold crack growth rates were monitored using d-c electrical potential techniques under load-shedding (decreasing ΔK) conditions, with the threshold ΔK_o defined in terms of a maximum growth rate of 10^{-8} mm/cycle [*16*]. All plotted data represent mean values from several individual tests. Full experimental details have been described elsewhere [*1,14-17*].

Crack surface oxide deposits were characterized using electron spectroscopy for chemical analysis (ESCA) and scanning Auger spectroscopy of fatigue fracture surfaces. Using a tantalum oxide standard, depth-concentration profiles were obtained using argon (Ar^+) sputtering to define the extent of oxidation, as described in detail elsewhere [*3,17*]. The resulting crack closure phenomena were assessed using ultrasonic techniques similar to those developed by Buck and co-workers [*18,19*]. Such procedures are described in Ref *17*.

TABLE 1—*Room temperature mechanical properties of steels investigated.*

Steel	Structure	Monotonic Yield Strength, MPa	Cyclic Yield Strength, MPa	Ultimate Tensile Strength, MPa	Reduction in Area, %	K_{Ic}, MPa$\sqrt{m}$	K_{Iscc} (H_2 gas), MPa$\sqrt{m}$
300 M-T300	martensite	1740	1700	2000	48	65	18 to 20
300 M-T650	martensite	1070	970	1200	56	152	...
SA542-2	martensite	769	568	820	56	...	80
SA542-3	bainite	500	400	610	77	295	85
SA516-70	ferrite-pearlite	327	...	496	...	233	...

[6]Plane-strain conditions were maintained such that cyclic plastic zone sizes did not exceed 1/15 of specimen thickness.

Results

Behavior in Lower-Strength Steels

The variation of fatigue crack growth per cycle with stress intensity range for a fully bainitic 2¼Cr-1Mo steel (SA542-3) is shown in Fig. 1 for environments of moist air and dry gaseous hydrogen (138 kPa pressure), representing tests at load ratios of 0.05 and 0.75 with frequencies between 0.5 and 50 Hz. As reported previously [*20*], the influence of hydrogen is evident in two growth rate regimes, namely at mid-growth rate levels above $\sim 10^{-5}$ mm/cycle and at near-threshold levels below $\sim 10^{-6}$ mm/cycle. In the mid-growth rate regime, at maximum stress intensities K_{max} in excess of ~ 20 MPa$\sqrt{m}$[7] and where frequencies (for $R = 0.05$) are below 5 Hz, crack growth rates are increased abruptly in hydrogen gas coincident with a fracture mode transition from predominately transgranular to predominately intergranular cracking, as shown in Fig. 2*b* and *d*. The major difference in growth rates between hydrogen and air, however, occurs progressively as the threshold ΔK_o is approached. In this regime at $R = 0.05$, even at high frequencies (50 Hz), crack propagation rates are up to two orders of magnitude faster in hydrogen with ΔK_o values reduced by as much as 27 percent, although the fracture surface morphology (predominately transgranular) remains unchanged (Fig. 2*a* and *c*). Significantly, however, near-threshold growth rates at high load ratios ($R = 0.75$) appear comparable in both environments. Similar behavior for air and dry hydrogen environments has been observed in bainitic-ferritic 2¼Cr-1Mo (SA387) steels [*1*] and in the pearlitic-ferritic SA516-70 pipeline steel shown in Fig. 3. In the near-threshold regime at 50 Hz, the presence of hydrogen similarly results in faster growth rates at low load ratios ($R = 0.15$), whereas behavior in moist air and hydrogen is almost identical at $R = 0.75$. Also shown in Fig. 3 are mid-growth rate data [*21*] for moist air and high-pressure (6900 kPa) hydrogen tests on the same heat of steel at frequencies of 0.1 to 10 Hz. A fifty-fold increase in hydrogen pressure can be seen to increase growth rates by up to a factor of 20, coincident with a reduction in the stress intensity $K_{max}{}^{T}$, above which the mid-growth rate effect of hydrogen is first observed.

In Fig. 4, the influence of a number of environments on near-threshold growth is compared with moist air data for SA542-3 at $R = 0.05$ (50 Hz). What is perhaps most significant about these results is that near-threshold growth rates are approximately 100 times higher in dry hydrogen, yet in wet hydrogen this effect totally disappears. In distilled water, growth rates are marginally *slower* compared to air, whereas they are markedly *faster* in dry

[7]This critical value for the onset of hydrogen-assisted growth, termed $K_{max}{}^{T}$, is of the order of 20 MPa$\sqrt{m}$ in SA542-3. This value is found to be independent of load ratio and can be considered, in this case, as an effective threshold for sustained load hydrogen embrittlement contributions to fatigue crack growth [*20*].

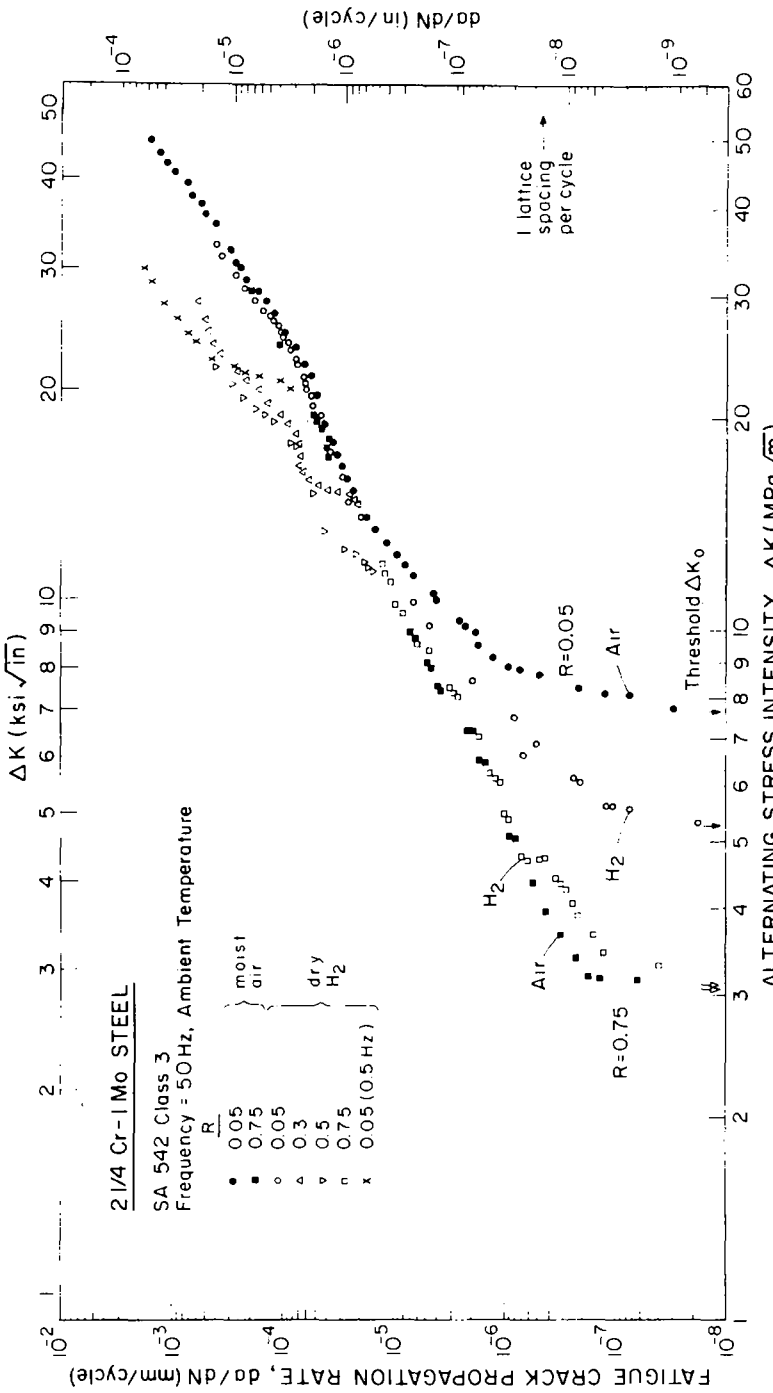

FIG. 1—*Fatigue crack propagation in bainitic 2¼Cr-1Mo steel (SA542-3) tested in moist air and dry hydrogen gas, showing two regimes of hydrogen-assisted growth.*

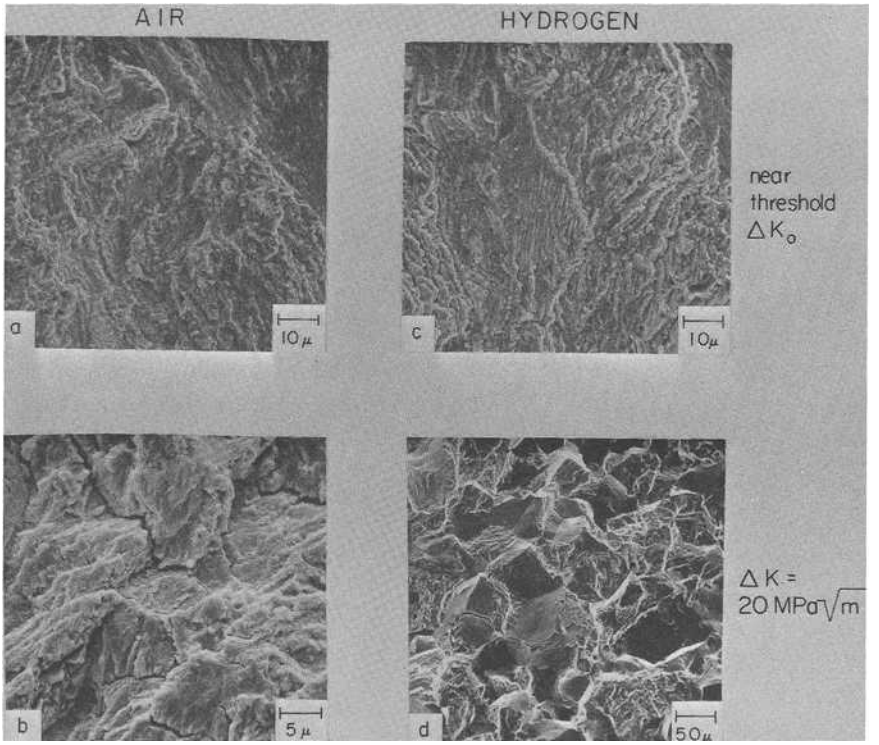

FIG. 2—Fractography of fatigue crack growth in moist air and dry hydrogen (R = 0.05, 50 Hz) at near-threshold levels and at ΔK = 20 MPa√m.

gaseous helium. Helium in fact behaves very similarly to dry hydrogen in that no effect is seen at high load ratios ($R = 0.75$), as shown for martensitic SA542-2 steel in Fig. 5.

Thus, environmental influences at near-threshold levels predominate at low load ratios, and are characterized by the fact that growth rates are substantially higher in dehumidified environments such as dry hydrogen and helium gases, compared to moist environments such as wet hydrogen, moist air, and distilled water. Such results appear at variance with classical mechanisms of corrosion fatigue, yet can be understood by considering a contribution from oxide-induced crack closure.

Behavior in Ultrahigh-Strength Steels

The variation of fatigue crack propagation rates in 300-M steel as a function of stress intensity range at $R = 0.05$ is shown in Fig. 6 for the highest strength 300°C tempered structure tested in moist air and hydrogen. As for

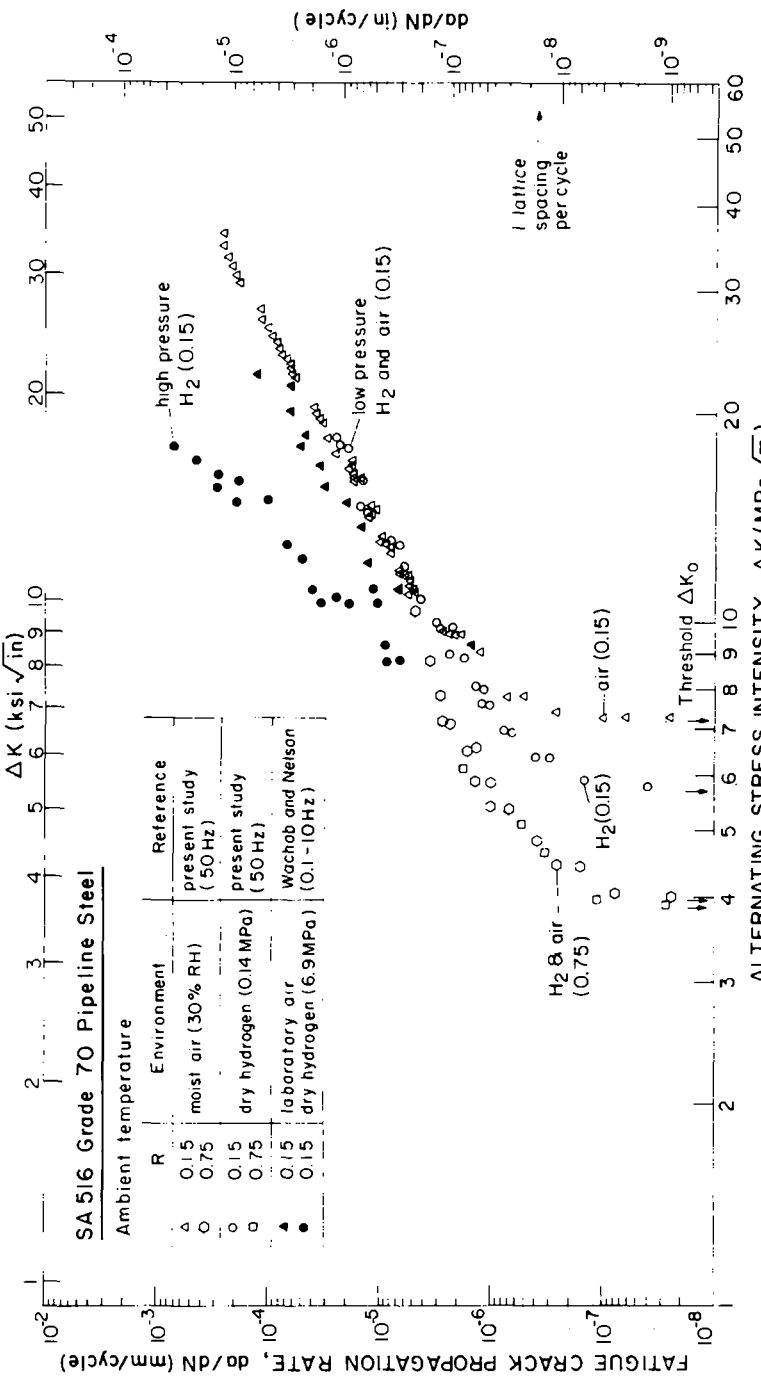

FIG. 3—*Fatigue crack propagation in ferritic-pearlitic SA516-70 steel tested in moist air and dry hydrogen gas at pressures of 0.14 and 6.9 MPa. High pressure data from Ref 21.*

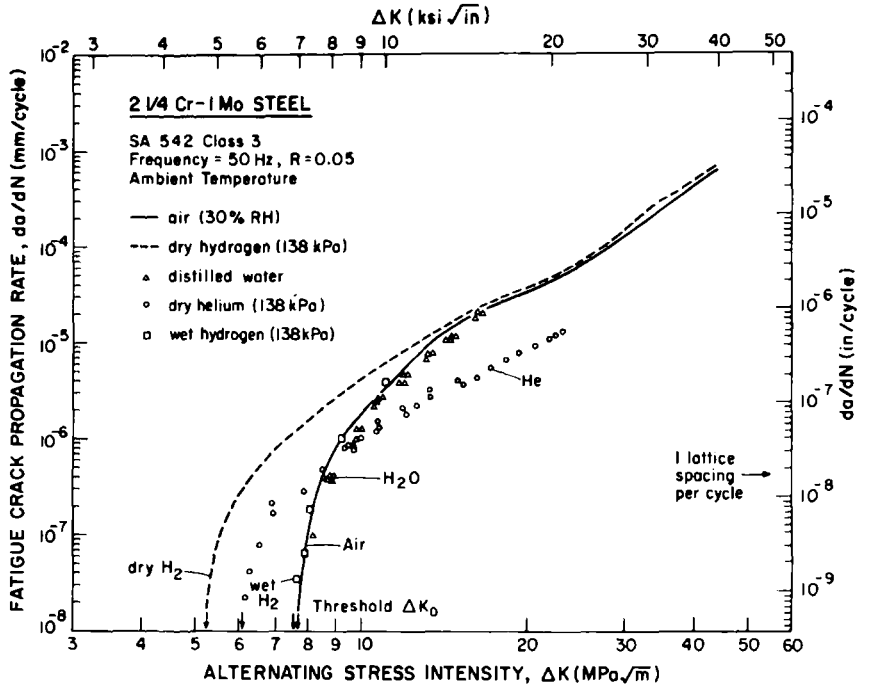

FIG. 4—*Environmentally influenced fatigue crack propagation in bainitic SA542-3 at* R = *0.05 (50 Hz) in moist air, distilled water, dry helium, and wet and dry hydrogen gas.*

lower strength steels (Figs. 1 and 3), two distinct regimes of environmentally influenced crack growth are seen. Above 10^{-5} mm/cycle, although growth rates in air and hydrogen are similar at 50 Hz, lowering the frequency to 5 Hz results in significantly faster growth rates in hydrogen. This behavior, which has been reported by others [*22-24*], is accompanied by a marked increase in intergranular fracture for hydrogen-assisted failures. What is intriguing, however, is the observation that at growth rates below 10^{-6} mm/cycle at 50 Hz frequency, the presence of hydrogen gas actually results in *slower* near-threshold propagation rates and a 16 percent higher threshold ΔK_o value compared to air.

Similar behavior is seen in the lower-strength T650 microstructure where, at both high and low load ratios (R = 0.05 and 0.70) at 50 Hz, growth rates in air and hydrogen are similar until near-threshold levels, whereupon they become *slower* in hydrogen, as shown in Fig. 7. Threshold ΔK_o values in hydrogen are again between 11 to 15 percent higher than in air. Similar to lower strength steels (Fig. 2), fracture surfaces close to the threshold were predominately transgranular and indistinguishable between air and hydrogen environments. Once again, the role of environment at near-threshold levels appears distinctly different from more familiar behavior

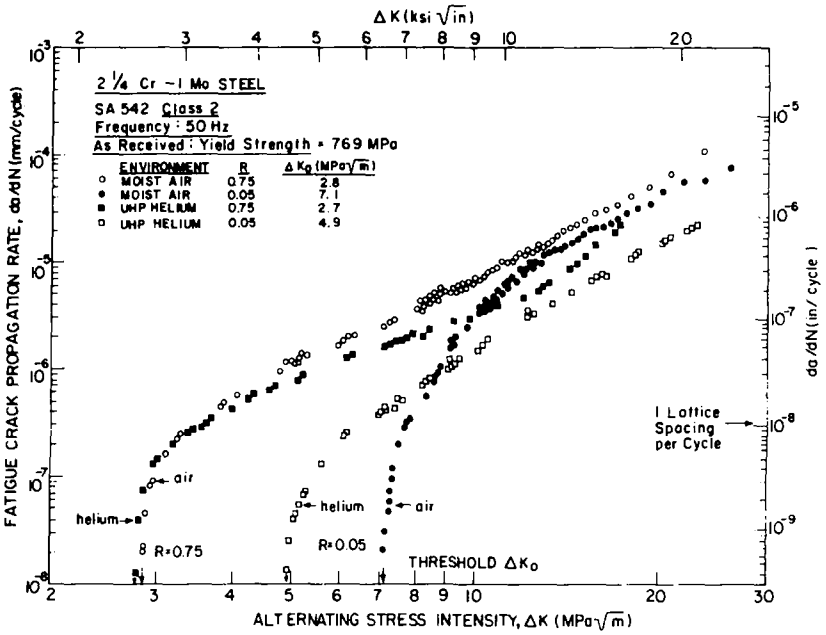

FIG. 5—*Fatigue crack growth in martensitic SA542-2 tested in moist air and dry helium gas at* R = *0.05 and 0.75 (50 Hz), showing faster near-threshold growth in helium at low load ratios.*

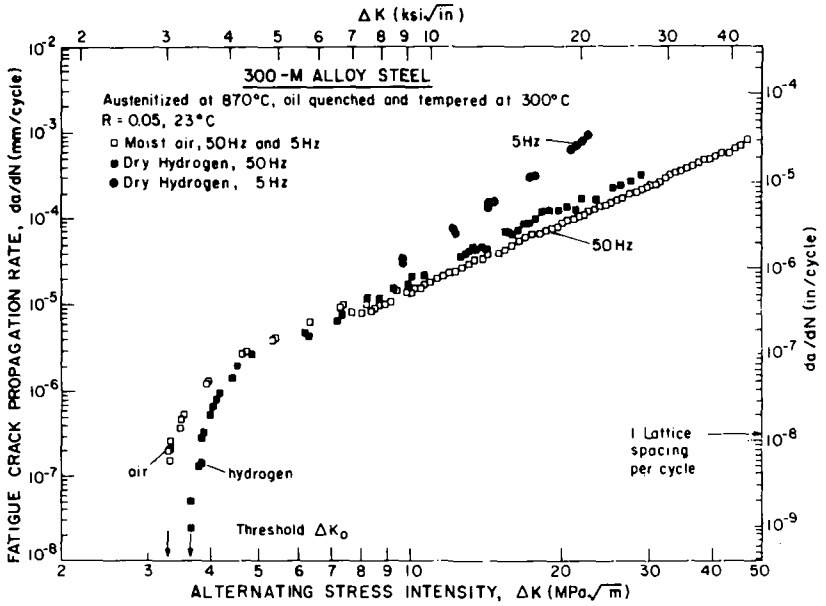

FIG. 6—*Fatigue crack growth in martensitic 300-M ultrahigh-strength steel, tempered at 300°C, tested in moist air and dry hydrogen at 5 and 50 Hz* (R = *0.05).*

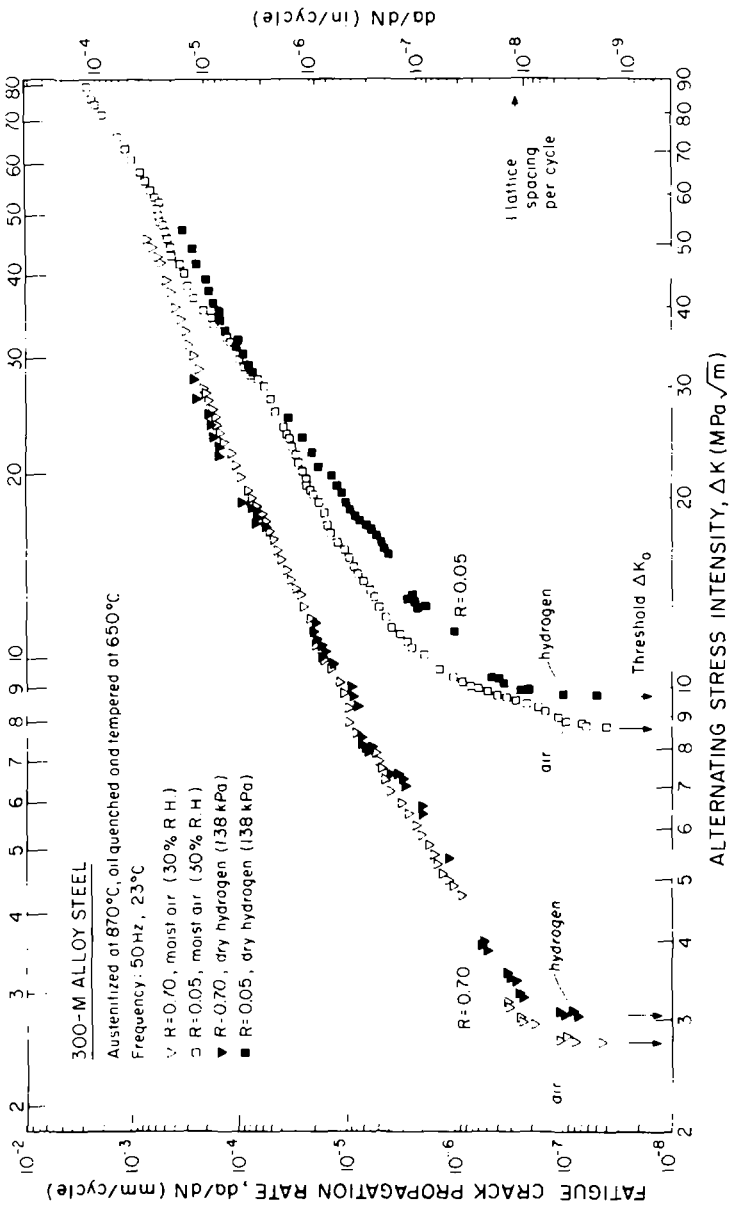

FIG. 7—*Fatigue crack growth in martensitic 300-M steel, tempered at 650°C, showing slower near-threshold growth rates in dry hydrogen compared to moist air at* R = *0.05 and 0.70 (50 Hz).*

commonly observed in higher growth rates, and is seemingly at variance with classical corrosion fatigue mechanisms.

Discussion

It is well established that in the mid-growth rate regime above $\sim 10^{-5}$ mm/cycle, hydrogen-containing or producing environments can cause significant accelerations in fatigue crack growth rates in both high-strength [*20–24*] and lower-strength [*20,25*] steels. Hydrogen-assisted growth in this region is sensitive to load ratio, frequency, and pressure (Figs. 1 and 3), and in many materials is accompanied by a change from a predominately transgranular to a predominately intergranular fracture mode (Fig. 2). Mechanistically, reaction kinetic studies [*22,23*] have indicated that such environmentally assisted cracking can be attributed to hydrogen embrittlement processes rate-limited by surface reactions at the crack tip. It appears that in gaseous hydrogen atmospheres this rate-limiting step involves chemisorption of hydrogen, whereas in water/water vapor environments crack growth is limited by the rate of hydrogen production which results from the reactions with (or oxidation of) freshly exposed surfaces at the crack tip [*23*].

However, an even more pronounced effect in the presence of hydrogen has been shown in the current work for near-threshold growth rates below 10^{-6} mm/cycle, an effect which is characteristically very different from behavior at higher growth rates. Steels such as 300-M, for example, which are known for their marked susceptibility to hydrogen embrittlement, show marginally *slower* growth rates in hydrogen compared to air at near-threshold levels. On the other hand, lower-strength steels, which traditionally have been considered to be relatively immune to hydrogen embrittlement, show faster rates in dry hydrogen, no effect in wet hydrogen, and marginally slower rates in water, again with reference to room air. Previous models [*16,26–29*] for the role of environment at ultralow growth rates relied on very limited data and were based on classical corrosion-fatigue mechanisms, specifically hydrogen embrittlement in steels. While such mechanistic processes may still occur at near-threshold levels, even at high frequencies, it is clear that in light of the current results, competing processes such as those based on crack closure must play a dominant role.

Models [*1–3*] based on the role of corrosion debris formed inside the crack can provide such a description of environmentally influenced crack growth at near-threshold levels, at least for lower-strength steels. Moist environments, such as humid air, water, and wet hydrogen, simply allow oxide products to build up on the crack surfaces due to fretting and abrasion from plasticity-induced closure and Mode II displacements, as shown in Fig. 8. Provided such deposits are of a size comparable with crack-tip opening displacements, the effective stress intensity (ΔK_{eff}) at the crack tip will be reduced correspondingly through oxide-induced crack closure [*1–3*] and possibly addi-

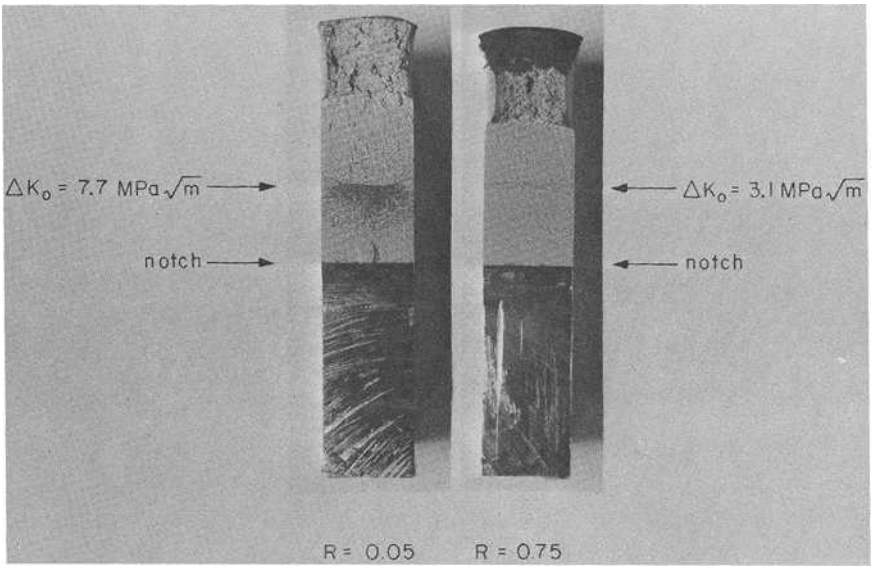

FIG.8—*Zones of corrosion deposits formed on near-threshold fatigue fracture surfaces of SA542-3, tested in air at* R = *0.05 and 0.75.*

tional crack blunting [*7,30*] effects. In dry atmospheres, such as dehumidified hydrogen and helium, where less oxide can be generated, the reduced role of closure promotes faster propagation rates. At high load ratios, the relative absence of such closure mechanisms results in similar growth rate behavior in both wet and dry environments (Figs. 1, 3, and 5).

Supporting evidence for this mechanism has been obtained through oxide thickness and closure measurements [*17*]. ESCA and Auger analyses of fracture surfaces in SA542-3 [*3*] revealed that corrosion deposits were predominately iron oxide (Fe_2O_3) and varied in thickness with crack length (and hence crack growth rate) in the manner shown in Fig. 9. It is apparent that the thickness of the oxide scale varies inversely with growth rate, is independent of the time spent from crack initiation to final failure, and is at a maximum close to the threshold ΔK_o. *At* $R = 0.05$ for tests in moist air, the maximum oxide thickness is approximately 0.2 μm, roughly 20 times larger than oxides formed naturally under similar environmental conditions for the same length of time. Even in dry hydrogen at $R = 0.05$, the oxide formed close to the threshold was 0.1 μm thick, presumably because oxide formation can occur via fretting mechanisms even in the presence of minute traces of moisture in dehumidified atmospheres. Conversely, at high load ratios ($R = 0.75$) where closure and fretting effects would be negligible, oxide thicknesses in air and hydrogen environments were of the order of naturally formed oxide (that is, ~ 0.01 μm).

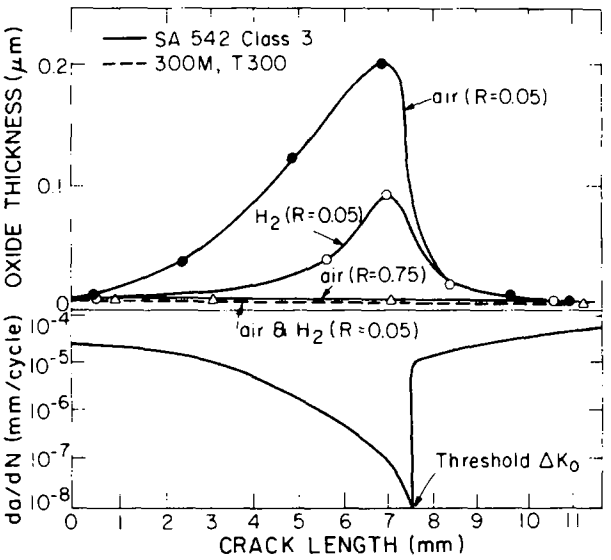

FIG. 9—*Ar^+ sputtering data showing variation of crack flank oxide thickness with crack length (measured from the notch tip) and crack growth rate* (da/dN) *for SA542-3 and 300-M steels tested in moist air and hydrogen gas at* R = *0.05 and 0.75.*

The suggestion that the presence of such oxides at low load ratios can increase crack closure loads can be verified experimentally by using ultrasonics to detect the opening and closing of a near-threshold crack [*18,19*]. Such measurements on SA542-3 steel [*17*] indicated that closure loads[8] were roughly 50 percent larger in moist air environments compared to dry hydrogen, in support of oxide-induced closure concepts.

Since one unit volume of iron produces 2.13 unit volumes of Fe_2O_3, the measurements in Fig. 9 represent approximately the total excess material inside the crack, assuming an equal thickness on each crack face. A comparison of such oxide thickness data measured for a number of steels with computed crack-tip opening displacements[9] indicates that, at threshold, ΔCTOD is of the order of the maximum excess oxide thickness, as shown in Fig. 10. Whereas Auger thickness measurements and ΔCTOD computations are somewhat uncertain, this "model" for the existence of a threshold is clearly physically appealing since it indicates that the crack will no longer propagate when it becomes "wedged closed" with corrosion deposits such

[8]Estimates of the stress intensity at closure (K_{cl}), determined from such measurements, were found to be of the order of the threshold stress intensity levels for both air and hydrogen environments at $R = 0.05$ [*17*].

[9]Following the finite-element analyses of Shih [*31*], crack tip displacements were calculated from the expression $\Delta CTOD = 0.5\ \Delta K^2/2\ Y_c E$, valid for a material of yield strain ~0.002, strain hardening exponent ~0.1, deformed in plane strain. Y_c is the cyclic yield stress and E the appropriate elastic modulus.

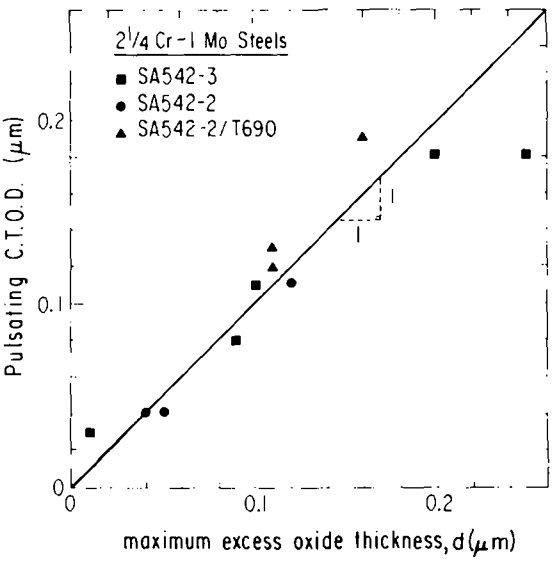

FIG. 10—*Data for 2¼Cr-1Mo steels* [3] *showing correspondence of maximum excess oxide thickness* (d) *with ΔCTOD at the threshold.*

that the effective stress intensity range becomes small. It follows from this that one might not expect to see a threshold for tests *in vacuo*, and while interpretations of such a result may be clouded by re-welding effects [*2,16*], the vacuum data of Cooke et al [*26*] and Skelton and Haigh [*32*] on medium-strength steels do in fact show no well-defined threshold!

Behavior in ultrahigh-strength steel, however, appears considerably more complicated [*4*]. Early data on high-strength rotor steels by Stewart [*2*] indicated that thresholds in air and hydrogen were identical (no growth rate measurements were made). Such an observation is at least consistent with the idea of oxide-induced closure, since oxide formation should be reduced with increasing strength level. This follows from decreased fretting-oxidation effects arising from less plasticity-induced closure and less abrasion of the oxide debris on the harder steel substrate, and from the fact that the extent of oxide buildup will be limited by the smaller crack-tip displacements. Auger measurements on the present 300M-T300 condition (Fig. 9) indicated excess oxide thicknesses of approximately 0.01 μm at $R = 0.05$, which are comparable with the ΔCTOD value at the threshold. The oxide films, though, are considerably smaller than those in lower-strength steels and measurements often approach background noise levels. What is surprising, however, is that careful experimentation on ultrahigh-strength steels subsequent to Stewart's work [*2*] shows that threshold values are in fact marginally ***higher*** in hydrogen compared to moist air, at both low and high load ratios (Figs. 6 and 7). This result, which has been confirmed in 300-M by testing at con-

stant ΔK with changing environment [*4*], and independently verified by Liaw et al [*8*] on rotor steels, remains largely unexplained at this time.

Nevertheless, it is conceivable that in such high-strength steels, known for their susceptibility to degradation from hydrogen, environmentally affected near-threshold growth still may be associated predominantly with hydrogen embrittlement mechanisms even at high frequencies [*4*]. The results in Figs. 6 and 7, however, imply that at the partial pressures and periods (reciprocal frequency) relevant to these data, hydrogen uptake into the matrix, and hence the extent of embrittlement, would need to be more efficient in water vapor than in gaseous hydrogen. Although contrary to behavior in steels at higher growth rates [*25,33*], this behavior is similar to aluminum alloys [*34*], and presumably occurs because at the small ΔCTOD's associated with near-threshold levels, where fretting-oxidation can promote enhanced oxide growth even in nominally dry environments (Fig. 9), crack surface corrosion deposits may be thicker than naturally formed oxide. Since it is this formation of the oxide which is the source of hydrogen for water vapor environments, whereas the oxide provides a barrier for hydrogen permeation for hydrogen gas phase environments, moist air atmospheres may well be more aggressive than hydrogen gas for steel at near-threshold levels.

Thus, the results presented in this paper provide an indication that environmental influences on fatigue crack growth behavior at near-threshold levels and at higher growth rates may be governed by entirely different mechanisms. Although classical processes such as hydrogen embrittlement and active path corrosion may be effective mechanisms controlling corrosion fatigue behavior over a wide range of growth rates, at near-threshold levels it is clear that competing mechanisms, namely oxide-induced crack closure, can become active, particularly in lower-strength steels, and dominate overall behavior. Near-threshold behavior in ultrahigh-strength steels similarly shows marked differences compared to higher growth-rate behavior, but remains largely unexplained at this time.

The competing role of oxide-induced closure becomes significant at near-threshold levels because the size-scale of the corrosion debris is of the order of the crack-tip displacements. Size-scales of the fracture surface morphology or roughness, however, also may approach this dimension, thus providing additional sources of closure [*35*]. Given the small ΔCTOD's and Mode II displacements near ΔK_o, a rougher fracture surface may lead to increased closure simply by wedging open the crack at discrete contact points along the crack faces [*36–38*]. In terms of this mechanism, one might expect increasing threshold ΔK_o values in coarser-grained materials due to the occurrence of rougher fracture surfaces, which is consistent with reported data [*16*]. Further, threshold values should be decreased in higher-strength materials due to reduced plasticity-induced closure, less fretting [*1–3*] and perhaps smoother fracture surfaces [*37*], again consistent with reported data

for steels [*16*]. Although these crack closure explanations for observed microstructural effects are at present somewhat speculative, they are in keeping with one prominent characteristic of near-threshold behavior, that in general the beneficial effects of increasing grain size and decreasing strength are markedly reduced at high load ratios (that is, $R \gtrsim 0.5$). Thus, similar to the lack of environmental effects at high load ratios at near-threshold levels in lower-strength steels, this strongly suggests a dominant role of fatigue crack closure.

Conclusions

Based on a study of environmentally influenced fatigue crack propagation at high frequencies (0.2 to 50 Hz) in a wide range of steels, it is apparent that at near-threshold levels, below $\sim 10^{-6}$ mm/cycle, the overall growth rate behavior results from competing mechanisms. In higher-strength steels where the role of crack closure is minimized, conventional corrosion fatigue processes, that is, hydrogen embrittlement, appear to dominate, although unlike behavior at higher growth rates, moist air/water vapor environments seem marginally more aggressive than dry hydrogen gas. In lower-strength steels, however, the production of copious corrosion deposits in moist environments can promote large crack wedging effects, which at near-threshold levels and low load ratios can markedly influence the overall growth rate behavior through the mechanism of oxide-induced crack closure.

Acknowledgments

The work was supported by the Director, Office of Energy Research, Office of Basic Energy Sciences, Materials Science Division of the U.S. Department of Energy, under Contract Nos. W-7405-ENG-48 and DE-AC02-79ER10389.A000, with additional support from the Division of Fossil Energy Research. Thanks are due to A. Joshi, R. E. Lewis, and J. Martin for help with the Auger measurements, R. Fuquen-Molano, C. White, and D. M. Parks for experimental assistance and helpful discussions, and J. D. Landes, D. M. McCabe, H. Wachob, and R. P. Wei for generously providing the lower-strength steels.

References

[*1*] Ritchie, R. O., Suresh, S., and Moss, C. M., *Journal of Engineering Materials and Technology*, Transactions of the American Society of Mechanical Engineers, Vol. 102, 1980, pp. 293–299.

[*2*] Stewart, A. T., *Engineering Fracture Mechanics*, Vol. 13, 1980, pp. 463–478.

[*3*] Suresh, S., Zamiski, G. F., and Ritchie, R. O., *Metallurgical Transactions A*, Vol. 12A, 1981, pp. 1435–1443.

[*4*] Toplosky, J. and Ritchie, R. O., *Scripta Metallurgica*, Vol. 15, 1981, pp. 905–908.

[5] Paris, P. C., Bucci, R. J., Wessel, E. T., Clark, W. G., and Mager, T. R. in *Stress Analysis and Growth of Cracks, ASTM STP 513,* American Society for Testing and Materials, 1972, pp. 141-176.

[6] Tu, L. K. L. and Seth, B. B., *Journal of Testing and Evaluation,* American Society for Testing and Materials, Vol. 6, 1978, pp. 66-74.

[7] Ford, F. P., *BWR Environmental Cracking Margins for Carbon Steel Piping,* Final Report RP 1248/1, Electric Power Research Institute, Palo Alto, Calif., 1981.

[8] Liaw, P. K., Hudak, S. J., Jr., and Donald, J. K. in this publication, pp. II-370-II-388.

[9] Thompson, A. W. and Bernstein, I. M., *Advances in Corrosion Science and Technology,* Vol. 7, R. W. Staehle and M. G. Fontana, Eds., Plenum Press, New York, 1978, p. 53.

[10] Benoit, D., Namdar-Irani, R., and Tixier, R., *Materials Science and Engineering,* Vol. 45, 1980, p. 1.

[11] Elber, W. in *Damage Tolerance in Aircraft Structures, ASTM STP 486,* American Society for Testing and Materials, 1971, pp. 230-262.

[12] Davidson, D. L., *Fatigue of Engineering Materials and Structures,* Vol. 3, 1981, pp. 229-236.

[13] Horn, R. M. and Ritchie, R. O., *Metallurgical Transactions A,* Vol. 9A, 1978, pp. 1039-1053.

[14] Ritchie, R. O., *Journal of Engineering Materials and Technology,* Transactions of the American Society of Mechanical Engineers, Vol. 99, 1977, pp. 195-204.

[15] Ritchie, R. O. and Fuquen-Molano, R., M.I.T. Fatigue and Plasticity Laboratory Report No. FPL/R/80/1035, Massachusetts Institute of Technology, Cambridge, Mass., 1980.

[16] Ritchie, R. O., *International Metals Reviews,* Vol. 20, 1979, pp. 205-230.

[17] Suresh, S., Parks, D. M., and Ritchie, R. O., in *Fatigue Thresholds,* International Conference Proceedings, Stockholm, J. Bäcklund, A. F. Blom, and C. J. Beevers, Eds., Engineering Materials Advisory Service, Warley, Vol. I, 1982, pp. 391-408.

[18] Frandsen, J. D., Inman, R. V., and Buck, O., *International Journal of Fracture,* Vol. 11, 1975, pp. 345-348.

[19] Mahulikar, D. S. and Marcus, H. L., *Fatigue and Engineering Materials and Structures,* Vol. 3, 1981, pp. 257-264.

[20] Suresh, S., Moss, C. M., and Ritchie, R. O., *Transactions of Japan Institute of Metals,* Vol. 21, 1980, pp. 481-484.

[21] Wachob, H. F. and Nelson, H. G., *Hydrogen Effects in Metals, Proceedings of the Third International Conference on Hydrogen,* I. M. Bernstein and A. W. Thompson, Eds., The Metallurgical Society of the American Institute of Mining, Metallurgical, and Petroleum Engineers, 1981, pp. 703-711.

[22] Wei, R. P. and Landes, J. D., *Materials Research and Standards,* American Society for Testing and Materials, Vol. 9, 1969, p. 25.

[23] Simmons, G. W., Pao, P. S., and Wei, R. P., *Metallurgical Transactions A,* Vol. 9A, 1978, p. 1147.

[24] Austen, I. M. and McIntyre, P., *Metal Science,* Vol. 13, 1979, pp. 420-428.

[25] Brazill, R. L., Simmons, G. W., and Wei, R. P., *Journal of Engineering Materials and Technology,* Transactions of the American Society of Mechanical Engineers, Vol. 101, 1979, pp. 199-204.

[26] Cooke, R. J., Irving, P. E., Booth, G. S., and Beevers, C. J., *Engineering Fracture Mechanics,* Vol. 7, 1975, pp. 69-77.

[27] Irving, P. E. and Beevers, C. J., *Metallurgical Transactions,* Vol. 5, 1974, pp. 391-398.

[28] Gerberich, W. W. and Moody, N. R. in *Fatigue Mechanisms, ASTM STP 675,* American Society for Testing and Materials, 1979, pp. 292-334.

[29] Stanzl, S. and Tschegg, E., *Acta Metallurgica,* Vol. 29, 1981, pp. 21-33.

[30] Radon, J. C., Branco, C. M., and Culver, L. E., *International Journal of Fracture,* Vol. 12, 1976, p. 467.

[31] Shih, C. F., *Journal of Mechanics and Physics of Solids,* Vol. 29, 1981, pp. 305-330.

[32] Skelton, R. P. and Haigh, J. R., *Materials Science and Engineering,* Vol. 36, 1978, pp. 17-25.

[33] McIntyre, P. in *Mechanics and Mechanisms of Crack Growth,* M. J. May, Ed., British Steel Corp., Rotherham, U.K., 1973, pp. 130-155.

[34] Wei, R. P., Pao, P. S., Hart, R. G., Weir, T. W., and Simmons, G. W., *Metallurgical Transactions A*, Vol. 11A, 1980, pp. 151–158.
[35] Purushothaman, S. and Tien, J. K., in *Strength of Metals and Alloys, Proceedings of the International Conference*, P. Haasen, V. Gerold, and G. Kostotz, Eds., Pergamon Press, New York, Vol. 2, 1979, pp. 1267–1271.
[36] Beevers, C. J., *Metal Science*, Vol. 14, 1980, pp. 418–423.
[37] Mayes, I. C. and Baker, T. J., *Fatigue of Engineering Materials and Structures*, Vol. 4, 1981, pp. 79–96.
[38] Ritchie, R. O. and Suresh, S., *Metallurgical Transactions A*, Vol. 13A, 1982, pp. 937–940.

G. R. Yoder,[1] *L. A. Cooley,*[1] *and T. W. Crooker*[1]

A Critical Analysis of Grain-Size and Yield-Strength Dependence of Near-Threshold Fatigue Crack Growth in Steels

REFERENCE: Yoder, G. R., Cooley, L. A., and Crooker, T. W., "**A Critical Analysis of Grain-Size and Yield-Strength Dependence of Near-Threshold Fatigue Crack Growth in Steels,**" *Fracture Mechanics: Fourteenth Symposium—Volume I: Theory and Analysis, ASTM STP 791*, J. C. Lewis and G. Sines, Eds., American Society for Testing and Materials, 1983, pp. I-348-I-365.

ABSTRACT: Near-threshold fatigue crack growth behavior has been analyzed for a broad selection of steels surveyed from the literature. It is clear first of all that apparent values of the threshold stress-intensity factor (ΔK_{th}) can vary widely, roughly an order of magnitude. Though in many instances actual ΔK_{th} values are difficult to define rigorously, a pronounced transition point or "knee" is apparent in the near-threshold region of the conventional logarithmic plot of fatigue crack growth rate (da/dN) as a function of stress-intensity range (ΔK). Though the values of ΔK associated with these transition points (ΔK_T) for an individual steel may tend to exhibit a functional dependence on yield strength (σ_{ys}) or grain size ($\bar{\ell}$)—as is the case, for example, with a low-carbon ferritic steel—it is unmistakably clear that for the *gamut* of steels examined (15 cases), the transition points do not order on the basis of either σ_{ys} or $\bar{\ell}$ alone. Rather, values of ΔK_T for the gamut of steels order on the basis of a synergetic interaction of σ_{ys} and $\bar{\ell}$, according to the equation, $\Delta K_T = 5.5\ \sigma_{ys}\sqrt{\bar{\ell}}$. This relationship was derived in the cyclic plastic zone model of fatigue crack growth established in our prior work with titanium alloys. In further agreement with this model, ΔK_T has been identified for these steels as the point at which the cyclic plastic zone attains the mean grain size. The significance and implications of these findings appear far-reaching, as the steels surveyed include those of both high and low strength, a wide range of effective grain sizes (mean free path in the case of high-strength steel), and a host of microstructural types (ferritic, martensitic, pearlitic, bainitic, and austenitic).

KEY WORDS: fatigue (materials), crack propagation, steels, ferrous alloys, yield strength, grain size, microstructure, structure-sensitive crack growth, cyclic (reversed) plastic zone, near-threshold fatigue crack growth, fracture mechanics

Though a number of investigators have examined the influence of microstructural variables on near-threshold fatigue crack growth rates in steels, a

[1] Metallurgist, metallurgist, and mechanical engineer, respectively, Mechanics of Materials Branch, Material Science and Technology Division, Naval Research Laboratory, Washington, D.C. 20375.

comprehensive understanding of the dependence of near-threshold growth rates on grain size, yield strength, and microstructural morphology in steels has yet to emerge, as noted in an excellent review by Ritchie [*1*].[2] Recently, however, from our own extensive studies with α/β titanium alloys, the basis for microstructural dependence of widely different fatigue crack growth rates was established for titanium alloys [*2–6*]. Inasmuch as the micromechanistic model from that work does not depend uniquely on alloy family, it is of great interest to explore its applicability to steels, especially since it predicts quantitatively the influence of yield strength and grain size in the near-threshold region for steels. Thus, the purpose of this paper is to analyze critically the near-threshold fatigue crack growth behavior, as reported in the literature, for steels of widely different strength level, grain size, and microstructural morphology in the search for a systematic ordering of near-threshold fatigue crack growth rates that pertains to the whole gamut of steels.

Survey and Analysis

A summary of the near-threshold fatigue crack growth behavior surveyed from the literature is presented in Fig. 1, together with symbols that identify the steel and respective investigator(s) in Table 1 [*7–15*]. For each of the 15 materials represented in this logarithmic plot of fatigue crack growth rate (da/dN) versus stress-intensity range (ΔK), the growth-rate data exhibit a bilinear form with a transition point or "knee" as illustrated in Fig. 1. The level of stress-intensity range associated with the transition point is designated as ΔK_T. Since the observed value of ΔK_T for each material in the figure is unique, it serves in Table 1 to distinguish the yield strength (σ_{ys}) and grain size ($\bar{\ell}$) of that material in those instances where a given symbol pertains to multiple growth-rate curves. It is important to point out that virtually all of the growth-rate data represented in this figure were generated at roughly the same value of stress ratio, namely $0.0 \leq R \leq 0.1$.[3]

As shown in Fig. 1, apparent values of the threshold stress-intensity range (ΔK_{th}) can vary widely among the different steels, by roughly as much as an order of magnitude.[4] Though in many instances actual ΔK_{th} values are difficult to define rigorously, Fig. 1 indicates a spectrum of values from about 3 to 18 MPa·m$^{1/2}$. Note, however, that in the case of each material, the transition point ΔK_T closely approximates ΔK_{th}, since the slope of the hypotransitional branch of the growth-rate curve is so steep, that is, the exponent in the growth rate law [*18*]

$$da/dN = C(\Delta K)^m \tag{1}$$

[2] The italic numbers in brackets refer to the list of references appended to this paper.

[3] The data of Taira, Tanaka, and Hoshina [*15*] are treated as though $R = 0$, as the authors originally published.

[4] Earlier surveys of ΔK_{th} [*16,17*] which were based upon more limited data did not reveal the broad range of near-threshold behavior that is now evident.

TABLE 1—*Identification of materials.*

Symbol	Steel	Microstructure[a]	R	f, Hz	$\bar{\ell}$, μm	σ_{ys}, MPa	Observed ΔK_T, MPa·m$^{1/2}$	Predicted ΔK_T, MPa·m$^{1/2}$	Investigators
⬢	1005	F	0.1	100	24	411	10.3	11.07	Benson [7]
					70	368	12.8	16.93	
●	4Cr—0.35C	M + A + C	0.05	50	0.83	1324	5.09	6.63	Carlson and Ritchie [8] (see Carlson, Narasimha, Rao, and Thomas [9])
					0.47	1324	3.82	4.99	
					0.41	1303	3.66	4.59	
					0.38	1324	3.57	4.49	
Δ	1055	P	0.05	85	27	399	14.4	11.42	Cooke and Beevers [10]
○	304 stainless	A	0.0	0.07	76	273	17.8	13.09	James and Schwenk [11]
⬡	1007	F	0.1	50	19	219	9.2	5.25	Masounave and Bailon [12]
					40	192	9.4	6.68	
▽	2 1/4Cr—1Mo	B + F	0.05	50	36	290	9.5	9.57	Ritchie et al [13]
▷	1018	F + M	0.05	1-30	36	293	9.8	9.67	Suzuki and McEvily [14]
▲	1020	F + P	−1.0	30	7.8	366	5.47	5.62	Taira, Tanaka, and Hoshina [15]
					20.5	275	6.47	6.85	
					55	194	7.95	7.91	

[a]A = austenite, B = bainite, C = carbide (Fe_3C), F = ferrite, M = martensite, P = pearlite.

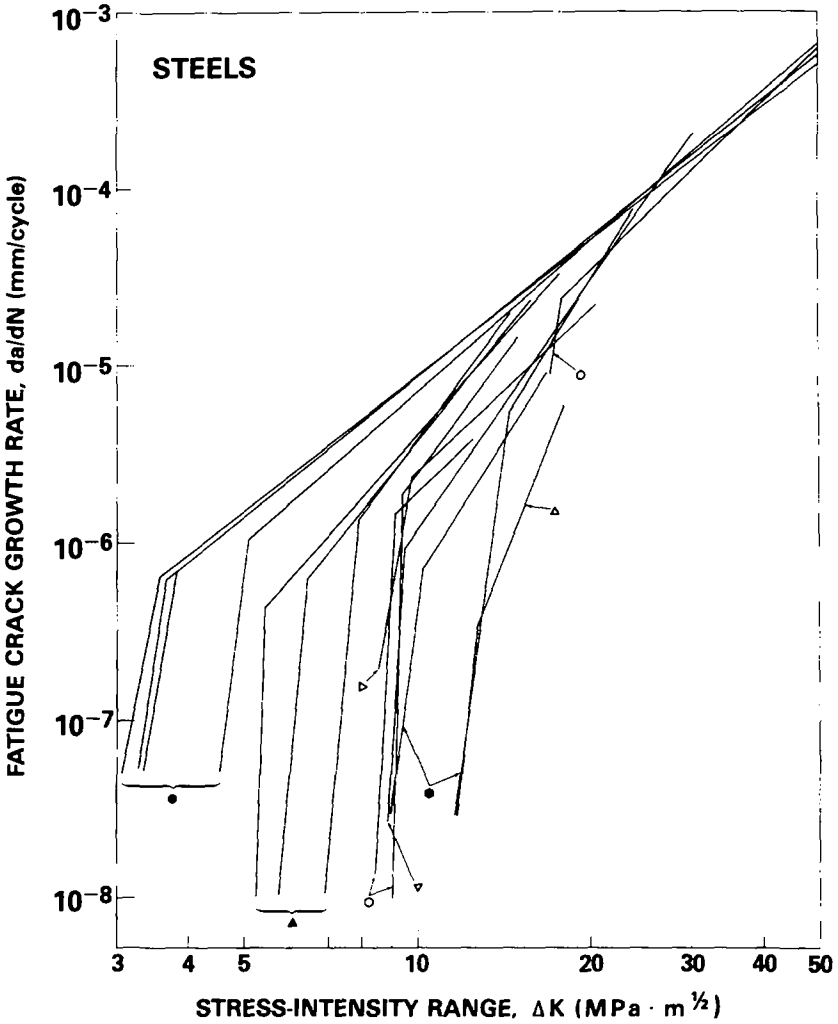

FIG. 1—*Near-threshold fatigue crack growth behavior of a broad selection of steels. Symbols refer to identification in Table 1, see text for further details.*

is very large. Inasmuch as the transition points ΔK_T are found to order systematically for the 15 materials in Fig. 1, on the basis of a synergetic interaction of the yield strength and grain size, which will be elucidated in this paper, this point is of potentially prime engineering significance with regard to the estimation of thresholds ΔK_{th}.

The broad spectrum of ΔK_T values represented in Fig. 1 derives from steels that vary widely in terms of composition, microstructural morphology, yield strength, and grain size, as indicated in Table 1. Microstructural types range, for example, from basically martensitic 4Cr-0.35C steel to primarily ferritic

1005, 1007, and 1020 steels, pearlitic 1055 steel or austenitic 304 stainless, etc. Both high- and low-strength steels are represented, with yield strengths ranging from 192 MPa $\leq \sigma_{ys} \leq$ 1324 MPa. Effective grain sizes (*transformed* grain size or mean free path in the case of high-strength steel) range from 0.38 μm $\leq \bar{\ell} \leq$ 76 μm.[5]

In prior work with low-strength steels, it has been reported that fatigue crack growth rates decrease with increased grain size, or that the threshold ΔK_{th} itself increases with increased grain size, or both [*7,12,15,21-24*]. Figure 2 illustrates behavior found typically for a *particular* steel: Though the said effects appear operative as the grain size is increased through heat treatment of the given plate of steel, it is also clear that the yield strength (σ_{ys}) has been simultaneously decreased. Thus, the isolation of any grain-size effect is obscured, as pointed out by Ritchie [*1*] and Benson [*7*]. Others also have noted a decrease in ΔK_{th} with an increase in σ_{ys} [*12,24-26*]. Though the data in Fig. 2 will be considered further later in this paper, it is worthwhile to note at this point the degree to which the data support the bilinear form of the growth-rate curves shown here and in Fig. 1.

In contrast to Fig. 2, if behavior for the broad spectrum of steels described in Fig. 1 and Table 1 is examined, there is no clearly discernible influence of σ_{ys} and $\bar{\ell}$ on the ordering of the growth-rate curves, when each variable is considered separately. This point is illustrated in Fig. 3, where a random sampling of data from Fig. 1 and Table 1 is represented. As the growth-rate curves (in terms of ΔK_{th} or ΔK_T) are traversed from left to right, values of $\bar{\ell}$ exhibit no consistent trend, nor do those of σ_{ys}. When the functional dependence of ΔK_T on σ_{ys} and $\bar{\ell}$ is examined for all 15 of the materials of Fig. 1 and Table 1, as shown in Figs. 4 and 5 respectively, again the data patterns of ΔK_T versus σ_{ys} and $\bar{\ell}$ appear highly random. For the sake of completeness, data from our own work with titanium alloys [*4,27*] have been included in these and subsequent

[5] For the basically ferritic steels or the 304 stainless, $\bar{\ell}$ is the ferrite or austenite grain size, respectively. For the 1055 steel, $\bar{\ell}$ is the pearlite colony size, since all α-phase lamellae in a colony exhibit the same variant of the Kurdjumov-Sachs transformation relationship—so that, accordingly, slip bands or slip-band cracks can transmit across α-lamellae with carbide platelets cracking very readily under tensile load [*10,19,20*] as though the colony were a pseudo single crystal. In the case of the dual-phase, ferritic-martensitic 1018 steel, which is nearly 65 percent ferrite, $\bar{\ell}$ is taken as the ferrite grain size, consistent with Suzuki and McEvily's observation that crack growth preferentially followed a path through the ferrite [*14*]. For the martensitic 4Cr-0.35C steel, $\bar{\ell}$ would be the size of the packet of martensite laths which have a common variant according to the Kurdjumov-Sachs or the Nishiyama-Wasserman transformation relations—were there no austenite remaining at the lath boundaries as an effective barrier to the transmission of slip bands between adjacent laths [*9*]. In those cases where virtually continuous films of retained austenite line the lath boundaries (namely for austenitizing temperatures of 1000, 1100, and 1200°C), values of $\bar{\ell}$ are taken as the lath widths reported by Carlson, Narasimha Rao, and Thomas, namely $\bar{\ell} =$ 0.47, 0.41, and 0.38 μm, respectively. By contrast, for the material quenched from the lowest austenitizing temperature (870°C), the austenite film is highly discontinuous; in this instance, the appropriately modulated value of mean free path is estimated (from quantitative metallographic methods by the present authors) from the thin film transmission electron micrograph [*9*] to be $\bar{\ell} =$ 0.83 μm.

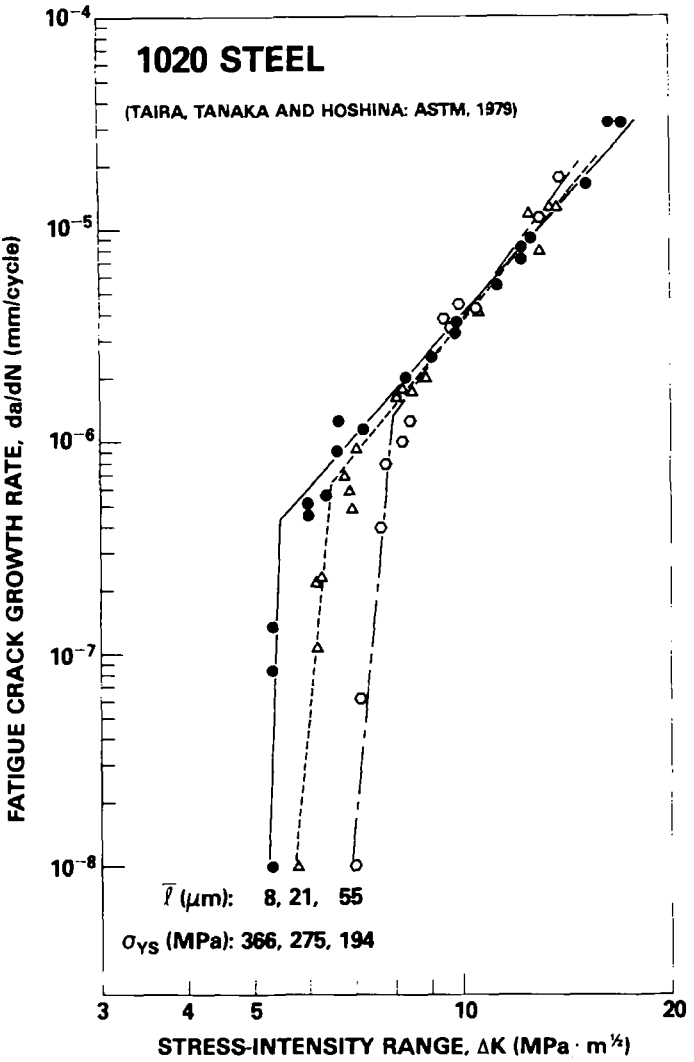

FIG. 2—*Near-threshold fatigue crack growth behavior of a 1020 steel heat-treated to the indicated levels of grain size* ($\bar{\ell}$) *and yield strength* (σ_{ys}), *after Ref* 15, *adapted from Fig. 11, p. 151.*

plots, denoted by the symbol "X." All other data symbols in these figures are identified in Table 1.

If ΔK_T does not order on the basis of either σ_{ys} or $\bar{\ell}$, when the full gamut of steels is considered, then what is the system to the ordering of the growth-rate curves in the near-threshold region? Happily, there appears to be a straightforward answer to this question: In accord with the cyclic plastic zone model for the ordering of growth-rate curves, as developed from work with titanium

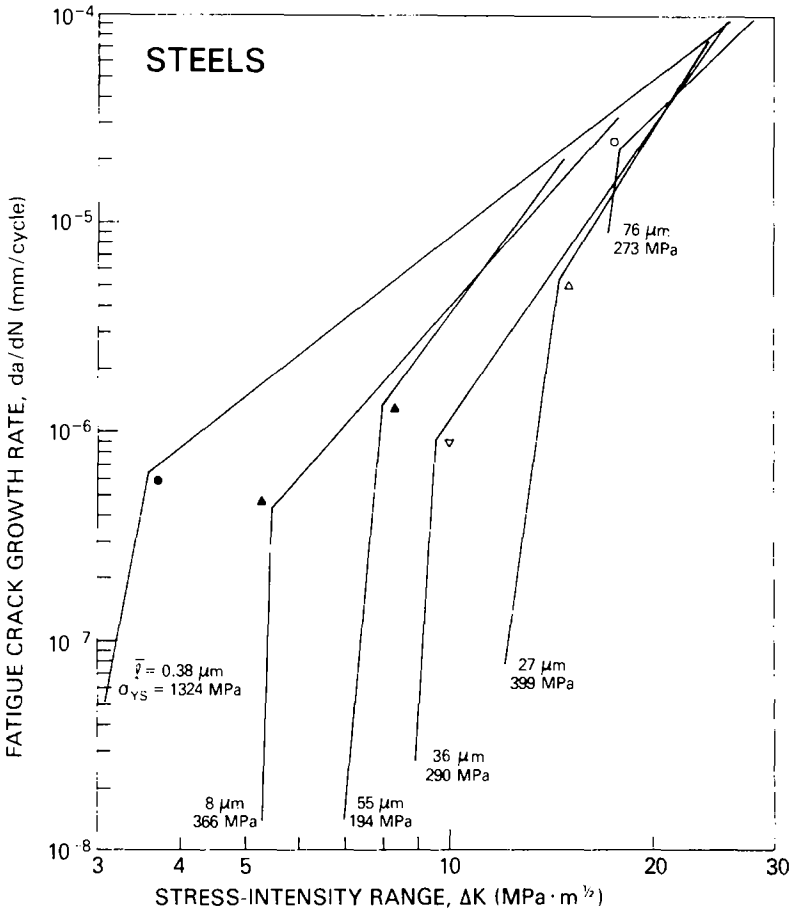

FIG. 3—*As illustrated with selections from Fig. 1 and Table 1, near-threshold growth-rate behavior for the whole gamut of steels fails to order on the basis of either grain size* ($\bar{\ell}$) *or yield strength* (σ_{ys}) *alone.*

alloys [*2-6*], observed values of ΔK_T for the whole spectrum of steels examined in this study are in remarkable agreement with the quantitative predictions of that model. In further agreement with the model, values of $\bar{\ell}$ for all these steels, independent of microstructural morphology or composition, are found equal to respective values of the cyclic plastic zone size at the transition point, ΔK_T.

To begin with: In the work with titanium alloys, a bilinear growth-rate behavior was observed as illustrated in Fig. 6, with two distinct branches that independently obey the power law of Eq 1 and that join together at the transition point (T). In the hypotransitional region where the cyclic (or "reversed") plastic zone size (sketched for plane strain conditions) is less than the grain size, $r_y^c < \bar{\ell}$, a microstructurally sensitive (or "structure-sensitive") mode of

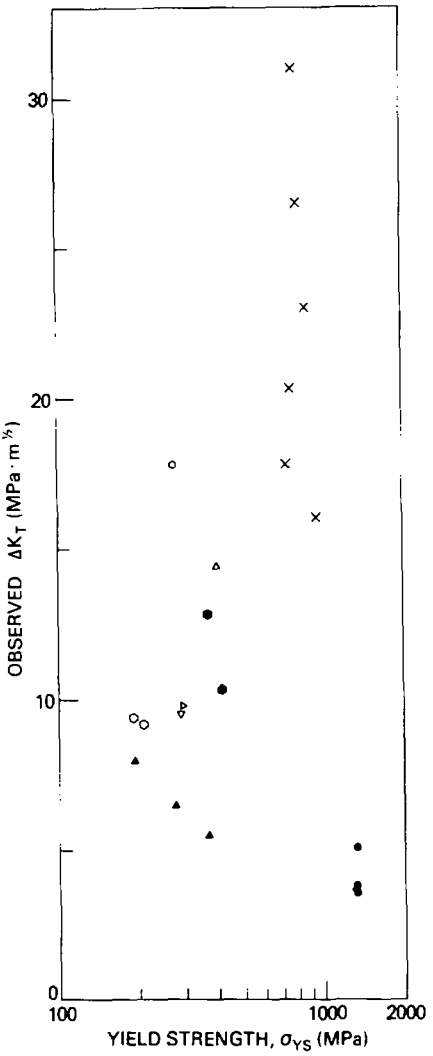

FIG. 4—*Values of stress-intensity range observed at transition points or "knees" in the growth-rate data trend lines* (ΔK_T) *of Fig. 1 versus yield strength* (σ_{ys}). *Symbols refer to Table 1: additional symbol "X" refers to data from Refs* 4, 27.

crack growth occurs that involves crystallographic bifurcation in grains adjacent to the Mode I crack plane. This bifurcation causes a reduction in the effective ΔK and consequently da/dN, and thus the appearance of the transition itself. By contrast, in the hypertransitional region where $r_y^c > \bar{\ell}$, the grains within the larger r_y^c must necessarily deform as a continuum, which results in a microstructurally insensitive, nonbifurcated mode of crack growth [*4,5*]. It should be noted that bifurcation has been observed in the microstructurally

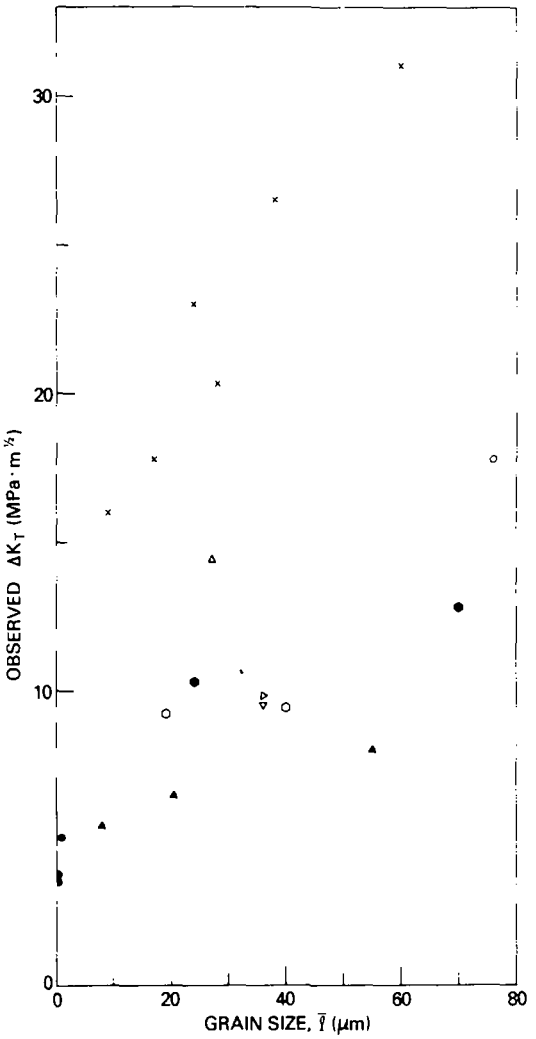

FIG. 5—*Observed values of transitional stress-intensity range* (ΔK_T) *versus effective grain size* ($\bar{l}$).

sensitive region for a wide range of microstructures [*28,29*]. Moreover, it is appropriate to mention that Wanhill and Döker [*30*] have observed a difference in the dislocation substructures associated with the structure-sensitive and structure-insensitive modes of crack growth. Quantitatively, a shift in the fatigue crack growth rate curve can be predicted, since the transition point (T) in Fig. 6 is the point at which the reversed plastic zone size [*31-33*]

$$r_y^c = 0.033\,(\Delta K/\sigma_{ys})^2 \tag{2}$$

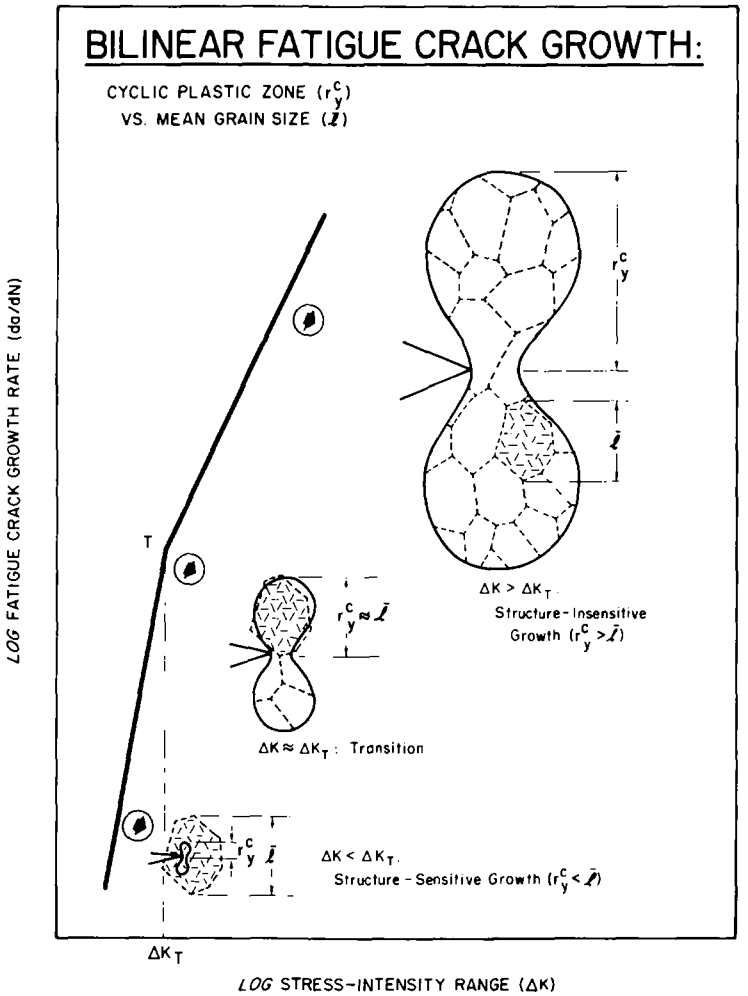

FIG. 6—*Influence of cyclic (reversed) plastic zone size, relative to grain size, upon development of bilinear fatigue crack growth behavior. Note transition from structure-sensitive mode of crack growth in lower branch to structure-insensitive mode in upper branch.*

attains the mean grain size [*2-6,27-29*]. Thus at the transition point, where $r_y^c = \bar{\ell}$, it follows that

$$\Delta K_T = 5.5\, \sigma_{ys} \sqrt{\bar{\ell}} \tag{3}$$

This shift in the *da/dN* data plot, as sketched in Fig. 7, is well documented for titanium alloys [*2-6,27-29*].

To examine the applicability of this model to the near-threshold fatigue

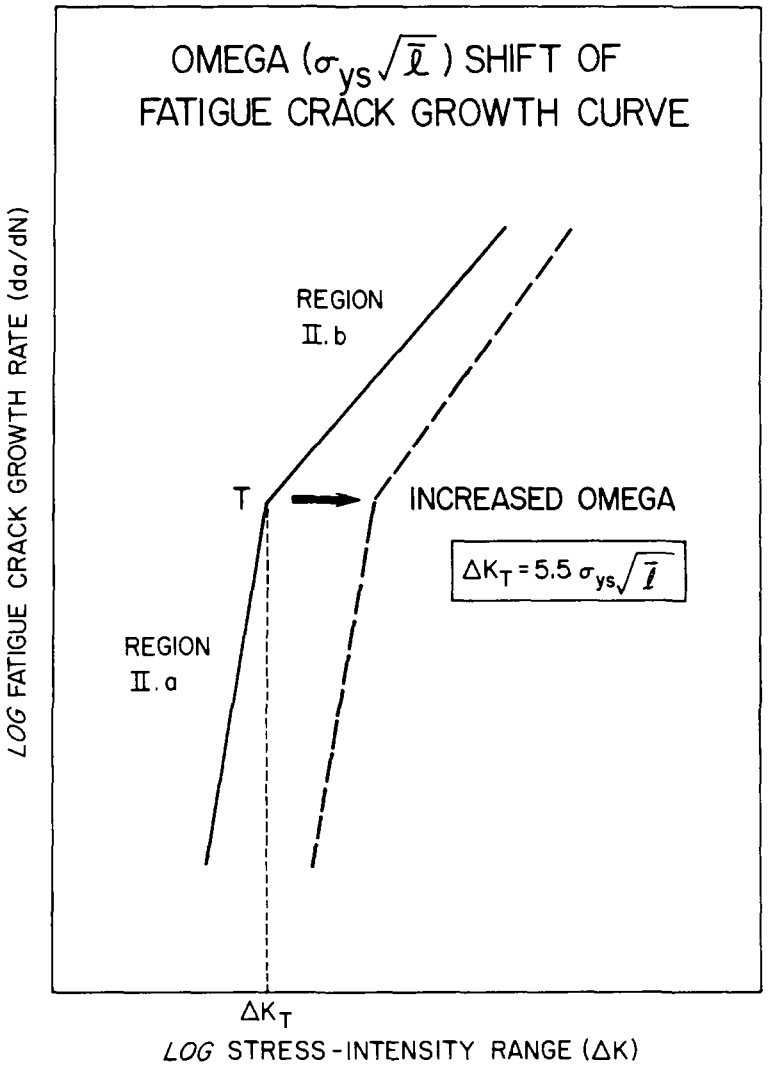

FIG. 7—*From Fig. 6 and Eq 3, shift in the fatigue crack growth-rate curve is predicted quantitatively from the synergetic interaction of yield strength* (σ_{ys}) *and grain size* ($\bar{\ell}$).

crack growth behavior of the whole gamut of steels described by Fig. 1 and Table 1, values of $\bar{\ell}$ are compared in Fig. 8 to respective values of the cyclic plastic zone size from Eq 2, computed at the transition point, ΔK_T. The agreement appears to be excellent. In further accord with Fig. 6, a number of investigators have reported a structure-sensitive mode of crack growth when the cyclic plastic zone size was less than the grain size, which made the transition to a structure-insensitive mode of crack growth when the cyclic plastic zone

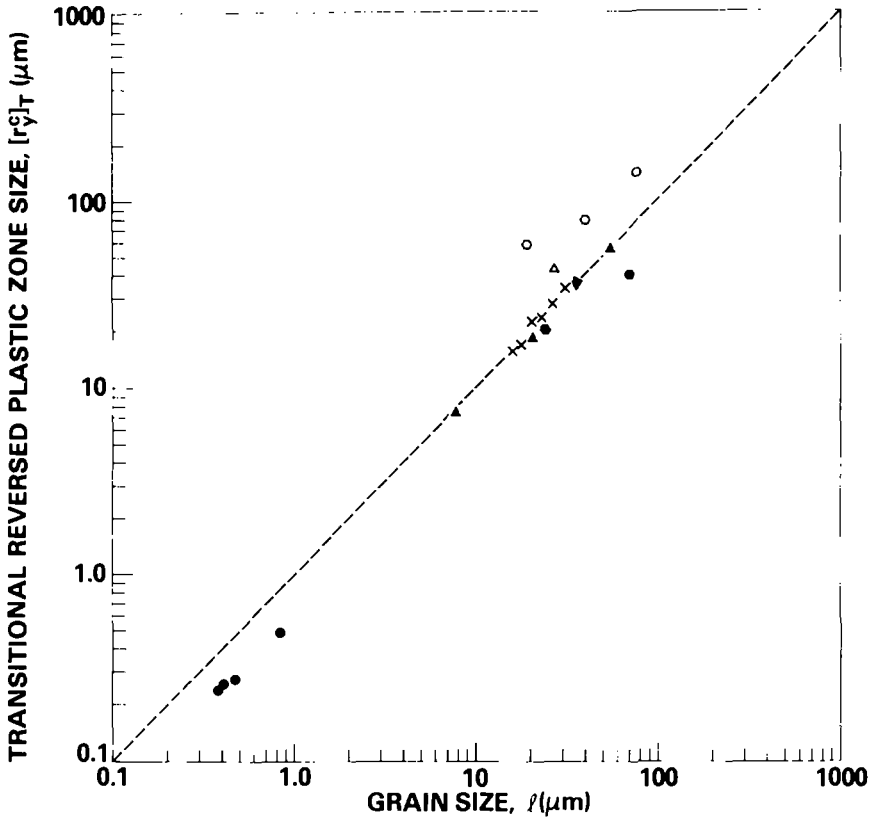

FIG. 8—*Comparison of cyclic (reversed) plastic zone size at the transition point in bilinear growth-rate curve,* $[r_y^c]_T$, *versus effective grain size* ($\bar{\ell}$).

exceeded the grain size; for example, see Aita and Weertman [*19,20*], Suzuki and McEvily [*14*], and Cooke, Irving, Booth, and Beevers [*34*]. Finally, to examine whether the wide spread in near-threshold growth-rate curves in Fig. 1 is simply a consequence of the "omega" shift predicted in Fig. 7 via Eq 3, values of ΔK_T observed for the whole gamut of steels in Fig. 1 are compared in Fig. 9 to values of ΔK_T computed from Eq 3. The level of agreement is considered remarkable, particularly in view of uncertainties involved in the measurements made by different investigators.[6] Thus, the broad spectrum of near-threshold growth-rate curves for the gamut of 15 steels in Fig. 1 clearly orders in accord with the predictions of Fig. 7 and Eq 3.

[6] For example, inasmuch as there is as yet no ASTM standard for the relatively difficult measurement of growth rates in the near-threshold region, the data represented in Fig. 1 were obtained by a multitude of different procedures. Moreover, as pointed up in a recent paper by Vosikovsky, Trudeau, and Rivard [*35*], residual stresses can affect enormously determinations of apparent near-threshold growth rate behavior.

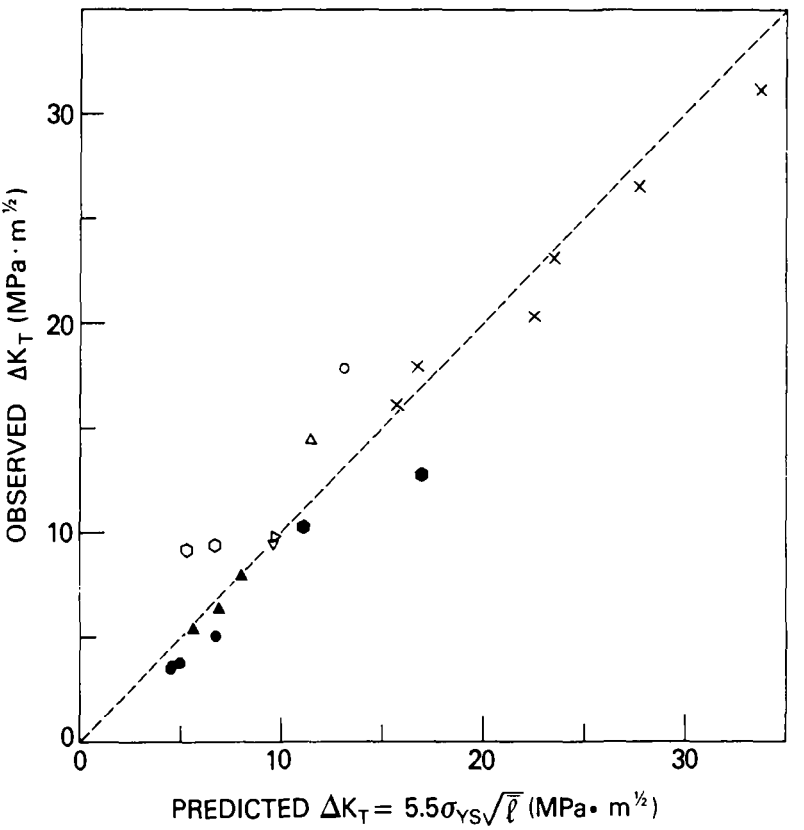

FIG. 9—*Comparison of observed values of transitional stress-intensity range* (ΔK_T) *versus predicted values from model according to Eq 3.*

Discussion

Evidence has been presented for a systematic ordering of near-threshold growth rates for steels, based on the synergetic interaction of yield strength (σ_{ys}) and grain size ($\bar{\ell}$) expressed by Eq 3. Inasmuch as this finding pertains to the whole gamut of steels, regardless of strength level, microstructural morphology, or composition, it would appear to be extraordinarily significant. In particular, from an engineering standpoint, it is suggested that estimation of the threshold for fatigue crack growth ΔK_{th} ought to be considered via Eq 3, which requires knowledge of only σ_{ys} and $\bar{\ell}$, to obviate the need for direct measurements of ΔK_{th}, which though elegant, are very time-consuming and expensive.

Though the near-threshold growth-rate curves for the whole *gamut* of steels do not order on the basis of grain size alone, it is pertinent to readdress the case

of an *individual* steel, heat-treated to generate different levels of $\bar{\ell}$ (and σ_{ys}) as illustrated in Fig. 2. Since the Hall-Petch relation provides the tradeoff between σ_{ys} and $\bar{\ell}$ in steels [*36,37*]

$$\sigma_{ys} = \sigma_o + k(\bar{\ell})^{-1/2} \tag{4}$$

where σ_o and k are material constants, then for an individual steel it follows from Eq 3 that

$$\Delta K_T = 5.5\,(\sigma_o\sqrt{\bar{\ell}} + k) \tag{5}$$

or

$$\Delta K_T \propto \sqrt{\bar{\ell}} \tag{6}$$

Thus it is possible to understand micromechanistically the "grain-size" effects reported by Taira, Tanaka, and Hoshina [*15*] and Masounave and Bailon [*12*], namely

$$\Delta K_{th} \propto \sqrt{\bar{\ell}} \tag{7}$$

It is of further interest to note that in the case of titanium alloys, the Hall-Petch relation in Eq 4 is inoperative—that is, the dependence of σ_{ys} on $\bar{\ell}$ is very weak, at best [*3,38*]. Consequently, the $\sqrt{\bar{\ell}}$ term dominates the right-hand side of Eq 3, so that a grain-size effect is observed for titanium alloys [*2–4,21,38,39*]. In that case, the inverse dependence of fatigue crack growth rates upon grain size is directly relatable to the microstructurally sensitive mode of crack growth—since larger bifurcated cracks (thought to be slip-band cracks [*5*]) occur as the grain size is increased, thus dispersing the strain-field energy of the macroscopic crack over increased volumes of material in the crack-tip region—to further reduce the effective ΔK and consequently, da/dN.[7]

As shown by Hertzberg and Mills [*41*] for a wide range of alloy families, slip-band cracking or decohesion is characteristic of near-threshold growth-rate behavior, or the microstructurally sensitive mode of fatigue crack growth. For steels, Taira, Tanaka, and Nakai [*42*] have developed a blocked slip band model, with particular reference to the results of Ref *15*, in which the ferrite grain boundaries served as the blocking obstacles.[8] If the structure-sensitive mode of crack growth can occur only so long as the cyclic plastic zone size is less than the maximum dimension to which a slip-band (or slip-band crack)

[7] In recent work by J. P. Lucas and W. W. Gerberich with a high-strength low-alloy steel, the Hall-Petch relation similarly was found to be inoperative for $\bar{\ell}$ in excess of 50 μm, with a large grain-size effect observed on ΔK_{th} [*40*]; moreover, a dislocation model for the ΔK_{th} behavior has been developed.

[8] Recently, Sadananda [*43*] has developed a dislocation model to explain the crystallographic, faceted mode of fatigue crack growth.

can develop unimpeded by an (insurmountable) obstacle, then ℓ must in the general sense represent the *mean free path* between such obstacles. For α/β titanium alloys and low-strength steels, $\bar{\ell}$ is thus the effective grain size—inasmuch as the grain boundaries are the controlling obstacles. In the case of the high-strength steels of Carlson et al [*8,9*], as noted previously in Footnote 5, the appearance of retained austenite in the martensite lath boundaries truncates the mean free path for slip-band transmission, which otherwise would be the lath packet dimension.

If application of the model represented by Eq 3 and Fig. 7 were to be extended to the near-threshold, transitional growth-rate behavior observed in precipitation-hardened alloys such as those in the aluminum family [*44-47*] or others [*48*], thin-foil transmission electron microscopy might well be required to determine the mean free path $\bar{\ell}$ between obstacles that effectively obstruct slip-band transmission. Such potential obstacles might include constituent or intermetallic particles, dispersoids, or precipitates formed upon aging.[9]

In closing this discussion, it is appropriate at least to mention a further pair of issues concerning ΔK_T. On the one hand, in view of the work of Wilhem [*49*] some years ago, the question might be raised as to whether ΔK_T reflects a tensile to shear mode fracture transition. The answer appears to be a resounding no, since it appears that shear lip development was not involved in the case of any of the 15 materials in Fig. 1 and Table 1. Moreover, calculation of the limits for plane strain constraint indicates that levels of ΔK_T are nowhere near the calculated limits, except for possibly 1 or 2 of the 15 cases. On the other hand, the question of stress-ratio (R) influence on ΔK_T might be raised. From a micromechanics standpoint, it is not clear that R should have any influence on ΔK_T as formulated in Eq 3. Rather, there is growing evidence that stress-ratio effects may be primarily environmental in their influence on the near-threshold growth-rate behavior: Witness, for example, the results for steels, aluminum, and titanium alloys which indicate that ΔK_{th} (or ΔK_T) is insensitive to R in an inert environment, namely vacuum conditions [*1,34,47*]. Moreover, it is relevant to note that ΔK_{th} values reported for vacuum over a wide range of R values are similar to ΔK_{th} values observed near $R = 0$ for an air environment. Thus the case can be made that environmental influence had negligible bearing on the results for the 15 steels analyzed in this paper.[10]

Conclusions

1. Resistance to fatigue crack growth in the near-threshold region varies widely among steels. When logarithmic plots of growth rate (da/dN) versus stress-intensity range (ΔK) are analyzed in a bilinear form with a transition point

[9] Hertzberg has raised the question whether subgrain boundaries might act as the controlling obstacles in an extruded aluminum alloy. Personal communication, 3 April 1981.

[10] With regard to stress-ratio effects and environmental modeling, the interested reader might wish to consult the work of Krafft, J. M., this publication, pp. I-380–I-406.

or "knee" at ΔK_T, values of ΔK_T are observed to range from 3 to 18 MPa $\cdot$ m$^{1/2}$ for the different steels. These values of ΔK_T appear to be good approximations to actual threshold values of ΔK below which cracks do not propagate (ΔK_{th}).

2. Values of ΔK_T for the gamut of steels examined do not order on the basis of either yield strength (σ_{ys}) or grain size ($\bar{\ell}$) alone. Rather, values of ΔK_T order on the basis of the synergetic parameter, $\sigma_{ys}\sqrt{\bar{\ell}}$.

3. Specifically, in accord with the cyclic plastic zone model developed in prior work with titanium alloys, observed values of ΔK_T are in remarkable agreement with predictions according to the equation, $\Delta K_T = 5.5\,\sigma_{ys}\sqrt{\bar{\ell}}$.

4. Applicability of these findings appears to be far-reaching, as the steels surveyed span a wide variety of yield strengths (192 to 1324 MPa), effective grain sizes (0.4 to 76 μm), and microstructural types (ferritic, martensitic, pearlitic, bainitic, and austenitic).

5. A simple predictive equation (see Conclusion 3) thus is offered as a reasonable approximation of the threshold, ΔK_{th}, for any steel, from knowledge of only σ_{ys} and $\bar{\ell}$.

6. Though near-threshold growth-rate curves for the whole *gamut* of steels do not order on the basis of grain size alone, for the case of an *individual* steel, by contrast, ΔK_T does increase with $\sqrt{\bar{\ell}}$. This result is shown to be a direct consequence of the Hall-Petch relation, in combination with the equation for ΔK_T given in Conclusion 3.

7. The grain-size parameter in the cyclic plastic zone model, namely $\bar{\ell}$, is recognized in the more general sense to be the mean free path between (insurmountable) obstacles to slip-band transmission.

Acknowledgment

The authors gratefully acknowledge the Office of Naval Research and the Naval Air Systems Command for support of our studies on fatigue crack propagation. Special thanks are extended to Prof. W. W. Gerberich for his thorough and thoughtful review of the preliminary manuscript.

References

[1] Ritchie, R. O., *International Metals Reviews*, Vol. 24, Nos. 5 and 6, Review 245, 1979, pp. 205-230.

[2] Yoder, G. R., Cooley, L. A., and Crooker, T. W. in *Titanium '80, Proceedings of the 4th International Conference on Titanium*, H. Kimura and O. Izumi, Eds., Vol. 3, The Metallurgical Society of the American Institute of Mining, Metallurgical, and Petroleum Engineers, Warrendale, Pa., 1981, pp. 1865-1874.

[3] Yoder, G. R., Cooley, L. A., and Crooker, T. W., *Journal of Engineering Materials and Technology, Transactions of the American Society of Mechanical Engineers*, Series H, Vol. 101, No. 1, Jan. 1979, pp. 86-90.

[4] Yoder, G. R., Cooley, L. A., and Crooker, T. W., *Engineering Fracture Mechanics*, Vol. 11, No. 4, 1979, pp. 805-816.

[5] Yoder, G. R., Cooley, L. A., and Crooker, T. W., *Metallurgical Transactions A*, Vol. 8A, No. 11, Nov. 1977, pp. 1737-1743.

[6] Yoder, G. R., Cooley, L. A., and Crooker, T. W. in *Proceedings of the Second International Conference on Mechanical Behavior of Materials,* American Society for Metals, Metals Park, Ohio, 1976, pp. 1010-1014.
[7] Benson, J. P., *Metal Science,* Vol. 13, Sept. 1979, pp. 535-539.
[8] Carlson, M. F. and Ritchie, R. O., *Scripta Metallurgica,* Vol. 11, No. 12, Dec. 1977, pp. 1113-1118.
[9] Carlson, M. F., Narasimha Rao, B. V., and Thomas, G., *Metallurgical Transactions A,* Vol. 10A, No. 9, Sept. 1979, pp. 1273-1284.
[10] Cooke, R. J. and Beevers, C. J., *Materials Science and Engineering,* Vol. 13, No. 3, March 1974, pp. 201-210.
[11] James, L. A. and Schwenk, E. B., Jr., *Metallurgical Transactions,* Vol. 2, No. 2, Feb. 1971, pp. 491-496.
[12] Masounave, J. and Bailon, J. P., *Scripta Metallurgica,* Vol. 10, No. 2, Feb. 1976, pp. 165-170.
[13] Ritchie, R. O., Suresh, S., and Moss, C. M., *Journal of Engineering Materials and Technology, Transactions,* American Society of Mechanical Engineers, Series H, Vol. 102, No. 3, July 1980, pp. 293-299.
[14] Suzuki, H. and McEvily, A. J., *Metallurgical Transactions A,* Vol. 10A, No. 4, April 1979, pp. 475-481.
[15] Taira, S., Tanaka, K., and Hoshina, M. in *Fatigue Mechanisms, ASTM STP 675,* American Society for Testing and Materials, 1979, pp. 135-162.
[16] Rolfe, S. T. and Barsom, J. M., *Fracture and Fatigue Control in Structures,* Prentice-Hall, Englewood Cliffs, N. J. 1977, p. 224.
[17] Weiss, V. and Lal, D. N., *Metallurgical Transactions,* Vol. 5, No. 8, Aug. 1974, pp. 1946-1949.
[18] Paris, P. C. and Erdogan, F., *Journal of Basic Engineering, Transactions,* American Society of Mechanical Engineers, Series D, Vol. 85, No. 4, Dec. 1963, pp. 528-533.
[19] Aita, C. R. and Weertman, J., *Metallurgical Transactions A,* Vol. 10A, No. 5, May 1979, pp. 535-544.
[20] Aita, C. R. and Weertman, J., *Scripta Metallurgica,* Vol. 14, No. 4, April 1980, pp. 425-429.
[21] Gerberich, W. W. and Moody, N. R. in *Fatigue Mechanisms, ASTM STP 675,* American Society for Testing and Materials, 1979, pp. 292-341.
[22] Priddle, E. K., *Scripta Metallurgica,* Vol. 12, No. 1, Jan. 1978, pp. 49-56.
[23] Yokobori, T. in *Fatigue Mechanisms, ASTM STP 675,* American Society for Testing and Materials, 1979, pp. 683-701.
[24] Masounave, J. and Bailon, J. P. in *Proceedings of the Second International Conference on Mechanical Behavior of Materials,* American Society for Metals, Metals Park, Ohio, 1976, pp. 636-641.
[25] Kitagawa, H., Nishitani, H., and Matsumoto, T. in *Proceedings of Third International Conference on Fracture,* Vol. 6, Paper V-444/A, Verein Deutscher Eisenhüttenleute, Düsseldorf, 1973, pp. 1-6.
[26] Vosikovsky, O., *Engineering Fracture Mechanics,* Vol. 11, No. 3, 1979, pp. 595-602.
[27] Yoder, G. R., Cooley, L. A., and Crooker, T. W. in *Advances in Materials Technology in the Americas—1980, Proceedings of the 6th Inter-American Conference on Materials Technology,* I. LeMay, Ed., Vol. 2, American Society of Mechanical Engineers, New York, 1980, pp. 135-140.
[28] Irving, P. E. and Beevers, C. J., *Materials Science and Engineering,* Vol. 14, No. 3, June 1974, pp. 229-238.
[29] Yoder, G. R., Cooley, L. A., and Crooker, T. W., *Metallurgical Transactions A,* Vol. 9A, No. 10, Oct. 1978, pp. 1413-1420.
[30] Wanhill, R. J. H. and Döker, H., Paper No. A78-35, The Metallurgical Society of American Institute of Mining, Metallurgical, and Petroleum Engineers, Warrendale, Pa., 1978; Wanhill, R. J. H. and Döker, H., Report NLR MP 78002 U, National Aerospace Laboratory NLR, Amsterdam, The Netherlands, Dec. 1977.
[31] Paris, P. C. in *Fatigue—An Interdisciplinary Approach,* J. J. Burke, N. L. Reed, and V. Weiss, Eds., Syracuse University Press, Syracuse, N.Y., 1964, pp. 107-127.
[32] Rice, J. R. in *Fatigue Crack Propagation, ASTM STP 415,* American Society for Testing and Materials, 1967, pp. 247-311.

[33] Hahn, G. T., Hoagland, R. G., and Rosenfield, A. R., *Metallurgical Transactions,* Vol. 3, No. 5, May 1972, pp. 1189-1202.

[34] Cooke, R. J., Irving, P. E., Booth, G. S., and Beevers, C. J., *Engineering Fracture Mechanics,* Vol. 7, No. 1, March 1975, pp. 69-77.

[35] Vosikovsky, O., Trudeau, L. P., and Rivard, A., *International Journal of Fracture,* Vol. 16, No. 4, Aug. 1980, pp. R187-R190.

[36] Hall, E. O., *Proceedings of the Physical Society,* Section B, Vol. 64, Part 9, No. 381B, Sept. 1951, pp. 747-753.

[37] Petch, N. J., *Journal of the Iron and Steel Institute,* Vol. 174, May 1953, pp. 25-28.

[38] Robinson, J. L. and Beevers, C. J., *Metal Science Journal,* Vol. 7, Sept. 1973, pp. 153-159.

[39] Moody, N. R. and Gerberich, W. W., *Metal Science,* Vol. 14, No. 3, March 1980, pp. 95-100.

[40] Lucas, J. P., personal communication, 16 April 1981, paper to be submitted to *Materials Science and Engineering* by J. P. Lucas and W. W. Gerberich.

[41] Hertzberg, R. W. and Mills, W. J. in *Fractography—Microscopic Cracking Processes, ASTM STP 600,* American Society for Testing and Materials, 1976, pp. 220-234.

[42] Taira, S., Tanaka, K., and Nakai, Y., *Mechanical Research Communications,* Vol. 5, No. 6, 1978, pp. 375-381.

[43] Sadananda, K. in *Dislocation Modelling of Physical Systems,* M. F. Ashby et al, Eds., Pergamon Press, Oxford, 1981, pp. 69-73.

[44] Forsyth, P. J. E. and Bowen, A. W., *International Journal of Fatigue,* Vol. 2, No. 1, Jan. 1981, pp. 17-25.

[45] Bucci, R. J., Vasudevan, A. K., Bretz, P. E., and Malcolm, R. C., "Effect of Microstructure on 7XXX Aluminum Alloy Fatigue Crack Growth at Low Stress Intensities," Alcoa Laboratories, Interim Report, Contract N00019-79-C-0258, Naval Air Systems Command, Washington, D. C., 31 Oct. 1980.

[46] Coyne, E. J., Jr. and Starke, E. A., Jr., *International Journal of Fracture,* Vol. 15, No. 5, Oct. 1979, pp. 405-417.

[47] Kirby, B. R. and Beevers, C. J., *Fatigue of Engineering Materials and Structures,* Vol. 1, No. 2, 1979, pp. 203-215.

[48] Salgat, G. W. and Koss, D. A., *Materials Science and Engineering,* Vol. 35, No. 2, Oct. 1978, 263-272.

[49] Wilhem, D. P. in *Fatigue Crack Propagation, ASTM STP 415,* American Society for Testing and Materials, 1967, pp. 363-380.

J. D. Bertel,[1] *A. Clerivet,*[1] *and C. Bathias*[1]

On the Relation Between the Threshold and the Effective Stress-Intensity Factor Range During Complex Cyclic Loading

REFERENCE: Bertel, J. D., Clerivet, A., and Bathias, C., **"On the Relation Between the Threshold and the Effective Stress-Intensity Factor Range During Complex Cyclic Loading,"** *Fracture Mechanics: Fourteenth Symposium—Volume I: Theory and Analysis, ASTM STP 791*, J. C. Lewis and G. Sines, Eds., American Society for Testing and Materials, 1983, pp. I-366-I-379.

ABSTRACT: Overload effects have been studied for center-cracked tension (CCT) specimens of aluminum alloy 2124-T351. The results show that the retardation of crack propagation due to overloading, which is not taken into account by the Paris relation, can be explained by variation in the U ratio as defined by Elber. The crack length over which this retardation occurs was found equivalent to the diameter of the plastic zone as calculated by the Irwin relation. It was verified that the minimum value of ΔK_{eff} reached after overloading could be calculated from threshold measurements taking into account the loading history. The threshold after overloading was related to the overload ratio, implying that two kinds of tests are sufficient to determine the threshold after any overload ratio and hence the minimum ΔK_{eff}. The relationship between ΔK_{eff} and the plastic zone size gives the ΔK_{eff} value for a given crack length in the affected zone without measurement of crack tip opening displacement.

KEY WORDS: aluminum alloys, effective stress-intensity factor range, threshold, R-ratio influence, overloading effects, spectrum loadings, prediction of retardation, fracture mechanics

Nomenclature

- a Crack length
- a_o Overload crack length
- a_D Crack length affected by overloading
- N_D Number of cycles of retardation due to overloading
- P_{max} Maximum applied load

[1]Research assistant, research assistant, and professor of Engineering Mechanics, respectively, University of Technology, France 60206.

P_{min}	Minimum applied load
P_{op}	Load level at which the crack is fully open
P_o	Applied load just before overloading
P_p	Magnitude of applied overload
P_m	Maximum load at which the crack is arrested after overloading
ΔK_o	Stress-intensity factor range before overloading
ΔK_{peak}	Overload stress-intensity factor range
ΔK_{th}	Maximum stress intensity factor range at which the crack is arrested after overloading
$\Delta K_{(ND)}$	ΔK value at which the crack is no longer affected by overloading
ΔK_{eff}	Effective stress-intensity factor range
ΔK_{effmin}	Minimum value of ΔK_{eff} due to overloading
$\Delta K_{eff(ND)}$	ΔK_{eff} value at which the crack is no longer affected by overloading
U	Effective stress-intensity range ratio
U_E	U-value for uniform loading
U_{min}	Minimum value of U due to overloading
T_p	Overload ratio ($\Delta K_{peak}/\Delta K_o$)
T	Threshold ratio ($\Delta K_o/\Delta K_{th}$)
m, C	Constants of Paris relation
C_E	Constant of Paris relation modified by Elber relation
δ	Gage displacement at the crack tip
r_{po}	Plastic zone size due to K_o
r_{ppeak}	Plastic zone size due to K_{peak}
r_{pth}	Plastic zone size due to K_{th}

The reduction in crack growth rate resulting from an overload preceded and followed by the same level of cyclic loading has been studied by many investigators.

Crack growth retardation is known to be related to many factors. After the overload, there is generally a rapid decrease in the growth rate to a minimum level followed by a gradual increase back to the steady-state growth rate.

Wheeler related the retardation only to the plastic zone size affected by the overload. Systematic agreement between the Wheeler model and test results is not always found. Actually, the number of variables of complex load time histories is rather large. Hence it is necessary to incorporate crack closure to get a more realistic model.

The effective ΔK determination is not easy and requires sophisticated appliances [*1,2*].[2] So a threshold concept after overload has been introduced in order to determine more easily the part of the cycle that contributes to propagating the crack effectively.

[2]The italic numbers in brackets refer to the list of references appended to this paper.

Procedure

Center-cracked tension (CCT) specimens of 2124-T351 aluminum alloy were tested under tensile cyclic loading in plane stress conditions. The specimens were 1.6 mm thick and 200 mm wide. The chemical composition of this alloy was

Si	Fe	Cu	Mn	Mg	Cr	Zn	Ti
0.11	0.23	4.35	0.6	1.45	0.01	0.04	0.02

Its mechanical properties in the longitudinal transverse direction were σ_y = 274 MPa, ultimate tensile strength = 440 MPa, reduction in area = 18 percent, and K_{Ic} = 32 MPa $\sqrt{m}$.

A servo-hydraulic fatigue machine controlled by a minicomputer was used for the overloading tests. The cracks were propagated at a frequency of 10 Hz. One millimetre before application of the overload the frequency was changed to 0.1 Hz. A clip gage was positioned just ahead of each crack tip and in the affected zone, at an average crack length chosen to have the stress-intensity factor range, ΔK_o, approximately equal to 12 MPa $\sqrt{m}$, just before the overload. Another clip gage straddling the central notch was used to record the load-displacement curves.

On the other specimens, cracks were propagated at a frequency of 20 Hz and with an R-ratio of 0.01. When the stress-intensity factor range, ΔK_o, was 12 MPa$\sqrt{m}$, different overload values were applied at a frequency of 10 Hz. The stress-intensity factor range was subsequently decreased to a level such that the crack did not propagate during 10^6 cycles. This level called threshold, K_{th}, has been determined for the following load configurations, as shown in Fig. 1:

1. Determine the overload value (ΔK_{peak}) which induces crack arrest such that the threshold (ΔK_{th}) after overloading is equal to the stress-intensity factor range which preceded the overload, ΔK_o [*3*].
2. Determine the ΔK_{th} value during uniform loading such that the overload ratio T_p is 1 [*3*].
3. Determine the threshold after a given overload ratio. Two values have been investigated here: T_p = 1.5 and 2 [*4*].

Experimental Program

To study crack growth mechanisms in terms of effective stress-intensity factor range, ΔK_{eff}, the influence of different parameters on the retardation due to overloading has been investigated. These parameters are: the frequency before and after overloading; the crack length; the steps at a maximum and minimum value of load; the stress state; the overload ratio, T_p = 1.5 and 2; and the R-ratio influence.

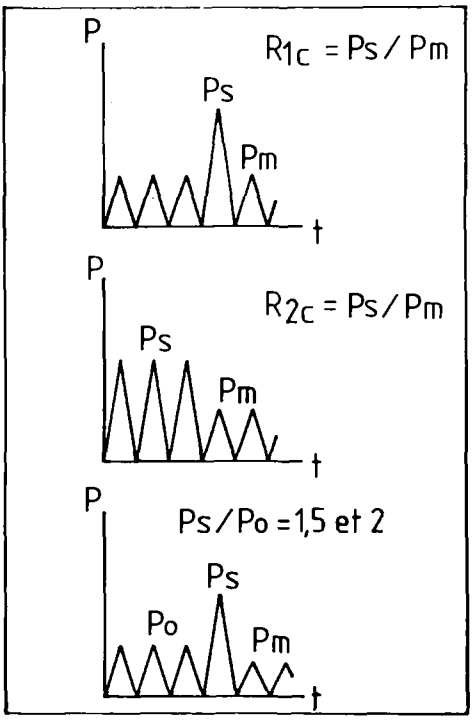

FIG. 1—*Determination of the threshold after overloading* [3].

Our results show [*5,6*] first that the affected crack length, a_D was influenced only by the value of the overload ratio, T_p; a value of $a_D \simeq 0.9$ mm has been found both for 12-mm-thick compact-tension (CT) specimens and 1.6-mm-thick CCT specimens tested with a stress-intensity factor range $\Delta K_o \simeq 12$ MPa$\sqrt{\text{m}}$ and an overload ratio $T_p = 1.5$. Secondly, important variations were observed on the number of cycles of delay, N_D, principally due to variations in the coefficient, C, and exponent, m, of the Paris law established from different tests, associated with a particular crack length, as shown in Tables 1 and 2. Consequently, the crack growth rate, the overload ratio, and the R-ratio are the principal parameters to be considered in the determination of crack growth retardation after overloading.

Overloading Effect on the Effective Stress-Intensity Factor

Because an overload ratio, $T_p = \Delta K_{peak}/\Delta K_o$ of 1.5 is not sufficient to record variations in the load displacement relationship, due to the poor retardation ($\simeq$4000 cycles), we decided to test the CCT specimens with an overload ratio $T_p = 2$, with two R-ratios: 0.01 and 0.5 [*4*]. For this value of

TABLE 1—*Comparison between measured and calculated affected zones.*

Specimen Reference	a_o, mm		Measured Values of a_D, mm	a_D, Determined from U Ratio, mm	Calculated Plastic Zone Diameter, $2ry$, mm	Calculated Values of a_D, [15], mm
MO 2.2	average	24.91	2.7	...	2.56	1.9
MO 3.2	average	24.91	2.98	...	2.56	1.9
MO 4.1	side 1	15.66	2.85	2.65	2.63	1.97
	side 2	14.34	2.96		2.4	1.8
MO 5.1	average	15.1	3.6	2.55	2.54	1.9
MO 6.1	side 1	14.42	2.38	2.4	2.42	1.8
	side 2	15.45	2.92	2.55	2.6	1.95
MO 7.2	side 1	24.37	2.8	...	2.5	1.87
	side 2	25.49	2.8		2.63	1.97

overload ratio, variations of P opening have been recorded by the clip gages located in front of each crack tip in the zones affected by the overload. Figure 2 shows an example of P opening variations determined from the $P - \delta$ recordings.

For each value of P_{op}, there exists a corresponding value of U

$$U = \frac{\Delta P_{eff}}{\Delta P} = \frac{P_{max} - P_{op}}{P_{max} - P_{min}}$$

These values have been calculated in order to determine $\Delta K_{eff} = U\,\Delta K \simeq U\Delta\sigma\sqrt{\pi a}$, where a is the crack length. Figure 3 shows that when the crack growth rate is plotted versus ΔK_{eff}, instead of ΔK as shown in Fig. 4, all the experimental points obtained in the affected zone lie on a unique straight line that corresponds to the relation $da/dN = C_E\,\Delta K_{eff}^m$ determined from the Paris relation $da/dN = C\,\Delta K^m$ without considering the points obtained in the affected zone (Fig. 4). In this case the ratio U is constant for a given R-ratio, and hence $da/dN = C_E\,U\,\Delta K^m$ [2]. A similar relation $da/dN = C_E\Delta K_{eff}^m$ has been obtained for an R-ratio equal to 0.5 [4,5], shown in Fig. 5. Secondly, we have verified that the ratio U is again constant after the overload effect [2,5,7,8] confirming the previous relation $da/dN = C_E\,\Delta K^m$, established in the case of fatigue crack propagation under constant amplitude loading.

This method for the determination of a_D, the crack length affected by the overload, appears to be more precise than measuring a_D on the curves of $da/dN = f(a)$ (Table 1). The values of a_D determined when U is again constant are in good agreement with values of the plastic zone diameter, $2ry$, calculated with the Irwin relation

$$2ry = \frac{1}{\pi}\left(\frac{K_{peak}}{\sigma_y}\right)^2$$

TABLE 2—*Influence of the coefficients* m *and* C_E *variations on* N_D *calculation.*

Specimen Reference	a_o, mm		Measured Values of N_D, mm	Calculated Values of N_D, $m = 3.8$					$m = 3.4$	$m = 4$
				$C_E = 10^{-7}$	1.2×10^{-7}	1.4×10^{-7}	1.6×10^{-7}	1.8×10^{-7}	$C_E = 2.10^{-7}$	$C_E = 10^{-7}$
MO 2.2	average	24.91	299 500	282 300	...	...	...	...	...	...
MO 3.2	average	24.91	258 500	282 300	...	...	...	...	...	...
MO 4.1	side 1	15.66	160 000	287 200	239 350	205 150	179 500	159 600	196 500	...
	side 2	14.34	181 500	...	...	194 300	170 000	...	...	...
MO 5.1	average	15.1	169 350	280 800	...	...	175 500	...	...	240 600
MO 6.1	side 1	14.42	167 300	...	...	...	...	...	...	...
	side 2	15.45	224 800	284 800	237 300	...	...	...	...	...
MO 7.2	side 1	24.37	134 500	278 200	...	198 700	...	...	...	...
	side 2	25.49	257 300	286 700	239 000	...	...	...	...	...

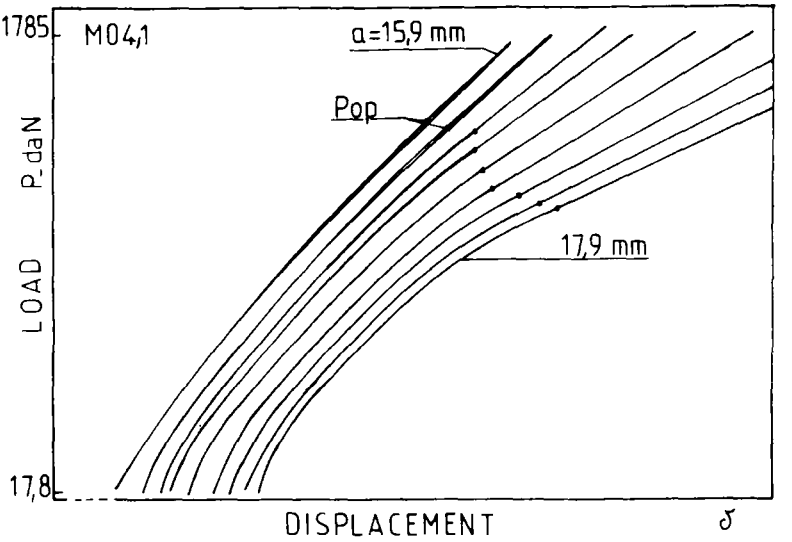

FIG. 2—P *opening variations detected in the affected zone.*

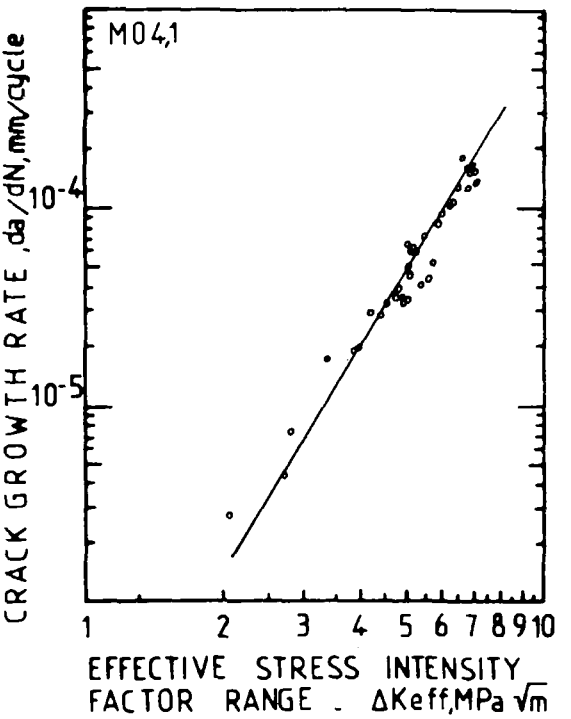

FIG. 3—*Fatigue crack growth rate versus the effective stress-intensity factor range:* R = *0.01.*

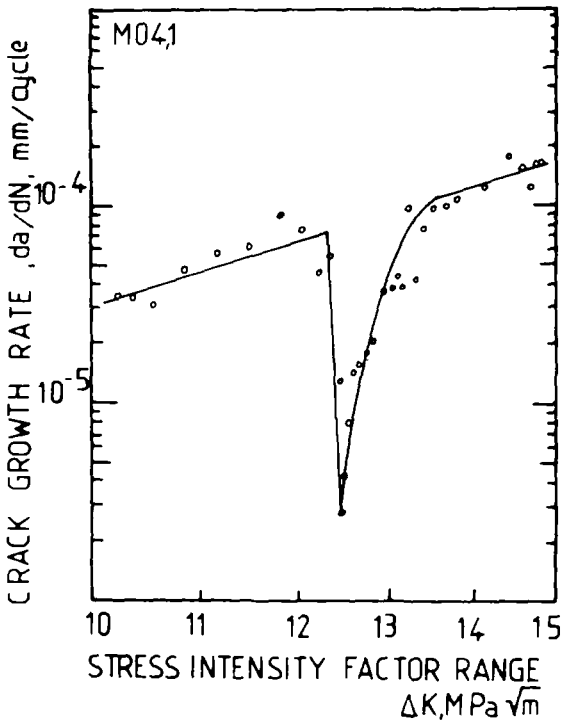

FIG. 4—*Fatigue crack growth rate versus the stress-intensity factor range;* R = *0.01.*

Knowledge of the integration limits, 0 and $2ry$, is not sufficient to calculate the number of cycles of delay, N_D, from the relation $dN = da/C_E \Delta K_{\text{eff}}^m$ because U and ΔK_{eff} are a function of the retarded crack length a_D. As a first approximation, we have considered the linear relation between U^3 and a or $2ry$, and also between ΔK_{eff}^2 and a or $2ry$, as shown in Fig. 6.

The new relation becomes

$$dN = \frac{da}{C_E (Aa + B)^{m/2}} \tag{1}$$

The coefficients A, B are calculated for *each case* from the relations for a_o (overload crack length)

$$\Delta K_{\text{effmin}} = U_{\min} \Delta K_{\text{o}}$$

for $2ry$

$$U = C^t = U_E; \qquad \Delta K_{(\text{ND})} \simeq \Delta\sigma\sqrt{\pi(a_o + 2ry)}$$

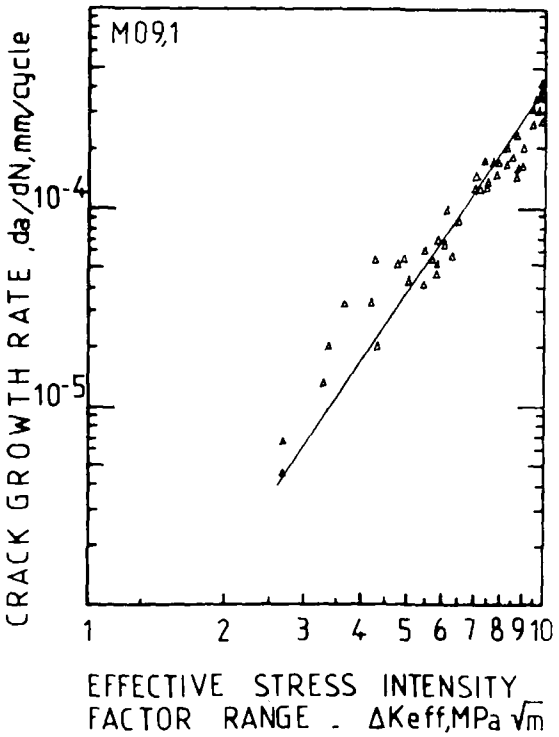

FIG. 5—*Fatigue crack growth rate versus the effective stress-intensity factor range:* R = *0.5.*

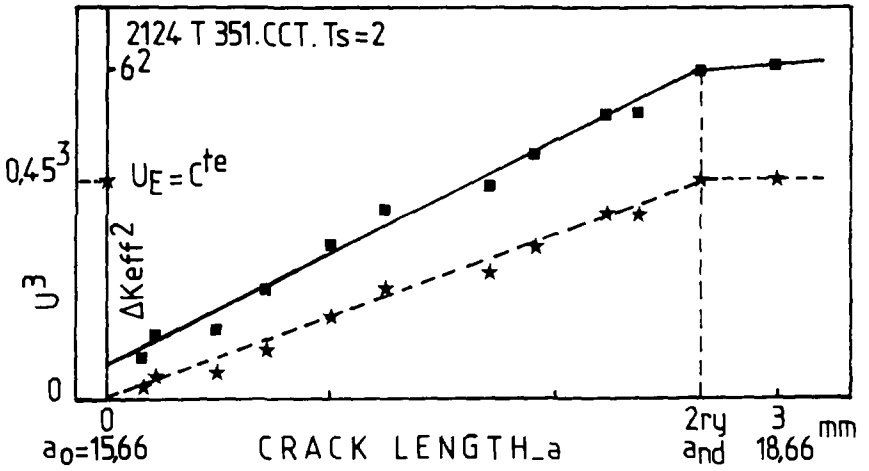

FIG. 6—U *(star) and* ΔK_{eff} *(solid square) variations versus the affected zone size:* $T_p = 2$.

So

$$\Delta K_{\text{eff(ND)}} = U_E \Delta K_{\text{(ND)}} \simeq U_E \Delta\sigma\sqrt{\pi(a_o + 2ry)}$$

The relation $\Delta K_{\text{eff}} = f(a)$ becomes

$$\Delta K_{\text{eff}} = \sqrt{Aa + B} = \sqrt{\frac{\Delta K^2_{\text{eff (ND)}} - \Delta K^2_{\text{effmin}}}{2ry} a + \Delta K^2_{\text{effmin}}} \qquad (2)$$

The integration of Eq 1 has been made by Simpson's method over the limits a_o, $a_o + \Delta a$. The results found for $\Delta a = 2ry$ are given in Table 2. These results are given for different coefficients m and C_E found in different tests, but for each test, with its determined values of m, C_E, the calculated retardation is in good agreement with the experimentally measured value.

Relation Between the Effective Stress-Intensity Factor Range and the Threshold After Overloading

From the previous results we know that it is possible to calculate the delay due to an overload by means of ΔK_{eff} measurements. To avoid the determination of ΔK_{eff} in the affected zone by crack opening displacement, the threshold concept after overloading, K_{th}, has been introduced [3] in Paris's law $da/dN = C(K_{\text{max}} - K_{\text{th}})^m$.

Because the crack does not propagate for ΔK values less than ΔK_{th}, we shall consider that the crack propagates for ΔK_{eff} values equal to $K_{\text{max}} - K_{\text{th}}$. So the ΔK_{eff} value, immediately after overloading called previously ΔK_{effmin}, will be determined from the following hypothesis: $\Delta K_{\text{o}} = \Delta K_{\text{eff}} + \Delta K_{\text{th}}$. From the results obtained for the three configurations [9], a linear relation has been established between

$$T_p^2 = \left(\frac{\Delta K_{\text{peak}}}{\Delta K_{\text{o}}}\right)^2 = \frac{r_{\text{p peak}}}{r_{\text{po}}} \quad \text{and} \quad T^2 = \left(\frac{\Delta K_{\text{o}}}{\Delta K_{\text{th}}}\right)^2 = \frac{r_{\text{po}}}{r_{\text{p th}}} \quad (\text{for } R = 0)$$

where r_p is the radius of the plastic zone, as shown in Fig. 7. It appears that two tests are sufficient to determine this relation for the two extreme cases a, b defined previously [3]. From this relation, for any given T_p and ΔK_{o}, the ΔK_{th} value immediately after overloading can be determined, and hence ΔK_{effmin}, being the lower integration limit of Eq 1. The higher limit can be calculated from Eq 2. Hence, the retardation due to an eventual overload can be predicted without measurement of crack opening displacement variations.

Discussion

It is interesting to notice that no variation of crack opening was obtained by the central clip gage while the crack crossed the affected zone. The ex-

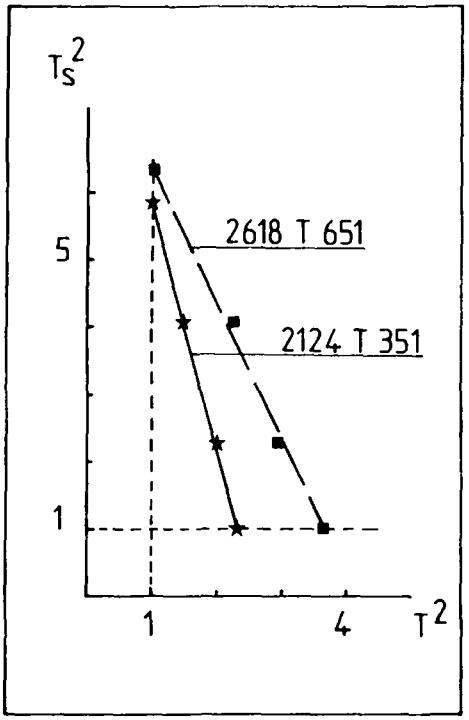

FIG. 7—*Threshold determination for a given overload ratio* T_p; $\Delta K_o = 12\ MPa\sqrt{m}$ *and* R = *0.01.*

planation is that the variations of P_{op} are due to the extra residual deformations, which affect only the tip of the crack, induced by the overload. The variations of P_{op} were obtained only with the two clip gages located in front of the crack tips in the affected zone [*1,7,8,10-14*].

The results given in Table 1 show that the values of a_D determined by the U ratio are in good agreement with the values of the diameters of the plastic zones due to overloading, calculated for $K_{peak} \simeq 24\ MPa\sqrt{m}$. This method gives less scatter in results than those obtained by measuring a_D from $a = f(N)$ or $da/dN = f(a)$, as they depend greatly on the manipulator. However, Elber and Schijve [*2,7*] have found them to be in a good agreement. Good relations have also been found by Bertel [*6*] between a_D and $2ry$ for sheets of 2124-T351 and 2618-T651 aluminum alloys tested with two R-ratios, 0.01 and 0.5, and different overload ratios. Consequently, it is more accurate to consider $2ry$ for determining the length of the affected crack than to consider the value of a_D determined by Wheeler [*15*] (Table 1) or only ry, as proposed by different authors, at least for the aluminum alloys.

The relation $T_p = f(T)$ gives the threshold just after a given overload (when $T_p = 1$, as is the case of uniform loading or many successive overloads). It

appears that the threshold is easily determined, but the use of ΔK_{eff} is more practical in the prediction of retardation for the following reasons:

1. When the crack growth rate is plotted against ΔK_{eff}, in logarithmic coordinates, a linear relationship is obtained even in the case of overloading with different R-ratios.

2. This relation is the same for different R-ratios in plane stress propagation (Figs. 3 and 5) verifying the Elber relation $U = \alpha + \beta R$ established in the case of propagation under uniform loading as well as for overloading.

3. The threshold concept gives only the extreme points: the threshold value just after overloading and that after a uniform loading, that is, for $2ry$. The relation between U and a gives the ΔK_{eff} value for a given crack length Δa, even if Δa is less than $2ry$.

This last remark is very important for application of the ΔK_{eff} concept in the case of complex spectrum loading. In fact, ΔK_{eff} is calculated cycle by cycle by the different relations established in this paper, satisfying

$$\frac{da}{dN} = C_E \Delta K_{eff}^m \quad \text{hence} \quad \Delta a_N = C_E \Delta K_{effN-1}^m$$

An example of applying this method is given in Table 3 for the spectrum loading, represented in Fig. 8, composed of repeated blocks of 18 cycles. The results show that the prediction of crack propagation is in good agreement with measurements for a range of crack length up to 8.18 mm.

The ΔK_{eff} concept indicates that only five cycles are effectively propagating the crack (Fig. 8).

The ΔK_{eff} concept appears to be a good criterion to explain the crack propagation mechanisms under variable amplitude loading with different R-ratios, at least for thin sheets. This concept permits the prediction of crack propagation under complex spectrum loadings encountered in aeronautics.

Conclusions

1. The variations of the U ratio calculated from $P\delta$ records in the affected zone by overloading permit plotting a linear relation in logarithmic coor-

TABLE 3—*Predicted crack propagation for spectrum loading (CCT specimen).*

	Measured Number of Blocks		Calculated Crack Propagation		Measured Crack Propagation	
a_o, mm	ΔN_o	ΣN	Δa	Total a	Δa	Total a
32.32	3010	3010	2.28	34.6	2.68	35
34.6	1400	4410	1.1	35.7	1.35	36.35
35.7	5300	9710	4.9	40.6	4.15	40.5
...	...	$N = 9710$	$\Sigma \Delta a = 8.28$	40.6	$\Sigma \Delta a = 8.18$	40.5

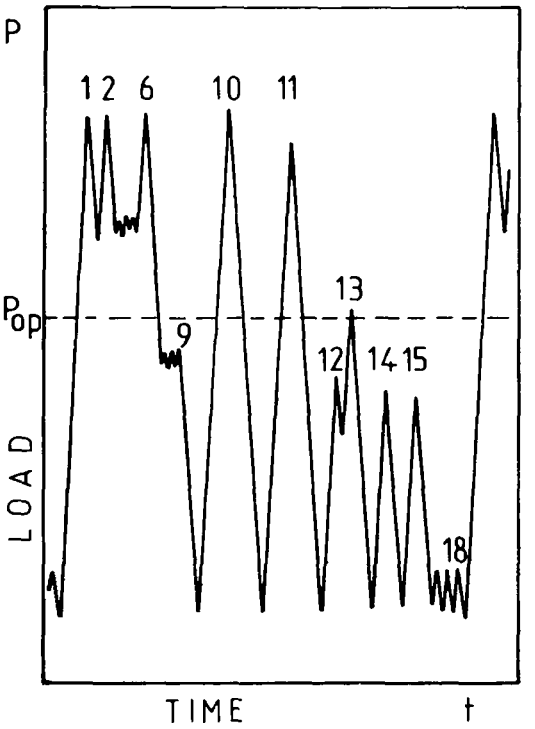

FIG. 8—*Applied spectrum loading as repeated blocks.*

dinates between the crack propagation rate da/dN and the effective stress-intensity factor range ΔK_{eff}.

2. This relation has been found the same in the case of propagation under a cyclic loading with R-ratio of 0.5, affected by an overload.

3. The value of a_D, affected crack length, calculated from the U variations has been found in good agreement with the diameter of the plastic zone, $2ry$, induced by the overload.

4. The relation $U = f(2ry)$ permits the prediction of the number of cycles delayed, N_D, due to an overload with good precision by integrating $dN = da/C_E \Delta K_{eff}^m$.

5. The range of results obtained for calculated values of N_D is the same as that observed during testing. Consequently, an eventual error of N_D values is due not to the calculation method (ΔK_{eff} concept) but to the variations of the coefficient C_E observed for different tests.

6. The threshold concept after overloading defined in the literature is a simple and indirect means for determination of ΔK_{eff}.

7. The ΔK_{eff} concept permits the prediction of crack growth in plane stress conditions under complex spectrum loadings.

References

[1] Clérivet, A. and Bathias, C., *Engineering Fracture Mechanics*, Vol. 12, 1979, pp. 599-611.
[2] Elber, W. in *Damage Tolerance in Aircraft Structures, ASTM STP 486*, American Society for Testing and Materials, 1971, pp. 230-242.
[3] Pellas, J., Baudin, G., and Robert, M., *Fracture 1977: 4th International Conference on Fracture*, Vol. 2, 1977, pp. 1353-1360.
[4] Bertel, J. D., Clérivet, A., and Bathias, C., *5th International Conference on Fracture*, Vol. 2, 1981, pp. 943-951.
[5] Bertel, J. D., Clérivet, A., and Bathias, C., "Influence du rapport R et des surcharges sur les mécanismes de fissuration par fatigue," Ecole d'été Franco-Québecoise No. 2, Montréal, July 1980.
[6] Bertel, J. D., "Influence de l'état de contrainte sur les mécanismes de fissuration par fatigue sous chargement comportant des surcharges. Cas des alliages d'aluminium à hautes caractéristiques," thesis, University of Technology at Compiègne, Jan. 1981.
[7] Schijve, J., *Engineering Fracture Mechanics*, Vol. 11, 1979, p. 182.
[8] Ogura, K. and Ohji, K., *Engineering Fracture Mechanics*, Vol. 9, 1977, pp. 471-480.
[9] Bertel, J. D., Clérivet, A., and Bathias, C., *International Symposium on Fatigue Threshold*, Vol. 1, 1981, pp. 12:1, 12:19.
[10] Sewell, G. and Marcus, H. L. *Scripta Metallurgica*, Vol. 11, 1977, p. 521.
[11] Ewalds, H. L. and Furnée, R. T., "Crack Closure Measurement Along the Fatigue Crack Front of Center Cracked Specimens," *International Journal of Fracture*, Vol. 14, 1978.
[12] Ohta, A., Kosuge, M., and Sasaki, E., "Change of Fatigue Crack Closure Level with Gauge Location Along Crack Line," *International Journal of Fracture*, Vol. 15, 1979.
[13] Lindley, T. C. and Richards, C. E., *Materials Science and Engineering*, Vol. 14, 1974, pp. 281-293.
[14] Newman, J. D., Jr. in *Mechanics of Crack Growth, ASTM STP 590*, American Society for Testing and Materials, 1976, pp. 281-301.
[15] Wheeler, O. E., *Journal of Basic Engineering, Transactions of the American Society of Mechanical Engineers*, 1972, pp. 181-186.

J. M. Krafft[1]

Plastic Flow Normalizing the Fatigue Crack Propagation Data of Several Steels

REFERENCE: Krafft, J. M., **"Plastic Flow Normalizing the Fatigue Crack Propagation Data of Several Steels,"** *Fracture Mechanics: Fourteenth Symposium—Volume I: Theory and Analysis, ASTM STP 791*, J. C. Lewis and G. Sines, Eds., American Society for Testing and Materials, 1983, pp. I-380–I-406.

ABSTRACT: Taken from a recent Naval Research Laboratory (NRL) report, this paper advances author's earlier efforts to associate plastic flow with fatigue crack growth characteristics. Success with this could lessen the data required for estimates of fatigue crack propagation life of structural elements. The model sees crack growth as a means of strain hardening material elements adjacent to the crack tip to counteract strength losses due to transient stress relaxation/creep and environmental surface attack. It defines limiting growth rates in terms of fixed as well as of strain-limited environmental action. Data on some 16 steels are compared to measured stress-strain data using the same model equations. Data fits are rather close, and values of the three kinds of data fitting parameters show consistent trends with respect to the yield strength of the steels.

KEY WORDS: fatigue crack propagation, corrosion fatigue of steels, fatigue propagation model, plastic flow versus fracture model, fracture mechanics

Fatigue crack propagation data are needed in important life-prediction problems such as: air-frame structural integrity and damage tolerance; fatigue stress allowables of welded structures; tolerance for nondestructive testing (NDT) indications under the American Society of Mechanical Engineers (ASME) pressure vessel code; and total fatigue endurance of jet engine parts. The ideal measure of structural fatigue endurance is by testing in direct simulation of service environment and loading spectrum. However, it is usually less costly to estimate life from steady-state crack growth rate data, modified by suitable overload retardation models. Even here, the effort required to simulate all stress ratios, frequencies, and environmental conditions can be substantial. A goal of propagation modeling, the subject of this paper, is to reduce

[1] Head, Structural Mechanics Branch, Naval Research Laboratory, Washington, D.C. 20375.

the time and cost of acquiring such data. As in earlier papers on this endeavor [*1,2,3*],[2] this one puts forth refinements that were required to cope with an enlarged data base. It describes the ferrous alloy results of Naval Research Laboratory (NRL) Memorandum Report 4161 [*4*], which also contains data on titanium and aluminum alloys. Copies of the full report are available from the NRL.

Model Concept and Development

This model explores the hypothesis that stability of crack propagation requires the maintenance of a state of constant-load stability within a specific region of material very close to the crack tip. The crack extension during each cycle is determined as the means of just maintaining such stability. For simplicity, it considers the specific region of material as a crack-tip front with rows of cylindrical tensile ligaments of fixed diameter $d_T(=2r_T)$. These are elongated by remote loading of the crack as well as by crack growth in each cycle. As with any specimen subjected to tensile strain, strain-hardening enhances stability, while Poisson contraction reduces it. Additional load-reducing effects are transient stress relaxation (a volume effect) and environmental attack (a surface effect), modeled as load-bearing material removed from the ligament surface. This surface attack can be considered to be limited in two ways. First, it may be limited by exposure time in the cycle, up to a saturation condition. Second, it may be limited alternatively by insufficient surface-disturbing plastic strain due to crack loading and propagation. The following analysis provides a deterministic way of considering both limits.

Constant Load Stability

Consider a simple tension specimen of sectional area A, subjected to load P, for which the true stress σ is defined

$$\sigma = P/A; \qquad P = \sigma A; \qquad dP = \sigma dA + A d\sigma \tag{1}$$

For the constant-load creep conditions, $dP = 0$, whence Eq. 1 becomes

$$\sigma dA = -A d\sigma \tag{2}$$

These total differentials of area and stress, on a ligament of radius $r_T = d_T/2$, can be replaced by the following partials

$$\partial A_v = 2\nu\pi r_T^2 d\epsilon_p; \qquad \partial A_s = -2\pi r_T dr_T \tag{3}$$

$$\partial\sigma_\theta = \theta_p d\epsilon_p \qquad \partial\sigma_m = -m\sigma dt/t \tag{4}$$

[2]The italic numbers in brackets refer to the list of references appended to this paper.

Here ν is the Poisson ratio, ϵ_p is the plastic strain, Θ_p is the plastic strain hardening rate ($d\sigma/d\epsilon_p$), m is the stress relaxation exponent ($d\ell n\sigma/\ell nt \simeq -d\ell n\sigma/d\ell n\dot{\epsilon}_p$), t is time, and subscript s denotes a surface effect. The plastic strain ϵ_p, and plastic strain hardening rate $d\sigma/d\epsilon_p = \Theta_p(\Theta_p{}^{-1} = \Theta^{-1} - E^{-1})$ are used since stress relaxation, or strain rate sensitivity, is a plastic-flow effect and the elastic part of the Poisson contraction is relatively small, $2\nu \simeq 1.0$. With this simplification, combining Eqs 3 and 4 with Eq 2 results in

$$d\epsilon_p = \left(2\frac{dr_T}{r_T} + m\frac{dt}{t}\right)\left(\frac{\theta_p}{\sigma} - 1\right)^{-1} \tag{5}$$

Crack-Tip Straining

In Eq 5, $d\epsilon_p$ may be regarded as the strain differential required to maintain the constant load condition, $dP = 0$. An expression is needed for how such strain derives from the loading and growth of the crack. This model employs, provisionally, the simple analogue of the linear elastic crack tip stress field, providing an inverse half power strain singularity near the crack tip

$$\sigma_y = K/\sqrt{2\pi r}; \qquad \epsilon = K/\sqrt{2\pi r}\,E \tag{6}$$

Differentiating Eq 6 gives

$$d\epsilon = \left(r^{-1/2}dK - \frac{K}{2}r^{-3/2}dr\right)/\sqrt{2\pi}\,E \tag{7}$$

where K is the opening mode stress-intensity factor, r is distance ahead of the crack tip, E is Young's modulus, and ϵ is total elastic plus plastic strain.

As a further simplification, the crack-tip strain singularity is truncated within the distance equal to the ligament diameter, $r = d_T$. Substituting $r = d_T$, $dr = -da$ where a is crack length, and $\epsilon = K/\sqrt{2\pi d_T}\,E$, then Eq 7 becomes

$$d\epsilon = d\epsilon_L + \frac{\epsilon_G}{4r_T}da \tag{8a}$$

Here $d\epsilon_L$ designates a strain differential due to crack loading, while ϵ_G is a strain associated with the strain gradient $d\epsilon/dr$, hence $-d\epsilon/da$, at the point $r = d_T$. For constant-load stability during the dwell period after loading has ceased in the fatigue cycle, the loading strain differential $d\epsilon_L$ is neglected. Of the propagation strain remaining, its elastic component is unchanged by the growth increment da, hence $d\epsilon$ may be regarded as a plastic-only strain, that is

$$d\epsilon_p \equiv \frac{\epsilon_G}{4r_T}da \tag{8b}$$

Substituting Eq 8b in Eq 5 gives

$$da = \left(8dr_T + 4mr_T \frac{dt}{t}\right)\left[\epsilon_G\left(\frac{\theta_p}{\sigma} - 1\right)\right]^{-1} \tag{9}$$

Specifics for the Growth Rate Equation

The general crack growth relationship, Eq 9, shows the principal impediment to crack growth as the strain hardening rate of the material. Cyclic and monotonic strain hardening characteristics differ markedly. Both are involved in some way at the crack tip in fatigue. Cyclic loading produces cyclic straining at the crack tip. Yet if there is substantial growth during the period of sustained load, the crack may invade material of virgin characteristics, unaffected by the cycling. After trials of many correlation algorithms, the option chosen is to divide the effects decisively on the basis of limiting cases of crack propagation, namely, to associate cyclic strain hardening, a function of the strain excursion, with impedance to stress-relaxation induced growth, and to associate monotonic strain hardening, a function of the maximum strain, with impedance to environmentally induced growth. This defines two different kinds of the flow property-dependent term of Eq 9

$$G_1 \equiv \left[\epsilon_1\left(\frac{\theta_{1p}}{\sigma_1} - \frac{\sqrt{3}}{2}\right)\right]^{-1} \tag{10}$$

and

$$G_2 \equiv \left[\epsilon_2\left(\frac{\theta_{2p}}{\sigma_2} - \frac{\sqrt{3}}{2}\right)\right]^{-1} \tag{11}$$

where subscripts 1 and 2 denote monotonic and cyclic properties, respectively, and G is called a specific growth rate factor.

In calculating G-values from measured tensile data, the monotonic stress σ_1 is measured from zero-stress origin, and converted to true stress. However the cyclic stress is the positive excursion of a cyclic loop assumed in balance with its negative excursion as results from prolonged cycling [5]. The strains ϵ_1 and ϵ_2 are total (elastic plus plastic) strains measured from these origins, and the corresponding values of stress and strain hardening rate are considered functions of these total strains. The term $\sqrt{3/2}$, slightly less than unity, is substituted as a plane-strain triaxiality effect on the instability condition [6]. It has the effect of increasing the strain for tensile instability in a way found to be helpful in correlating materials with very flat monotonic stress-strain curves. With these selections, Eq 9 can be expressed as a crack growth differential

$$da = 4r_T m G_2 dt/t + 8G_1 dr_T \tag{12a}$$

An increment of crack growth in an excursion from K_{min} to K_{max} in an interval t_L, and then holding on K_{max} for an interval t_H can be expressed

$$\Delta a = 4r_T m \ell n(1 + t_H/t_L)G_2 + 8\Delta r_T G_1 \tag{12b}$$

or abbreviated

$$\Delta a = f_2 G_2 + f_1 G_1 \tag{12c}$$

A summed or averaged growth-rate factor (GRF) may be defined as

$$GRF = \Delta a/f_2 = G_2 + \frac{f_1}{f_2} G_1 \tag{13}$$

In this paper, a single value for the loading wave-form factor $\ell n(1 + t_H/t_L) = 0.3$ (versus 0.4 in Ref *3*) is used to fit data for both sinusoidal and triangular wave forms used in the fatigue crack growth rate (FCGR) tests. Substituting this value in Eq 13

$$GRF \equiv \frac{\Delta a}{1.2mr_T} = G_2 + \left[\frac{\Delta r_T}{r_T}\right] G_1/0.15m \tag{14}$$

where *GRF* is a general/total growth-rate factor.

Curves of Time- and of Strain-Limited Surface Attack

The two different ways in which environmental attack may be limited were mentioned earlier. The effect of varying these limits is displayed by two families of curves. One is a parametric set of constant values of r_T-normalized surface attack intrusion $[\Delta r_T/r_T]$; the second is a set for such intrusion relative to the *plastic* tensile straining of the d_T-ligament during one loading cycle, $[\Delta r_T/r_T/\Delta\epsilon_p]$.

For the first family, Eq 14 is restated

$$GRF = G_2 + [\Delta r_T/r_T]\, G_1/0.15m \tag{15}$$

or for a parametric N-family

$$G(N) = G_2 + [2^N]G_1/0.15m \tag{16}$$

The crack growth rate is thus

$$\left(\frac{da}{dN}\right)_t = 1.2mr_T G(N) \tag{17}$$

For the second family, Eq 14 is restated

$$GRF = G_2 + \Delta\epsilon_p \left[\frac{\Delta r_T/r_t}{\Delta\epsilon_p}\right] G_1/0.15m \tag{18}$$

Here the $\Delta\epsilon_p$ term is intended to include plastic strain due to both the loading and the propagation of the crack. It is calculated from Eq 8, approximated here in incremental form, with Eq 14 substituted for Δa

$$\Delta\epsilon_p = \Delta\epsilon_L + 0.3m\epsilon_G GRF \tag{19}$$

The loading (plastic) strain $\Delta\epsilon_L$ is associated with the total strain of the cyclic stress-strain curve, less its elastic strain

$$\Delta\epsilon_L = \epsilon_{2p} = \epsilon_2 - 2\sigma_2/E_2 \tag{20}$$

Considering the term $0.3\, m\epsilon_G GRF$, what value to use for ϵ is unclear since, in effect, ϵ_2 is used for it in the G_2 term of GRF, while ϵ_1 is used in the G_1 term, per Eqs 10, 11, and 13. Corresponding values of these strains differ at nonzero stress ratio. To obtain a closed-form solution, only one can be used. In this case, the gradient strain is set equal to the maximum strain ϵ_1, corresponding to its value in G_1. This is the more accurate value in regions where the environmental effects dominate. When they do not, the choice is of little consequence. With this approximation then, Eq 18 becomes

$$GRF = G_2 + \left[\epsilon_2 - \frac{2\sigma_2}{E_2} + \epsilon_1 0.3m GRF\right]\left[\frac{\Delta r_T/r_T}{\Delta\epsilon}\right] G_1/0.15m \tag{21}$$

Solving for GRF, then

$$GRF = \frac{G_2 + \left[\dfrac{\Delta r_T/r_T}{\Delta\epsilon}\right] G_{2p} G_1/0.15m}{1 - \left[\dfrac{\Delta r_T/r_T}{\Delta\epsilon}\right] 2\epsilon_1 G_1} \tag{22}$$

or for a parametric M-family

$$G(M) = \frac{G_2 + [2^M]\epsilon_{2_p} G_1/0.15m}{1 - [2^M]2\epsilon_1 G_1} \tag{23}$$

Similarly to Eq 17, the crack growth rate for this family is simply

$$\left(\frac{da}{dN}\right)_t = 1.2mr_T G(M) \tag{24}$$

Corresponding K-Strain Excursion

The effects of load ratio R (K_{min}/K_{max}) on the values of G_1 and G_2 is considered next. If the load ratio is zero and crack tip strain is proportional to the stress-intensity factor, then total elastic plus plastic strains of measurement in the two cycles can be compared directly. However, if R is greater than zero, then one should associate monotonic properties, hence G_1, with a strain larger than that for cyclic properties, hence G_2. If the strain excursion corresponding to ΔK is taken as a base, then a basis of association is

$$\Delta\epsilon = \epsilon_2 = (1 - R)\epsilon_1 \tag{25}$$

This means that to calculate a GRF for a given value of strain excursion $\Delta\epsilon$, one uses cyclic properties at strain $\epsilon_2 = \Delta\epsilon$ to compute G_2, while using monotonic properties at strain $\epsilon_1 = \Delta\epsilon/(1 - R)$ to compute the corresponding value of G_1.

What level of stress-intensity factor excursion ΔK is required to produce a strain $\Delta\epsilon$ at d_T? This model recognizes a slight degree of ineffectiveness, or "slack," in coupling the overall K-excursion to the strain excursion at the crack tip, analogous to the Elber's crack closure effect [*7*]. The amount of this slack is fixed as one-half the monotonic tensile yield point strain as justified in Ref *3*. This "closure strain," $\epsilon_{CL} = TYS/2E$, is taken as a fixed increase of the monotonic form of $\Delta\epsilon$. In the cyclic form, it is added only to the extent that the minimum strain, $R\Delta\epsilon/(1 - R)$, is less than the closure strain, or the difference greater than zero. With this, the ΔK proportional strain is defined as

$$\Delta\epsilon_K = \Delta\epsilon + \epsilon_{CL} \tag{26}$$

$$= \epsilon_2 + [\epsilon_{CL} - R\epsilon_2/(1 - R)]_{>0} \tag{27}$$

$$= (1 - R)\epsilon_1 + \epsilon_{CL} \tag{28}$$

The cyclic excursion ΔK may now be defined, after Eq 6, for the point $r = d_T = 2r_T$

$$\Delta K = \sqrt{4\pi r_T}\, E\Delta\epsilon_K \tag{29}$$

An illustration of foregoing considerations is attempted in Fig. 1.

This model version differs from that of Refs *3* and *8* in one major respect, as well as in several minor ones. The major change is that the gradient strain in G_1 (Eq 10) and in $G(M)$ (Eq 21) is taken as the maximum strain rather than the strain excursion. This and the minor changes are detailed in Ref *4*.

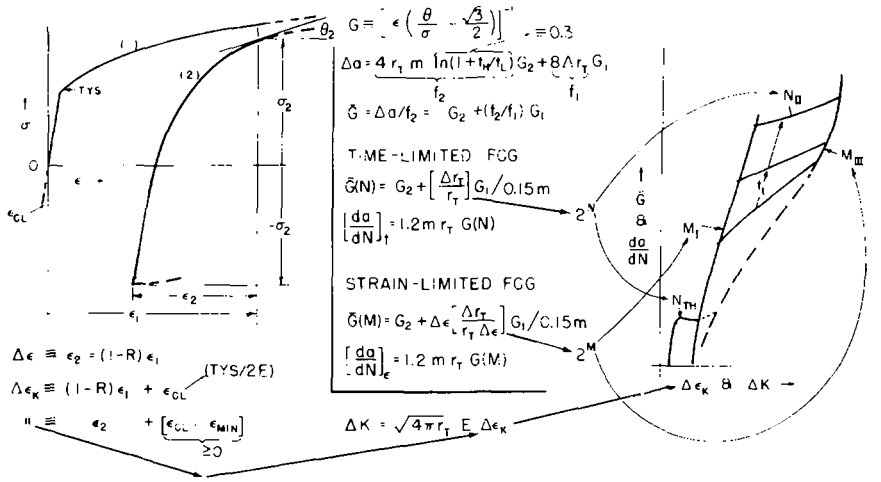

FIG. 1—*Outline of procedure for converting measured shape of monotonic (1) and cyclic (2) stress-strain curves into paths of up to four stages of corrosion-fatigue crack growth rate.*

Tension Tests of Conversion to GRE Parametric Curves

To compare the previously developed algorithm with plotted fatigue crack growth data requires monotonic and cyclic stress-strain measurement and its conversion to parametric curve sets of $G(N)$ and $G(M)$ versus $\Delta\epsilon_K$. The computational task, too laborious for manual calculation and graphing, is readily accomplished with a suitable computer program, large digital computer, and plotter. The general procedure is summarized in sections to follow. References *3* and *4* contain greater detail, and the BASIC language calculation program is available from the Naval Research Laboratory to those interested.

Measuring Stress-Strain-Time Curves

The model requires a mechanical stress-strain test of the material of interest. Specimens are taken preferably from used fatigue test specimens, with the longitudinal axis normal to the fracture plane; ours are 4.32 mm (0.170 in.) diameter, with about 9 mm (0.35 in.) length of uniform cylindrical section between fillets to threaded end buttons. With some skimping on thread length, they can be made from broken halves of a 1-T compact tension specimen in accordance with the ASTM Test for Plane-Strain Fracture Toughness of Metallic Materials (E 399-81). These are subjected to tensile and compressive deformation on a subpress installed in the lower head space of 45-kN (10-kip) screw-driven Instron machine. The crosshead was biased with heavy coil springs to remove backlash in load reversal, in the manner of Coffin and

Tavernelli [9]. A four-finger, resistance-strain-gage-instrumented clip gage was used to measure longitudinal strain recorded versus load on an x-y plotter. The Instron was set up to give a constant-load strain rate of about 10^{-3} s^{-1}. Data for the stress relaxation exponent m is obtained on the flat region of the cyclic curve by arresting the head and timing, with the highest available amplification, the decay in load. The slope of a log plot of load versus time after arrest is used in the measure of m.

Reading and Correcting Flow Data

Values of stress and tangent modulus are scaled directly on the stress-strain curves at selected strain stations, then converted to true values using

$$\sigma = \sigma_T(1 + \epsilon_T) \tag{30}$$

$$\theta = [\theta_T + \sigma_T/(1 + \epsilon_T)]\,(1 + \epsilon_T)^2 \tag{31}$$

$$\epsilon = \ell n(1 + \epsilon_T) \tag{32}$$

where the subscript T denotes tensile values. For the cyclic curve, stress is measured from the compressive toe, converted to true stress, then divided by two for the applicable tensile portion.

Removing Upper-Yield-Point Effects

Monotonic properties of structural steel usually exhibit an upper/lower yield point effect where zero or negative Θ_T produces an intractable G_1 infinity. It is removed by fitting a power-hardening equation to the region beyond that of the lower yield point, then extrapolating with it back under the measured lower yield plateau, using the equations

$$\sigma_1 = \sigma_0(\epsilon_p/\epsilon_0)^n \tag{33}$$

$$\theta_1 = \left(\frac{\epsilon_o}{n\,\sigma_o\epsilon_p} + \frac{1}{E_1}\right)^{-1} \tag{34}$$

$$\epsilon_1 = \epsilon_p + \sigma_1/E_1 \tag{35}$$

The strain hardening exponent n is determined as the slope of a log plot of measured σ versus ϵ beyond the lower yield range, and E_1 is the measured monotonic elastic modulus. Estimated values of Θ_1 are used only to replace lesser measurement-derived values. By this rule, measurements around the proportional limit are used, as desirable to ascertain ΔK threshold values. Only measured values of σ_T are used in the program.

Computer Processing

The monotonic and cyclic flow data are listed in separate data file programs in computer storage. The file for a given material is withdrawn and inserted in the calculational program using the BASIC-language WEAVE instruction capability in preparing the program to run. The program performs the numerical interpolations, providing monotonic and cyclic characteristics at fixed logarithmically spaced strain intervals of $\Delta\epsilon_K$. The output is plotted on a graphics terminal, generally with $G(M)$ and $G(N)$ versus $\Delta\epsilon_K$ maps, in contrasting colors, superimposed.

Installing Matching Guidelines

The matching process involves finding what values of r and the two surface attack fitting parameters, $\Delta r_T/r_T$ or N, $\Delta r_T/r_T/\Delta\epsilon$ or M, provide the best fit of the data. This is done by graphical superposition of *GRF* versus $\Delta\epsilon_K$ maps upon the *da/dN* versus ΔK data, both of identical (logarithmic) scaling. In doing this, it is convenient to install match guidelines on both the plots. Our convention is to find the point on the crack growth data plot $da/dN = 10$ μm/cycle; $\Delta K = 10$ MPa$\sqrt{\text{m}}$. Solving Eqs 14 and 29 using these coordinates, plus an arbitrary value of $d_T = 100$ μm, gives a corresponding point on the *GRF* plot

$$GRF_{\text{ref}} = 1/6m$$
$$\Delta\epsilon_{K-\text{ref}} = 1000\ (MPa)/\sqrt{2\pi}\,E_1 \tag{36}$$

Other values of d_T can be substituted to establish a line; alternatively, one of slope +2 can be drawn from the previously designated reference points, by regarding the 2:1 d_T-sensitivity of *GRF* versus $\Delta\epsilon_K$. The matching lines shown on the various data-match figures follow this convention. Comparison of *G*-maps with *da/dN* data involves superposition of the respective plots on a light box, with matching lines held coincident. The position of $\Delta\epsilon_K$ on the ΔK scale at best match is, conveniently, a value whose square is the size of the d_T process zone in microns.

Number of Fitting Parameters

This model requires from one to five fitting parameters of three different kinds. The size parameter d_T is always required. If there is little or no environmental effect, the data should correspond to $G(N) \simeq G_2$-only, for a one-parameter (d_T-only) fit. If there is a sensitivity to the air environment, data generally will correspond to a curve of constant $M = M_{\text{III}}$, for a two-parameter fit. In aggressive liquid environments, two additional stages must be charac-

terized: Stage I growth by another higher value of $M = M_I$, and Stage II bridging I to III with a path of constant $N = N_{II}$, for a four-parameter fit. Finally, at high stress ratios, one can detect a "knee" protruding down from the constant-M_I, Stage I trace which appears to be matched by a curve of very low $N = N_{TH}$ value. With it, a maximum of five fitting parameters is needed. However, the same parameters apply to all positive stress ratios without change.

The two curve families differ in frequency sensitivity. Curves of constant M, like the Stages I and III of corrosion-fatigue crack growth (CFCG) which they track, tend to be frequency-independent, presumably because the amount of surface attack is limited by the degree of surface distortion or plastic deformation of the ligament. On the other hand, the curves of constant N, as the Stage II they track, tend to be frequency/cycle-duration dependent, which presumably is related to the time dependency of surface attack or corrosion.

Case Studies

The overall collection reported in Ref *4* contained some 13 alloys of titanium and aluminum in addition to the 16 steels shown here. Table 1 provides a listing of steel compositions, and Table 2 provides the heat treatments and mechanical properties. The sources of tension specimen material and FCGR data are referenced in the figure captions. For brevity, the GRF maps for the first case are shown. For the other cases, only the map portions found in correspondence with the data are shown. The characterizing values of d_T, N_{TH}, M_I, N_{II}, and M_{III}, where appropriate, are shown on each figure.

Figures 2 to 10 display analyses of the 16 steels of differing composition or heat treatment or both. The full example is shown in Fig. 2 using the unusually complete data set of Vosikovsky [*10*] on X-70 line pipe steel. Values of true stress and strain hardening rates are given in Fig. 2*a*, followed in Fig. 2*b* by the combined $G(M)$ and $G(N)$ maps for each stress ratio. (A selection of these is overlaid the data in Fig. 2*c*.)

Of the various cases shown, the matches are generally encouraging. In the softest materials, such as the A-36 of Fig. 3, specimen yielding tends to cut off the upper limit of agreement. Steels in the middle strength range seem to model best. Two higher strength steels, HY-80 and HY-130, show a greater ΔK range of stable fatigue growth than can be predicted from the strain range of stable plastic deformation. The extreme flatness of their monotonic stress-strain curve causes, as with the lower yield point of mild steel, an uncertainty in the estimate of stability. However, at present the match of these two must be regarded as less than satisfactory. It is notable of the whole data set of Ref *4* that the eleven titanium alloys modeled rather well, but two aluminum alloys did not model as well.

TABLE 1—*Alloy composition.*

Alloy	Base + weight %	C	Si	Mn	Ni	Cr	Mo	V	Co	Cu	Al	Nb	S	P
A-36	Fe	0.17	0.29	0.86	...	...	...	...	...	0.03	...	...	0.021	0.015
BS 4360-50D	Fe	0.17	0.358	1.35	0.07	0.09	0.01	...	...	0.17	0.05	0.03	0.023	0.037
X-65	Fe	0.16	0.33	1.34	...	...	...	0.046	...	...	...	0.031	0.009	0.006
X-70	Fe	0.06	0.28	1.90	0.25	...	0.39	...	...	...	0.073	0.058	0.009	0.002
SM-58-Q	Fe	0.14	0.32	1.30	0.024	0.020	0.023	0.038	...	...	...	...	0.006	0.022
HT-80	Fe	0.13	0.19	0.94	0.025	0.46	0.14	0.027	...	0.051	...	...	0.007	0.014
HY-130	Fe	0.09	0.26	0.69	5.0	0.48	0.47	0.08	...	0.05	...	...	0.007	0.009
10 Ni	Fe	0.12	0.07	0.28	10.29	7.03	1.03	...	8.07	...	...	...	0.006	0.008
4340	Fe	0.40	0.31	0.72	1.85	0.82	0.22	...	...	...	...	...	0.020	0.010
300M	Fe	0.42	1.59	0.76	1.76	0.76	0.41	0.10	...	...	...	...	0.002	0.007

TABLE 2—*Alloy heat treatment, grain size and mechanical properties.*

Fig. No.	Alloy	Thickness, mm	Heat Treatment, deg C[a]	Direc-tion	E, GPa	Tensile Yield Strength, GPa[b]	Ultimate Tensile Strength, GPa[b]	ϵ_u	m[c]	Grain Size, μm	d_T μm
	Steel										
3	A-36	25	AR	TL	207	0.26/	0.48/	≃0.18	0.0072	...	77
4	BS 4360-50D	38	AR	...	207	0.37/0.37	0.53/0.54	0.26	0.0078	...	87
5	X-65	13	API spec. 5LX	TL	207	0.45/0.46	0.59/0.57	≃0.2	0.0064	18	25
2	X-70	19	Control-rolled, API spec. 5LX	LT	207	0.46/0.53	0.63/0.67	0.16	0.0065	4.5	20
6	SM-58-Q	12	930°, WQ; 650° T, AC	LT	210	0.59/0.59	0.68/0.67	0.09	0.0059	...	18
6	HT-80	12	880°, WQ; 570° T, AC	LT	207	0.74/0.79	0.79/0.82	0.06	0.0052	...	9.6
7	HY-130	13	830°, WQ; 643° T, WQ	LT	207	0.96/	1.09	0.08	0.0054	...	6.0
8	10 Ni steel	...	...	LT	195	1.32/1.31	1.40/1.35	...	0.0065	...	...
9	4340/538°	13	843°, OQ; 538° T, AC	TL	...	1.03/	1.08/	0.08	0.0066	...	9.5
	4340/427°	13	843°, OQ; 427° T, AC	TL	...	1.25/	1.37/	0.06	0.0059	...	9.5
	4340/316°	13	843°, OQ; 316° T, AC	TL	...	1.41/	1.61/	0.05	0.0048	...	9.5
	4340/204°	13	843°, OQ; 204° T, AC	TL	...	1.49/	1.88/	0.11	0.0065	...	2.6
10	300M/650°	13	870°, OQ; 650° T	...	208	1.01/1.08	1.17/1.19	...	0.0057	20[d]	13
	300M/470°	13	870°, OQ; 470° T	...	207	1.28/1.50	1.63/1.68	...	0.0047	20	6.0
	300M/300°	13	870°, OQ; 300° T	...	207	1.59/1.73	1.97/2.00	0.045	0.0041	20	4.0
	300M/100°	13	870°, OQ; 100° T	...	...	1.07/1.50	2.17/2.34	...	0.0033	20	1.4

[a] Heat treatment abbreviations:
AR = as received, Normal heat treatment presumed,
WQ = water quench,
OQ = oil quench,
T = temper,
AC = air cool,
FC = furnace cool.
[b] Measured/author's values shown
[c] Room temperature value of m
[d] Prior austenite grain size

Trends in Model Fitting Parameters

One measure of plausibility of a fracture model is the consistency among fitting parameters for various materials. In the titanium alloys from the source report [4], the d_T process zone was found to correlate with the average grain size. In the steels, grain size generally was not measured. However, if a similar correspondence were to carry over, then the process zone size should follow a Hall-Petch type correlation with yield strength. The upper bound of Fig. 11 shows such a plot. The slope of -2.0 for the overlaid band is as would be expected from the usual -0.5 power of grain size to yield strength relationship. Some of the other fitting parameters also are displayed in Fig. 11. In each case, the M or N value of the parametric curve family member has been converted to an absolute length using the process zone size as a multiplier.The parameters used are N_{TH} and M_{III} for the air fatigue data. Some degree of consistency among the values is indicated by the shaded bands.

The frequency-dependent parameter of the tensile ligament instability model (TLIM) is the value of N_{II} or corresponding Δr_T per cycle, found to fit the Stage II corrosion-fatigue growth region. Such values as are available in this collection are shown in Fig. 12 where, on a logarithmic plot, the value of Δr_T is plotted against loading time of the cycle. Using loading time as the time parameter governing corrosion-fatigue below K_{Iscc} follows the finding of Barsom [17] and of Kawai and Koibuchi [18]. Loading time is taken as 0.35 of cycle period for a sinusoidal wave form and 0.5 for a triangular wave form. The 4340 steel data also are plotted this way, although for most specimens the cycling was at a $K_{\max}$ generally exceeding the K_{Iscc} threshold.

In evaluating trends of Fig. 12, one should place less confidence in the low values of Δr_T, as the small difference between M_{I} and M_{III} paths in this region make it difficult to fit. Also, small values of the environmental term correspond to the transition of control between cyclic and monotonic curve shapes, where simple addition of limiting cases in the model is a questionable procedure. A slope of $+1$ on this plot indicates a constant value of surface attack rate, called V_s in earlier papers. There appears to be a tendency for V_s to decrease with cycle period at longer cycle durations, presumably due to some sort of time-saturation effect on environmental attack.

The model algorithm permits a direct estimate of the threshold for fatigue crack growth. In the nonvacuum environment, ΔK_{TH} is proportional to the monotonic yield point strain, or

$$\Delta K_{TH} = (1.5 - R)\,TYS\,\sqrt{2\pi d_T} \tag{37}$$

which results from combining Eqs 28 and 29. This is a slight overestimate, as the program detects the proportional limit, rather than the 0.2 percent yield stress. The observation in titanium alloys [4] of $d_T \simeq 2\bar{\ell}$ substituted in Eq 37 gives for $R = 0$

$$\Delta K_{TH} \simeq 5.3\,TYS\,\sqrt{\bar{\ell}} \tag{38}$$

a

VOSIKOVSKY X70 LINE PIPE STEEL, R=.0065, #7361

FIRST EXCURSION TRUE FLAW DATA, REF. STRESS=0

N	STRAIN	STRESS (MPA)	STRESS (KSI)	THETA (MPA)	THETA (KSI)
1	0.000000	0	0.0	207453	30038
2	0.000100	193	28.0	207453	30038
3	0.000150	255	37.1	140774	20390
4	0.000900	324	47.1	112009	17115
5	0.000750	373	54.1	86992	12606
6	0.000300	414	60.0	56480	8208
7	0.000389	456	66.1	26847	3896
8	0.000598	478	69.4	15613	2264
9	0.000807	486	70.6	11347	1645
10	0.001015	494	71.7	9015	1307
11	0.001222	509	73.9	7505	1091
12	0.001430	510	74.0	6490	941
13	0.001687	516	75.0	5718	829
14	0.001931	541	78.5	4901	709
15	0.002430	553	80.9	3950	573
16	0.002937	574	83.4	3337	484
17	0.003440	582	85.8	2808	407
18	0.003927	602	87.4	2615	379
19	0.004479	622	90.3	2218	321
20	0.005397	641	93.1	1940	284
21	0.006748	656	95.2	1601	232
FF	0.007496	670	97.2	1394	202
23	0.008618	683	99.0	1175	170

FULL-CYCLIC TRUE-FLAW DATA, REF. STRESS = UCS

N	STRAIN	STRESS (MPA)	STRESS (KSI)	THETA (MPA)	THETA (KSI)
1	0.000000	0	0.0	183394	26588
2	0.000098	178	25.9	183394	26588
3	0.000199	364	52.9	183394	26588
4	0.000300	537	77.9	173250	25127
5	0.000400	689	100.0	164794	24101
6	0.000500	834	121.0	146380	21230
7	0.000598	951	138.0	97824	14234
8	0.000698	1041	151.0	77251	11204
9	0.000797	1094	159.0	52938	7678
10	0.000896	1148	166.5	37653	5461
11	0.000995	1176	170.7	28614	4150
12	0.001190	1224	177.9	19585	2840
13	0.001390	1254	182.0	12982	1882
14	0.001590	1275	185.0	9981	1448
15	0.001980	1303	189.0	6060	879
16	0.002430	1320	191.0	3590	512
17	0.002960	1331	193.0	2626	381
18	0.003440	1342	216.0	1620	235
19	0.003920	1349	195.0	1041	151
20	0.004400	1372	199.0	827	120
21	0.004900	1379	199.0	751	109
FF	0.005400	1379	200.0	689	100

TIME= 3.11 SECS.

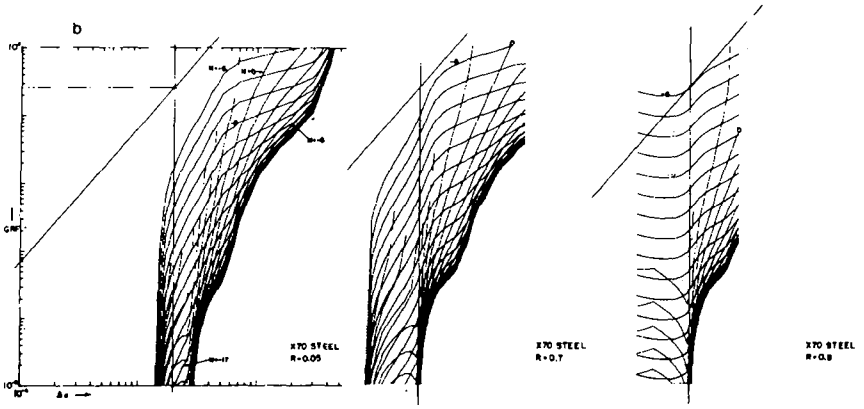

FIG. 2—*Stress-strain data and GRF curves for X-70 line pipe steel at three stress ratios matched to air and salt water environment FCGR data of Vosikovsky* [10].

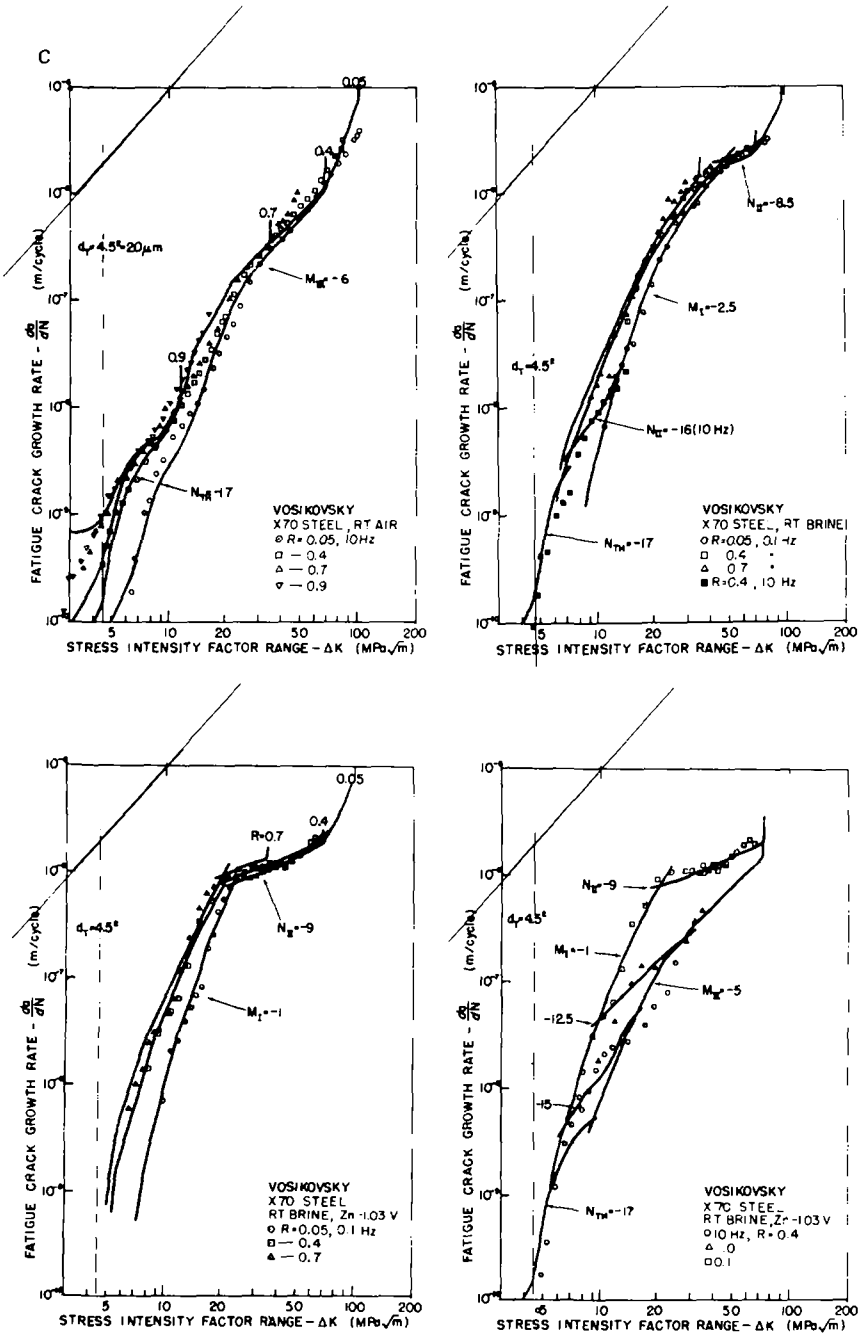

FIG. 2—*(Continued.)*

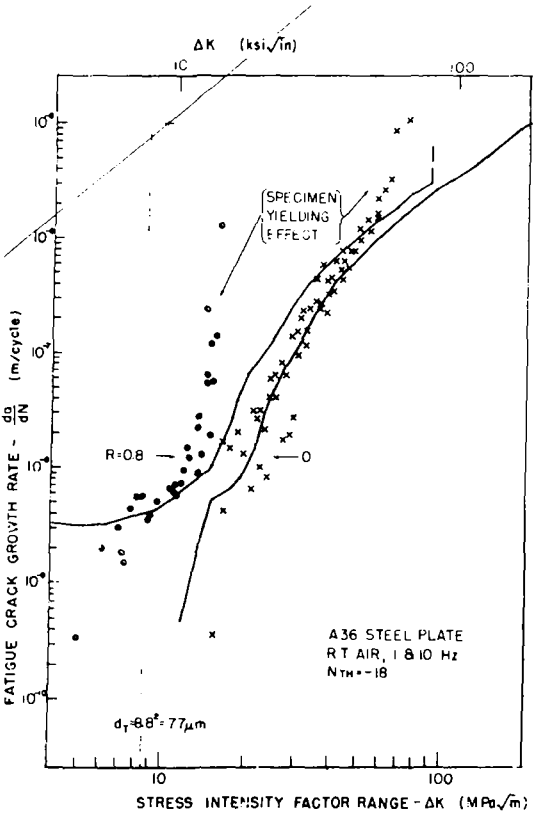

FIG. 3—*GRF parametric curves matched to Stonesifer FCGR data on A-36 steel [20].*

where $\bar{\ell}$ is the average (effective) grain size. This result is consistent with the expression put forth by Yoder et al [*19*].

One should be cautious in attempting to use this model for FCGR predictions when cleavage is part of the fracture process. This model implicitly assumes a ductile tear type of separation as a local process. The additional growth due to local bursts of cleavage was observed by Stonesifer [*20*] and Richards and Lindley [*21*] to accelerate the average crack propagation rate. The model does not account for this, and our (unpublished) attempts to apply it to predict the low temperature fatigue crack propagation rate in steel have been unsuccessful. On the other hand, the modeling seems quite adequate in cases when the environmental attack has resulted in intragranular separation. Presumably, here the stability of grain size ligaments limits the rate at which the separation around them may proceed. In general, the reflection of the widely differing shapes of stress-strain curves in the crack growth rate maps suggests some truth in the method. It does provide a way of normalizing effects

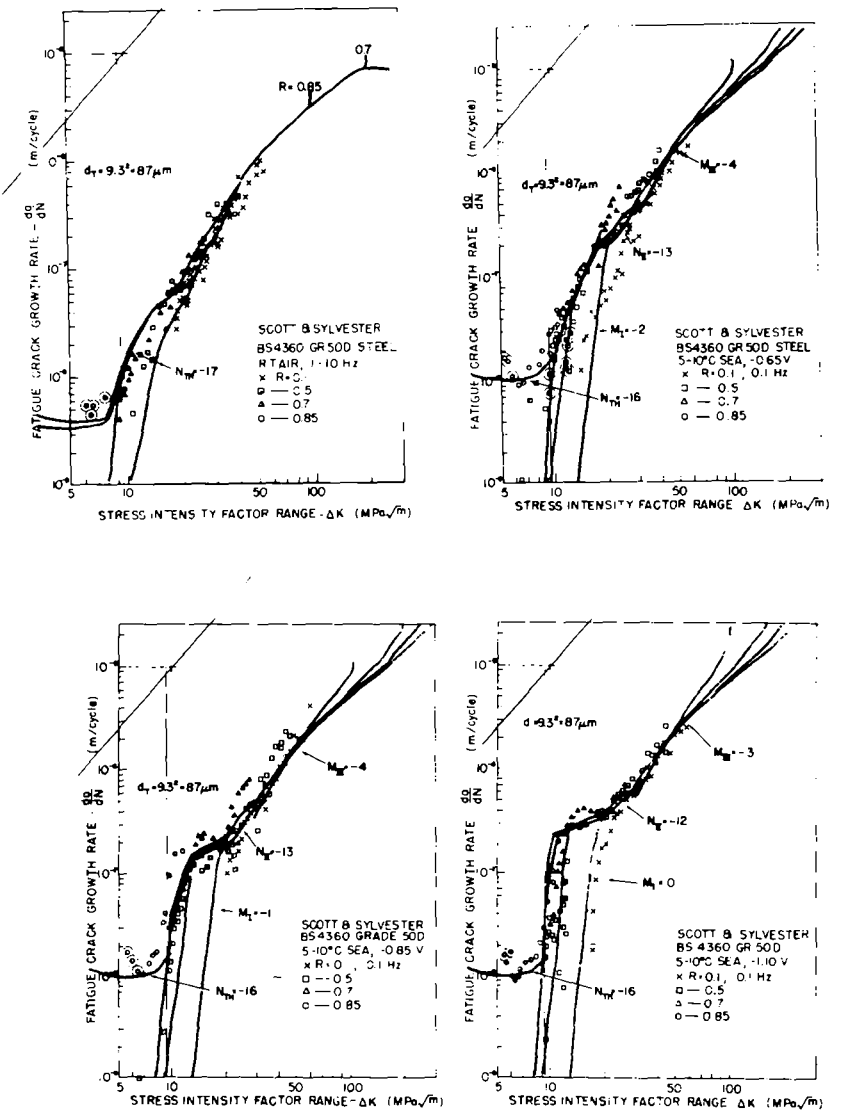

FIG. 4—*GRF curves for BS 4360 Grade 50D steel matched to corrosion-fatigue crack growth rate data of Scott and Silvester [11]. The curves shown are from stress-strain data at ≃ 7°C except the air data, which were at 25°C. Authors designate experimental artifact by enlarged circles around data points.*

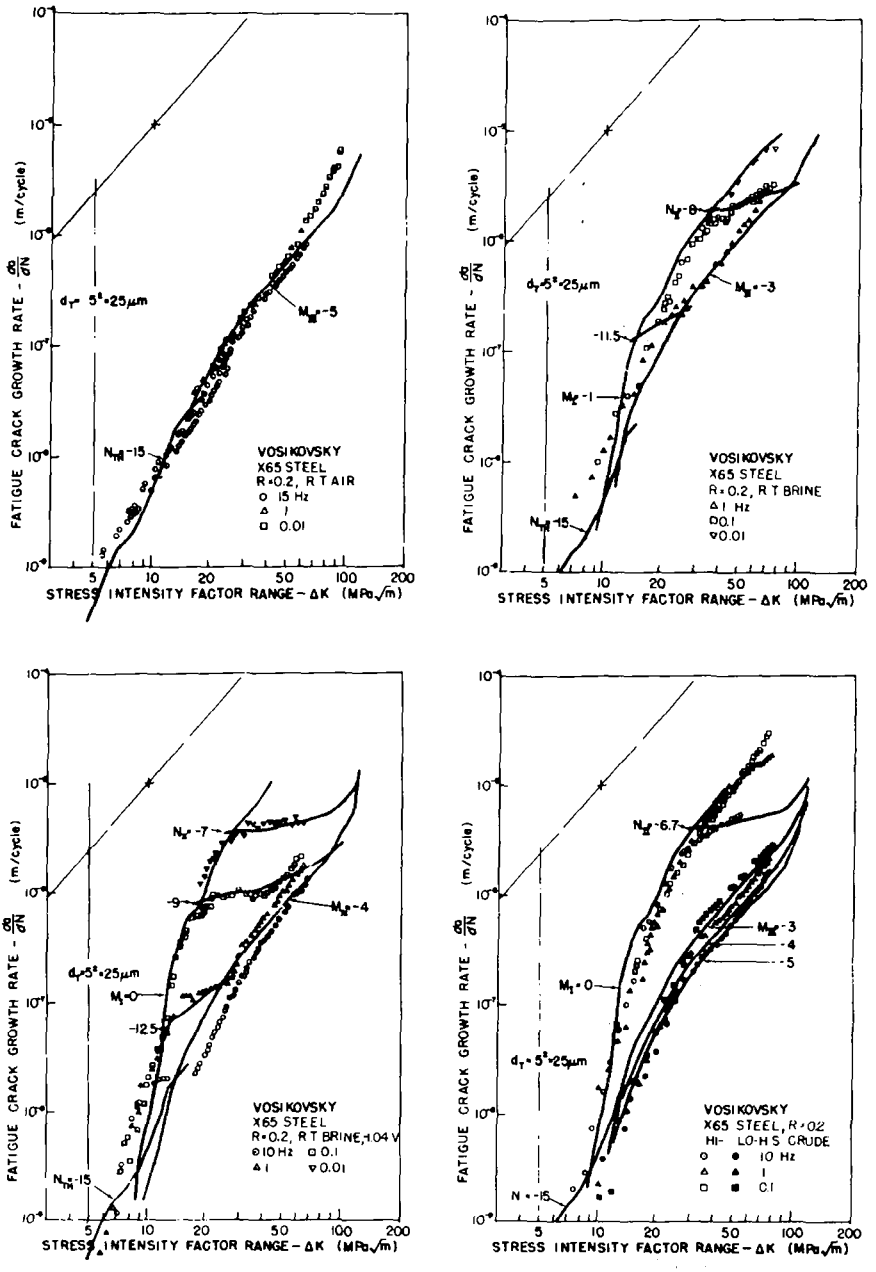

FIG. 5—*GRF curve family for X-65 line pipe steel at the single stress ratio* R = *0.2, matched to room temperature, air, salt water, and sour crude oil environment data of Vosikovsky [12].*

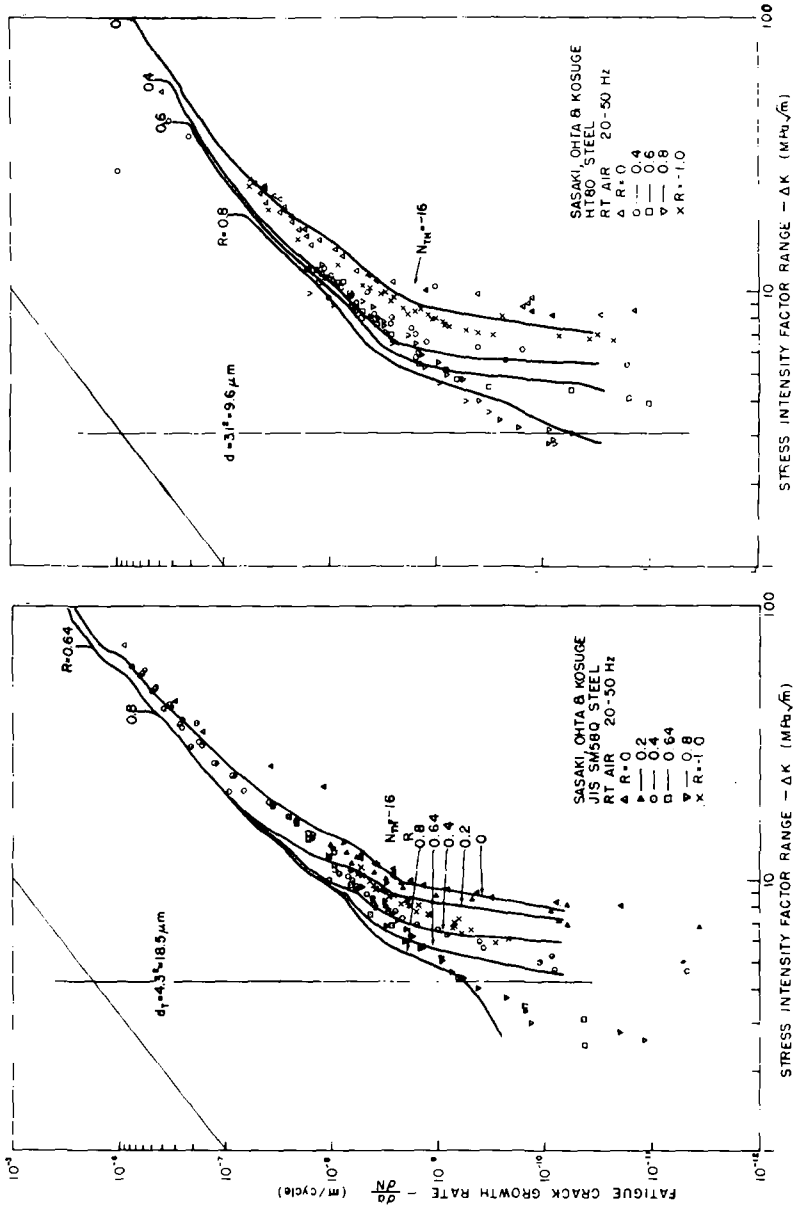

FIG. 6—*GRF curves for SM-58-Q steels and HY-80 at several stress ratios matched to air environment FCGR data of Sasaki et al [13].*

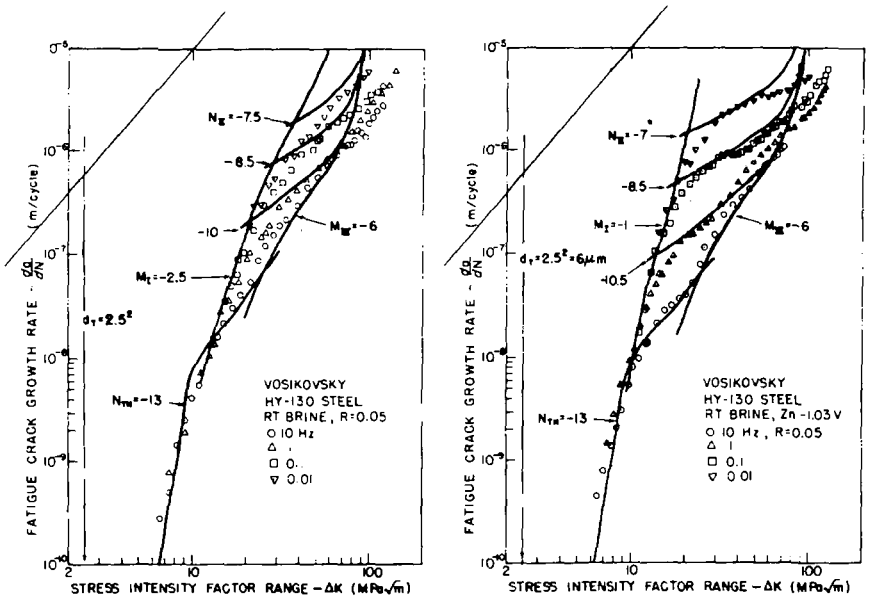

FIG. 7—*GRF curves for HY-130 steel at three stress ratios matched to air and salt water environment data of Vosikovsky [14].*

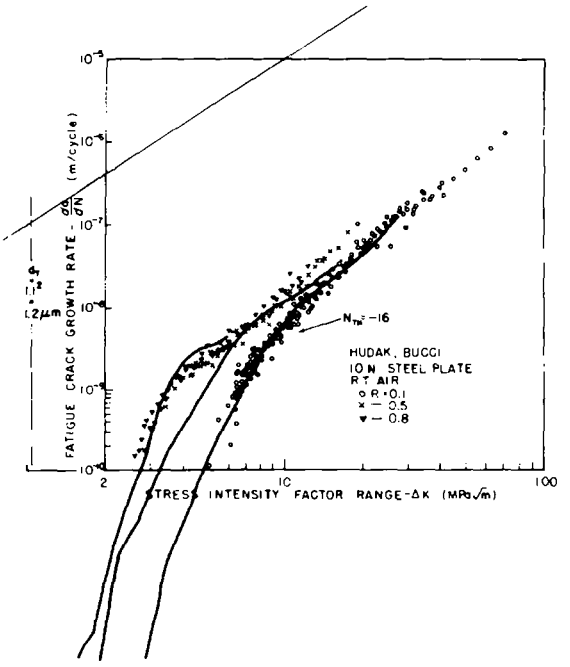

FIG. 8—*GRF curves for 10-nickel steel at three stress ratios matched to air FCGR data of Hudak and Bucci [15].*

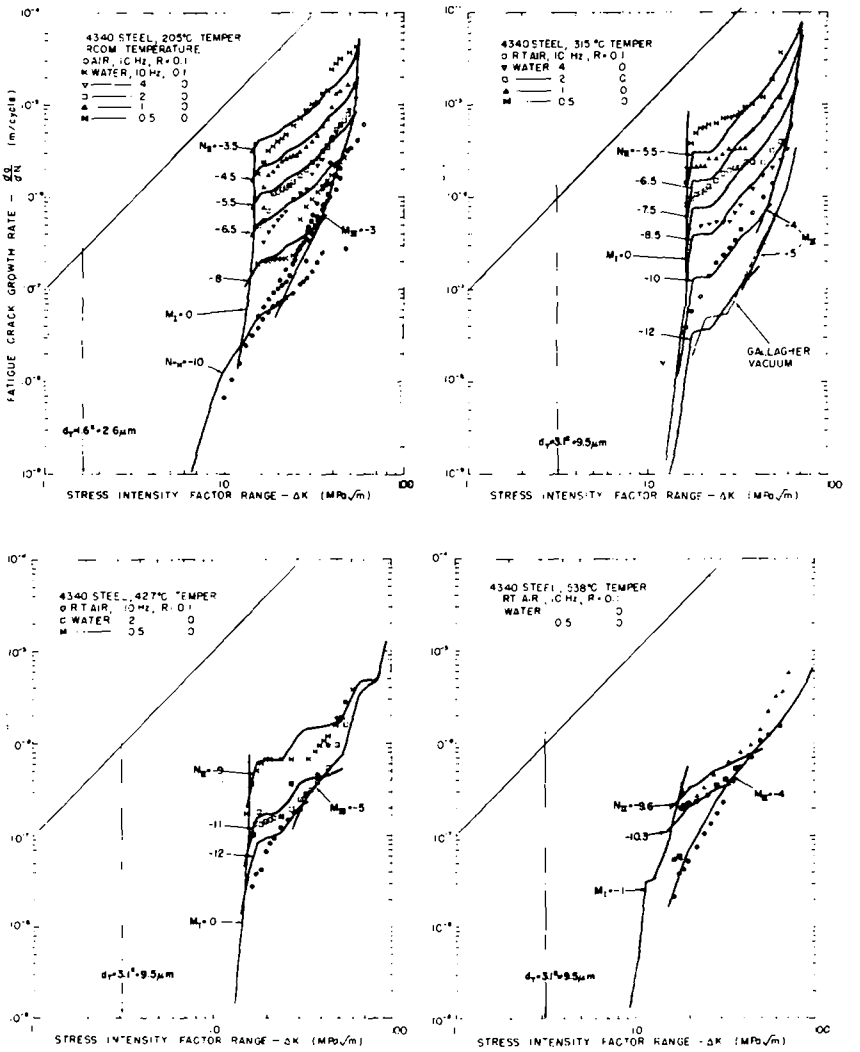

FIG. 9—*GRF curves for each of four tempers of 4340 steel matched to corrosion-fatigue crack growth rate data in air and fresh water environments by Stonesifer, reported in Ref 2.*

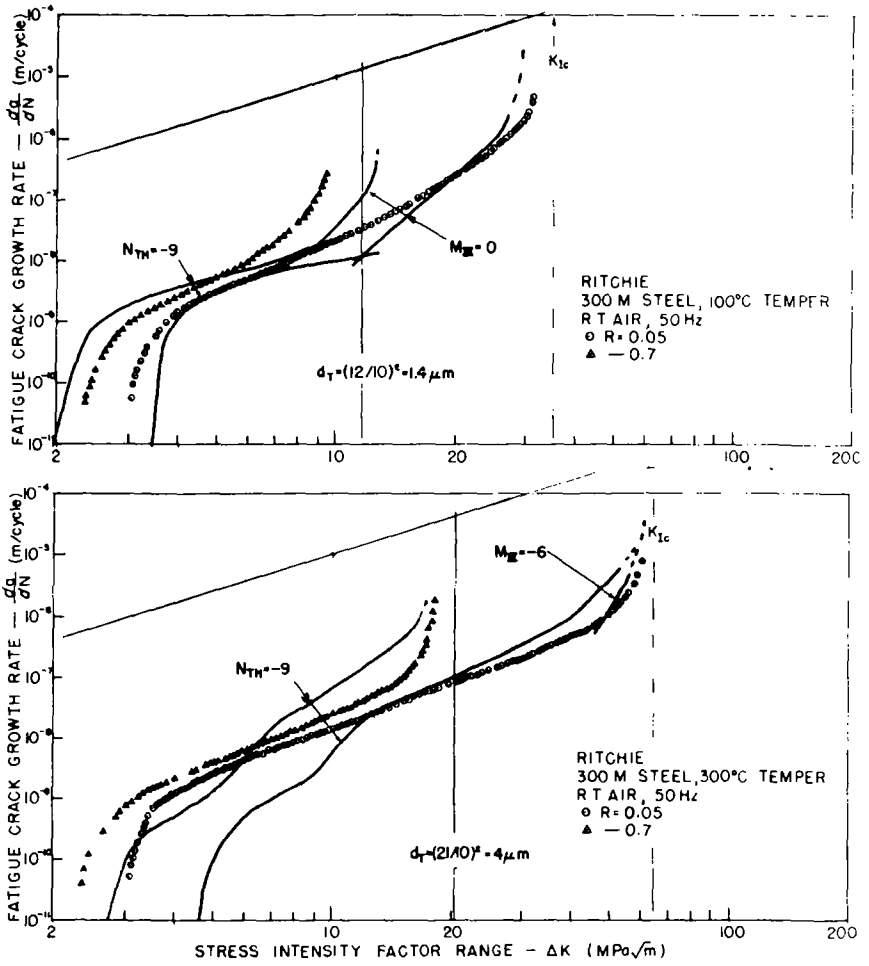

FIG. 10—*GRF curves for 300M steel tempered at four different temperatures at* R = *0.05 and 0.7 matched to air environment data of Ritchie [16].*

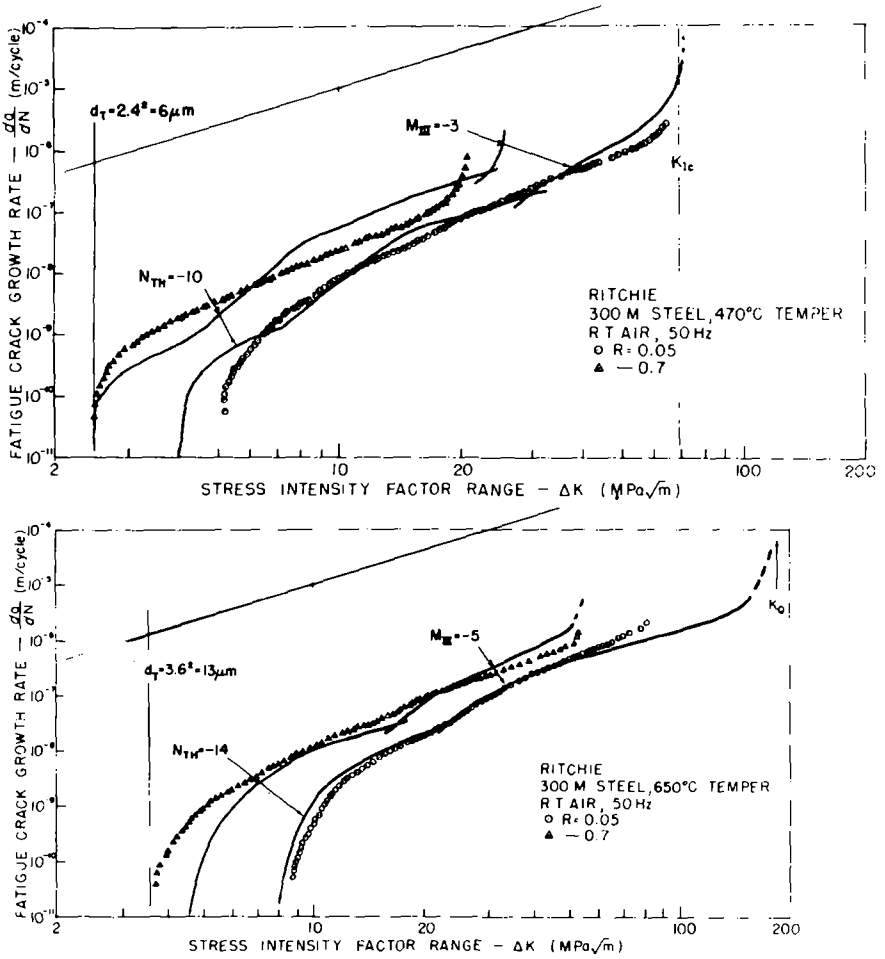

FIG. 10—*(Continued.)*

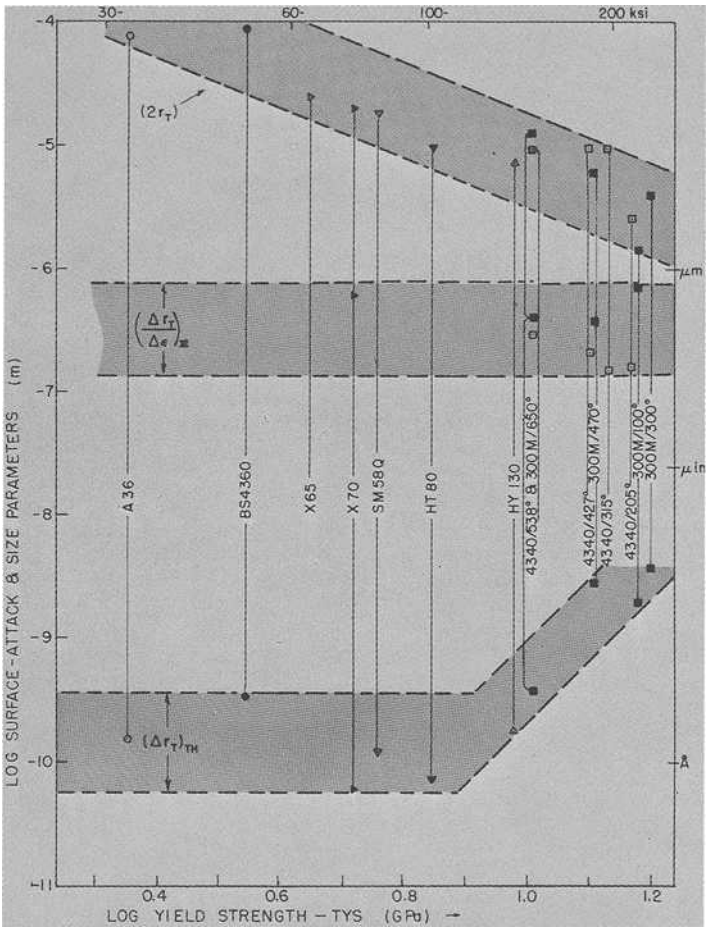

FIG. 11—*Size and surface-attack depth values derived from TLIM matching of the various iron base alloys shows an internal consistency.*

of plastic flow properties, allowing more effort to be devoted to studies of the remaining, more complex, influences of material and environment.

Conclusions

From this further development of a model which views crack growth as a means of strain hardening material elements at the crack tip to balance strength losses due to transient creep and surface attack, the following conclusions are reached.

1. A fit of threshold and three later stages of growth, including stress ratio

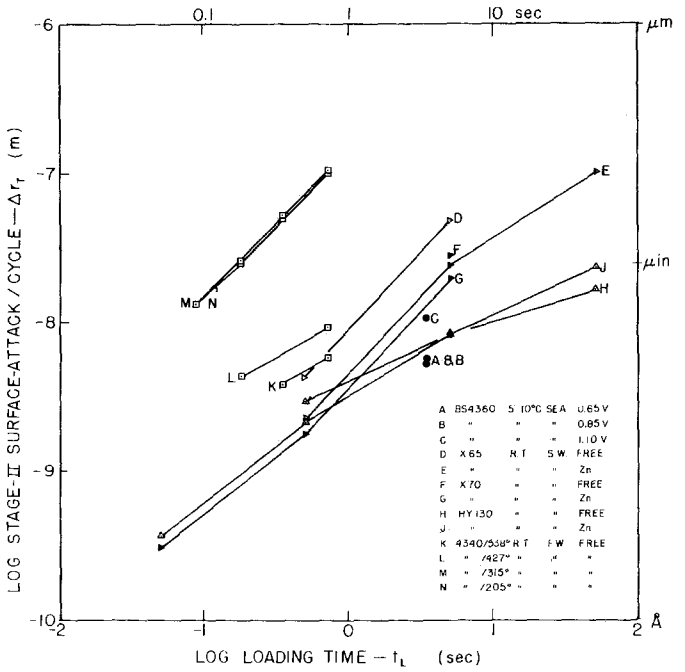

FIG. 12—*Values of the depth of surface attack in Stage II growth derived from TLIM matching are plotted versus loading rise time of the cycle.*

effects, can be obtained with two values of two kinds of disposable surface attack parameters and a process zone size parameter.

2. In the steels, the process zone size decreases with increasing yield strength of the materials in a manner suggesting its correspondence to grain size.

3. Values of the surface attack parameters show a consistent trend with the yield strength of the steels.

4. Although conversion of measured monotonic plus cyclic stress-strain curves to growth tracking curve families is tedious, a computer program is available that makes this a feasible task that is believed to be well worth the effort.

References

[*1*] Krafft, J. M., "Strain-Hardening versus Stress-Relaxation Effects on Fatigue Crack Propagation," Report of Naval Research Laboratory Progress, July 1971, pp. 1–10.

[*2*] Krafft, J. M. and Smith, H. L. in *Proceedings of the Conference on Stress-Corrosion and Hydrogen Embrittlement of Iron Base Alloys*, Unieux-Firminy, France, 10–12 June 1973, National Association of Corrosion Engineers, Houston, Tex., 1977, pp. 482–494; see also Naval Research Laboratory Memorandum Report 2598, April 1973.

[3] Krafft, J. M. and Cullen, W. H., Jr., *Engineering Fracture Mechanics*, Vol. 10, 1979, pp. 609-650; see also Naval Research Laboratory Memorandum Report 3505, July 1977.
[4] Krafft, J. M., "Case Studies of Fatigue Crack Growth Using an Improved Microligament Instability Model," Naval Research Laboratory Memorandum Report 4161, Jan. 1980.
[5] Landgraf, R. W. in *Cyclic Stress-Strain Behavior—Analysis, Experimentation, and Failure Prediction, ASTM STP 519*, American Society for Testing and Materials, 1973, pp. 213-228.
[6] Williams, J. G. and Turner, C. E., *Applied Mathematical Research*, Vol. 3, 1964, pp. 144-147.
[7] Elber, W., *Engineering Fracture Mechanics*, Vol. 2, 1970, pp. 37-45.
[8] Krafft, J. M. in *Proceedings of the Third International Conference on Mechanical Behavior of Materials (ICM3)*, Cambridge, England, Aug. 1979, pp. 383-396.
[9] Coffin, L. F., Jr. and Tavernelli, J. F., *Transactions of the Metals Society*, American Institute of Mining, Metallurgical, and Petroleum Engineers, Vol. 215, 1959, pp. 794-807.
[10] Vosikovsky, O., "Effects of Stress Ratio on Fatigue Crack Growth Rates in X-70 Line Pipe Steel in Air and Salt Water," Canada Centre for Mineral and Energy Technology, Report ERP/PMRL 79-12(J), Feb. 1979.
[11] Scott, P. M. and Silvester, D. R. V., "The Influence of Mean Tensile Stress on Corrosion Fatigue Crack Growth in Structural Steel Immersed in Sea Water," Atomic Energy Research Establishment, Harwell, United Kingdom Offshore Steels Research Project (UKOSRP) Report 3/02, May 1977.
[12] Vosikovsky, O., *Journal of Engineering Materials and Technology, Transactions of the American Society of Mechanical Engineers*, Vol. 97, 1975, pp. 298-304.
[13] Sasaki, E., Ohta, O., and Kosugi, M., *Transactions, National Research Institute for Metals (Japan)*, Vol. 19, No. 4, 1977, pp. 29-46.
[14] Vosikovsky, O., "Frequency, Stress Ratio, and Potential Effects on Fatigue Crack Growth of HY-130 Steel in Salt Water," Canada Mineral Research Program Report MRP/PMRL-77-6(J), May 1977.
[15] Hudak, S. J., Saxena, A., Bucci, R. J., and Malcolm, R. C., "Development of Standard Methods of Testing and Analyzing Fatigue Crack Growth Rate Data," Technical Report AFML-TR-78-40, Air Force Materials Laboratory, Wright-Patterson Air Force Base, Ohio, May 1978.
[16] Ritchie, R. O., *Metal Science*, Aug./Sept. 1977, pp. 368-381.
[17] Barsom, J. M., "Effect of Cyclic-Stress Form on Corrosion-Fatigue Crack Propagation Below K_{Iscc} in a High Yield-Strength Steel," *Proceedings of the First International Conference on Corrosion Fatigue*, University of Connecticut, Storrs, Conn., June 1971.
[18] Kawai, S. and Koibuchi, K., *Fatigue of Engineering Materials and Structures*, Vol. 1, 1979, pp. 395-407.
[19] Yoder, G. R., Cooley, L. A., and Crooker, T. W. in this publication, pp. I-348-I-365.
[20] Stonesifer, F. R., *Engineering Fracture Mechanics*, Vol. 10, 1978, pp. 305-314.
[21] Richards, C. E. and Lindley, T. C., *Engineering Fracture Mechanics*, Vol. 4, 1972, pp. 951-978.

A. R. Ingraffea,[1] *G. E. Blandford,*[2] *and J. A. Liggett*[1]

Automatic Modelling of Mixed-Mode Fatigue and Quasi-Static Crack Propagation Using the Boundary Element Method

REFERENCE: Ingraffea, A. R., Blandford, G. E., and Liggett, J. A., **"Automatic Modelling of Mixed-Mode Fatigue and Quasi-Static Crack Propagation Using the Boundary Element Method"** *Fracture Mechanics: Fourteenth Symposium—Volume I: Theory and Analysis, ASTM STP 791*, J. C. Lewis and G. Sines, Eds., American Society for Testing and Materials, 1983, pp. I-407-1-426.

ABSTRACT: A multidomain boundary element model for the automatic analysis of mixed-mode fatigue and quasi-static crack propagation problems is described. Starting with the initial structural discretization, the new model automatically computes stress-intensity factors, direction of propagation, and load increment or number of cycles required to advance the crack tips a requested distance. This process is repeated, again automatically, until crack instability occurs or the requested number of crack increments is reached. Traction singular quarter-point boundary elements are used on each side of the crack tips. These elements contain both the dominant $1/\sqrt{r}$ traction singularity and the dominant $\sqrt{r}$ displacement variation at the crack tip. Any of four mixed-mode interaction theories may be activated for angle and instability predictions. Solutions of example problems are presented. The predicted boundary element results show good correlation with both experimental and other numerically obtained results.

KEY WORDS: mixed-mode, fatigue, crack propagation, boundary element method, fracture mechanics

Except for very simplified problems, the computations involving crack propagation must be done numerically. Within the scope of linear elastic fracture mechanics computer modelling of crack propagation problems is characterized by the following three difficulties.

1. Topology: The extension of a crack changes the boundary configuration and places the problem into the class of moving boundary problems. Thus, a numerical discretization of the solution region must change at each step. The

[1]School of Civil and Environmental Engineering, Cornell University, Ithaca, N.Y. 14853.
[2]Department of Civil Engineering, University of Kentucky, Lexington, Ky. 40506.

new discretization has required the intervention of the analyst, who submits new data on punched cards [*1,2*][3] or graphically using interactive computer graphics [*3*]. The latter method is more efficient from the point of view of the analyst (although it uses more computer time), but requires access to graphic hardware and software. Ingraffea et al [*4*] discuss the graphics type of algorithm.

2. Singularity: A linear elastic fracture mechanics approach to discrete cracking requires recognition of the theoretically singular nature of the crack tip stress field. If fracture toughness, K_{Ic}, is to be the controlling material parameter, stress-intensity factors, K_I and K_{II}, must be found for a given crack configuration and loading. In the boundary element context, this implies the ability to compute accurately and efficiently the stress-intensity factors through the use of elements which reflect the singular behavior in the vicinity of the crack tip.

3. Stability: Cracking is not always immediately catastrophic. Quasi-static growth can occur if the energy release rate is decreasing with crack length. Subcritical growth can occur during cyclic loading. Nor is cracking always pure Mode I, either in a quasi-static or fatigue growth environment. For a given load increment or number of cycles of loading on a structure, methods must be available for predicting the length and direction of the corresponding crack increments.

This paper presents a new and comprehensive solution to two-dimensional crack propagation problems. The computer code described herein automatically generates data required to analyze sequentially the changing boundary configuration corresponding to a propagating crack. The user need only supply the initial input data; as output, the user obtains the final crack trajectory and a load/position or cycle number/position history.

The operation of the model is controlled by the length of the crack increment selected by the user. For each new crack configuration, mixed-mode stress-intensity factors are computed automatically. These are substituted into a user-selected interaction formula which predicts the direction of the next crack increment and determines its stability. For quasi-static propagation, the load increment corresponding to the selected crack increment length is computed automatically using an energy balancing algorithm [*1*]. In the case of fatigue, the user selects a mixed-mode fatigue crack model from which the number of cycles corresponding to the crack increment is determined. This process is repeated for as many crack increments as the user selects, or until crack instability is detected.

The boundary element method (BEM) is used herein as the numerical algorithm. Since only the boundary is discretized, the topological changes introduced by the crack extension require a minimal one-dimensional boundary change in the vicinity of the crack tip. Only the nodal coordinates along the crack are recomputed (Mode I and mixed-mode fracture problems), and one

[3]The italic numbers in brackets refer to the list of references appended to this paper.

or two elements are added to represent the extended crack (mixed-mode fracture problems). In contrast, the finite element method requires a two-dimensional change which is more extensive [5] and can be used for the present purpose only in an interactive graphics environment.

A multidomain approach is used since that is the only accurate and efficient means of analyzing mixed-mode problems using the BEM [6].

Both mixed-mode fatigue and quasi-static cracking problems are considered in this paper. The techniques to be described are used to analyze the problems shown in Fig. 1. These problems have been studied experimentally and numerically in previous investigations [2, 7]. Results of those investigations are compared to the predictions of the present method.

Stable Crack Propagation

The characteristics of the two types of crack propagation which the present method is capable of modelling are described in this section.

Quasi-Static Crack Propagation

Quasi-static propagation occurs when, under the assumptions of linear elastic fracture mechanics, a continuously increasing load is required to maintain crack instability. This implies a decreasing energy release rate with respect to crack advance under a constant load. Three classes of structures which exhibit this type of behavior are of interest.

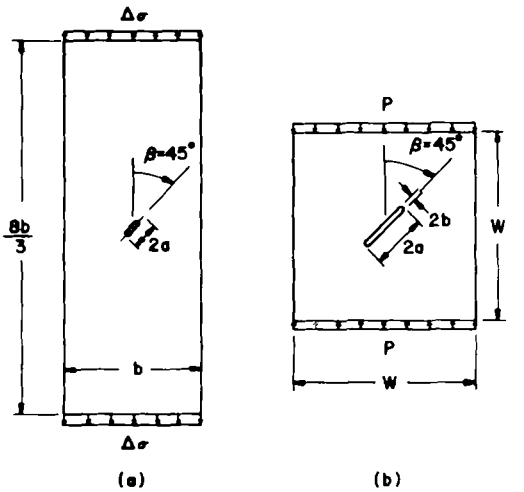

FIG. 1—(a) *Mixed-mode fatigue crack problem (2a = 13.5 mm, b = 76.2 mm, Δσ = 155.3 MPa, R = 0.1).* (b) *Quasi-static crack propagation problem (a = 10.16 mm, b = 0.1016 mm, w = 101.6 mm).*

In the first class are structures loaded in tension, bending, or by wedging action which, by nature of their geometry, exhibit quasi-static growth. The tapered or contoured double cantilever [*8*], the short rod [*9*], and the wedge-opened crack specimens [*10*] are examples which are of current interest for their value in fracture toughness testing of concrete and rock.

In the second class are those structures in which quasi-static growth occurs because of the existence of mechanical crack arrest capability. Reinforced concrete is a good example [*11*].

Finally, there is the class of cracked or notched structures, loaded in compression, such as an underground opening in rock (Fig. 1*b*).

In order to model crack propagation in these classes of structures, it is necessary to predict:

1. the load required to initiate a crack increment,
2. the direction of that crack increment, and
3. the length of that crack increment.

In the present model, mixed-mode crack initiation theory is employed to obtain the first two predictions. Four theories have been implemented in the developed code: maximum circumferential tensile stress, $\sigma(\theta)_{max}$ [*12*]; maximum energy release rate, $G(\theta)_{max}$ [*13*], and $J(\theta)_{max}$ [*14*]; and minimum strain energy density $S(\theta)_{min}$ [*15*]. Each of these theories predicts critical mixtures of the Mode I and Mode II stress intensity factors (K_I and K_{II}) and the direction of propagation at local instability. For example, the interaction equation for the $\sigma(\theta)_{max}$ theory is

$$1 = \cos\frac{\theta_o}{2}\left[\frac{K_I}{K_{Ic}}\cos^2\frac{\theta_o}{2} - \frac{3}{2}\frac{K_{II}}{K_{Ic}}\sin\theta_o\right] \tag{1}$$

and the direction of propagation is found by solving

$$[K_I\sin\theta_o + K_{II}(3\cos\theta_o - 1)] = 0 \tag{2}$$

for θ_o (Fig. 2).

An algorithm, first proposed by Ingraffea [*7*], computed the length of each increment of cracking caused by a given increment in load. The opposite point of view is taken herein; the increment in load which causes the crack to extend a given distance is computed. The scheme is based on the release of potential energy to form surface energy. Let R be the energy required to create a new unit of crack length, and G the potential energy release rate due to creation of that unit. If for a given crack configuration G is greater than R, a local instability occurs and the crack will extend. As the crack propagates, G may increase, resulting in an unstable crack growth. Alternatively, G may decrease and lead to stable crack growth.

For stable crack growth, the question is then how far the crack extends un-

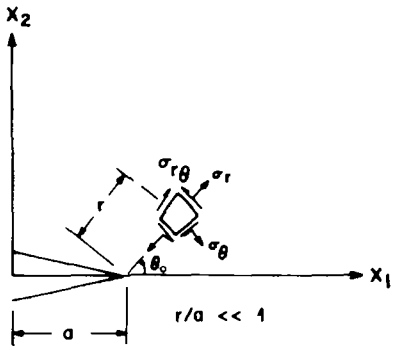

FIG. 2—*Crack tip polar coordinate system and stress notation.*

der a given fixed load before it stops. An equilibrium state will be reached when a balanced energy transfer occurs from G to R as shown in Fig. 3 and in the following form

$$\int_0^{\Delta a} G(a,\theta,K_{\mathrm{I}},K_{\mathrm{II}})\,d\Delta a = \int_0^{\Delta a} R(K_{\mathrm{Ic}})\,d\Delta a \tag{3}$$

where Δa represents the point of crack arrest and the origin is taken at the original crack tip.

Given a structure, analyzed for four crack positions, all with the same load P_i, a curve through the four corresponding values of G can be defined. The area under the G-curve, A_G, is the amount of energy released, and the area under the R-curve, A_R, is the amount of energy needed to create a new crack length corresponding to the increment Δa (Fig. 3).

If A_G is greater than A_R, then a form of instability occurs. It will be a local instability if G decreases with crack length and the energy balance transfer can be satisfied before the crack reaches a free surface. Alternatively, if G in-

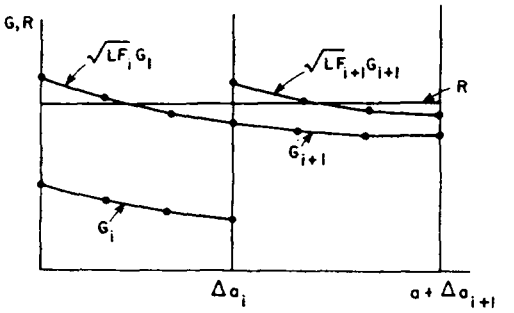

FIG. 3—*Graphical form of energy balance algorithm for crack length prediction.*

creases with crack extension, then a global instability takes place resulting in failure.

If A_G is smaller than A_R, A_G should be increased by shifting the G-curve upward in order to satisfy the energy balance transfer. Since G is proportional to the square of stress intensity, which in turn is directly proportional to the load, the multiplication factor for the current increment of load is

$$LF = \sqrt{\frac{A_R}{A_G}} \tag{4}$$

The determination of A_G is accomplished by dividing each crack increment into three subincrements, each with its own direction and value of G, fitting a curve through the four G-values, and integrating the resulting expression over the crack increment length. This process is done automatically for each crack increment.

Further details of the algorithms for predicting crack increment direction and length can be found in Ref *16*.

Fatigue Crack Propagation

The present model is capable of predicting mixed-mode fatigue crack propagation under constant amplitude loading. The four theories mentioned previously are available for predicting direction of propagation. Rate of growth for Mode I loading is predicted using the Paris model [*17*],

$$\frac{da}{dN} = C(\Delta K_I)^n \tag{5}$$

in which N is the number of load cycles, C and n are material properties, and ΔK_I is the stress intensity factor range.

The generalized Paris model of Tanaka [*18*]

$$\frac{da}{dN} = C(\Delta K_{eff})^n \tag{6}$$

is used for mixed-mode loading. Two expressions for the effective stress-intensity factor range, ΔK_{eff}, are user-selectable,

$$\Delta K_{eff} = (\Delta K_I^4 + 8\Delta K_{II}^4)^{1/4} \tag{7}$$

$$\Delta K_{eff} = (\Delta K_I^2 + 2\Delta K_{II}^2)^{1/2} \tag{8}$$

Rewriting Eq 6 and integrating both sides gives

$$\int_0^{\Delta a} \frac{da}{C(\Delta K_{\text{eff}})^n} = \int_0^{\Delta N} dN = \Delta N \tag{9}$$

where Δa is the user-selected crack length increment and ΔN is the required load cycle increment.

The evaluation of the left side of Eq 9 depends on the relationship between ΔK_{eff} and crack length, $\Delta K_{\text{eff}} = f(a)$. To establish that function, ΔK_{eff} is calculated by the BEM at four points

$$\begin{aligned} a_i^o &= a_{i-1} \\ a_i^1 &= a_i^o + \frac{\Delta a}{3} \\ a_i^2 &= a_i^1 + \frac{\Delta a}{3} \\ a_i^3 &= a_i^2 + \frac{\Delta a}{3} = a_{i-1} + \Delta a \end{aligned} \tag{10}$$

in which a_{i-1} is the crack length at the end of Step $i - 1$. A cubic polynomial, generated by using Lagrangian interpolation, is passed through the four points on the $\Delta K_{\text{eff}} = f(a)$ curve [*16*]. Using this polynomial as the required functional relationship, six point Gaussian quadrature is used to evaluate the integral on the left side of Eq 9, thus obtaining the required number of load cycles to extend the crack the fixed distance, Δa.

The Boundary Integral Equation

The boundary integral equation formulation discretizes only the boundary and thus effectively reduces the dimension of the computation by one. The governing Navier-Cauchy equations of elasticity are replaced with a boundary integral operator using Betti's reciprocal theorem [*19,20*].

Dividing the plane into subdomains $\Omega^{(k)}$, the boundary integral equation is written as [*21*][4]

$$\begin{aligned} c_{ij}^{(k)}(P) u_j^{(k)}(P) + \int_{\Gamma^{(k)}} T_{ij}^{(k)}(P,Q) u_j^{(k)}(Q) d\Gamma \\ = \int_{\Gamma^{(k)}} U_{ij}^{(k)}(P,Q) t_j^{(k)}(Q) d\Gamma \end{aligned} \tag{11}$$

[4]The usual indicial notation of Cartesian tensor analysis is used. Latin subscripts have the range (1,2) and summation over repeated subscripts is implied. Commas are used to denote partial differentiation.

in which $c_{ij}^{(k)}(P)$ is the rigid body translation solution of Eq 11 [*22,23*]. For a smooth boundary, $c_{ij}^{(k)}(P) = \frac{1}{2}\delta_{ij}$, in which δ_{ij} is the Kronecker delta. The displacement vector is u_j and the traction vector is t_j. The points P and Q are field points on the boundary, $\Gamma^{(k)}$. The second-order tensors $T_{ij}^{(k)}(P,Q)$ and $U_{ij}^{(k)}(P,Q)$ are the fundamental traction and displacement solutions, respectively, which are [*19,20*]

$$T_{ij}^{(k)}(P,Q) = \frac{-1}{4\pi\mu^{(k)}(\tau^{(k)}+\mu^{(k)})}\left(\frac{1}{r(P,Q)}\right)$$
$$x\left\{\frac{\partial r}{\partial n^{(k)}(Q)}\left(2(\mu^{(k)})^2\delta_{ij} + 4\tau^{(k)}\mu^{(k)} r_{,i}(P,Q)\right.\right.$$
$$r_{,j}(P,Q) + 2(\mu^{(k)})^2\left[r_{,j}(P,Q)n_i^{(k)}(Q)\right.$$
$$\left.\left.-r_{,i}(P,Q)n_j^{(k)}(Q)\right]\right\} \tag{12}$$

$$U_{ij}^{(k)}(P,Q) = \frac{-1}{4\pi\mu^{(k)}(\tau^{(k)}+\mu^{(k)})}\{(\tau^{(k)} + 2\mu^{(k)})\ln r(P,Q)\,\delta_{ij}$$
$$-\tau^{(k)} r_{,i}(P,Q)\, r_{,j}(P,Q)\}$$

in which $\mu^{(k)}$ is the shear modulus for subdomain, k, $\tau^{(k)} = \mu^{(k)}/(1-2\nu^{(k)})$ for plane strain, $\tau^{(k)} = 2\mu^{(k)}(1+\nu^{(k)})$ for plane stress, and $\nu^{(k)}$ in the Poisson ratio for subdomain k. The distance measured from point P to point Q is $r(P,Q)$ and $n^{(k)}$ is the unit outward normal to the boundary at point Q. The fundamental solutions given in Eqs 12 represent the traction and displacement in the jth direction at point Q due to a unit point force in the ith direction at point P.

At a point along the interface between subdomains $\Omega^{(k)}$ and $\Omega^{(\ell)}$, the displacement continuity and the traction equilibrium are enforced through

$$u_i^{(k)}(P) = u_i^{(\ell)}(P)$$
$$t_i^{(k)}(P) = -t_i^{(\ell)}(P) \tag{13}$$

The Numerical Model

An isoparametric formulation of the multidomain boundary integral equation (Eq 11) is used in the present formulation. The isoparametric BEM represents the geometric, displacement, and traction variations as quadratic polynomials

$$x_i = \sum_{\beta=1}^{3} N^{\beta}(\xi)\, x_i{}^{\beta} = \lfloor N(\xi) \rfloor \{x_i\}$$

$$u_i = \lfloor N(\xi) \rfloor \{u_i\}$$

$$t_i = \lfloor N(\xi) \rfloor \{t_i\} \tag{14}$$

where $\lfloor N(\xi) \rfloor$ is the row vector of shape functions given in Fig. 4 and the terms in braces are the element nodal values of the parameter.

Substituting the polynomial expressions of Eqs 14 into Eq 11 results in the multidomain boundary element formulation [*6, 16*]

$$c_{ij}^{(k)}(P_\zeta)\, u_j^{(k)}(P_\zeta) + \sum_{\sigma=1}^{M^{(k)}} \left[\int_{-1}^{+1} T_{ij}^{(k)}(P_\zeta, Q(\xi))\, N^{\beta}(\xi)\, J_\Gamma(\xi)\, d\xi \right] (u_j^{(k)})^{\beta\sigma}$$

$$= \sum_{\sigma=1}^{M^{(k)}} \left[\int_{-1}^{+1} U_{ij}^{(k)}(P_\zeta, Q(\xi))\, N^{\beta}(\xi)\, J_\Gamma(\xi)\, d\xi \right] (t_i^{(k)})^{\beta\sigma} \tag{15}$$

in which P_ζ is the fixed boundary point, $Q(\xi)$ is the variable boundary point, $M^{(k)}$ is the number of elements in subdomain k, $J_\Gamma(\xi)$ is the boundary Jacobian, that is

$$J_\Gamma(\xi) = \left[\left(\frac{dx_1}{d\xi} \right)^2 + \left(\frac{dx_2}{d\xi} \right)^2 \right]^{1/2} = \left[\left(\frac{dN^{\beta}}{d\xi} x_1{}^{\beta} \right)^2 + \left(\frac{dN^{\beta}}{d\xi} x_2{}^{\beta} \right)^2 \right]^{1/2}$$

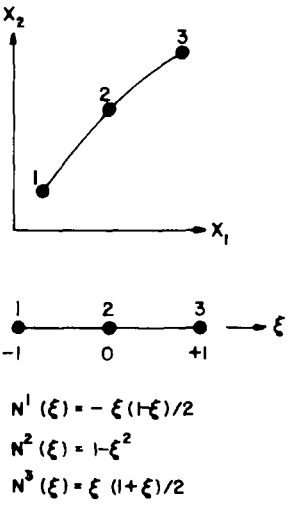

FIG. 4—*Isoparametric quadratic boundary element.*

and $(u_j^{(k)})^{\beta\sigma}$, $(t_j^{(k)})^{\beta\sigma}$ are the element node components of displacement and traction, respectively. Evaluating Eq 15 for each boundary node in each subdomain and imposing the interface constraint conditions of Eqs 13, leads to an algebraic system of equations.

Stress-Intensity Factor Computation

Using the boundary element shown in Fig. 4 in the vicinity of the crack tip would give a quadratic variation of the displacements and tractions whereas the theoretical crack-tip displacement and traction functions are proportional to $\sqrt{r}$ and $1/\sqrt{r}$, respectively, where r is the distance from the crack tip. Since the interpolating polynomials do not contain these terms, the tractions never can be represented correctly by the interpolating functions, and the displacements can be modelled adequately only by using a refined mesh in the vicinity of the crack tip.

It has been shown, however, that by moving the midpoint node of the quadratic element to the quarter-point position, the $\sqrt{r}$ displacement variation is obtained [*24*]. Unfortunately, the traction variations will not possess the $1/\sqrt{r}$ singularity. The inclusion of the $1/\sqrt{r}$ singularity into the traction interpolations is obtained by moving the midpoint node to the quarter-point position, and then multiplying the traction interpolations by $\sqrt{l/r}$ where l is the crack tip element [*24*]. The resulting displacement and traction interpolations are

$$u_i = A_{u_i}{}^1 + A_{u_i}{}^2\sqrt{r} + A_{u_i}{}^3 r \tag{16a}$$

$$\begin{aligned} t_i &= (A_{t_i}{}^1 + A_{t_i}{}^2\sqrt{r} + A_{t_i}{}^3 r)\sqrt{\frac{l}{r}} \\ &= B_{t_i}{}^1\sqrt{r} + B_{t_i}{}^2 + B_{t_i}{}^3\sqrt{r} \end{aligned} \tag{16b}$$

Equations 16*a* and 16*b* show that both the dominant $\sqrt{r}$ displacement variation and the dominant $1/\sqrt{r}$ traction variations are included in the crack tip element interpolations. The expression $\sqrt{l/r}$ in Eq 16*b* is written in the nondimensionalized coordinate system as shown in Figs. 5*a* and *b*. The terms $A_{u_i}{}^j$, $B_{t_i}{}^j$ $(j = 1,2,3)$ are generalized constants which are functions of displacements and tractions, respectively, at the node points. The boundary elements with interpolations given by Eqs 16 are known as "traction singular quarter-point" boundary elements [*6,16*].

The displacement correlation method [*25*] is employed with these elements for the computation of the stress-intensity factors. Denoting the displacements along the crack axis as u (crack sliding displacement) and the displacements

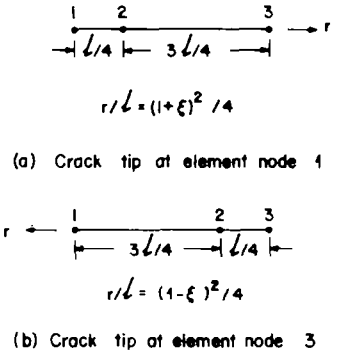

FIG. 5—*Traction singular quarter-point boundary elements.*

normal to the crack axis as v (crack opening displacement), the evaluation of the mixed-mode stress-intensity factors for $\theta = 180$ deg is [*1*],

$$K_I = \frac{\mu}{\kappa+1}\sqrt{\frac{2\pi}{l}}\,[4(v_B - v_D) + v_E - v_C]$$
$$K_I = \frac{\mu}{\kappa+1}\sqrt{\frac{2\pi}{l}}\,[4(u_B - u_D) + u_E - u_C] \tag{17}$$

in which the points B, C, D, and E are defined in Fig. 6, μ is the shear modulus, and $\kappa = 3 - 4\nu$ for plane strain in which ν is Poisson's ratio.

Crack Propagation Algorithms

A boundary element program, entitled Boundary Element Crack Propagation Program (BECPP), was developed to analyze both Mode I and mixed-mode quasi-static or fatigue fracture problems [*16*]. As currently written, the calculation is limited to the propagation of a single crack in an isotropic and homogeneous material.

The program steps for quasi-static crack propagation are summarized later. The calculations begin with an elastic analysis based upon the geometry of the structure, including the initial crack geometry, and unit applied loads. Then:

1. The stress-intensity factors, K_I and K_{II}, are computed from the elastic analysis and Eq 17. The direction of propagation is computed from direction of propagation equation, for example, Eq 2.
2. An increment of crack length, Δa, is chosen.
3. The $G(P,a)$ and $R(K_c)$ curves (Fig. 3) are calculated by
   (a) Dividing the crack length by 3.

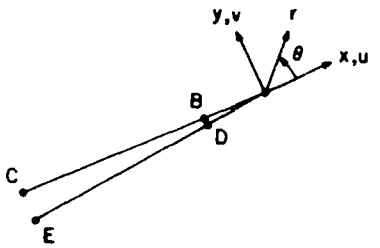

FIG. 6—*Element geometries and nodal lettering for mixed-mode stress-intensity factor calculations.*

(b) Performing the elastic analysis and stress-intensity factor calculation for each $\Delta a/3$ increment of crack length.

4. The areas A_R and A_G are computed and compared. The load then is increased according to

$$P_1 = (LF)P_i$$

where

P_1 = first fracture increment initiation load,
P_i = initial applied load, and
LF = load amplification factor, Eq 4.

5. Return to Step 1 with updated geometry and loads.

The modification of the procedure for fatigue crack propagation is straightforward. The number of load cycles replaces the load increment as the driving mechanism. Steps 1 and 2 are performed as before. Steps 3 and 4 are replaced by the integration implied in Eq 9 from which the number of load cycles required for the specified crack increment is computed.

Example Problems

Fatigue Crack Propagation

The analysis of the problem shown in Fig. 1*a* is discussed in this section. The boundary element results are compared with the numerical and experimental results of Pustejovsky [*2*]. Those numerical results were obtained using the dislocation-superposition method.

The initial mesh used to perform the boundary element analysis is shown in Fig. 7. The boundary element program was used to extend the crack four increments with each crack increment of length Δa = 1.9 mm. The predicted crack path from the boundary element analysis is compared with the experi-

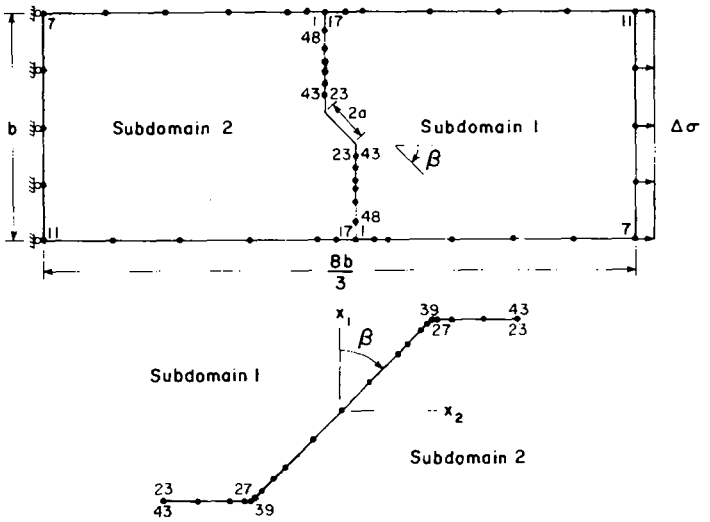

FIG. 7—*Initial boundary element mesh for the fatigue crack propagation problem of Fig. 1a.*

mentally observed crack paths of Pustejovsky [2] in Fig. 8*a*. The $\sigma(\theta)_{max}$ theory [12] was used for angle predictions in the present analysis.

The experimental results of Pustejovsky were obtained on a titanium Ti-6Al-4V plate. The reported material properties of the specimen were $E = 110\,316$ MPa, $\nu = 0.29$ and $K_{Ic} = 82.4$ MPa $\sqrt{m}$. The titanium specimen was subjected to a stress range of $\Delta\sigma = 155.3$ MPa with a stress ratio of $R = 0.10$.

The C and n values to be used in Eq 6 were not reported in Ref 2. However, in Fig. 2 of that paper, results of fatigue crack growth rate tests on two center-cracked plate specimens are reported. From that figure, a value of $n = 3.37$ was measured in the ΔK_I range applied in the angled-crack test under analysis. Although this value of n was measured for both tests, values of C measured from the two test results were not equal. Results of load cycle computations for three values of C, those derived directly from the test results and the average value, are compared to experimental results in Fig. 8*b*. It is obvious that there was substantial variation in the value of C among the specimens tested, and that load cycle computations are quite sensitive to the value chosen. The load-cycle computations were found to be totally insensitive to the form of effective stress-intensity factor range, Eqs 7 and 8.

The experimental results plotted in Fig. 8 were obtained for an actual crack orientation of $\beta = 43$ deg rather than the $\beta = 45$ deg orientation used in both the present BEM analyses and the dislocation-superposition analyses of Pustejovsky [2]. Correction for this discrepancy would bring the BEM trajectory (Fig. 8*a*) and load-cycle (Fig. 8*b* with average C-value) predictions into even better agreement with the experimental results.

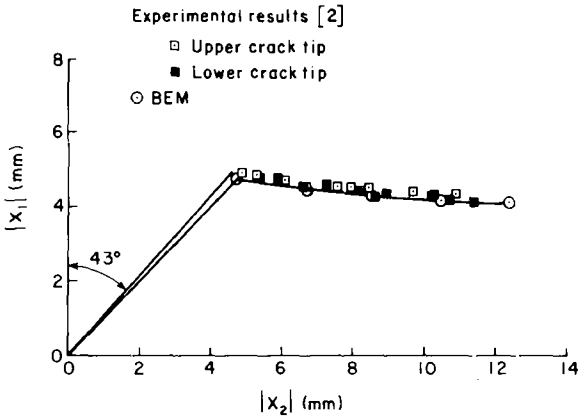

(a) Crack trajectory comparisons

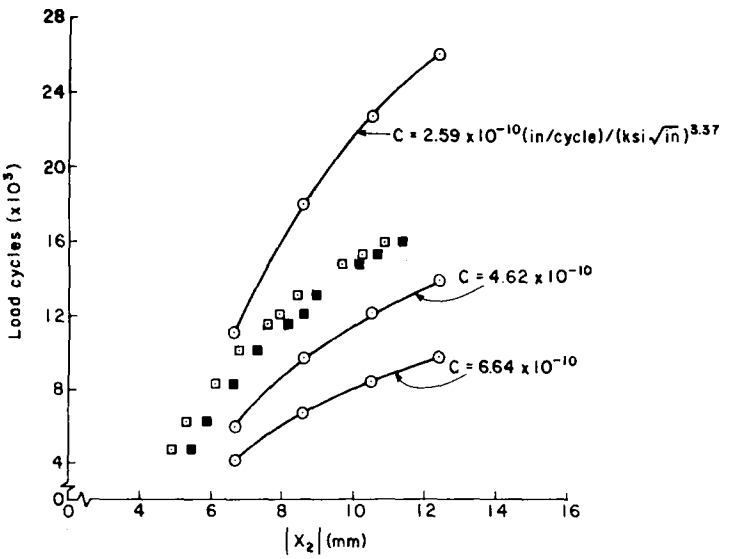

(b) Load cycle comparisons

FIG. 8—*Comparison of BEM results with the experimental results of Pustejovsky [2].*

The computed Mode I stress-intensity factor ranges using the BEM and the superposition-dislocation results of Pustejovsky [2] are compared in Fig. 9. These results show a consistent correlation of the two projected crack paths and the Mode I stress-intensity factor ranges, particularly for the first several crack increments. The boundary element stress-intensity factor ranges become higher than the dislocation-superposition results as the fatigue crack

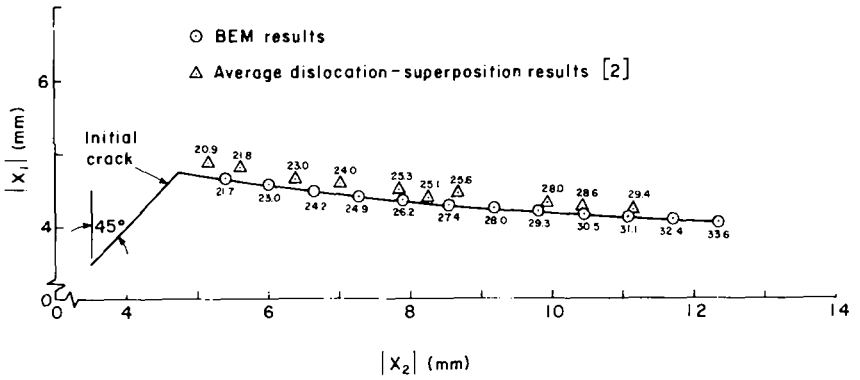

FIG. 9—*Comparison of the computed Mode I stress intensity factor ranges (units: MPa* $\sqrt{m}$*).*

lengthens. The dislocation-superposition analysis was performed on a plate assumed infinite in length and width [*2*], whereas the BEM employed here models the actual test geometry. It is to be expected, therefore, that the BEM results should increase more rapidly as the fatigue crack begins to sense the finite width effect.

The results shown in Figs. 8*a* and 9 indicate that the center slant fatigue crack propagates primarily in Mode I. The Mode II stress intensity factor ranges are two orders of magnitude smaller than the corresponding Mode I stress intensity factor ranges [*16*].

Quasi-Static Crack Propagation

The quasi-static crack propagation analysis of the angled notch problem of Fig. 1*b* is discussed in this section. The boundary element results using the $\sigma(\theta)_{max}$, $S(\theta)_{min}$, and $G(\theta)_{max}$ mixed-mode fracture initiation theories are compared with the same analyses using the finite element method as well as the experimental results of Ingraffea [*1, 7*]. The initial mesh used to perform the boundary element analysis is shown in Fig. 10*a* and *b*. The initial crack length emanating from the notch was chosen to be 0.762 mm, which is the same as the chosen crack increment, Δa.

The boundary element program was used to perform seven crack increment analyses. The computed crack path is compared with the experimentally observed results obtained by Ingraffea [*7*] in Fig. 11. Ingraffea performed experiments on 19-mm-thick Salem limestone with the initial geometry of Fig. 1*b*. The material properties assumed in the analyses were [*7*] $E = 36200$ MPa, $\nu = 0.21$, $K_c = 9.55 \times 10^{-6} a^3 - 1.17 \times 10^{-3} a^2 + 4.89 \times 10^{-2} a + 0.252$ for $a \leq 50.8$ mm, and $K_{Ic} = 0.97$ MPa $\sqrt{m}$ for $a > 50.8$ mm. The BEM results shown in Fig. 11 were obtained using the $S(\theta)_{min}$ [*15*] fracture initiation theory. The predicted crack paths of the $\sigma(\theta)_{max}$ and $G(\theta)_{max}$ mixed-mode fracture ini-

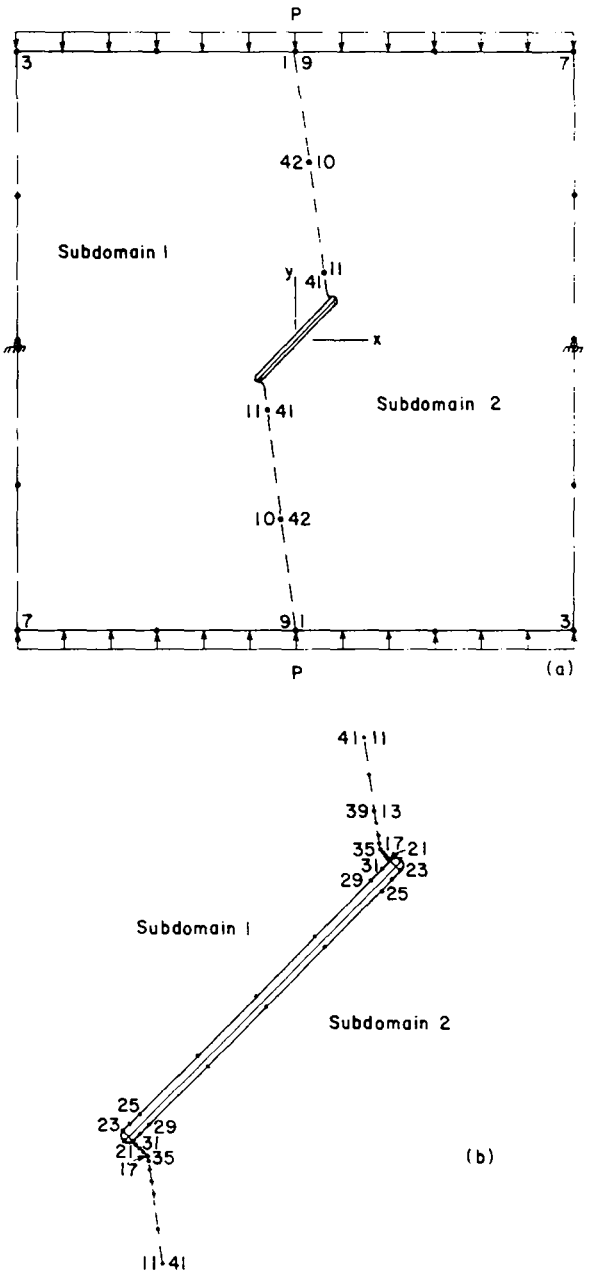

FIG. 10—(a) *Initial boundary element mesh for the quasi-static crack propagation problem of Fig. 1*b. (b) *Detail of mesh around notch.*

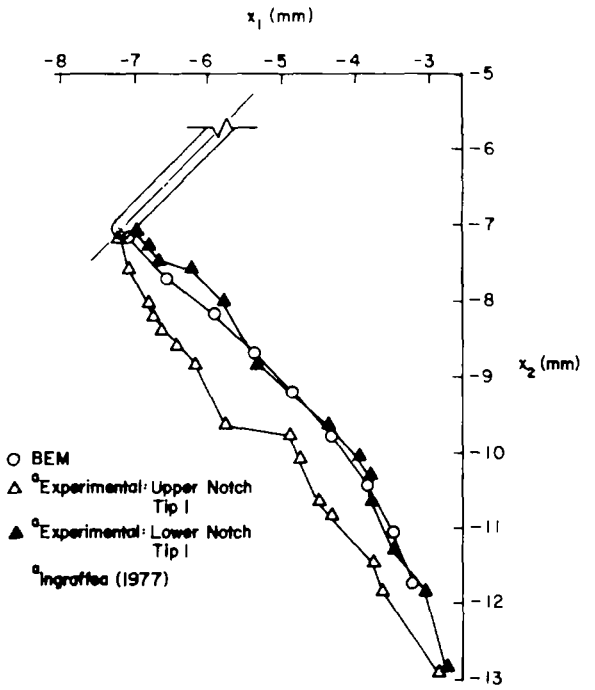

FIG. 11—*Comparison of the BEM predicted primary crack path with the experimental results of Test 1 [8].*

tiation theories are not shown because the results are virtually identical. The reason that the results agree so closely is that the Mode II stress-intensity factors are at least an order of magnitude smaller than the corresponding Mode I stress-intensity factors.

The BEM and finite element [*1, 7*] crack path predictions are shown in Fig. 12. There is good agreement between the BEM and the $\sigma(\theta)_{max}$ and $G(\theta)_{max}$ finite element results. The finite element crack path predictions using the $S(\theta)_{min}$ theory agree less with the other results. This discrepancy is most likely due to small errors in crack topology introduced by the irregularity of a finite element mesh. Using the BEM approach, the crack trajectory is modelled more smoothly and element distribution is more regular. The resulting stress intensity factor evaluation is more accurate, especially for the small K_{II} values which control trajectory.

The average solution times required for the automatic crack propagation analysis using the BEM are given in Table 1. (The average time was obtained by summing the $\sigma(\theta)_{max}$, $S(\theta)_{min}$, and $G(\theta)_{max}$ solution times and dividing by three.) The initial time corresponds to a single analysis using the boundary element mesh of Fig. 10. The solution times in each fracture step represent a total

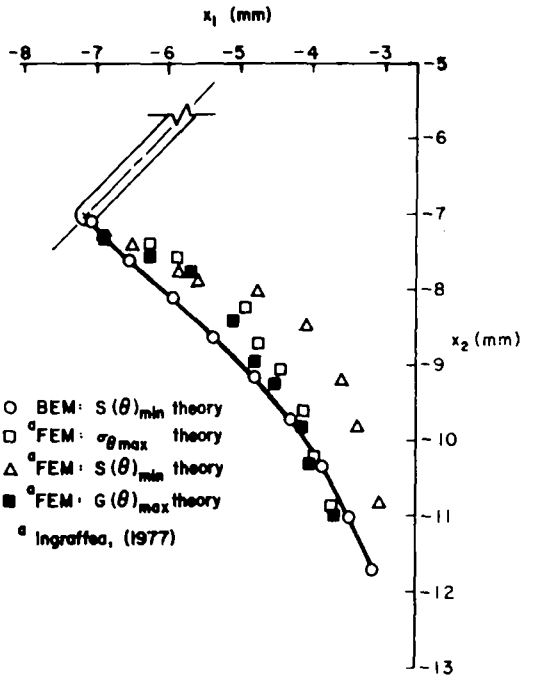

FIG. 12—*Comparison of BEM and Finite element [8] crack path predictions.*

TABLE 1—*CPU timing statistics for the angle notch problem. IBM 370/168.*

Analysis[a]	Average Time, s
Initial	13.29[b]
FS 1	50.17
FS 2	62.82
FS 3	77.58
FS 4	94.24
FS 5	112.9
FS 6	133.9
FS 7	157.0
Total	701.9

[a]FS—fracture step.
[b]Single analysis on initial mesh.

of three analyses, one for each subincrement of crack propagation. The central processing unit (CPU) times increase with each fracture step since a total of eight new unknowns (two displacements in each subdomain for each propagating crack tip) are introduced with each fracture step.

Discussion

Examination of Figs. 8 and 11 shows that the present method accurately reproduced observed fatigue and quasi-static crack propagation. Although both of the problems studied herein are laboratory simplifications rather than actual structural configurations, they do show the versatility of the developed code. They integrate physical phenomena necessary to test all the algorithms described in this paper.

Figures 9 and 12 show that the proposed model is at least as accurate as previously employed numerical methods. Moreover, it should be emphasized that previous approaches to crack propagation modelling have not been automatic; the new method requires only initial input data from the user, the code generating all subsequent data without the possibility of human error.

This observation, coupled with the reasonable CPU times shown in Table 1, means that the new model is extremely efficient. Analyses which previously required man-days to perform and check now can be done, with more confidence in the results, in man-hours.

The present, initial version of the code does have some major drawbacks. Problem size grows rapidly with the number of crack increments. This effect can be countered by automatically eliminating unnecessary elements behind the propagating crack-tips. For fatigue modelling, only constant amplitude loading is allowed currently. User-selectable load spectra should be implemented and Eq 9 and its solution generalized accordingly. During quasi-static propagation in materials with relatively low tensile strength, secondary crack nucleation often occurs [*1,3*]. The code should have the capability for automatically locating likely points of nucleation, and ideally, remeshing for a new crack. Work on these and other improvements is currently underway.

Conclusions

In this paper the BEM has been used as a new approach to the modelling of quasi-static and fatigue crack propagation problems within the limitations of linear elastic fracture mechanics. The advantages include:

1. The inherent accuracy of boundary methods in that all approximations are confined to the boundary;
2. The ease of the use of singular elements to reproduce the crack tip singularity;
3. The ease in which the discretization can follow a moving boundary;
4. The fact that the user need supply mesh data only on the boundaries (plus a short segment of line from the crack tips to a free boundary); and
5. The inherent efficiency of the BEM which greatly reduces computing time.

Thus, the crack propagation program can be made automatic whereby the user does not have to intervene from one step to the next.

The examples in this paper and in Ref *16* have indicated that the method is at least as accurate as alternate techniques. These examples illustrate the advantages cited previously.

References

[*1*] Ingraffea, A. R. and Heuze, F., *International Journal for Numerical and Analytical Methods in Geomechanics*, Vol. 4, 1980, pp. 25-43.

[*2*] Pustejovsky, M. A., *Engineering Fracture Mechanics*, Vol. 11, 1979, pp. 9-15 and 17-31.

[*3*] Ingraffea, A. R., *Proceedings 20th Symposium on Rock Mechanics*, Austin, Tex., 1979, pp. 153-162.

[*4*] Ingraffea, A. R., Saouma, V., Blandford, G. E., and Chappell, J. C., "Crack Propagation in Rock and Concrete Structures," to appear in the *Proceedings of the International Symposium on Absorbed Specific Energy and Strain Energy Density Criterion*, Budapest, Hungary, Sept. 1980.

[*5*] Saouma, V., *Interactive Finite Element Analysis of Reinforced Concrete: A Fracture Mechanics Approach*, Ph.D. dissertation, Cornell University, Ithaca, N.Y., 1981.

[*6*] Blandford, G. E., Ingraffea, A. R., and Liggett, J. A., "Two-Dimensional Stress Intensity Factor Computations Using the Boundary Element Method," to appear in the *International Journal for Numerical Methods in Engineering*, 1981.

[*7*] Ingraffea, A. R., *Discrete Fracture Propagation in Rock: Laboratory Tests and Finite Element Analysis*, Ph.D. dissertation, University of Colorado, Boulder, Colo., 1977.

[*8*] Mostovoy, S., Crosley, P. B., and Ripling, E. J., *Journal of Materials*, Vol. 2, No. 3, 1967, pp. 661-681.

[*9*] Ingraffea, A. R. and Beech, J., "Three-Dimensional Finite Element Calibration of the Short-Rod Specimen," to appear in the *International Journal of Fracture*, 1981.

[*10*] Saouma, V., Ingraffea, A. R., and Catalano, D., "Fracture Toughness of Concrete—K_{Ic} Revisited," Department of Structural Engineering Report 80-9, Cornell University, Ithaca, N.Y., 1980.

[*11*] Saouma, V. and Ingraffea, A. R., "Fracture Mechanics Analysis of Discrete Cracking," to appear in the *Proceedings of the Colloquium on Advanced Mechanics of Reinforced Concrete*, Delft, the Netherlands, 2-4 June 1981.

[*12*] Erdogan, F. and Sih, G. C., *Journal of Basic Engineering*, American Society of Mechanical Engineers, Vol. 85, 1963, pp. 519-527.

[*13*] Hussain, M. A., Pu, S. L., and Underwood, J. in *Fracture Analysis, ASTM STP 560*, 1974, pp. 2-28.

[*14*] Tirosh, J., *Engineering Fracture Mechanics*, Vol. 9, 1977, pp. 607-616.

[*15*] Sih, G. C., *International Journal of Fracture*, Vol. 10, 1974, pp. 305-321.

[*16*] Blandford, G. E., *Automatic Two-Dimensional Quasi-Static and Fatigue Crack Propagation Using the Boundary Element Method*, Ph.D. dissertation, Cornell University, Ithaca, N.Y., 1981.

[*17*] Paris, P. C., *The Growth of Fatigue Cracks Due to Variation in Load*, Ph.D. dissertation, Lehigh University, Bethlehem, Pa., 1962.

[*18*] Tanaka, K., *Engineering Fracture Mechanics*, Vol. 6, 1974, pp. 493-507.

[*19*] Rizzo, F. J., *Quarterly of Applied Mathematics*, Vol. 25, 1967, pp. 83-95.

[*20*] Cruse, T. A., "Mathematical Foundations of the Boundary-Integral Equation Method in Solid Mechanics," AFSOR-TR-77-1002, Air Force Scientific Office of Research, 1977.

[*21*] Lachat, J. C. and Watson, J. O., *International Journal for Numerical Methods in Engineering*, Vol. 10, 1976, pp. 991-1005.

[*22*] Cruse, T. A., *Computers and Structures*, Vol. 4, 1974, pp. 741-754.

[*23*] Rizzo, F. J. and Shippy, D. J., *International Journal for Numerical Methods in Engineering*, Vol. 11, 1977, pp. 1753-1768.

[*24*] Cruse, T. A. and Wilson, R. B., "Boundary Integral Equation Method for Elastic Fracture Mechanics," AFSOR-TR-78-0355, Air Force Scientific Office of Research, 1977.

[*25*] Shih, C. F., de Lorenzi, H. G., and German, M. D., *International Journal of Fracture*, Vol. 12, 1976, pp. 647-651.

G. Glinka[1] *and R. I. Stephens*[2]

Total Fatigue Life Calculations in Notched SAE 0030 Cast Steel Under Variable Loading Spectra

REFERENCE: Glinka, G. and Stephens, R. I., **"Total Fatigue Life Calculations in Notched SAE 0030 Cast Steel Under Variable Loading Spectra,"** *Fracture Mechanics: Fourteenth Symposium—Volume I: Theory and Analysis, ASTM STP 791*, J. C. Lewis and G. Sines, Eds., American Society for Testing and Materials, 1983, pp. I-427-I-445.

ABSTRACT: A method of fatigue life calculation based upon low-cycle fatigue and fracture mechanics concepts is presented. Two arbitrary crack initiation criteria were analyzed regarding experimental results with SAE 0030 cast steel and theoretical solutions proposed by other authors. Four different load histories based upon the Society of Automotive Engineers (SAE) transmission history using a keyhole compact specimen with two different notch diameters were analyzed. The results showed that the criterion $\Delta a = 0.25$ mm (0.01 in.) for crack initiation is practical. However, the exact value of crack length at initiation is not of the greatest importance in total fatigue life calculations. Similarly, fatigue crack growth retardation was not as important as that found with other spectra discussed in the literature. It was found that proper modeling of fatigue crack growth near notches can improve fatigue life calculations. With the present state of knowledge it was possible to calculate the total life within a factor of two. The calculation methods developed primarily for wrought metals were quite acceptable for this cast steel.

KEY WORDS: fatigue (materials), notches, cracks, low cycle fatigue, fracture mechanics, linear elastic fracture mechanics, crack initiation, crack growth, spectra loading, overloads, cast steel

The common failure mode of structures and components subjected to cyclic stresses and strains is fatigue; thus, calculating the fatigue life of critical elements must be emphasized. For analysis, the fatigue life has been separated into two stages: (1) a portion of life spent in crack initiation, and (2) a portion spent in crack propagation. It should be noted that this distinction is arbitrary and both stages are not adequately defined.

[1] Faculty, Warsaw Technical University, Warsaw, Poland; formerly postdoctoral fellow, The University of Iowa, Iowa City, Iowa 52242.

[2] Professor, Materials Engineering Division, The University of Iowa, Iowa City, Iowa 52242.

Low-cycle fatigue concepts have often been used to estimate crack initiation lives of notched members [*1-3*].[3] Techniques based on fracture mechanics concepts have been used for estimating crack propagation life [*4, 5*]. There has been only limited work combining the two methods for variable-amplitude loading. Socie [*6*] has used both criteria in conjunction with the experimental Society of Automotive Engineers (SAE) fatigue program, which involved two wrought steels and a keyhole test specimen, that is related to this work. The purpose of this paper is to combine theoretical evaluations of fatigue life under complex load spectra for a cast steel using both low-cycle fatigue and fracture mechanics concepts. The analytical models, load histories, material, and notched specimens will be reviewed.

Low-Cycle Fatigue Concept

The basic hypothesis of the low-cycle fatigue concept is that if stresses and strains at the critical location of a component are known, then crack initiation life at this location can be related to the life of strain-controlled unnotched laboratory specimens. Thus, the analysis reduces to determining the local stresses and strains and relating them to the known strain-life fatigue behavior. The local stresses and strains can be estimated from nominal stresses, loads, or strains on the basis of the cyclic stress-strain behavior and Neuber's rule [*1*]. The cyclic stress-strain curve has to be obtained from smooth laboratory specimens. It is usually given in the form of Eq 1

$$\frac{\Delta\epsilon}{2} = \frac{\Delta\sigma}{2E} + \left(\frac{\Delta\sigma}{2K'}\right)^{1/n'} \tag{1}$$

where

$\Delta\epsilon$ = strain range,
$\Delta\sigma$ = stress range,
E = modulus of elasticity,
K' = cyclic strength coefficient, and
n' = cyclic strain hardening exponent.

Neuber's rule relates the theoretical stress concentration factor and the nominal stresses and strains with the local stresses and strains of the notch for plane-stress conditions.

$$K_t^2(\Delta S \times \Delta e) = (\Delta\sigma \times \Delta\epsilon) \tag{2}$$

where

ΔS = nominal stress range,
Δe = nominal strain range,

[3]The italic numbers in brackets refer to the list of references appended to this paper.

$\Delta\sigma$ = local (notch) stress range,
$\Delta\epsilon$ = local (notch) strain range, and
K_t = theoretical stress concentration factor.

It has been shown that under cyclic loading it may be better to use a fatigue strength reduction factor K_f in Eq 2 instead of the theoretical stress concentration factor K_t. The fatigue strength reduction factor K_f can be determined experimentally but very often the empirical formula proposed by Peterson [7] is used.

$$K_f = 1 + \frac{K_t - 1}{1 + \frac{\alpha}{r}} \tag{3}$$

where

α = material constant and
r = notch radius.

Fatigue resistance of metals is characterized by a strain-life relationship determined from smooth laboratory specimens and is expressed in the following form

$$\frac{\Delta\epsilon}{2} = \epsilon'_f(2N_f)^c + \frac{\sigma'_f}{E}(2N_f)^b \tag{4}$$

where

ϵ'_f = fatigue ductility coefficient,
c = fatigue ductility exponent,
σ'_f = fatigue strength coefficient,
b = fatigue strength exponent, and
$2N_f$ = number of reversals to failure.

For mean stress considerations the following modified strain-life relationship accounting for mean stress σ_m is often used.

$$\frac{\Delta\epsilon}{2} = \epsilon'_f(2N_f)^c + \frac{\sigma'_f - \sigma_m}{E}(2N_f)^b \tag{5}$$

Notch root stresses and strains are determined on a reversal-by-reversal basis using Eqs 1 and 2 and a cycle counting scheme (often rainflow). Then fatigue damage for each reversal is calculated using Eq 5. The total damage is determined as a sum of damages by individual reversals which is equivalent to Miner's rule.

Crack Propagation Concept

The most commonly used formula for relating fatigue crack growth rate and applied loads was proposed by Paris [4].

$$\frac{da}{dN} = C(\Delta K)^n \tag{6}$$

where

da/dN = fatigue crack growth rate,
C = crack growth coefficient,
n = crack growth exponent, and
ΔK = stress-intensity factor range.

Crack propagation lives are obtained by integrating Eq 6 with the following result

$$N_p = \int_{a_i}^{a_f} \frac{da}{C(\Delta K)^n} \tag{7}$$

where

a_i = initial crack size,
a_f = final crack size, and
N_p = crack propagation life.

In practice the integral in Eq 7 is usually replaced by a cycle-by-cycle summation for each cycle such that

$$a_f - a_i = \sum_{i=1}^{N_p} C(\Delta K_i)^n \Delta N_i \tag{8}$$

For variable-amplitude loading, fatigue crack growth retardation due to load interaction can be taken into account. There are several simple models that approximately calculate this retardation. The Willenborg model [*8*] was used in this research. Thus Eq 8 can then be written in the form

$$a_f - a_i = \sum_{i=1}^{N_p} C_{ri} C(\Delta K_i)^n \Delta N_i \tag{9}$$

where

C_{ri} = the retardation factor calculated on the basis of Willenborg's model.

The use of specific retardation models is still an open issue, and discussion of different retardation models can be found in the literature [*5, 9*].

Material, Specimens, and Tests

SAE 0030 cast steel was used in all experiments. The chemistry, foundry history, and heat treatment are given in Table 1. The monotonic and cyclic properties taken from Ref *10* are given in Table 2. The cyclic stress-strain

TABLE 1—*Chemical composition, weight percent.*

C	Mn	Si	S	P	Cr	Ni	Cu	Mo	Al	Ti
0.24	0.71	0.44	0.026	0.015	0.10	0.10	0.05	0.08	0.06	0.013

NOTE—Heat treatment: normalize 30 min at 900°C (1650°F); temper 90 min at 677°C (1250°F).

TABLE 2—*Monotonic and cyclic properties* [10].

0.2% monotonic yield strength σ_y, MPa (ksi)	303 (44)
Ultimate strength σ_u, MPa (ksi)	496 (72)
Modulus of elasticity E, GPa (psi)	207 (30 × 10^6)
0.2% cyclic yield strength σ'_y, MPa (ksi)	317 (46)
Strength coefficient K', MPa (ksi)	708 (103)
Strain hardening exponent n'	0.13
Fatigue strength coefficient σ'_f, MPa (ksi)	653 (95)
Fatigue strength exponent b	−0.082
Fatigue ductility coefficient ϵ'_f	0.28
Fatigue ductility exponent c	−0.51

properties were previously obtained from strain-controlled tests with unnotched polished uniaxial specimens [*10*]. The cyclic stress-strain and strain-life curves are shown in Fig. 1 [*10*] and Fig. 2 [*10*], respectively. Baseline constant-amplitude fatigue crack growth rate (FCGR) data were obtained using compact tension specimens. FCGR data using four different R ratios ranging from −1 to 0.5 are shown in Fig. 3. Even though the compact specimen is not recommended in the ASTM Test for Constant-Load-Amplitude Fatigue Crack Growth Rates Above 10^{-8}m/Cycle (E 647-81) for negative R ratio testing, the $R = -1$ test results can still be considered quite reasonable. Some influence of R ratio on FCGRs was found under high stress intensities, but R ratio had little effect on total fatigue crack propagation life. In general, there was no systematic R ratio effect and the scatter between results obtained from different specimens tested under the same R ratio was similar to differences due to the R ratio. It was assumed that the R ratio effects could be neglected. The constants for Eq 6 found from these data by a least-square method are $n = 3.30$, $C = 1.67 \times 10^{-9}$ for ΔK in MPa$\sqrt{\text{m}}$ ($C = 8.97 \times 10^{-11}$ for ΔK in ksi$\sqrt{\text{in.}}$), and da/dN in mm/cycle (in./cycle). Note that $\Delta K = K_{max}$ for $R \leq 0$.

Keyhole specimens shown in Fig. 4 were used for experiments presented in Ref *10* involving crack initiation and propagation under variable-amplitude load histories. Two keyhole notch diameters were used: 4.7 mm (3/16 in.) and 9.5 mm (3/8 in.) The distance from the load centerline to the notch end (a_N) was 19.6 mm (0.77 in.) for both notches. All specimens were 8.2 mm (0.325 in.) thick.

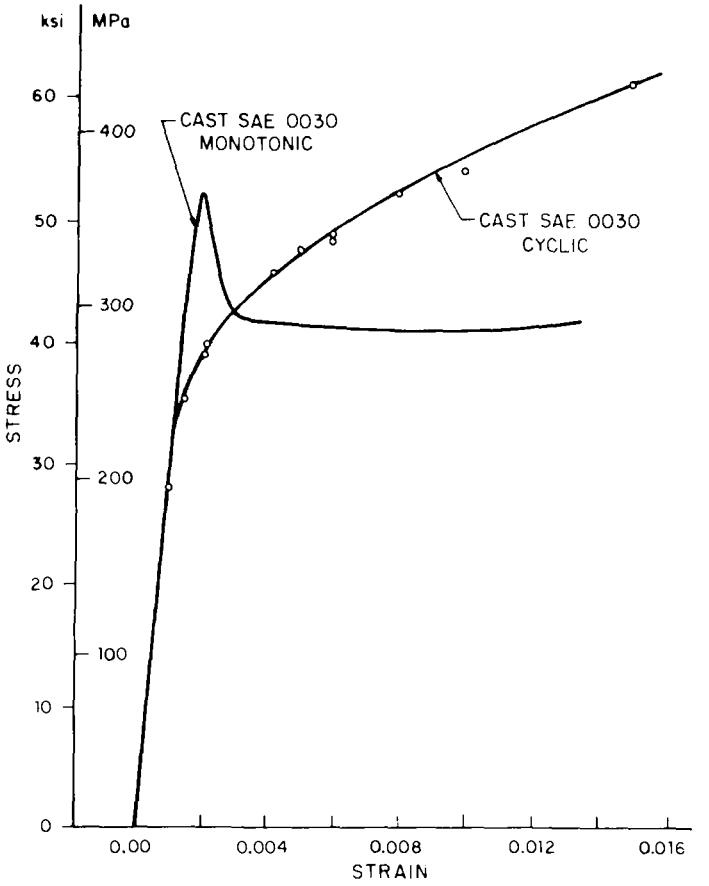

FIG. 1—*Cyclic stress-strain behavior of SAE 0030 cast steel [10].*

Loading Histories and Test Results

The SAE transmission history [*11*] was chosen as shown in Fig. 5*a* as the base spectrum and will be referred to as T/H. This T/H spectrum was modified to form additional spectra. Figure 5*b* shows one modification labeled "mod T/H" that eliminates all compressive loadings. A total of 1710 load reversals make up one T/H history block. The mod-T/H history has only 1694 reversals per block since 16 reversals were eliminated by removing the compressive loads. Two other modifications were formed by applying two single tensile overloads to the T/H and mod-T/H spectra. One overload was applied at the beginning of the test, and the second was applied after a crack increment of $\Delta a = 5.8$ mm (0.23 in.), which corresponds to a total crack length of 25.4 mm (1.0 in.). Thus, overload influence on both crack initiation

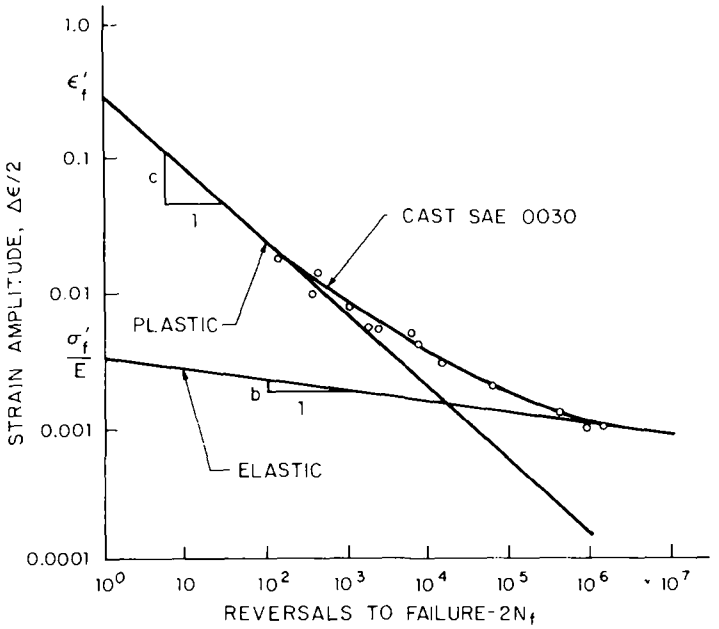

FIG. 2—*Low-cycle strain-control fatigue behavior of SAE 0030 cast steel [10].*

and crack growth could be considered. The overloads were equal to 1.6 times the highest peak in the T/H or mod-T/H spectra. These histories are called T/H + 2OL and mod-T/H + 2OL, respectively.

An automated profiler was used in conjunction with an 89-kN (20-kip) closed-loop electrohydraulic test system in load control to apply the four histories to the specimens. The block history was repeated until specimen fracture. Fatigue crack initiation and crack growth were monitored with an electropotential system and a ×45 traveling microscope using stroboscopic lighting and a 0.25-mm (0.01-in.) least division scale fastened to the specimen. Crack initiation was defined and recorded in the experiments at the first visible surface crack of $\Delta a = 0.25$ mm (0.01 in.). A crack length of $\Delta a = 2.5$ mm (0.1 in.) was also specifically monitored since this value had been selected by the SAE Fatigue Design and Evaluation Committee as a limiting value of crack initiation used with low-cycle fatigue analysis prediction methods.

The T/H history was applied with both keyhole specimen diameters using three different relative peak load levels. This peak load occurs as the first and last load within a block. Values chosen for these peaks were 22.24 kN (5 kips), 17.8 kN (4 kips), and 15.57 kN (3.5 kips). Nominal elastic stresses caused by the peaks were 393 MPa (57 ksi), 314 MPa (46 ksi), and 275 MPa (40 ksi), respectively, which indicates plasticity occurred at the notches on the first loading. Two load levels, 17.8 kN (4 kips) and 15.57 kN (3.5 kips), respec-

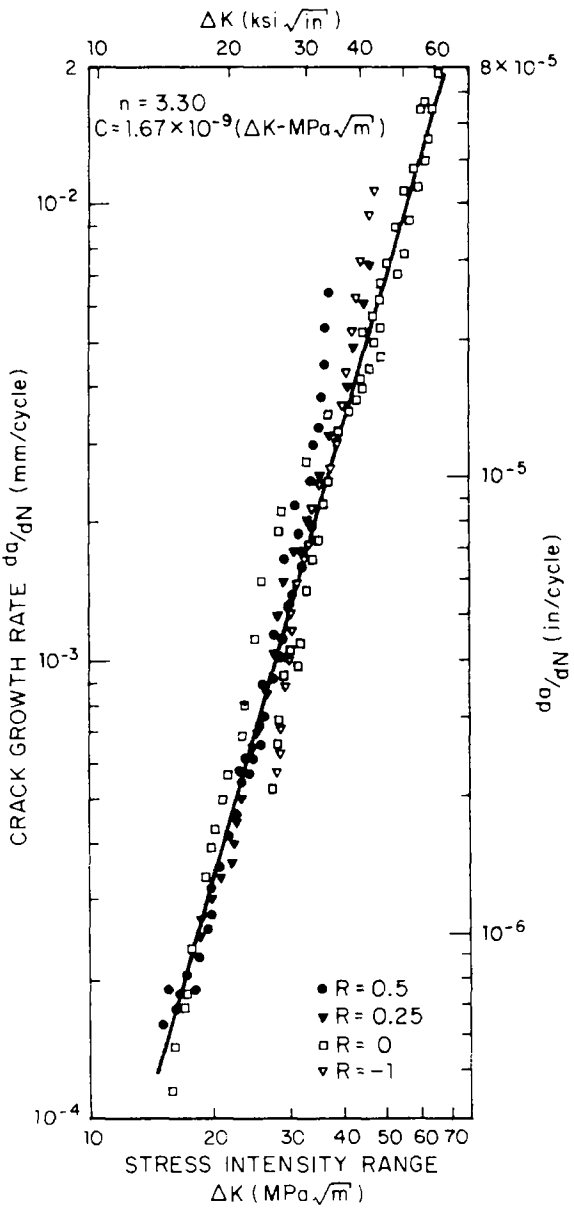

FIG. 3—*Fatigue crack growth behavior under constant-amplitude loading for SAE 0030 cast steel.*

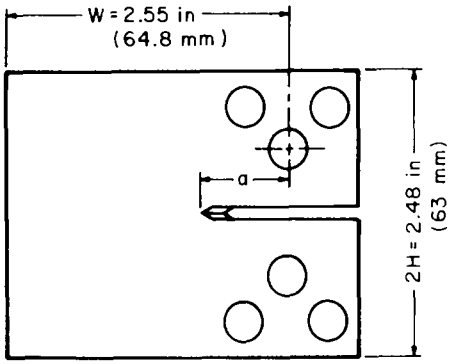

(a) CRACK GROWTH SPECIMEN

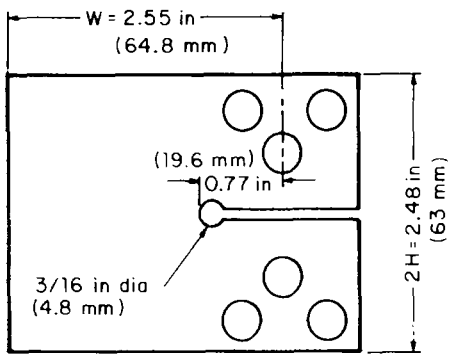

(b) KEY HOLE FATIGUE SPECIMEN

FIG. 4—*Keyhole fatigue specimen.*

tively, were used to scale the T/H + 2OL and mod-T/H spectra. Only the smaller diameter keyhole specimens were tested with these two spectra. One load level was used with the mod-T/H + 2OL history and the smaller diameter keyhole specimen. The experimental results from Refs 10 and 12 are presented in Table 3. Duplicate or triplicate tests were made for each history and stress level.

Theoretical Calculation of Fatigue Crack Initiation Lives

To simulate stress-strain behavior near the notch tip using Neuber's rule one needs to know the theoretical stress concentration factor K_t. This was found for both keyhole notch diameters by interpolation of results published

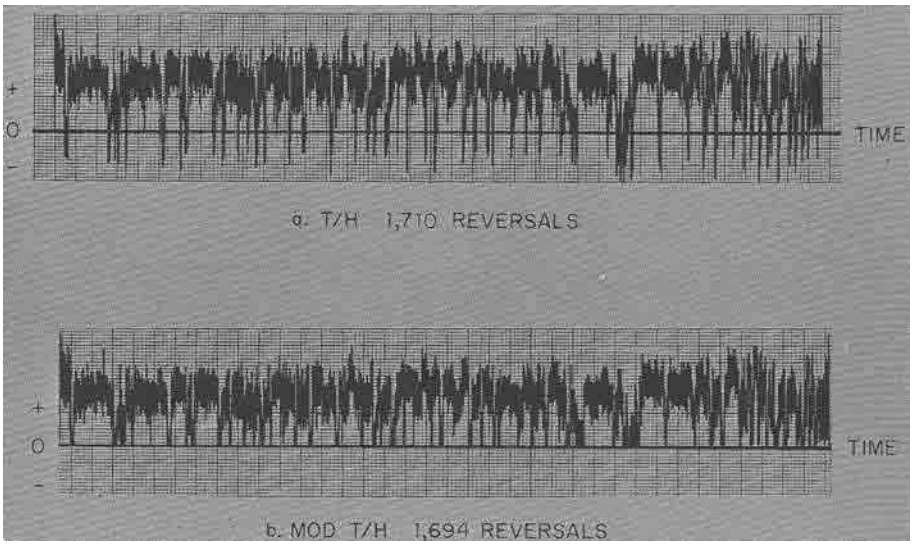

FIG. 5—*Variable-amplitude load spectra T/H and mod T/H.*

TABLE 3—*Number of blocks to specific crack lengths and fracture with four load histories and three load levels* [10,12] *(duplicate or triplicate tests per condition).*

	Peak Load Levels P_{max}, kN (kips)				
Crack Length Δa, mm (in.)	22.24 (5)	17.8 (4)	15.57 (3.5)	17.8 (4)	15.57 (3.5)
	4.7-mm (3/16-in.) Notch Dia T/H History			4.7-mm (3/16-in.) Notch Dia T/H + 2 OL History	
0.25 (0.01)	18, 16	67, 35	82, 52	100, 74	141, 181
2.54 (0.1)	39, 27	77, 78	134, 130	140, 114	200, 207
Fracture	54, 54	141, 130	270, 213	200, 203	367, 381
		Mod-T/H History		Mod-T/H + 2 OL History	
0.25 (0.01)	...	247, 113	249, 308	237, 257	...
2.54 (0.1)	...	354, 193	298, 388	460, 335	...
Fracture	...	453, 340	447, 567	876, 632	...
	9.5-mm (3/8-in.) Notch Dia T/H History				
0.25 (0.01)	24, 20, 19	140, 111, 121	193, 288, 103	...	...
2.54 (0.1)	45, 55, 45	180, 153, 156	209, 332 ...	...	...
Fracture	55, 82, 57	256, 218, 241	351, 489, 297	...	...

by Wilson [*13*] and Neal [*14*]. The values were $K_t \approx 3.65$ and $K_t \approx 2.8$ for specimen with holes 4.7 mm (3/16 in.) diameter and 9.5 mm (3/8 in.) diameter, respectively. The fatigue strength reduction factors were calculated using Eq 3. Material constant $\alpha = 0.000326$ m (0.0128 in.) was calculated from the empirical expression in Eq 10 based on the fatigue results presented by Peterson [*7*].

$$\alpha = 2.5 \times 10^{-5}\left(\frac{2068}{\sigma_u}\right)^{1.8} \quad \text{for } \sigma_u \text{ in SI units} \tag{10}$$

The fatigue strength reduction factors were $K_f = 3.33$ for the small hole and $K_f = 2.62$ for the large hole. The notch root stress and strains were simulated using a method proposed by Wetzel [*15*]. Following this method the cyclic stress-strain curve (Fig. 1) used for calculations was represented by a series of ten straight-line segments. The fatigue damage for separate reversals was calculated following Wetzel's method by using Eq 5 rearranged by Landgraf [*2*].

$$\frac{\text{Damage}}{\text{Reversal}} = \left[\left(\frac{\sigma'_f}{\epsilon'_f E}\right)\left(\frac{\Delta\epsilon_p}{\Delta\epsilon_e}\right)\left(\frac{\sigma'_f}{\sigma'_f - \sigma_m}\right)\right]^{\frac{1}{b-c}} \tag{11}$$

where

$\Delta\epsilon_p$ = plastic strain range and
$\Delta\epsilon_e$ = elastic strain range.

A similar approach to fatigue damage calculations was presented by Nelson and Fuchs [*3*]. The first calculation showed that for longer lives (small $\Delta\epsilon_p$) Eq 11 overestimated lives due to the use of the plastic-to-elastic strain range ratio as a damage parameter. A similar tendency was found by Nelson and Fuchs [*3*]. Therefore, for reversals with total strain amplitude less than $\Delta\epsilon/2 = 0.001$, the elastic part of Eq 5 was used for damage calculations in the form

$$\frac{\text{Damage}}{\text{Reversal}} = \left[\frac{2(\sigma'_f - \sigma_m)}{\Delta\epsilon \times E}\right]^{1/b} \tag{12}$$

A total fatigue damage was calculated for one block history. The inverse of the damage value caused by one block gives the number of blocks to initiation. Numbers of blocks to specific crack lengths $\Delta a = 0.25$ mm (0.01 in.) and $\Delta a = 2.54$ mm (0.1 in.) obtained from experiments were compared with calculated lives to initiation for both notches. The crack initiation results for the four load histories with $\Delta a = 0.25$ mm (0.01 in.) are shown in Fig. 6, where it can be seen that, considering a scatter factor of 2, substantial good agreement was obtained for $\Delta a = 0.25$ mm (0.01 in.) using the theoretical

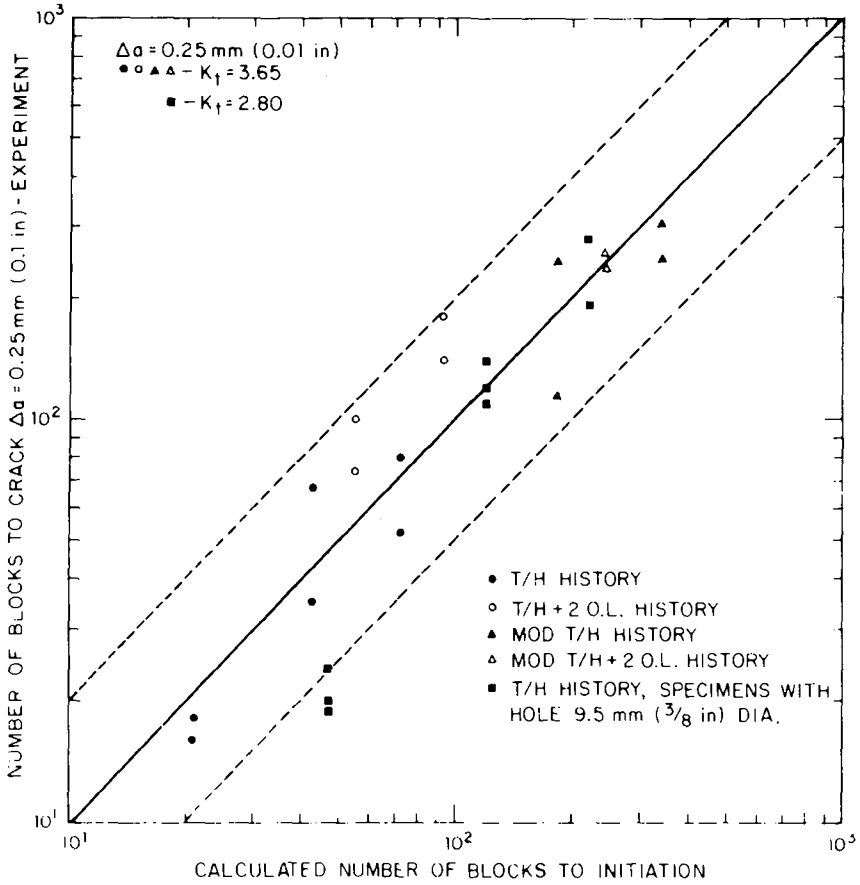

FIG. 6—*Comparison of experimental lives to crack length* Δa = *0.25 mm (0.01 in.) with calculated lives using* K_t.

stress concentration factor, K_t. Over 90 percent of the data were within the ±2.0 scatterband shown by the dashed lines in Fig. 6.

As mentioned previously, the separation of the fatigue process into initiation and propagation stages is strictly arbitrary because the initiation stage has not yet been properly defined. In this paper the crack initiation period was defined once as life to a crack Δa = 0.25 mm (0.01 in.), and second as life to a crack Δa = 2.54 mm (0.1 in.). The first criterion is related to the accuracy of equipment used in experiments and to what a design engineer might realistically comprehend or visualize. The crack Δa = 0.25 mm (0.01 in.) was the shortest crack that was reasonable to detect. The criterion Δa = 2.54 mm (0.1 in.) was suggested by SAE. This suggestion was based upon wide experimental research.

Many researchers agree that the crack Δa defining the initiation period is below $\Delta a = 2.5$ mm (0.1 in.) Dowling [*16*] suggests defining crack length initiation at a notch as a crack equal to the length of the notch effect. For the keyhole specimens the values are $\Delta a = 0.4$ mm (0.017 in.) for the small notch and $\Delta a = 0.8$ mm (0.033 in.) for the large notch. El Haddad et al [*17*] suggest that the crack length at initiation is a material constant related to the threshold stress intensity ΔK_{th} and fatigue limit strain amplitude e_a. Simplified calculations based on this model gave $\Delta a = 0.25$ (0.01 in.) Socie's results [*18*] suggested that the crack length to initiation should not be a material constant because initiation depends upon material properties, loading level, and geometric parameters. Calculations based on Socie's model made by Lawrence and Chen[4] for AISI 1020 steel (which is similar to the cast SAE 0030 steel) suggest that the crack length to initiation varies in the range from 0.25 mm (0.01 in.) to 0.5 mm (0.02 in.) depending on the stress level. The model discussed by Smith and Miller [*19*] gives a value $\Delta a = 0.9$ mm (0.035 in.). In general, all the models mentioned previously predict the crack length to initiation in the range $\Delta a = 0.25$ mm (0.01 in.) to 0.9 mm (0.035 in.). Also, crack length to fracture or failure in strain-controlled low-cycle fatigue tests will vary from about 0.25 mm (0.01 in.) to 5 mm (0.2 in.) depending upon stress level and fracture toughness.

The criterion $\Delta a = 0.25$ mm seems to be very reasonable for fatigue crack initiation in cast SAE 0030 steel. The applied method of notch stress-strain simulation and fatigue damage calculation properly predicted the effect of the first overload in T/H + 20L and mod-T/H + 20L histories. The overloads in T/H + 20L and mod-T/H + 20L increased fatigue life to crack initiation about 50 percent in comparison to the T/H and mod-T/H histories, respectively. The same tendency was obtained from the calculated results.

Theoretical Calculation of Fatigue Crack Propagation Lives

Equations 6 and 7 were used for predicting fatigue crack propagation life along with an effective stress-intensity factor concept based upon the Willenborg model [*8*], which accounts for fatigue crack growth retardation due to variable load history. The plastic zones r_y at the crack tip were calculated from Eq 13 assuming plane stress conditions.

$$r_y = \frac{1}{2\pi}\left(\frac{K}{\sigma_y}\right)^2 \tag{13}$$

Short cracks at notches, however, behave differently than long cracks that are beyond the notch affected area, and therefore, a model proposed by Jergéus [*20*] was used to determine the notch effect on fatigue crack growth.

Jergéus showed that the effect is equivalent to an additional crack increment e calculated from Eq 14

$$e = a_N\left\{1 - \exp\left[-4\left(1 + \frac{a_N}{b}\right)\frac{\Delta a}{b}\right]\right\} \tag{14}$$

where

a_N = notch depth, a_N = 19.5 mm (0.77 in.),
Δa = crack increment measured from notch tip,
$b = \sqrt{a_N \times \rho}$, and
ρ = notch radius.

The effective crack length used for calculating the effective stress-intensity factor is

$$\Delta a_{\text{eff}} = \Delta a + e \tag{15}$$

An analysis of Eq 14 shows that the notch effect is negligible for longer Δa. For the specimen shown in Fig. 4, with $a_N/W = 0.308$, e was practically equal to zero for $\Delta a = 2$ mm (0.08 in.). This means that the model overestimates the notch effect in comparison to results presented by Dowling [*16*] and Smith [*19*]. However, there is no solution that exactly satisfies the geometry in Fig. 4. Therefore, Eq 14 was used as a reasonable model, which is also very convenient in computer calculations. The improved (relating to specimen geometry, notch effect, and stress computations) program "CRACKS II—Crack Propagation Analysis Program" [*21*] was used for fatigue propagation life calculations. The life was calculated beginning from $\Delta a = 0.25$ mm (0.01 in.) until the current maximum stress-intensity factor $K_{\max}$ reached a value $K_c = 77$ MPa$\sqrt{\text{m}}$ (70 ksi$\sqrt{\text{in.}}$). The value of $K_c = 77$ MPa$\sqrt{\text{m}}$ was determined at fracture from previously described fatigue crack growth tests under constant amplitude.

Fatigue crack growth lives were calculated with and without retardation. It was found that including the retardation effect in the calculations did not contribute significantly to the calculated crack growth life with these four histories. The highest calculated increment in crack growth life due to retardation for the tensile overload histories was 18 percent over that calculated without retardation. The experiments, however, showed that the tensile overloads increased crack propagation life by a factor of about two. The fatigue crack propagation lives calculated without retardation are shown in Fig. 7. About half of the results had overestimated lives. There are many reasons for this. The first is natural scatter of fatigue crack growth rates. With $P_{\max} = 17.8$ kN (4 kips) and $P_{\max} = 22.24$ kN (5 kips) some peaks gave nominal stresses higher than the yield strength. However, the basic crack growth rate data (Fig. 3) were obtained under nominal elastic conditions. The basic

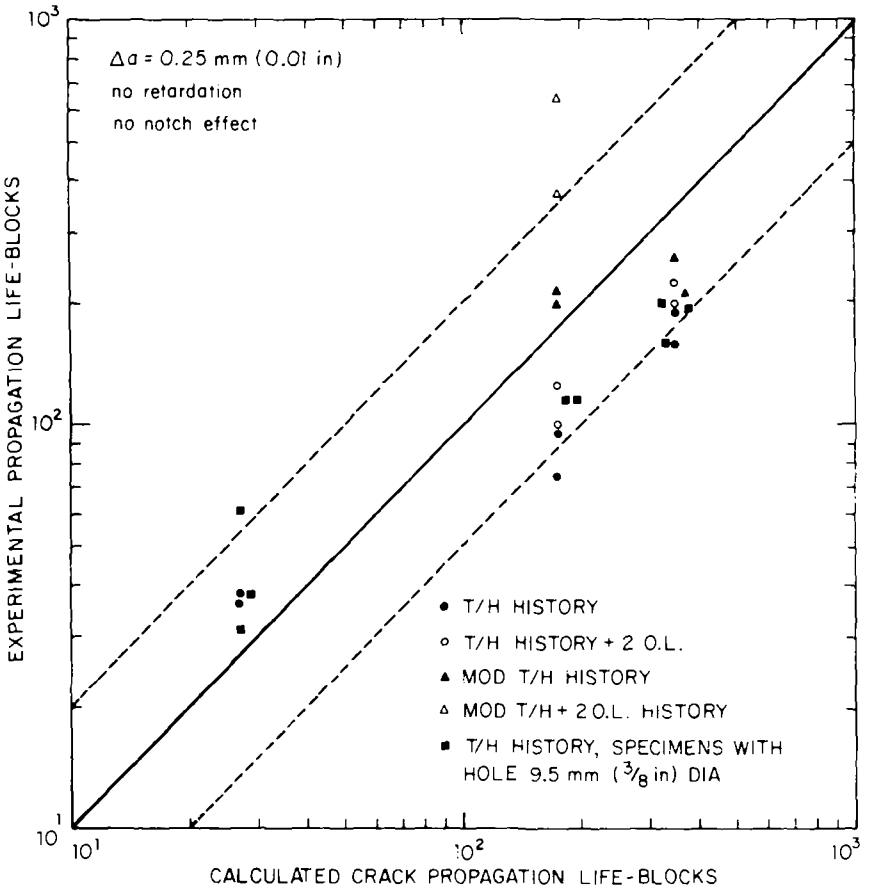

FIG. 7—*Comparison of experimental and calculated fatigue crack propagation lives calculated from* Δa = *0.25 mm (0.01 in.) until fracture without retardation.*

crack growth data (Fig. 3) did not show appreciable R ratio effects, but it is possible that under lower stress intensities that existed in the spectra the effect is more distinct. It should be noted from Table 3 that experiments showed differences in fatigue propagation lives between the T/H and the mod-T/H histories by less than a factor of two. Unfortunately, the crack growth models used here do not take into account compressive loads and therefore cannot show the difference. The Paris equation and Willenborg model used in the present study thus give the same life for the T/H and the mod-T/H histories, which disagrees with the experimental results.

In terms of fatigue accuracy, the crack propagation calculations without load interaction effects are acceptable. About 80 percent of the calculated lives (Fig. 7) do not differ by more than a factor of two (dashed lines) from

the experimental lives. It can be concluded that for the spectra analyzed, fatigue crack growth retardation is not as important as in other spectra. Barsom [22] indicated that spectra with frequently applied similar peak loads will not have significant fatigue crack growth retardation.

Total Life Predictions

It was shown in the previous sections that good agreement regarding life to initiation was found for $\Delta a = 0.25$ mm (0.01 in.) using K_t (Fig. 6). These lives were added to the respective propagation lives with and without retardation. Comparison of experimental and calculated lives is shown in Fig. 8 without retardation. Calculations with retardation were within scatter ranges similar to Fig. 8. The same calculations were made using $\Delta a = 2.5$ mm (0.1 in.) for crack initiation. These results in terms of total lives are shown in Fig. 9, also without retardation. It is surprising that for both crack initiation criteria, the calculations in Figs. 8 and 9 are quite similar considering that differences less than a factor of two are acceptable. Thus it can be concluded for these experiments using two different keyhole notch sizes ($K_t \approx 2.8$ and 3.65) that crack length to crack initiation, Δa, was not that important from the viewpoint of acceptable practical total fatigue life calculations.

Lawrence and Chen[4] also recently indicated that in some reasonable range the crack length Δa to initiation does not substantially affect the total predicted fatigue life. The previously discussed theoretical models suggested that the crack length to initiation is in the range 0.25 mm (0.01 in.) to 0.9 mm (0.035 in.). The present studies show that the criterion $\Delta a = 0.25$ mm is reasonably good for both notches and all load histories applied. Therefore, it seems reasonable to recommend $\Delta a = 0.25$ mm (0.01 in.) as a crack initiation criterion until a nonarbitrary criterion is found.

Summary and Conclusions

An approach to fatigue life calculations was presented. Low-cycle fatigue concepts were applied to fatigue life initiation calculations and fracture mechanics concepts for fatigue crack propagation life estimation. Two arbitrary criteria for fatigue crack initiation were chosen: $\Delta a = 0.25$ mm (0.01 in.) and $\Delta a = 2.54$ mm (0.1 in.). It was found that the method of damage calculation in the form of Eq 11 overestimated lives (unconservative predictions) especially for spectra that consist of many reversals with low strain amplitudes. Theoretical calculations were improved distinctly for strain amplitudes lower than 0.001 when the elastic part of the strain-life equation was used in the form of Eq 12. Good agreement with experimental results was found for

[4]Lawrence, F. and Chen, W. C., University of Illinois, Urbana, Ill., private communications.

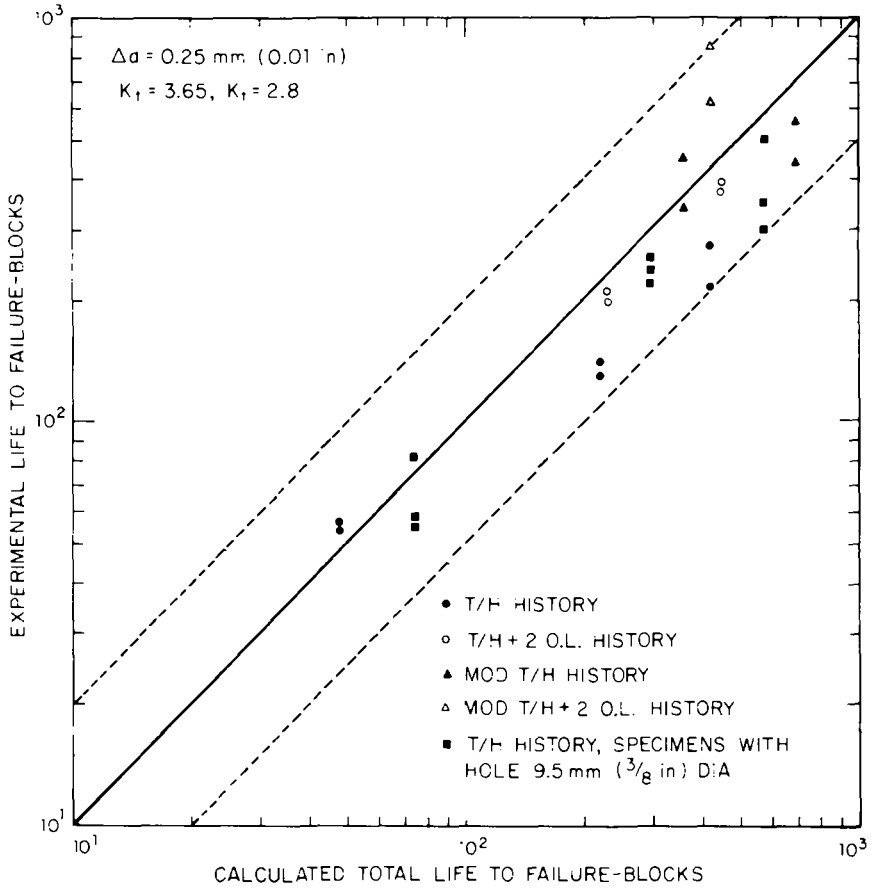

FIG. 8—*Experimental and calculated total lives using crack initiation criterion* Δa = *0.25 mm (0.01 in.) and crack propagation lives calculated without retardation.*

the crack initiation criterion $\Delta a = 0.25$ mm (0.01 in.) and the stress concentration factor K_t. The fatigue strength reduction factor K_f overestimated lives for both assumed crack initiation criteria. The crack propagation calculations for the four spectra suggest that fatigue crack growth retardation did not contribute to the fatigue life significantly, assuming that disagreement between theoretical and experimental results by a factor of two is acceptable.

The analysis of total lives showed that both the criteria for fatigue initiation were reasonably good. It can be suggested that in some reasonable range the crack length to initiation does not appreciably affect the predicted initiation lives.

Fatigue life calculation methods that have been used primarily in comparing experimental wrought metals were quite acceptable for this cast steel.

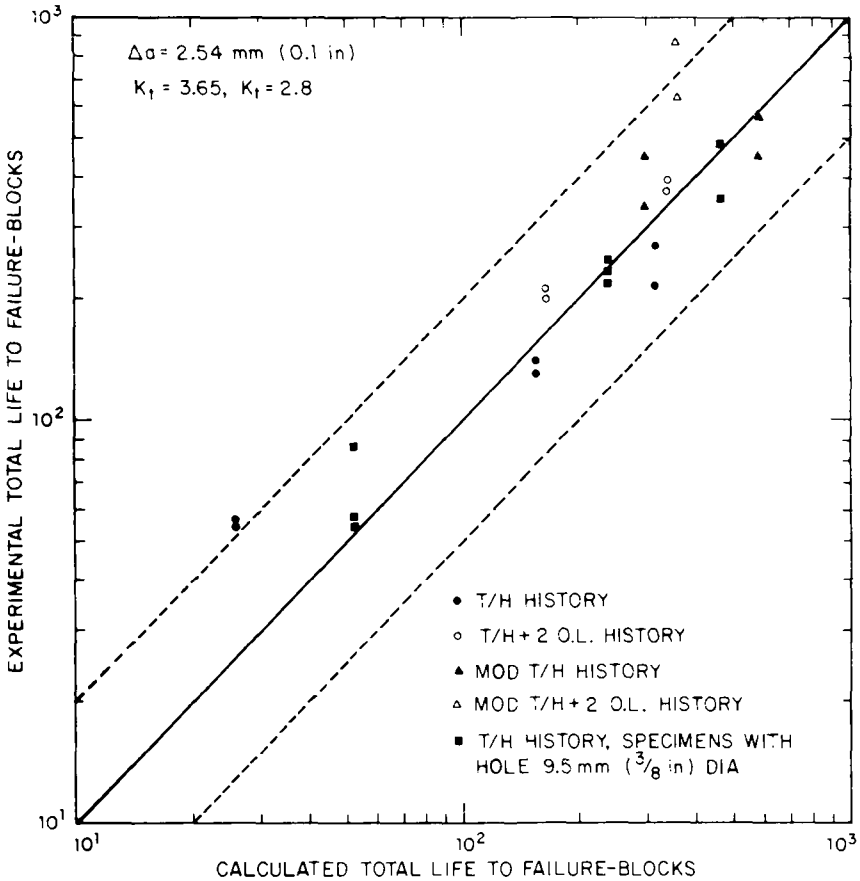

FIG. 9—*Experimental and calculated total lives using crack initiation criterion* $\Delta a = 2.54$ *mm (0.1 in.) and crack propagation lives calculated without retardation.*

References

[1] Dowling, N. E., Brose, W. R., and Wilson, W. K. in *Fatigue Under Complex Loading: Analyses and Experiments,* R. M. Wetzel, Ed., Society of Automotive Engineers, Warrendale, Pa., 1977, pp. 55–84.

[2] Landgraf, R. W., Richards, F. D., and La Pointe, N. R. in *Fatigue Under Complex Loading: Analyses and Experiments,* R. M. Wetzel, Ed., Society of Automotive Engineers, Warrendale, Pa., 1977, pp. 95–106.

[3] Nelson, D. V. and Fuchs, H. O. in *Fatigue Under Complex Loading: Analyses and Experiments,* R. M. Wetzel, Ed., Society of Automotive Engineers, Warrendale, Pa., 1977, pp. 163–187.

[4] Paris, P. C., "The Fracture Mechanics Approach to Fatigue," *Proceedings of the 10th Sagamore Conference,* Syracuse University Press, 1963.

[5] Gallagher, J. P., *Experimental Mechanics,* Vol. 16, No. 11, 1976, pp. 425–433.

[6] Socie, D. F., *Journal of Engineering Materials and Technology, Transactions, American Society of Mechanical Engineers,* Vol. 102, No. 1, Jan. 1980, pp. 153–158.

[7] R. E. Peterson in *Proceedings of the Symposium on Fatigue of Aircraft Structures*, 1959, pp. 273-299; Wright Air Development Center Technical Report 59-507, Aug. 1959.
[8] Willenborg, J. D., Engle, R. M., and Wood, H. A., "A Crack Growth Retardation Model Using an Effective Stress Concept," AFFDL-TM-FBR-71-1, Air Force Flight Dynamics Laboratory, Wright-Patterson Air Force Base, Ohio, Jan. 1971.
[9] Schijve, J., "Prediction Methods for Fatigue Crack Growth in Aircraft Material," *Fracture Mechanics (12th Conference), ASTM STP 700*, American Society for Testing and Materials, 1980, pp. 3-34.
[10] Stephens, R. I., Mauritzson, G., Benner, P. H., and Galliart, D. R., *Journal of Steel Castings Research*. No. 83, July 1978, pp. 1-12.
[11] Tucker, L. and Bussa, S. in *Fatigue Under Complex Loading: Analyses and Experiments*, R. M. Wetzel, Ed., Society of Automotive Engineers, Warrendale, Pa., 1977, pp. 1-53.
[12] Stephens, R. I., Benner, P. H., Mauritzson, G., and Tindall, G. W., *Journal of Testing and Evaluation*, Vol. 7, No. 2, March 1979, pp. 68-81.
[13] Wilson, W. K., *Journal of Pressure Vessel and Technology*, American Society of Mechanical Engineers, Vol. 96, No. 4, 1974, pp. 293-298.
[14] Neal, S., Zachary, L. W., and Burger, C. P., "Three-Dimensional Stress Analysis of the SAE Keyhole Fatigue Specimen," SAE Paper No. 780104, Society of Automotive Engineers, Warrendale, Pa., March 1978.
[15] Wetzel, R. M., "A Method of Fatigue Damage Analysis," Scientific Research Staff Report No. SR 71-107, Ford Motor Co., Dearborn, Mich., Sept. 1971.
[16] Dowling, N. E. in *Fracture Mechanics: 11th Conference, ASTM STP 677*, American Society for Testing and Materials, 1979, pp. 247-273.
[17] El Haddad, M. H., Smith, K. N., and Topper, T. H. in *Fracture Mechanics (11th Conference), ASTM STP 677*, American Society for Testing and Materials, 1979, pp. 274-289.
[18] Socie, D. F., Morrow, J., and Chen, W. C., *Engineering Fracture Mechanics*, Vol. 11, No. 4, 1979, pp. 851-860.
[19] Smith, R. A. and Miller, K. J., *International Journal of Mechanical Science*, Vol. 19, No. 1, 1977, pp. 11-22.
[20] Jergéus, H. Å., *International Journal of Fracture*, Vol. 14, No. 4, 1978, pp. R113-R116.
[21] Engle, R. M., "Cracks II—Crack Propagation Analysis Program," Air Force Flight Dynamics Laboratory, Wright-Patterson Air Force Base, Ohio, 1974.
[22] Barsom, J. M. in *Progress in Flaw Growth and Fracture Toughness Testing, ASTM STP 536*, American Society for Testing and Materials, 1973, pp. 147-167.

Y. H. Kim[1] *and S. D. Manning*[1]

A Superposition Model for Corrosion-Fatigue Crack Propagation in Aluminum Alloys

REFERENCE: Kim, Y. H. and Manning, S. D., **"A Superposition Model for Corrosion-Fatigue Crack Propagation in Aluminum Alloys,"** *Fracture Mechanics: Fourteenth Symposium—Volume I: Theory and Analysis, ASTM STP 791*, J. C. Lewis and G. Sines, Eds., American Society for Testing and Materials, 1983, pp. I-446-I-462.

ABSTRACT: The mechanism for fatigue crack growth in aluminum alloys under a chemically aggressive environment is discussed, based on the current understanding of hydrogen embrittlement phenomena. This mechanism is discussed quantitatively in terms of the three-term superposition model proposed by Wei et al. A diffusion-controlled model, characterizing the cycle-dependent interaction of fatigue loading and environmental attack, is developed, based on the assumption that crack growth enhancement results from microvoid nucleation due to hydrogen accumulation at inhomogeneities ahead of a crack tip. This model is evaluated with limited data on Aluminum 7075-T6. The model developed in this paper accounts for the significant parameters affecting corrosion-fatigue crack growth enhancement. Integration of this model into the superposition scheme is discussed, including the application to predicting crack growth behavior in a corrosive environment for spectrum loading.

KEY WORDS: corrosion fatigue, crack growth enhancement, crack propagation (growth), environment, fracture mechanics, hydrogen embrittlement, Paris' region, retardation, spectrum loading, superposition model, sustained load crack growth

Environment assisted fatigue crack growth in aluminum alloys is often an important factor in many structural applications. Specifically, it is one of the major considerations in aircraft structural design and analysis, since it can significantly affect aircraft safety-of-flight, operational readiness, and overall maintenance costs. Thus, quantitative understanding of the characteristics of and mechanisms for corrosion fatigue is essential to assure structural integrity, durability, and reliability, together with optimum structural efficiency.

Fatigue crack growth behavior of aircraft structural materials in chemically

[1]Senior research scientist and engineering specialist senior, respectively, Materials Research Laboratory, General Dynamics, Fort Worth, Tex. 76101.

aggressive environments has been extensively studied during the last 20 to 25 years [*1-6*].[2] According to previous research, the primary parameters influencing crack growth behavior of a material in a corrosive environment include the following: (1) cyclic stress amplitude, (2) mean stress level, (3) load frequency, (4) sustained-load holding time, (5) severity of environments (or water vapor pressure), and (6) cyclic material properties, etc. Significant progress in understanding the effects of load frequency and gas pressure on crack growth in a gaseous environment has been made recently by Wei et al [*7-9*]. Based on considerations of surface reactions and gas transport, they established a framework for estimating frequency and pressure dependence on cycle-dependent crack growth enhancement for single component gaseous environments [*7,8*] and for binary gas mixtures [*9*].

Meanwhile, understanding of fatigue crack growth behavior in aqueous environments is considered to be less advanced. Saff et al [*10,11*] recently have made a significant step towards quantitatively predicting crack growth behavior in synthetic seawater, by applying the Wei-Landes linear superposition approach [*12*] to several landing gear steels subjected to various load spectra. However, Wei-Landes' superposition scheme [*12*] implicitly assumed that crack growth enhancement results only from sustained-load contribution, and thus did not consider the load-environment interaction.

The main purposes of this paper are: (1) to qualitatively describe the probable mechanism for fatigue crack growth of aluminum alloys in an aqueous environment, and (2) to quantitatively relate this mechanism to the superposition model later suggested by Wei and Simmons [*13*], in order ultimately to derive a predictive methodology traceable to fundamental behavior. Techniques for applying this model to spectrum loading conditions also will be discussed.

Corrosion-Fatigue Crack Propagation Mechanism

Environment assisted crack growth generally is believed to result from hydrogen embrittlement in conjunction with the mechanical driving force for crack growth. Based on the current understanding, Fig. 1 schematically illustrates the corrosion-fatigue process during crack propagation.

Free hydrogen atoms are produced at the crack tip by the chemical reactions of the hydrogeneous environments with the freshly created crack surface, as described in Fig. 1*a*. Hydrogen atoms then must be driven from the metal surface layers of the crack tip to various internal destinations in the microstructure (Fig. 1*b*). This process is governed by classical lattice diffusion, or by dislocation transport of hydrogen atoms, or both. Under cyclic loading, hydrogen atoms transferred into the matrix lattice will segregate at inhomogeneities, such as grain boundaries, matrix/constituent particle in-

[2]The italic numbers in brackets refer to the list of references appended to this paper.

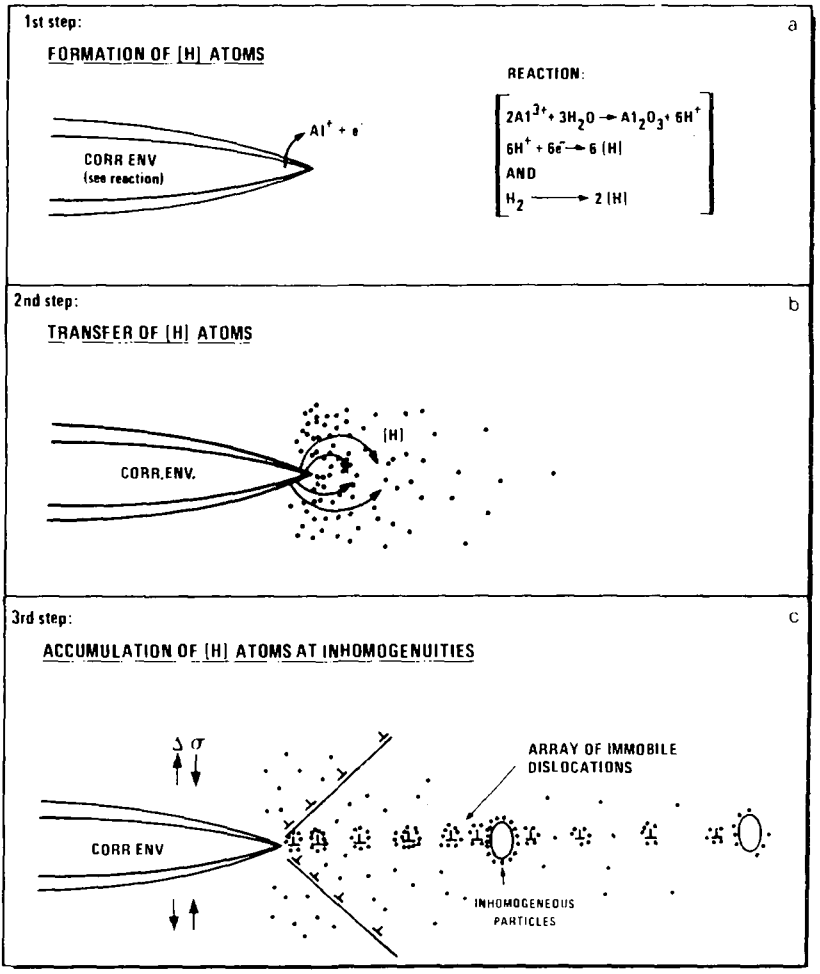

FIG. 1—*Schematic representation of a mechanism for corrosion-fatigue crack propagation due to hydrogen embrittlement.*

terfaces, or sessile dislocations, depending upon which sites provide the highest binding energy with hydrogen. Segregation of hydrogen at favorable sites makes this process completely irreversible, resulting in the continuous accumulation of hydrogen atoms (Fig. 1*c*). When the local hydrogen concentration exceeds the limit of solubility, hydrogen-filled microvoids nucleate easily. Fracture type and morphology, therefore, are affected by the type of site which is dominant in hydrogen trapping. A generalized relationship between the fracture morphology and various hydrogen segregation sites has been presented by Thompson [*14*].

The sequence of processes described previously is represented schematically in Fig. 2. Hydrogen evolution at crack-tip surfaces and subsequent transfer into the matrix, segregation at inhomogeneities, and accumulation at these sites result in nucleation of hydrogen-filled microvoids ahead of the crack tip, as shown in Fig. 2. Microvoid nucleation ahead of the actual crack tip is expected to lead to accelerated crack propagation or so-called crack growth enhancement. Corrosion-fatigue crack growth response, then, is governed by one or more of various processes, operating in sequence, that seem to involve embrittlement of high-strength aluminum alloys by hydrogen.

As a result, corrosion-fatigue fracture surfaces in general are expected to show dimples with a somewhat brittle fracture morphology. This morphology is in sharp contrast with ductile striations which usually are observed on the fracture surface of most aluminum alloys after fatigue testing in a nonaggressive environment.

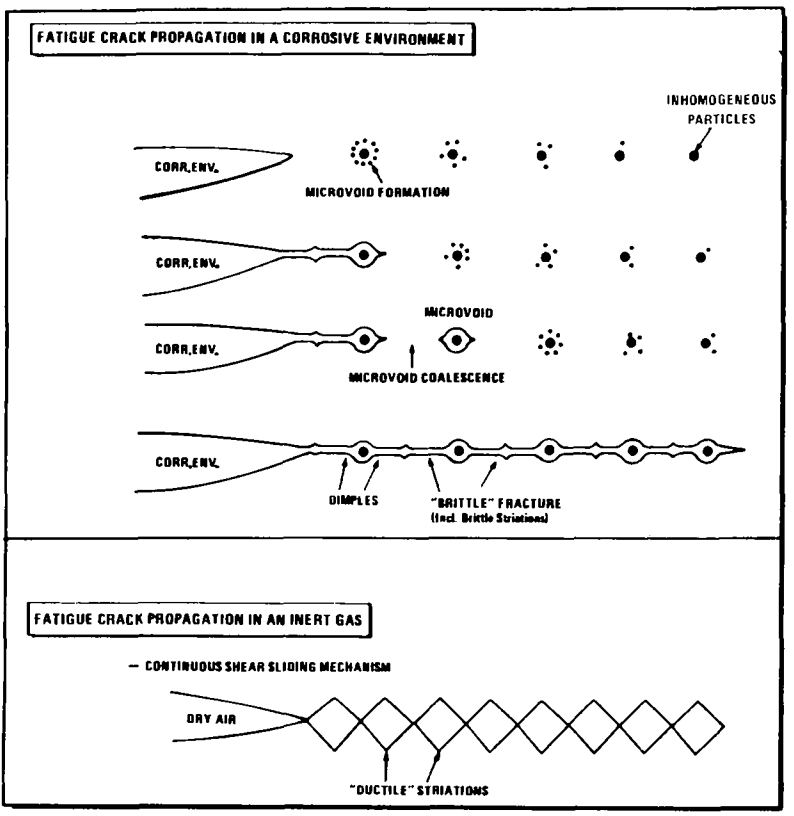

FIG. 2—*Sequence of corrosion-fatigue crack propagation based on hydrogen embrittlement mechanism and comparison of fatigue fracture surface for dry air versus corrosion environment.*

Figure 3 shows scanning electron microscopy of Aluminum 7075-T6 fatigue fracture surfaces tested in dry air and in a 3.5 percent sodium chloride (NaCl) solution. As expected from the mechanism described previously, the fracture surface in a 3.5 percent NaCl has a high density of dimples with a brittle morphology attributed to hydrogen embrittlement along the crack path; on the other hand, in lab air the fracture surface shows well-defined striations. Figure 4 shows that crack growth is nearly 100 percent transgranular for a frequency of 1 Hz, from a polished and slightly etched surface of 7075-T6 after fatigue loading in a 3.5 percent NaCl solution. This figure also indicates that the crack path is associated with constituent particles. There-

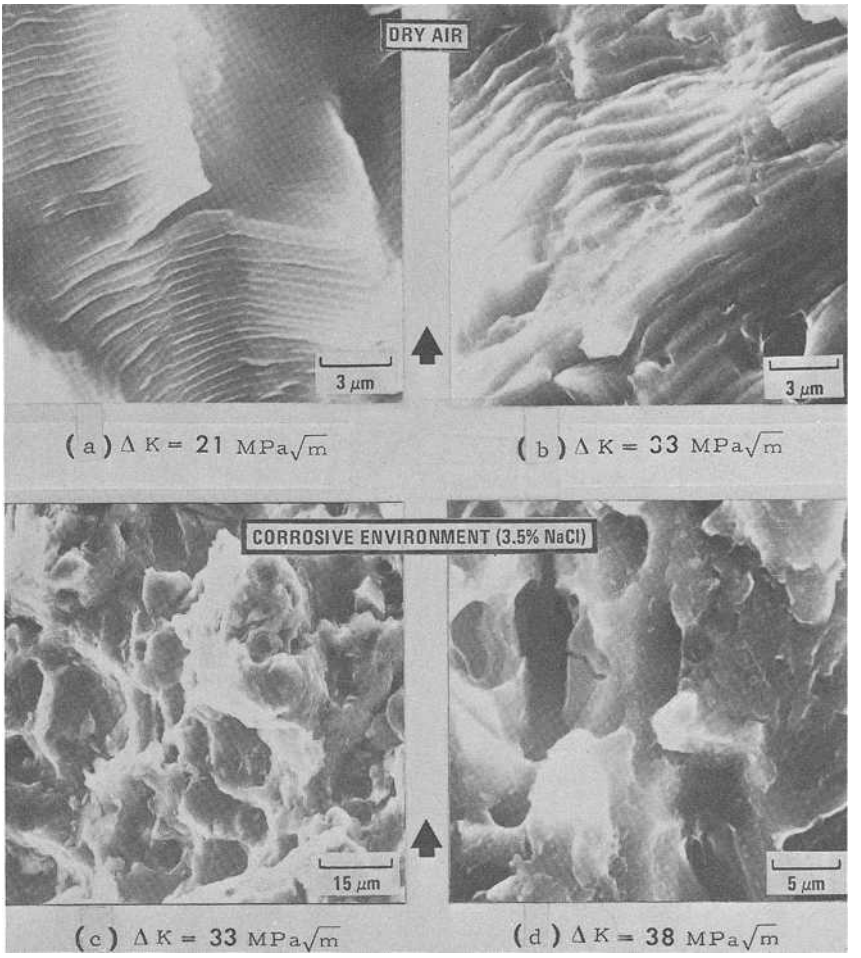

FIG. 3—*Scanning electron micrographs of 7075-T6 fatigue fracture surfaces in dry air and in a 3.5 percent NaCl solution.*

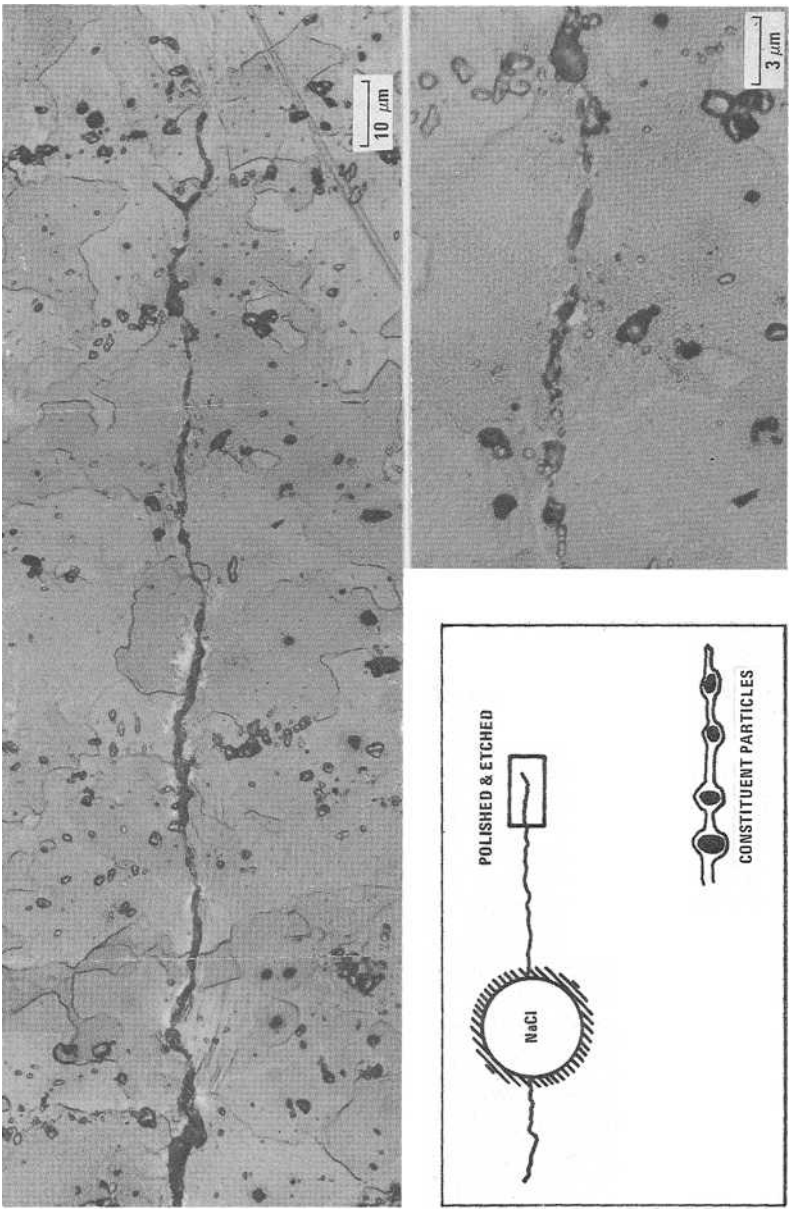

FIG. 4—*Polished and etched surface for a fatigue crack originating from an open hole in 7075-T6 after constant amplitude fatigue loading in 3.5 percent NaCl.*

fore, in 7075-T6 alloy, constituent particle interfaces and dislocation tangles are considered the dominant hydrogen accumulation sites of interest in the corrosion-fatigue crack propagation process.

Quantitative Analysis of Corrosion-Fatigue Crack Growth Rate

According to the superposition model proposed by Wei et al [*13*], fatigue crack growth rate in an aggressive environment, $(da/dN)_e$, can be expressed by the sum of three components, as described by Eq 1

$$\left(\frac{da}{dN}\right)_e = \left(\frac{da}{dN}\right)_i + \left(\frac{da}{dN}\right)_c + \left(\frac{da}{dN}\right)_{scc} \tag{1}$$

The first term, $(da/dN)_i$, is the crack growth rate in an inert environment, representing the contribution of purely mechanical fatigue. The second term, $(da/dN)_c$, is a cycle-dependent contribution requiring synergistic interaction of fatigue and environmental attack. The third term, $(da/dN)_{scc}$, is the contribution of sustained-load crack growth per cycle, that is, stress-corrosion cracking at K-levels above K_{scc}.

$(da/dN)_i$, which is the purely mechanical term, has been formulated by many people, at least for the so-called Paris' region (Region II). The pseudostatic crack growth region (Region III) is not considered to be very important in terms of total fatigue life, while the near-threshold region (Region I) is extremely important, if an initial flaw size is small enough, or if the stress level is low enough. Near-threshold fatigue crack propagation resistance in nonaggressive environments has been correlated to grain size [*15,16*] or yield strength [*17,18*], or both [*19*]. However, to the best of our knowledge, a general agreement has not been reached on a quantitative relationship between these material parameters and fatigue crack propagation rates in this region. Furthermore, the corrosion-fatigue mechanism described in this paper is believed to be more applicable to the intermediate ΔK region, where increase in crack closure stress due to oxide film formation at a crack tip [*20–22*] may not be significant.

For the materials having K_{scc} values close to K_c (that is, high relative index of stress-corrosion cracking susceptibility, K_{scc}/K_c), contribution of the sustained-load crack growth is not an important factor, since most crack growth occurs at cyclic stress intensities below the K_{scc} level. Such materials include most 7XXX series aluminum alloys in the longitudinal direction. Therefore, $(da/dN)_{scc}$ may be only of academic interest, while $(da/dN)_c$ is quite important for these alloys. However, transverse directions for aluminum alloys and some high-strength titanium and steel alloys [for example, *10,11*] often indicate a low stress-corrosion cracking susceptibility index. For these conditions, both terms are believed to be equally important. These cases, however, will not be explored in this paper.

Crack Growth Enhancement Due to Load-Environment Interaction

The second term of the superposition model, shown in Eq 1, represents the cycle-dependent contribution from the synergistic interaction of fatigue loading and environmental attack. Based on the mechanism previously described, this term can be interpreted as the crack growth enhancement resulting from microvoid nucleation due to hydrogen accumulation at inhomogeneities ahead of a crack tip. It can be derived mathematically using two plausible assumptions: (1) hydrogen penetration distance (PD) is proportional to the plastic zone size (PZS) and the diffusion distance, and (2) hydrogen concentration in the matrix varies linearly as a function of distance from the crack tip. These assumptions are schematically represented in Fig. 5.

PD then is expressed by Eq 2

$$\text{PD} = \alpha[(\Delta K)^2/\pi(\sigma'_0)^2]\sqrt{Dt} \tag{2}$$

where α is a proportional constant, ΔK the cyclic stress-intensity amplitude, σ'_0 the cyclic yield stress, D the diffusivity of hydrogen in aluminum, and t the time available for reaction. The hydrogen concentration around a sessile dislocation at a crack tip, $C_\perp$, has been reported in the literature [*23*] as given by Eq 3

$$C_\perp = C\sqrt{p}\exp(-G_B/RT) \tag{3}$$

where C is the hydrogen concentration in the surrounding matrix, p the pressure, G_B the binding energy of hydrogen atoms to a dislocation, R the gas constant, and T the absolute temperature.

From the assumption of a linear variation of the hydrogen concentration as a function of distance, the number of hydrogen atoms accumulated during the nth cycle at a dislocation located at a distance X from the crack tip, $D_n'(X)$ may be expressed by Eq 4

$$D_n'(X) = \beta \times C_\perp\left(1 - \frac{X}{PD}\right) \tag{4}$$

where β is a proportional constant.

An arbitrary point (X_0) can be chosen at or within PD for calculation purposes. However, it is more convenient to select a point at the boundary of PD and PZS, where the first cycle considered in calculation results in the first accumulation of hydrogen atoms. If some other reference points within PD are chosen, one has to calculate the number of hydrogen atoms already accumulated during the prior cycles.

At $X_0 = PD$, the distance X is also a function of the number of cycles (n) and is given by $PD - \{(2n - 1)/2\} \times \delta a$, where δa represents crack growth

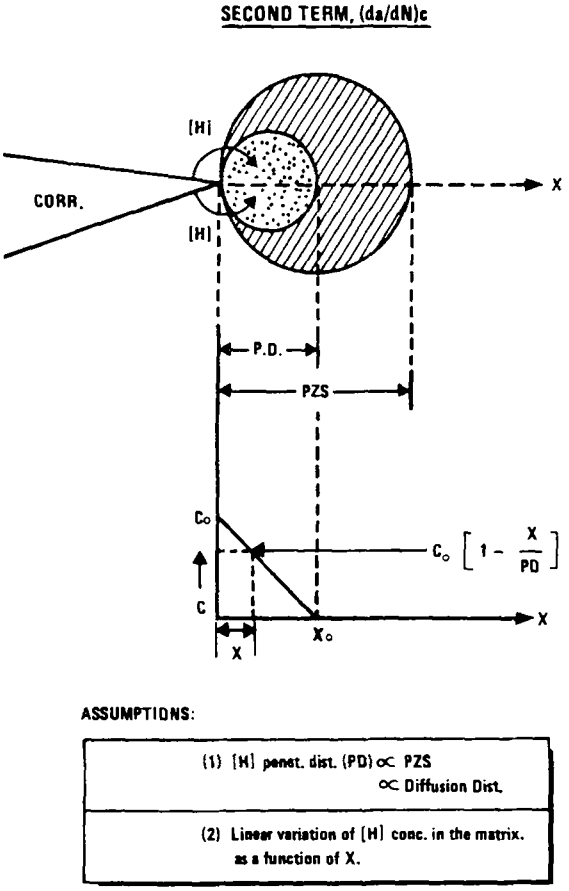

FIG. 5—*Schematic illustration of the assumptions used for deriving* $(da/dN)_c$.

increment per cycle. Using the criterion that a local fracture occurs at $X_0 = PD$ when the accumulated damage exceeds a critical value, D_c^*, Eq 5 may be established when $PD/\delta a \gg 1$. (In general, PD is considered to be several hundred times greater than δa in the Paris region.)

$$\sum_{n=1}^{PD/\delta a} D_n'(X) = \tfrac{1}{2}\beta C_\perp \frac{PD}{\delta a} = D_c^* \tag{5}$$

Substituting Eqs 2, 3, and 4 into Eq 5 leads to Eq 6

$$\left.\frac{da}{dN}\right|_c = \delta a = A \times \exp(-G_B/RT) \times \sqrt{pDt} \times \left(\frac{\Delta K}{\sigma_0'}\right)^2 \tag{6}$$

In Eq 6, A is a proportional constant and the other parameters already have been defined.

Equation 6 provides a quantitative basis for predicting the effect of various parameters on the cycle-dependent crack growth enhancement. For example, an increase in pressure increases the degree of crack growth enhancement; whereas an increase in frequency (which is the reciprocal of the time available for reaction) decreases the degree of enhancement. An increase in ΔK amplifies the crack growth enhancement in proportion to the square of ΔK.

Crack growth rates, da/dN, were obtained using simple dog-bone 7075-T6 specimens. Each specimen contained a single open fastener hole and reflected a K_t of 2.4. Crack growth rates were determined for lab air and a 3.5 percent NaCl solution. Plots of da/dN versus ΔK are shown in Fig. 6 in a log-log scale. Based on Fig. 6, the crack growth rates in a 3.5 percent NaCl solution are approximately 70 to 100 percent faster than in dry air. Figure 7 also shows that the crack growth rates for 0.3 Hz are about 30 to 60 percent faster than for 1 Hz in a 3.5 percent NaCl solution.

Some of the crack growth rate data in dry air was subtracted from the corresponding 3.5 percent NaCl data for 1 Hz and 0.3 Hz, so that the resulting values may correspond to the second term of the superposition model. Experimental values so determined were plotted against ΔK in a log-log scale, as shown in Fig. 8. The slope for 0.3 Hz was 2.8 and that for 1 Hz was 2.5 while our predicted value from Eq 6 was 2.

Application of the Superposition Model to Spectrum Loading Case

Spectrum loading can be input into a computer as a series of stresses and corresponding time increments. The stress history is simplified, so that it contains only peaks and valleys and the time at which they are applied. Stress levels are then joined by a haversine wave, as shown in Fig. 9.

For spectrum loading, the superposition model described in the previous sections must be modified for load interaction and load fluctuation. Since the present algorithm accounts for the effects of cyclic stress-intensity amplitude (ΔK), R ratio, frequency, and cyclic yield stress along with some other factors, it can be applied to various loading spectra, assuming that currently existing load interaction models [*24-26*] are applicable. The amount of retardation was reported [*27,28*] to be substantially less in a corrosive environment than in dry air for the same ΔK and overload ratio. However, this observation does not necessarily imply that a retardation model for a nonaggressive environment cannot be used for the corrosion fatigue case. This may be attributed simply to the fact that fewer cycles are required in the corrosive environment for a fatigue crack to propagate through the previously formed zone created by the overload, because the crack growth rate is higher in the corrosive environment. Further investigation, however, is needed for this presumption.

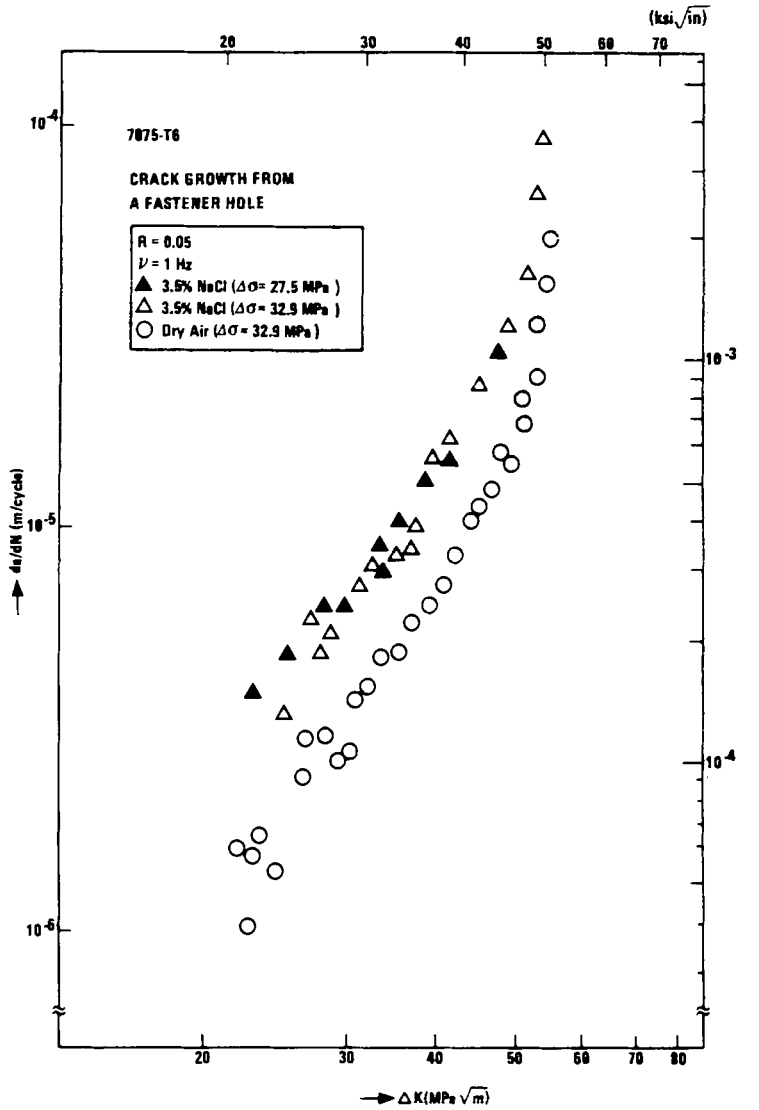

FIG. 6—da/dN *versus* ΔK *for an open hole* (K_t = *2.4) in dry air and in 3.5 percent NaCl for 7075-T6 alloy.*

The mean stress level of each cycle, denoted by R_j for the jth cycle in Fig. 9, is expected to affect the sustained load crack growth, if it is higher than one half of the K_{scc} level. However, the effects of mean stress on the sustained crack growth for the aluminum alloys investigated in this study are considered to be negligible, as discussed earlier. Thus, R_j mainly affects the first term of superposition model, while the second term is primarily a function of

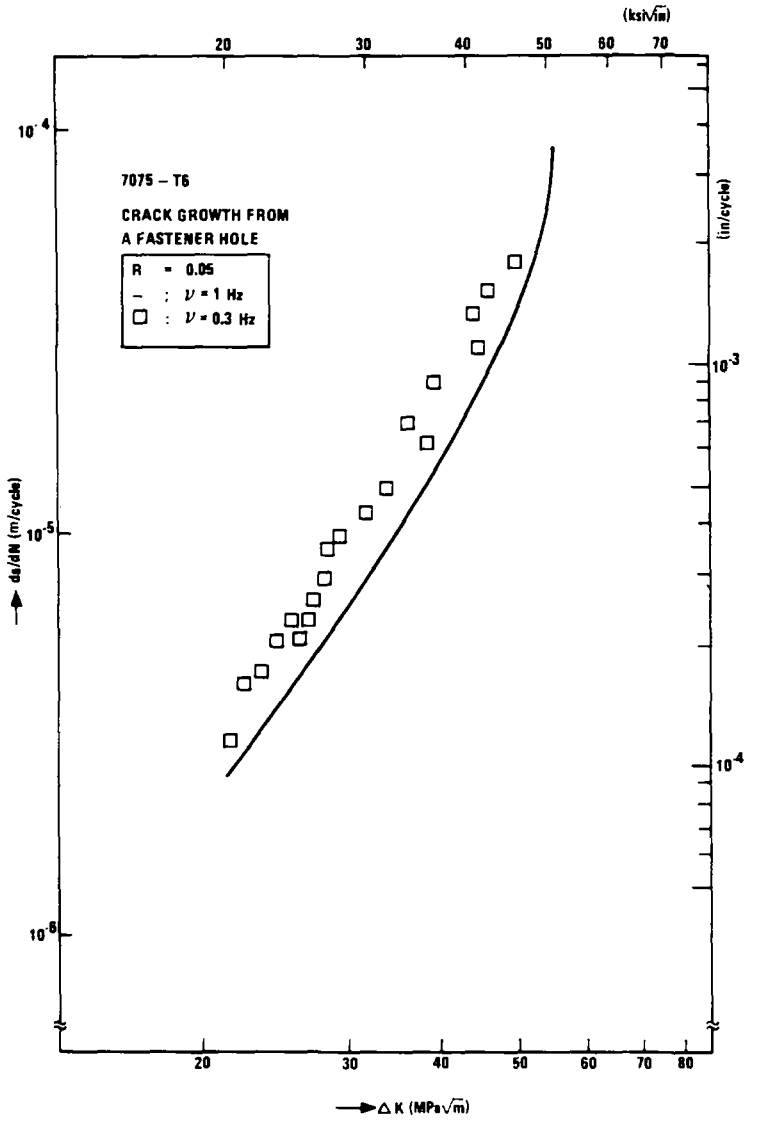

FIG. 7—da/dN *versus* ΔK *for an open hole* (K_t = *2.4) at frequencies of 1 Hz and 0.3 Hz in 3.5 percent NaCl for 7075-T6 alloy.*

time available for the cycle.[3] For both terms, the effective cyclic stress amplitude, $(\sigma_j - \sigma_{j-1})_{\text{eff}}$, adjusted for the retardation effect should be used.

[3]However, we also recognize that some work addressing the effect of the mean stress on the crack growth enhancement, based on the surface-reaction controlled process, is in progress by R. P. Wei's group at Lehigh University.

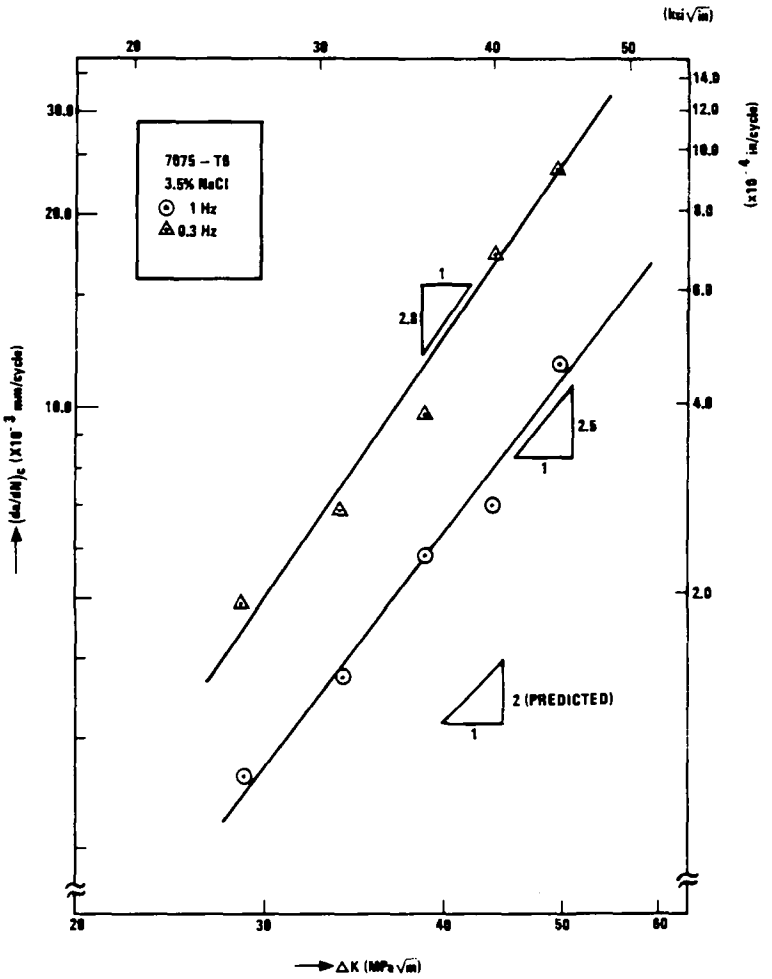

FIG. 8—$da/dN|_c$ *(cycle-dependent crack growth enhancement) versus* ΔK *at frequencies of 1 Hz and 0.3 Hz in 3.5 percent NaCl for 7075-T6 alloy.*

The equations shown in Fig. 9 illustrates how the superposition model can be used for spectrum loading. A, B, n, and m are empirical constants required as input information, and mean stress (R_j) and reciprocal of frequency (t_j) are automatic inputs from the spectrum tape for equivalent cycle-by-cycle loading. Therefore, a total crack length can be obtained by iterative evaluation of the equations in Fig. 9 for all the cycles.

Figure 10 is a part of a simplified flow chart for programming to predict crack growth behavior in a corrosive environment. It includes the following steps: (1) calculate ΔK_{eff} either by the Wheeler model [*24*] or by the MPYZ

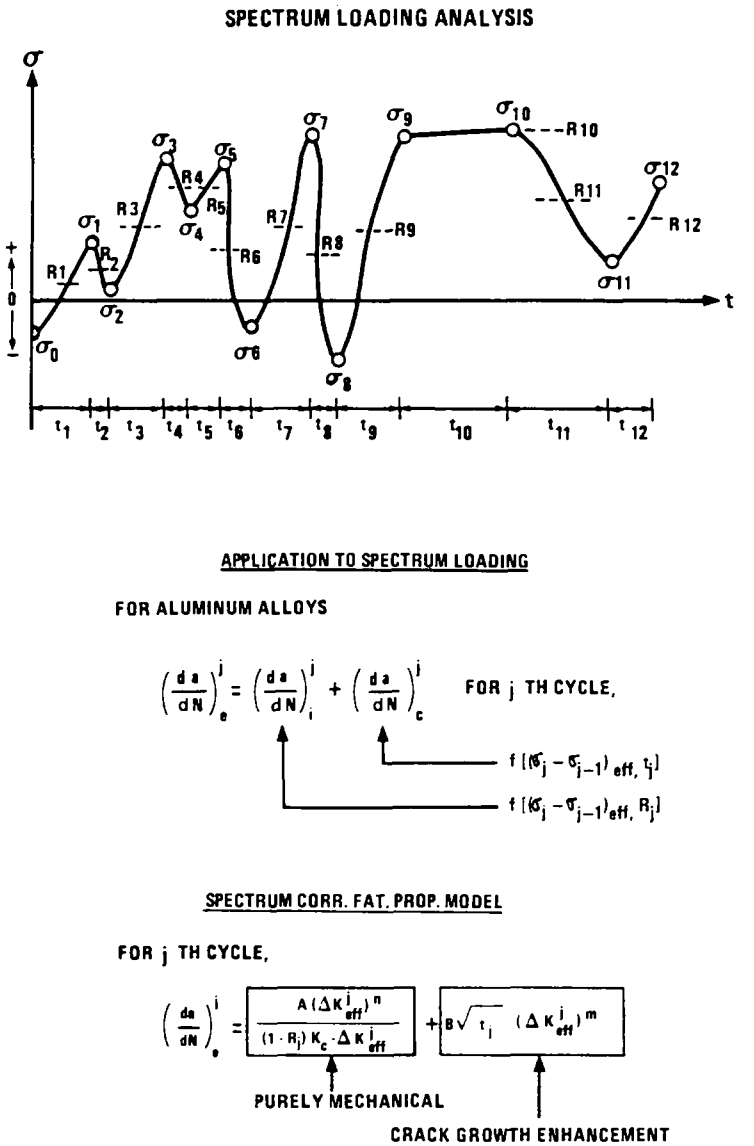

FIG. 9—*Schematic illustration of the application of the superposition model for spectrum loading.*

model [*26*], (2) calculate the first term either by Paris' equation or by Forman's equation, using the ΔK_{eff} determined, (3) calculate the second term by our proposed model, using same ΔK_{eff}, (4) sum the two terms, and (5) add the crack growth increment to the original crack size. This procedure can be

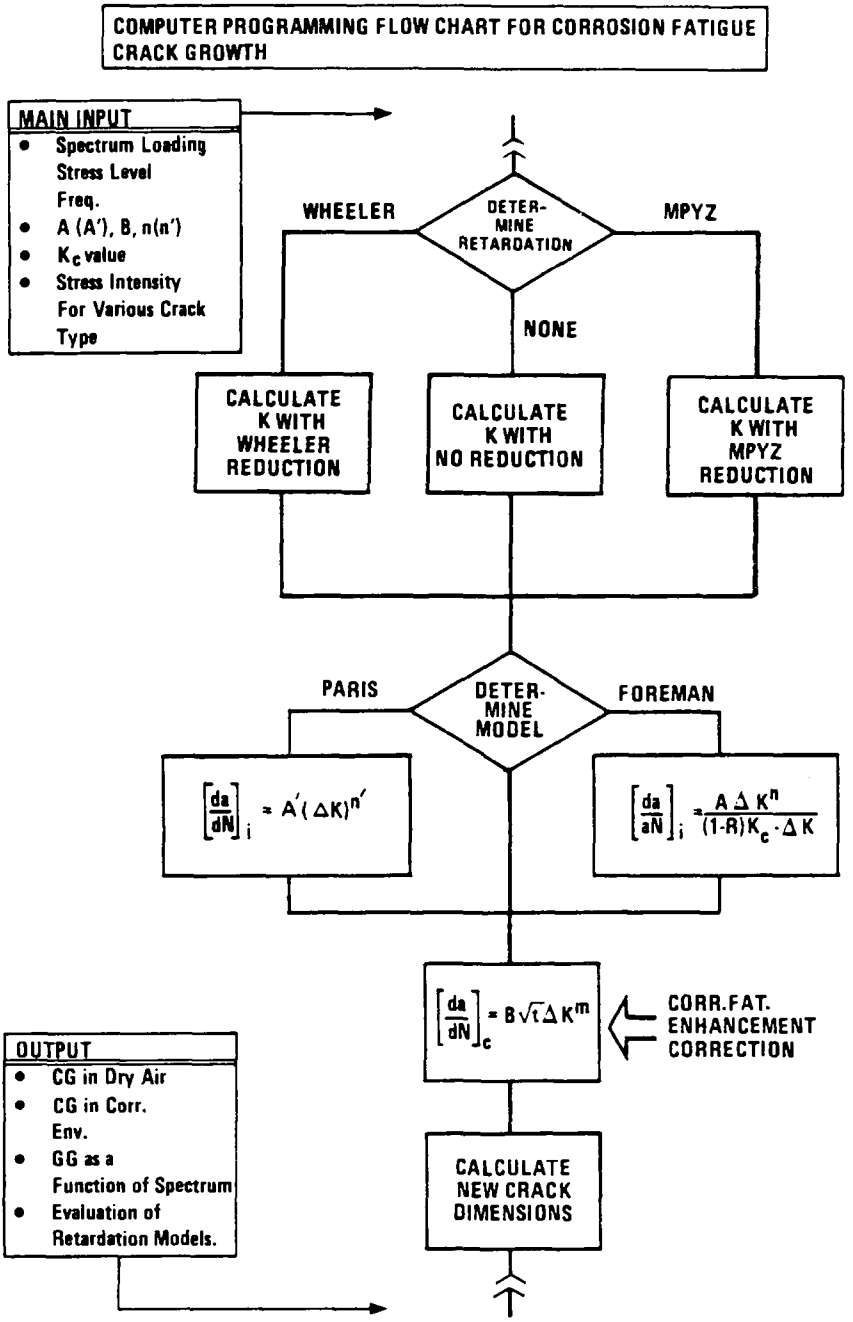

FIG. 10—*A simplified flow chart for progamming corrosion-fatigue crack growth predictions under spectrum loading.*

done iteratively to predict corrosion-fatigue crack lengths, as a function of time or number of cycles of peak stresses. The model described for characterizing crack propagation due to the cycle-dependent interaction of spectrum fatigue loading and environment will be developed further and evaluated under an ongoing Navy program [*29*].

Summary

1. A three-step procedure for corrosion-fatigue crack growth behavior for aluminum alloys was proposed based on the current understanding. This procedure includes the following processes: (1) formation of hydrogen atoms at a crack tip, (2) transfer of the hydrogen into microstructure, and (3) continuous accumulation of the hydrogen at inhomogeneities while cycling.

2. The second term of the superposition model (cycle-dependent enhancement) was determined theoretically based on the mechanism described previously. Our limited experimental data agreed reasonably well with the predicted dependence of ΔK on this term.

3. Quantification of the superposition model for various load spectra was described briefly.

Acknowledgments

This research was supported by General Dynamics, Fort Worth Division. The authors thank M. S. Rosenfeld, P. Kozel, and E. Lee of the Naval Air Development Center for stimulating discussions and R. P. Wei of Lehigh University for critically reviewing the manuscript.

References

[*1*] Krafft, J. M. and Cullen, W. H., Jr., *Engineering Fracture Mechanics*, Vol. 10, 1978, p. 609.

[*2*] Crooker, T. W. and Lange, E. A. in *Effects of Environment and Complex Load History on Fatigue Life, ASTM STP 462*, American Society for Testing and Materials, 1970, pp. 258-271.

[*3*] Fisher, P. and DeLuccia, J. J. in *Environmental Effects on Advanced Composite Materials, ASTM STP 602*, American Society for Testing and Materials, 1976, pp. 50-66.

[*4*] Gallagher, J. P. and Wei, R. P. in *Corrosion Fatigue: Chemistry, Mechanics and Microstructure*, NACE-2, O. F. Devereux, A. J. McEvily, and R. W. Staehle, Eds., Univeristy of Connecticut, Storrs, Conn., June 1971, p. 409.

[*5*] Duquette, D. J. in *Fatigue and Microstructure*, M. Meshii, Ed., American Society for Metals, Oct. 1978, p. 335.

[*6*] Marcus, N. L. in *Fatigue and Microstructure*, M. Meshii, Ed., American Society for Metals, Oct. 1978, p. 365.

[*7*] Wei, R. P., Pao, P. S., Hart, R. G., Weir, T. W., and Simmons, G. W., *Metallurgical Transactions A*, Vol. 11A, 1980, p. 151.

[*8*] Lu, M., Pao, P. S., Weir, T. W., Simmons, G. W., and Wei, R. P., *Metallurgical Transactions A*, Vol. 12A, 1981, p. 805.

[*9*] Wei, R. P. and Simmons, G. W., "Surface Reactions and Fatigue Crack Growth," presented at 27th Sagamore Army Materials Research Conference, New York, July 1980.

[10] Dill, H. D. and Saff, C. R., "Environment-Load Interaction Effects on Crack Growth," Technical Report AFML-TR-78-137, McDonnell Aircraft Co., St. Louis, Mo., Nov. 1978.

[11] Saff, C. R. and Rosenfeld, M. S., "Load-Environment Interaction Effects on Crack Growth in Landing Gear Steels," presented at 14th National Symposium on Fracture Mechanics, 1981; Saff, C. R., "Environment-Load Interaction Effects on Crack Growth in Landing Gear Steels," Technical Report No. NADC-79095-60, McDonnell Aircraft Co., St. Louis, Mo., Dec. 1980.

[12] Wei, R. P. and Landes, J. D., *Materials Research and Standards*, Vol. 9, No. 7, 1969, p. 25.

[13] Wei, R. P. and Simmons, G. W., "Recent Progress in Understanding Environment Assisted Fatigue Crack Growth," Technical Report No. 8, Office of Naval Research Contract N00014-75-C-0543, NR 036-097, Jan. 1979.

[14] Thompson, A. W. in *Environmental Degradation of Engineering Materials*, M. R. Louthan, Jr. and R. P. McNitt, Eds., Virginia Polytechnic Institute, Blacksburg, Va., 1977, p. 3.

[15] Kim, Y. H., unpublished work, General Dynamics, Fort Worth, Tex., 1981.

[16] McKittrick, J., Liaw, P. K., Kwun, S. I., and Fine, M. E., *Metallurgical Transactions A*, Vol. 12A, 1981, p. 1535.

[17] Ritchie, R. O., *Journal of Engineering Materials and Technology, Transactions*, American Society of Mechanical Engineers, Series H, Vol. 99, 1977, p. 195.

[18] Suzuki, H. and McEvily, A. J., *Metallurgical Transactions A*, Vol. 10A, 1979, p. 475.

[19] Yoder, G. R., Cooley, L. A., and Crooker, T. W., in this publication, pp. I-348–I-365.

[20] Ritchie, R. O., Suresh, S., and Moss, C. M., *Journal of Engineering Materials and Technology, Transactions*, American Society of Mechanical Engineers, Series H, Vol. 102, 1980, p. 293.

[21] Suresh, S., Toplosky, J., and Ritchie, R. O., in this publication, pp. I-329–I-347.

[22] Liaw, P. K., Hudak, S. J., Jr., and Donald, J. K., in this publication, pp. II-370–II-388.

[23] West, A. J. and Louthan, M. R., Jr., *Metallurgical Transactions A*, Vol. 10A, 1979, p. 1675.

[24] Wheeler, O. E., *Journal of Basic Engineering, Transactions*, American Society of Mechanical Engineers, Series D, Vol. 94, 1972, p. 181.

[25] Willenborg, J. D., Engle, R. M., Jr., and Wood, H. A., "A Crack Growth Retardation Model Using Effective Stress Concept," Technical Report AFFDL-TM-71-1-FBR, Air Force Flight Dynamics Laboratory, Jan. 1971.

[26] Garver, W. R. and Johnson, W. S., "An Evaluation of the MPYZ Crack Growth Retardation Model for Durability and Damage Tolerance Analysis," ERR-FW-1956, General Dynamics, Fort Worth, Tex., Dec. 1978.

[27] Chanani, G. R. in *Corrosion Fatigue Technology, ASTM STP 642*, American Society for Testing and Materials, 1978, p. 51–73.

[28] Hagemeyer, J. W., "Overload Induced Retardation of Fatigue Cracks in Several Aluminum and Titanium Alloys," ERR-FW-1779, General Dynamics, Forth Worth, Tex., Dec. 1976.

[29] "Development of Fatigue and Crack Propagation Design and Analysis Methodology in a Corrosive Environment for Typical Mechanically Fastened Joints," Solicitation No. N62269-80-R-0273, Report FZP-2049, General Dynamics, Fort Worth, Tex., July 1980.

W. R. Brose[1]

Correlation of Smooth and Notched Body Stress Corrosion Crack Initiation

REFERENCE: Brose, W. R., **"Correlation of Smooth and Notched Body Stress Corrosion Crack Initiation,"** *Fracture Mechanics: Fourteenth Symposium—Volume I: Theory and Analysis, ASTM STP 791*, J. C. Lewis and G. Sines, Eds., American Society for Testing and Materials, 1983, pp. I-463-I-481.

ABSTRACT: A method is presented for predicting the stress corrosion crack initiation (environment-induced crack initiation) resistance of notched components from the results of smooth (unnotched) specimen tests. The predictive procedure is based on the maximum principal surface strain failure criterion and uses Neuber's rule to estimate notch root strains. It is capable of handling elastic-plastic notch stress-strain behavior. The method is shown to be accurate in predicting the results of tests on two notched geometries, representing very different stress gradients, and a number of notch radii corresponding to a wide range of stress concentration factors. A material-environment system was employed in which hydrogen-induced cracking occurs, specifically a 1194 MPa (173 ksi) yield strength NiCrMoV steel exposed to 345 kPa (50 psig) hydrogen sulfide gas. Some additional data pertaining to the definition of crack initiation and the effect of constraint were generated and discussed in terms of their effect on the accuracy of the prediction procedure. The results of the work indicate that the stress corrosion crack initiation resistance of structures and machine parts which contain stress raisers can be predicted by laboratory tests with specimens of much simpler geometries.

KEY WORDS: prediction, stress corrosion crack initiation, notches, nickel-chromium-molybdenum-vanadium steel, hydrogen sulfide, geometry effects, Neuber's rule, fracture mechanics

Little information is available regarding geometry effects on stress corrosion crack initiation (environment-induced crack initiation) behavior. Of the information available, much is qualitative or fails to distinguish between crack initiation and crack propagation performance. Geometry effects include stress concentration, state-of-stress, and stress gradient. Consideration of these factors is necessary when applying stress corrosion data developed

[1]Senior engineer, Materials Engineering Dept., Westinghouse Research and Development Center, Pittsburgh, Pa. 15235.

with one type of test specimen geometry to a component with a different geometry and possibly a different loading mode. Also, laboratory data generated with different specimen geometries should correlate, of course.

Recently, Lee, Goldenberg, and Hirth [*1,2*][2] and Hirose and Tanaka [*3*] were able to correlate the environment-induced crack initiation behavior of notched specimens. Lee's correlation was based on measured principal notch strain, while Hirose's involved the $K/\sqrt{\rho}$ parameter, an indirect measure of notch stress-strain level. Each study employed a single notched specimen geometry and several radii.

The present work is concerned with the relationship between smooth (unnotched) and notched body performance. Often, stress corrosion data are generated with a smooth specimen geometry and the results are applied to a part containing a notch of some type. In light of this practice, a quantitative procedure is established here for predicting the stress corrosion crack initiation resistance of notched parts from stress corrosion tests on smooth uniaxial tension specimens. The proposed prediction procedure involves the maximum principal strain failure criterion and employs Neuber's rule to estimate notch root strains. An important feature of the procedure is that it can handle strains beyond yield as easily as completely elastic strains.

In order to establish the limits of applicability of the predictive method, experimental data were obtained on a wide range of specimen geometry-notch radii combinations, as well as on smooth tension specimens. Specifically, two notched specimen types were selected, representing the extremes of stress gradient (uniform tension versus bending) across their net sections. Notch radii were chosen giving stress concentration factors from 2.8 to 16.4. One material-environment system was employed, a 1194 MPa (173 ksi) yield 3.5 percent nickel-chromium-molybdenum-vanadium (NiCrMoV) steel exposed to 345 kPa (50 psig) hydrogen sulfide (H_2S) gas. This system results in hydrogen-induced cracking, and was selected because it is fast-acting and convenient in terms of test result interpretation.

In general, a complete picture of the environment-induced crack initiation behavior of a given material-environment system can be represented by a stress (or strain) versus time-to-cracking curve. The curve may or may not involve a threshold level below which the time to crack initiation is infinite. For the present material-environment system, this threshold level apparently does exist, and above it crack initiation occurs almost instantaneously. All the test results in this paper represent this threshold level.

The test data are presented in terms of specimen failure (separation in two pieces). However, crack initiation was essentially coincident with failure for the subject material-environment system, as will be demonstrated experimentally. Thus, the terms "initiation" and "failure" are interchangeable in this report.

[2]The italic numbers in brackets refer to the list of references appended to this paper.

Some additional data on the effect of constraint also are given, as are fractographic observations.

Analysis

In this paper, the prediction of notch stress corrosion crack initiation is based on the notch surface stress-strain behavior. However, it is often inconvenient to deal with notch stress and strain directly. Therefore, analysis is provided for relating the notch conditions to two other parameters: nominal stress, S, and the fracture mechanics term, stress intensity, K. The representation employing K is addressed in the following paragraph.

Consider a part under load with a notch of a given depth and radius. If the part is treated as if it contains a crack (instead of a notch) whose depth equals that of the notch, a pseudo-stress intensity, K, can be calculated with the appropriate fracture mechanics K-solution. A "fictitious elastic stress," σ_e, which is the notch surface stress assuming completely elastic conditions, is calculated by the so-called $K/\sqrt{\rho}$ relationship [4]

$$\sigma_e = \frac{2}{\sqrt{\pi}} \frac{K}{\sqrt{\rho}} \tag{1}$$

where ρ is the notch radius. This relationship first was employed in the analysis of stress corrosion crack initiation data by Clark [5]. Its accuracy has been established by finite element results [6]. While widely applicable, it should be noted that there are certain geometries for which the equation results in significant error [7].

The nominal stress, S, on a notched part is calculated without accounting for the effects of stress concentration or plasticity. The relation between true notch surface stress, σ, and strain, ϵ, and nominal stress is given by Neuber's rule [8]

$$\sigma \epsilon = \frac{(k_t S)^2}{E} \tag{2}$$

where k_t is the theoretical stress concentration factor and E is the elastic modulus. Note that k_t must be defined in a manner consistent with the method of determining S, so that the product $k_t S$ is the same for different methods of calculating these factors (for example, gross section versus net section stress). Also, the nominal stress must be below yield for this version of Neuber's rule to be valid.

Since the fictitious elastic stress from Eq 1 is identical to $k_t S$

$$\sigma_e = k_t S \tag{3}$$

Equations 1 and 2 can be combined and rearranged to form

$$\frac{K}{\sqrt{\rho}} = \frac{\sqrt{\pi\sigma\epsilon E}}{2} \tag{4}$$

For a stress-strain point representing the threshold resistance to stress-corrosion crack initiation in a smooth specimen, a specific value of $K/\sqrt{\rho}$ is indicated. That is, the resistance of a notch with a given radius is predicted in terms of its pseudo-stress intensity. On a plot of initiation K versus $\sqrt{\rho}$, different notch radii are expected to be correlated by a straight line representing the appropriate value of $K/\sqrt{\rho}$. (Such a plot is shown later in this paper in Fig. 4.)

The $K/\sqrt{\rho}$ criterion predicts that the notch resistance approaches zero as the notch becomes sharper. But the cracked body behavior, represented by K_{Iscc}, is considered to be the lower bound on notch resistance. This limit is represented by a horizontal line on the K versus $\sqrt{\rho}$ plot. The overall prediction scheme then is represented by a two-segment line (the solid line in Fig. 4).

Another method of characterizing notched part stress corrosion crack initiation behavior is through the use of nominal stress. Neuber's rule, Eq 2, can be rearranged to give

$$k_t S = \sqrt{\sigma\epsilon E} \tag{5}$$

Recalling that smooth specimen resistance is represented by a stress-strain point, notched behavior is given by a specific value of the product $k_t S$. On a plot of critical (for initiation) nominal stress versus k_t, notched specimen performance would be correlated by a hyperbola representing the appropriate value of $k_t S$. (As shown later, Fig. 5 is an example of such a plot.) A different lower bound line (value of S) corresponding to K_{Iscc} is needed for each geometry since the relationship between K and S is geometry dependent.

The analyses defined in the preceding section will be employed to predict notch resistance, from the smooth specimen test results, in terms of both K and S. The analyses are done only once since plots are constructed that yield a prediction for any notch. For a given notched part, K and S are linearly related to load. Thus, the notched specimen test results can be converted easily to values of K and S, which in turn can be compared with the predicted values.

Experimental Procedure

The test material used in this investigation was a 3.5NiCrMoV steel [similar to the ASTM Specification for Vacuum-Treated Alloy Steel Forgings for Turbine Rotor Disks and Wheels, A 471-77 (1982)] with a yield strength of about 1194 MPa (173 ksi) and a bainitic microstructure. The range of room

temperature tensile, Charpy, and fracture toughness properties found in the original piece of material is given in Table 1.

Four specimen types were tested, as shown in Fig. 1. Two of them, the straight tension and tapered tension, are considered "smooth" specimens, and the other two are notched specimens. Most of the smooth specimen testing was conducted with the straight tension specimen. The tapered tension specimen [9] is sometimes favored in static load stress corrosion testing because it can provide information over the range of stresses along its length. The stress at the maximum diameter of the test section is 54 percent of that at the minimum diameter.

The two notched specimens are the notched compact and circumferentially notched round, here simply called notched round. Table 3 gives the notch radii and k_t values employed. The compact specimen is common in fracture mechanics testing where a fatigue-induced precrack is used instead of a finite radius notch. Some fatigue precracked compact specimens also were tested in this investigation.

TABLE 1—*Mechanical properties at room temperature.*

3.5NiCrMoV Steel, 1194 MPa (173 ksi) nominal yield strength	
Yield strength, MPa (ksi)	1173 to 1214 (170 to 176)
Ultimate tensile strength, MPa (ksi)	1311 to 1352 (190 to 196)
True fracture strength, MPa (ksi)	1856 to 2077 (269 to 301)
Reduction in area, %	45 to 55
Charpy impact energy, m·N (ft·lb)	48 to 54 (35 to 40)
Fracture toughness, MPa·$m^{1/2}$ (ksi·$in.^{1/2}$)	160 to 182 (145 to 165)

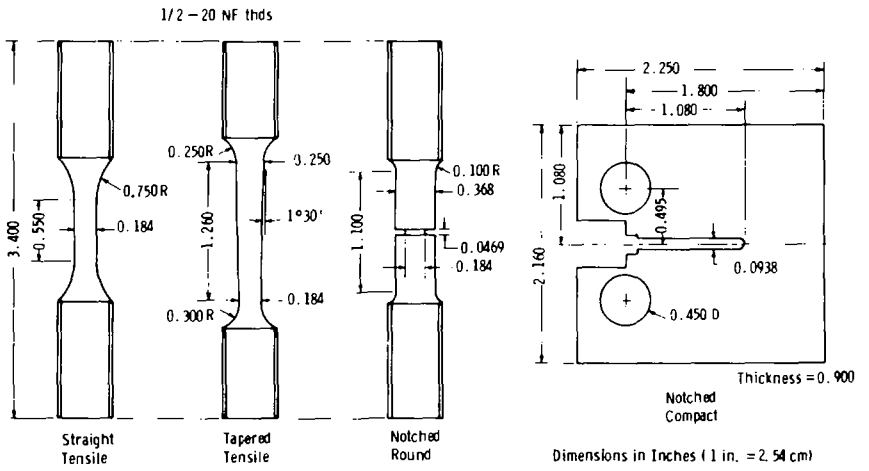

FIG. 1—*Smooth and notched stress-corrosion crack initiation specimens.*

The two notched geometries represent very different nominal stress gradients across their net sections. The stress distribution across the minimum diameter of the round is uniform, while a decreasing stress gradient exists across the ligament of the compact specimen due to the bending forces present.

The smooth specimens were fabricated by single-point machining on a lathe. To minimize surface metal disturbance, the last few passes were shallow and then several polishing steps were performed with successively finer grit. The notched specimens also were fabricated by a point machining type process, although the techniques involved are somewhat different than that for the smooth specimens. The notched specimens also are polished, but by honing rather than by using abrasive paper.

The environmental tests were conducted in an austenitic stainless steel chamber. Force was transmitted from a servo-controlled electro-hydraulic test machine to the specimen inside the chamber via O-ring sealed pull rods extending through the chamber walls. After installing a specimen in the chamber and sealing it, the chamber was evacuated. It then was backfilled with H_2S gas to a pressure of 345 kPa (50 psig). The bottled gas was commercial purity (CP) grade, minimum purity 99.5 percent.

A rising load technique [*10*] was employed in which, as opposed to static load testing, the load slowly and continuously increases. All tests were conducted under stroke (ram deflection) control at a stroke rate maintained constant throughout a given test. Specimens were brought to an initial load (preload) corresponding to a true stress of about one half of yield before applying the stroke rate to be used for the remainder of the test. The stroke rates selected (different for each specimen geometry) corresponded to a strain rate of about 2×10^{-6} s^{-1}. More detail on strain rate will be given with the test results.

In the H_2S tests on the straight tension specimens it was inconvenient to attach a deflection gage directly to the specimen test section. Consequently, a clip gage was used to measure deflection between the two clevises into which specimens were threaded. This arrangement also was used for the tapered tension and notched round specimens. For the compact specimens, a similar type of gage was employed, but deflection was measured directly on the specimen at the load line. A heavy wax coating prevented the gages from being affected by the H_2S. Load versus deflection was recorded autographically in all tests.

Some air environment tests were conducted on the straight tension specimens in which a 1.27-cm (0.5-in.) clip-on gage with knife edges was attached to the specimen test section; a clevis-to-clevis clip gage also was attached to these specimens. A comparison between results from both gages was made, yielding an accurate calibration for subsequent testing in H_2S gas. A similar calibration was obtainced for the tapered tension specimens by using metal foil strain gages at the minimum section. The foil gages had a gage length of

about 0.041 cm (0.016 in.) and were accurate up to a strain of 0.06, according to manufacturer's specifications.

In both air and H_2S gas environments, some tests were terminated before failure and the specimens were examined for evidence of stable crack growth. In the case of the smooth specimens, their surfaces were examined via a scanning electron microscope (SEM). In one case, a straight tension specimen tested in air, a longitudinal metallographic section was prepared and examined for the presence of cracks by optical microscopy at $\times 1000$ magnification. The notched specimens, both compact and round, that were terminated before failure were heat tinted, then cooled with liquid nitrogen and fractured. A small crack extending from a notch root would be visible due to the heat tint.

Results and Discussion

In this section, the smooth specimen test results are presented first, along with information on the effect of strain rate. The notched specimen results then are given and are compared with the predictions based on the smooth specimen results. Following this discussion, test results are presented that bear on two factors possibly affecting the observed stress corrosion crack initiation behavior, these being constraint and the difference between crack initiation and propagation.

Smooth Specimen Behavior

All the smooth specimen test results are given in Table 2. The stress-strain behavior obtained on a straight tension specimen of the test material is shown in Fig. 2 along with the median failure strain in H_2S. Up to the H_2S failure point, the stress-strain curves in air and H_2S had the same shape. The fracture strain in H_2S was much less than in air, of course, around 0.054 compared to a true fracture strain of 0.892. The latter value was converted from a measured reduction in area of 59 percent. The most important feature illustrated in Fig. 2 is that the critical point for failure (which coincides with crack initiation) is well into the plastic range of deformation behavior. The stress corrosion predictive methodology presented here is capable of handling this plasticity.

The baseline strain rate for the H_2S tests on the straight tension specimens was about 2×10^{-6} s^{-1}. A few tests were conducted at other strain rates, and the results are displayed in Fig. 3. These tests indicate little effect of strain rate below about 10^{-5} s^{-1}. Above this rate the effect of H_2S is apparently less severe, perhaps due to insufficient exposure time, and higher fracture strains result. The strain rates in H_2S at the minimum section of the ta-

TABLE 2—*Smooth specimen test results.*

Specimen Number	Machining Procedure	Test Environment	$\dot{\varepsilon}$, Strain Rate, s^{-1}	Failed or Stopped Before Failure	Strain at Failure or Where Test Stopped	Comments
			STRAIGHT TENSION SPECIMENS			
1A6-T17	point machined	H_2S	1.8×10^{-6}	failed	0.054	SEM fracture surface—intergranular mode
1A6-T19	point machined	H_2S	1.8×10^{-6}	failed	0.054	...
1A6-ST4	point machined	H_2S	2.2×10^{-6}	failed	0.055	...
1A6-ST1	point machined	H_2S	6.3×10^{-7}	failed	0.058	...
1A6-ST2	point machined	H_2S	6.8×10^{-6}	failed	0.059	...
1A6-ST8	point machined	H_2S	2.3×10^{-5}	failed	0.082	...
1A6-ST6	point machined	H_2S	7.5×10^{-5}	failed	0.094	...
1A6-ST5	point machined	H_2S	2.2×10^{-6}	stopped	0.048	SEM specimen surface—no cracking
1A6-ST7	point machined	air	7.3×10^{-5}	failed	0.892	calibration test; SEM fracture surface—ductile mode; strain from reduction in area
1A6-T18	point machined	air	1.8×10^{-4}	stopped	0.065	calibration test; SEM specimen surface—no cracking
			TAPERED TENSION SPECIMENS			
1A6-T25	point machined	H_2S	...	failed	0.056	...
1A6-T26	point machined	H_2S	...	failed	>0.06	...
1A6-T27	point machined	H_2S	...	failed	>0.06	...

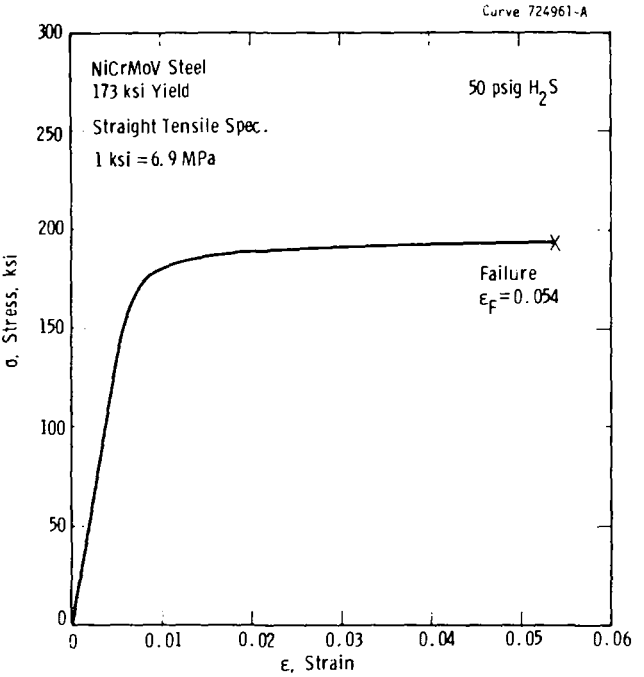

FIG. 2—*Stress-strain behavior in H_2S.*

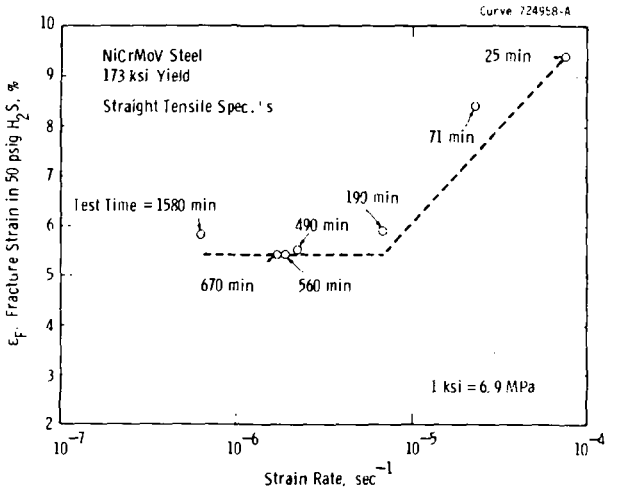

FIG. 3—*Fracture strain versus strain rate in H_2S.*

pered tension specimens and at the notch roots of the notched specimens were all within the range where strain rate is unimportant.

While the straight tension and tapered tension specimen results are in general agreement (see Table 2), the resistance of the latter specimen appeared to be slightly higher. The straight tension specimen median failure strain was 0.054. But the failure point on two of the tapered tension specimens was beyond the calibration limit strain of 0.06.

Notched Specimen Results

Table 3 contains the notched specimen test results. Figure 4 shows these results and the prediction from smooth specimen results on a plot of K_F versus $\sqrt{\rho}$. The horizontal line representing the lower bound of the prediction at K_{Iscc} is based on the precracked specimen results, which are plotted at zero radius. The critical value of $K/\sqrt{\rho}$ is based on a strain of 0.054. The figure clearly shows the increased resistance to stress corrosion cracking at a notch compared to the precracked condition. The predicted line shows the correct

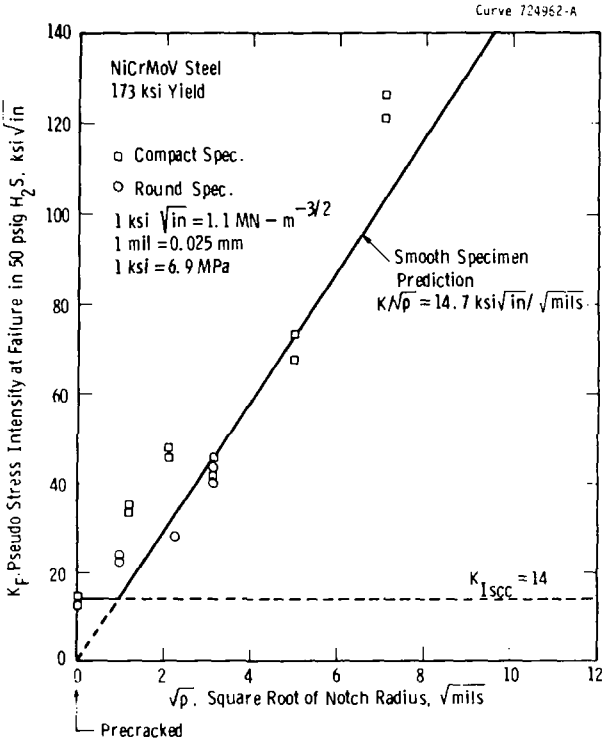

FIG. 4—*Test data and predicted line for failure of notched specimens in H_2S.*

trend of notched specimen stress corrosion behavior, and is generally in good agreement with the data. The largest factors of error between prediction and test data are for the sharpest radii, and it is important to note that these errors are conservative.

Another means of portraying the data is in terms of the nominal stress at failure, S_F, on a plot of S_F versus k_t, as shown in Fig. 5. While the predicted line in Fig. 4 represents a constant value of $K/\sqrt{\rho}$, the predicted line in Fig. 5 represents a constant value of k_tS. The hyperbolic shape of the predicted line reveals that stress corrosion crack initiation in the subject material-environment system is very sensitive to changes in stress concentration factor at the low end of the scale. In spite of this, the plot clearly shows the good agreement between notched specimen test data and prediction in this region of stress concentration factor, between about three and six. It is significant that the predictions in this region are the most accurate, because higher stress concentration factors are rare in service. At the higher stress concentration factors, the increased resistance over that predicted is also clearly visible.

Fractography was conducted on the fracture surfaces of some of the failed specimens, as indicated in Tables 2 and 3. In the H_2S environment tests, the cracking mode near the origin of fracture was predominantly intergranular for all specimen types. This is illustrated in Fig. 6. Farther from the point of origin, as the mechanical overload point was approached, the fracture mode changed to a ductile one. In the air environment tests, the fracture mode was entirely ductile.

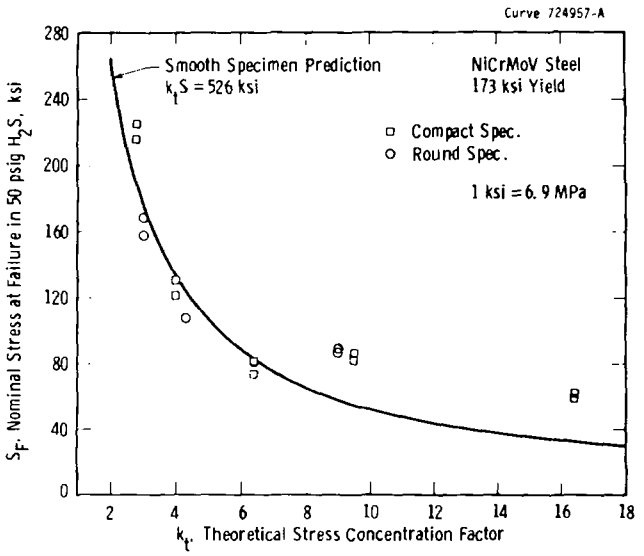

FIG. 5—*Predicted line and test data for failure of notched specimens in H_2S.*

TABLE 3—*Notched specimen test results.*

Specimen Number	ρ, Notch Root Radius, In.	k_t	Test Environment	Failed or Stopped Before Failure	Point at Failure or Where Test Stopped		Comments
					K, Pseudo-Stress Intensity, ksi·in.$^{1/2}$	S, Nominal Stress, ksi	
				NOTCHED ROUND SPECIMENS			
1A6-T1	0.010	3	H_2S	failed	40.6	158	SEM fracture surface—intergranular mode
1A6-T2	0.010	3	H_2S	failed	43.7	169	...
1A6-T4	0.010	3	H_2S	stopped	35.4	137	Heat tint—no cracking
1A6-T3	0.010	3	air	stopped	50.3	195	Heat tint—no cracking
1A6-T5	0.005	4.3	H_2S	failed	27.9	108	...
1A6-T7	0.005	4.3	air	stopped	32.8	127	Heat tint—no cracking
1A6-T9	0.001	9	H_2S	failed	22.8	88.4	SEM fracture surface—intergranular mode
1A6-T10	0.001	9	H_2S	failed	22.5	87.4	...
				NOTCHED COMPACT SPECIMENS			
1A4-1	0.050	2.8	H_2S	failed	126.6	225	...
1A4-2	0.050	2.8	H_2S	failed	121.5	216	...
1A4-3	0.050	2.8	H_2S	stopped	103.2	184	Heat tint—no cracking
1A4-2a	0.050	2.8	air	failed	220	392	SEM fracture surface—ductile mode; K from maximum load

1A4-4	0.050	2.8	air	stopped	145.8	259	Heat tint—no cracking
1A5-2a	0.025	4	H_2S	failed	73.5	131	...
1A5-3a	0.025	4	H_2S	failed	67.8	121	...
1A5-1	0.010	6.4	H_2S	failed	41.4	73.6	SEM fracture surface—intergranular mode
1A5-2	0.010	6.4	H_2S	failed	45.9	81.6	...
1A5-3	0.010	6.4	H_2S	stopped	35.6	63.3	Heat tint—no cracking
1A5-4	0.010	6.4	air	stopped	49.7	88.4	Heat tint—no cracking
4D4-1	0.0045	9.5	H_2S	failed	48.4	86	...
4D4-2	0.0045	9.5	H_2S	failed	46.2	82.2	...
4D4-3	0.0045	9.5	H_2S	stopped	40.1	71.4	Heat tint—no cracking
4D4-4	0.0045	9.5	air	stopped	55.5	98.7	Heat tint—no cracking
4D6-1	0.0015	16.4	H_2S	failed	35	62.3	SEM fracture surface—intergranular mode
4D6-2	0.0015	16.4	H_2S	failed	33.3	59.3	...
4D6-3	0.0015	16.4	H_2S	stopped	28.3	50.3	Heat tint—no cracking
1A4-1-2	0.0015	16.4	H_2S	failed	35.4	62.9	Thin specimen, $B = 0.090$ in.
1A4-1-3	0.0015	16.4	H_2S	failed	28.3	50.3	Thin specimen, $B = 0.090$ in.
1A4-4a	0.0015	16.4	air	failed	174	309	SEM fracture surface—ductile mode; K from max. load
4D6-4	0.0015	16.4	air	stopped	41.2	73.4	...
1A6-1	precracked		H_2S	failed	13.6	24.1	...
1A6-2	precracked		H_2S	failed	14.5	25.7	...
1A6-3	precracked		H_2S	stopped	13.3	23.7	Heat tint—subcritical cracking; estimated $K = 10.6$ at initiation
1A6-4	precracked		air	stopped	17.3	30.8	Heat tint—no cracking

NOTE—Conversion factors: 1 in. = 2.54 cm, 1 ksi·in.$^{1/2}$ = 1.1 MPa·m$^{1/2}$; 1 ksi = 6.9 MPa.

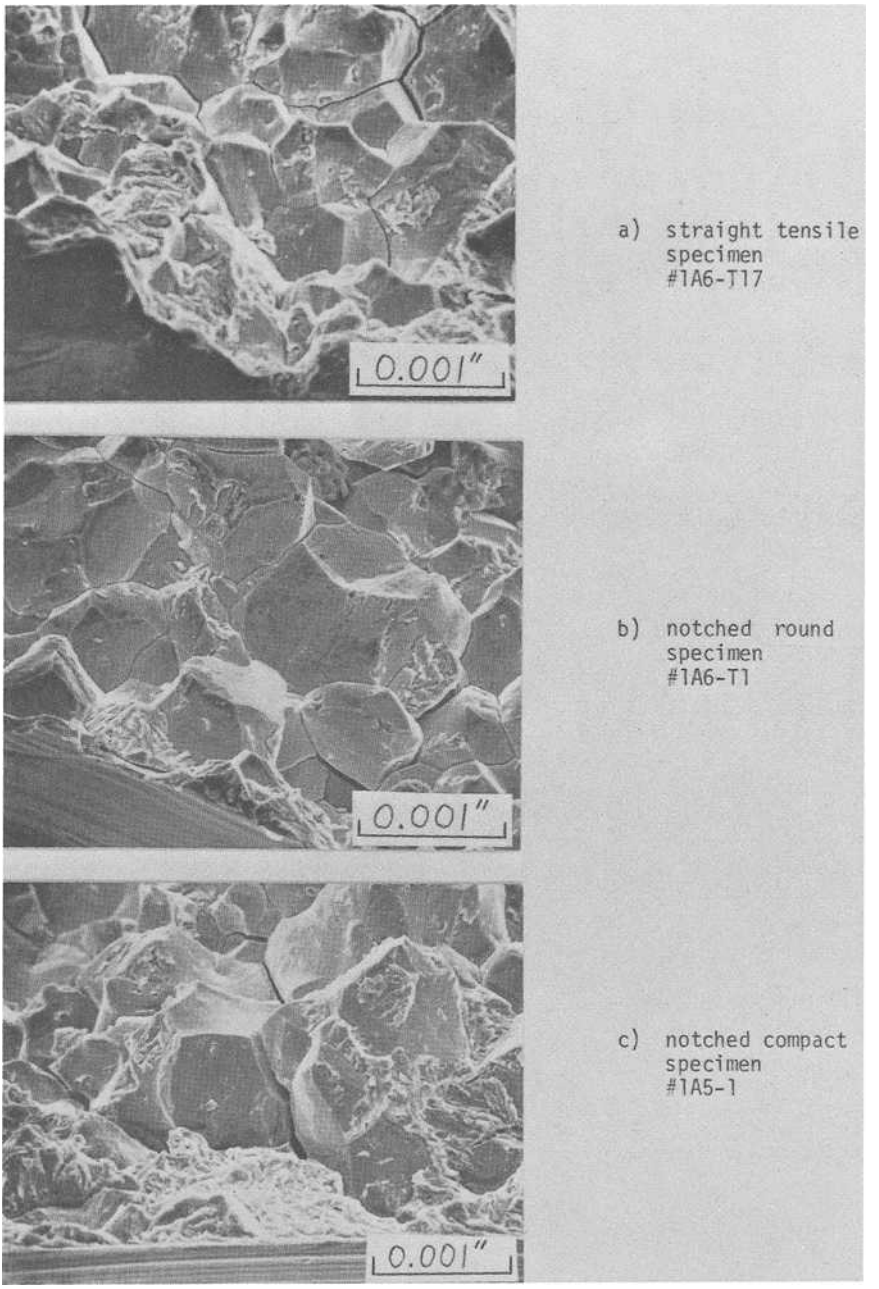

FIG. 6—*Fracture surfaces of smooth and notched specimens failed in* H_2S.

Effect of Constraint

Maximum principal surface strain has been proposed as the controlling parameter for failure in H_2S, implying that the value of the other principal strain (which acts in the transverse direction) is unimportant. The ratio of the principal strains represents the overall state-of-strain, which in turn is related to the state-of-stress. But data do exist which show a possible influence of state-of-stress on environment-induced crack initiation behavior [*11*].

In compact specimens, the state-of-stress (or state-of-strain) at the notch surface can be characterized by what is known as transverse constraint. Constraint is determined by the ratio of notch radius to specimen thickness, ρ/B. As this constraint factor, ρ/B, decreases, the constraint is said to increase, and the state-of-stress approaches the plane strain condition and departs from plane stress. For the compact specimens tested which were of the same thickness, a different degree of constraint is represented by each notch radius. Therefore, constraint was investigated as a possible cause for the sharp notches having greater resistance than predicted while the blunter notches agreed with prediction.

Several "thin" compact specimens were fabricated with a notch radius equal to the sharpest in the full-thickness specimens, 0.0038 cm (0.0015 in.), but with a thickness of 0.229 cm (0.090 in.) instead of 2.29 cm (0.900 in.). The resulting constraint factor, ρ/B, was in the range of that of the larger radii (lower k_t) specimens for which the failure predictions were accurate. However, reducing the thickness, and thus constraint, of the sharp-notch specimens did not significantly change the stress corrosion resistance, as shown in Fig. 7. Thus the higher constraint (compared to the blunter notches) existing in the sharp-notch specimens is not responsible for their failure performance exceeding that predicted. Two other possible explanations for this increased stress corrosion resistance are size of the highly stressed area (weakest link argument) and notch surface condition (residual stress and degree of cold-work), the latter being more difficult to control as notch radius decreases. The influence of these factors was not addressed in the present work.

Crack Initiation Versus Propagation

Due to the high crack growth rates that occur in H_2S for metals of the type tested [*10*], crack initiation generally is expected to be virtually coincident with specimen failure. Some testing was conducted to verify this assumption. Again, there was interest in the sharp notch test data that did not agree with prediction. Perhaps stress corrosion crack initiation occurred at a lower load, closer to that predicted, than did failure. Such a phenomenon might be expected for a sharp notch based on an argument employed in the area of fatigue [*12*]. That is, as a crack grows out of the notch-affected strain field into

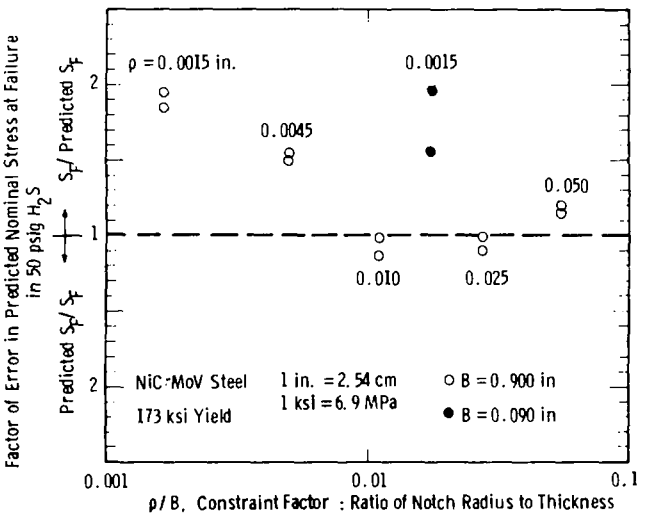

FIG. 7—*Effect of transverse constraint on the failure of notched compact specimens in H_2S.*

an area of lower strain, it may slow down relative to a crack growing from the surface of a notch of a larger radius that would have a deeper notch-affected strain field.

Tests were conducted in H_2S on smooth (straight tension), notched, and precracked specimens that were terminated before failure and inspected for the presence of cracks as described in the Experimental Procedure section. For each set of tests to failure with a given geometry and radius, a test was run to about 85 percent of the lowest failure point. The results are shown in Fig. 8. The smooth and notched specimens inspected contained no cracks. Interestingly, the only geometry in which subcritical crack growth did occur was the precracked compact.

One example of the inspection findings is in Fig. 9*a*. This is an SEM photo of the surface of a straight tension specimen from an H_2S test that was stopped before failure. Surface "rumpling" associated with the plastic strain endured is evident, but no cracks were found. The feature near the center of the top photo, which is shown at a higher magnification in the bottom photo, is apparently a slip step.

Some tests were also run in air and stopped before failure. For each set of tests to failure in H_2S with a given geometry and radius, a test was run in air to about 15 percent beyond the highest failure point. Figure 8 contains the results. In no case were cracks found. Figure 9*b* is a representative sample of the surface condition of a straight tension specimen. This shows that the H_2S test results do not represent a situation where cracks initiated due to purely mechanical effects and propagated rapidly due to H_2S. In other words, crack

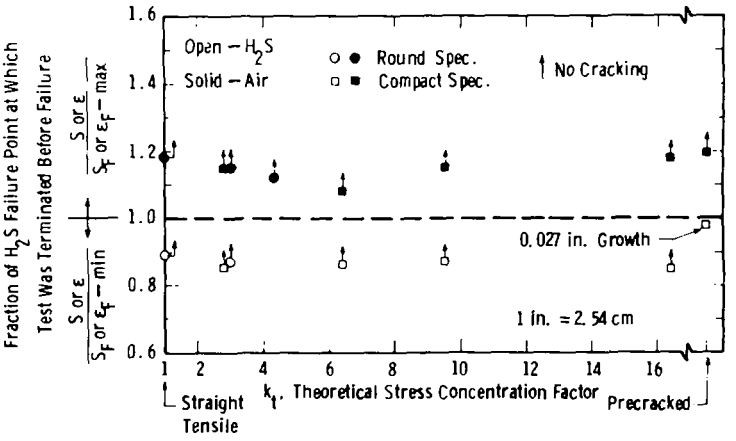

FIG. 8—*Results of tests terminated before failure and inspected for cracking.*

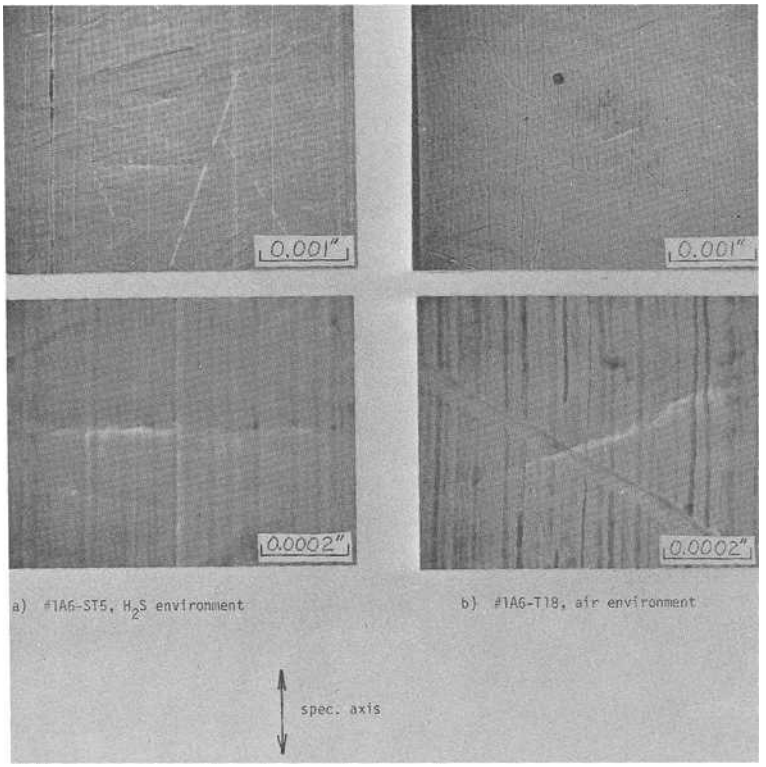

FIG. 9—*Surfaces of straight tension specimens stopped before failure.*

initiation in the subject material in H_2S is truly an environment-induced phenomenon.

Conclusions

1. The environment-induced crack initiation resistance of notched parts can be predicted accurately from smooth specimen tests with a maximum principal surface strain failure criterion. The predictive methodology can handle elastic-plastic notch stress-strain behavior. Experimental verification was obtained with notched specimens of different stress gradients and a wide range of stress concentration factors, in a material-environment system where hydrogen cracking occurred.

2. Very sharp notches ($k_t > 9$) not normally found in service portray greater environment-induced crack initiation resistance than predicted. Higher levels of transverse constraint in these specimens compared to those with larger radii notches are not responsible for this discrepancy. Therefore, the predictive method has a built-in conservatism, for reasons presently unclear, for very sharp notches.

3. The cracking mode in H_2S at the point of crack initiation was predominantly intergranular for all geometries. This is further evidence that the observed environment-induced crack initiation results represent a geometry-independent phenomenon and can be treated by a single failure criterion.

4. Crack initiation in H_2S was essentially coincident with total specimen failure, as expected. Thus, crack propagation was not a factor in the test results obtained.

5. Tests of the type conducted here should be performed for a wider range of stress states, for example, pure shear and equibiaxial conditions. Also, the experiments should be repeated in an environment where dissolution mechanisms rather than hydrogen cracking alone are operable. Such tests would expand the range of situations in which the proposed predictive methodology could be applied confidently.

Acknowledgments

The author would like to acknowledge the careful experimental work conducted by members of the Structural Behavior of Materials Laboratory, especially P. J. Barsotti. This work was sponsored by the Westinghouse Steam Turbine Generator Division.

References

[1] Lee, T. D., Goldenberg, T., and Hirth, J. P., *Metallurgical Transactions A*, Vol. 10A, Feb. 1979, pp. 199-208.

[2] Lee, T. D., Goldenberg, T., and Hirth, J. P., *Metallurgical Transactions A*, Vol. 10A, April 1979, pp. 439-448.
[3] Hirose, Y. and Tanaka, K. in *Third International Conference on Mechanical Behavior of Materials*, Vol. 2, Pergamon Press, Elmsford, N.Y., 1979, pp. 409-420.
[4] Paris, P. C. and Sih, G. C. in *Fracture Toughness Testing and Its Applications, ASTM STP 381*, American Society for Testing and Materials, 1965, pp. 30-83.
[5] Clark, W. G., Jr. in *Flaw Growth and Fracture, ASTM STP 631*, American Society for Testing and Materials, 1977, pp. 121-138.
[6] Wilson, W. K., *Journal of Pressure Vessel Technology*, Vol. 96, No. 4, Nov. 1974, pp. 293-298.
[7] Dowling, N. E. in *Fracture Mechanics (Eleventh Conference), ASTM STP 677*, American Society for Testing and Materials, 1979, pp. 247-273.
[8] Neuber, H., *Journal of Applied Mechanics*, Dec. 1961, pp. 544-550.
[9] Jonas, O., *Journal of Testing and Evaluation*, Vol. 6, No. 1, Jan. 1978, pp. 40-47.
[10] Clark, W. G., Jr. and Landes, J. D. in *Stress Corrosion-New Approaches, ASTM STP 610*, American Society for Testing and Materials, 1976, pp. 108-127.
[11] Smith, P. W., Louthan, M. R., and McNitt, R. P., *Scripta Metallurgica*, Vol. 14, 1980, pp. 199-204.
[12] Dowling, N. E., *Fatigue of Engineering Materials and Structures*, Vol. 2, 1979, pp. 129-138.

I. S. Abou-Sayed,[1] *J. Ahmad,*[1] *F. W. Brust,*[1] *and M. F. Kanninen*[1]

An Elastic-Plastic Fracture Mechanics Prediction of Stress-Corrosion Cracking in a Girth-Welded Pipe

REFERENCE: Abou-Sayed, I. S., Ahmad, J., Brust, F. W., and Kanninen, M. F., "**An Elastic-Plastic Fracture Mechanics Prediction of Stress-Corrosion Cracking in a Girth-Welded Pipe,**" *Fracture Mechanics: Fourteenth Symposium—Volume I: Theory and Analysis, ASTM STP 791*, J. C. Lewis and G. Sines, Eds., American Society for Testing and Materials, 1983, pp. I-482-I-496.

ABSTRACT: Despite the fact that weld-induced residual stresses arise as a result of thermoplastic material deformation, current analyses of crack growth in welds assume that linear elastic fracture mechanics (LEFM) conditions are valid. In particular, the stress-intensity factor K, the LEFM-based measure of the crack driving force, is calculated using the linear superposition techniques that strictly hold for linear elastic material behavior. Another common idealization is that only the normal component of the residual stress field that acts on the crack plane is significant.

To assess the importance of these assumptions, a heuristic elastic-plastic fracture mechanics analysis procedure is developed in this paper and applied to determine the rate of stress-corrosion crack growth in an axially-loaded 102-mm (4-in.)-diameter girth-welded Type 304 stainless steel pipe. It is found that the more rigorous elastic-plastic analysis predicts higher crack growth rates than do the currently used LEFM-based calculations. It is concluded that more rigorous prediction methods may be needed for safety assessments of welded structures than those now in use.

KEY WORDS: residual stresses, stress-corrosion cracking, Type 304 stainless steel, elastic-plastic fracture mechanics, weld cracking, fracture mechanics

Intergranular stress-corrosion cracking (IGSCC) in the heat-affected zones (HAZ) around girth welds in austenitic stainless steel piping of boiling water reactors (BWR) is a problem of some concern to the nuclear industry. As described by Fox [*1*],[2] the three factors that are required for IGSCC to occur—

[1]Battelle Columbus Laboratories, Columbus, Ohio 43201.

[2]The italic numbers in brackets refer to the list of references appended to this paper.

material sensitization, a deleterious environment, and tensile stresses—are all present in BWR piping. In particular, the weld-induced residual stresses at the inner surface of a pipe are generally tensile so that IGSCC can occur even in the absence of an applied stress. Several studies [*2–5*] have shown that the welding-induced residual stresses can be quite high, in some cases approaching the room temperature yield stress of the material. Hence, it would appear that direct consideration must be given to the residual stresses induced by the welding process in assessing the integrity of nuclear piping systems.

Thermoplastic finite-element analyses have been developed for the direct computation of the residual stresses arising in the welding process [*6–10*]. But, these generally do not consider the effect of applied stresses and the flaw size. Conversely, the analyses that have been made of crack growth in residual stress fields do not admit the plastic deformation, but instead treat the problem within the confines of linear elasticity.

Treatments of the influence of residual stresses on stress-corrosion cracking in sensitized weldments in austenitic stainless steel piping in BWR piping have been given by several investigators [*11–13*]. Earlier studies on the temperature distributions and residual stresses due to welding are given by Masubuchi [*14*]. All of these analyses have employed the same two rather severe assumptions: that linear elastic fracture mechanics (LEFM) conditions are valid, and that only the normal component of the residual stress field that acts on the crack plane is significant. The work reported in this paper avoids these two assumptions by coupling an elastic-plastic fracture mechanics treatment of crack growth with a thermoplastic analysis of weld-induced residual stresses. Thus, both the complete plastic deformation field and a more appropriate elastic-plastic fracture parameter is used to determine the crack growth rates.

In this paper a brief outline of a general analysis procedure is given first. Next, a heuristic approach is developed and applied to determine the rate of stress-corrosion crack growth in an axially-loaded 102-mm (4-in.)-diameter girth-welded Type 304 stainless steel pipe. These results then are contrasted with the current LEFM-based approaches for a preliminary assessment of the importance of pursuing an elastic-plastic fracture mechanics approach for stress-corrosion cracking in nuclear plant piping.

Basis of the Analysis

Thermal elastic-plastic mechanical models for residual stresses due to welding generally consist of two parts: a weld-layer dependent temperature analysis and a corresponding stress analysis. Most of the early models concentrated on plate type configurations and girth-butt welds in pipes and pressure vessels [*15*]. More recent work has centered on the improvement and control of residual stresses by alterations in the welding process [*16*] or by

post-welding treatments [*17*]. It is now generally agreed that such analyses are reliable for general trends, but do not always give a high degree of precision. Nevertheless, because experimental residual stress determinations are quite expensive and are also subject to uncertainties, finite-element analyses can be useful for quantitative studies such as this.

Considerable progress has been made towards the development of elastic-plastic fracture mechanics analysis techniques for nuclear components [*18*]. The incentive for these developments can be attributed to the inability of LEFM to treat conditions where the plastic deformation occurring in real structures is important. The tough and ductile nuclear plant materials (for example, A533B steel, Type 304 stainless steel) undergo large plastic deformation before the onset of crack growth. Moreover, crack growth instability in such materials generally is preceded by some stable crack growth. Of most importance here, investigations aimed at the development of a plastic fracture methodology [*19-20*] have revealed that the local crack-tip opening displacement tends to remain a constant, even for extended amounts of stable crack growth. While comparable observations for IGSCC have not been made, this fact is highly suggestive for the latter process as well.

Due to the inherent limitations and uncertainties of current inspection and detection techniques, some cracks are always left undetected, even in fracture-sensitive components. (As examples, stress-corrosion cracks that were detected in a BWR pipe [*21*] are shown in Fig. 1.) Thus, it is important to have a reasonably accurate prediction of the time required for such cracks to grow to a critical size. This depends upon the crack growth rate, which in turn depends on the controlling crack growth mechanism, the loading, and the operating conditions. Of primary interest here is stress-corrosion cracking that occurs under conditions such that

$$\frac{da}{dt} = CK^m \tag{1}$$

where da/dt is the time rate of crack growth, K is the applied stress-intensity factor, while C and m are supposed to be material constants. For example, Eq 1 was used in recent studies to determine the integrity of sensitized BWR piping welds [*11,12*].

One basic difficulty involved in the use of Eq 1 is its explicit reliance on LEFM. Commonly, data are collected with small-scale laboratory test specimens and used to determine the empirical parameters C and m for application to full-scale structures. However, if either the test specimen or the structure experiences extensive plastic deformation during crack growth, the resulting relation could be quite inappropriate. Nevertheless, because there currently is no generally acceptable alternative, such relations are sometimes used when they are not valid. It is one aim of this work to utilize the constancy of the crack-tip opening displacement observed in plastic fracture mechanics investigations in an attempt to improve upon this situation.

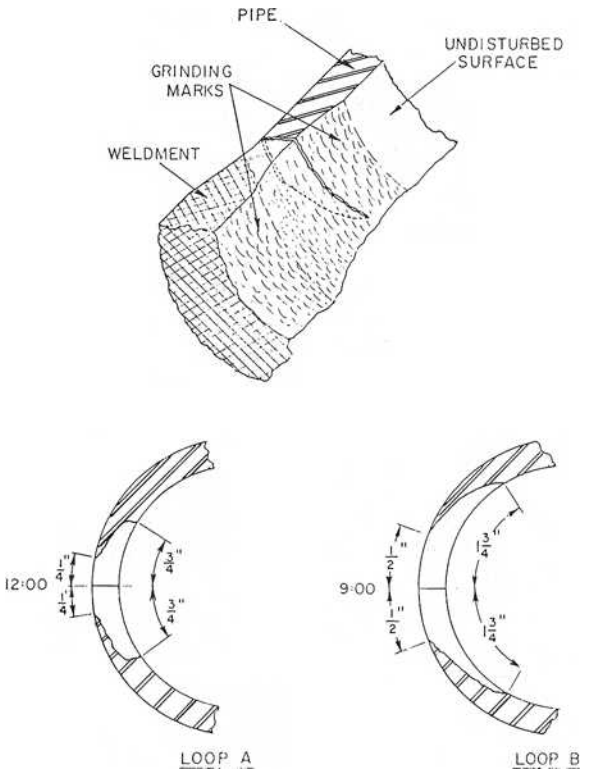

FIG. 1—*Profiles of circumferential cracks detected in 102-mm (4-in.)-diameter recirculation bypass line of the Dresden II boiling water reactor plant, after Cheng et al* [21].

Analysis Procedure

The analysis procedure is composed of three steps. In the first step the residual stresses induced during the girth welding of a 102-mm (4-in.)-diameter, Schedule 80, Type 304 stainless steel pipe are calculated under axisymmetric conditions. In the second, the radial growth of the circumferential part-through-wall crack is simulated to obtain the elastic-plastic crack driving force at successive stages of the crack growth process. The third step introduces a plausible, albeit hypothetical, elastic-plastic stress-corrosion cracking criterion to deduce the crack length-time behavior.

Analysis Model for a Girth-Welded Pipe

The residual stress analysis approach for a girth-welded pipe consists of first predicting the temperature versus time history experienced in the pipe when depositing each individual weld pass. The temperature model is based

on the solution for a point heat source moving in an infinite solid at a constant velocity with appropriate modifications made to account for the finite wall thickness. These temperature histories then serve as the loading history for a subsequent thermoelastic-plastic finite-element analysis. The finite-element program that was used is based on incremental plasticity theory and includes large deformations. A modified isotropic hardening law which permits strain softening to occur at higher temperatures is used in this model.

The temperature-dependent material properties for Type 304 stainless steel shown in Fig. 2 were used in the analysis together with a bilinear representation of the stress-strain curve. The temperature analysis was performed using the welding parameters in an experimental program by Argonne National Laboratories [5]. Welding parameters are shown in Table 1. The weld pass geometry was obtained from a photograph of the weld cross section. While the actual weldment consisted of a total of seven passes, these were modeled with four layers using a weld centerline symmetry assumption.

The finite-element grid used to model the welding process and to perform the subsequent crack growth analysis is shown in Fig. 3. This mesh consists of a total of 286 nodes and 238 elements. The elements are constant strain triangles and quadrilaterals consisting of an assemblage of four triangles. A condition of axisymmetry is imposed on the nodal deformations for the girth-weld analysis together with the weld centerline symmetry condition. Therefore, only radial deformations are permitted in the nodes along the weld centerline, with stress-free boundary conditions imposed on the nodes at the opposite end of the pipe model.

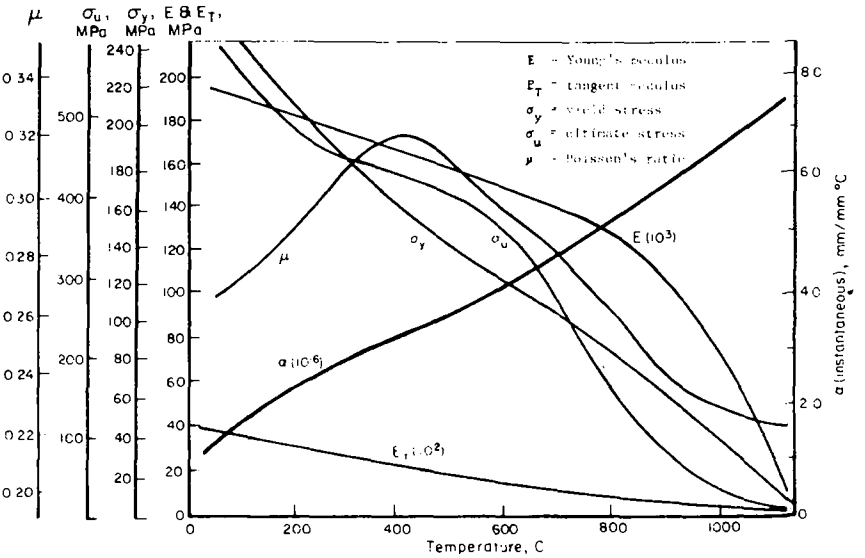

FIG. 2—*Temperature-dependent properties of Type 304 stainless steel.*

TABLE 1—*Welding parameters and weld geometry for a 102-mm (4-in.)-diameter Schedule 80 Type 304 stainless steel pipe.*[a]

Layer	Welding Current, A	Arc Voltage, V	Travel Speed, mm/s	Heat Input, J/mm
Root	100	13	1.14	1137
Two	85	13	1.09	1012
Three	95	23	3.05	717
Four	95	24	3.05	717

[a]Data of Shack et al [5].

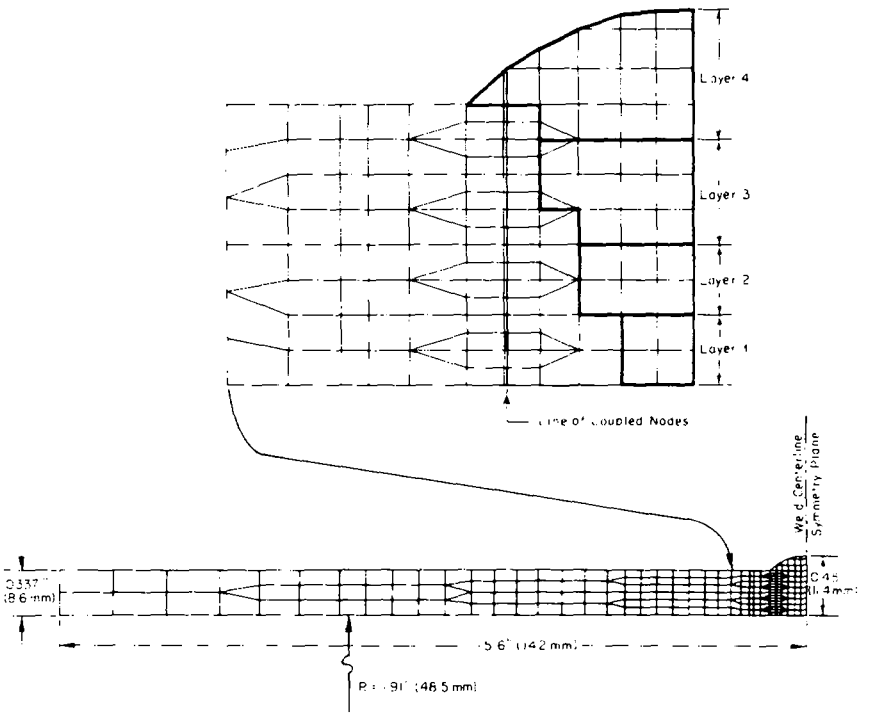

FIG. 3—*Finite-element model for residual stress and crack growth analysis in a girth-welded 102-mm (4-in.)-diameter Schedule 80, Type 304 stainless steel pipe.*

A comparison between the residual stresses computed at the inner surface of the pipe and Argonne's measured values [5] is presented in Fig. 4. It can be seen that the analysis predictions agree quite well with the experimental data. Notice that both the axial and circumferential residual stresses are tensile in the HAZ at the inner surface of the pipe. Therefore, this pipe is definitely a candidate for IGSCC.

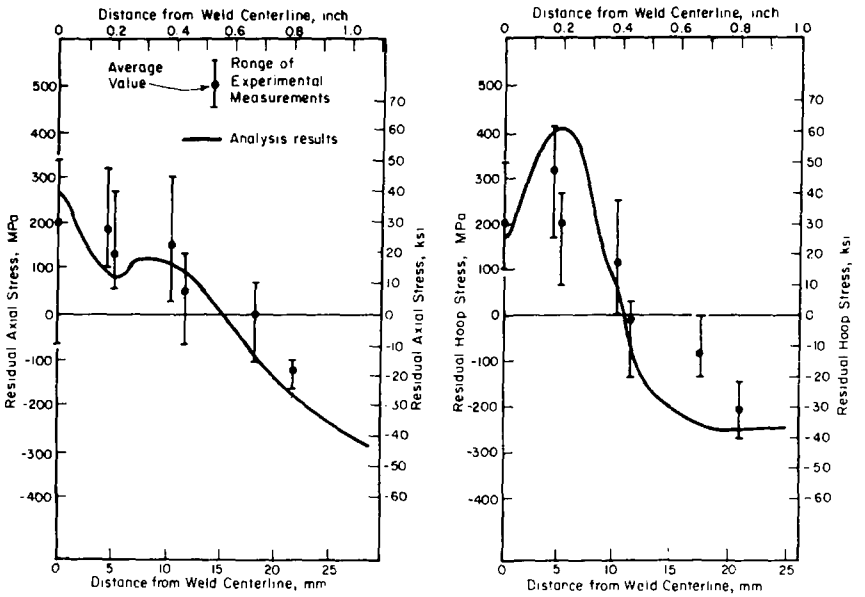

FIG. 4—*Axial and circumferential stresses along the inner surface of a girth-welded 102-mm (4-in.)-diameter Schedule 80, Type 304 stainless steel pipe.*

The axial residual stresses calculated through the pipe wall thickness at the crack line are shown in Fig. 5. It is seen that tensile residual stresses of 96.5 MPa (14 ksi) exist at the pipe inner surface and reverse to compression at the pipe outer surface. These stresses are self equilibrating through the pipe wall.

Crack Growth Analysis

As appropriate for a preliminary investigation, the work described in this paper was based upon simple geometric conditions. Specifically, a complete circumferential annular crack shape was considered with a symmetry plane considered to exist at the weld centerline. This implies that there actually are two parallel cracks, one existing on each side of the weld. A crack was simulated in the finite-element model by placing a line of double nodes along a radial line in the weld HAZ where intergranular stress-corrosion cracks tend to occur. This is shown in Fig. 3. The nodal spacing along this line was 0.53 mm (0.021-in.). All of the crack growth calculations were made by introducing a small initial radial crack into the finite-element model of length equal to 1.5 mm (0.06-in.).

Each pair of double nodes was coupled with a spring that was assigned a very high stiffness. Then, as shown schematically in Fig. 6, the simulation of

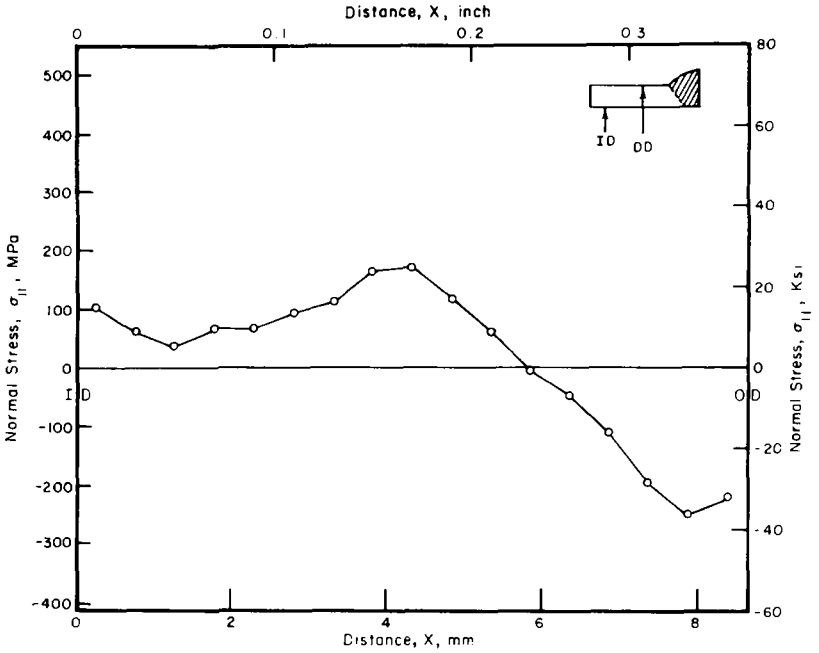

FIG. 5—*Axial residual stresses plotted through the pipe wall at the crack line.*

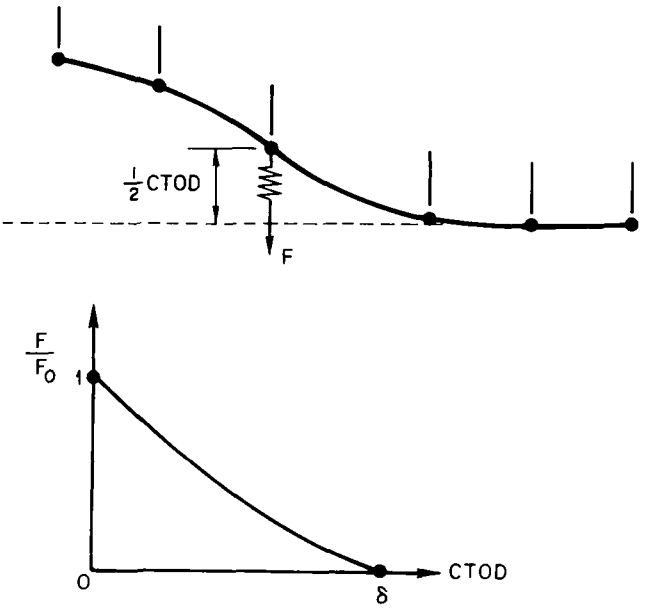

FIG. 6—*Simulation of crack growth by node release in the finite-element model.*

an increment of crack growth was achieved by gradually releasing the force developed in a spring to zero. The crack grows by sequentially eliminating the spring forces along the preselected crack path. Notice that this procedure does negative work on the body which removes an amount of energy corresponding to the material's energy dissipation rate.

Where LEFM is valid, a relation exists between the stress-intensity factor and the crack-tip opening displacement. This can be written as

$$\delta = \alpha \frac{K^2}{EY} \tag{2}$$

where δ is the crack-tip opening displacement, K is the LEFM stress-intensity factor, E is the elastic modulus, Y is the yield stress, and α is a dimensionless constant. The exact value of α depends upon the problem formulation and loading conditions; for example, see Atkinson and Kanninen [*22*]. This relation is important here because of the key role played by δ in plastic fracture mechanics applications [*8–20*]. In particular, as shown by Shih [*23*]

$$\delta = d_n \frac{J}{Y} \tag{3}$$

where J is the J-integral—the crack-tip characterizing parameter for a deformation plasticity representation of the near-tip region—and d_n is a function of the strain-hardening exponent of the material; note that for LEFM conditions, $J \propto K^2/E$ whereupon Eq 3 agrees with Eq 2. It follows that, if δ is computed as a function of crack growth, it can serve to characterize the propensity for crack growth under both the elastic and the elastic-plastic conditions examined in this study.

Starting from the arbitrary initial crack, progressive subcritical crack growth was simulated in the model by successively releasing the stiff springs connecting the double nodes on the crack plane. At the point where the nodes were completely uncoupled, the crack-tip opening displacement was taken as equal to δ (see Fig. 6). In this way, a record of $\delta = \delta\ (a - a_0)$ was obtained where a_0 denotes the initial crack length. Parallel computations were performed for the simple elastic case, where only the normal component of the residual stress field on the crack plane was included. Figure 7 shows the results.

One interesting aspect of these results is shown in Fig. 8. This is that the stress redistribution that occurs due to crack growth, even in the absence of an applied stress, will give rise to a positive stress at the crack tip well beyond the point at which the initial residual stresses become negative. Hence, even if a region of compressive residual stress exists, there could be a positive crack driving force as crack growth proceeds that will drive the crack to a critical size. It follows that reliance on a region of compressive stress to assure crack arrest may not be realistic.

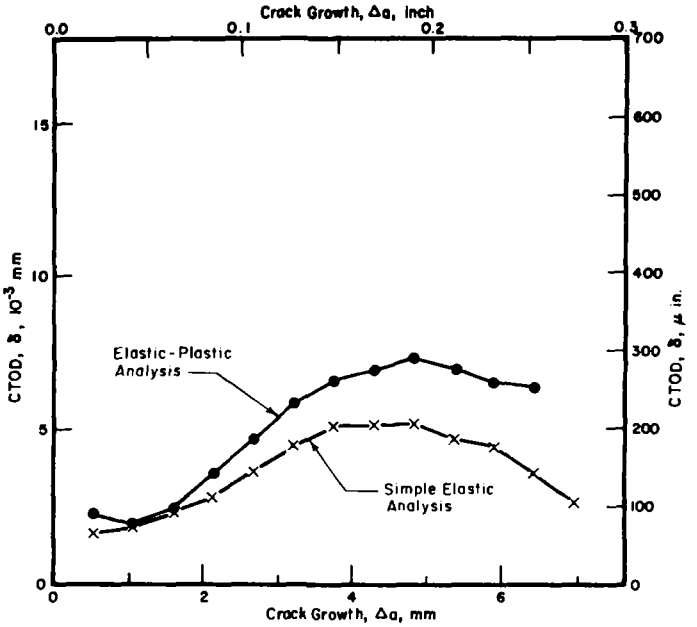

FIG. 7—*Crack-tip opening displacement calculated as a function of crack growth* (Δa) *for 102-mm (4-in.)-diameter Type 304 stainless steel pipe subjected to welding-induced residual stresses and zero applied stress.*

Simulation of Stress-Corrosion Cracking

By combining Eq 1 and 2, an expression for the crack growth rate in stress-corrosion cracking can be obtained in terms of the crack-tip opening displacement. This is

$$\frac{da}{dt} = C'\delta^{m/2} \tag{4}$$

where $C' = C\,(EY/\alpha)^{m/2}$ is a material constant. Of interest is the extent of crack growth as a function of time. With δ known as a function of crack length (compare Fig. 7), integration of Eq 4 can be obtained most easily in the form

$$t = \frac{1}{C'} \int_{a_0}^{a} \frac{da}{\delta^{m/2}} \tag{5}$$

To keep the following results as general as possible it is convenient to introduce a dimensionless time parameter, t^*. This gives

$$t^* = \int_{a_0}^{a} \frac{h^{m/2-1}}{\delta^{m/2}}\, da \tag{6}$$

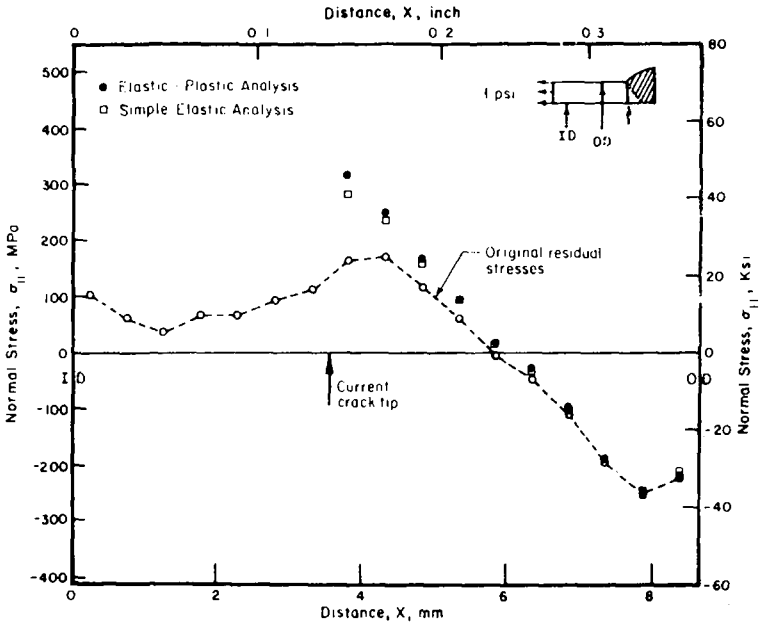

(a) AFTER 1.5 mm OF CRACK GROWTH

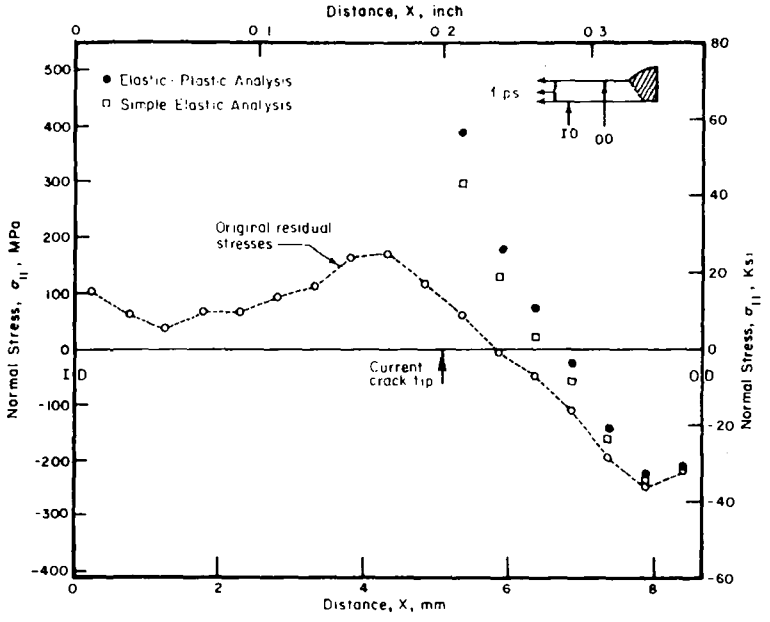

(b) AFTER 3.21 mm OF CRACK GROWTH

FIG. 8—*Normal stress distribution across the uncracked remaining ligament for a 102-mm (4-in.)-diameter Type 304 stainless steel pipe subjected to welding-induced residual stresses.*

where t^* is related to real time by

$$t = \frac{t^*}{C' h^{m/2-1}} \tag{7}$$

where h is the pipe wall thickness.

By this device, the following computational results are independent of at least one of the parameters in the stress-corrosion crack growth rate relation. But the results do depend on the material parameter m and, of course, on the calculated $\delta = \delta(a - a_0)$ results for the conditions being examined here.

A value appropriate for Type 304 stainless steel is $m = 8$ [*11,12*]. Using this value and the results shown in Fig. 7, Eq 6 can be integrated (numerically) to obtain $t^* = t^*(a - a_0)$. The results are shown in Fig. 9. These results are very significant in that they reveal the nonconservative nature of the conventional crack growth prediction technique. That is, as indicated by these calculations, the simple elastic analysis overpredicts the time required for a crack to grow to a given length.

Discussion

The work presented in this paper was designed to address two separate assumptions that are made in all previous analyses of crack growth in weld-induced residual stress fields. These are the following:

1. Only the normal component of the residual stress field that acts on the crack plane is significant.
2. Linear elastic conditions (including linear superposition and the existence of the characteristic LEFM singularity) are valid in weld-induced thermoplastic deformation fields.

To assess the validity of these assumptions, two different types of crack growth analyses can be carried out. First, a calculation can be made in accord with the conventional assumptions. This result will be referred to as a "simple elastic analysis." Second, an "elastic-plastic analysis" can be performed in which neither assumption is used. As described in the foregoing, this calculation can be conducted by introducing the initial crack directly into the plastically deformed weld-induced residual stress analysis model.

It also may be of interest to determine the crack growth rates under an applied load. Figure 10 gives the results when an axial stress of 138 MPa (20 ksi) (approximately one half the yield stress for Type 304 stainless steel) is imposed. Of perhaps most interest here, it can be seen in Fig. 10 that the simple elastic analysis gives a consistently lower value of the crack-tip opening displacement than the elastic-plastic analysis.

It is important to recognize that only one problem was analyzed here—a girth-welded Type 304 stainless steel 102-mm (4-in.)-diameter Schedule 80

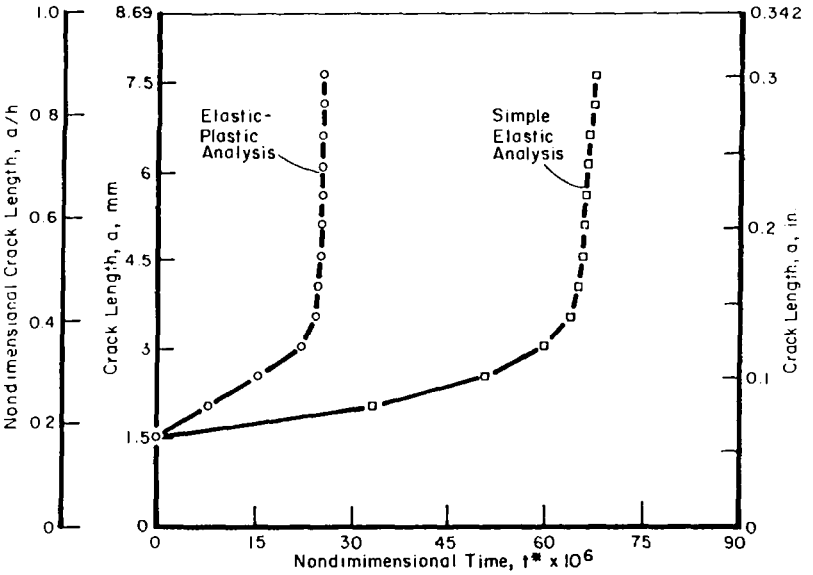

FIG. 9—*Nondimensional time t* as a function of crack growth for 102-mm (4-in.)-diameter Type 304 stainless steel pipe subjected to welding-induced residual stresses.*

pipe—and that this was done for a highly idealized crack/structure geometry. Hence, conclusions drawn from these results must be viewed cautiously. It would be desirable to carry out similar analyses for a range of pipe diameters, wall thicknesses, and welding procedures. But, before this can be done effectively, further attention must be paid to two key aspects of the work: the limitations in current residual stress analyses and the present lack of a suitable crack growth parameter valid for crack growth in a plastically deformed material.

Conclusions

Based on the results obtained in this paper, the calculation of stress-corrosion crack growth rates in the HAZ's around welds—based on analyses that (1) do not include the full residual stress field and (2) assume that linear superposition is valid—could be substantial underestimates. More reliable calculations based upon a combination of thermoplastic residual stress analyses and plastic fracture mechanics concepts appear to be needed. The approach described in this paper indicates how this calculation can be done.

Acknowledgment

This work was prepared in connection with Battelle's Workshop Conference on Computations of Crack Growth and Residual Stresses in Welded

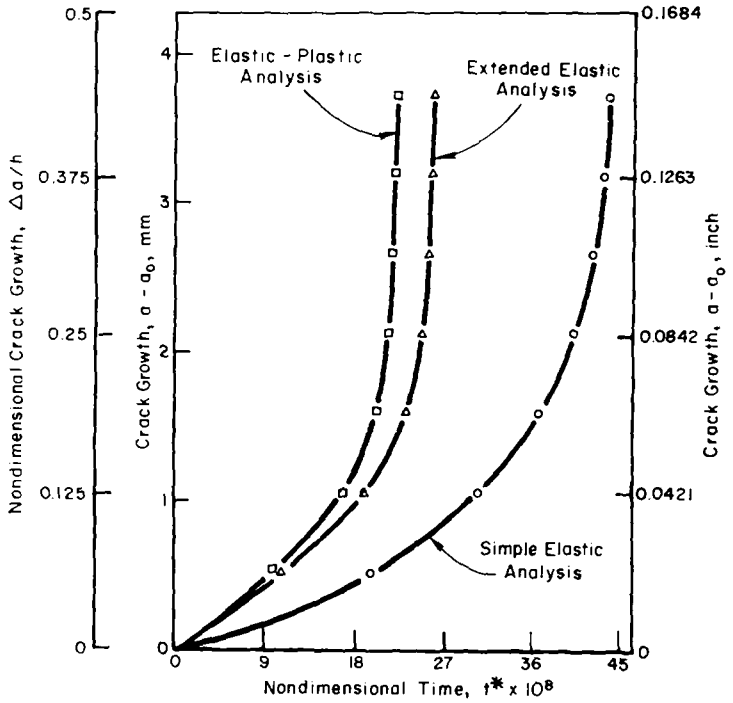

FIG. 10—*Nondimensional time* t* *as a function of crack growth for 102-mm (4-in.)-diameter Type 304 stainless steel pipe subjected to welding-induced residual stresses and an axial stress of 138 MPa (20 ksi).*

Structures. The authors would like to express their appreciation to Battelle's Transportation and Structures Department, D. K. Snediker, Manager, for its support of this activity. The work was a natural outgrowth of the plastic fracture mechanics and residual stress analysis projects performed at Battelle with support from the Electric Power Research Institute. The authors therefore also wish to thank T. Giannuzzi, R. Jones, T. U. Marston, and D. M. Norris, Jr. for their guidance on these projects.

References

[1] Fox, M., "An Overview of Intergranular Stress Corrosion Cracking in BWR's," Seminar on Countermeasures for Pipe Cracking in BWR's, Electric Power Research Institute Report WS-79-174, May 1980.

[2] Klepfer, H. H. et al, "Investigation of Cause of Cracking in Austenitic Stainless Steel Weldments," Report NEDO-21000, General Electric Co., Nuclear Energy Division, San Jose, Calif., July 1975.

[3] "Investigation and Evaluation of Cracking in Austenitic Stainless Steel Piping of Boiling Water Reactor Plants," Report NUREG-75/067 (NTIS No. PB-246 645), Pipe Cracking Study Group, Nuclear Regulatory Commission, Washington, D.C., Oct., 1975.

[4] "Studies on AISI Type-304 Stainless Steel Piping Weldments for Use in BWR Applica-

tions," Report EPRI NP-944, RP449-2, Electric Power Research Institute, Palo Alto, Calif., Dec. 1978.

[5] Shack, W. J., Ellingson, W. A., and Pahis, L. E., "The Measurement of Residual Stresses in Type-304 Stainless Steel Piping Butt Weldments," Final Report on Electric Power Research Institute EPRI RP449-1, Dec. 1978.

[6] Rybicki, E. F., McGuire, P. M., and Stonesifer, R. B., "Effect of Weld Parameters on Residual Stresses in Boiling Water Reactor Piping Systems," First Semiannual Progress Report, 1 April-1 Oct. 1978, RP1174, Electric Power Research Institute, Palo Alto, Calif.

[7] Brust, F. W. and Stonesifer, R. B., "Effect of Weld Parameters on Residual Stresses in BWR Piping Systems," Battelle-Columbus Laboratories Final Reports to Electric Power Research Institute on RP1174, June 1980.

[8] Kanninen, M. F., Barber, T. E., Brust, F. W., Mishler, H. W., "Controlling Residual Stresses by Heat Sink Welding," Battelle-Columbus Laboratories Final Report to Electric Power Research Institute on RP1576-1 (T109-1), Dec. 1980.

[9] Hepworth, J. K., "Finite Element Calculation of Residual Stresses in Welds," Central Electricity Generating Board, Marchwood Engineering Laboratories Report, Nov. 1980.

[10] Brust, F. W. and Kanninen, M. F. in *Failure Prevention and Reliability—1981*, F. T. C. Loo, Ed., American Society of Mechanical Engineers, 1981, pp. 1-6.

[11] Harris, D. C., "The Influence of Crack Growth Kinetics and Inspection on the Integrity of Sensitized BWR Piping Welds," Final Report on EPRI NP-1163, Project 1325-2, Sept. 1979.

[12] Egan, G. R. and Cipolla, R. C., "Stress Corrosion Crack Growth and Fracture Predictions for BWR Piping," American Society of Mechanical Engineers, Paper No. 78-Mat-23, 1978.

[13] Rybicki, E. F., Stonesifer, R. B., and Olson, R. J., *Journal of Pressure Vessel Technology*, Vol. 103, 1981, p. 66.

[14] Masubuchi, K., *Analysis of Welded Structures*, International Series on Materials Science and Technology, Vol. 33, Pergamon Press, New York, 1980.

[15] Rybicki, E. F., Schmueser, D. W., Stonesifer, R. B. Groom, J. J., and Mishler, H. W., "Residual Stresses at Girth-Butt Welds in Pipes and Pressure Vessels," Report NUREG-0376, Nuclear Regulatory Commission, Washington, D.C., Nov. 1977.

[16] Brust, F. W and Kanninen, M. F., "Analysis of Two Methods for Retarding Stress Corrosion Cracking by Controlling Residual Stresses in Girth Welded Type 304 Stainless Steel Pipes," *American Society for Metals (ASM) Journal*, in press, 1981.

[17] Rybicki, E. F. and McGuire, P. A., "A Computational Model for Improving Weld Residual Stresses in Small Diameter Pipes by Induction Heating," to appear in *Journal of Pressure Vessel Technology*.

[18] Kanninen, M. F., Popelar, C. H., and Broek, D., "A Critical Survey on the Application of Plastic Fracture Mechanics to Nuclear Pressure Vessels and Piping," Battelle-Columbus Laboratories Report to the U.S. Nuclear Regulatory Commission, NUREG CR-2110, May 1981.

[19] Kanninen, M. F. et al, "The Development of a Plastic Fracture Methodology," Battelle-Columbus Laboratories Report to Electric Power Research Institute on RP601-1, EPRI NP-1734, Dec. 1980.

[20] Shih, C. F. et al, "Methodology for Plastic Fracture," General Electric Co. report to the Electric Power Research Institute on RP 601-2, EPRI NP-1735, March, 1981.

[21] Cheng, C. F., Ellingson, W. A. and Park, J. Y., "Effect of Residual Stress and Microstructure on Stress-Corrosion Cracking in BWR Piping," *Corrosion/76*, National Association of Corrosion Engineers, Houston, Tex., March 1976.

[22] Atkinson, C. and Kanninen, M. F., *International Journal of Fracture*, Vol. 13, 1977, p. 151.

[23] Shih, C. F., "Relationships Between the J-Integral and the Crack Opening Displacement for Stationary and Extending Cracks," *Journal of the Mechanics and Physics of Solids*, in press, 1981.

J-Integral and R-Curve

H. A. Ernst[1]

Unified Solution for *J* Ranging Continuously from Pure Bending to Pure Tension

REFERENCE: Ernst, H. A., **"Unified Solution for *J* Ranging Continuously from Pure Bending to Pure Tension,"** *Fracture Mechanics: Fourteenth Symposium—Volume I: Theory and Analysis, ASTM STP 791*, J. C. Lewis and G. Sines, Eds., American Society for Testing and Materials, 1983, pp. I-499–I-519.

ABSTRACT: This paper addresses the problem of determining *J* for a ligament subjected to arbitrary tension-bending loading, presenting a solution for *J* in terms of the load displacement characteristics. Several aspects of the problem are considered. First the Merkle-Corten analysis (MCA) for the compact specimen (CT) is reviewed, emphasizing its basic assumptions. Then the problem is stated in a general way and solved for *J* by assuming suitable relations between load and displacement. This results in a unified solution ranging continuously from pure bending to pure tension. The result agrees with previous investigators in the limits of pure bending and pure tension and closely approximates the MCA result for small tensile component ($0.6 < a/W$) in the CT. The two analyses are extensively discussed in the light of the constitutive equation used. The present work is also compared with finite-element results obtained by other investigators for the CT and the single-edge-notch specimen.

KEY WORDS: fracture mechanics, materials, J-integral, bending, tension, single-edge notch, solutions, calibration

With the increasing success of the J-integral [*1,2,3,4,5*][2] as the parameter describing fracture properties, significant effort has been devoted to reduce as much as possible the number of specimens needed for its experimental determination. Rice et al [*6*] made a significant contribution with their analysis of different deep cracked specimens relating *J* to area under the load-displacement record, which included a very small remaining ligament subjected to either pure bending or pure tension. In fact, for many years their analysis provided the only available tool to determine *J* from a single load-

[1]Senior research engineer, Materials Engineering Department, Westinghouse Research and Development Center, Pittsburgh, Pa. 15235.

[2]The italic numbers in brackets refer to the list of references appended to this paper.

displacement record. In particular, it became popular to use their formula for bending even when the starting assumption of a small remaining ligament subject to pure bending was not the actual testing condition (that is, compact specimen with a/W as low as 0.4).

Merkle and Corten [7] provided a significant step further by including the effect of the tensile component in their already classical analysis (MCA) of the compact specimen (CT). Their solution was shown to slightly overestimate J, for $a/W > 0.5$, but if the term involving the complementary energy is neglected as proposed by Landes et al [8], it gives excellent agreement with the J obtained with the multispecimen technique [4]. However, for situations where the tensile component becomes more important (that is, short cracks in the CT or the single-edge-notch specimen subject to tensile pin-load, SEN) a formula to experimentally determine J from a single P-δ record of a real material tested (arbitrary constitutive equation) is still needed.

Recently, Shiratori and Miyoshi [9] developed expressions for the location of the stress reversal point in the SEN and CT, of a rigid-perfectly plastic material based on lower bound, upper bound, and slip line approaches. They also obtained expressions for J in terms of load point displacement and its relation with crack-tip opening displacement (CTOD) for the perfectly plastic material, their expressions being "essentially the same as those of Merkle and Corten (1974) though the expressions are a little different" [9].

In this work, several aspects of the problem are considered. First the MCA [7] is briefly reviewed, emphasizing its basic assumptions. Then the problem of a ligament subject to arbitrary tension-bending combination is stated in a general way and solved in terms of J by assuming suitable relations between load and displacement. This results in unified solution, ranging continuously from pure bending to pure tension. It is also shown that the CT and the SEN are particular examples of the general formulation.

The analysis agrees with the Rice et al [6] result in the limit of pure tension and pure bending and closely follows the MCA for small tensile component ($a/W > 0.6$) in the CT. Moreover, the latter is shown to be in error when extrapolated to pure tension. The two analyses are discussed extensively in the light of the constitutive equations used. The present work is also compared with the Kumar et al [10] finite-elements results for the CT and SEN.

Merkle-Corten Analysis

As a starting point, consider briefly the MCA [7] for the CT shown in Fig. 1. The internal resisting moment per unit thickness at plastic collapse is given by

$$M_0 = \sigma_0 c^2(1 - \alpha^2) \tag{1}$$

and the limit load per unit thickness is

$$P_0 = \sigma_0 c(2\alpha) \tag{2}$$

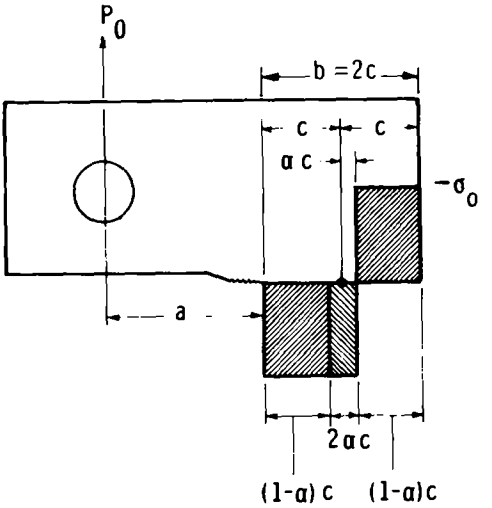

FIG. 1—*Stress conditions in a CT at plastic collapse.*

where σ_0 is the yield stress, c is half of the remaining ligament length, and α is the ratio of the internal stress block equilibrating the applied load to the remaining ligament length, $b = 2c$.

Equating the plastic moment M_0 to the moment of the applied load P_0 about the centroid of the net section gives

$$M_0 = P_0(a + c) \tag{3}$$

Equations 1, 2, and 3 can be combined to eliminate P_0 and M_0, and thus an equation for α can be obtained

$$\alpha^2 + 2\left(\frac{a}{c} + 1\right)\alpha - 1 = 0 \tag{4}$$

with solution

$$\alpha = \left[\left(\frac{a}{c}\right)^2 + \frac{2a}{c} + 2\right]^{1/2} - \left(\frac{a}{c} + 1\right) \tag{5}$$

Note that with α given by Eq 5, the dependence of the moment and load on crack length (Eqs 1 and 2 is completely specified.

As pointed out in the MCA, Eqs 1 through 5 "represent a lower bound plastic limit analysis of the net section, based on equilibrium ignoring the state of stress triaxiality caused by the crack tip" [*7*]. In any case, the particular value of the yield stress does not affect the value of J obtained when the latter is

related to area under the P-δ record. Note also that the presence of all boundaries, other than the back face, are ignored. Or in other words, the only two length parameters affecting (or describing) the problem are the distance from the crack tip to the back surface b, and the distance from the load-line to the back surface D. The MCA would give the same result independently of the location of all other boundaries.

Displacement Diagram and Constitutive Equation

The displacement diagram for a CT, as shown in Fig. 2, is obtained using a trigonometric type relation, assuming rigid rotation about the point of stress reversal. Thus, the plastic angle of rotation θ_{PL} is given by

$$\theta_{PL} = \frac{\delta_{PL}}{\alpha + (1 + \alpha)c} \tag{6}$$

where δ_{PL} represents the plastic part of the displacement measured at the load line.

Regarding the relation between load and displacement, a constitutive equation has to be assumed since it cannot be derived from the perfectly plastic analysis. In fact, in the MCA it is assumed that the plastic angle is a function of the ratio of the applied to the limit load only.

$$\theta_{PL} = \tilde{g}(P/P_0) \tag{7}$$

or inverting

$$P = P_0 g(\theta_{PL})$$

This equation indicates that the total dependence of the load on a/W is given through the limit load and the expression relating θ_{PL} and δ_{PL}. As indicated in the MCA, this is consistent with Rice's approach [6], although it is obviously not the only possible one.

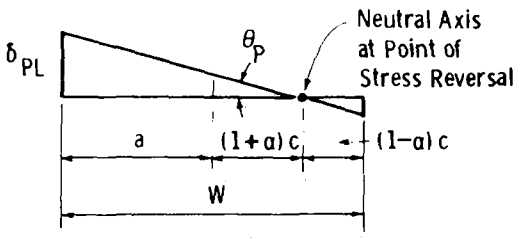

FIG. 2—*Displacement diagram for a CT at plastic collapse.*

Using Eq 7, the expression for J can be obtained in a straightforward manner, following the definition.

The displacement due to the crack δ can be separated in its elastic and plastic parts [*6,11,12*] δ_{EL} and δ_{PL}

$$\delta = \delta_{EL} + \delta_{PL} \tag{8}$$

Then J

$$J = -\int_0^P \left(\frac{\partial \delta}{\partial b}\right)_P dP = -\int_0^P \left(\frac{\partial \delta_{EL}}{\partial b}\right)_P dP - \int_0^P \left(\frac{\partial \delta_{PL}}{\partial b}\right)_P dP \tag{9}$$

The first term is the elastic part of J, that is, Griffith's G, and the second term following Ernst et al [*11,12*] can be written as

$$-\int_0^P \left(\frac{\partial \delta_{PL}}{\partial b}\right)_P dP = \int_0^{\delta_{PL}} \left(\frac{\partial P}{\partial b}\right)_{\delta_{PL}} d\delta_{PL} \tag{10}$$

giving for the total J

$$J = G + J_{PL} = G + \int_0^{\delta_{PL}} \left(\frac{\partial P}{\partial b}\right)_{\delta_{PL}} d\delta_{PL} \tag{11}$$

The expression relating P with δ_{PL} and b can be obtained from Eqs 5, 6, and 7, and then used for J_{PL} in Eq 11, giving

$$J_{PL} = \int_0^{\delta_{PL}} \frac{\partial P}{\partial b}\,\delta_{PL}\,d\delta_{PL} = g\int_0^{\delta_{PL}} \frac{\partial P_0}{\partial b}\,\delta_{PL}\,d\delta_{PL} + P_0\int_0^{\delta_{PL}} \frac{\partial g}{\partial \theta_{PL}}\,\frac{d\theta_{PL}}{d\delta_{PL}}\,d\delta_{PL} \tag{12}$$

Using Eqs 5, 6, and 7, Eq 12 can be written in the form (see the MCA [*7*] for details)

$$J_{PL} = \frac{2}{b}\,\frac{(1+\alpha)}{(1+\alpha^2)}\int_0^{\delta_{PL}} P\,d\delta_{PL} + \frac{2}{b}\,\alpha\left(\frac{1-2\alpha-\alpha^2}{(1+\alpha^2)^2}\right)\int_0^P \delta_{PL}\,dP \tag{13}$$

where α is given by Eq 5 and the integrals refer to the area and the complementary area under the load per unit thickness, P, versus plastic displacement, δ_{PL}, record respectively.

Or as defined in the MCA

$$J_{PL} = \frac{\eta}{b}\int_0^{\delta_{PL}} P\,d\delta_{PL} + \frac{\eta_c}{b}\int_0^P \delta_{PL}\,dP \tag{14}$$

where

$$\eta = 2\frac{(1+\alpha)}{(1+\alpha^2)}$$

$$\eta_c = \frac{2\alpha(1 - 2\alpha - \alpha^2)}{(1+\alpha^2)^2} \tag{15}$$

In Table 1, values of α, η, and η_c are listed for different a/W. It can be seen that for the case of pure bending ($b/W \to 0$, $\alpha \to 0$) the value of η approaches 2 while η_c approaches 0, thus Eq 14 converges to the familiar Rice et al result as it should.

As was mentioned before, for many years the MCA has provided the only way of obtaining J for the CT from a single P-δ record. It has been shown that this formula gives excellent results when compared to the multispecimen J for $a/W > 0.5$, if the term involving the complementary energy is neglected (that is, $\eta_c = 0$). For smaller a/W, it is believed to overestimate J although very limited work has been done.

The basic points of the analysis are the following: (1) Perfect plastic behavior is assumed to obtain the limit load P_o and the point of stress reversal (relation between θ_{PL} and δ_{PL}, Eq 6); however, the value of J does not depend on the particular value of P_o when referred to area under the curve. (2) The problem is described in terms of two length parameters only, b and D, and the location of the boundaries other than the back surface does not enter into the analysis. (3) A constitutive relation has been assumed between load and angle with Eq 7, or load and displacement if Eq 6 is used. As will be seen later, the last assumption is more suitable for situations where bending predominates. In fact, if the analysis is extended to situations where tension predominates by redefining terms, it fails to meet the required value in the limit (see next sections).

TABLE 1—*Merkle-Corten analysis.*

a/W	α	η	η_c
0	0.414	2.414	0.000
0.1	0.357	2.407	0.089
0.2	0.303	2.387	0.154
0.3	0.252	2.355	0.193
0.4	0.205	2.313	0.207
0.5	0.162	2.265	0.200
0.6	0.123	2.213	0.176
0.7	0.088	2.159	0.141
0.8	0.055	2.104	0.097
0.9	0.026	2.051	0.049
1.0	0.000	2.000	0.000

Ligament Subject to Arbitrary Bending Tension Loading

Consider now a cracked body, with a remaining ligament b, subject to a tension load per unit thickness P, applied perpendicular to the crack along a line lying at an arbitrary distance D from the back surface, as shown in Fig. 3. Note that depending on the relation between b and D different situations arise. If the load is applied very far from the back surface, $b/D \to 0$, the ligament is essentially subjected to pure bending; if, instead, the load is applied in the middle of the remaining ligament, $b/D \to 2$ and from a plastic analysis point of view the ligament is in pure tension. For $0 < b/D < 2$ all bending-tension combinations result.

According to Fig. 3, let d be the coordinate (positive or negative) of the crack tip taking the load line-crack line intersection as origin; let $x = d/D$ be the generalized dimensionless coordinate, and s the distance from the load line to the middle of the remaining ligament $s = D(1 + x)/2$. Let us assume as before that the plastic problem can be described in terms of two parameters, b and D (or b and x), implying that the only boundary taken into consideration is the back surface. The load diagram in terms of the general coordinates is shown in Fig. 4.

The plastic limit moment and limit load per unit thickness M_0 and P_0, respectively, are given by

$$M_0 = \sigma_0 \frac{b^2}{4}(1 - \alpha^2) = \frac{\sigma_0}{4} D^2 (1 - x)^2 (1 - \alpha^2) \tag{16}$$

$$P_0 = \sigma_0 b\alpha = \sigma_0 D (1 - x)\alpha \tag{17}$$

$$M_0 = P_0 s = \sigma_0 \frac{D^2}{2} (1 - x^2) \tag{18}$$

where

$$\begin{aligned} b &= D(1 - x) \\ s &= \frac{D}{2}(1 + x) \end{aligned} \tag{19}$$

As before, combining Eqs 16 through 18, an equation for α can be obtained

$$\alpha^2(1 - x) + 2\alpha(1 + x) - (1 - x) = 0 \tag{20}$$

with solution

$$\alpha = \left[\left(\frac{1 + x}{1 - x}\right)^2 + 1\right]^{1/2} - \left(\frac{1 + x}{1 - x}\right) \tag{21}$$

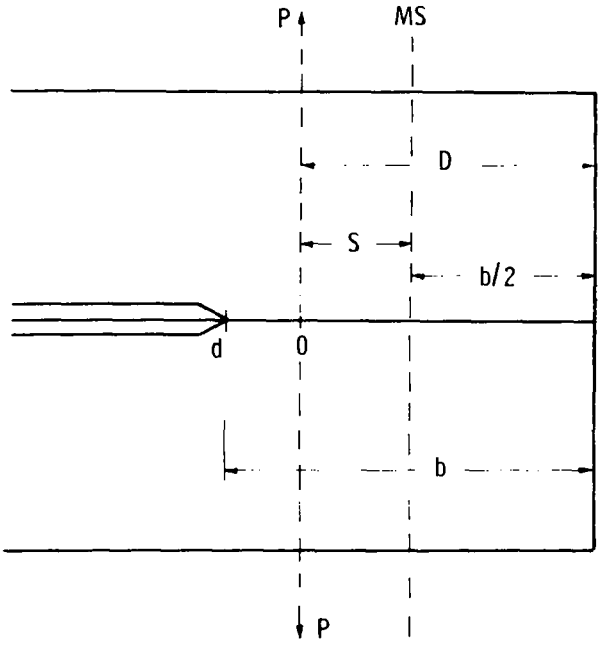

FIG. 3—*Extension of the MCA redefinition of coordinates.*

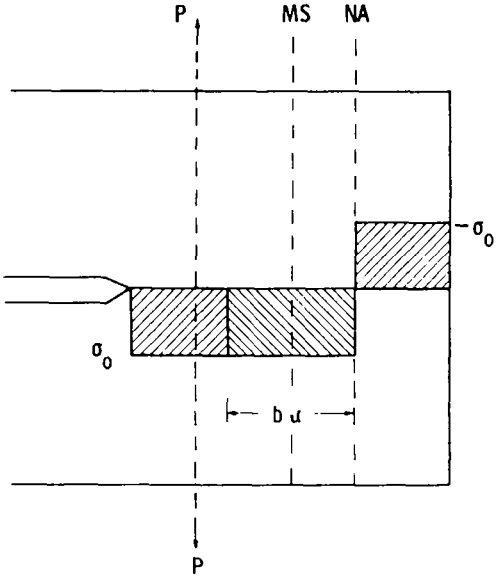

FIG. 4—*Stress conditions for a ligament subject to arbitrary tension-bending loading at plastic limit.*

The foregoing equation obviously coincides with Eq 5 for $x > 0$, because so far nothing more than a redefinition of coordinates has been made. However, the problem has been set now in a general way. The load line is not restricted to being left of the crack tip as in the original MCA ($b < D$), and that allows the extension of the problem to pure tension. By allowing x to range from 1 to -1 all situations from pure bending to pure tension are obtained (the CT and SEN being just special cases of the general formulation).

In this spirit, the MCA can be extended to situations where tension prevails. In fact α can be obtained from the more general Eq 21 and η and η_c can be still calculated from Eq 15. Nevertheless, as it can be seen from Table 2 and Fig. 5, for $x \to -1$, $\eta \to 2$, J becomes

$$J = \frac{2}{b}\int_0^{\delta} P d\delta = \frac{2}{b} P\delta$$

for pure tension in a perfectly plastic material; on the other hand, Rice's [6] limit for this case is

$$J = \frac{P\delta}{b}$$

TABLE 2—*Extension of the Merkle-Corten analysis.*

x	η
−1.0	2.000
−0.9	2.051
−0.8	2.104
−0.7	2.159
−0.6	2.213
−0.5	2.265
−0.4	2.313
−0.3	2.355
−0.2	2.387
−0.1	2.407
0	2.414
0.2	2.407
0.2	2.387
0.3	2.355
0.4	2.313
0.5	2.265
0.6	2.213
0.7	2.159
0.8	2.104
0.9	2.051
1.0	2.000

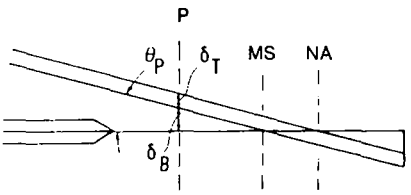

FIG. 5—*Displacement diagram for a ligament subject to arbitrary tension-bending loading at plastic limit.*

Thus, even though the MCA can be extended using a redefinition of coordinates, it does not give the correct value at the limit. This result shows that the problem of a ligament subjected to arbitrary tension-bending loading cannot be approached by a mere extension of the already available MCA using a generalization of coordinates.

Instead, a major change in the basic assumptions is needed to better describe the problem from a physical point of view. Specifically, the MCA was originally intended to serve for the CT, and this is reflected in the particular constitutive relation used, Eq 7, which best suits situations where bending prevails. For the more general case, the constitutive equation has to be able to accurately describe the problem in its whole range. In the following sections this approach is presented as well as its consequences in terms of J.

Displacement Diagram and Constitutive Equations

Let us assume here that the plastic displacement δ_{PL} can be separated in a part due to bending δ_{PB} and a part due to tension δ_{PT}. As shown in Fig. 5, the total plastic displacement δ_{PL} is still obtained (in the plastic limit) from a trigonometric type relation, but here the final "position of the transverse line" (displacement profile) can be thought as being the result of a rigid rotation about the midsection point plus a rigid translation producing zero displacement at the point of stress reversal. Thus according to Fig. 5

$$\delta_{PL} = \delta_{PB} + \delta_{PT} \tag{22}$$

$$\delta_{PB} = \delta_{PL}\left(\frac{s}{s + \alpha b/2}\right) \tag{23}$$

$$\delta_{PT} = \delta_{PL}\left(\frac{\alpha b/2}{s + \alpha b/2}\right)$$

or using Eq 19

$$\frac{\delta_{PB}}{\delta_{PL}} = \frac{(1 + x)}{(1 + x) + \alpha(1 - x)} \tag{24}$$

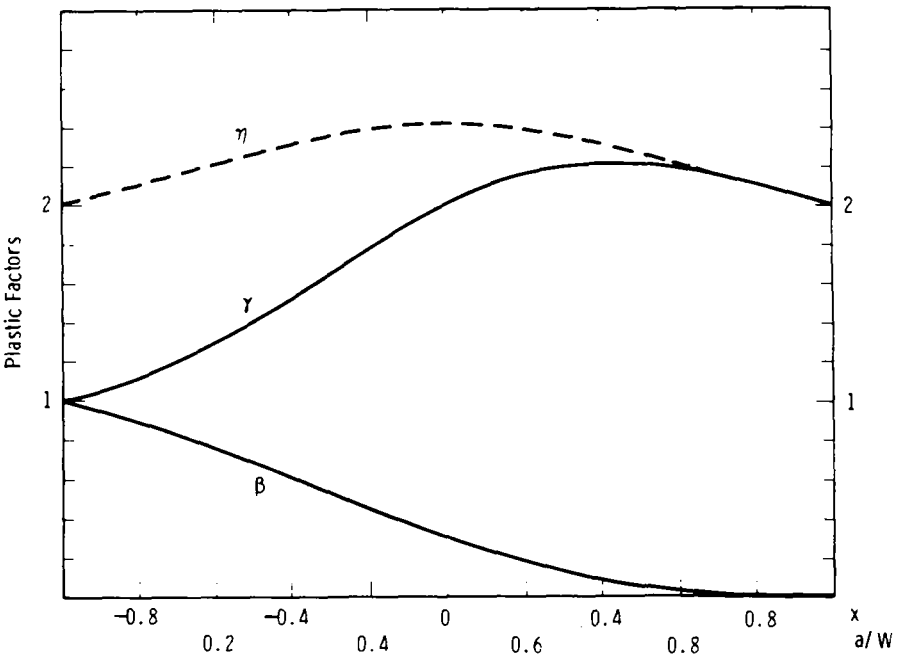

FIG. 6—*Plastic factor* η, γ, *and* β *versus generalized coordinate* x *and single-edge notch* a/W.

$$\frac{\delta_{PT}}{\delta_{PL}} = \frac{\alpha(1-x)}{(1+x)+\alpha(1-x)} \tag{24}$$

In real situations the different displacements are connected in a more complex way than just the simple rigid rotation model. In fact, hardening exponent, level of deformation, and changes in location of the point of stress reversal due to increasing deformation are variables expected to modify the picture.

However, these displacements are expected to be affected proportionally by the previously mentioned variables. Thus, ratios of "individual" displacements δ_{PB} and δ_{PT} to the total plastic one δ_{PL} are not expected to be very different than those shown in Eq 24 obtained from a rigid rotation model. As emphasized before when referring to actual value of σ_0, no attempt is made to predict the absolute value of these quantities: they will be determined from the P-δ record itself. Nevertheless, even if no statement is made about the absolute value, the functional form can be proposed following the spirit of the dimensional analysis in Rice's work [*6*]. Therefore, the bending part of the plastic displacement δ_{PB} can be written as

$$\frac{\delta_{PB}}{D} = \tilde{g}(P/P_0) \tag{25}$$

or inverting

$$P = P_0 g(\delta_{PB}/D)$$

On the other hand, the tension part of the plastic displacement δ_{PT} can be written as

$$\frac{\delta_{PT}}{b} = \tilde{h}(P/b) \tag{26}$$

or inverting

$$P = b\, h(\delta_{PT}/b)$$

AS discussed later, Eq 24 coincides with the MCA for $\chi \to 1$ ($a/W \to 1$), but for shorter cracks the former departs the latter.

J Analysis

Once the constitutive relations of Eqs 24, 25, and 26 have been established, *J* can be calculated in a rather straightforward (although sometimes laborious) manner just by applying the definition

$$J = \int_0^P \left(\frac{\partial \delta}{\partial a}\right)_p dP \tag{27}$$

or following Refs *6, 7,* and *11-13*

$$J = G + \int_0^P \left(\frac{\partial \delta_{PL}}{\partial a}\right)_p dP \tag{28}$$

for this case using Eq 22

$$\begin{aligned} J &= G + J_{PL} \\ &G + \int_0^P \frac{\partial}{\partial a}(\delta_{PB})\, dP + \int_0^P \frac{\partial}{\partial a}(\delta_{PT})\, dP \end{aligned} \tag{29}$$

The last equation can be evaluated by using Eqs 25 and 26 (see Appendix for detailed analysis) giving as a result

$$J = G + \frac{\gamma}{b}\int_0^P P d\delta_{PL} - \frac{\beta}{b}\int_0^P \delta_{PL}\, dp \tag{30a}$$

or rearranging

$$J = G + \frac{(\gamma + \beta)}{b} \int_0^P P d\delta_{PL} - \beta \frac{P\delta_{PL}}{b} \tag{30b}$$

with

$$\gamma = \left[\frac{2(1+\alpha)(1+x)}{(1+\alpha^2)} + \alpha(1-x) \right] \times \left[\frac{1}{(1+x) + \alpha(1-x)} \right] \tag{31}$$

and

$$\beta = \frac{\alpha}{\alpha + \left(\frac{1+x}{1-x} \right)} \tag{32}$$

Values of γ, β as functions of x (or a/W) can be found in Table 3 and in Fig. 5.

Discussion

Limits

When the limit of pure bending is approached, that is, $x \to 1$, as it can be seen in Fig. 5 and Table 3, $\gamma \to 2$ and $\beta \to 0$; as a result Eq 30 gives for J_{PL} the correct Rice's limit for pure bending [*6*]

$$J_{PL} = \frac{2}{b} \int_0^{\delta_{PL}} P d\delta_{PL}$$

On the other hand when the limit of pure tension is approached, as shown in Fig. 5 and Table 3, $\gamma \to 1$ and $\beta \to 1$, the result from Eq 30 becomes

$$J_{PL} = \frac{1}{b} \int_0^{\delta_{PL}} P d\delta_{PL} - \frac{1}{b} \int_0^P \delta_{PL} dP$$

$$= \frac{2}{b} \int P d\delta_{PL} - \frac{P\delta_{PL}}{b}$$

which again is the correct Rice's limit for pure tension [*6*].

It is emphasized (as can be seen from Fig. 5 and Table 3) that the present analysis completely agrees with the MCA in the region $0.6 < x \leq 1$, where the latter has been extensively checked.

TABLE 3—*Ligament subjected to arbitrary tension-bending loading.*

x	$(a/W)_{SEN}$	$(a/W)_{CT}$	γ	β
−1.0	0.00	...	1.000	1.000
−0.9	0.05	...	1.055	0.947
−0.8	0.10	...	1.122	0.890
−0.7	0.15	...	1.201	0.826
−0.6	0.20	...	1.294	0.758
−0.5	0.25	...	1.400	0.684
−0.4	0.30	...	1.517	0.606
−0.3	0.35	...	1.643	0.526
−0.2	0.40	...	1.769	0.445
−0.1	0.45	...	1.891	0.367
0.0	0.50	0.0	2.000	0.293
0.1	0.55	0.1	2.089	0.226
0.2	0.60	0.2	2.154	0.168
0.3	0.65	0.3	2.193	0.119
0.4	0.70	0.4	2.207	0.081
0.5	0.75	0.5	2.200	0.051
0.6	0.80	0.6	2.177	0.030
0.7	0.85	0.7	2.141	0.015
0.8	0.90	0.8	2.097	0.006
0.9	0.95	0.9	2.050	0.001
1.0	1.00	1.0	2.000	0.000

Constitutive Equations

The present work follows the spirit of the MCA although a different constitutive relation between load and displacement is used. As was mentioned before, the relationships given in Eqs 6 and 7 are for situations where bending is the main component. In fact, if the arm s (or D) is big compared with $b/2$, Eqs 6 and 7 are expected to be accurate. On the other hand, for cases where the tension component is more important, that is, the arm s is not so large and D is nearly $b/2$, Eqs 6 and 7 are not expected to be adequate; in fact, the errors in the angle and plastic displacement prediction might be large.

A better description of the problem can be achieved by separating the plastic displacement in its bending and tension parts, δ_{PB} and δ_{PT}, respectively. In this way even if Eq 7 is not too accurate, the relative contribution of bending to the total displacement is small and Eq 13 is in order.

At the same time, following previous analyses [*11,12,13*], the angle has been replaced by δ_{PB}/W.

With respect to the tension part: if a load P is applied at a certain distance D from the back surface, the ligament is subjected to a tension load that is precisely P. Thus, the Rice et al analysis [*6*] was followed, resulting in constitutive Eq 26.

Applicability: Rule of Similarity

This work gives an expression for J based on the load displacement record of a single specimen ranging continuously from pure tension to pure bending. The solution is presented in terms of the plastic factors γ and β, which are functions of the general dimensionless variable x *only*. Therefore a solution can be obtained for a ligament subjected to *any arbitrary* bending tension combination. In fact, the percent of bending (POB) and the percent of tension (POT) can be defined via the nominal stress in terms of the variable x. The nominal stresses due to bending and tension, σ_{NB} and σ_{NT}, can be defined as [*14*]

$$\sigma_{NB} = \frac{P}{D} 3 \frac{(1+x)}{(1-x)^2}$$

$$\sigma_{NT} = \frac{P}{D} \frac{1}{(1-x)}$$

and as a consequence the POT and POB are given by

$$\text{POT} = \frac{\sigma_{NT}}{\sigma_{NT} + \sigma_{NB}} = \frac{(1-x)}{2(2+x)} \times 100$$

$$\text{POB} = \frac{\sigma_{NT}}{\sigma_{NT} + \sigma_{NB}} = \frac{3}{2} \frac{(1+x)}{(2+x)} \times 100$$

Thus the following rule of similarity can be stated: Two specimens having the same POB or POT or both (that is, the same x) behave similarly and thus the same value of γ and β must be used for both. This means that the curves γ and β versus x can be used as master curves to solve any two-dimensional problem of a ligament subject to arbitrary POB (or POT). In fact, for any given specimen the value of x can be easily obtained from specimen geometry, crack length, total width, and so forth. With the particular value of x, the corresponding values of γ and β can be obtained from this analysis.

For example, using the nomenclature defined in Fig. 3 for the CT

$$W = D$$

$$a = d$$

thus

$$x = d/D = a/W \tag{33}$$

For the SEN instead, if W is the total width

$$a - \frac{W}{2} = d$$

thus

$$x = d/D = (2a/W - 1) \tag{34}$$

Then using Eqs 33 and 34, a CT and a SEN will have the same plastic factors γ and β when

$$(a/W)_{CT} = \left(\frac{2a}{W} - 1\right)_{SEN} \tag{35}$$

Note that this analysis ignores all boundaries other than the back face, and the whole plastic problem is described using two length parameters, b and D (or x and D). Thus, the obtained equations are not expected to hold in situations where the front face is close to the tip of the crack (that is, ratio of crack length to total width <0.3).

Comparison with Finite-Element Results

As a way of checking the present analysis and the Rule of Similarity stated previously, a crucial comparison was made with the finite-elements results of Kumar et al [*10*]. In their work, expressions for J and load-point displacement δ in terms of P, a, and the hardening exponent n for different geometries were obtained.

$$\begin{aligned} J &= J(a, P, n) \\ \delta &= \delta(a, P, n) \end{aligned} \tag{36}$$

In particular, their results for the CT and SEN were re-expressed, after some algebra in the form

$$J = \frac{\mu}{b} \int_0^{\delta} P\, d\delta$$

$$\text{with } \mu = \mu(a/W, n) \tag{37}$$

In both cases (CT and SEN), the values of a/W were converted to x using the Rule of Similarity of Eqs 33 and 34, and thus values of $\mu = \mu(x, n)$ were obtained. This allows the plotting values of μ for *both configurations* in the *same curve*.

On the other hand, if a pure power relation is assumed, $P = k\, \delta_{PL}^{1/n}$, (as in Kumar et al [*10*]), Eq 30 becomes

$$J = G + \frac{\gamma}{b} \int_0^{\delta_{PL}} P\, d\delta_{PL} - \frac{\beta}{b} \int_0^{P} \delta_{PL}\, dP$$

can be restated as

$$J = G + \frac{\gamma_t}{b} \int_0^{\delta_{PL}} P d\delta_{PL} \tag{38}$$

$$\text{with } \gamma_t = (\gamma - \beta/n) \tag{39}$$

In Fig. 7, a plot of γ_t and μ from Eqs 37 and 30 versus x for $n = 10$ is shown.

The good agreement indicates the accuracy of the present analysis as well as the viability of using the Rule of Similarity.

Conclusions

1. The problem of determining J for a ligament subjected to arbitrary tension-bending loading was considered.

2. It was shown that by proper redefinition of coordinates the MCA for the CT can be extended to situations where tension prevails over bending, but it does not give the correct result for pure tension.

3. By assuming a proper constitutive equation, an expression for J was obtained based on the P-δ record for arbitrary tension-bending combination.

4. The present analysis agrees with the Rice limits [6] for pure bending and pure tension, and closely approximates the MCA for $a/W > 0.6$ ($x > 0.6$).

5. A Rule of Similarity was stated, allowing the use of this analysis for the general problem.

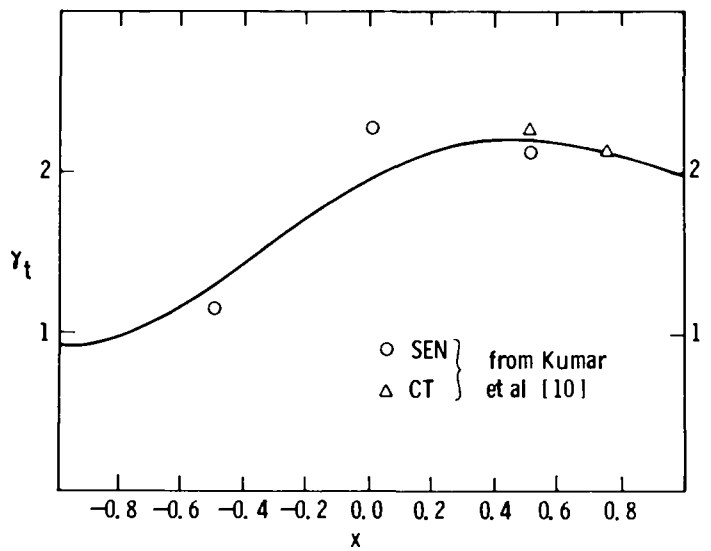

FIG. 7—*Total plastic factor* γ_t *and* μ *versus* x *for the CT and SEN hardening exponent* n = *10 (plane strain).*

6. A successful comparison with finite-element results regarding both the Rule of Similarity and the analysis itself was made.

Acknowledgments

This investigation was partially supported by the Electric Power Research Institute (EPRI) under Contract No. RP-1238-2, D. M. Morris, Project Manager. The author wants to thank J. D. Landes from Westinghouse Research and Development Center for his valuable contribution regarding several aspects of this work.

Appendix

J Analysis for a Ligament Subjected to Arbitrary Tension-Bending Loading

As was mentioned, the plastic displacement δ_{PL} can be separated in its bending and tension parts, δ_{PB} and δ_{PT}, as

$$\delta_{PL} = \delta_{PB} + \delta_{PT} \tag{40}$$

And thus for J_{PL}, one gets

$$J_{PL} = -\int_0^P \frac{\partial \delta_{PL}}{\partial b}\Big)_P dP = -\int_0^P \frac{\partial \delta_{PT}}{\partial b}\Big)_P dP - \int_0^P \frac{\partial \delta_{PB}}{\partial b}\Big)_P dP \tag{41}$$

The first integral of the right-hand side can be evaluated using the constitutive relation

$$\delta_{PT} = b\tilde{h}(P/b) \tag{42}$$

In fact, by differentiating and integrating by parts

$$\begin{aligned} -\int_0^P \frac{\partial \delta_{PT}}{\partial b}\Big)_P dP &= \int_0^P b\tilde{h}' \frac{P}{b}\frac{dP}{b} - \int_0^P \tilde{h}\, dP \\ &= -\int_0^P \tilde{h}\, dP + \tilde{h}P - \int_0^P \tilde{h}\, dP \\ &= \frac{2}{b}\left\{\int_0^{\delta_{PT}} P d\delta_{PT} - \frac{P\,\delta_{PT}}{2}\right\} \end{aligned} \tag{43}$$

The second integral in Eq 41 can be evaluated with the help of the constitutive relations

$$\frac{\delta_{PB}}{W} = \tilde{g}(P/P_0) \tag{44}$$

$$P_0 = \sigma_0 b\alpha \tag{45}$$

As a first step, the second integral can be written as

$$-\int_0^P \frac{\partial \delta_{PB}}{\partial b}\Big)_P dP = -W\int_0^P \tilde{g}'\,\frac{P}{P_0^2}\,\frac{\partial P_0}{\partial b}\,dP \tag{46}$$

but from Eq 42

$$\frac{\partial P_0}{\partial b} = \sigma_0(\alpha + b\,\partial\alpha/\partial b) \tag{47}$$

Now using Eq 4

$$\alpha^2 + \left(\frac{4a}{b} + 2\right)\alpha - 1 = 0$$

or replacing $a = W - b$

$$\alpha^2 + \left(\frac{2W}{b} - 2\right)\alpha - 1 = 0 \tag{48}$$

By differentiating Eq 48 and reusing it to eliminate b/W one gets

$$\frac{\partial\alpha}{\alpha b} = \frac{1}{b}\,\frac{(1 + 2\alpha - \alpha^2)\,\alpha}{(1 + \alpha^2)} \tag{49}$$

Combining Eqs 49 and 47,

$$\frac{\partial P_0}{\partial b} = \sigma_0\,\frac{2\alpha(1 + a)}{(1 + \alpha^2)} \tag{50}$$

Replacing Eq 50 in Eq 46 gives

$$\begin{aligned}
-\int_0^P \frac{\partial \delta_{PB}}{\partial b}\Big)_P dP &= -W\int_0^P \tilde{g}'\,\frac{P}{P_0}\,\frac{2}{b}\,\frac{(1 + \alpha)}{(1 + \alpha^2)}\,dP \\
&= \frac{-2W}{b}\left(\frac{1 - \alpha}{1 + \alpha^2}\right)P_0\left\{\tilde{g}\,\frac{P}{P_0} - \int_0^P \frac{\tilde{g}}{P_0}\,dP\right\} \\
&= \frac{-2}{b}\left(\frac{1 + \alpha}{1 + \alpha^2}\right)\left\{\delta_{PB}\,P - \int_0^P \delta_{PB}\,dP\right\} \\
&= \frac{2}{b}\,\frac{1 + \alpha}{1 + \alpha^2}\int_0^{\delta_{PB}} P\,d\delta_{PB}
\end{aligned} \tag{51}$$

Adding Eqs 43 and 51 gives

$$J_{PL} = \frac{2}{b}\,\frac{1 + \alpha}{1 + \alpha^2}\int_0^{\delta_{PB}} P\,d\delta_{PB} + \frac{2}{b}\int_0^{\delta_{PT}} P\,d\delta_{PT} - \frac{P\delta_{PT}}{b} \tag{52}$$

Using Eq 24 for the relative displacements

$$\frac{d\delta_{PB}}{d\delta_{PL}} = \frac{(1+x)}{(1+x)+\alpha(1-x)} \qquad (53)$$

$$\frac{d\delta_{PT}}{d\delta_{PL}} = \frac{\alpha(1-x)}{(1+x)+\alpha(1-x)}$$

one gets for J_{PL}

$$J_{PL} = \frac{\gamma}{b}\int_0^{\delta_{PL}} P d\delta_{PL} - \frac{\beta}{b}\int_0^{P} \delta_{PL}\, dP \qquad (54)$$

or

$$J_{PL} = \frac{\gamma + \beta}{b}\int_0^{\delta_{PL}} P d\delta_{PL} - \frac{\beta P \delta_{PL}}{b}$$

with γ and β given by

$$\gamma = \frac{\dfrac{2(1+\alpha)(1+x)}{(1+\alpha^2)} + \alpha(1-x)}{(1+x)+\alpha(1-x)} \qquad (55)$$

$$\beta = \frac{\alpha}{\alpha + \dfrac{1+x}{1-x}}$$

References

[1] Rice, J. R., *Journal of Applied Mechanics*, Vol. 35, 1968, pp. 379-386.

[2] Hutchinson, J. W., *Journal of the Mechanics and Physics of Solids*, Vol. 16, No. 1, 1968, pp. 13-31.

[3] Rice, J. R. and Rosengren, G. F., *Journal of the Mechanics and Physics of Solids*, Vol. 16, No. 1, 1968, pp. 1-12.

[4] Begely, J. A. and Landes, J. A. in *Fracture Toughness. ASTM STP 514*, American Society for Testing and Materials, 1972, pp. 1-23.

[5] Landes, J. D. and Begley, J. A. in *Fracture Toughness, ASTM STP 514*, American Society for Testing Materials, 1972, pp. 24-39.

[6] Rice, J. R., Paris, P. C., and Merkle, J. G. in *Progress in Flaw Growth and Fracture Toughness Testing, ASTM STP 536*, American Society for Testing and Materials, 1973, pp. 231-245.

[7] Merkle, J. and Corten, H., *Journal of Pressure Vessel Technology Transactions of American Society of Mechanical Engineers*, 1974, pp. 286-292.

[8] Landes, J. D., Walker, H., and Clarke, G. A. in *Elastic-Plastic Fracture, ASTM STP 668*, American Society for Testing and Materials, 1979, pp. 266-287.

[9] Shiratori, M. and Miyoshi, T., "Evaluation of Constraint Factor and J-Integral for Single Edge Notched Specimen," Third International I. Smith, Ed., Pergamon Press, 1980.

[10] Kumar V., German, M. D., and Shih, C. F, "Estimation Techniques for the Prediction of Elastic-Plastic Fracture of Structural Components of Nuclear Systems," Combined 2nd and 3rd Semiannual Report to Electric Power Research Institute (EPRI), General Electric Co., 1 June 1980.

[11] Ernst, H. A., Paris, P. C., Rossow, M., and Hutchinson J. W. in *Fracture Mechanics, ASTM STP 677*, American Society for Testing and Materials, 1979, pp. 581-599.

[12] Ernst, H. A. and Paris, P. C., "Techniques of Analysis of Load-Displacement Records by J-Integral Methods," Nuclear Regulatory Commission, NUREG/CR-1222, Jan. 1980; also available as H. A. Ernst, PhD Thesis, Department of Mechanical Engineering, Washington University, St. Louis, Mo., Dec. 1979.

[13] Ernst, H. A., Paris, P. C., and Landes, J. D. in *Fracture Mechanics (13th Conference), ASTM STP 743*, American Society for Testing and Materials, 1981, pp. 476-502.

[14] Tada H., Paris, P. C., and Irwin, G. R., "The Stress Analysis of Cracks Handbook," Del Research Corporation, Hellertown, Pa., 1973.

R. H. Dodds, Jr.,[1] *D. T. Read,*[2] *and G. W. Wellman*[1]

Finite-Element and Experimental Evaluation of the J-Integral for Short Cracks

REFERENCE: Dodds, R. H., Jr., Read, D. T., and Wellman, G. W., **"Finite-Element and Experimental Evaluation of the J-Integral for Short Cracks,"** *Fracture Mechanics: Fourteenth Symposium—Volume I: Theory and Analysis, ASTM STP 791*, J. C. Lewis and G. Sines, Eds., American Society for Testing and Materials, 1983, pp. I-520–I-542.

ABSTRACT: Fitness-for-service assessments of critical metal structures such as piping systems, pressure vessels, and ships require accurate predictive methods for fracture of parts containing small flaws or short cracks. Flaw size, geometry, applied loads, fabrication, and material characteristics often combine to produce large-scale plastic zones inappropriate for evaluation by linear elastic fracture mechanics. The J-integral is widely advocated as a suitable parameter to characterize both material fracture toughness and the driving force in elastic-plastic fracture. Procedures have been proposed to measure the material fracture toughness, J_{Ic}, for standard test specimen geometries containing large crack lengths. However, there are no generally accepted methods to predict or experimentally measure the applied J-integral within a structural element containing a small crack (defined here by a crack length to remaining ligament ratio, a/W, < 0.25).

This paper describes analytical studies conducted using the finite-element method (FEM) to predict applied J-integral values in single-edge-notch tensile panels (width/thickness $\approx$ 9) of HY-130 steel for crack lengths in the range $0.02 \leq a/W \leq 0.22$. Nominal strain levels beyond yield are addressed specifically. Comparisons are made with preliminary experimental J-values obtained by integrating strain and displacement quantities measured along an instrumented contour. FEM plane stress predictions for applied J increasingly exceed experimentally measured values for decreasing crack lengths with large discrepancies observed at strain levels above nominal yield. The introduction of a small stiffened zone that provides partial through-thickness constraint around the crack tip, using a plane stress-plane strain overlay scheme, considerably reduces the disagreement. Near tip stiffening also improves results in the regime between elastic and fully plastic response and slightly elevates the predicted limit loads.

These computational results suggest a strong dependence of the applied J on partial through-thickness constraint near the tips of short cracks under conditions normally considered plane stress. The effect of near tip stiffening diminishes for crack lengths greater than the specimen thickness, but does reduce the small remaining discrepancy between

[1]Assistant professor of civil engineering and graduate research assistant, respectively, University of Kansas, Lawrence, Kans. 66044.

[2]Fracture and Deformation Division, National Bureau of Standards, Boulder, Colo. 80303.

FEM plane stress and experimental J-values for longer cracks. Both experimental and computational evidence imply the existence of a transition range of crack lengths in which the applied J begins to decrease significantly at strains above yield as the crack length approaches zero. Given the existence of a small flaw in a critical structural component, knowledge of this transition range behavior may prove essential for defect assessment. Two-dimensional FEM plane stress models do not predict this behavior unless augmented with the partial thickness constraint capability near the crack tip. The modeling scheme adopted in this study can be utilized without modification of standard elastoplastic analysis software and appears to minimize the necessity of expensive, three-dimensional nonlinear computations.

KEY WORDS: J-integral, finite-element method, experimental results, plane stress, plane strain, near tip constraint, fracture mechanics

Fitness-for-service assessments of critical metal structures such as piping systems, pressure vessels, and ships require accurate predictive methods for fracture of parts containing small flaws or short cracks. The majority of flaws that develop in critical structures are generally quite small with respect to in-plane dimensions of the affected component. Flaw size, geometry, fabrication, applied loads, and material characteristics often combine to produce large scale plasticity conditions inappropriate for evaluation by linear elastic fracture mechanics (LEFM). There is a considerable absence of experimental data, and consequently, verified analytical techniques to describe the elastic-plastic fracture behavior of small flaws (defined here by crack length to remaining ligament ratios $a/W < 0.25$). This paper describes parallel experimental and analytical investigations of small flaw effects within the framework of a J-integral based elastic-plastic fracture methodology.

The J-integral, introduced by Rice [*1*],[3] is widely advocated as both a measure of elastic-plastic deformation intensity near a crack tip and as a means of characterizing material fracture toughness [*2,3*]. Compared with the crack-opening displacement method (COD), the J-integral offers several advantages including a precise definition of the fracture characterizing parameter and direct correspondence with LEFM under purely elastic conditions. Previous experimental studies of the J-integral have concentrated largely on standard material fracture toughness test specimen geometries (3 point bend, compact tension, etc.) for moderate to deep initial flaw lengths ($0.5 < a/W < 0.75$). Within this range of crack lengths, the applied J has been found to be nearly independent of a/W for a specified load point displacement. This important result combined with analytical methods relating absorbed energy from load point displacement records to applied J spurred development of the ASTM Test for J_{Ic}, a Measure of Fracture Toughness (E 813-81) to determine J_{Ic} for correlation with plane strain fracture tough-

[3]The italic numbers in brackets refer to the list of references appended to this paper.

ness K_{Ic}. The J-integral concept now is adopted widely for the evaluation of material fracture toughness, as measured by J_{Ic}, for relatively ductile materials.

The multiple specimen test procedure developed by Begley and Landes [2] provides a general technique to experimentally determine the applied J as a function of load point displacement. However, the procedure breaks down for small a/W as compliance changes become increasingly difficult to measure. Similarly, J prediction schemes that use limit load solutions to estimate the terminal slope of the applied J versus load point displacement curves become suspect as a/W ratios decrease. The simple limit load solutions, which idealize the behavior as either plane stress or plane strain, neglect thickness direction constraint near notch tips and changes in behavior that occur between net and gross section yield. The center cracked tensile panel illustrates this problem. The limit load is given by $2B(W - a)$ σ_y, where B is specimen thickness, W the width per crack tip, a the crack length per crack tip, and σ_y the material yield stress. This expression predicts a terminal J-displacement slope (dJ/dV, where V is the load point displacement) that is independent of a/W and given by 1.0 σ_y (plane stress) or 1.15 σ_y (plane strain). The implication is that as a/W approaches zero, the terminal J-displacement slope abruptly vanishes because for $a = 0$, J also must be zero. Such a sudden change in behavior seems unrealistic, and indeed, experimental and computational results presented herein suggest the existence of a transition range of a/W during which the slope of the J-displacement relationship gradually decreases to zero. Given the existence of a flaw in a large structural component such that a/W is quite small, knowledge of whether the flaw lies within or beyond an a/W transition limit may prove essential in assessing the defect significance.

In this work, the finite-element method (FEM) has been applied to study the relationship between flaw size, loading, and applied J interpreted as the fracture driving force for small cracks. To date, studies have been completed for single edge notch (SEN) tensile panels of HY-130 steel containing through-thickness notches of $a/W < 0.25$. The primary purpose here is to examine the adequacy of analytical techniques to predict applied J-values for small flaw sizes in the plastic range. A nonlinear finite-element approach that employs a hybrid plane stress-plane strain model of material behavior near the crack tip is explored in addition to conventional plane stress and plane strain procedures. Comparisons are made with experimental J-values obtained by integrating strain and displacement quantities measured along an instrumented contour. Finite-element predicted crack-mouth opening displacement (CMOD) and the overall load displacement response are similarly compared with experimental results. A brief description of the experimental procedure to measure J by instrumenting a contour is included for completeness.

Experimental Procedure

This section provides a brief summary of the experimental procedure and methods employed to evaluate the J-integral from test measurements. Full details of the experimental program and data reduction process are described elsewhere [*4*].

Test specimens were machined to the dimensions shown in Fig. 1 from 2.54-cm-thick, annealed HY-130 steel plate. The chemical composition and mechanical properties of this material are summarized in Tables 1 and 2. The reference axis shown on the figure parallels the principal rolling direction. A gage test section 9 by 30 cm and 1 cm thick was used for all experiments. Specimens were instrumented with strain gages and by linear variable differential transformers (LVDT's) to measure overall extension and cross-section rotation as shown in Fig. 1. Tests were conducted for 1, 2, 4, 7, and 20-mm single edge notches. Saw cut notches of width 0.46 mm were used rather than fatigue cracks to postpone the onset of stable crack growth. This permitted overall gage strains (ϵ_g) of 3 to 8 times nominal yield prior to observed tearing. The gage strain, defined as the average of the three LVDT readings divided by the gage length (30 cm), provides a convenient measure of the extensional deformation.

Measured strains and displacements obtained during a test permit evaluation of the *J*-integral defined by Rice [*1*] as

$$J = \int_\Gamma \overline{W}\, dy - \int_\Gamma \{t\}^T \frac{\partial}{\partial x} \begin{Bmatrix} u \\ v \end{Bmatrix} ds \tag{1}$$

for two-dimensional problems. In this equation, $\{t\}$ represents Cartesian components of the traction vector directed along the outward normal to path Γ. Displacement components u and v are also directed along the x-y axes; where y is perpendicular to the notch plane. The strain energy density, $\overline{W}$, is defined by

$$\overline{W} = \int_0^\epsilon \{\sigma\}^T \{d\epsilon\} \tag{2}$$

for nonlinear material behavior.

The contour, Γ, selected for experimental J evaluation as shown in Fig. 1, follows free edges where possible and traverses the gage section far from the notch. The contour consists of three straight segments denoted A-B, B-C, and C-D. Equation 1 for this particular contour is conveniently split into three simple integrals, one for each segment. Only the first term of Eq 1 contributes to J for free edge segments A-B and C-D. Moreover, the strain energy density is entirely determined by ϵ_{yy} along these edges and is given numerically by the area under the tensile stress-strain curve for the material. Measured strains were used in conjunction with a nonlinear curve fitting pro-

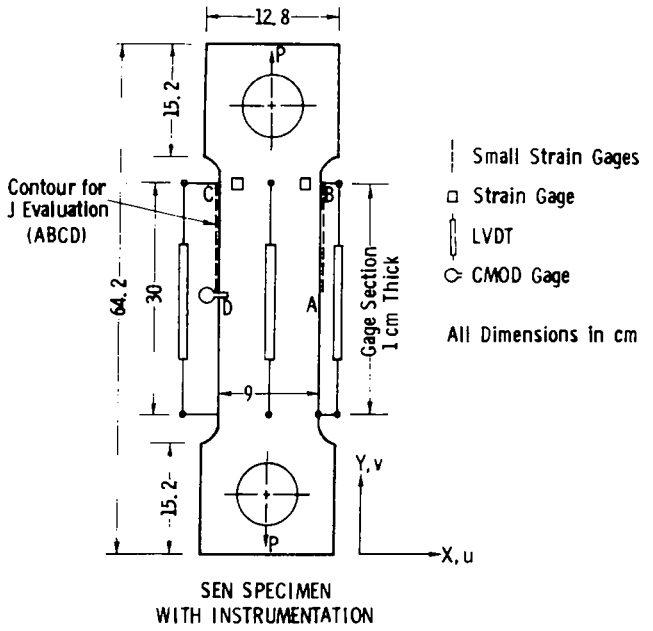

FIG. 1—*Specimen geometry and instrumentation along the contour for J evaluation.*

TABLE 1—*Chemical composition of HY-130 steel, weight percent.*

C	Mn	P	Si	Ni	Cr	Mo	V	S	Cu	Al	Co	Ti
0.11	0.76	0.005	0.03	5.0	0.42	0.53	0.043	0.004	0.022	0.021	0.02	0.008

TABLE 2—*Mechanical properties of HY-130 steel.*

Yield Strength (0.2 percent offset), MPa	Ultimate Tensile Strength, MPa	Elongation in 51 mm (2 in.), %
933	964	21

cess to construct continuous strain and $\overline{W}$ functions for these edges. Application of standard numerical integration procedures then yielded the J contribution from these edges. The J contribution from contour segment B-C is simplified by noting that: (1) $dy = 0$ and $ds = dx$, (2) σ_{yy} is the dominant stress component of the far field, and (3) $\partial v/\partial x$ is the required displacement gradient. Thus, J computation requires only the stress σ_{yy} (obtained from

measured strain and the material σ-ϵ curve) and the average contour rotation, θ_{BC}, provided by the gradient ($\partial v/\partial x$) of the LVDT readings.

In summary, the experimentally determined J-value is given by

$$J_{\text{exp}} = 2 \times \left(\int_A^B \overline{W} dy - \int_D^C \overline{W} dy - \sigma_{yy} \theta_{BC} W \right) \tag{3}$$

Reference *4* presents details of the curve fitting processes employed and a brief analysis that estimates uncertainty in the experimental J-values on the order of 5 percent once extensive plasticity develops.

Finite-Element Analysis

The FEM has been applied successfully by a number of investigators in nonlinear fracture related problems. All finite-element solutions reported here refer to two-dimensional (2-D) models that utilize linear strain-displacement relations based on small geometry change (SGC) assumptions. Large geometry change (LGC) analyses of a blunting notch in plane strain by McMeeking [*5*] and Alturi, Nakagaki, and Chen [*6*] showed J to be path dependent within the intensely deformed near tip zone. In the surrounding outer plastic field, however, negligible differences existed between SGC and LGC J predictions.

The following sections briefly describe special techniques employed here to address problems of nonlinear material characterization, stability of the incremental nonlinear solution, and through-thickness constraint near the notch tip. Numerical computations were performed with the POLO-FINITE [*7,8*] structural mechanics system operating in single precision on a computer with a 48-bit word length (11 to 12 decimal digits).

Element Grids and Material Representation

Figure 2*a* shows a typical element grid used for all models. Because experimental measurements occur only within the 1-cm-thick gage section, geometric details and nonlinear effects near the loading pin hole are neglected. Rectangular, eight node isoparametric elements with linear material properties adequately model this thicker (2.54 cm) region. Static condensation applied to this region reduces the grid to a row of nodes compatible with nonlinear elements in the gage section. One additional node located at the pin hole center, denoted A in the figure, also is retained after condensation for loading purposes. Condensation eliminates nodes and elements in the linear grip region (approximately ¼ of the total) from the iterative nonlinear solution and permits use of a rectangular mesh up to the point of thickness transition.

Eight node isoparametric elements also are used throughout the nonlinear test gage section. Figures 2*b* and *c* iilustrate typical mesh refinement schemes

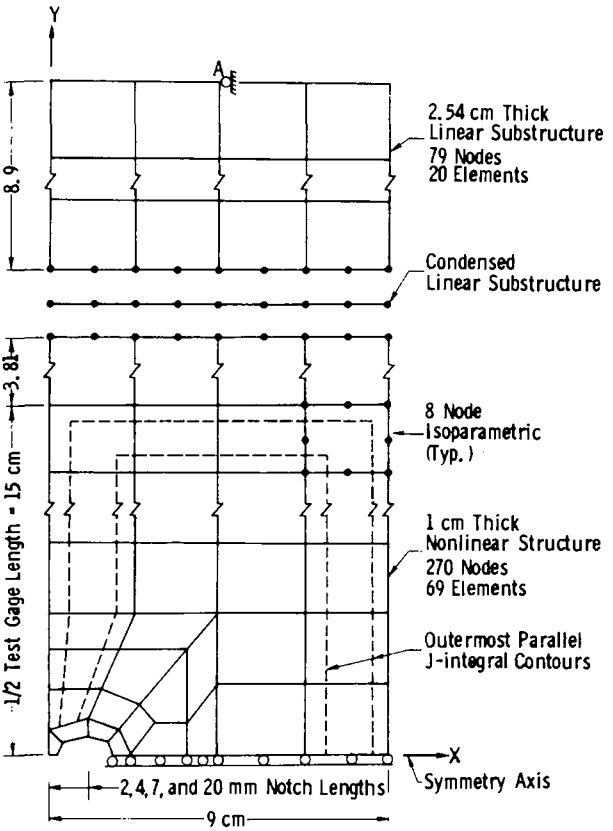

FIG. 2a—*Typical finite element grid with substructuring to reduce analysis cost.*

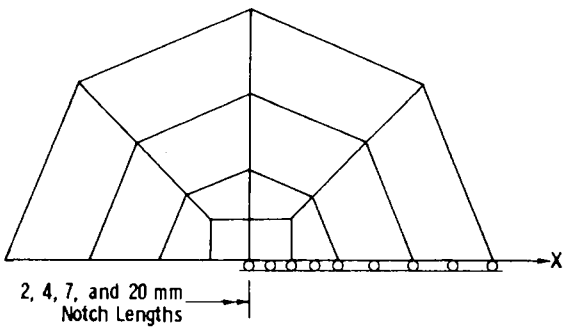

FIG. 2b—*Blunt notch tip model.*

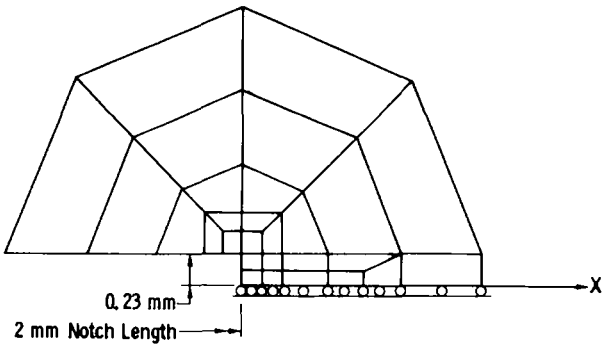

FIG. 2c—*Geometrically correct model of tip for 2-mm crack length analysis.*

employed near the notch tip. Degenerated singularity elements [*9*] were considered inapplicable at the tip of the blunt saw notch. Details of the notch tip geometry (width and corner radii) were not considered initially in finite-element models. To simulate the blunt notch condition, small square elements of size 0.25 mm at the tip were combined with constraint of displacements normal to the notch plane beginning at the tip (see Fig. 2*b*). A geometrically correct model for the notch tip (see Fig. 2*c*) also was considered for the 2-mm crack specimen to assess possible size effects of the notch width.

Incremental plasticity (J_2 flow theory) with the Mises yield surface, associated flow rule, and isotropic hardening applicable in monotonic loading situations adequately models the HY-130 material. Computational algorithms detailed by Nayak and Zienkiewicz [*10*] were utilized to ensure satisfaction of the incremental equations for finite size loading steps. Figure 3 shows the uniaxial tensile stress-strain curve for HY-130 steel. A pure power law hardening representation for this material does not appear realistic due to the extended plateau region; a simple 10-piece linear approximation gives an excellent fit with the experimental curve. Although the initial yield point for finite-element analysis is considered 827 MPa, a flow stress (σ_f) of 931 MPa corresponding to the plateau region is used in simple limit state calculations and to normalize results.

Plane Stress or Plane Strain

The dilemma facing analysts limited to 2-D solutions for through-thickness cracks involves selection of either the plane-stress or plane-strain condition, both of which neglect the complex variation of strain in the thickness direction near the tip. For thick specimens that satisfy, for example, the requirement in the ASTM Test for Plane-Strain Fracture Toughness of Metallic Materials (E 399-81) for valid K_{Ic} determination, plane strain dominates over

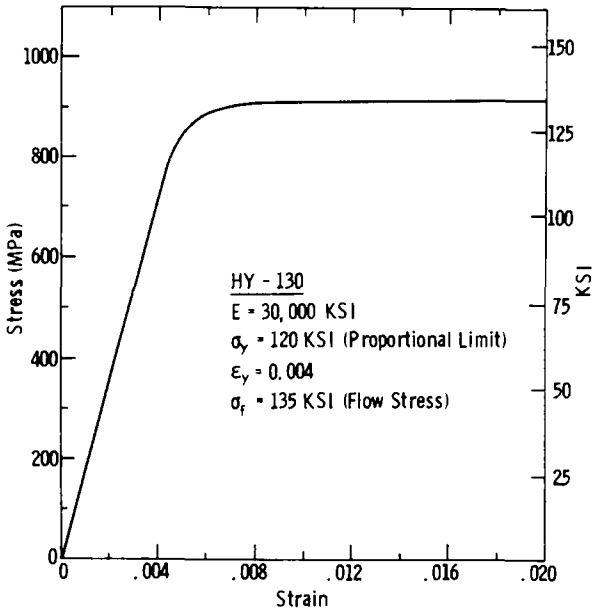

FIG. 3—*Uniaxial stress-strain curve for HY-130 employed in finite element analyses.*

most of the thickness with a rapid drop to the required plane-stress condition at free surfaces. Many practical situations involve thinner material, thus leading to relaxation of the perfect plane-strain condition. Specimen dimensions of 9 by 30 by 1-cm thick employed in the current experimental investigation strongly suggested idealization for 2-D finite-element analysis as plane stress. Preliminary finite-element solutions conducted assuming plane stress characteristically overestimated both the experimental CMOD and the applied J; yet excellent agreement was observed with the experimental load-gage displacement results including limit-load predictions. These computations suggested that the plane-stress assumptions are valid throughout the specimen except near the notch tip where localized through thickness constraint develops.

Several investigators, including Underwood and Kendall [*11*], Kobayashi, Engstrom, and Simon [*12*], and Ke and Liu [*13*], have measured strains near crack tips of SEN specimens using the Moiré method. Their results indicate a definite three-dimensional (3-D) influence even for thin material ($B = 0.32$ cm). Away from the crack tip, measured strains agreed very well with those obtained from plane-stress finite-element solutions. However, near the crack tip, beginning at a radius of approximately $B/2$, the measured surface strains decreased by 30 percent or more below plane-stress values. Hu and Liu [*14*] argue this behavior is due to partial restraint of thickness contraction at the highly strained crack tip by considerably less strained material

surrounding the tip. The degree of restraint provided naturally depends on the thickness, but the "stiffened" zone consistently showed a radius of $B/2$ to B in the experimental work. The partial restraint of contraction elevates stresses at the notch above simple plane-stress yield values but decreases the strain.

Analytical solutions to properly account for these effects require full 3-D elasto-plastic finite-element computations near the crack tip, which are prohibitively expensive for even simple test specimen geometries. To approximate the 3-D effect, Hu and Liu modified the plane-stress finite-element analysis by incorporating a fraction of idealized plane strain in a stiffened zone near the crack tip. They maintained two sets of stresses, one set for plane strain, the other for plane stress, for each simple constant strain triangle element within a radius $B/2$ from the crack tip. The degree of constraint is then expressed by

$$\{\Delta\sigma\} = \Omega[D_\epsilon]\{\Delta\epsilon\} + (1 - \Omega)[D_\sigma]\{\Delta\epsilon\} \tag{4}$$

where strain and stress increments are defined as

$$\{\Delta\sigma\} = \begin{Bmatrix} \Delta\sigma_{xx} \\ \Delta\sigma_{yy} \\ \Delta\sigma_{xy} \end{Bmatrix} \quad \text{and} \quad \{\Delta\epsilon\} = \begin{Bmatrix} \Delta\epsilon_{xx} \\ \Delta\epsilon_{yy} \\ \Delta\epsilon_{xy} \end{Bmatrix} \tag{5}$$

$[D_\sigma]$ and $[D_\epsilon]$ relate strain and stress increments in the elasto-plastic regime for plane-stress and plane-strain cases, respectively. Explicit forms of these matrixes are given by Nayak [*15*]. The stiffening parameter, Ω, was assumed to vary linearly from a specified value at the tip to zero (plane-stress condition) at a radius of $B/2$. In Ref *14*, Ω-values were selected to provide the best correlation between finite-element and measured surface strains near the crack tip. Neither J nor CMOD calculations were reported. Typical values of Ω ranged from 0.04 for 0.635-cm-thick plate to 0.08 for 1.27-cm-thick plate for tensile panel gage strains up to seven times nominal yield with 2024-0 aluminum specimens. These Ω-values, however, must be interpreted as minimums since no indication was given of special procedures to prevent "locking" of the triangle elements in plane-strain plasticity which provides an additional but unknown amount of stiffening.

A similar approach, but implemented differently, was adopted in this study to bring finite-element plane-stress results for CMOD and J into better agreement with experimental data. The stiffening effect represented by Eq 4 was incorporated without any change in the existing software through an overlay technique. Two isoparametric elements of the same shape and connectivity replace each single element appearing near the tip in a usual mesh. One of the elements is associated with a nonlinear plane-strain material model, the other with a nonlinear plane-stress material model. Simple appor-

tionment of the element thicknesses provides the desired value of the stiffening parameter. The stiffening effect is reduced linearly from the notch tip to zero at the boundary of the zones indicated in Fig. 4.

Computations for full plane-stress and plane-strain conditions were conducted to provide representative bounding solutions in addition to analyses performed to assess the influence of the stiffening parameter Ω. The incompressibility condition in plane strain implied by the Mises yield criterion was satisfied by using a reduced integration order (2 by 2) for all elements [*16*] to assure that no spurious stiffening developed.

Solution Procedures

Displacement control loading was used for the finite-element models corresponding to the test procedure. Specified extensional displacement increments imposed at node A in Fig. 2*a* loaded the model with horizontal translation at this node constrained to zero. Approximately 30 load increments of variable size were used to trace the nonlinear response and to obtain results at gage strains corresponding to experimental data points. Numerical refinements described by Nayak and Zienkiewicz [*10*] and Holt and Parsons [*17*] assured satisfaction of the material flow rule and controlled the spurious unloading phenomenon that occurs with high order isoparametric elements due to overestimation of yield zones. These techniques and the variable displacement increment magnitudes produced a stable solution process.

Incremental equations formulated in the initial stress approach described by Zienkiewicz [*18*] were solved with various forms of the Newton-Raphson scheme with occasional tangent stiffness updating. Application of the acceleration scheme originally proposed by Crisfield [*19*], based on the variable metric method, reduced by one-half the number of iterations required within each increment to attain the equilibrium configuration.

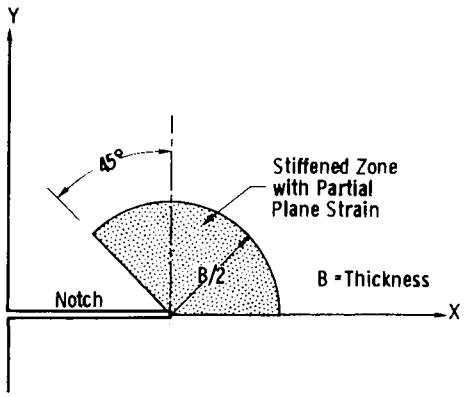

FIG. 4—*Region of mesh stiffened with the plane stress-plane strain overlay model.*

Numerical Evaluation of J

Finite-element strain-stress results permit evaluation of the J-integral defined in Eq 1 by direct numerical integration along contours that pass through specified Gauss points. Ten to twelve integration paths were typically employed with one path defined to closely follow the instrumented experimental contour. Plane-strain linear analyses were conducted to evaluate the accuracy of the numerical integration procedure and the degree of path independence attained. For all notch lengths, finite-element values of J exhibited less than a 5 percent individual contour deviation from the mean of all paths. Stress-intensity factors, K_I, derived from J consistently fell below exact results for a sharp crack as expected from the use of standard, not singularity, elements near the notch tip. For the longest notch, 20 mm ($a/W = 0.22$), the finite element K_I was 1 percent below the sharp crack solution. Similarly, for the shortest notch, 2 mm ($a/W = 0.22$), K_I was 4 percent lower and dropped slightly following modification of the element mesh to incorporate the blunt notch tip geometry (see Fig. 2*c*). These results reflect the diminishing influence of notch tip geometry with increasing notch length and provided additional justification for neglecting tip details of the 4, 7, and 20-mm notches.

Deviation of computed J-values between contours increased to 10 to 15 percent from the mean after the plastic zone began to propagate from the notch tip. Semicircular paths nearest the notch tip always produced the least variation of J (<5 percent). Contours outside the plastic zone also demonstrated negligible J variation and agreed well with near-tip path results. The onset of net section, then gross section yield and formation of the narrow slip band exacerbated the situation and caused 20 to 25 percent J variations between parallel paths traversing the same elements away from the notch tip (see Fig. 2*a*). However, simple averaging of the computed J for each pair of parallel contours produced a consistent set of values with less than 5 percent variation from the mean, including those paths near the tip. These observations reflect the severe strain gradients (ϵ_{yy}) present in the narrow slip band, which contribute significantly to the J-integral. At most, two elements are available to represent the complete slip band width for outermost J-integral contour segments parallel to the y-axis. Under such conditions the average J of parallel paths through these elements should provide a more reliable estimate. Contours near the tip pass through the most refined portion of the element mesh which experiences complete plastification with a comparatively smooth strain variation in the circumferential direction. Values of J for these contours showed negligible variation.

Results and Discussion

Figure 5 illustrates the qualitative elastic-plastic behavior of a tensile panel containing a short edge crack in terms of the plastic zone and the tensile

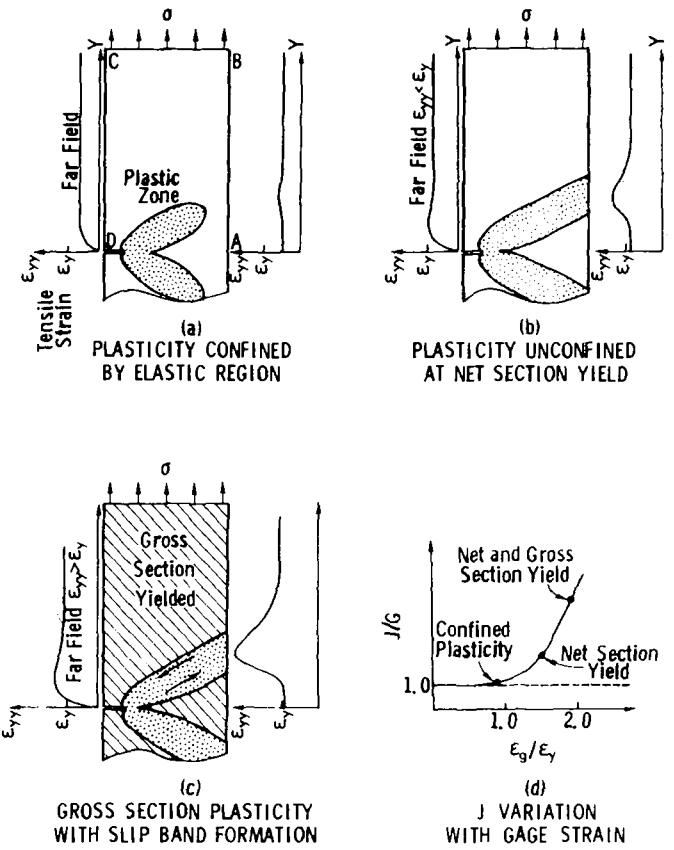

FIG. 5—*Qualitative elastic-plastic behavior and J-integral response for a tensile panel containing a short crack.*

strain variation along the free edges A-B and D-C. Gross section yield (GSY) accompanying net section yield (NSY) is attained only with very short cracks ($a/W < 0.05$) for which negligible in-plane bending develops. Longer crack lengths permit considerable bending that concentrates deformation in the narrow plastic zones and at the crack tip. In such cases, tearing occurs at gage strain levels near those corresponding to NSY.

Figure 5, in conjunction with Eq 3, offers insight into the physical meaning and computational aspects of the J-integral for shallow SEN specimens. J is the difference in area under the strain energy density, $\overline{W}$, curves along the free edges (similar to the strain variations shown) plus a traction-rotation term across the ends. For low gage strains, $\epsilon_g/\epsilon_y < 1$, a positive area difference and thus a positive J exist due to the drop of strain to zero at the crack mouth (point D). Almost no strain gradient occurs over the unnotched edge

A-B. For $a/W < 0.05$, the positive traction-rotation term, which reflects in-plane bending, is negligible. As the plastic zone extends across the section, J slightly increases above the LEFM energy release rate, G, as shown in Fig. 5*d*. When the plastic zone becomes unconfined at NSY, a slip band develops that is sensed along the J contour segment A-B by a narrow spike in the tensile strain distribution. Simultaneously, the notched edge strain increases but undergoes very minor redistribution. At this deformation for longer cracks, the traction-rotation term equals or exceeds the strain energy contribution and J increases linearly with deformation thereafter (the constant end traction rotates through an increasing angle).

For very short cracks, the traction-rotation term remains negligible compared with the strain spike contribution. Only after GSY does J begin to increase linearly with deformation. The strain spike height and width increase continuously as large shear deformations develop in the slip band. Within the spike, strains are well beyond yield such that the strain energy density increases at a constant rate ($\Delta \overline{W} = \sigma_f \Delta \epsilon$).

Early portions of the J-deformation curve follow LEFM predictions ($J = G$). The slope of the linear portion fully characterizes the response once extensive plasticity develops (NSY for long cracks, GSY for short cracks). These slopes are referred to symbolically as M, where

$$M = dJ/\sigma_f L_g d\epsilon_g = dJ/\sigma_f d\delta \tag{6}$$

in which L_g is the gage length and δ is the load point displacement. M is proposed as a direct indicator of the manner in which the specimen absorbs deformation in the plastic range. A large M-value indicates that displacements imposed at the specimen ends are transmitted in full to the crack tip, add significantly to the crack tip strain field, and produce large increases in applied J. Consequently, the correlation of finite-element and experimental M-values and the dependence of M on a/W as $a \rightarrow 0$ are of considerable interest.

Plane Stress-Plane Strain Analyses

Finite-element plane-stress analyses were performed for three crack lengths corresponding to $a/W = 0.022$, 0.044, 0.078, and 0.22. The computed limit load in each case fell below the experimental value. The discrepancy increased from 1 percent for the shortest crack to nearly 4 percent for the longest crack length. Figure 6 presents the experimental and finite-element J-integral response as a function of overall gage strain with the simple perfect plasticity approximation ($J = 1.0\sigma_f \delta$) included for reference. All curves follow the same qualitative trends: J first increases parabolically in accordance with LEFM, then makes a transition to a linear function of gage strain once sufficient plasticity develops.

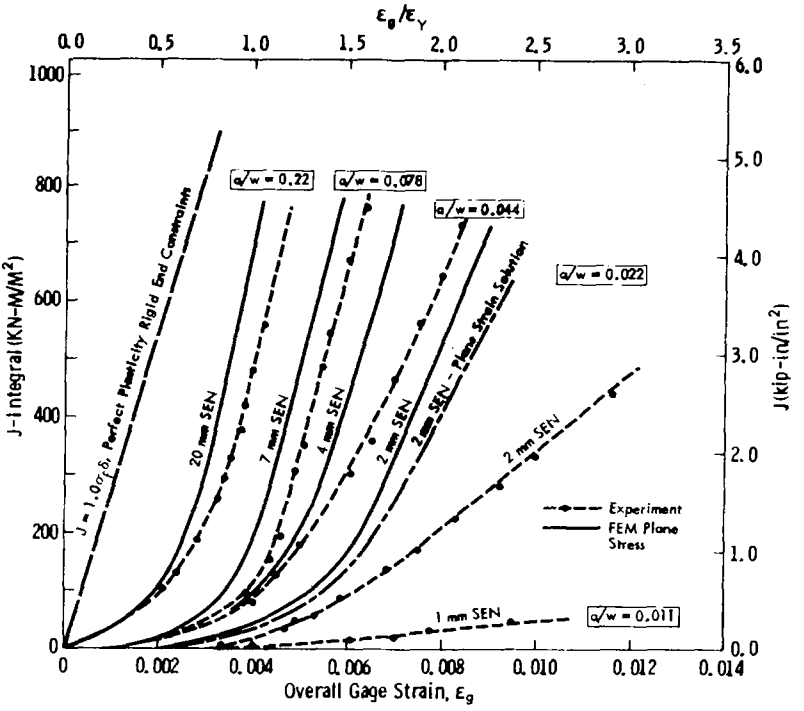

FIG. 6—*Finite element and experimental applied J-integral values for SEN tensile panel.*

Agreement between finite-element and experimental results for the longer crack lengths is quite good in the elastic region. As plasticity extends outward from the tip, the experimental and analytical curves separate but remain nearly parallel for subsequent deformation. Finite-element estimates of the J versus ϵ_g linear region slope, M, are slightly larger than experimental values. Slopes for both experimental and finite-element curves were determined with a least squares procedure. The close agreement of M-values and the gage strain shift between the curves indicate that the finite-element models are too flexible in the early stages of plastic deformation at the crack tip, but accurately represent conditions after extensive plasticity has developed. Further evidence of this is given in Fig. 7, which presents the finite element and experimental CMOD's. The CMOD curves exhibit the same qualitative trends as the J-integral and verify the greater near-tip deformation predicted by finite-element models.

Results for the 2- and 4-mm cracks ($a/W = 0.022$, 0.044) show considerable discrepancy for both J and CMOD beyond the elastic range despite excellent agreement of the limit loads. Beginning at an a/W of approximately 0.05 ($a/B = 1.0$), terminal slopes of the J and CMOD curves rapidly

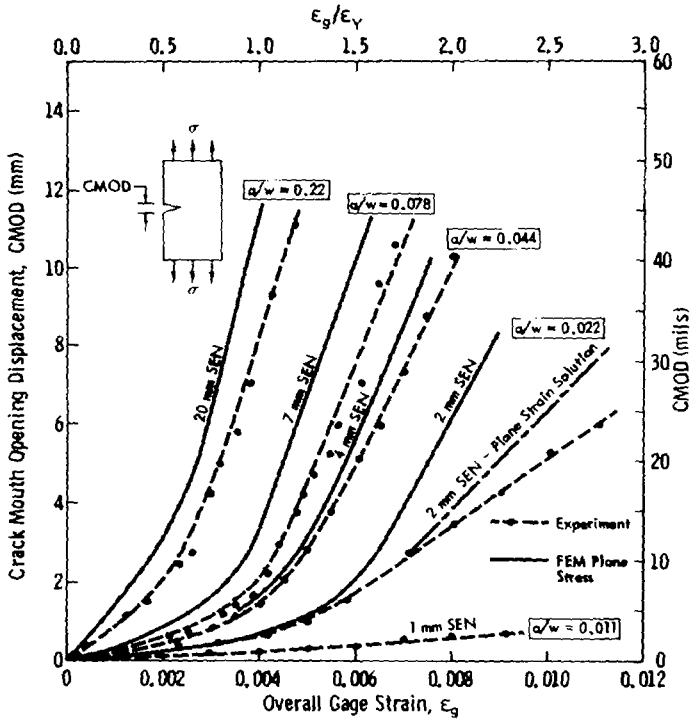

FIG. 7—*Finite element and experimental CMOD values for SEN tensile panel.*

decrease and approach zero for diminishing crack length. Finite-element plane-stress results indicate little sensitivity to decreasing crack length except for a lengthened region of elastic response. The computed M-values appear almost invariant of crack length and lead to a very large (320 percent) discrepancy with the 2-mm experimental value. The discrepancy arises because finite-element predictions of specimen rotation (line B-C of Fig. 1) exceed the experimental measurements (which indicate almost no rotation), and the finite-element ϵ_{yy} strain variation along the unnotched edge (A-B in Fig. 1) overestimates the strain spike height and width, although the spike center coincides with the experimental location. These effects comprise the two positive terms of the J-integral expression for the experimental contour.

Additional analyses were performed for the 2-mm crack specimen to investigate possible sources of and corrections for the near-tip flexibility. These included idealization of the test grips as frictionless pins, bluntness of the notch tip, and the use of plane-strain assumptions throughout the specimen. Rigidly constrained, rather than pinned, end conditions produced no changes in the computed limit load, J, or CMOD responses. The rigidly constrained model developed additional shear deformation in the narrow slip

band. The strain spike height and width increased sufficiently to offset loss of the positive J contribution at the constrained ends. No moment reaction developed across the constrained ends to suppress the rotation. This type of response is possible due to the nonuniqueness of slip-line fields at the limit load. Similar observations for the SEN tensile panel are described in Ref *20*. A geometrically correct model of the blunt notch tip (see Fig. 2*c*) had only minor effect on J in the elastic region and no effect on the final slope M. The plane-strain analysis predicted a limit load 1.155 times the experimental (and plane-stress) value, and decreased the finite-element and experimental discrepancy in J. More noticeable, however, is the significant improvement in CMOD correlation (Fig. 7) due to greatly reduced strain levels at the crack tip. The finite-element J-displacement relationship contradicts the trend predicted by simple limit load solutions, that is, the slope M decreases, rather than increases, for plane strain. The decrease of applied J for the plane-strain solution derives from a reduction of the cross section rotation about the pinned ends, and considerable reduction of the strain spike height along the unnotched edge with some width gain. The slip band angle relative to the crack plane also increased, thus causing the strain spike location to shift upwards well above the experimental and plane stress location. This change in fundamental response, coupled with the limit load elevation, demonstrates the inappropriateness of plane-strain assumptions over the complete specimen, but that some degree of plane-strain constraint exists in the crack tip vicinity.

Effects of Crack Tip Stiffening

The partial through-thickness constraint model was introduced near the crack tip to provide the required stiffening effect and yet preserve those aspects of the experimental and plane-stress solutions that agreed away from the tip. Analyses were performed to assess the influence of the stiffening parameter, Ω, on J, CMOD, and the limit load. For these analyses the stiffened zone was fixed as shown in Fig. 4 with an assumed variation of Ω that decreased linearly to zero at a radius of $B/2$. The only parameter varied in the present study was Ω at the crack tip.

Stiffening slightly increased the finite-element limit loads, which remained below experimental values. Fig. 8 shows the finite-element plane stress, stiffened crack tip, and experimental J-integral results as a function of gage strain. Stiffening the crack tip has a more pronounced effect on J as the crack length diminishes. The longest crack (20 mm) shows only slight improvement between experimental and finite element results for an Ω of 0.10. However, the same Ω reduces the discrepancy by more than one half over the complete curve for the 7-mm crack. M for both these specimens is reduced to very near or just below experimental values. For the 2-mm crack, an Ω of only 0.10

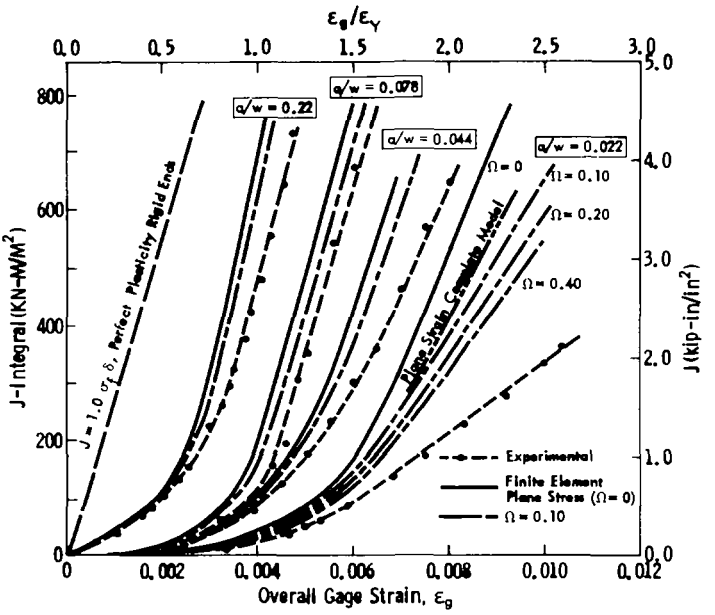

FIG. 8—*Effects of crack tip stiffening on computed J-integral.*

lowered the stiffened model curve below that for full plane strain and again decreased the difference with experimental results by nearly one half.

The 2-mm crack specimen was also analyzed for $\Omega = 0.20$ and 0.40 with the results shown in Fig. 8. These curves reveal an interesting trend in that large increases of Ω produce surprisingly small additional reductions of J and M. For example, increasing Ω from 0.10 to 0.40 provides less change than from plane stress ($\Omega = 0$) to an Ω of 0.10.

Effects of the crack tip stiffening parameter on M are summarized in Fig. 9. Finite-element plane-stress solutions exceed the experimental values, but with decreasing magnitude for increasing crack length. Differences between finite-element and experimental values are insignificant for the 20 and 7-mm cracks when $\Omega = 0.10$. The initial 300 percent difference of M with the experimental value for the 2-mm crack is reduced to approximately 35 percent as Ω increases to 0.40. The 2-mm crack length curve also shows the finite-element solution sensitivity to an initial small constraint but that additional constraint approaching full plane strain produces only a minor effect. Applied to actual specimens, this implies a very small portion of specimen thickness over which the behavior transforms from plane stress to plane strain.

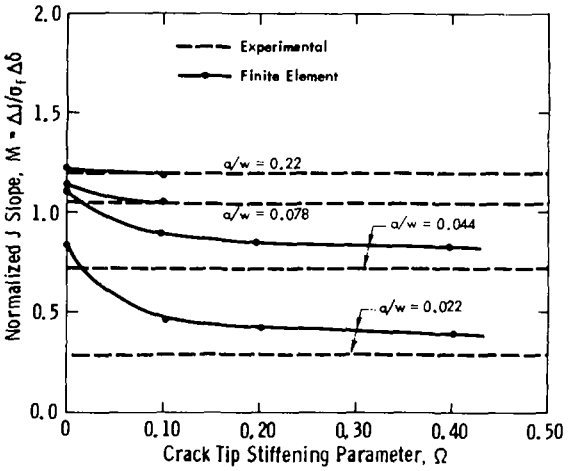

FIG. 9—*Effects of crack tip stiffening on the* M *parameter.*

Correlation of J *Predictions in Plastic Range*

The slope of the linear portion of J-displacement (or nominal strain) curves, normalized and termed M, has been postulated as a basic measure of the fracture response under fully plastic conditions—either net or gross section yield. M-values are available from finite-element analyses, experimental studies, and slip-line limit load approximations. The relation of J to displacement at the limit load is given by Ref *21*

$$dJ = -\frac{1}{B}\frac{\partial P_L}{\partial a}d\delta \tag{7}$$

where P_L is the limit load expression in terms of flow stress and geometry parameters. From such equations, M is derived as

$$M = -\frac{1}{B\sigma_f}\frac{\partial P_L}{\partial a} \tag{8}$$

Three limit load approximations [*22*] are available for the SEN tension specimen as listed in the following equations.

$$\begin{aligned} &\text{Rigid ends, plane stress} \\ &P_L = \sigma_f B\,(W - a) \end{aligned} \tag{9}$$

Pinned ends, plane strain

$$P_L = \sigma_f BW \{1 - 0.809(a/W) - 1.037(a/W)^2\} \quad (10)$$

Pinned ends, plane stress

$$P_L = \sigma_f BW \{[(1 - a/W)^2 + (a/W)^2]^{1/2} - a/W\} \quad (11)$$

Corresponding M relationships evaluated for the tensile panels tested are given in Fig. 10. The simplest expression for rigid ends, Eq 9, provides a reasonable average estimate of M. The solution for pinned end conditions with plane strain over the complete specimen, Eq 10, shows the closest agreement with finite-element and experimental results. The pinned-end, plane-stress solution, Eq 11, severely overestimates M for short cracks. Clearly, none of the limit load solutions predict the rapid decrease of M as the crack length approaches zero.

Summary and Conclusions

Experimental and finite-element results are presented for the J-integral and CMOD response of tensile panels (width/thickness = 9) containing short, single edge cracks. The behavior at nominal strain levels above yield was specifically addressed. Studies were conducted for a high-strength steel HY-130, (σ_f = 931 MPa) for crack length to remaining ligament ratios, a/W, in the range $0.02 < a/W < 0.22$. Experimental J-integral values were obtained by integrating strain and displacement quantities measured along an instrumented contour. Elasto-plastic finite-element 2-D analyses were

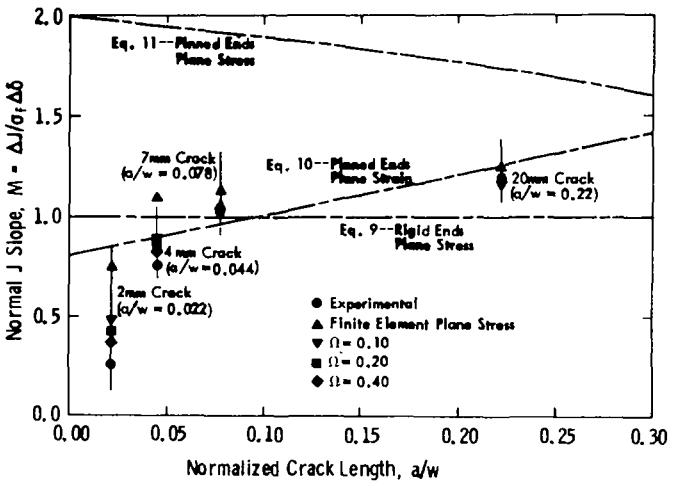

FIG. 10—*Correlation of estimates for the* M *parameter.*

performed using conventional plane-stress and plane-strain assumptions with high order isoparametric elements. A hybrid plane stress-plane strain modeling scheme was explored to provide partial through-thickness constraint near crack tips within the limitations of a 2-D analysis. The major findings of this investigation can be summarized as follows.

1. Plane-stress models predict limit loads slightly lower than experimentally measured values. For the longest crack length ($a/W = 0.22$) the discrepancy approached 4 percent. The difference decreased to approximately 1 percent for the shortest crack length ($a/W = 0.022$).

2. Plane-stress predictions for both J and CMOD in the plastic range exceed the experimental values for all crack lengths. The difference in applied J-values for the longest crack is in the range of 10 percent, but for the shortest crack exceeds 100 percent.

3. Experimental results imply the existence of a transition range of crack lengths ($a/W = 0.05$ or $a/B = 0.5$) in which the rate of J increase with additional deformation (M) decreases rapidly to zero for crack lengths approaching zero. Such behavior indicates that additional deformation after development of extensive plasticity is absorbed through uniform plastic strain over the complete length, and therefore does not promote ductile fracture or tearing. Finite-element plane-stress J predictions show only minor sensitivity to crack length in the plastic region.

4. Detailed comparisons of finite-element results with experimental measurements revealed excessive flexibility of the plane-stress models in the crack tip vicinity during the early stages of plastic deformation. Analyses conducted assuming plane strain over the entire model lowered the J and CMOD, but elevated the limit load by 15 percent over the experimental value and significantly raised the plastic slip band angle relative to the crack plane. Plane-stress solutions accurately predicted both the limit load and slip band angle.

5. The hybrid plane stress-plane strain model introduces the required partial through-thickness constraint near the crack tip and improves finite-element J predictions while preserving the essentially plane-stress behavior elsewhere in the model. Near-tip stiffening improves J predictions over the whole range of deformation and slightly elevates the limit loads, thereby improving agreement with experimental values. The effect of crack tip stiffening is most pronounced for the shortest crack lengths with an equivalent 10 percent plane-strain constraint reducing the applied J by 40 to 50 percent.

6. Both computational and experimental results suggest an increasing dependence of J on the through-thickness near-tip constraint as crack lengths approach zero under conditions normally considered plane stress. Finite-element 2-D models do not predict this behavior unless augmented with partial through-thickness constraint. Such a modeling scheme may minimize the necessity of expensive, 3-D nonlinear computations. Full 3-D

computations are in progress to define more fully the degree and region of near-tip stiffening.

This investigation has shown that short cracks in tensile panels ($a/W < 0.25$) have a radically different J-integral behavior than observed in tests of more traditional specimen geometries ($a/W > 0.5$). From the limited results presented in this study, it appears that conventional finite-element and limit load approaches for J-integral prediction are inadequate for short cracks commonly encountered in practice. These analytical methods predict applied J-values much larger than experimental results indicate, and thus may lead to grossly conservative designs or unnecessary costly repairs.

Acknowledgments

This report was prepared as part of the Fracture Control Technology Program under the sponsorship of H. H. Vandervelt, Naval Sea Systems Command (SEA-05 R15). The effort was directed by J. P. Gudas, David Taylor Naval Ship Research and Development Center under Program Element 62761N, Task Area SF-61-544-504. Computational support was provided by the Academic Computer Center and the Computer Aided Design Laboratory within the School of Engineering at the University of Kansas. The authors gratefully acknowledge many helpful discussions with Stanley Rolfe at the University of Kansas and Harry McHenry at the National Bureau of Standards.

References

[1] Rice, J. R., *Journal of Applied Mechanics, Transactions,* American Society of Mechanical Engineers, June 1968, pp. 379-386.

[2] Begley, J. A. and Landes, J. D. in *Fracture Toughness, ASTM STP 514*, American Society for Testing and Materials, 1972, pp. 1-23.

[3] Landes, J. D. and Begley, J. A. in *Fracture Toughness, ASTM STP 514*, American Society for Testing and Materials, 1972, pp. 24-39.

[4] Read, D. T. in this publication, pp. II-199-II-213.

[5] McMeeking, R. M. in *Flaw Growth and Fracture, ASTM STP 631*, American Society for Testing and Materials, 1977, pp. 28-41.

[6] Alturi, S. N., Nakagaki, M., and Chen, W. in *Flaw Growth and Fracture, ASTM STP 631*, American Society for Testing and Materials, 1977, pp. 42-61.

[7] Lopez, L. A., *International Journal for Numerical Methods in Engineering*, Vol. 11, 1977, pp. 851-866.

[8] Dodds, R. H. and Lopez, L. A., *International Journal for Advances in Engineering Software*, Vol. 2, No. 4, 1980, pp. 161-168.

[9] Barsoum, R. S., *International Journal for Numerical Methods in Engineering*, Vol. 11, No. 1., 1977, pp. 85-98.

[10] Nayak, G. C. and Zienkiewicz, O. C., *International Journal for Numerical Methods in Engineering*, Vol. 5, 1972, pp. 113-135.

[11] Underwood, J. H. and Kendall, D. P., "Measurement of the Strain Distribution in the Region of a Crack," presented to ASTM Committee E-24 on Fracture Testing of Metals, March 1967.

[12] Kobayashi, A. S., Engstrom, W. L., and Simon, B. R., *Experimental Mechanics*, Vol. 9, No. 4, 1969, pp. 163-170.

[13] Ke, J. S. and Liu, H. W., "Moiré Technique," *Experimental Techniques in Fracture Mechanics*, Vol. 2, Society for Experimental Stress Analysis monograph series, 1973.
[14] Hu, W. and Liu, H. in *Cracks and Fracture, ASTM STP 601*, American Society for Testing and Materials, 1976, pp. 522-534.
[15] Nayak, G. C., "Plasticity and Large Deformation Problems by the Finite Element Methods," Ph.D. thesis, University of Wales, Swansea, 1971.
[16] Dodds, R. H., *International Journal of Fracture*, to be published in Vol. 18, 1982.
[17] Holt, J. S. and Parsons, B. in *The Mathematics of Finite Elements and Applications III*, J. R. Whiteman, Ed., 1978, pp. 415-422.
[18] Zienkiewicz, O. C., *The Finite Element Method*, McGraw-Hill, London, 1977.
[19] Crisfield, M. A., *Computer Methods in Applied Mechanics and Engineering*, Vol. 20, 1979, pp. 267-278.
[20] Nagtegaal, J. C., Parks, D. M., and Rice, J. R., *Computer Methods in Applied Mechanics and Engineering*, Vol. 4, 1978, pp. 153-178.
[21] Bucci, R. J. et al in *Fracture Toughness, ASTM STP 514*, American Society for Testing and Materials, 1972, pp. 40-69.
[22] Chell, G. G., Milne, I., and Kirby, J. H., *Metals Technology* Vol. 2, 1975, pp. 549-553.

J. A. Joyce[1]

Static and Dynamic J-R Curve Testing of A533B Steel Using the Key Curve Analysis Technique

REFERENCE: Joyce, J. A., **"Static and Dynamic J-R Curve Testing of A533B Steel Using the Key Curve Analysis Technique,"** *Fracture Mechanics: Fourteenth Symposium—Volume I: Theory and Analysis, ASTM STP 791*, J. C. Lewis and G. Sines, Eds., American Society for Testing and Materials, 1983, pp. I-543-I-560.

ABSTRACT: Elastic-plastic J-R curves were obtained for compact specimens of A533B-02 plate tested at average load point velocities of 2.5×10^{-4} m/min and 0.25 m/s directly from the load displacement record using a key curve analysis technique. The slow velocity results compare well with J-R curves obtained on the identical specimens using an unloading compliance technique. The key curve method is shown to accurately predict the extent of crack extension. The J-R curves obtained from the high speed loading are shown to be elevated with respect to the slow test results in both the initial J_{Ic} and the tearing modulus T by from 50 to 100 percent.

KEY WORDS: elastic-plastic fracture, J-integral, fracture toughness J-R curves, A533 steel, key curve method, tearing modulus, high rate testing, crack propagation, fractures (materials), fracture mechanics

It has become common over the past few years to characterize the toughness of an elastic plastic material through the use of the J_{Ic} fracture parameter. A test procedure for the evaluation of J_{Ic} is presently approaching a consensus standard of ASTM using a multispecimen technique proposed by Clarke et al [*1*].[2] More recently the J-R curve has been suggested as an important measure of resistance to ductile tearing instability by Paris et al [*2*], and work by Paris et al [*3*] and Joyce and Vassilaros [*4*] has demonstrated that indeed fracture instability for a system can be accurately predicted if a material J-R curve is available. Static single specimen J-R curve testing has been done by various methods, but most commonly the technique used is that of unloading compliance as described by Clarke et al [*5*]. An alternate technique

[1]Associate professor, Mechanical Engineering Department, U.S. Naval Academy, Annapolis, Md. 21402.

[2]The italic numbers in brackets refer to the list of references appended to this paper.

for J-R curve evaluation using only load displacement records—without unloadings or additional instrumentation—was proposed by Ernst et al [6] and was termed the Calibration Function Method or Key Curve Method. This method was used by Joyce et al [7] on compact specimens of HY-130 steel, and it was demonstrated that accurate J-R curves could indeed be evaluated directly from load displacement records of 1T specimens if additional load displacement records of geometrically similar subscale 1/2T specimens were available. The advantages of the Key Curve Method are the following:

1. J-values incorporating crack extension effects are evaluated directly.
2. Crack extensions are available directly from the load displacement record without additional instrumentation.
3. Additional corrections like those for specimen rotation are included in the calculation of J and crack extension.
4. A J-R curve point is evaluated for each point on the load displacement record allowing accurate measure of the J-R curve slope and the $T_{material}$ tearing modulus quantity introduced by Paris et al [2].
5. J-R curves can be evaluated for high-speed tests—tests done at any rate at which an accurate load displacement record can be recorded. This is possible today at load point velocities up to 2.5 m/s.

In the present work key curve functions are obtained for compact specimens of A533B (HSST 02) plate material at two test speeds, a slow load point speed of approximately 2.5×10^{-4} m/min and a rapid load point velocity of 0.25 m/s. J-R curves are then developed from load displacement records of 1T compact specimens. For the slow-speed tests, the J-R curves are compared with results obtained earlier by an unloading compliance method and the slow and rapid J-R curves are compared to determine the effects of the load rate increase on the J_{Ic} value and the J-R curve for this material.

Experimental Program

Material Characterization

The material used in the study was obtained from an HSST-02 plate of A533B steel supplied in 0.3-m thickness. The chemical composition of the plate is described in Table 1 and the mechanical properties are presented in Table 2.

TABLE 1—*Chemical composition of HSST-02 A533B steel elements, weight percent.*

C	Mn	Ni	Mo	Si	S	P
0.22	1.48	0.68	0.52	0.25	0.018	0.012

TABLE 2—*Tensile mechanical properties of HSST-02 A533B steel.*

0.2% Yield Strength, MPa	Ultimate Tensile Strength, MPa	Total Elongation, % in 50 mm
448	620.1	19

Testing Details

Two sizes of compact specimens, 1/2T and 1T, were machined from the A533B plate with crack planes oriented in the T-L orientation. The small specimens were fatigue precracked to crack lengths from $a/W \cong 0.5$ to $a/W \cong 0.9$. A standard 6.35-mm (0.2-in.) travel fracture mechanics clip gage was attached to integral knife edges on the small specimens and load versus load point displacement curves were run for these specimens at 150°C.

Two loading rates were used, first 2.5×10^{-4} m/min and then $\cong 0.25$ m/s. The slow tests were conducted in a displacement controlled Instron Universal Test Machine; the fast tests were done on Materials Testing System (MTS) servohydraulic test machine.

For the larger specimens, the slow tests were completed and reported earlier [*8*]. All were done using the Instron screw machine and the computer interactive unloading compliance J-R test procedure of Joyce and Gudas [*9*]. The high speed 1T tests were conducted in stroke control on the MTS servohydraulic machine and a 19-mm (0.80-in.) travel clip-on load line crack-opening displacement (COD) gage mounted on razor blades was used in the specimen load line. Data from the high speed tests was taken by a digital oscilliscope connected via an Institute of Electrical and Electronics Engineers (IEEE) 488 interface to a Tektronix 4051 controller. All data were stored on magnetic tapes and disks for the key curve analysis.

After testing, each specimen was heat tinted at 370°C for 30 min and broken open at liquid nitrogen temperature. The fatigue crack length was measured on the 1/2T specimens while both the fatigue crack length and crack extension were measured optically using a 10 point average technique on the 1T specimens.

Key Curve Function Analysis

Previous work by Ernst et al [*6*] and Joyce et al [*7*] has shown that increments in J and crack extension Δa can be evaluated directly from a specimen load displacement record if a key curve function for the particular material geometry combination is available. The form of the key curve function assumed here was that

$$\frac{PW}{Bb^2} = F1\left(\frac{\Delta}{W}, \frac{a}{W}\right) \tag{1}$$

where

P = applied load,
Δ = total load line crack-opening displacement,
a = crack length,
b = uncracked ligament,
B = specimen thickness, and
$W = a + b$ = specimen width.

Increments in J and crack extension can then be evaluated from the equations of Joyce and coworkers [7] that

$$dJ = \left[\frac{2b}{W} F1 - \frac{b^2}{W^2}\frac{\partial F1}{\partial(a/W)}\right] d\Delta + \left[\int_0^{\Delta} -\frac{2}{W} F1 d\Delta + \int_0^{\Delta} \frac{4b}{W^2}\frac{\partial F1}{\partial(a/W)} d\Delta + \int_0^{\Delta} \frac{b^2}{W^3}\frac{\partial^2 F1}{\partial(a/W)^2} d\Delta\right] da \tag{2}$$

and

$$da = \frac{\frac{b^2}{W^2}\frac{\partial F1}{\partial(\Delta/W)} d\Delta - dP}{\frac{2b}{W} F1 - \frac{b^2}{W^2}\frac{\partial F1}{\partial(a/W)}} \tag{3}$$

Evaluating Eqs 2 and 3 at each point along a load displacement record and summing the increments gives a J-R curve for the specimen. Ernst et al have pointed out that the resulting J-R curve calculated in this fashion includes rotation corrections and corrections to J resulting from crack extension. Combining the results of Eqs 2 and 3 allows calculating the Paris [2] tearing modulus from the expression

$$T_{\text{mat}} = \frac{dJ}{da}\frac{E}{{\sigma_0}^2} \tag{4}$$

Development of the Key Curve File

The key curve file for each loading rate was obtained by assembling the load displacement records of eight 1/2T specimens with different a/W ratios in a

computer file as normalized triples. The result for the statically loaded case is shown in Fig. 1. This file is an experimentally obtained representation of the load displacement records of all geometrically similar specimens of this material loaded at similar rates at the temperature of 150°C. This file is obtained from small specimens so that it does not include the effects of crack extension, and checks were made of the fracture surfaces of each specimen after test to assure that very little if any crack extension was present when the test was terminated. It was found from these checks that crack initiation occurred very close to the first drop in load on the load displacement curve of each specimen, and this was used subsequently as a limitation to the load displacement record used to develop the key curve for the dynamically loaded tests. A similar key curve file was obtained from eight 1/2T specimens tested at the rapid rate. This file is shown in Fig. 2. The key curves are similar in a/W dependence but the high-speed tests resulted in elevated values of normalized load for a given a/W and Δ/W point.

Discussion of the Test Environment

Typical load displacement records for static and dynamic tests are shown in Fig. 3. The static test was run by unloading compliance as described previously. The dynamic test was conducted with the apparatus shown schematically in Fig. 4. All data were taken digitally and stored on magnetic disks to facilitate the key curve analysis.

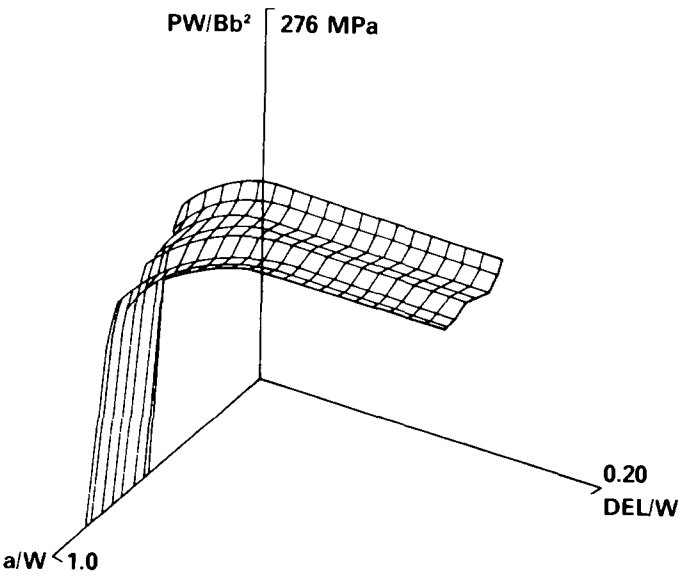

FIG. 1—*Static experimental key curve function for A533B steel at 150°C.*

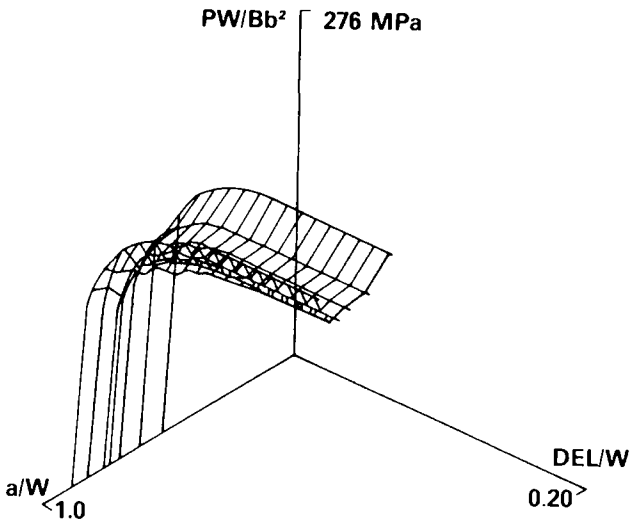

FIG. 2—*Dynamic experimental key curve function for A533B steel at 150°C.*

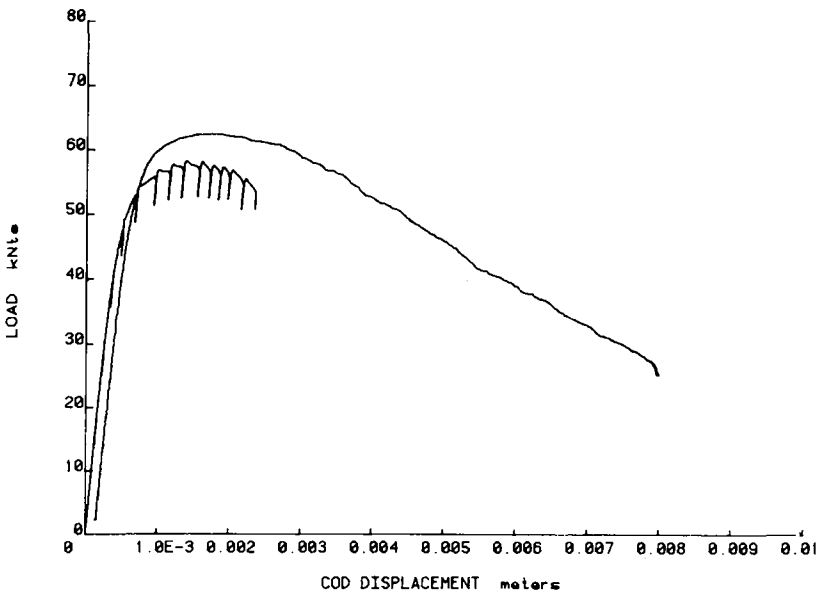

FIG. 3—*Static and dynamic load displacement records for A533B compact specimens.*

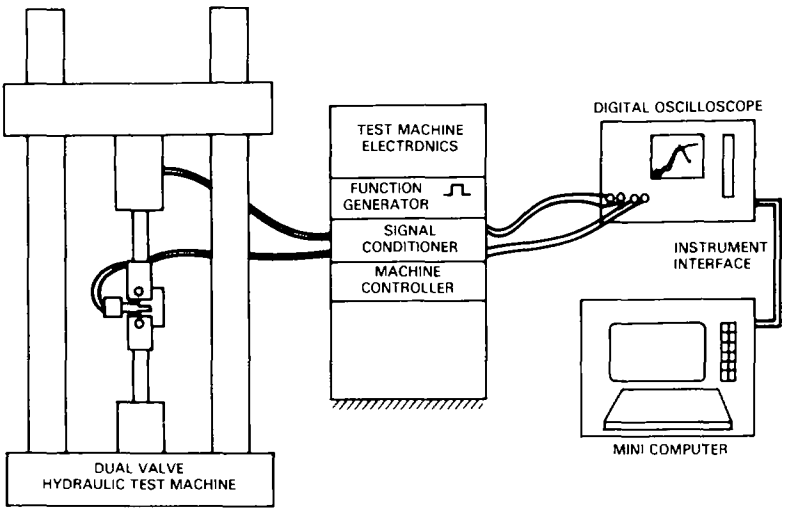

FIG. 4—*Schematic drawing of high speed loading apparatus and data acquisition system.*

The MTS servohydraulic machine was run in a single cycle mode with a 5-Hz-square wave excitation. The crack opening rate applied by this apparatus at the specimen load line is shown for 1T specimens of two crack lengths in Fig. 5. In both cases a maximum rate of between 0.25 and 0.35 m/s was reached, but the shorter cracked specimen, which required a considerably higher load, reached the maximum $d(COD)/dt$ rate much more slowly than the deeply cracked specimen. Looking at these same two specimens in terms of the rate at which the applied J singularity increased, a different picture results as shown in Fig. 6. For the short cracked specimen J is applied more slowly for about the first 0.01 s, but higher values of dJ/dt are reached for the short cracked specimen by about a factor of two in comparison with the deeply cracked compact specimen.

Discussion of the Static Test Results

For the static tests the 1T compact specimens were run as part of work reported previously using the computer interactive unloading compliance method of Joyce and Gudas [*9*] to investigate the effect of side grooves on J-R curves of A533B steel. For this work 1/2T specimens were machined as described previously, and slow-speed load-displacement tests were run to develop a key curve file. Then the analysis of the preceding sections was used to develop J-R curves for the 1T compact specimens that could be compared directly to the results of the unloading compliance tests. A typical comparison of the results of the two methods is shown in Fig. 7 for a 20 percent side grooved specimen with $a/W = 0.6$. The hollow triangles represent the re-

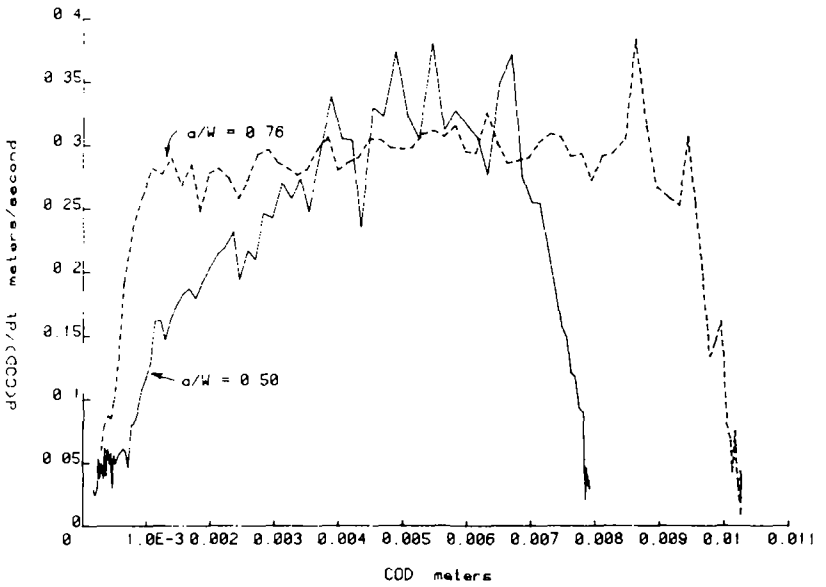

FIG. 5—*Load line displacement rate versus load line displacement for two high speed dynamic tests with different* a/W *ratios.*

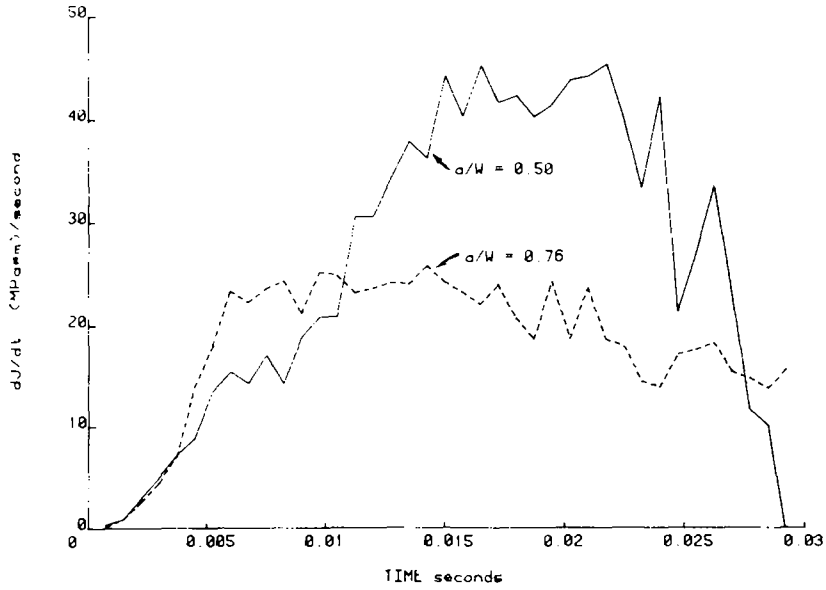

FIG. 6—*J-integral application rates versus elapsed time for tests with different* a/W *ratios.*

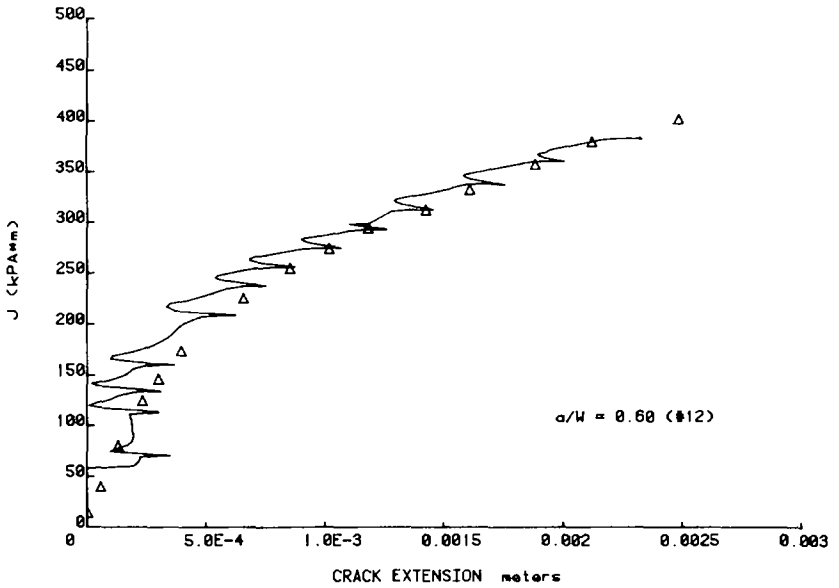

FIG. 7—*Static J-R curves for* a/W = *0.6 specimen obtained from unloading compliance and from the key curve methods.*

sults of the unloading compliance test where J is corrected for crack growth using the analysis of Ernst et al [*10*] and crack extension is corrected for rotation effects using the formula of Loss [*11*]. Similar close agreement was found for all 24 specimens of the matrix of geometries reported in the earlier work [*8*]. Figure 8 shows the results of the key curve analysis for four 20 percent side grooved specimens with different crack lengths, showing clearly the effect of constraint on the J-R curves of this material. This result was hinted at the unloading compliance results reported earlier, but was partially masked until the results were corrected for crack growth—a correction that is included in the key curve method.

Discussion of the Dynamic Results

The success of the static results reported here for A533B steel and previously for HY-130 steel gave incentive for an attempt to use the key curve method to develop J-R curves for compact specimens loaded at rates approaching those of impact testing. Typical load displacement records for 1T compact specimens tested at the 0.25 to 0.35 m/s loading rate are shown in Fig. 9. Applying the key curve analysis described previously to these and other similar load displacement records utilizing the key curve file of Fig. 2 gives the J-R curves shown in Fig. 10. It is clear immediately from comparing Figs. 8 and 10 that a similar dependence of the J-R curve on crack length is

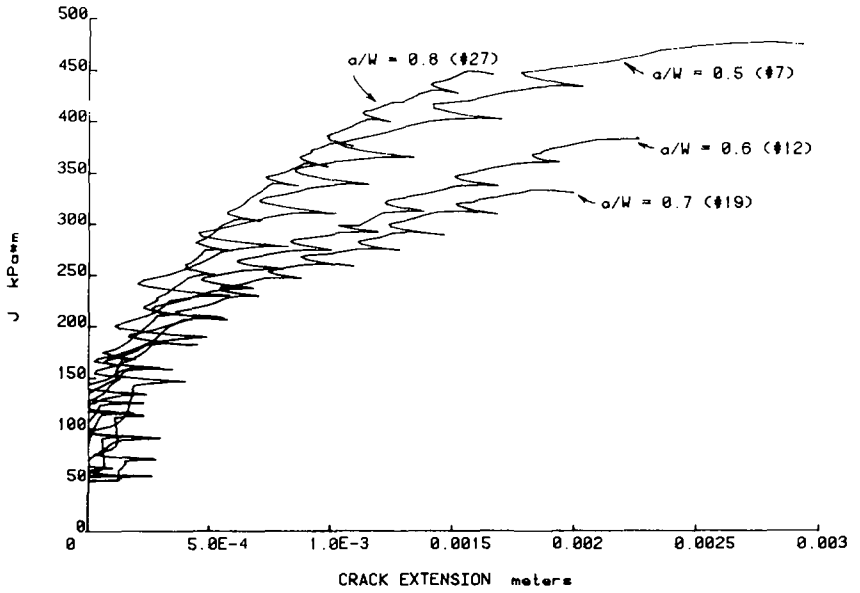

FIG. 8—*Static key curve J-R curves for compact specimens with a range of* a/W *ratios.*

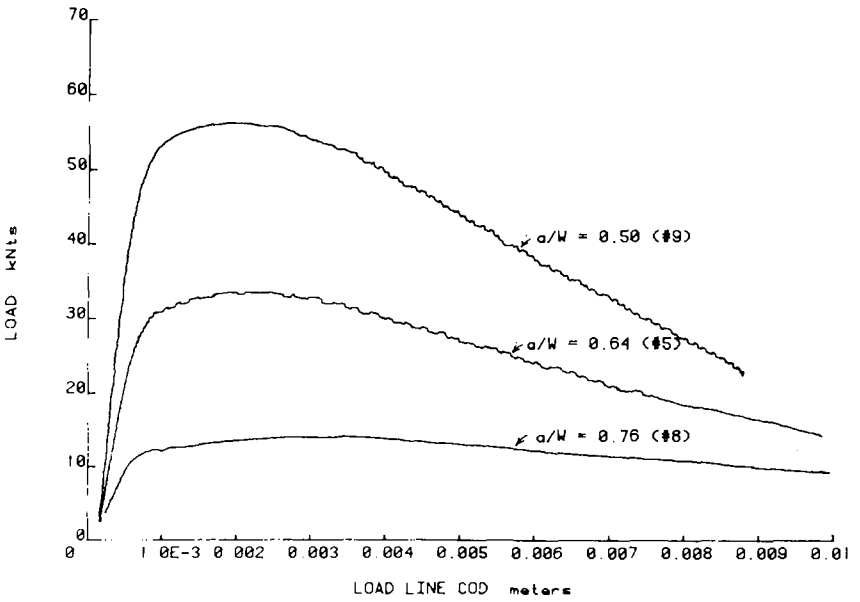

FIG. 9—*High rate load displacement records for compact specimens of varied* a/W *ratio.*

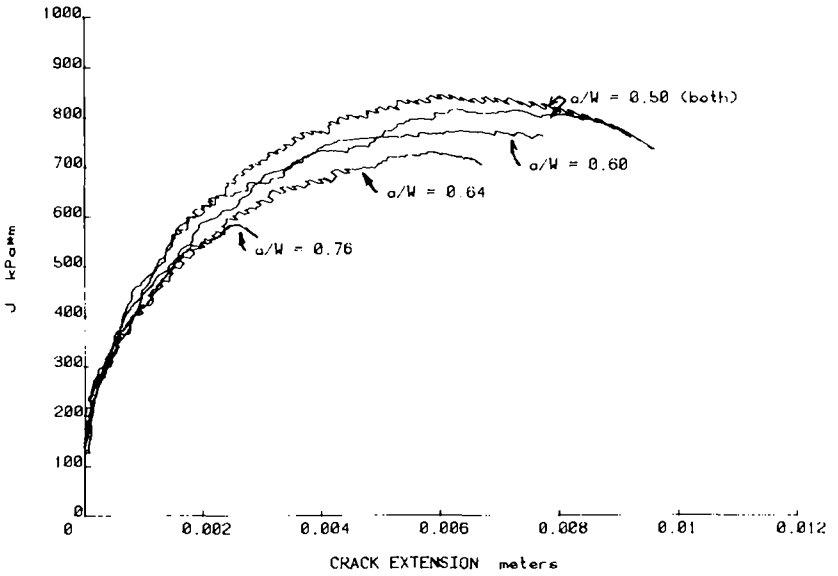

FIG. 10—*Dynamic key curve J-R curves for compact specimens with a range of* a/W *ratios.*

demonstrated at the high and low test rates. Also, it is clear that the high speed tests are considerably elevated in J_{Ic} and in dJ/da. Similar elevations of the J-R curve have been reported previously by the present author [*12*] on HY-130 steel tested in a similar manner.

Only the $a/W = 0.50$ specimens shown in Fig. 10 were analyzed to the full extent of their load-displacement records. For the longer crack length specimens, the key curve file did not extend far enough for a complete analysis. All J-R curves seem to become horizontal and then fall slightly as the end of the key curve file is approached. This might imply a limit has been reached to the region for which *J*-controlled crack growth can exist as discussed by Hutchinson et al [*13*], but it also might be that the key curve analysis was becoming inaccurate, possibly because of crack extension occurring in the subsize specimens used in the development of the key curve.

To evaluate the accuracy of the key curve method's J-integral value, a comparison is made in Fig. 11 between J-R curves utilizing four different equations for *J*.

The three additional equations used to determine *J* are, first, that due to Rice and coworkers [*14*]

$$J = \frac{2A}{Bb} \tag{5}$$

second, that due to Merkle and Corten [*15*]

$$J = \frac{\beta A}{Bb} \tag{6}$$

with $\beta(a/W)$ slightly greater than 2 to account for the additional component of tensile loading, and finally that due to Ernst and coworkers [*10*]

$$J_{(i+1)} = \left[J_i + \left(\frac{\eta}{b}\right)_i \frac{A_{i,i+1}}{B_N}\right]\left[1 - \left(\frac{\gamma}{b}\right)_i (a_{i+1} - a_i)\right] \tag{7}$$

where

$\eta = 2 + (0.522)\, b/W$,
$\gamma = 1 + (0.76)\, b/W$, and
$A_{i,i+1}$ = area under the load versus load line displacement record between lines of constant displacement at points i and $i + 1$.

The Rice equation is strictly accurate for deeply cracked bend specimens and contains no correction for crack extension. The Merkle-Corten equation includes a tensile correction, which makes it accurate for a compact specimen, but again this equation does not include a crack extension correction. The

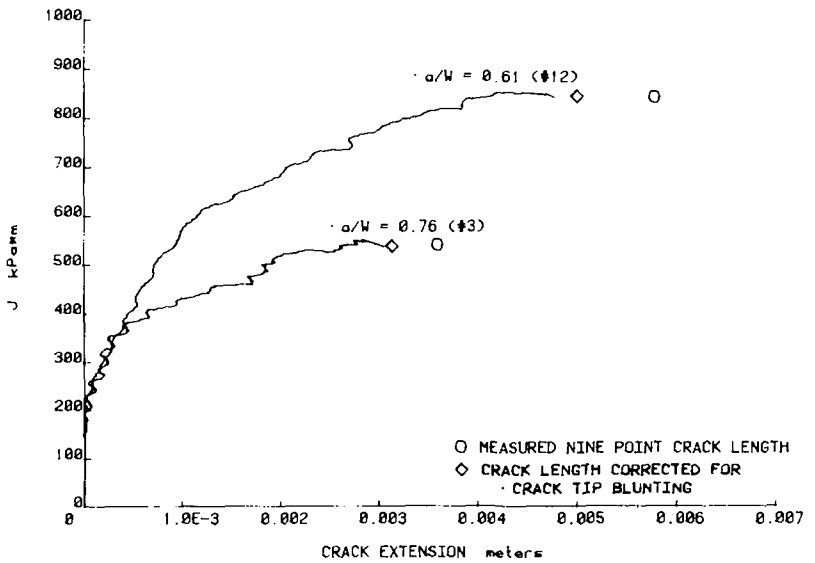

FIG. 11—*J-R curves for two high rate tests showing accuracy of final crack extension using the key curve method.*

Ernst equation contains corrections for both of these effects and thus should be most directly comparable with key curve results calculated here. Comparing the results in Fig. 11 shows that for small crack extensions, the Rice formula falls low because it does not include the tensile correction. When appreciable crack extension occurs, the two crack-growth corrected results start to fall away from the Merkle-Corten result back toward the Rice result. The key curve result agrees well with the Ernst formula for crack extension less than 0.002 m, but it falls always slightly below the Ernst results, with the difference growing to about 20 percent after 0.094 m of crack extension. The key curve result is of course vulnerable to experimental and numerical errors, while the Ernst result requires separable behavior of the load displacement relationship, which has not been experimentally verified for the compact specimen even without crack extension. The key curve result substantially agrees with numerical results of Shih et al [*16*], which predicted that the J singularity would begin to break down at around 6 to 10 percent crack growth or about 2.5 mm of crack extension in an $a/W = 0.5$ 1T compact specimen. The fact that this does in fact occur has apparently been masked up to now by a failure to crack-growth correct the J singularity values used for J-R curves.

For the two $a/W = 0.50$ specimens shown in Fig. 12, final crack extensions of about 9.6 mm were predicted by the key curve analysis and the heat tint nine-point average crack lengths for both specimens were found to be ~10.0 mm.

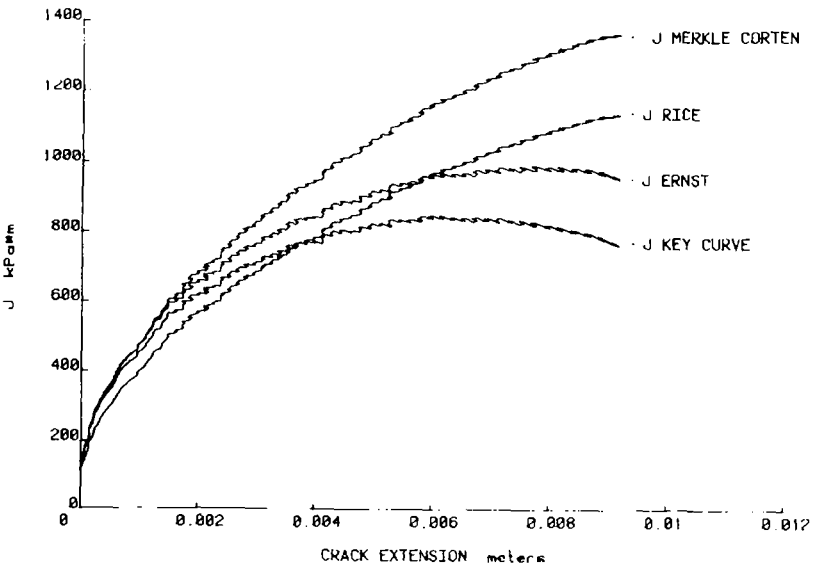

FIG. 12—*J-R curves for dynamic* a/W = *0.5 specimen obtained from equations for the* J *parameter taken from Merkle Corten [15], Rice [14], Ernst [10], and the present key curve method as designated.*

Two additional specimens containing deeper crack lengths were subsequently tested using the identical apparatus, but with a reduced square wave amplitude so that a reduced amount of crack extension would result. These specimens could be calculated to the end of their load displacement records without extending beyond the key curve file. The results are shown on Fig. 11 along with measured final crack length values. As in the case of the previous $a/W = 0.50$ specimens, the key curve result underestimates the crack extension by 10 to 15 percent. Part of this shortfall results from the fact that the key curve method does not include crack tip blunting in its crack extension measure since it occurs in both the small and large specimens and is subtracted out in the key curve analysis.

Data points were taken on the load displacement curves at fixed intervals of 50 μs for all these tests, and since crack extension at each data point was available from the key curve analysis, straight line segments could be fit to the crack length file to obtain estimates of the crack growth rates achieved in these tests. Figure 13 shows the average crack velocities achieved in these tests for two different crack length specimens using linear fits over 750-μs intervals. The short cracked specimens are seen to be subjected to considerably higher crack velocities than the deeply cracked specimens.

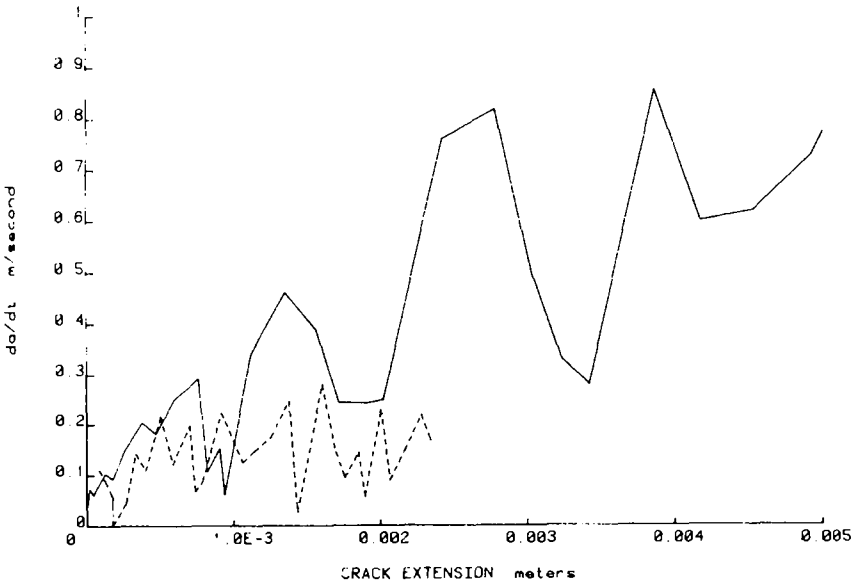

FIG. 13—*Average crack velocity versus crack extension for two specimens with varied* a/W *ratios.*

Comparison of Static and Dynamic Results

A comparison of the dynamic and static J-R curve files resulting from this work is shown in Figs. 14 to 16. In each case, the dynamic J-R curve is considerably elevated with respect to the static result. Greater elevation is found in the short cracked case, probably resulting from the higher dJ/dt applied and the higher da/dt that resulted in these specimens, as discussed in the previous sections. A tabulated summary of all J-R curve parameters is presented in Table 3.

Conclusions

The following conclusions can be drawn from this work.

1. The key curve method as utilized in this effort can be used to obtain accurate J-R curves directly from the load displacement record of a single specimen. Excellent agreement is found between the key curve analysis and a properly crack-growth corrected J-R curve resulting from unloading compliance methods.

2. The J-R curves of A533B-02 steel depend on crack length ratio in 1T 20 percent side grooved specimens with the most conservative J-R curve resulting from a/W ratios between 0.65 and 0.7.

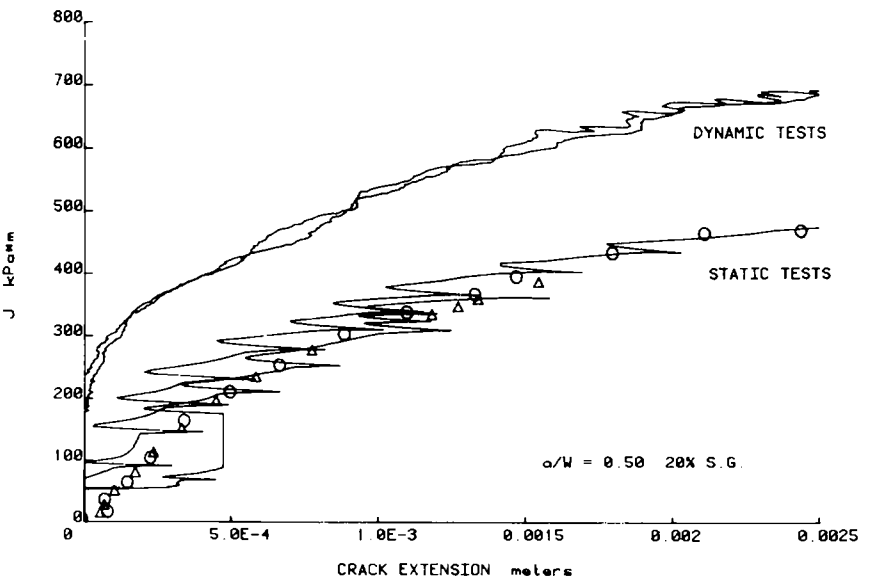

FIG. 14—*Comparison of dynamic and static J-R curves for A533B at 150°C,* a/W = *0.5.*

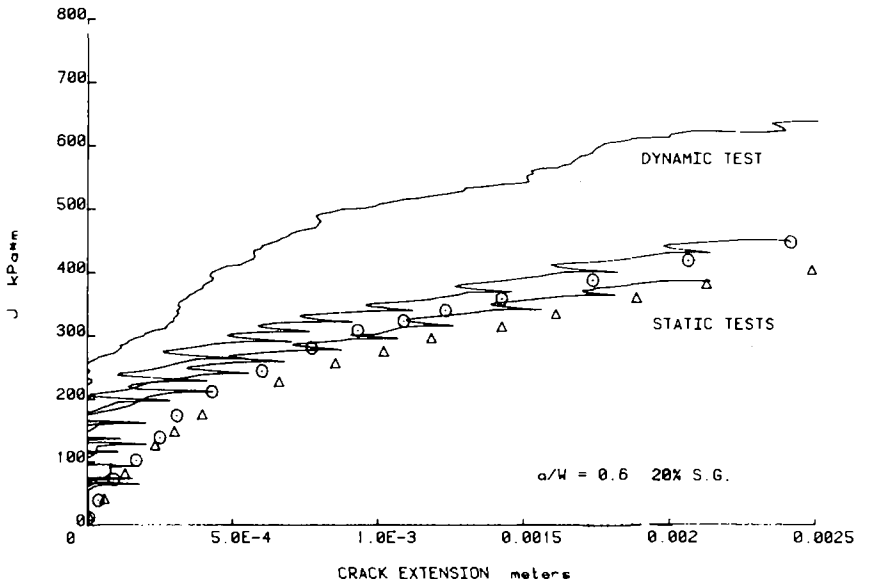

FIG. 15—*Comparison of dynamic and static J-R curves for A533B at 150°C,* a/W = *0.60.*

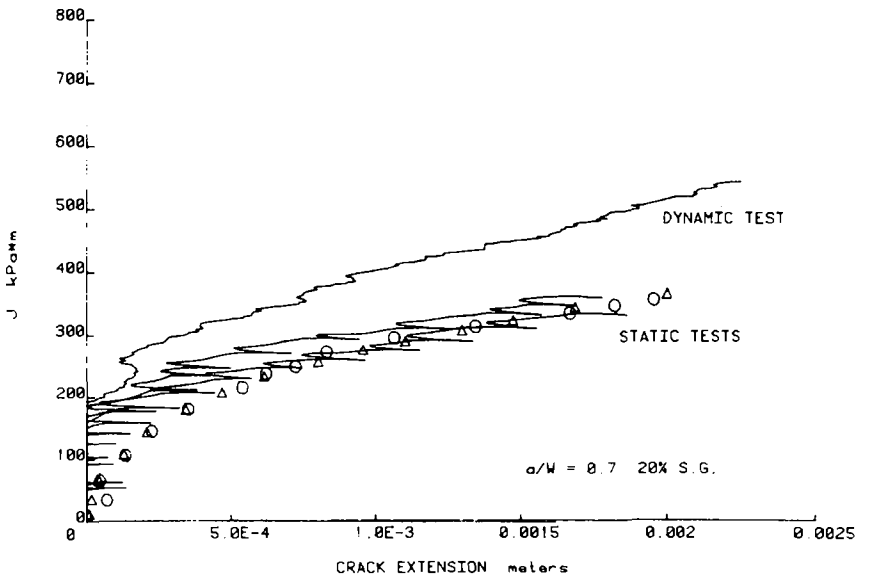

FIG. 16—*Comparison of dynamic and static J-R curves for A533B at 150°C,* a/W = *0.7.*

TABLE 3—*Summary of J-R curve test parameters, A533B-02 at 150°C.*

Specimen No.	Loading, m/sec	Analysis Method	a/W	J_{Ic}, kPa·m	dJ/da, MPa	T
8	4×10^{-6}	Key curve	0.5	125	161	86
		Unloading compliance	...	137	174	93
7	4×10^{-6}	Key curve	0.5	133	177	95
		Unloading compliance	...	146	181	97
12	4×10^{-6}	Key curve	0.6	185	103	56
		Unloading compliance	...	143	128	69
13	4×10^{-6}	Key curve	0.6	200	124	67
		Unloading compliance	...	173	146	78
19	4×10^{-6}	Key curve	0.7	173	94	50
		Unloading compliance	...	173	108	58
23	4×10^{-6}	Key curve	0.7	188	101	54
		Unloading compliance	...	185	100	54
27	4×10^{-6}	Key curve	0.8	151	199	107
		Unloading compliance	...	193	145	78
9D	0.25	Key curve	0.5	322	196	106
13D	0.25	Key curve	0.5	327	186	100
6D	0.25	Key curve	0.6	306	170	91
12D	0.25	Key curve	0.61	359	192	103
5D	0.25	Key curve	0.64	262	129	69
8D	0.25	Key curve	0.78	229	148	79
3D	0.25	Key curve	0.75	315	91.7	49

3. The key curve method is also effective for developing J-R curves from tests conducted at speeds up to 0.36 m/s COD rates at the specimen load line. It appears that the method would work at whatever velocity accurate load displacement records can be accurately measured.

4. High-rate J-R curves are elevated over those found at static speeds and the elevation approaches a factor of two when the crack velocity attained is on the order of 0.5 m/s. The slower loading rates generated for longer cracked specimens produced a smaller elevation of the high-rate J-R curve over that of the slow rate tests and it was not possible to determine whether this effect was due to the test rate or to a specimen constraint effect.

5. The key curve analysis when applied to the high-rate tests was shown to accurately predict the crack extension found by heat tinting and optically measuring the specimen after test was completed.

Acknowledgments

The author acknowledges the support of this work by the U.S. Nuclear Regulatory Commission (NRC) under Interagency Agreement RES-80-118

with the U.S. Naval Academy, Annapolis, Md. I especially wish to thank Milt Vagins of the NRC staff for his support and encouragement.

References

[1] Clarke, G. A., Andrews, W. R., Begley, J. A., Donald, J. K., Embley, G. T., Landes, J. D., McCabe, D. E., and Underwood, J. E., *Journal of Testing and Evaluation,* Vol. 7, No. 1, Jan. 1979, pp. 49–56.

[2] Paris, P. C., Tada, H., Zahoor, A., and Ernst, H. in *Elastic-Plastic Fracture, ASTM STP 668,* American Society for Testing and Materials, 1979, pp. 5–36.

[3] Paris, P. C. Tada, H., Zahoor, A., and Ernst, H. in *Elastic-Plastic Fracture, ASTM STP 668,* American Society for Testing and Materials, 1979, pp. 251–265.

[4] Joyce, J. A. and Vassilaros, M. G. in *Fracture Mechanics, ASTM STP 743,* American Society for Testing and Materials, 1981, pp. 525–542.

[5] Clarke, G. A., Andrews, W. K., Paris, P. C. and Schmidt, D. W. in *Mechanics of Crack Growth, ASTM STP 590,* American Society for Testing and Materials, 1976, pp. 27–42.

[6] Ernst, Hugo, Paris, P. C., Rossow, Mark, and Hutchinson, J. W. in *Fracture Mechanics, ASTM STP 677,* American Society for Testing and Materials, 1979, pp. 581–599.

[7] Joyce, J. A., Ernst, Hugo, and Paris, P. C. in *Fracture Mechanics, ASTM STP 700,* American Society for Testing and Materials, 1980, pp. 22–236.

[8] Vassilaros, M. G., Joyce, J. A., and Gudas, J. P. in *Fracture Mechanics, ASTM STP 700,* American Society for Testing and Materials, 1980, pp. 251–270.

[9] Joyce, J. A. and Gudas, J. P. in *Elastic-Plastic Fracture, ASTM STP 668,* American Society for Testing and Materials, 1979, pp. 451–468.

[10] Ernst, H., Paris, P. C., and Landes, J. D. in *Fracture Mechanics, ASTM STP 743,* American Society for Testing and Materials, 1981, pp. 476–502.

[11] Hawthorne, J. C., Ed., "Naval Research Laboratory-Electric Power Research Institute (NRL-EPRI) Research Program (RP886-2), Evaluation and Predictions of Neutron Embrittlement in Reactor Pressure Vessel Materials, Annual Report for 1978," NRL Report 327, Aug. 1979, p. 40.

[12] Joyce, J. A. and Czyryca, E. J., "Dynamic J_I-R Curve Testing of HY-130 Steel," David W. Taylor Naval Ship Research and Development Center, Report DTNSRDC/SME-81/57, Oct. 1981.

[13] Hutchinson, J. W. and Paris, P. C. in *Elastic Plastic Fracture, ASTM STP 668,* J. D. Landes, J. A. Begley, and G. A. Clarke, Jr., Eds, 1979, pp. 37–64.

[14] Rice, J. R., Paris, P. C., and Merkle, J. G. in *Progress in Flaw Growth and Fracture Toughness Testing, ASTM STP 536,* 1973, pp. 231–245.

[15] Merkle, J. G., and Corten, H. T., *Journal of Pressure Vessel Technology,* Nov. 1974, pp. 286–292.

[16] Shih, C. F., deLorenzi, H. G., and W. R. Andrews in *Elastic-Plastic Fracture, ASTM STP 668,* 1979, pp. 65–120.

D. E. McCabe[1] *and H. A. Ernst*[1]

A Perspective on R-Curves and Instability Theory

REFERENCE: McCabe, D. E. and Ernst, H. A., **"A Perspective on R-Curves and Instability Theory,"** *Fracture Mechanics: Fourteenth Symposium—Volume I: Theory and Analysis, ASTM STP 791*, J. C. Lewis and G. Sines, Eds., American Society for Testing and Materials, 1983, pp. I-561-I-584.

ABSTRACT: Several aspects of elastic-plastic R-curve theory and instability analysis are discussed. It is shown how material flow property effects can be incorporated into the R-curve in place of the more common practice of incorporation into J crack drive. Formulas for deformation theory J that adjust for slow-stable crack growth in compact (CT) and center cracked tension (CCT) specimens are presented. For cases of extremely large crack extension where conditions of deformation theory J are violated, an expression for modified J also is presented. J_R-curve data obtained from a 4T size compact specimen were used to predict instability in a displacement controlled CCT test for 2024-T351 aluminum.

KEY WORDS: R-curve, elastic-plastic fracture, J-integral, fracture mechanics, crack propagation

Nomenclature

- η A dimensionless factor used in area approximation for J
- A Area under force-displacement diagram in energy units
- B Specimen thickness
- W Specimen width
- b Remaining ligament dimension
- σ_0 Yield strength
- σ_u Ultimate strength
- ϵ_0 Yield strain
- α Coefficient in Ramberg-Osgood work hardening law
- n Work hardening exponent, Ramberg-Osgood law
- E Elastic modulus
- h_1 Handbook listed coefficients for plastic J determination

[1]Senior engineer, Materials Engineering Department, Westinghouse Research and Development Center, Pittsburgh, Pa. 15235.

J_R Crack growth resistance expressed in units of J
K_R Crack growth resistance expressed in units of K_I
J_{el} Elastic component of J
J_{pl} Plastic component of J
K_I Linear elastic stress-intensity factor, K
r_y Plastic zone adjustment
a_p Physical or real crack size
a_e Effective crack size, physical plus r_y
Δa_p Stable growth of physical crack size
Δa_e Stable growth of effective crack size
P Applied load
P_0 Calculated limit load
C_{CR} Compliance capacity remaining
K_M Spring constant of the structure
C_M Compliance of total structure ($1/K_M$)
Y Half-span of clip gage in CCT tests

R-curve technology had evolved initially as an extension of linear-elastic fracture mechanics, specifically designed to handle materials that display slow-stable crack growth prior to instability. Instability theory is implicit in R-curve theory through the relationships used to describe the balance between crack driving force supplied by loading conditions and crack growth resistance development in the materials. The fundamentals on the instability prediction procedure have been developed and used successfully on ultra-high-strength sheet materials for a number of years. Here linear-elastic conditions dominate stress field conditions and it has been shown that R-curves behave as a "material property," independent of initial flaw size, component planar size, and component geometry [*1*].[2] Most engineering grade steels also display slow-stable crack growth leading to instability provided that the service conditions are in the upper shelf transition temperature regime. Because these materials commonly display high upper shelf toughness, most laboratory specimens will deform progressively from linear elastic to confined plasticity to fully plastic conditions. Under high plastic deformation conditions, the so-called "material property" characteristics of R-curves have not been proved adequately. Experiments to evaluate specimen size requirements to obtain intrinsic R-curve behavior are few, and the appropriate specimen size requirements to be applied are not firmly established.

In the absence of a strong technical confirmation for the use of elastic-plastic J_R-curves, a J_{Ic} concept has been adopted as a temporary expedient. This concept directs attention to the point on the J_R-curve where stable crack growth initiates which generally occurs well below the in-service toughness performance capability of the materials. The principal advantage in J_{Ic} is

[2]The italic numbers in brackets refer to the list of references appended to this paper.

that specimen geometry effects are demonstrated to be negligible. Geometry effects have tended to develop only after appreciable crack growth and with the attendant increased plasticity development.

This paper is intended to present data applicable to the intrinsic J_R-curve behavior of elastic-plastic deforming materials. Methods of handling plasticity effects and crack growth effects in fracture toughness characterization will be discussed and the implications that J_R-curves have for instability prediction problems will be presented and demonstrated.

Elastic-Plastic Toughness Parameters

J-integral currently is regarded by many as the most suitable toughness parameter for handling plasticity effects, primarily because of the rigorous use of plasticity theory in its development. Specifically, J-integral is suitably justified for use in nongrowing crack situations. However, J initially was expected to be inappropriate for J_R-curve work precisely because of its origin in deformation theory. Theoretically, all nonlinear effects should be due to plasticity development in a specimen, and partial unloading due to stable crack growth violates the conditions assumed in the use of deformation theory. Despite this concern, J has been applied successfully to J_R-curve development for the purpose of determining J_{Ic}. In this specific application, the unknown variance from deformation theory J is not significant to J_{Ic} at incipient stable crack growth. Hence, simple equations employing total applied energy of the following form have been used liberally

$$J = \eta A/Bb \text{ (specimens in bending mode)} \tag{1}$$

In recent work, the relative impact of crack growth on the accuracy of J is better understood. Shih [*2*] has shown through numerical analysis that growth up to 6 percent of the initial ligament size can be tolerated, in the sense that J based on deformation theory still controls the crack growth process. Even more recently, Ernst [*3*] has developed a computational procedure whereby deformation theory J can be obtained from load-displacement records that contain significant additional displacement due to crack growth. This procedure, along with a newly developed expression for the center cracked tension (CCT) configuration, is described in the Appendix [*4*]. Unless otherwise stated, the J_R data shown in the present report were calculated with these expressions. The consequence of applying the Appendix calculations versus Eq 1 is demonstrated for the compact (CT) specimen geometry in Fig. 1 on a material that developed considerable crack growth. The 2024-T351 aluminum in 12.7-mm (½-in. thickness develops appreciable plasticity, but because the test was made with a 4T planview size CT specimen, the plasticity was confined within a dominant elastic stress field throughout the test. The elastic-plastic K_R^2/E shown in this comparison was obtained by the

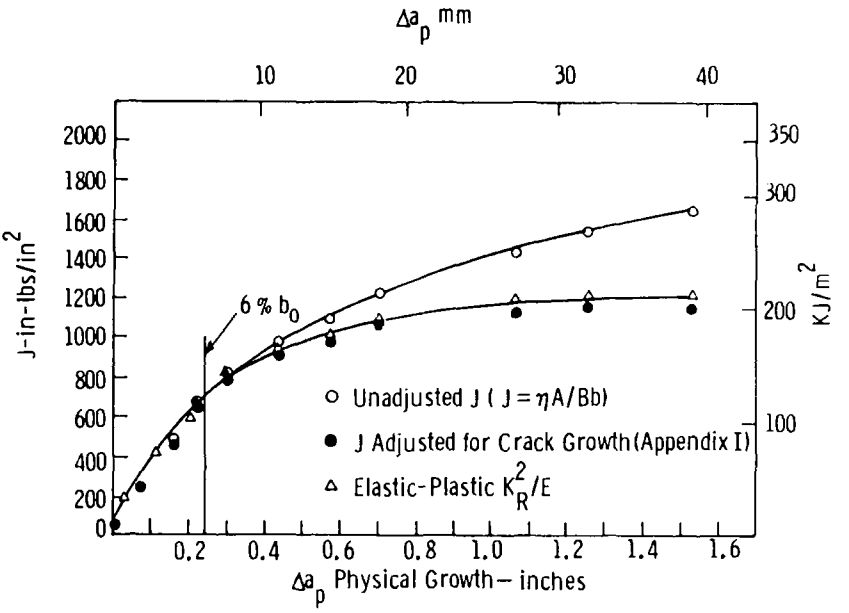

FIG. 1—J_R *curve from a 12.7-mm (0.5-in.)-thick 4T CT specimen of 2024-T351 aluminum. Comparison of* Δa_p *adjusted* J*-values.*

compliance procedure outlined in the ASTM Recommended Practice for *R*-Curve Determination (E 561-81), and for the present confined plasticity example can serve as the benchmark for comparison.

The use of deformation theory *J*, however, does not insure that geometry effects will be eliminated from J_R-curve behavior. In fact, the converse may exist when crack growth is substantial and when comparing two specimen types. Figure 2 is an example where deformation theory J_R-curves are compared for 12.7-mm (½-in.)-thick 2024-T351 aluminum with planview sizes of a 4T CT and 40-cm (16-in.)-wide CCT. The remaining ligament size was comparable in both specimen types.

Values of Δa_p were measured from unloading compliance, and deformation theory J_D for the CCT was calculated using the new procedure developed by Ernst (see Appendix). As can be seen, for crack extension up to 12.7 mm (½ in.), the results are consistent; beyond that size, data from the two geometries start deviating from each other. To improve calculations of *J* with extensive crack growth, it was decided to compute the results using a new parameter suggested by Rice et al [*5,6*]. This has been generalized very recently by Ernst [*7*] to obtain a modified J_M, expressed as

$$J_M = J_D - \int_{a0}^{a} \left. \frac{\partial J_{pl}}{\partial a} \right|_{\delta_{pl}} da \qquad (2)$$

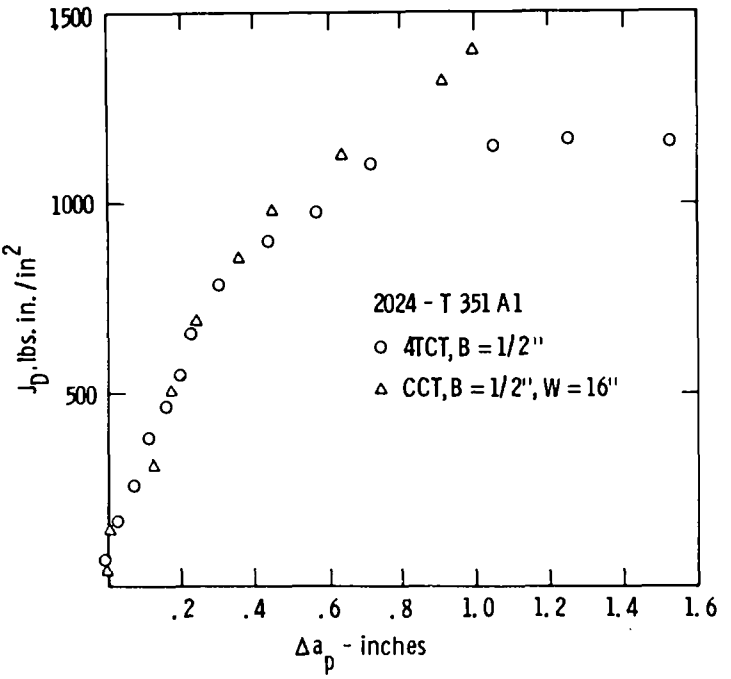

FIG. 2—*CT specimen and center cracked panel* J_R *curve comparison using deformation theory* J_D.

where a_0 and a are the initial and final value, respectively, of the crack length, and J_{pl} is the plastic part of J, ($J_{pl} = J_D - G$). (See Appendix.) The data were replotted in terms of J_M versus Δa, and a much better correlation resulted, as shown in Fig. 3. As was mentioned, the assumption that a universal material parameter exists with large amounts of crack growth is still an open question, but it seems that available results can be improved by properly modifying J.

Elastic-Plastic *J*-Calibration Values

In the previous section, formulas were presented for the experimental determination of deformation theory J. This information together with the value of the crack length represents the way the material behaves with crack growth, that is, the J_R-curve. On the other hand, J can be determined numerically as a function of, say, crack length and displacement, $J = J(a, \delta)$, with no crack growth assumed. These are calibration functions in the sense that they deal with the deformation behavior of the material in a fixed geometry.

Complete closed form elastic-plastic solutions for J do not exist for many configurations. However, solutions for the outer bounds of linear-elastic and

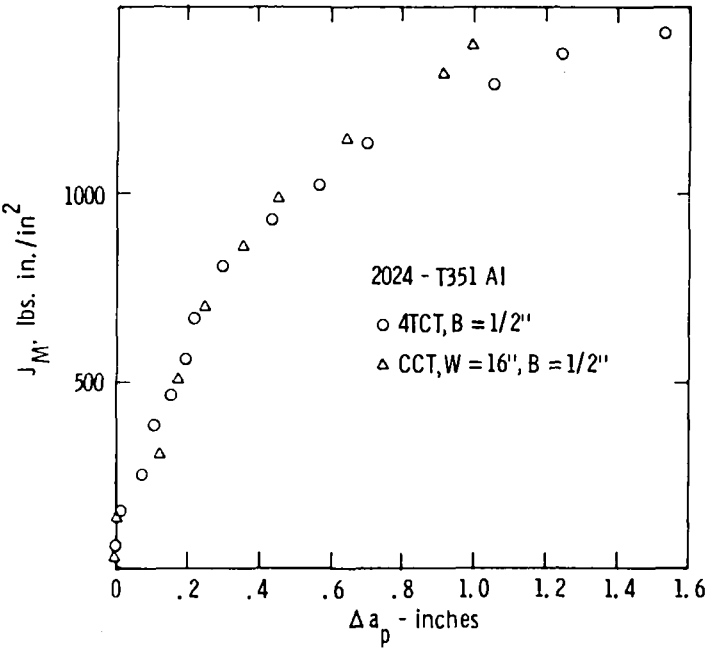

FIG. 3—*CT specimen and center cracked panel* J_R *curve comparison using modified* J_M.

fully plastic conditions are more common and are likely to be availble. Exact linear-elastic solutions are obtainable through linear-elastic handbook K_I formulas. At the other extreme of fully plastic displacements, general solutions have been developed for several cracked geometries [*8*]. To bridge the gap between elastic and fully plastic (confined plasticity cases), a common practice is to use plasticity-modified K_I values. Here, crack sizes are augmented with a plastic zone adjustment dimension, r_y, such that when these are applied in linear-elastic stress-intensity factor equations, K_R is obtained which is related to J_R through

$$J_R = K_R^2/E \tag{3}$$

The accuracy of J_R obtained in this way is, therefore, highly dependent on the accuracy of r_y in substitution for the plasticity effects. The well-known Irwin [*9*] formula is oftentimes used as a basis format and generally has been found to work best on high-strength nonhardening materials. For work hardening materials, Rice [*10*] has recommended the following to be more appropriate

$$r_y = \frac{1}{2\pi}\,\frac{n-1}{n+1}\left(\frac{K_R}{\sigma_0}\right)^2 \tag{4}$$

where n is the Ramberg-Osgood work hardening exponent. One additional modification is useful to make a smooth transition into the fully plastic mode of deformation. Since K_R is used for crack size adjustment to solve for K_R, solutions tend to become noncoverging as the fully plastic (limit load) condition is approached. A factor, ϕ, as proposed by Edmunds and Willis [*11*] can be added where

$$\phi = 1/[1 - (P/P_0)^2] \tag{5}$$

Plastic zone adjusted cracks commonly are referred to as effective crack size, and

$$a_e = a_p + \phi r_y \tag{6}$$

The experimental counterpart to the use of Eq 6 is a compliance procedure outlined in ASTM Method E 561-81. The procedure is relatively simple since it involves the use of the slope of secant lines constructed on the load-displacement test record. Values of K_R determined using these psuedolinear-elastic crack sizes have been shown to relate to deformation theory J_R for three common test specimen geometries [*12*]. This relationship is almost always exact up to limit load and moderately diverging beyond limit load, as illustrated in Fig. 4.

Crack Growth Resistance-Effective Crack Growth R-Curves

In ASTM Method E 561-81, it is suggested that R-curves can be plotted using either physical crack growth, Δa_p, or effective crack growth, Δa_e, on the abscissa. However, this particular method had been developed principally with high-strength sheet materials in mind. Here plastic zones are usually small such that the effect of this option would be of little consequence to an instability analysis. However, for the more ductile elastic-plastic behaving materials, plasticity effects can dominate, and the handling of material flow property effects can be highly significant to the accuracy of the predictions. If an R-curve is plotted in terms of Δa effective it will contain completely the material flow property effects. The compliance procedure outlined in ASTM Method E 561-81 or Eq 6 can be used to describe crack growth, Δa_e, on the abscissa. So long as plasticity is confined within dominant elastic stress fields, the resulting K_R-Δa_e R-curves can be shown to be independent of specimen planview size as represented by 1T and 4T CT specimen data shown in Fig. 5. In both cases, much of the data shown had been generated beyond maximum load.

An alternative and perhaps more laborious means of generating K_R-Δa_e R-curves is to use deformation theory J determined using the elastic-plastic

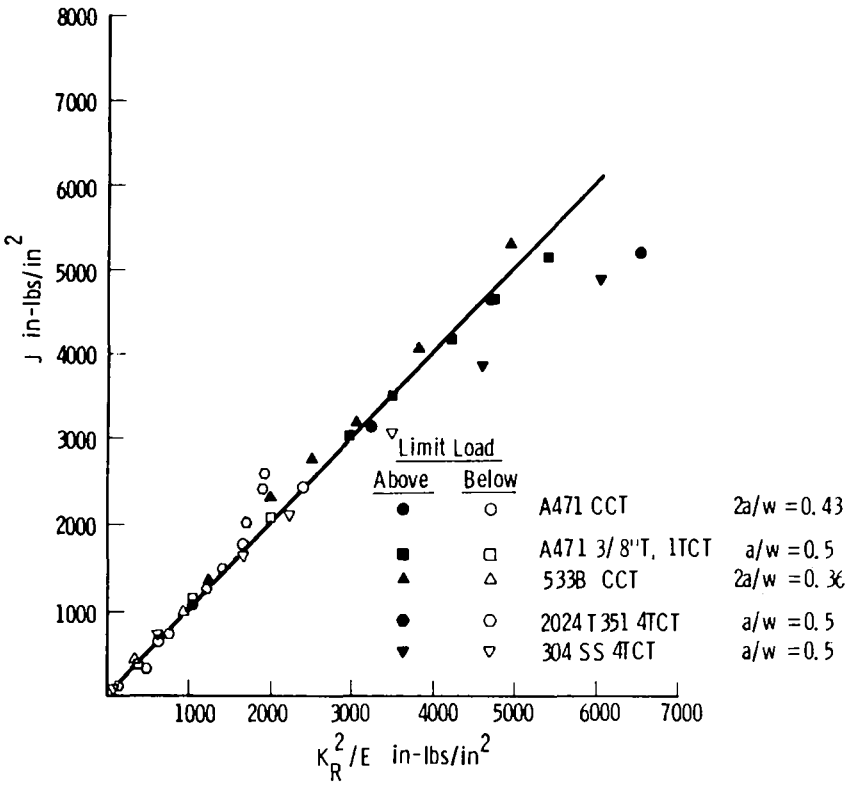

FIG. 4—*Correlation between* J *and* K_R^2/E *for four materials and two specimen types.*

formulations proposed by Shih and co-workers [*8*] in a handbook of elastic-plastic solutions. The material flow properties are contained within J calibrations and the plastic flow field effects can be transposed into K_R-Δa_e values for various crack geometries. Initially, J is developed using the Ramberg-Osgood work hardening properties of the material

$$\frac{\epsilon}{\epsilon_0} = \frac{\sigma}{\sigma_0} + \alpha\left(\frac{\sigma}{\sigma_0}\right)^n \tag{7}$$

where σ_0 and ϵ_0 are true yield strength and true yield strain, respectively. J is determined as the sum of the psuedoelastic J_{el} and fully plastic J_{pl}, where

$$J = J_{el} + J_{pl}(n, a/W) \tag{8}$$

$$J_{el} = K_R^2/E \tag{8a}$$

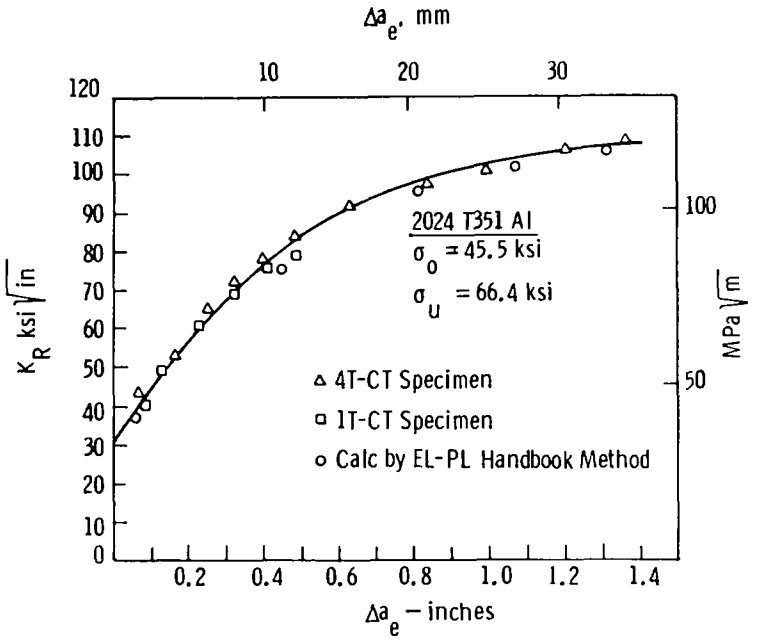

FIG. 5—K_R-Δa *effective R-curve for 12.7-mm (0.5-in.)-thick 2024-T351 aluminum.*

J_{el} is calculated using Eqs 4 through 6 and 8*a* with a_e applied in the linear elastic K_I equation for the subject geometry to obtain K_R. The second term, J_{pl}, in Eq 8 is for full plastic flow and two example solutions for CCT and CT specimens are as follows

$$(\text{CCT}) J_{pl} = \alpha \sigma_0 \epsilon_0 a (1 - 2a/W) h_1 (P/P_0)^{n+1} \tag{9}$$

$$(\text{CT}) J_{pl} = \alpha \sigma_0 \epsilon_0 (W - a) h_1 (P/P_0)^{n+1} \tag{9a}$$

In these, P_0 represents theoretical limit load, and the term h_1 is obtained through numerical analysis and is a function of relative crack size, a/W, and work hardening exponent n. Values of h_1 are tabulated in the handbook [*13*] in two sets: plane strain and plane stress. To illustrate, a family of calculated J calibration plots over variable crack sizes, a_p/W, for the 4T specimen of Fig. 5 is shown in Fig. 6. These calibration plots then can be used to calculate K_R versus Δa_e data points for Fig. 5. The procedure used was as follows:

1. Select a J level to be converted to K_R.
2. Use a J-Δa_p R-curve to determine the a_p/W at the selected J level.
3. Determine applied load from the appropriate calibration curve (a_p/W) in Fig. 6 (a_p = physical crack size).

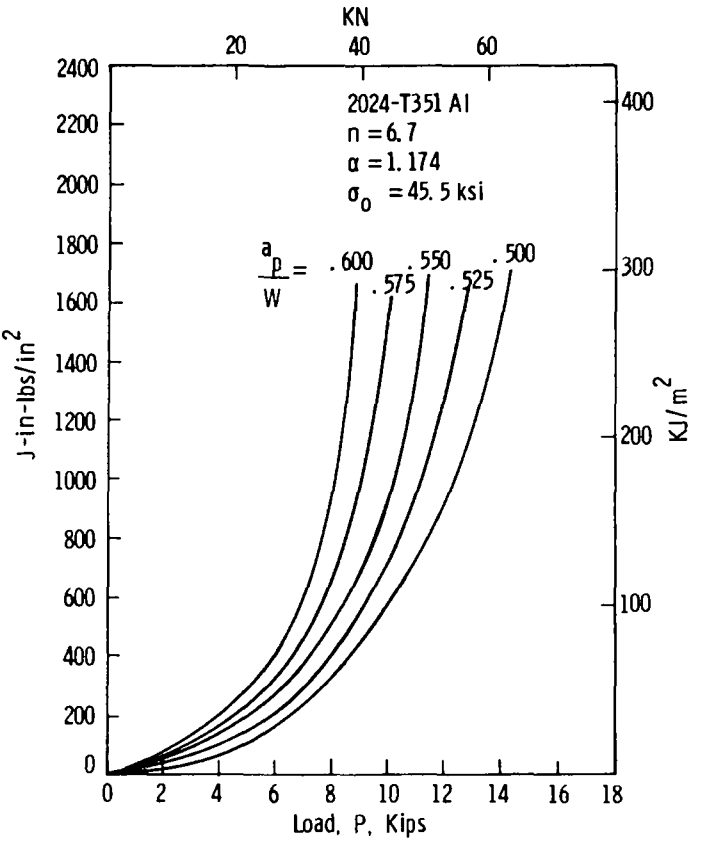

FIG. 6—J *calibration for 4T CT specimens of 2024-T351 aluminum.*

4. With K_R from Item 1 of this procedure and load from Item 3, determine the a_e that will satisfy the K_I equation for the CT specimen.

5. Then: $\Delta a_e = a_e - a_0$.

The results of the exercise over five levels of J are shown as data points in Fig. 5. The compatibility between these handbook-derived values and experimental values is unusually good. In effect, what has been demonstrated is that material flow property effects from elastic-plastic J solutions were effectively incorporated into the R-curve. The advantage of this alternative will be evident in a subsequent section on instability concepts.

Intrinsic R-Curves

To justify the validity of either J_R-curves or K_R-curves for use in instability predictions, the material property characteristics of independence from ini-

tial crack size and planview size must be demonstrated. This is accomplished experimentally by testing specimens of variable dimensions, and Figs. 7 and 8 are illustrative of typical findings. Figure 7 contains data on A533B tested as 25-mm (1-in.)-thick CT specimens, but with 1T, 2T, and 4T planview sizes. The Fig. 8 data were obtained from 200-mm (8-in.)-wide by 12-mm (0.494-in.)-thick CCT specimens of Ni-Cr-Mo-V (A471) rotor steel. In both figures, the plot on the left represents K_R versus Δa_e obtained using the ASTM Method E 561-81 described earlier. The right-hand plots were obtained using the Appendix calculations for J_R, and these are plotted against physical crack size obtained by unloading compliance. The preference of the authors is to always plot J_R against Δa_p and K_R against Δa_e as a convention for easy identification, but in the present case $\sqrt{J_R E}$ was used for the purpose of the comparison being made.

Both methods of data plotting show intrinsic R-curve behavior up to the onset of limit load (P_0) for the various size specimens. In these cases, limit load is also about coincident with the first attainment of maximum load. For CT specimens J_R-Δa_p R-curves are generally unaffected by the onset of limit load deformation. The equivalency between the toughness parameters of J_R and K_R is reasonably maintained to well beyond limit load, as was indicated earlier in Fig. 4. On the other hand, K_R-Δa_e type R-curves have been found to deviate consistently from intrinsic behavior at or near first onset of limit load. Since the equivalency between J_R and K_R is essentially maintained, the anomaly apparently develops in the abscissa, Δa_e. This perhaps results from

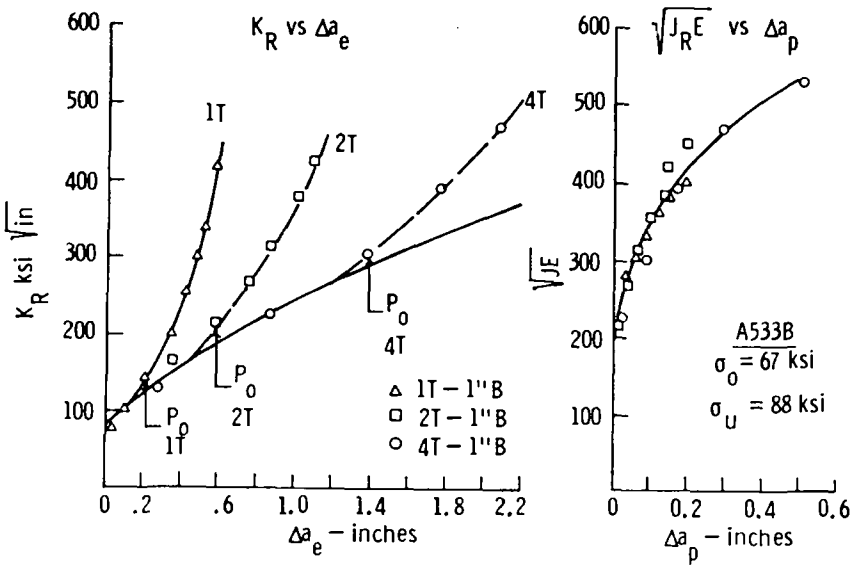

FIG. 7—*Comparison of R-curves for A533B of 25.4-mm (1-in.) thickness. 1T, 2T, and 4T plan view sizes. Test temperature +93.3°C (200°F),* $a_0/W = 0.5$.

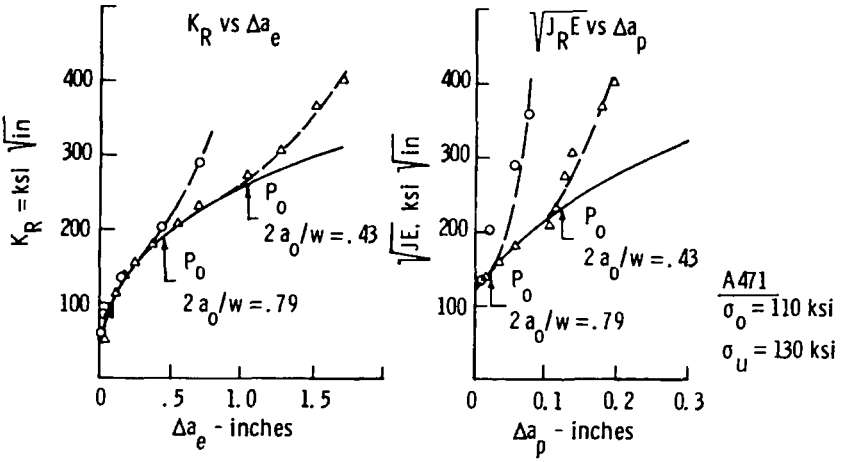

FIG. 8—*R-curves on A471 from 203.2-mm (8-in.)-wide CCT panels, thickness 12.3 mm (0.494 in.).*

the reality that the plastic zone representation loses physical significance once the remaining ligament transcends into full plastic flow. A procedure for extrapolation of Δa_e values to obtain intrinsic K_R-Δa_e beyond limit load, utilizing known plastic behavior characteristics, is thought to be possible, and a procedure is presently under evaluation.

In center cracked panel tests, it appears that both Δa_p and Δa_e type R-curves deviate from intrinsic behavior after the onset of limit load. This problem is generic to both methods, apparently because 45-deg slip lines develop that connect the crack tip to the free edges of the specimen. This type of deformation tends to disrupt the crack tip deformation fields such that the crack tip modeling of the fracture processes zone is progressively weakened with continued deformation. Therefore, it would appear that in order to develop substantial portions of intrinsic J_R curves in CCT tests, most of the data should be developed under confined plasticity conditions and this can be satisfied only by testing specimens with relatively large initial ligaments.

The following sections will address the various ways that intrinsic R-curves are used to make instability predictions.

Tearing Instability

Instability results from a lack of balance between an externally applied crack drive force and material crack growth resistance and will ensue when the rate of increase of the applied drive force exceeds that of the material resistance to crack growth. The general principles have been known since 1961 and are well documented in Ref *14*.

Recently, the basic implications of this concept were explored further by Paris et al [*15-16*], and as a result, it was demonstrated that the overall characteristics of the structure play a major role in instability and its effects have to be included in the rate balance mentioned. In this work, they introduced a nondimensional quantity called the tearing modulus, T, that in general has the form

$$T = \frac{E}{\sigma_0^2} \frac{dJ}{da} \tag{10}$$

where E is the elastic modulus and σ_0 is the flow stress. If Eq 10 is evaluated using the J resistance curve of the material, the resulting T is the material tearing modulus T_{mat}. If instead, dJ/da in Eq 10 is calculated as the rate of change of crack drive or the applied J, per unit virtual crack extension, with the condition of total displacement, δ_{tot}, kept constant (or other similar conditions specified), the resulting T is the applied tearing modulus T_{app}. And so following References [*15-16*], instability will occur when

$$T_{app} \geq T_{mat} \tag{11}$$

Using the condition of total displacement constant, the compliance of the structure, C_M, is introduced into the analysis and T_{app} becomes a function of C_M. Consequently, according to the theory, Eq 11 instability is predicted provided the values of T_{mat} and expressions for T_{app} are known. In their original work, Paris et al also performed the first experimental evaluation of the theory. In tests of three-point bend specimens loaded in series with a spring bar of adjustable length, the compliance of the system, C_M, was varied from test to test, producing stable or unstable behavior in complete agreement with the theory. In this work the expressions of T_{app} for different configurations were calculated by assuming that the material was perfectly plastic and that the crack was growing under limit load conditions.

Later on, Hutchinson and Paris [*17*] presented a more general expression for T_{app} for a specimen loaded in series with a spring, simulating the structure

$$T_{app} = \frac{E}{\sigma_0^2} \left\{ \left. \frac{\partial J}{\partial a} \right|_P - \left. \frac{\partial J}{\partial P} \right|_a \left. \frac{\partial \delta}{\partial a} \right|_P \frac{1}{\left[C_M + \frac{\partial \delta}{\partial P} \right]} \right\} \tag{12}$$

where δ is the displacement due to the crack and C_M is the compliance of the spring. All the terms appearing in Eq 12 are calibration functions, that is, they do not bear any information regarding the material response to crack growth. These functions can be obtained from finite-element analysis or experimentally from blunt notch specimen tests, and no "real" crack growth

test is needed for their determination. This scheme has been used [*18-19*] to obtain T_{app} for different configurations of practical interest, and, as was mentioned, instability can be predicted by comparing the value of T_{app} obtained from Eq 12 with the experimentally obtained T_{mat}.

In this section, the problem is approached from a different point of view, emphasizing the role of the actual P-δ test record. In fact, as shown by Ernst et al [*3*], both T_{mat} and T_{app} can be evaluated from a single specimen test record and the conditions for instability can be found directly.

The T_{mat} is defined as the rate of change of J with respect to crack length along the J-R curve, or actual test record.

$$T_{mat} = \frac{E}{\sigma_0^2}\left(\frac{dJ}{da}\right)_{mat} = \frac{E}{\sigma_0^2}\left(\frac{\partial J}{\partial a} + \frac{\partial J}{\partial \delta}\frac{\partial \delta}{\partial a}\right)_{mat} \tag{13}$$

At the same time, considering the load P as a function of displacement, δ, and crack length, a,

$$P = P(\delta, a) \tag{14}$$

it can be differentiated to give

$$dP = \frac{\partial P}{\partial a}\bigg|_{\delta} da + \frac{\partial P}{\partial \delta}\bigg|_{a} d\delta \tag{15}$$

or rearranging

$$\frac{d\delta}{da} = \frac{\dfrac{\partial P}{\partial a}\bigg|_{\delta}}{\left(\dfrac{dP}{d\delta} - \dfrac{\partial P}{\partial \delta}\bigg|_{a}\right)} \tag{16}$$

where the terms $(\partial P/\partial a)\,|_{\delta}$ and $(\partial P/\partial \delta)\,|_{a}$ are calibration functions, and the term $dP/d\delta$ is to be measured from the actual test record. Replacing Eq 16 in Eq 13 and noting that

$$\frac{\partial P}{\partial a}\bigg|_{\delta} = -\frac{\partial J}{\partial \delta}\bigg|_{a}$$

gives

$$T_{mat} = \frac{E}{\sigma_0^2}\left\{\frac{\partial J}{\partial a}\bigg|_{\delta} + \left(\frac{\partial J}{\partial \delta}\right)^2\bigg|_{a} \frac{1}{\dfrac{\partial P}{\partial \delta}\bigg|_{a} - \dfrac{dP}{d\delta}}\right\} \tag{17}$$

which is a general expression for T_{mat}.

The applied tearing modulus T_{app} is defined as the rate of change of J_{app} with crack length under the condition that the overall displacement is kept constant (or equivalent condition). Thus, T_{app} is given by

$$T_{app} = \frac{E}{\sigma_0^2}\left(\frac{dJ}{da}\right)_{\delta_{tot}} = \frac{E}{\sigma_0^2}\left(\frac{\partial J}{\partial a} + \frac{\partial J}{\partial \delta}\frac{d\delta}{da}\right)_{\delta_{tot}} \tag{18}$$

The condition δ_{tot} = constant, is equivalent to $d\delta_{tot} = 0$, or separating the total displacement into a part due to the crack, δ, and a part due to the rest of the structure (uncracked body part), δ_M

$$d\delta_{tot} = d\delta + d\delta_M = 0 \tag{19}$$

$$= d\delta + C_M dP = 0 \tag{19a}$$

where $C_M = (K_M)^{-1} = d\delta_M/dP$ can be associated with the linear compliance of the system (spring + testing machine + uncracked specimen). T_{app} then can be calculated using Eqs 15, 16, 18, and 19 to give

$$T_{app} = \frac{E}{\sigma_0^2}\left\{\left.\frac{\partial J}{\partial a}\right|_\delta + \left(\frac{\partial J}{\partial \delta}\right)_a^2 \frac{1}{\left.\frac{\partial P}{\partial \delta}\right|_a + K_M}\right\} \tag{20}$$

An alternative expression also can be found for T_{app} by combining Eqs 17 and 18, giving

$$T_{app} = \frac{E}{\sigma_0^2}\left\{\left.\frac{\partial J}{\partial a}\right|_\delta + \left(\frac{\partial J}{\partial \delta}\right)_a^2 \frac{1}{K_M + \frac{dP}{d\delta} + \frac{(\partial J/\partial \delta)^{-2}}{\frac{\sigma_0^2}{E}T_{mat} - \left.\frac{\partial J}{\partial a}\right|_\delta}}\right\} \tag{21}$$

Moreover, the calibration functions $\partial J/\partial a|_\delta$ and $\partial J/\partial \delta|_a$ can be expressed in terms of current values of J and P, respectively, if the expression for P in Eq 14 is known. As an example, as discussed in Ref *3* for the CT specimen

$$\left.\frac{\partial J}{\partial a}\right|_\delta = -\frac{\gamma J}{b} \tag{22}$$

$$\left.\frac{\partial J}{\partial \delta}\right|_a = \eta\frac{P}{b} \tag{22a}$$

where $\gamma = 1 + 0.76\, b/W$ and $\eta = 2 + 0.522\, b/W$.

As a result, Eqs 19 to 21, with the corresponding condition of Eq 22, allow us to obtain T_{mat} and T_{app} as a function of current values of J, P, and b, the slope $dP/d\delta$, and the stiffness of the structure K_M; all quantities obtainable from a single test record [*3*]. This different approach to the instability problem emphasizing the role of the load displacement record allows a new perspective to the instability phenomenon. That is, by comparing T_{mat} and T_{app}, an alternate physical meaning can be given to the instability condition of Eq 11. In fact, by comparing Eqs 19 and 20 one gets $T_{app} > T_{mat}$ when and only when

$$K_M = C_M^{-1} < -\frac{dP}{d\delta} \tag{23}$$

where $dP/d\delta$ refers to the slope (decreasing load part) of the load versus displacement test record (P-δ of the specimen alone). As a result, by just inspecting a test record of a certain specimen geometry, the amount of additional structural compliance needed to cause instability in an identical specimen test, or the needed additional compliance C_{CR} (compliance capacity remaining) [*3*] can be obtained readily.

So far, it is obvious that instability can be predicted by the C_{CR} concept for a given specimen geometry. Nevertheless, it is of much greater interest to be able to predict instability for a certain specimen without actually running a test. This also can be accomplished using the C_{CR} concept. In fact, $-dP/d\delta$ can be obtained from Eq 17 and substituted in Eq 23 to get

$$C_{CR}^{-1} = -\frac{dP}{d\delta} = -\left.\frac{\partial P}{\partial \delta}\right|_a + \left(\frac{\partial P}{\partial a}\right)^2 \frac{1}{\dfrac{\sigma_0^2}{E} T_{mat} - \left.\dfrac{\partial J}{\partial a}\right|_\delta} \tag{24}$$

as the instability condition for any configuration. Note that, as mentioned, $\partial P/\partial \delta|_a$, $\partial P/\partial a|_\delta$, and $\partial J/\partial a|_\delta$ are calibration functions and the only additional information needed is T_{mat} which comes from other specimen tests. Thus, instability can be predicted in a given configuration with no more than calibration functions and "universal material properties" (no actual test needed). In this approach, Eqs 23 and 24 are completely analogous to the previously mentioned method used by several authors. In fact, if the J_R-curve or K_R-Δa_{eff} is available (obtained for a certain specimen geometry) the P-δ record for an untested configuration can be predicted using Eqs 3 to 9 and the instability condition obtained following Eqs 23 and 24. Alternatively, with the material resistance curve information and the calibration functions known, the crack drive force, $J = J(\delta_{tot}, a)$, can be obtained. The tangency condition can be found, and instability predicted.

It is emphasized here that all of the preceding calculation makes use of the concept that a universal geometry-independent crack growth resistance ma-

terial property can be found. In situations where the universal parameter does not exist as such, some investigators have adopted the value of T_{mat} obtained by testing bend-type specimens as a conservative lower bound estimation. Nevertheless, the apparent variability of the J-R curve due to different geometries is still an open question which needs further exploration. This subject will be addressed again in the next section.

To illustrate the foregoing, a practical example of test specimen performance will be shown. Two specimens of 2024-T351 aluminum were tested in displacement control loading: (1) a 4T CT, thickness = 12.7 mm (½ in.), $a/W = 0.5$, and (2), a CCT, total width $W = 406$ mm (16 in.), thickness = 12.7 mm (½ in.) $2a/W = 0.4$. The P-δ test record for the CCT specimen was predicted from the J_M versus Δa_p R-curve generated from the 4T compact specimen, as shown in Fig. 9.

Measuring the slope of the dropping part of the curve beyond maximum load, the compliance C_{CR} needed to cause instability was estimated to be 1.95×10^{-9} m/N (3.41×10^{-7} in./lb), which predicts that a panel length of $L = 711$ mm (28 in.) [for the same $W = 406$ mm (16 in.) and thickness, $B = 6.35$ mm (¼ in.)] will cause crack instability. Considering that the estimated effective length was $L = 686$ mm (27 in.) and that the panel went unstable, it can be concluded that the prediction is in excellent agreement with the experimental result.

Graphical R-Curve Instability Methods

The tearing instability concept could be viewed as a numerical adaptation of principles that have been applied in the older and more conventional graphical methods. Crack drive is plotted against the material R-curve. See Fig. 10 as a schematic example. The R-curve indicates the trend of material fracture toughness development as a crack drive is increased. When the level of toughness, J_R, and development rate, dJ_R/da, are the same as crack drive, J, and crack drive rate, dJ/da, crack instability will develop. This, of course, is uniquely defined by the tangency condition shown with load P_3. As was pointed out earlier, material flow property effects are an important consideration in application of this model, and this is particularly important for structural materials that develop considerable plasticity and work hardening. The options are to incorporate the material flow properties in either the crack drive calculations or in the R-curve.

At present, the common practice is to use J_R-Δa_p R-curves and calculate elastic-plastic to fully plastic crack drive solutions for J-crack drive of the various geometries. As such, the material flow properties are contained in crack drive. The calibration behavior such as that shown in Fig. 6 is used to obtain crack drive, observing the trend in J at a fixed load over variable crack size. J-crack drive for the CCT panel of 2024-T351 aluminum in Fig. 9 was calculated using the handbook [*13*] of J solutions. The material crack growth

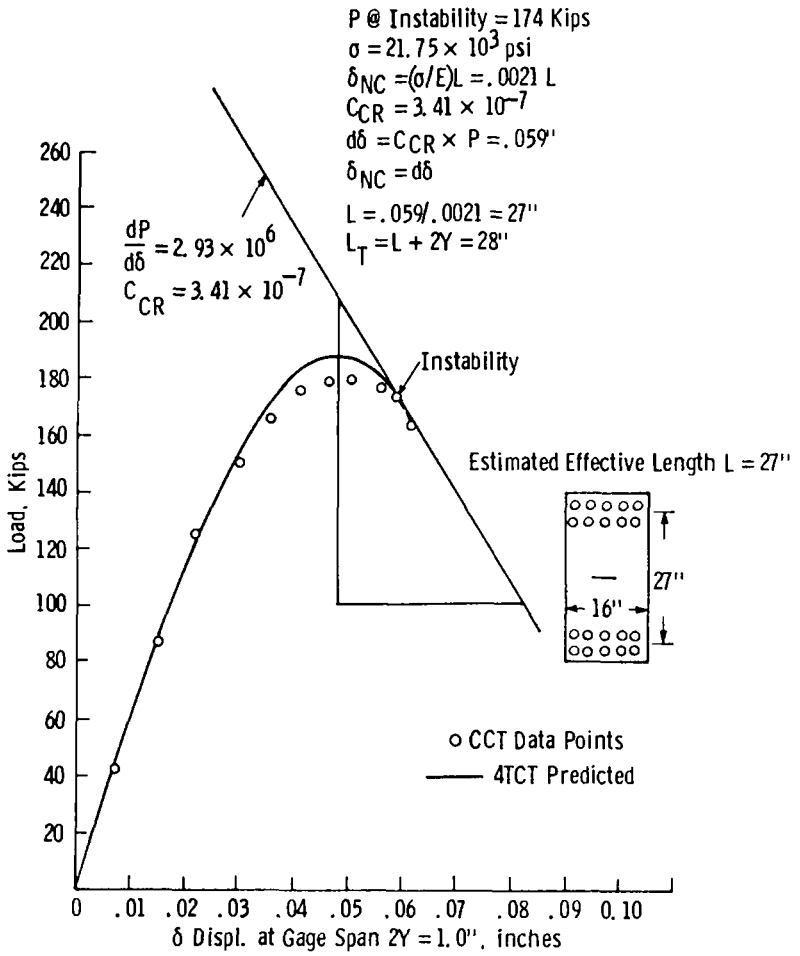

FIG. 9—*Load-displacement test record of CCT predicted from 4T CT J_R-curve. Results of* dP/dδ *slope to predict critical CCT length.*

resistance behavior was obtained from the 4T size compact specimen, as shown in Fig. 11. Here load control is implied, and instability occurs at maximum load. Therefore, we compare an experimental maximum load of 801 kN (179.9 kips) to a predicted maximum load of 779 kN (175 kips).

An alternative which is not presently widely recognized is to incorporate flow properties into the R-curve through the use of Δa_e on the abscissa as was described earlier. Since material flow properties are contained within the R-curve, crack drive can be calculated on the basis of simple linear-elastic K_I solutions. A comparison of the two alternate procedures is illustrated for the 4T CT specimen of 2024-T351 in Fig. 12. Again, the crack drive curves are for load control assumption such that instability is predicted at first attainment

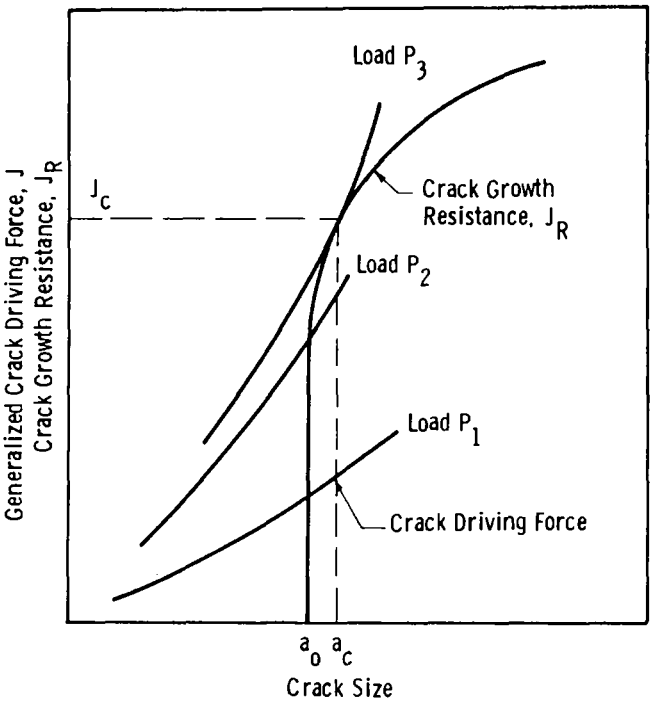

FIG. 10—*Schematic of crack driving force and crack growth resistance curves.*

of maximum load. The determinations for crack drive were made at 44.5 kN (10 kips) load. The maximum load in test was actually 45.8 kN (10.3 kips). Clearly, the instability prediction is suitably equivalent with either choice.

Finally, it will be useful to reexamine the T instability prediction example in terms of the conventional K_R-curve. Again, the R-curve is obtained from the 4T CT specimen test, but in this case effective crack growth Δa_e is plotted on the abscissa, as shown in Fig. 13. Crack drive is simply obtained from linear-elastic K_I, and because displacement controlled loading is used, specimen compliance behavior also is incorporated in crack drive. Load is set at 774 kN (174 kips), observed experimentally to be the failure load, and we predict a critical panel length for crack instability. As can be seen, the tangency condition occurs for a panel length, L = 480 mm (19 in.). Again, this result agrees well with the experimental observation.

Concluding Comment

The present study represents an attempt to review and to put into perspective several various R-curve approaches and instability concepts that have evolved over the past 20 years. In general, it is found that despite the highly varied origins of analytical developments, there is a strong coherence in the

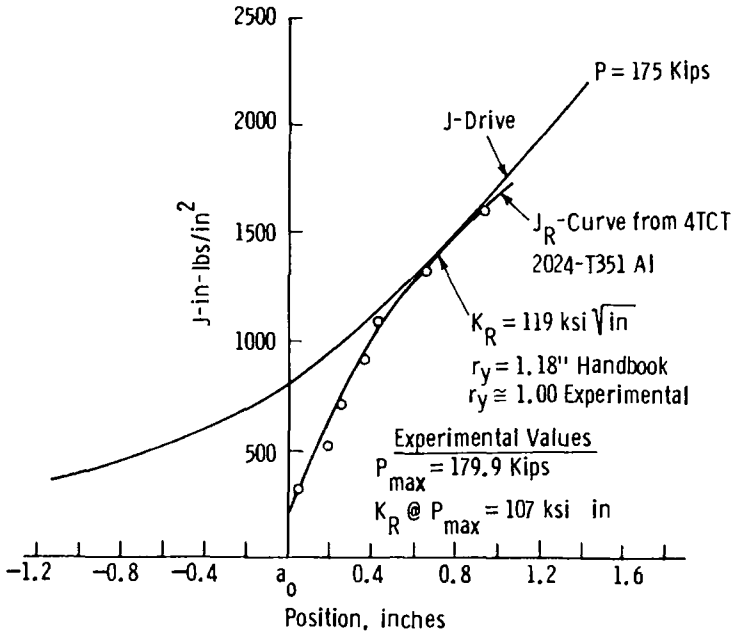

FIG. 11—*Prediction of instability under load control conditions for a 406.4-mm (16-in.)-wide CCT panel using the Shih et al [13] handbook J-values to obtain J crack drive.*

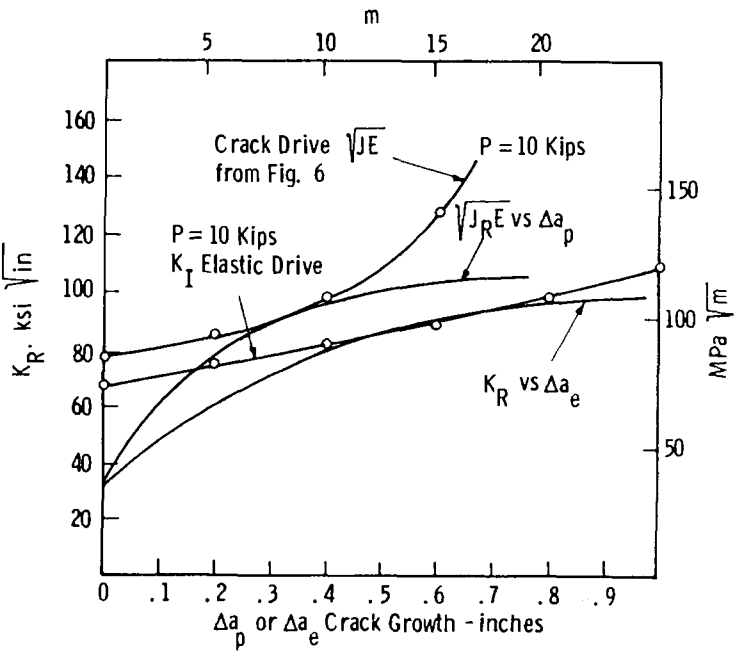

FIG. 12—*Instability prediction at 44 480 N (10 kips) load for a 4T 2024-T351 aluminum specimen. Comparison of* J_R *versus* Δa_p *methodology against* J_R *versus* Δa_e *methodology.*

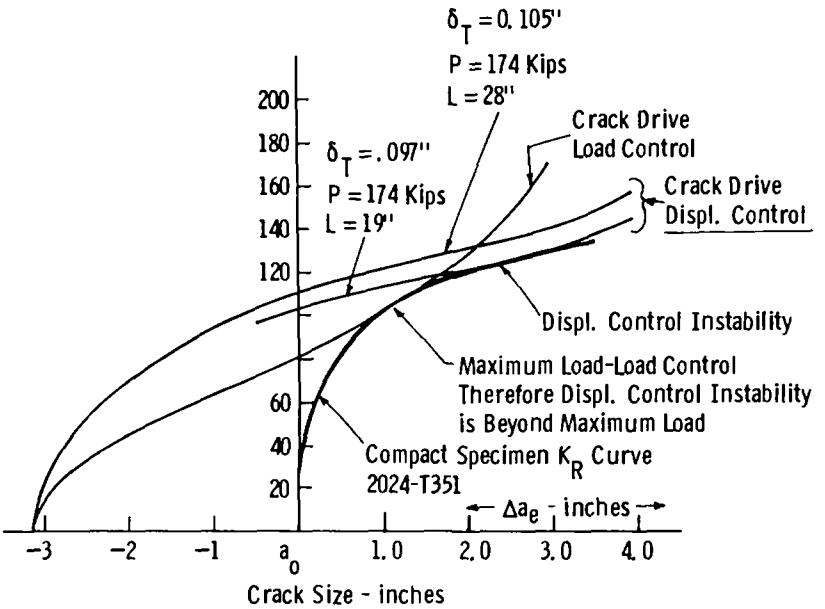

FIG. 13—*Use of* K_R-Δa_e *R-curve from the 4T CT specimen test to predict displacement-control instability for a CCT panel test. 2024-T351 aluminum, 12.7 mm (0.5 in.) thick.*

end results from the standpoint that predicted instability conditions generally agree within acceptable limits.

The *J*-calibration approximations from the work of Shih et al [*2,8,19*] appeared to predict suitable elastic-plastic *J*-crack drive relationships that can be used with J_R-Δa_p crack growth resistance curves. Alternatively, flow property effects can be incorporated into R-curves in the form of K_R versus Δa_e and linear-elastic K_I crack drive can be used to predict instability conditions.

Crack drive rate and material crack growth resistance properties also can be compared in terms of the dimensionless *T*-moduli. T_{app} represents the elastic-plastic *J*-crack drive slope and T_{mat} results from the J-Δa_p R-curve characterization. *T*-modulus was originally specialized to fixed displacement systems where system compliance was shown to exert an influence on instability occurrences. This specialization is not confining, however, in the sense that *T*, or for that matter, any of the other aforementioned approaches can be applied to either load- or displacement-controlled systems.

Generalized equations relating T_{app} to T_{mat} (again assuming displacement-controlled systems), have led to some interesting observations about the relationship between cracked body behavior and system compliance. Simply, the added compliance needed to cause component instability can be determined directly from test record slopes. In effect, material fracture toughness analysis information is not necessarily needed to demonstrate in-

stability experimentally. However, to predict instability on an untested geometry, calibration functions as well as information on material R-curve behavior are needed. From the point of view of the authors, this aspect of R-curve technology represents the major challenge, and for this, a complete understanding of constraint, geometry, and loading condition influences on material R-curve and flow property behavior is necessary.

Acknowledgments

The authors would like to express appreciation to the personnel of the Materials Testing Lab at Westinghouse Research and Development Center under the direction of R. E. Gainer, Jr., and in particular to R. C. Brown who conducted the CT and CCT panel tests.

APPENDIX

Deformation Theory J and the Growing Crack

Values of deformation theory of J, J_D, were obtained for the CT and CCT specimen geometries using the following formulas [*3-4*]. For the CT, J_D is given by

$$J_{i+1} = \left(J_i + \frac{\eta}{b}\bigg|_i A_{i,i+1}\right)\left(1 - \frac{\gamma}{b}\bigg|_i (a_{i+1_i} - a_i)\right) \tag{25}$$

where subscripts i or $i + 1$ indicate quantities evaluated at that step.

$$\eta = 2 + 0.522\, b/W$$

$$\gamma = 1 + 0.76\, b/W$$

$A_{i,i+1}$ refers to the area enclosed by the load per unit thickness versus displacement record between boundaries of constant displacement

$$\delta_i \quad \text{and} \quad \delta_{i+1}$$

In the same spirit, for the CCT, J_D is given by

$$J_D = G + J_{pl}$$

J_{pl} for CCT based on δ_{pl}

$$J_{i+1} = \left(J_i + \frac{P_i\delta_i}{b_i} + \frac{2}{b_i} A_{i,i+1}\right)\left(1 + \frac{\Delta a}{bi}\,\frac{P_i\delta_i - J_i b_i}{P_i\delta_i + J_i b_i}\right) - \frac{P_{i+1}\,\delta_{i+1}}{b_{i+1}} \tag{26}$$

where

$\Delta a = b_i - b_{i+1}$,
b = total remaining ligament ($W - 2a$),

δ = plastic component of displacement, and
J_{pl} = plastic component of J.

Modified J

The foregoing results showed how to calculate the correct J_D from a P-δ record for a CT and CCT. In this section a different concept is introduced. Rice et al [5-6] suggested that if two specimens subjected to pure bending with different initial remaining ligaments are tested, the resulting $J_D - \Delta a$ curves would be slightly different and that eventually consistent results would be obtained if instead of J_D, a far field J, J_f, were used. The slope of the $J_f - \Delta a$ being

$$\frac{dJ_f}{da} = \frac{dJ_D}{da} + \frac{J_D - G}{b} \tag{27}$$

Very recently, this concept was generalized by Ernst [7] for other configurations: the expression for this modified J, J_M being

$$J_M = J_D - \int_{a_0}^{a} \frac{\partial J_{pl}}{\partial a}\bigg|_{\delta_{pl}} da \tag{28}$$

for pure bending J_M coincides with Rice's J_f

$$\frac{\partial J_{pl}}{\partial a} = -\frac{J_{pl}}{b} \tag{29}$$

and thus

$$\frac{dJ_M}{da} = \frac{dJ_f}{da} = \frac{dJ_D}{da} + \frac{J_{pl}}{b} \tag{30}$$

but at the same time Eq 25 provides a general way of modifying J.

In this work, J_M for the CT was calculated as

$$J_M = J_D + \int_{a_0}^{a} \gamma \frac{J_{pl}}{b}\, da \tag{31}$$

with $\gamma = 1 + 0.76\, b/W$.

For the CCT, the difference between J_M and J_D is almost negligible. In fact, following Rice, Paris, and Merkle [20], for the CCT, J_{pl} is

$$J_{pl} = \frac{2}{b} \int_0^{\delta_{pl}} P\, d\delta_{pl} - \frac{p\delta_{pl}}{b} \tag{32}$$

Now if the load and displacement are connected by a pure power law $P = \alpha\, \delta^{1/n}$, then

$$\frac{\partial J_{pl}}{\partial a}\bigg|_{\delta_{pl}} = \frac{J}{bn} \tag{33}$$

which in general is a small modification to J_D. In fact in the limit of perfect plastic material ($n \to \infty$)

$$\left.\frac{\partial J_{pl}}{\partial a}\right|_{\delta_{pl}} \to 0 \tag{34}$$

and thus

$$J_M = J_D \tag{35}$$

References

[1] Heyer, R. H. and McCabe, D. E., *Engineering Fracture Mechanics*, Vol. 4, 1972, pp. 413-430.

[2] Shih, C. F. et al, "Methodology for Plastic Fracture," Fifth Quarterly Report, EPRI Contract RP601-2, Electric Power Research Institute, Palo Alto, Calif., 31 Aug. 1977.

[3] Ernst, H. A., Paris, P. C., and Landes, J. D. in *Fracture Mechanics—13th Conference, ASTM STP 743*, American Society for Testing and Materials, 1981, pp. 476-502.

[4] Ernst, H. A., "Expressions for Deformation and Modified *J*," work in progress.

[5] Rice, J. R., Drugan, W. J., and Sham, T. L., "Elastic-Plastic Analysis of Growing Cracks," Brown University Report No. 65, May 1979.

[6] Herman, L. and Rice, J. R., "Comparison of Experiment and Theory for Elastic-Plastic Plane Strain Crack Growth," Brown University Report No. 76, Feb. 1980.

[7] Ernst, H. A., "Material Resistance and Instability Beyond *J*-Controlled Crack Growth" in *Elastic-Plastic Fracture: Second Symposium—Volume I: Inelastic Crack Analysis, ASTM STP 803*, American Society for Testing and Materials, 1983.

[8] Kumar, V., German, M. D., and Shih, F. G., "Estimation Technique for the Prediction of Elastic-Plastic Fracture of Structural Components of Nuclear Systems," Combined 2nd and 3rd Semiannual EPRI Report, Electric Power Research Institute, Palo Alto, Calif., 1 June 1980.

[9] Irwin, G. R., Kies, J. A., and Smith, H. L., *ASTM Proceedings*, American Society for Testing and Materials, 1958, pp. 640-657.

[10] Rice, J. R., *Fracture*, Vol. 2, H. Libowitz, Ed., Academic Press, New York, 1968, pp. 191-311.

[11] Edmunds, T. M. and Willis, J. R., "Matched Asymptotic Expansions in Nonlinear Fracture Mechanics," *Journal of Mechanics and Physics of Solids*, Vol. 24, 1976.

[12] McCabe, D. E. and Landes, J. D. in *Elastic-Plastic Fracture, ASTM STP 668*, American Society for Testing and Materials, 1979, pp. 229-248.

[13] Kumar, V., German, M. D., and Shih, C. F., "An Engineering Approach for Elastic-Plastic Fracture Analysis," NP1931, Electric Power Research Institute, Palo Alto, Calif., July 1981.

[14] *Fracture Toughness Evaluation by R-Curve Methods, ASTM STP 527*, American Society for Testing and Materials, 1973.

[15] Paris, P. C., Tada, H., Ernst, H., and Zahoor, A. in *Elastic-Plastic Fracture, ASTM STP 668*, American Society for Testing and Materials, 1979, pp. 251-265.

[16] Paris, P. C., Tada, H., Zahoor, A., and Ernst, H. in *Elastic-Plastic Fracture, ASTM STP 668*, American Society for Testing and Materials, 1979, pp. 5-36.

[17] Hutchinson, J. W., and Paris, P. C. in *Elastic-Plastic Fracture, ASTM STP 668*, American Society for Testing and Materials, 1979, pp. 37-64.

[18] Zahoor, A., "Tearing Instability of Elastic-Plastic Crack Growth," Ph.D. thesis, Department of Mechanical Engineering, Washington University Report, Aug. 1978.

[19] Kumar, V. and Shih, C. F. in *Fracture Mechanics—12th Conference, ASTM STP 700*, American Society for Testing and Materials, 1980, pp. 406-438.

[20] Rice, J. R., Paris, P. C., and Merkle, J. G. in *Progress in Flaw Growth and Fracture Toughness, ASTM STP 536*, American Society for Testing and Materials, 1973, pp. 231-245.

Summary

Summary

The papers in this Special Technical Publication have been divided into two volumes. Volume I contains papers dealing with fracture theory and analyses. The papers in Volume II primarily describe test methods or fracture mechanics data about specific applications or materials.

Volume I has five sections: Fracture Theory, Stress-Intensity Factors, Surface Cracks, Fatigue and Stress Corrosion, and J-Integral and R-Curves.

In the section on Fracture Theory, various theoretical models are proposed in six papers for different aspects of fracture mechanics. Chona, Irwin, and Sanford describe photoelastic methods to determine the influence of specimen size and shape on the coefficients of a series representation of the stresses around the crack tip. The authors compare the multiparameter representation to a "singular" solution in an effort to quantify the "singularity-dominated zone." In the second paper, de Wit proposes a crack-opening displacement model for failure that encompasses the whole range of fracture mechanics from linear elastic fracture mechanics through elastic-plastic fracture mechanics and plastic collapse. Shukla and Fourney report on studies of the energy loss during the fracture process using photoelastic methods. In their paper, Vassilaros, Joyce, and Gudas explore the tearing instability theory of Paris and coworkers for applicability to materials having high tearing moduli. Gavigan and Queeney propose a theoretical model for the fracture resistance of particle-hardened brittle solids based on strain energy concepts. In the last paper of this section, Wnuk and Mura describe a final stretch model for predicting stable crack growth under three-dimensional elastic-plastic conditions.

The section on Stress-Intensity Factors contains six papers that give stress-intensity factor solutions for various physical conditions or structural geometries. Rossmanith and Shukla describe the use of photoelastic techniques to determine mixed-mode stress-intensity factors for both static and dynamic crack fronts interacting with elastic stress waves. Shah and Lin use finite-element analysis to calculate stress-intensity factors for partially cracked stiffeners on stiffened panels. Hsu and Kathiresan report on the calculation of stress-intensity factors for an attachment lug having an interference-fit bushing. The next two papers in this section use different analytical approaches to determine stress-intensity factors for radial cracks in pressurized thick-wall cylinders: Pu and Hussain treat the partially autofrettaged case, and Parker et al treat the fully autofrettaged case. Finally, Newman and Raju report stress-intensity factors for imbedded cracks, surface cracks, corner cracks, surface cracks at holes, and corner cracks at holes for finite bodies under three-dimensional stresses.

Four papers are included in the section on Surface Cracks. Smith and Kirby describe methods to determine stress-intensity factor distributions for deep surface cracks and the relative influence of bending stresses on deviations from the classical semielliptical shape. Lim, Dedhia, and Harris report approximate influence functions that can be used to estimate Mode I stress-intensity factors for circumferential surface cracks of arbitrary size in pipes subjected to arbitrary stresses and loadings. Jolles and Tortoriello propose a methodology for predicting the geometrical crack growth patterns for surface cracks growing under cyclic tension or cyclic bending stresses. Finally, Dedhia, Harris, and Lim use the influence functions described in their previous paper to predict the effect of nonuniform thermal stresses on fatigue crack growth of surface cracks in nuclear reactor piping.

Nine papers constitute the section on Fatigue and Stress Corrosion. Suresh, Toplosky, and Ritchie extend earlier work on a proposed new mechanism for the effect of environment on crack growth rates in steels near the crack-growth threshold. In the second paper, Yoder, Cooley, and Crooker propose a model, based on yield strength and grain size, for predicting the transition point at which the slope of the logarithmic plot of da/dN versus ΔK changes in steels. Bertel, Clerivet, and Bathias argue for the use of Elber's ΔK_{eff} to describe crack growth under complex cyclic loading. Krafft presents numerous additional case studies of fatigue crack growth using his improved micro-ligament instability model. Ingraffea, Blandford, and Liggett use a boundary element method to predict two-dimensional Mode I and mixed-mode quasi-static growth and fatigue crack growth. Glinka and Stephens present a method of fatigue life calculation based on a combination of fracture mechanics and low-cycle fatigue notch strain analysis. Kim and Manning describe a model for predicting corrosion fatigue crack growth under spectrum loading in a chemically aggressive environment.

The last two papers in this section are about stress corrosion. Brose reports on investigations of the effect of state-of-stress and surface condition on stress-corrosion crack initiation. Abou-Sayed et al compare stress-corrosion crack growth rates calculated with an elastic-plastic fracture mechanics analysis to rates calculated by superposition of linear elastic fracture mechanics conditions.

The last section of this volume contains four papers about the J-integral and R-curves. In the first paper, Ernst proposes a single solution for J that describes crack growth in a single specimen when the state-of-stress starts as pure bending, moves into combined bending and tension, and ends as pure tension. Dodds, Read, and Wellman compare experimentally measured J-integral values for specimens having large yielded zones to those determined analytically using a nonlinear finite-element method. Joyce reports on the use of load-displacement records to develop J-R curves at a load point velocity of approximately 0.25 m/s. In the last paper of Volume I, McCabe and Ernst

propose that it is possible to incorporate all material flow plasticity effects into the R-curve description for a given material.

J. C. Lewis

Space and Technology Group, TRW, Redondo Beach, Calif. 90278; symposium co-chairman and co-editor.

George Sines

School of Engineering and Applied Science, University of California at Los Angeles, Los Angeles, Calif. 90024; symposium co-chairman and co-editor.

Index

This Index combines entries for both volumes of STP 791. "I" denotes entries for Volume I, and "II" denotes entries for Volume II.

R

S